Application of Optical Fibre Sensors

for Structural Health and Usage Monitoring

Daniel C. Betz

A thesis submitted for the Degree of Doctor of Philosophy

June 2004

Dynamics Research Group

Mechanical Engineering Department

University of Sheffield

Abstract

Structural Health and Usage Monitoring has gained considerable interest throughout the engineering technologies. Especially for the aircraft industry, where damage can lead to catastrophic and expensive failures, and the vehicles involved undergo regular cost intensive inspections, a Health and Usage Monitoring System (HUMS) has one of the highest payoffs. Furthermore, HUMS allow new design principles for the realisation of lightweight aircraft structures. Different approaches towards a HUMS can be found in the literature. A system based on load monitoring and damage detection could provide highest potential for implementation in future aircrafts.

This thesis investigates the use of multifunctional fibre Bragg grating (FBG) sensors for structural health and usage monitoring. It is shown, how FBG sensors can be used simultaneously for both, a strain sensing based load monitoring system and a Lamb wave based damage detection system. Several fundamental areas are addressed analytically and experimentally.

This work adds new approaches towards the implementation of large area FBG sensor networks using fibre optical rosettes and temperature compensated strain sensors. A miniaturised build-up technique for a FBG temperature sensor is demonstrated which allows multiplexing of several strain and temperature sensors within a single fibre network. The use of a backing patch for FBG sensors is studied numerically and experimentally.

In this thesis, surface mounted and structural integrated FBG sensors are used to detect Lamb waves. The theoretical approach that leads to the development of an appropriate ultrasonic interrogation system for FBG sensors is introduced. Numerical simulations on the influence of the grating dimensions on its ability to detect ultrasonic strain fields and their experimental validation are presented.

Three different tasks of damage identification based on Lamb waves are considered: detection of damage, localisation of damage and severity of damage. Experimental results on all three tasks show that FBG sensors can compete with existing technologies. As part of the experimental work, a reliable, temperature independent damage index is introduced and a novel detection scheme using fibre grating rosettes and Genetic Algorithms for the localisation of damage is developed. The results of a simple fatigue test experiment on which the same FBG sensors were used to measure the load parameters and the crack size agree very well with the results using standard technologies.

Acknowledgements

I would like to sincerely thank my supervisor Dr. Wieslaw Staszewski from Sheffield University for his guidance and support throughout my research. I have very much enjoyed working with him. He always made me feel at home, when I stayed over at Sheffield.

I also thank my co-supervisor Prof. Brian Culshaw from Strathclyde University, who provided so much advice and resources necessary for me to accomplish my goals.

Thanks go to Dr. Eberhard Zeeb from the DaimlerChrysler Research Laboratories in Ulm, who enabled and supported my work on fibre optic sensors at the Optoelectronic Department REM/CO.

Welcome support in various forms has been provided by the members of the Structural Health Monitoring and Dynamics Research Group at Sheffield University. They are Prof. Christian Boller, who was one of the initiators of the PhD project, when he still worked for EADS Military Aircraft and who added much contribution to the work; Boon Chuan Lee, who gave me all the practical assistance inside and outside the University; Dr. Graeme Manson and Dr. Gareth Pierce who gave assistance and revisions of various publications.

The people from the Optoelectronics Department at Strathclyde University provided valuable assistance for the project. These are Dr. Graham Thursby, who contributed so much for the experimental work on fibre optics, Borja Sorazu, not only for the technical matters related to the thesis, but also for his friendship, and Dr. Fengzhong Dong for all his practical assistance.

I would like to thank my colleagues from the Optoelectronic Department REM/CO at DaimlerChysler, especially the colleagues from the fibre Bragg grating project: Lothar Staudigel and Marcel Krieg who always assisted me in the Laboratory, my former colleagues Dr. Michael Trutzel and Dr. Pascale Müller, and all the students who contributed with their work to the overall task of this thesis: Thiemo Kastel, Sigmar Siedler and Thorsten Baier.

I would also like to acknowledge: Dr. Michael Kehlenbach from EADS Germany, for his cooperation in the field of fibre optic sensing and Lamb wave analysis; Christoph Chojetzki and Manfred Rothhardt from IPHT Jena, for supplying the Bragg grating sensors and for useful discussion on the subject; York Roth from IVW Kaiserslautern for implementation of the FE model, Andreas Schäufele from DaimlerChrysler AG Ulm for assistance with the fatigue test machine.

The acknowledgements would be incomplete without personal thanks to my family – Katharina and Helena – for their love and patience over the last few years.

Contents

Abbreviations

A/D	Analogue/Digital
CCD	Charge Coupled Device
CFRP	Carbon Fibre Reinforced Plastic
CM	Conventional Monitoring
CWT	Continuous Wavelet Transform
DFT	Discrete Fourier Transform
ECL	External Cavity Laser
ESG	Electrical Strain Gauge
FBG	Fibre Optic Bragg Grating
FBGS	Fibre Optic Bragg Grating Sensor
FFA	Federal Aviation Authority
FFT	Fast Fourier Transform
FRP	Fibre Reinforced Plastic
FWHM	Full Width Half Maximum
GFRP	Glass Fibre Reinforced Plastic
GPIB	General Purpose Interface Bus
HBM	Hottinger Baldwin Messtechnik
HUMS	Health and Usage Monitoring Systems
IPHT	Institut für Physikalische Hochtechnologie Jena e.V.
IVW	Institut für Verbund Werkstoffe Kaiserslautern
LED	Light-Emitting Diode
NDE	Non-Destructive Evaluation
NDT	Non-Destructive Testing
OPD	Optical Phase Difference
ORMOCER®	Organically Modified Ceramics
OTDR	Optical Time Domain Reflectometry
Prepreg	Preimpregnated
PZT	Lead Zirconate Titanate (Piezoceramic)
RIN	Relative Intensity Noise
RMS	Root Mean Square
RMSE	Root Mean Square Error
SDM	Spatial Division Multiplex
SHM	Structural Health Monitoring
SLD	Superluminescent Diode
SNR	Signal-to-Noise Ratio

SOP	State Of Polarisation
TDM	Time Division Multiplex
TOF	Time-Of-Flight
UV	Ultraviolet
VCSEL	Vertical Cavity Surface Emitting Laser
WDM	Wavelength Division Multiplex

Nomenclature

A	Amplitude
a	Dilation or scale parameter
a	Crack length
$A;B;C;D$	Arbitrary constants
A_{em}	Amplitude of the electrical part of the electromagnetic field
$a_{i,j}$	Arbitrary fit constants
A_m	Arithmetic mean
B	Crack's strength preservation factor
b	Translation parameter
c_g	Group velocity
c_L	Longitudinal wave velocity
c_P	Phase velocity
c_T	Transversal wave velocity
d	Distance or thickness
d_{clad}	Diameter of fibre cladding
d_{coat}	Diameter of fibre coating
d_{core}	Diameter of fibre core
D_i	Dielectric displacement
d_{kij}	Piezoelectric constants
dn/dT	Coefficient of the thermo-optic effect
E	Youngs modulus
E_d	Demarcation energy
E_{em}	Vector of the electrical part of the electromagnetic field
E_k	Electric Field
E_l	Energy level
E_{PA}	Error as a proportion of plate area
$\mathcal{F}$	Cumulative fracture probability
f	Frequency
$\mathcal{F}$	Fourier transform of a function
f	Fitness function
G	Modulus of rigidity or modulus of elasticity in shear
G_m	Geometric mean
$\mathcal{H}$	Hilbert transform of a function
H	Safe operational life
I	$\sqrt{-1}$

i,j,k,l,m,n	Indices
k	Gauge factor (strain sensitivity)
K	Stress intensity factor
k_B	Boltzmann constant
k_{em}	Wave number of the electromagnetic wave
K_r	Kurtosis
k_{us}	Wave number of the ultrasonic wave
L	Length of the Bragg grating
m_d	Scaling parameter for the width of a Weibull plot
Med	Median
n	Corrosion susceptibility factor
n_0	Refractive index of the unstrained fibre
n_{clad}	Refractive index of fibre cladding
n_{coat}	Refractive index of fibre coating
n_{core}	Refractive index of fibre core
n_{eff}	Effective refractive core index
$\overline{n}_{eff}$	Mean effective refractive index
p	Dielectric constant (permittivity)
P	Optical Power
p_{11},p_{12}	Pockel's components of the strain optic tensor
p^{eff}	Effective strain-optic constant
P_F	Failure probability
R	Reflection
R_{el}	Electrical resistance
R_{max}	Maximum grating reflectivity
$S(t)$	Fibre strength
S_i	Fibre initial strength
s_{ijkl}	Compliance tensor
T	Temperature
t	Time
$t_{fcyclic}$	Lifetime under cyclic loading
$t_{fstatic}$	Lifetime under pure static loading
T_P	Period of a sinusoidal modulated function
U	Voltage
u,w	Longitudinal and Transverse component of displacement
W	Wavelet transform
x,y,z	Variables e.g. to define a rectangular coordinate system
x_{max}	Maximum value

x_{min}	Minimum value
x_{RMS}	RMS value
Y	Geometrical Factor
ΔT	Temperature change
Γ	Confinement factor
Λ	Grating period
Ψ	Wavelet function
α	Coefficient of thermal expansion
α^s	Thermal expansion coefficient of the structure
α,β	Arbitrary angles
χ_{AC}	AC coupling coefficient in coupled mode theory
δ	Detuning factor
ε	Strain
$\varepsilon_{1,2}$	Principal strains
ε_i	Principal components of the strain tensor
ε_{ij}	Strain tensor
$\varepsilon_x, \varepsilon_y, \varepsilon_z$	Strain components along the x,y,z - axes
ε_z^m	Mechanically induced strain along fibre axis
$\phi(t)$	Phase of the electrical part of the electromagnetic field
γ_{max}	Maximum shear strain in the x-y plane
γ_{xy}	Shear stress in xy direction
η	Normalised integrated coupling constant
κ	Amplitude modulation for a cyclic loading
λ	Wavelength.
λ_B	Bragg wavelength
λ_D	Design wavelength for an infinitesimally weak index of refraction change grating
λ_{in}	Arbitrary wavelength of light coupled into a fibre
λ_{US}	Ultrasonic Wavelength
λ,μ	Lamé constants
ν	Poisson's ratio
ν_0	Fit parameter in the electron release rate equation
ν_{rel}	Release rate
ρ	Densitiy
ρ_{sp}	Specific resistance
σ	Standard deviation
$\sigma(t)$	Applied stress

σ_0	Scaling parameter for the mean of a Weibull plot
$\sigma_{1,2}$	Principal stress
σ_d	Fracture stress
σ_{DC}	DC coupling coefficient in coupled mode theory
σ_{kl}	Stress tensor
$\sigma_{x,y,z}$	Stress along the x,y,z-axes
τ_{xy}	Shear strain in xy direction
ω	Angular frequency

1 INTRODUCTION

1.1 STRUCTURAL HEALTH AND USAGE MONITORING

Structural health and usage monitoring has become a respected and established discipline in engineering. Health and Usage Monitoring Systems (HUMS) deal with the development of autonomous systems for continuous monitoring, inspection, and damage detection of structures with minimum labour involvement. The ultimate goal of Structural Health Monitoring (SHM) is to increase reliability, improve safety, enable light weight design and reduce maintenance costs for all kind of structures. An overview of the subject can be found in [1-3]. A selection of conference papers on the subject is given in [4-7].

1.1.1 TERMINOLOGY

Health and Usage Monitoring is a highly interdisciplinary field of work. This does not only include the different fields of engineering this can be applied to, covering the whole area of civil

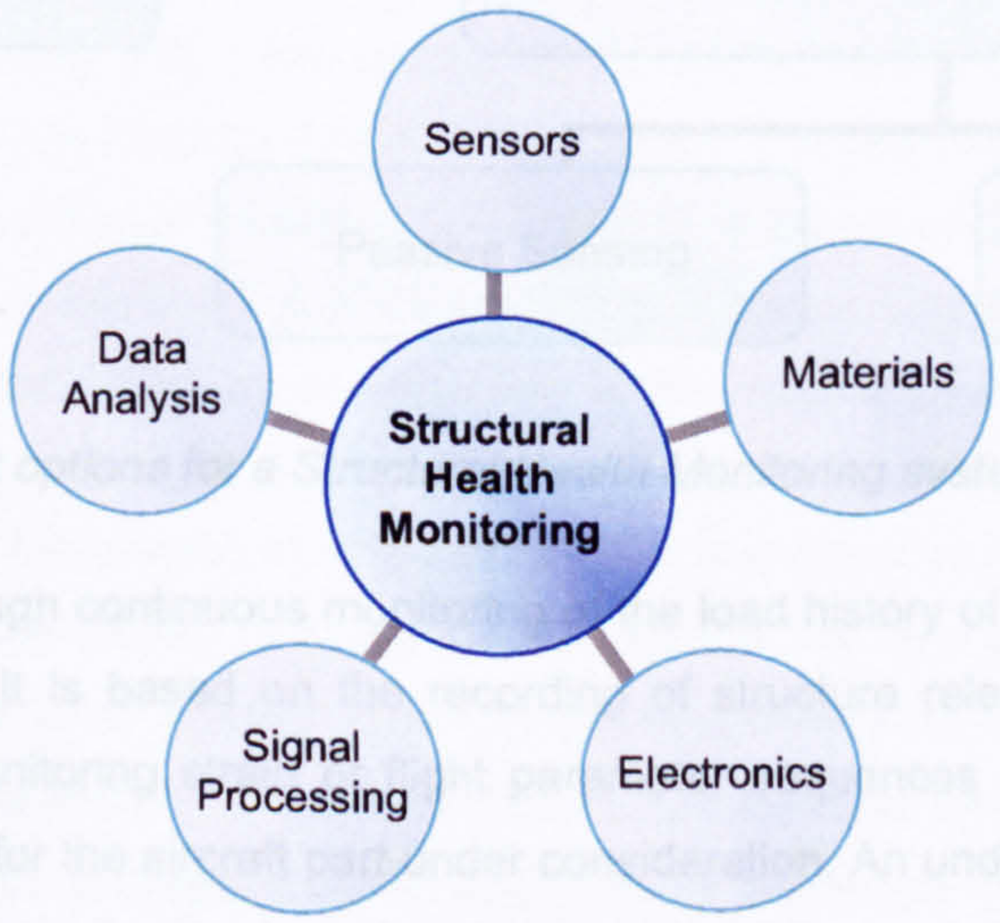

Figure 1.1: Disciplines involved in Structural Health Monitoring.

engineering, power systems, aeronautics, automotive and possibly many more, but also the variety of disciplines being involved, depending on the field of SHM which is focussed on.

Among the disciplines that are involved in SHM are sensors, electronics, materials, signal processing, and data analysis as illustrated in Figure 1.1. Many of the advances in all of these disciplines can contribute to the progress in SHM. The work presented here focuses on the development of novel sensors and advancement in the analysis of their data with a special emphasis on aeronautic applications.

It is generally acknowledged that two complementary approaches can be followed to attain the objectives of Health and Usage Monitoring [8-12]. The first approach is the implementation of an integrated system that provides damage predictive capabilities, e.g. by continuously monitoring the usage of the structure. The second approach requires the ability to detect unpredicted damage. SHM is the process of damage identification (detection, location, classification and severity of damage) and prognosis. Identification of damage falls into two camps, either damage can be detected as it occurs (passive sensing), or it can be accessed through periodical interrogations of the structure (active sensing). The different approaches towards an SHM system are depicted in Figure 1.2.

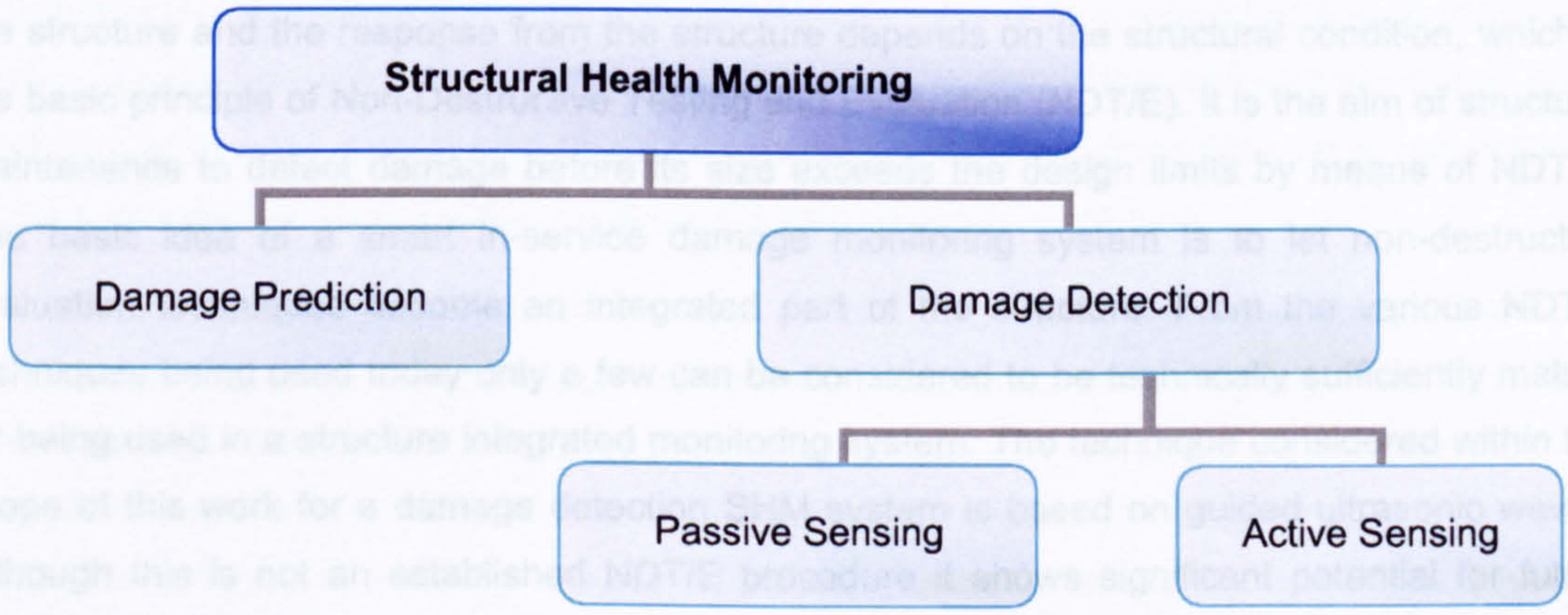

Figure 1.2: Different options for a Structural Health Monitoring system.

Damage prediction through continuous monitoring of the load history of a structure can be used for damage prediction. It is based on the recording of structure relevant parameters and is performed by either monitoring strain or flight parameter sequences which are then used to derive a load sequence for the aircraft part under consideration. An understanding of the fatigue properties of the structure is required for interpretation of the data in terms of life time consumption and maximum permitted loads. From these data, the occurrence of overloads may be identified and a resulting catastrophic damage to the structure avoided, by warning the

operator of any exceedances in time. From the actual load spectrum recorded the fatigue life of the structure can be assessed in more detail than from an estimated load spectrum. However, the predicted fatigue life still depends on a variety of assumptions. The algorithms describing the load transfer information from the sensor signals and for the prediction of the remaining fatigue life are therefore part of a load monitoring system.

In contrast to the damage prediction methods, the goal of damage detection system is either to detect damage as it occurs or to detect damage at regular inspection intervals. The detection of damage as it stands today is mainly related to the sensing of impacts with composites and monitoring of crack growth in metallic structures. It is the aim of a damage detection system to determine if damage has occurred and where it is located. Impact detection or Acoustic Emission are passive sensing techniques as only sensors can measure these events. Sensor measurements are constantly taken in real time while the structure is in service. The energy of the impact event or the acoustic emission is enough to trigger the sensors and to record the impact signature. In order not to miss damage that occurs during maintenance, direct analysis of such signatures requires the sensors to be permanently active, even when the structure is out of use since dropping of a tool may even cause damage when the structure is out of operation. By contrast, active sensing systems only need to be activated on demand at regular or event driven inspection intervals. External mechanical or non-mechanical loads are implied to the structure and the response from the structure depends on the structural condition, which is the basic principle of Non-Destructive Testing and Evaluation (NDT/E). It is the aim of structural maintenance to detect damage before its size exceeds the design limits by means of NDT/E. The basic idea of a smart in-service damage monitoring system is to let non-destructive evaluation techniques become an integrated part of the structure. From the various NDT/E techniques being used today only a few can be considered to be technically sufficiently mature for being used in a structure integrated monitoring system. The technique considered within the scope of this work for a damage detection SHM system is based on guided ultrasonic waves. Although this is not an established NDT/E procedure it shows significant potential for future health monitoring systems. Lamb wave inspection is the most widely used damage detection technique based on guided ultrasonic waves [13]. The technique is based on Lamb waves propagating in plate-like structures [14, 15]. Lamb wave inspection requires two probes, one of which is used to introduce ultrasonic stress waves into the structure and the other to pick up these stress waves at another position. The use of Lamb waves for ultrasonic inspection has become very attractive especially for large structures. Lamb waves can be excited at one point of a structure and can be propagated over considerable distances. Hence, a relatively large area of the structure can be interrogated between actuator and sensor. The Lamb wave method involves the analysis of the transmitted and/or reflected wave. The presence of damage is

identified when the detected ultrasonic signal deviates from the reference signal of the undamaged structure, see Figure 1.3.

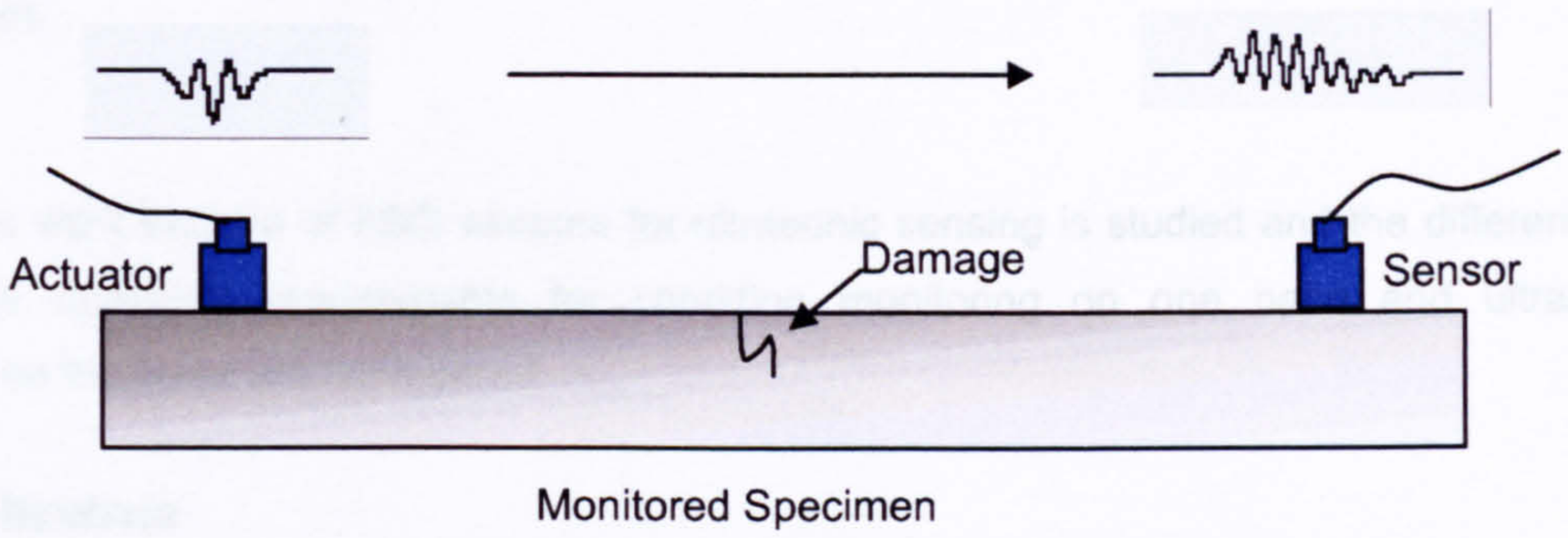

Figure 1.3: Structural damage detection based on Lamb waves.

It is obvious that a complementary use of damage prediction and damage detection offers increased reliability and accuracy. Each approach could profit from the additional information gained from the other method. For example the result of the predicted fatigue life gained from continuous loads monitoring can vary compared to the real fatigue life. Therefore, damage identification can help to identify whether a possible overload has caused damage to the structure or not. On the other hand, damage inspection could be triggered by a load monitoring system. Today inspection intervals are based on flight hours, independent of flight conditions. From the information gained from loads monitoring resulting in fatigue damage accumulated or impacts occurred, an event driven inspection schedule could be derived.

The present research project focuses on the development of a Health and Usage Monitoring System that is capable of monitoring both operational loads as well as damage. The basic idea is to use only one multifunctional sensor which is sensitive to strain as a meaure of the operational loads and ultrasound as a measure of Lamb waves. The main advantage of such a system is obvious: a dramatic reduction of costs related to sensor installation and sensor interrogation compared to a system that uses different sensors for each measurement. Not only will the overall number of sensors required be reduced, but also only one interrogation unit will be necessary to obtain the relevant data. In addition, the combination of information from both systems can increase the overall reliability of the damage prognosis by an appropriate data fusion algorithm. Therefore, a single sensor that is capable of sensing the relevant data for the loads and the damage monitoring system may be advantageous. It is obvious that such a multifunctional sensor has to fulfil the highest demands on reliability, accuracy and lifetime. The failure of a single sensor would bring with it the loss of data for a number of systems, which in the worst case could mean the breakdown of the whole SHM system. Within this thesis the fibre optic Bragg grating (FBG) is proposed as the sensor with the highest potential to meet all the

necessary requirements. This type of sensor has been shown to exhibit excellent performance as a strain sensor and has become known as the fibre optic analogue of the electrical resistance strain gauge [16-18]. This makes the sensor ideally suited for condition monitoring deployment.

Within this work the use of FBG sensors for ultrasonic sensing is studied and the different and sometimes opposing requirements for condition monitoring on one hand and ultrasonic detection on the other are considered.

1.1.2 Benefits

The major benefits of a SHM system for aeronautic and possibly many other applications can be divided into design and maintenance benefits [11, 19-21]. SHM systems may lead to significant weight reductions as advanced damage tolerant design criteria for the structure can be implemented or to reduced maintenance costs due to real-time monitoring and reporting, minimum human involvement, and automation of inspection.

In aeronautics two major different philosophies for structural design co-exist. *Safe-life* is designed to achieve the required life time without any visible crack initiating. After its defined life has expired the structure is taken out of service, irrespective of whether a crack has been identified or not. To guarantee the *safe life* in any case, often a large margin of safety is acknowledged during the design of the structure. However, this may contradict to the requirements of economy or performance. On the other hand the *fail-safe* or *damage-tolerant* concept allows cracks in a structure, provided there is enough remaining undamaged structure that could takeover the loads once carried by the now damaged part. This concept inherently requires an inspection scheme to monitor the crack propagation. Should the crack reach a critical dimension which has to be detected during inspection and appropriate measures, repair or replacement have to take place. Today most parts of civil aircraft are designed according to the *damage tolerant* concept, which allows lighter weight of the structure.

The inspection scheme that is required for the *damage-tolerant* concept can be significantly influenced by a SHM system. Inspection in this context means the work related to structural inspections carried out when the aircraft is grounded at regular intervals. One of the major parameters determining the inspection interval is the operational stress in the structure. Figure 1.4 shows the inspection interval as a function of the operational stress for a structural element in case of conventional monitoring (CM) and for a structure equipped with an SHM system. For a certain stress level $\sigma_{structure}$ different inspection intervals are required for a SHM and a CM structure. Due to the permanent monitoring of an SHM system and the permanent knowledge of

structural conditions, the inspection interval for which the aircraft has to be grounded can be significantly increased, which as a consequence cuts down the maintenance costs.

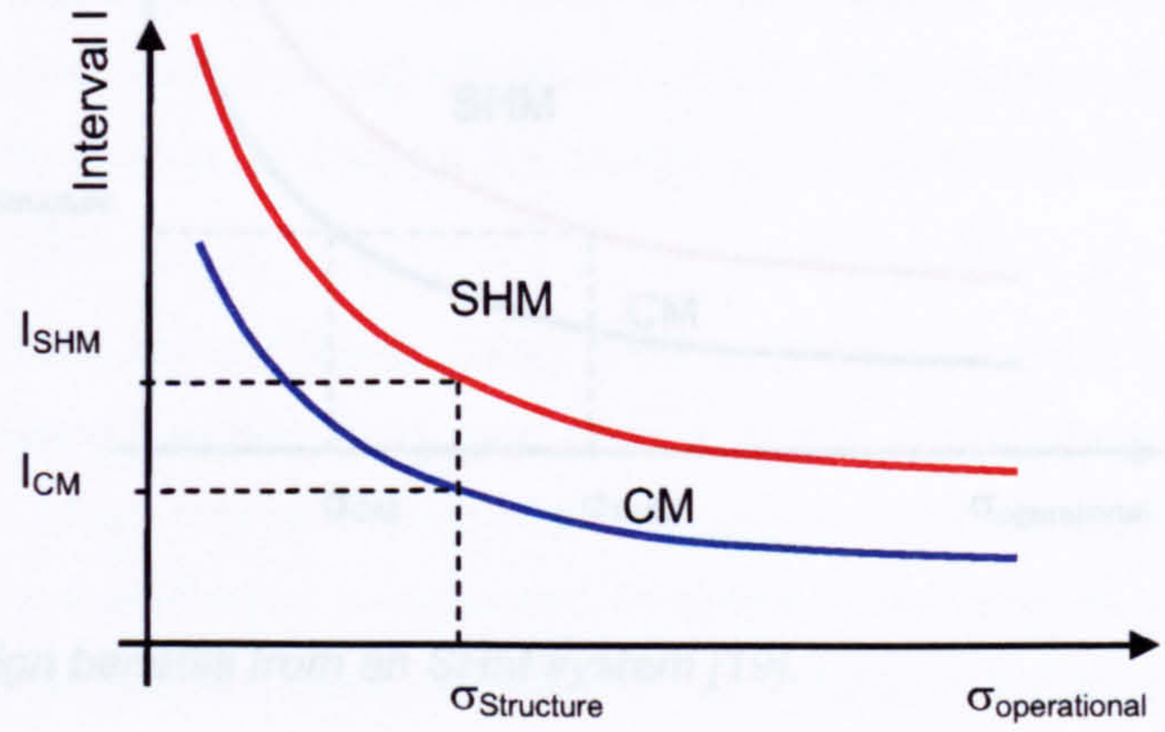

Figure 1.4: Maintenance benefits from an SHM system [19].

In addition to the increased inspection intervals, an SHM system can contribute to reducing the labour work necessary for inspection, therefore reducing the ground time and minimising human error, due to automated and autonomous systems being deployed. Furthermore, an integrated SHM system, with sensors permanently installed on the components of interest, reduces the efforts related to dismantling the structure for inspection, again reducing maintenance time and costs. However, it is seen that the new inspection intervals have to be fitted into the scheduled maintenance program which is still required and depends mainly on the requirements for corrosion inspections and systems. In addition, if anomalies are detected by the SHM system, traditional NDT/E methods for detailed inspection to verify the damage at locations predicted by the SHM system, can be applied. Ground based NDT/E methods usually have more power for the identification of damage.

In the case of regular inspection intervals the aircraft operator can profit from the design benefits. This is illustrated in Figure 1.5. A constant inspection interval suitable for the operator is assumed. It can be seen that the allowed operational stresses for SHM structures are significantly increased compared to CM structures. Increased allowable operational stresses can lead to a reduction of the structural weight in all aircrafts which are designed according to the *damage-tolerant* principle. This is because an increase in allowable stresses at constant loads is achieved through reduction of structural cross-sections and thus leading to a reduction in weight. The overall cost saving for the aircraft is significantly higher than only due to the weight saving in the monitored areas. For example lighter structures could also lead to considerable reductions of production costs as less material is needed, which would improve the efficiency of both, the manufacturers and the operators.

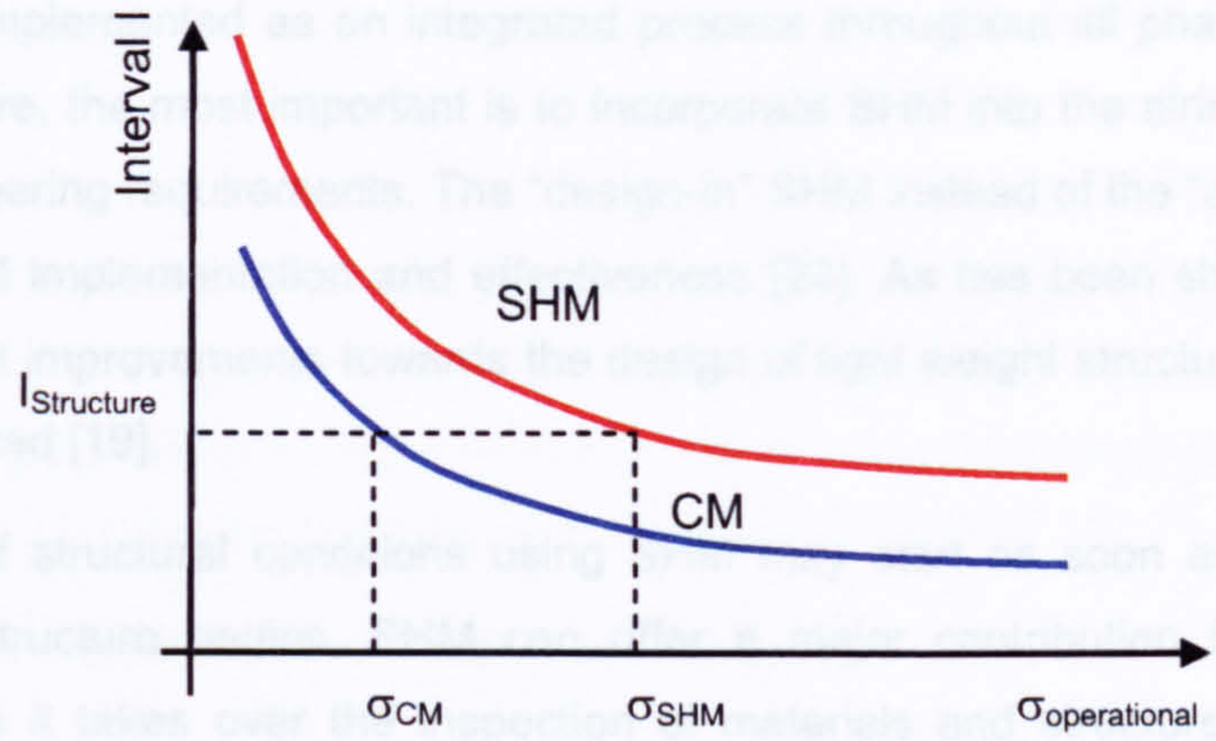

Figure 1.5: Design benefits from an SHM system [19].

1.2 Fibre Bragg Gratings for Structural Monitoring

The sensor that is considered within the scope of this work for implementation of an SHM system is the fibre Bragg grating sensor (FBGS) [16-18]. FBGS are very attractive for SHM systems as they provide excellent potential for multiplexing and multifunctional sensing networks to obtain simultaneously data on stress/strain, temperature, pressure or ultrasonic waves. Therefore, FBGS could help to implement an integrated SHM system which is applicable to all phases of the entire life cycle. In addition to the applications mentioned before in section 1 which are related to the in-service phase, the sensors could also be used during the manufacturing phase, qualification phase and for recovery of the structure [22, 23]. This new life cycle monitoring strategy is based on a feedback loop through the entire life cycle of the structure, where SHM provides the necessary additional knowledge about specific design performances, material quality, structural condition and reusability diagnosis respectively. The respective process is illustrated schematically in Figure 1.6.

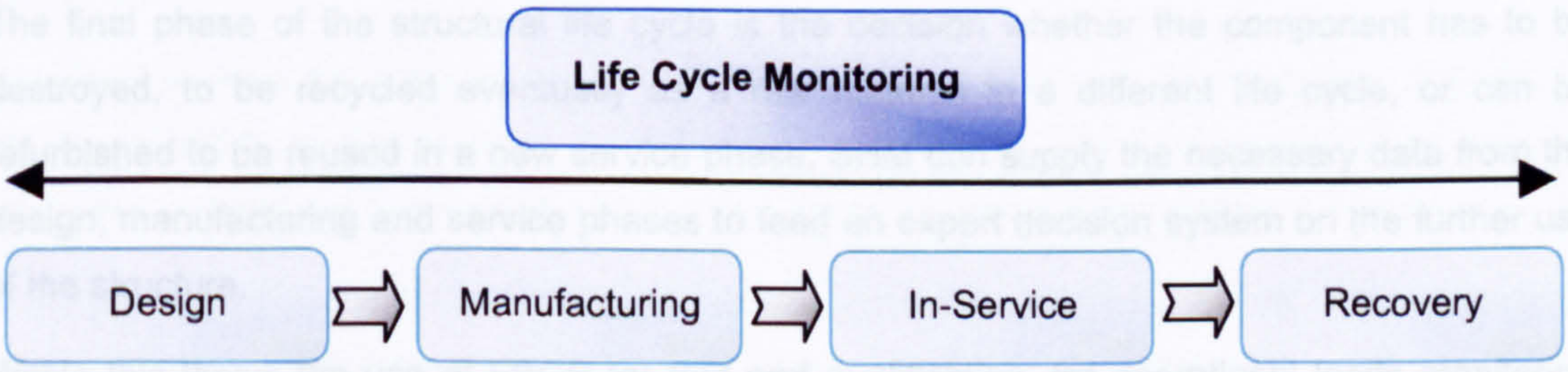

Figure 1.6: Integrated SHM strategy for life cycle monitoring of structures.

SHM should be implemented as an integrated process throughout all phases of the structural life cycle. Therefore, the most important is to incorporate SHM into the airframe design through the system engineering requirements. The "design-in" SHM instead of the "add-on" SHM system is the key to SHM implementation and effectiveness [23]. As has been shown in the previous section, significant improvements towards the design of light weight structures can be achieved if SHM is considered [19].

The monitoring of structural conditions using SHM may start as soon as the manufacturing process of the structure begins. SHM can offer a major contribution to quality control of manufacturing, as it takes over the inspection of materials and structures for manufacturing defects. Especially for manufacturing composite materials, a real-time sensing technique based on FBGS can help to monitor and control the resin flow and curing process and as a consequence guarantee a constant and assessed quality [23-29]. At the final stage of the manufacturing stage, testing and qualification of the structure takes place. For both ground and flight testing major benefits can be expected when FBGS instead of conventional electrical strain gauges are deployed [30-32].

Clearly, the major contribution of SHM relates to the monitoring of the structural conditions and the identification of damage during the in-service phase. The advantages of such an approach have been discussed in Section 1. FBGS have been shown to be capable for monitoring the loads during in-flight service on-line [33-35]. A damage detection scheme using FBGS has been suggested that makes use of local changes in the strain field due to the presence of damage [36-38]. However, this approach will only work, if the sensors are located close to the possible failure, for example for bonded repairs [39, 40]. Another approach towards damage detection uses the changes in the spectral properties of the FBGS due to a non-uniform strain field, that indicates the presence of damage [41-43]. Again this is a very localised method and not suitable for monitoring large areas. A new approach is followed within the scope of this thesis, using FBGS for sensing ultrasonic Lamb waves and identifying damage by evaluation of the Lamb wave signals.

The final phase of the structural life cycle is the decision whether the component has to be destroyed, to be recycled eventually as a raw material in a different life cycle, or can be refurbished to be reused in a new service phase. SHM can supply the necessary data from the design, manufacturing and service phases to feed an expert decision system on the further use of the structure.

Within this thesis the use of FBGS for test and qualification, for operational loads monitoring and for Lamb wave based damage detection will be discussed.

1.3 OBJECTIVES

The overall goal of this thesis is to investigate the use of fibre Bragg grating sensors (FBGS) for a structural Health and Usage Monitoring System, where FBGS can be used simultaneously for both, strain sensing (load monitoring) and a Lamb wave sensing (damage detection). In order to achieve that goal a number of objectives have been set. These are:

- to review the state-of-the-art in Structural Health and Usage Monitoring;
- to design a FBG sensor arrangement for a multiplexed strain and temperature network;
- to investigate the use of backing patches for FBG sensors using numerical methods;
- to confirm the numerical results experimentally;
- to develop a FBG sensor capable to sense strain and ultrasound (Lamb waves);
- to model the interaction between the FBG sensor and the ultrasonic strain field;
- to validate the model by appropriate experimental work;
- to test the FBG ultrasonic sensor under various conditions and for various structures;
- to apply the ultrasonic sensor for damage detection and location;
- to use recent developments in signal processing for damage identification;
- to validate the load and damage based methodology using a fully controlled fatigue test.

1.4 SCOPE OF THE WORK

The order of the chapters approximately follows the chronological order in which the work was carried out.

Chapter 2 reviews the basic principles of fibre Bragg grating sensors, where special attention is on the reliability of the sensors for industrial applications. The advantages of draw-tower fabricated sensors are highlighted, and the importance of appropriate coating is discussed.

In chapter 3 the focus is on the Bragg grating as a sensor for structural strains. The necessity of advanced strain measurement methods for structural engineering, particularly in the aerospace industry, is discussed. The advantages of Bragg gratings compared to other conventional methods such as electrical strain gauges are emphasised. The chapter presents a novel, technique to build-up strain-isolated FBGS for accurate temperature measurements. These

temperature sensors could be used for temperature compensation of other FBG strain sensors. The unique advantages of the technique presented are the small size and the multiplexing capabilities. This allows the formation of sensor networks with temperature compensated Bragg grating rosettes. One issue of particular interest when using Bragg grating rosettes is the use of a backing material to prearrange the sensors and to simplify the installation. A finite element model is used to study the influence of the backing material on the sensor function. The chapter also presents results of experimental work that validate the results from the FE modelling.

In Chapter 4 an overview of current NDT/E technologies is given and their potential for future HUM systems is discussed. The basic principles of Lamb waves are reviewed and conventional techniques for Lamb wave sensing are presented. Special focus is on the use of optical techniques for the generation and detection of ultrasound

Chapter 5 describes the analytical and experimental work carried out to develop a FBG ultrasonic sensor system, which is capable of detecting ultrasonic Lamb waves for the identification of damage. In addition to the established technologies, the use of FBGS for receiving Lamb waves is suggested. The sensor function is derived and an appropriate interrogation system is described. The chapter goes on to present the results of initial tests on the detection of Lamb waves. A numerical simulation of the sensor function follows, which reveals the influence of the grating length on the sensor function for different acoustical wavelengths. The chapter closes with the experimental results on Lamb wave detection in a composite plate using structural embedded FBGS. It is the first time, surface mounted and structural integrated FBGS have been used to detect Lamb waves.

In order to use FBGS for damage identification, the relevant signal processing tools for the analysis of the Lamb wave signals are presented in Chapter 6. The chapter discusses various aspects of signal processing, such as signal conditioning and feature extraction. The latter becomes important when the information from the Lamb wave signals has to be translated into a diagnosis of location and severity of damage. The basic concepts of Genetic Algorithms are reviewed, as they play an important role in the location of damage as presented in chapter 6.

Chapter 7 presents the results of the damage identification experiments. This chapter starts with a description of the experimental set-up. The different aspects of damage identification - detection of damage, localisation of damage, and severity of damage – are addressed in the corresponding sections. For the localisation of damage a novel method that uses a Genetic Algorithm to analyse the response of two fibre Bragg grating rosettes is presented. A method to predict the severity of damage independently of the temperature of the structure is developed in the final section. The experimental results are also discussed there.

In Chapter 8 the layout of a demonstrator is described, on which the dual use of FBGS for load monitoring and damage detection is shown. The idea is to conduct a fatigue test, where the

FBGS are used to obtain the load parameters and the crack length. Based on this knowledge a prediction of the remaining lifetime of the structure is possible. The chapter begins with an introduction to the fatigue of materials, in order to provide the necessary terminology. Next, the experimental set-up is described. The results of two fatigue tests are presented, and the performance of FBGS and conventional sensors are compared.

Finally in Chapter 9, the main conclusion from chapters 2 to 8 are summarised and recommendations for future work are presented.

2 FIBRE OPTIC BRAGG GRATING SENSOR

Fibre optic sensors have been studied extensively in the literature. There exist several books that give a comprehensive overview of the subject [44-46]. Almost every book introduces fibre optic Bragg grating sensors (FBGS), indeed there are two textbooks that are dedicated to fibre Bragg gratings (FBG) [16, 17]. Recent developments can also be found in relevant journal publications [47-49]. Despite the emerging interest in the use of FBG for sensing applications, only a few publications deal with the requirements of the grating, the fibre, and the coating that come along with the demands of the potential user, see for example [50]. The intention of this chapter is to introduce the terminology, briefly review the current state-of-art and make some amendments with own results related to draw tower gratings.

2.1 INTRODUCTION

The realisation of optical fibres for the transmission of light in the 1960s has revolutionised telecommunication. Data transmission over several kilometres without additional amplifiers has become feasible using low attenuation of optical signals in silica fibres [51, 52]. Fibre-based communication still offers highest data rates. The development of high performance equipment for the telecommunication market also had a high impact on the fibre optic sensor business [53]. Significant improvements on the technical performance have come along with a price reduction due to the mass production for the huge telecommunication market. Today, in the beginning of the 21st century fibre optic sensors have gained access to the market and started their way to replace conventional electrical or mechanical sensors [54].

Fibre optical sensors offer several advantages compared to their conventional electronic and electrical counterparts. With their intrinsic nature they are suitable for the deployment under harsh environmental conditions, e.g. in areas with high electro-magnetic fields, high voltage, increased exposure to radiation and in explosive or chemically aggressive environments. The flexibility and the ease of miniaturisation allows the unobtrusive installation of distributed sensor networks with several hundreds of sensor locations. Of most interest is the capability of structural integration of the fibre optic sensors into composite materials or concrete [24, 55-68].

Especially in the aerospace industry where fibre-reinforced plastics (FRP) have started to replace metallic structures this leads to advantages over conventional sensors not suited for structural integration [28, 32, 69-75].

Light propagates through the optical fibre because of total reflection of the guided light inside the fibre core. Total reflection occurs at interfaces where the refractive index of the outer material is smaller than the one of the inner material and the angel of incidence is less than the critival angle. The propagation of the light is characterised by the appearance of modes. The characteristics of the modes can be described using Maxwell's equations [76-78]. The most common layout of the fibres for high performance sensor applications is the single mode fibre. For this type of fibre only the fundamental mode can propagate. The geometry and the index profile of a step index single mode fibre are shown in Figure 2.1.

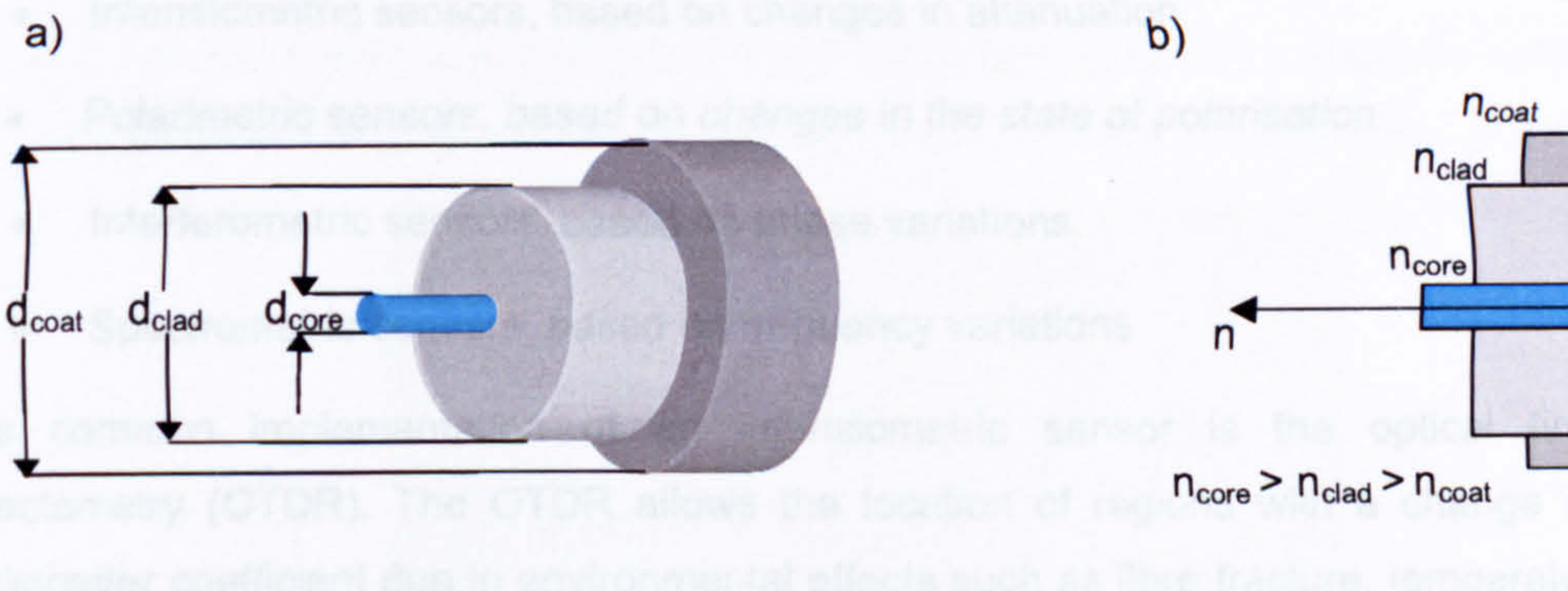

Figure 2.1: Single mode fibre: a) Geometry; b) refractive index profile.

a) typical values:	*diameter of fibre core*	d_{core} = *4 - 10 µm*
	diameter of fibre cladding	d_{clad} = *125 µm*
	diameter of fibre coating	d_{coat} = *150 - 250 µm*
b) typical values:	*index of fibre core*	n_{core} = *1.46 - 1.48*
	index of fibre cladding	n_{clad} = *1.44 - 1.45*
	index of fibre coating	n_{coat} = *< 1.44*

The most common approach to give a mathematical description of light is that of an electromagnetic wave. For a monochromatic plane wave travelling along the z-direction, presented by its electric field E_{em}, the following expression can be derived from Maxwell's equations [76]:

$$E_{em}(x,y,z,t) = A_{em}(x,y)\exp i\left(k_{em}z - \omega t + \phi(t)\right) \tag{2.1}$$

Here A_{em} is the amplitude of the wave which can vary in space, $k_{em} = 2\pi/\lambda_{em}$ is the free-space wave number, ω is the angular frequency, λ is the free-space wavelength and $\phi(t)$ is a time-depending phase shift. For light travelling in a medium other than vacuum the free-space propagation constant will be replaced by the general propagation constant $\beta = nk$, where n is the index of refraction of the material. In general there exist two independent waves even in a single mode fibre that differ in their state of polarisation (SOP), i.e. they have different propagation characteristics. Any effect that alters either the phase, amplitude, frequency or state of polarisation of the wave can be measured if an appropriate interrogation system, i.e. a system that is sensitive to a change in one of these properties, is available. For any of the above mentioned effects numerous interrogation systems exist. Depending on the property of light affected, the sensors can be classified into [54]:

- Intensiometric sensors, based on changes in attenuation
- Polarimetric sensors, based on changes in the state of polarisation
- Interferometric sensors, based on phase variations
- Spectrometric sensors, based on frequency variations

One common implementation of an intensiometric sensor is the optical time domain reflectometry (OTDR). The OTDR allows the location of regions with a change in the local backscatter coefficient due to environmental effects such as fibre fracture, temperature change, etc. Intensiometric sensors suffer from relatively low spatial resolution and low sensitivity [44, 54].

Polarimetric sensors require control of the SOP for the whole fibre optic system. Although high resolutions can be achieved, these sensors suffer from the complexity of polarisation control. Examples of polarimetric sensors can be found in [79-86].

A large and important class of high-performance fibre optic sensors today is based on the interferometric principle. In an interferometer there exist two or more optical paths through which a propagating wave can travel. At some point these two paths combine again and any relative change in phase between the two waves travelling along the two paths is translated into a change of intensity, provided that the two waves are coherent. The interferometer works best if both waves have the same optical power and same SOP. In that case the fringe contrast is maximum, for orthogonal SOP there is no interferemce at all. Interferometers appear in different lay-outs, for example as a Michelson, a Mach-Zehnder, or a fibre optic Fabry-Perot interferometer. Especially the Fabry-Perot sensor offers high sensitivity and high spatial resolution due to its short sensing region. Due to its popularity several examples of Interferometric sensors can be found in the literature. Relevant publications can be found in [27, 87-98].

The category of spectrometric sensors can be divided into two sub-categories. The first includes sensors based on Raman and Brillouin backscatter. Both are non-linear effects that produce additional components besides the central wavelength in the reflected spectrum, called the Stokes and Anti-Stokes radiation. Combined with OTDR these effects have been used for determining the temperature and strain profile along an optical fibre. Such systems however suffer from only modest spatial resolution and sensitivity [44, 54]. The second sub-category of spectrometric sensors comprises fibre optic Bragg grating sensors, which will be described in detail in the next section.

2.2 General Description

Figure 2.2 shows a photograph of a fibre optic Bragg grating beside a match to demonstrate the size of the device. The grating extends itself only over the black marked region of the fibre.

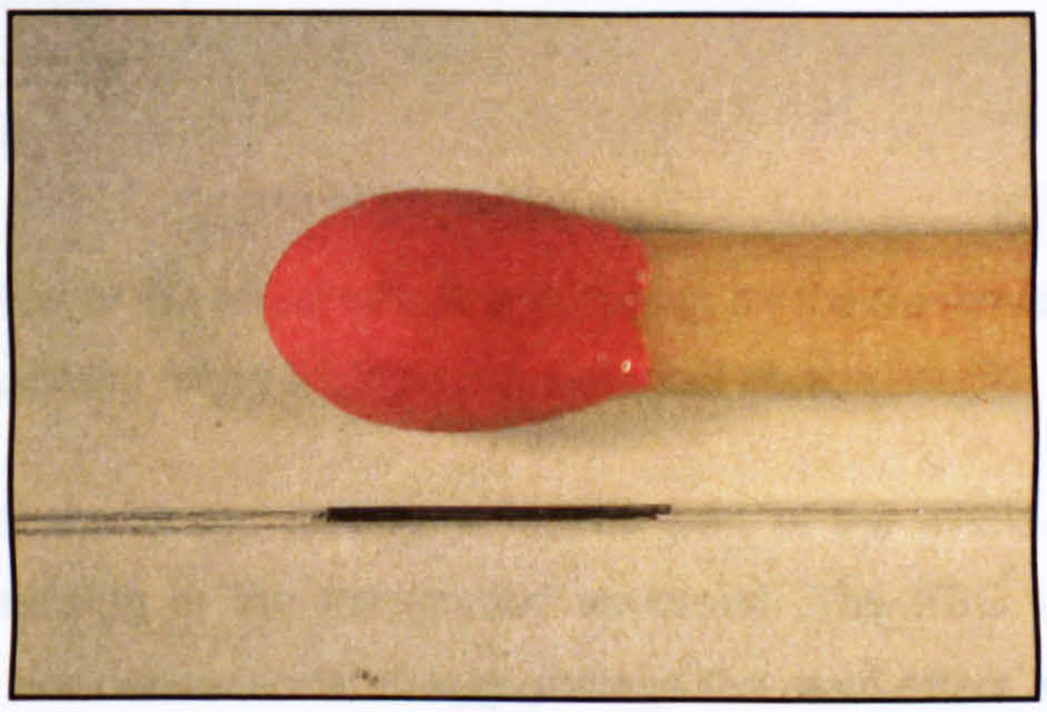

Figure 2.2: Photograph of a fibre Bragg grating and a match.

A FBG is a permanent, periodic perturbation of the refractive index which is laterally exposed into the core of a photosensitive optical fibre, extending over a limited length of the fibre. The grating is characterised by its period, amplitude, and length, usually 1-20 mm. The structure is called a Bragg grating, because it has a similar effect on light travelling along the fibre as has the crystal lattice of a solid on incoming X-rays, which was discovered by W.H. and W.L. Bragg [99]. The Bragg grating acts as a filter for light travelling along the fibre line. It has the property of reflecting light in a predetermined range of wavelength centred around a peak wavelength value. Figure 2.3 shows the transmission and reflection characteristics of a FBG. In this case light of a broadband light source, e.g. a light emitting diode (LED) or super luminescent LED (SLED), is coupled into a single mode optical fibre.

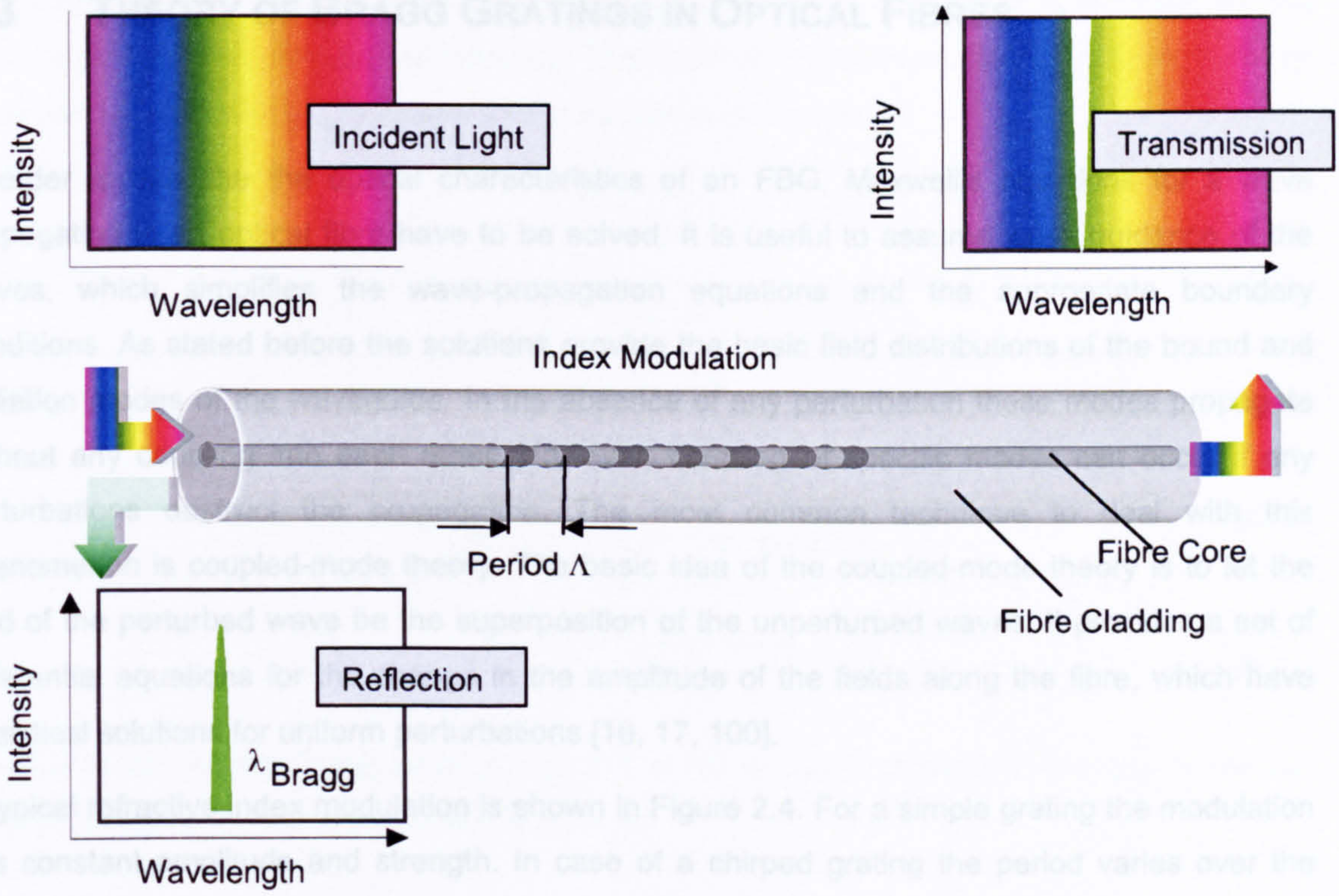

Figure 2.3: Illustration of the effect of a Bragg grating on the transmission and reflection of light travelling along a single mode optical fibre.

Due to the presence of the Bragg grating, a narrow part of the whole spectrum is reflected, whereas this part is missing in the transmitted spectrum. The FBG acts as a filter for the electromagnetic wave. For conventional Bragg gratings the main effect is the coupling between the forward and backward propagating core modes [100]. This will be investigated in more detail in Section 2.3.

The wavelength for which the contributions of the reflected light from each grating plane add constructively in the backward direction is called the Bragg wavelength λ_B. Let Λ be the grating period and $\overline{n}_{eff}$ the mean effective refractive index in the grating region then the Bragg wavelength can be calculated as the product of these values, see Section 2.3. External forces such as strain, pressure or a temperature change lead to changes in the grating period and in the effective refractive index. Consequently, the wavelength of the light reflected from the grating varies. By measuring the actual reflected wavelength an efficient interrogation system for the external forces can be obtained. The layout of the interrogation system will always be adapted to the actual requirements in terms of interrogation frequency, accuracy and other boundary conditions such as geometrical size, weight and last but not least costs. Therefore, interrogation systems will be discussed in the corresponding Sections.

2.3 THEORY OF BRAGG GRATINGS IN OPTICAL FIBRES

In order to describe the optical characteristics of an FBG, Maxwell's equations for a wave propagating in an optical fibre have to be solved. It is useful to assume weak guidance of the waves, which simplifies the wave-propagation equations and the appropriate boundary conditions. As stated before the solutions provide the basic field distributions of the bound and radiation modes of the waveguide. In the absence of any perturbation these modes propagate without any coupling into each other. However, coupling of specific modes can occur if any perturbations obstruct the propagation. The most common technique to deal with this phenomenon is coupled-mode theory. The basic idea of the coupled-mode theory is to let the field of the perturbed wave be the superposition of the unperturbed waves. It provides a set of differential equations for the change in the amplitude of the fields along the fibre, which have analytical solutions for uniform perturbations [16, 17, 100].

A typical refractive index modulation is shown in Figure 2.4. For a simple grating the modulation has constant amplitude and strength. In case of a chirped grating the period varies over the grating length, an apodised grating varies in the amplitude of the index modulation over the grating length. Figure 2.4 defines the ac part of the index modulation Δn_{ac} and the dc part Δn_{dc}.

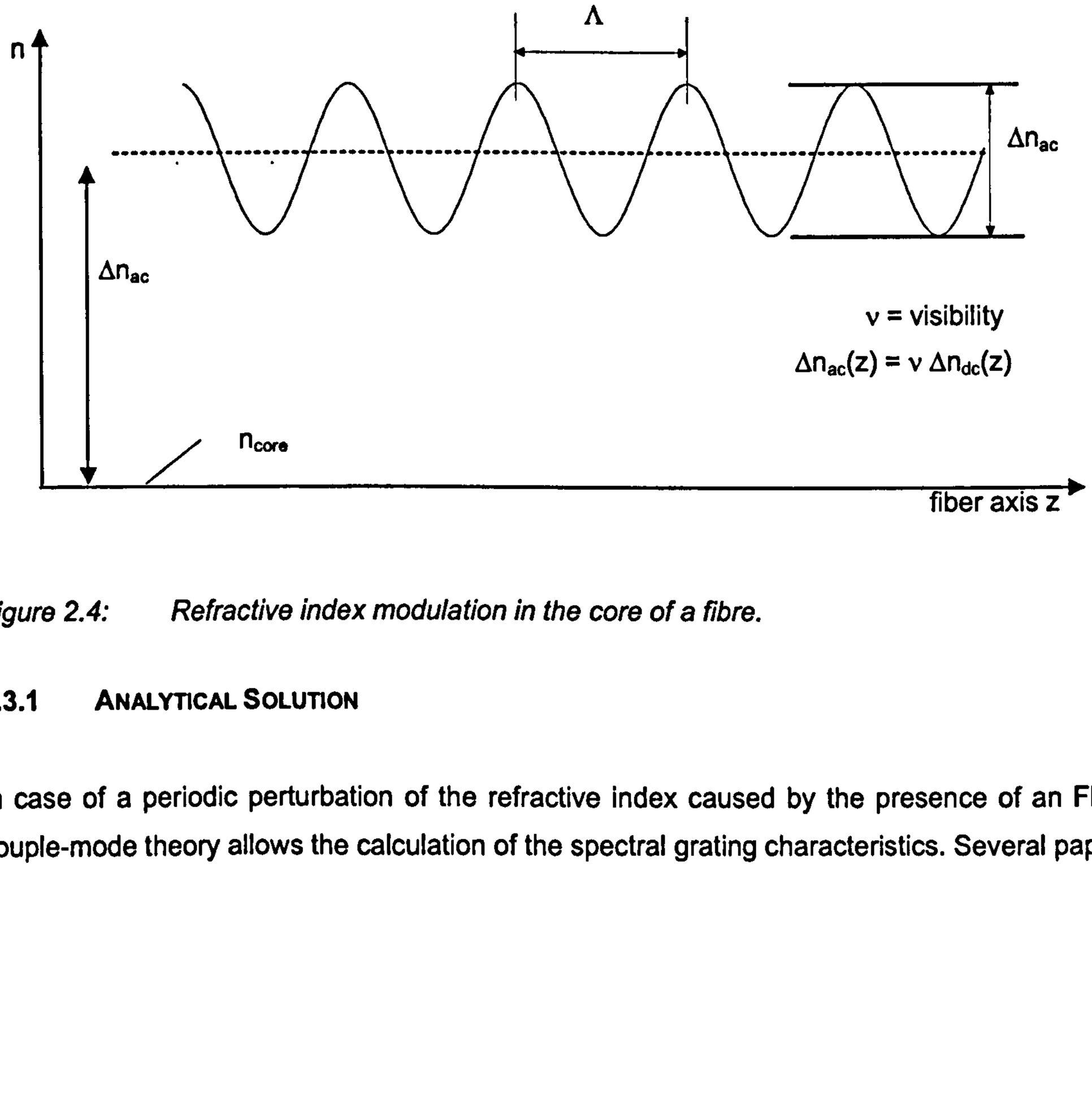

Figure 2.4: Refractive index modulation in the core of a fibre.

2.3.1 ANALYTICAL SOLUTION

In case of a periodic perturbation of the refractive index caused by the presence of an FBG, couple-mode theory allows the calculation of the spectral grating characteristics. Several papers

and textbooks have discussed these calculations in detail [16, 17, 101]. It is sufficient for this work to give the resulting power reflection coefficient *R* and transmission coefficient *T*, which allow the calculation of the reflection and/or transmission spectrum.

$$R = \frac{\frac{\chi^2}{\gamma_B^2} \cdot \sinh^2(\gamma_B \cdot L)}{\cosh^2(\gamma_B \cdot L) + \frac{\sigma^2}{\gamma_B^2} \cdot \sinh^2(\gamma_B \cdot L)} \tag{2.2}$$

$$T = \frac{1}{\cosh^2(\gamma_B \cdot L) + \frac{\sigma^2}{\gamma_B^2} \cdot \sinh^2(\gamma_B \cdot L)} \tag{2.3}$$

where

$$\gamma_B = \sqrt{(\chi^2 - \sigma^2)} \tag{2.4}$$

L is the length of the Bragg grating, χ_{AC} is the AC coupling coefficient and σ_{DC} is the DC coupling coefficient. The coefficients are given as

$$\chi_{AC} = \frac{\pi}{\lambda} \cdot \Gamma \cdot \Delta n_{ac} \tag{2.5}$$

$$\sigma_{DC} = \delta + \frac{2\pi}{\lambda} \cdot \Gamma \cdot \Delta n_{dc} \tag{2.6}$$

$$\delta = 2\pi \cdot n_{eff} \left(\frac{1}{\lambda} - \frac{1}{\lambda_D} \right) \tag{2.7}$$

The following definitions have been used to introduce the above equations:

Γ is the confinement factor, which gives the ratio of the power guided in the core to the total power of the fundamental mode; δ is the detuning factor and λ_D is the design wavelength for an infinitesimally weak index of refraction change grating; n_{eff} is the effective refractive core index and λ is the variable of the wavelength.

The maximum reflectivity R_{max} of the grating follows from the differentiation of (2.2):

$$R_{\max} = \tanh^2(\chi \cdot L) \tag{2.8}$$

The maximum occurs when the DC coupling coefficient σ_{DC} becomes zero, as then all reflected waves are phase matched. Using Equations (2.6) and (2.7) the exact expression of the Bragg wavelength λ_B can be derived as

$$\lambda_B := \lambda\big|_{\sigma=0} = \lambda_D \cdot \left(1+\Gamma\cdot\frac{\Delta n_{dc}}{n_{eff}}\right) = 2\cdot n_{eff}\cdot\Lambda\cdot\left(1+\Gamma\cdot\frac{\Delta n_{dc}}{n_{eff}}\right) = 2\cdot \bar{n}_{eff}\cdot\Lambda \qquad (2.9)$$

In contrast to Equation (A.2) an additional term, the modification of the index by the DC part of the UV induced modulation, appears. As $\Delta n_{dc} << n_{eff}$ and $\Gamma < 1$, this additional term is often neglected, and the mean effective index $\overline{n}_{eff}$ is replaced by the effective index n_{eff}.

Figure 2.5 shows calculated reflection and transmission spectra as a function of wavelength of a uniform Bragg grating. The maximum reflectivity R_{max} and the full-width-half maximum FWHM are also shown. The following parameters have been chosen to calculate the spectra of Figure 2.5: $\Delta n_{ac} = \Delta n_{dc} = 7*10^{-5}$, $\Gamma = 0.65$, $\lambda_D = 1530$ nm, $n_{eff} = 1{,}445$ and $L = 10$ mm. Using (2.8) the maximum reflectivity can be calculated $R_{Max} = 53{,}6$ %.

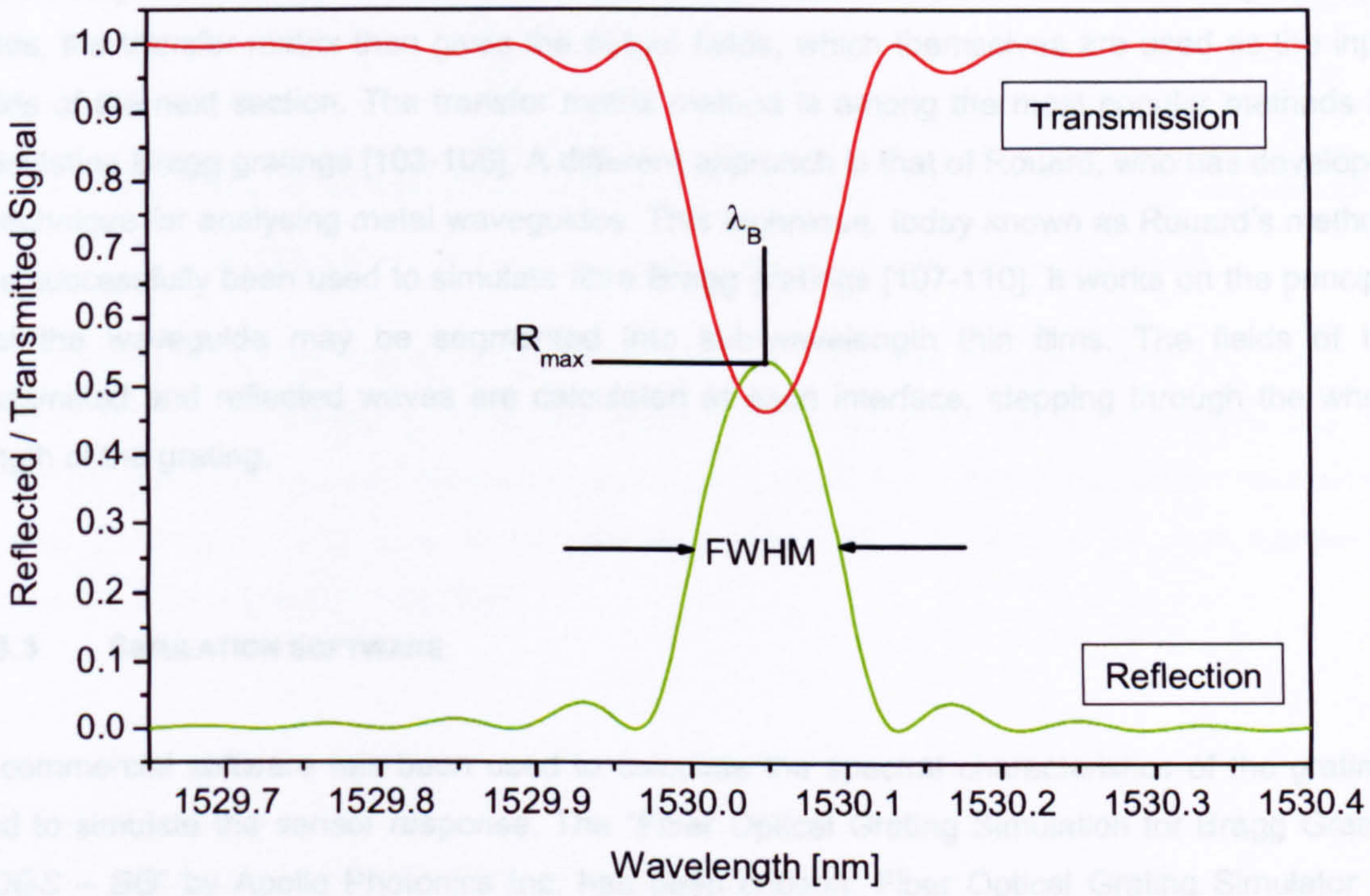

Figure 2.5: Typical reflection and transmission spectra of a Bragg grating as a function of wavelength.

2.3.2 NUMERICAL METHODS

Throughout this work uniform gratings have been used. Uniform gratings work very well for sensor applications, where a small grating spectrum is needed. They are easier to fabricate than special chirped, apodized or phase-shifted gratings. Yet, as will be explained in more detail

in section 2.5, a sensor grating may be subjected to non-uniform strain or temperature profiles. As a consequence the index modulation of the grating will be altered and behave like a chirped grating. For analysing the spectral response of the sensor gratings to arbitrary strain and temperature profiles non-uniform gratings have to be considered. In the case of a non-uniform grating a numerical solution has to be found for the equations of the coupled-mode theory. Many different techniques differing in their degree of complexity for simulating fibre Bragg gratings exist. The simplest method is the straightforward numerical integration of the coupled-mode equations. The transfer matrix method offers a fast and accurate way for calculating the spectral response of a non-uniform grating. In this approach the coupled mode equations are used to calculate the output fields of a short section of the grating for which the parameters are assumed to be constant [102, 103]. Transfer matrixes are popular in Electronic Engineering where they are used to calculate the characteristics of a four-port device. Knowing the input fields, the transfer matrix then gives the output fields, which themselves are used as the input fields of the next section. The transfer matrix method is among the most popular methods for calculating Bragg gratings [103-106]. A different approach is that of Rouard, who has developed a technique for analysing metal waveguides. This technique, today known as Rouard's method, has successfully been used to simulate fibre Bragg gratings [107-110]. It works on the principle that the waveguide may be segmented into sub-wavelength thin films. The fields of the transmitted and reflected waves are calculated at each interface, stepping through the whole length of the grating.

2.3.3 SIMULATION SOFTWARE

A commercial software has been used to calculate the spectral characteristics of the gratings and to simulate the sensor response. The "Fiber Optical Grating Simulation for Bragg Grating *FOGS – BG*" by Apollo Photonics Inc. has been chosen. Fiber Optical Grating Simulator for Bragg Grating (FOGS-BG) is a powerful and user-friendly computer-aided simulation and optimisation tool for design and analysis of optical fibre devices based on Bragg grating [111]. The software has the feature of parameter scanning which enables the user to optimize the grating performance by varying a parameter in a defined range. This is important when the influence of any parameter on the FBG response has to be studied. Especially for the study of the influence of ultrasonic acoustical waves on the grating response, this feature has been of particular importance.

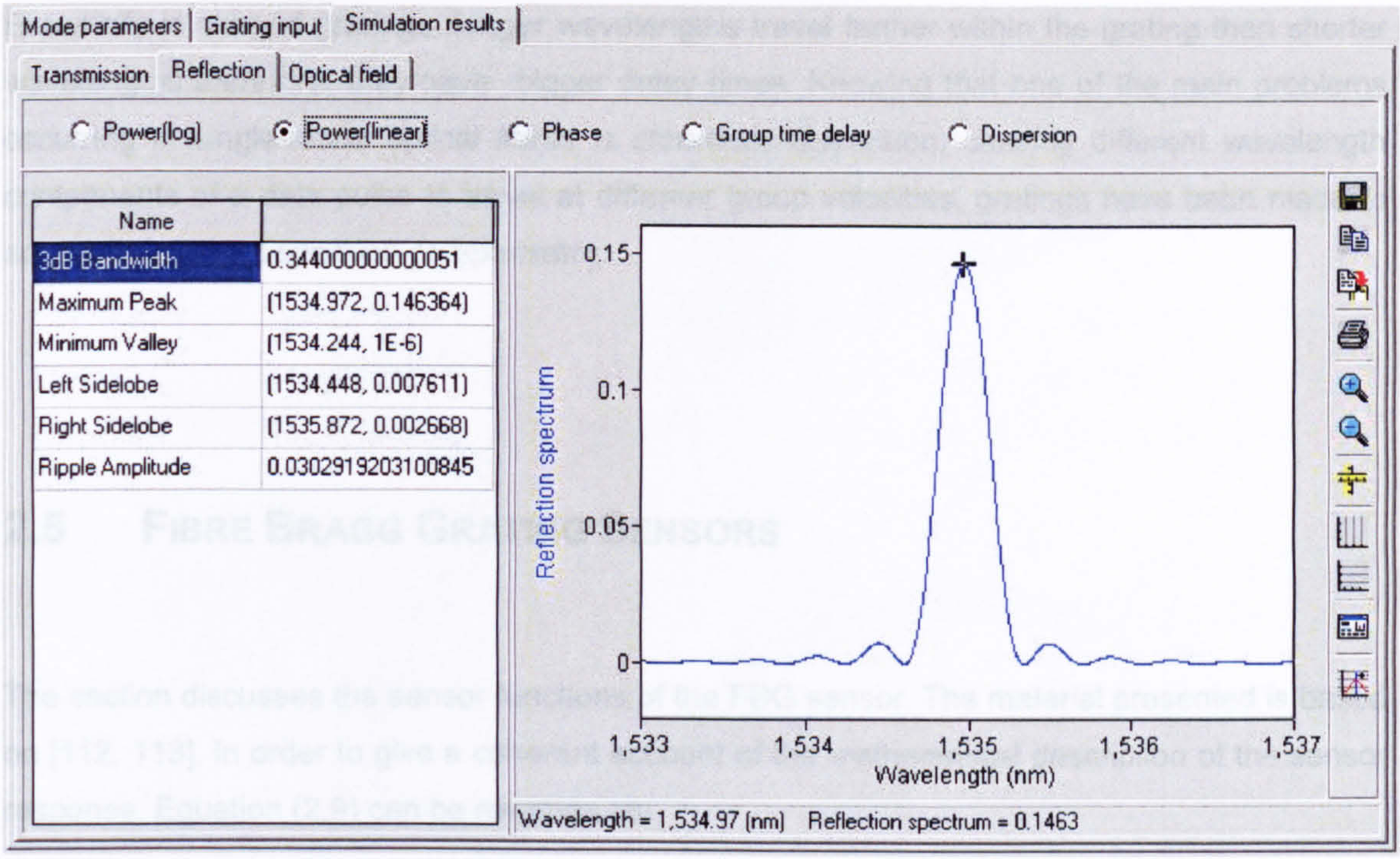

Figure 2.6: FOGS-Software: Window showing the calculated grating spectrum.

The software calculates the spectrum of the grating using the transfer matrix approach (see Section 2.3.2). For simple gratings the results of the software can be compared with the analytical solution. Figure 2.6 shows the graphical result of the software calculation for a simple grating. It is very close to what can be calculated analytically. The error in the peak wavelength is within 1.1 % and can be neglected.

2.4 Applications in Telecommunication

Fibre Bragg gratings have found many applications in telecommunication. For the sake of completeness the most common applications are listed in this brief overview of fibre Bragg gratings. As shown in Section 2.3, FBGs offer unique filtering properties. Combined with their versatility as in-fibre devices they offer enhanced performance for wavelength-stabilised lasers, fibre lasers and fibre amplifiers. Their filter characteristics are used to form important devices for modern WDM (Wavelength Division Multiplex) networks, e.g. multiplexers and demultiplexers and add/drop multiplexers. Another property of the FBG not mentioned before is their dispersion characteristic. Each wavelength has a different delay time when being reflected at the grating.

Especially in chirped gratings, longer wavelengths travel farther within the grating than shorter wavelengths therefore, they have bigger delay times. Knowing that one of the main problems occurring in single-mode optical fibres is chromatic dispersion, causing different wavelength components of a data pulse to travel at different group velocities, gratings have been made to act as an in-fibre dispersion compensator.

2.5 Fibre Bragg Grating Sensors

The section discusses the sensor functions of the FBG sensor. The material presented is based on [112, 113]. In order to give a coherent account of the mathematical description of the sensor response, Equation (2.9) can be rewritten as:

$$\lambda_B = 2 \cdot \bar{n}_{eff} \cdot \Lambda \tag{2.10}$$

In fact this equation is only valid for a uniform grating. For apodised gratings the mean refractive index has to be calculated numerically and for chirped gratings the spatial dependence of the grating period has to be accounted for. For the shift of the Bragg wavelength due to external forces this is of minor impact. It is however important, that the external effect does not change the spectral characteristics of the grating, i.e. no additional chirp or apodisation must be generated. This is true if the external effect is constant on a scale compared to the size of the grating.

When the response of a Bragg grating to ultrasound is considered, these effects, i.e. chirp and apodisation have to be considered (see Section 0). What further has to be thought of is the polarisation dependence of all the variables in Equation (2.10). Throughout this work only gratings will be considered that have been inscribed perpendicular to the fibre axis, i.e. no blazed gratings will be taken into account.

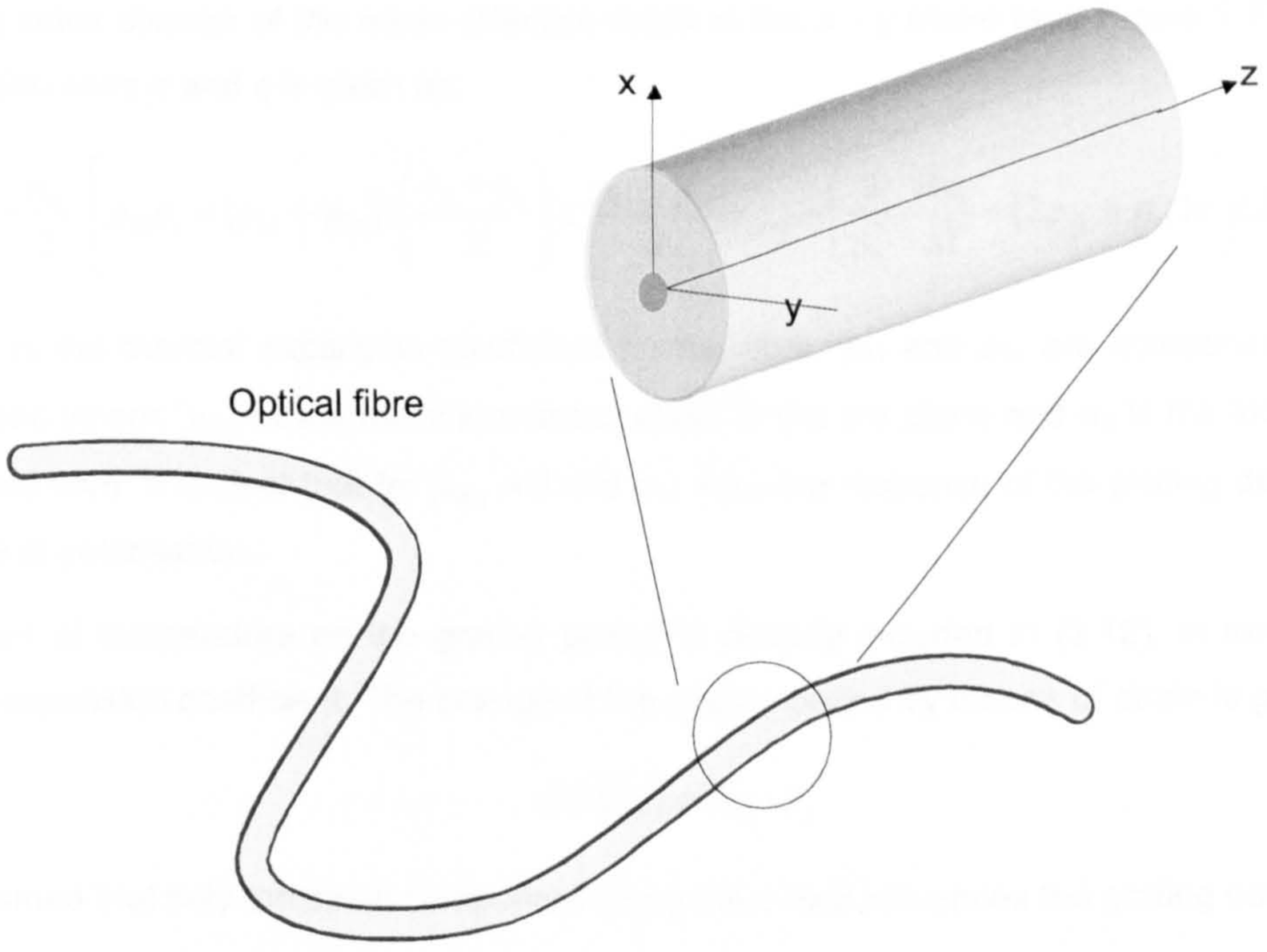

Figure 2.7: Path along optical fibre and definition of coordinate system.

From Equation (2.10) it is apparent that a fibre Bragg grating can be used for sensing purposes, as both the mean refractive index $\overline{n}_{eff}$ and the grating period Λ are functions of external forces such as strain or temperature. Therefore, a change in the Bragg wavelength can be a measure of temperature and strain.

2.5.1 General Sensor function

The shift in the Bragg grating centre wavelength for a freestanding sensor can be estimated using a linear approach, i.e. the total differential of Equation (2.10) is calculated as

$$\frac{\Delta\lambda_B}{\lambda_{B_0}} = \frac{\Delta\Lambda(\varepsilon_i, \Delta T)}{\Lambda_0} + \frac{\Delta\overline{n}_{eff}(\varepsilon_i, \Delta T)}{\overline{n}_{eff_0}} \tag{2.11}$$

The subscript "0" refers to the initial state without any strain and at temperature T_0. ΔT is the temperature change related to the initial temperature T_0, i.e. $\Delta T = T - T_0$, ε_i are the components of the strain tensor along the coordinate axes. The change of the refractive index as a function of temperature is covered by the thermo-optic effect, whereas its change as a function of strain is described by the photo-elastic effect. The grating period is changed by temperature due to the thermal expansion of the material and by the strain which is the relative change of the period compared to the initial period. The calculation of the refractive index as a function of strain and temperature under consideration of the polarisation has been performed in [112]. The

resulting index change of the mean effective index in the x – y plane (see Figure 2.7) for both polarisation axes *p* and *q* is given as:

$$\Delta\bar{n}_{eff}^{p,q} = -\frac{n_0^3}{2}\cdot\left[p_{12}\varepsilon_z + (p_{11}+p_{12})\cdot\left(\frac{\varepsilon_y+\varepsilon_x}{2}\right)\pm\frac{p_{11}-p_{12}}{2}\gamma_{\max} - \left(\frac{2}{n_0^3}\cdot\frac{dn_0}{dT} + (2p_{12}+p_{11})\alpha\right)\Delta T\right] \quad (2.12)$$

where α is the thermal expansion coefficient for the fibre, p_{11} and p_{12} are components of the strain optic tensor, γ_{max} is the maximum shear strain in the x-y plane and n_0 is the index of the unstrained fibre. It is clear that for $\gamma_{max} \neq 0$ and $p_{11} \neq p_{12}$ the response of the grating depends on the state of polarisation.

The effect of temperature on the grating period is already included in (2.12), in terms of the thermal expansion coefficient. The change of the grating period by means of strain is given as

$$\Delta\Lambda(\varepsilon_i) = \Lambda_0 \cdot \varepsilon_z \quad (2.13)$$

It is assumed that only the strain component along the z-axis influences the grating period.

Substituting (2.12) and (2.13) into (2.11) gives the desired general expression of the shift of the Bragg wavelength when exposed to strain or a change in temperature.

For most experiments only special sub-cases of the general expression are of interest. The following sections will provide the basis equations for the relevant thermo-mechanical load cases considered in this work

2.5.2 Pure Temperature

If all the mechanical strains are zero and the only strains are thermally induced, the shift of the Bragg wavelength for a freestanding sensor can be calculated using

$$\frac{\Delta\lambda_B}{\lambda_{B_0}} = \left(\alpha + \frac{1}{n_0}\frac{dn_0}{dT}\right)\cdot\Delta T \quad (2.14)$$

The first term describes the thermal expansion and the second term the thermo-optic effect. The coefficients depend on the composition of the fibre material and can be found in the literature. It has been shown that for different amounts of germanium in the fibre silicate matrix the thermal expansion coefficient varies from $0.55 - 1.1\cdot10^{-6}$ for a GeO_2 part of 0 – 13 mol%. The thermal expansion coefficient is assumed to be independent of temperature. The change of the refractive index with temperature is dominated by the change in the density of the material. It has been shown that $dn/dT \approx 1\cdot10^{-5}$ 1/K. Although this quantity is in the literature often assumed to be independent of the temperature, some references show an increase with raising temperature. If high precision or a broad temperature range is required a non-linear wavelength

shift should be anticipated. From Equation (2.14) the expected linear sensitivity for a 1530 nm grating ($n_0 = 1.445$) is approximately 11 pm/K at room temperature. The thermo-optic effect clearly dominates the temperature sensitivity of the Bragg grating, as shown in [112].

2.5.3 Strain

Considering the case of uni-axial load along the fibre axis without any change in temperature, the Bragg wavelength for a freestanding sensor is obtained by

$$\frac{\Delta\lambda_B}{\lambda_{B_0}} = \left(1 - \frac{n_0^2}{2}\cdot\left[p_{12} - \nu\cdot\left(p_{11} + p_{12}\right)\right]\right)\cdot\varepsilon_z = \left(1 - P^{eff}\right)\cdot\varepsilon_z \qquad (2.15)$$

This is the expression most often found in the literature to describe the strain sensitivity of an FBG. P^{eff} is the effective strain-optic constant and ν is the Poisson's ratio. For a typical germanosilicate fibre the constants are $p_{11} = 0.113$, $p_{12} = 0.252$ and $\nu = 0.17$ [16]. The Poisson's ratio is a function of strain that varies from 0.15 at low strain to 0.17 for strain levels around 0.1 to 1 %. Using these parameters an effective strain-optic constant $P^{eff} = 0.198$ ($n_0 = 1.445$) can be found. For the shift off the Bragg wavelength follows at 1530 nm a strain sensitivity of approximately 1.22 pm/μstrain. One μstrain has been defined as the strain of 1 μm/m = 10^{-4} %. The shift of the Bragg wavelength is linear with strain and has been found to be independent of temperature [112].

2.5.4 Uni-axial load and Temperature

In the more general case of combined thermal and mechanical loads the following expression for the wavelength shift under uni-axial load can be found as

$$\frac{\Delta\lambda_B}{\lambda_{B_0}} = \left[1 - P^{eff}\right]\cdot\varepsilon_z + \left[\alpha\cdot P^{eff} + \frac{1}{n_0}\frac{dn}{dT}\right]\cdot\Delta T = \left[1 - P^{eff}\right]\cdot\varepsilon_z^m + \left[\alpha + \frac{1}{n_0}\frac{dn}{dT}\right]\cdot\Delta T \qquad (2.16)$$

where ε_z^m is the mechanically induced strain, so that $\varepsilon_z = \varepsilon_z^m + \alpha\Delta T$ is the sum of mechanically and thermally induced strain. It becomes apparent that any change in the Bragg wavelength, associated with an external perturbation, is the sum of strain and temperature terms. This complicates the use of Bragg grating sensors, as for normal applications only one perturbation is of interest and the other one is just a source of error. Therefore, several methods for the deconvolution of temperature and strain have been suggested in the literature. A practical solution is considered in Section 3.3 when the implementation of a FBG load monitoring sensor is discussed.

2.5.5 Surface Mounted and Embedded Sensors

The strain and temperature function become more complex when surface mounted or structural embedded sensors are studied. On the one hand, for the cases studied in the previous section, the strains were symmetrical and constant so that no polarisation dependence occurred; on the other hand the applied strains and temperature were applied only to the bare fibre. But for mounted and embedded fibres it is the structure that bears the loads. The question is in what way these thermal and mechanical loads are transferred from the structure to the sensor, in particular into the fibre core and the region of the Bragg grating.

It is desirable to have a sensor response only for loads applied along the main sensor axis, i.e. along the fibre axis. This is for example true for resistive strain gauges. A high directivity of the sensor causes low cross sensitivity and therefore a minimisation of the corresponding errors. It is furthermore advantageous if one is able to use the calibration factors found in Equation (2.15). It has been shown by Betz and Trutzel that surface mounted sensors possess the desired properties [112, 114-116]. In the case of surface mounted sensors the transfer functions of the structural strains into the fibre are known and can be given as follows

$$\begin{aligned} \varepsilon_z &= \varepsilon_z^s = \varepsilon_z^{s,m} + \alpha^s \cdot \Delta T \\ \varepsilon_x &= -\nu \cdot \varepsilon_z = -\nu \cdot \varepsilon_z^{s,m} - \nu \cdot \alpha^s \cdot \Delta T \\ \varepsilon_y &= -\nu \cdot \varepsilon_z = -\nu \cdot \varepsilon_z^{s,m} - \nu \cdot \alpha^s \cdot \Delta T \\ \gamma_{\max} &= 0 \end{aligned} \tag{2.17}$$

Here ε_x, ε_y and ε_z are the strain components and γ_{max} is the shear strain in the fibre core. The structural strain ε_z^s is separated into its thermal $\alpha^s \cdot \Delta T$ and mechanical $\varepsilon_z^{s,m}$ strain components. Also, ν is Poisson's ratio of the fibre and α^s is the thermal expansion coefficient of the structure. Equation (2.17) ensures that only the strain components along the fibre z-axis are transferred into the FBGS. Substituting (2.17) in (2.11) - (2.13) gives the following expression for the shift of the Bragg wavelength as a function of structural strain

$$\frac{\Delta\lambda_B}{\lambda_{B_0}} = \left[1 - P^{eff}\right] \cdot \varepsilon_z^{s,m} + \left[\left(1 - P^{eff}\right) \cdot \alpha^s + \frac{1}{n_0}\frac{dn}{dT}\right] \cdot \Delta T \tag{2.18}$$

As for most structures the thermal expansion of the material is much higher than that for silica fibre, the thermal expansion of the fibre has been neglected in Equation (2.18). Especially for the materials used in the automotive and aerospace industries, such as metals (α□= 10-23*10^{-6} 1/K) and composites (α = 3*10^{-6} 1/K), the temperature sensitivity of the mounted sensors is much higher than that for single fibres (α = 1*10^{-6} 1/K).

2.6 LIFETIME AND RELIABILITY OF BRAGG GRATING SENSORS

Fibre Bragg gratings used for sensor applications have much higher demands on the thermal and mechanical performance and reliability than the ones used in telecommunication. The standard requirements for applications in the automotive and aircraft industry for the temperature range is -50 to +100 °C and for the strain range is -2000 to +2000 µstrain (see also Section 3.3.1. There are however some applications that require even higher temperatures for example for monitoring vehicle engines or aircraft turbines, where temperature goes up to 1000 °C . High loaded aircraft structures, for example rotor blades of a helicopter, are strained up to 30 000 µstrain. If the Bragg grating sensor technology wants to compete in such applications the sensors of course have to fulfil these high demands.

2.6.1 THERMAL DECAY

Both, refractive index modulation and mean index change, induced by UV-illumination of the fibre core with an interference pattern during grating production, decay with time, especially at elevated temperature. On the one hand, reflectivity and wavelength changes of the FBG with time can cause errors in sensor applications and on the other hand, which is the worst case scenario, the grating can totally disappear, its reflectivity approaching zero. The thermally induced decay implies that the UV-induced defects (see 7.1.1.1Appendix A:) are not thermodynamically stable. The refractive index change during UV-illumination is described with carriers trapped in energy states of certain stability [117]. For a given energy level E_l thermal depopulation of the mean occupation number is assumed to be exponential with time t and dependent of the temperature T. The function of the release rate ν_{rel} modelled with an Arrhenius approach is given as

$$\nu_{rel}(E_l) = \nu_0 \exp\left(-\frac{E_l}{k_B T}\right) \tag{2.19}$$

Here k_B is the Boltzmann constant and ν_0 a fit parameter.

The total number of occupied states is assumed to be proportional to the UV-induced refractive index change. After some time t at temperature T the demarcation energy E_d divides the states in approximately two groups. The demarcation energy can be written as

$$E_d(T,t) = k_B T \ln(\nu_0 \cdot t) \tag{2.20}$$

For $E_l < E_d$ the states are depopulated, for $E > E_d$ most states are still occupied.

From equations (2.5) and (2.8) the relation of modulated index change and maximum reflectivity is given. It follows that the total number of trapped electrons remaining at a given time *N(t)* is a function of the remaining reflectivity *R* of the grating. In a normalised form these quantities can be plotted over the demarcation energy E_d. The relation is shown in Equation (2.21). The plot is called a master curve, which is a function of demarcation energy. With the master curve, combined influence of time and temperature can be studied. The initial state distribution can be calculated from the slope of the master curve, given as

$$\eta = \frac{N(t)}{N(0)} = \frac{\operatorname{arctanh}\left(\sqrt{R}\right)}{\operatorname{arctanh}\left(\sqrt{R_0}\right)} = f\left(E_D\right) \tag{2.21}$$

From the master curve predictions of the thermal stability and the lifetime of the FBG can be made. The decay mechanisms of the grating allow the annealing of the gratings. This means that by an accelerated aging of the gratings at elevated temperatures it is possible to keep only the stable component of the index change at subsequent applications. Once the sensor is in service, no more change in reflectivity or initial Bragg wavelength will occur. Figure 2.8 shows an example of the master curve for draw-tower gratings.

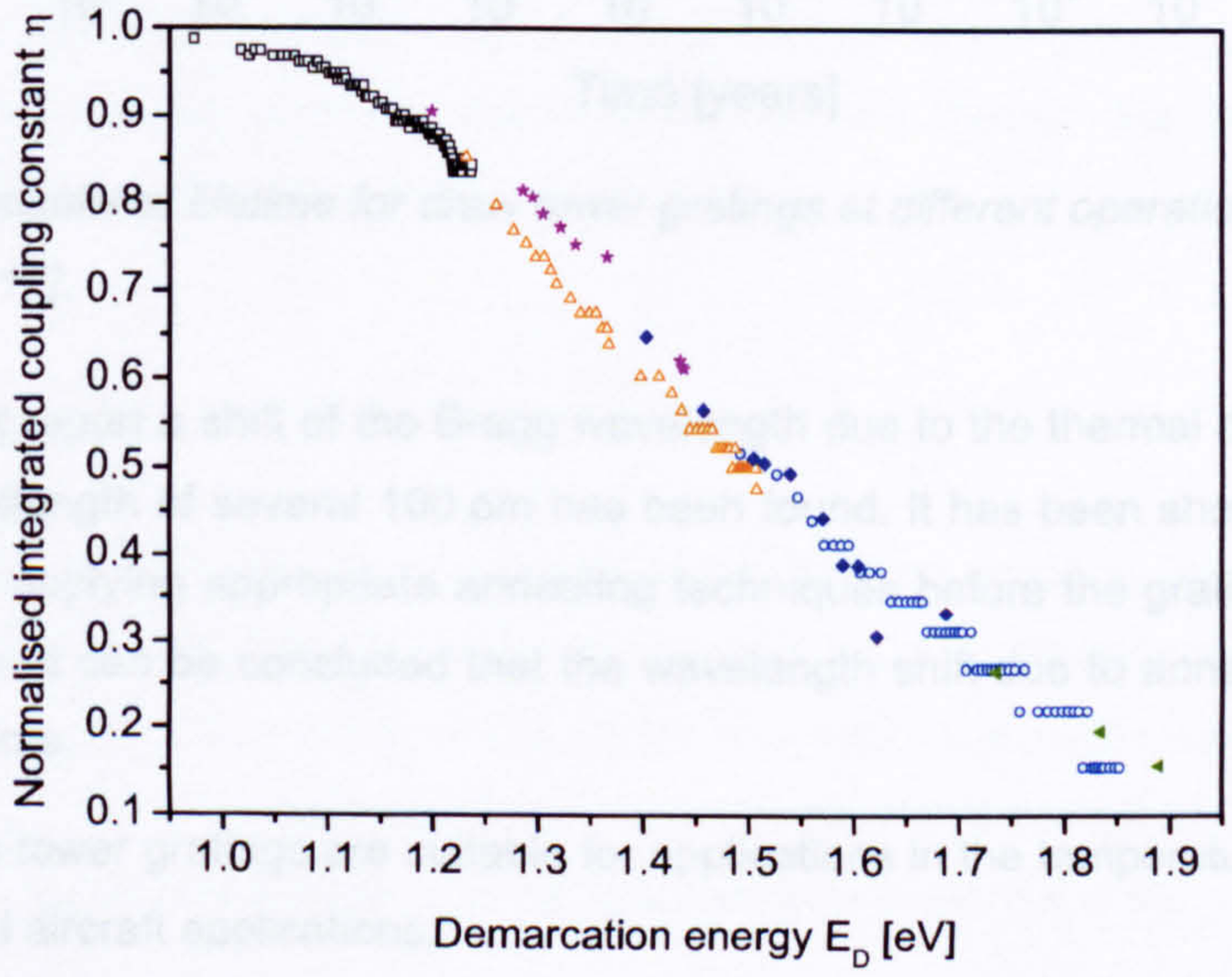

Figure 2.8: Plot of the master curve for draw-tower gratings [112]. The different symbols correspond to different decay experiments performed at various temperatures.

The master curve can be used to calculate the thermal decay of the grating at any temperature and subsequently give a lifetime estimation for sensor in service. In [112, 118, 119] the lifetime and reliabilty of low-reflective (10 %) draw-tower gratings are discussed. Figure 2.9 shows the calculated lifetime curves for a grating at different operational temperatures. For draw tower Bragg gratings the lifetime is several decades if their application is limited to temperatures

below 100 °C. The limit for the sensors is around 200 °C, but varies strongly with the required minimum reflectivity, which is a parameter of the interrogation system used. Today's draw-tower gratings have improved reflectivity (>15 %), therefore the temperature range of the sensors is extended.

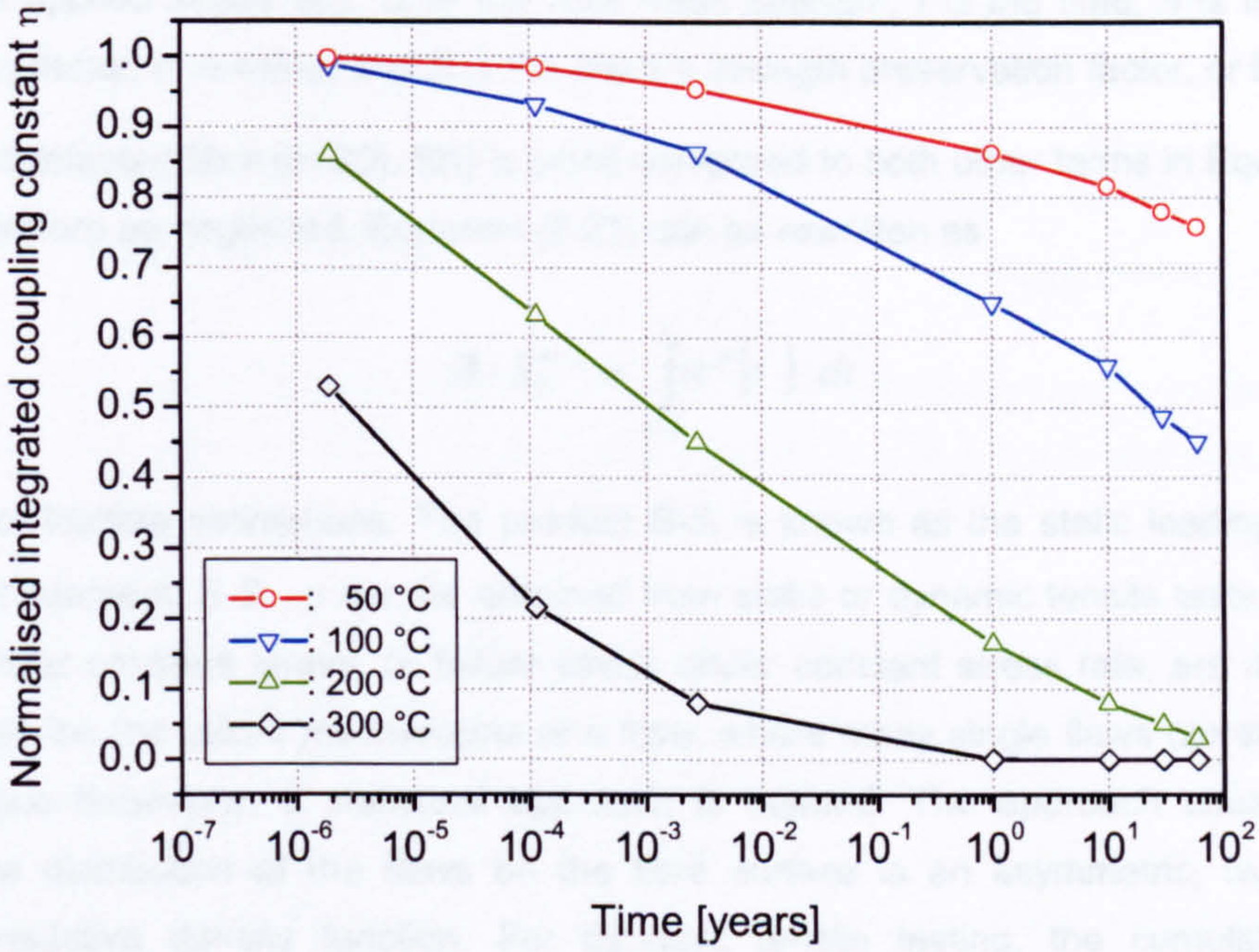

Figure 2.9: Calculated lifetime for draw tower gratings at different operational temperatures [112].

Mauron *et al* [120] report a shift of the Bragg wavelength due to the thermal decay. A decrease of the Bragg wavelength of several 100 pm has been found. It has been shown that this effect can be erased by applying appropriate annealing techniques before the grating is used for the sensor application. It can be concluded that the wavelength shift due to annealing is negligible during operation time.

In summary, draw-tower gratings are suitable for applications in the temperature range required for automotive and aircraft applications.

2.6.2 Mechanical Strength

Mechanical strength and fatigue of optical fibres are commonly described by a fracture mechanical model where a fibre is treated as a ceramic-like brittle material: surface flaws introduced during fibre drawing prior to the coating process start growing, due to any applied mechanical loads or intrinsic residual stresses. Glass dissolution due to water also reduces fibre strength. The power-law based general lifetime equation can be written as [118, 121]

$$S^{n-2}(t) = S_I^{n-2} - \frac{1}{B} \cdot \int_{t=0}^{t} \sigma^n(t') \cdot dt' \tag{2.22}$$

Failure due to stress corrosion occurs when the continuously decreasing fibre strength *S(t)* reaches the applied stress $\sigma(t)$. S_I is the fibre initial strength, *t* is the time, *n* is the corrosion susceptibility factor, or n-value, and *B* is the crack's strength preservation factor, or B-value.

For standard telecom fibre (n>20), S(t) is small compared to both other terms in Equation (2.22) and can therefore be neglected. Equation (2.23) can be rewritten as

$$B \cdot S_I^{n-2} \approx \int_{t=0}^{t} \sigma^n(t') \cdot dt' \tag{2.23}$$

and used for lifetime estimations. The product $B \cdot S_I$ is known as the static loading unit stress intercept, or intercept; $B \cdot S_I$, n can be obtained from static or dynamic tensile tests, where time to failure under constant stress, or failure stress under constant stress rate, are measured. In order to describe the failure mechanisms of a fibre, where many single flaws correspond to the overall fatigue behaviour, a statistical approach is needed. The approach usually taken to describe the distribution of the flaws on the fibre surface is an asymmetric, two-parameter Weibull cumulative density function. For dynamic tensile testing, the cumulative fracture probability *F* is given as

$$F = 1 - \exp\left[-\left(\frac{\sigma_d}{\sigma_0}\right)^{m_d}\right] \tag{2.24}$$

The cumulative fracture probability as function of the fracture stress σ_d, or the corresponding survival probability or reliability R = 1 – F, depend on the dynamic shape and scaling parameters m_d and σ_0, which are a measure for the width and mean value of the fracture strength distribution. On a double logarithmic scale the results of the dynamic tensile tests can be plotted and the scaling parameters can be obtained by a linear curve fit.

Although pristine optical fibres posses high mechanical strength, the mechanical performance of the fibre after inscription of a Bragg grating is dramatically reduced by the fibre decoating/recoating process. Several studies confirm this observation. It has been shown as well that the mechanical strength of the grating also depends on the parameters of the grating inscription process (pulse energy, number of pulses, exposure intensity, etc.). For sensor applications, where high mechanical strength is required, the solution is the use of draw-tower gratings. It has been shown that draw-tower gratings have the same mechanical strength as standard telecom fibres [118, 121-123]. Figure 2.10 illustrates the difference in the mechanical strength for standard FBGs (off-line fabricated) and draw-tower FBGs (on-line fabricated).

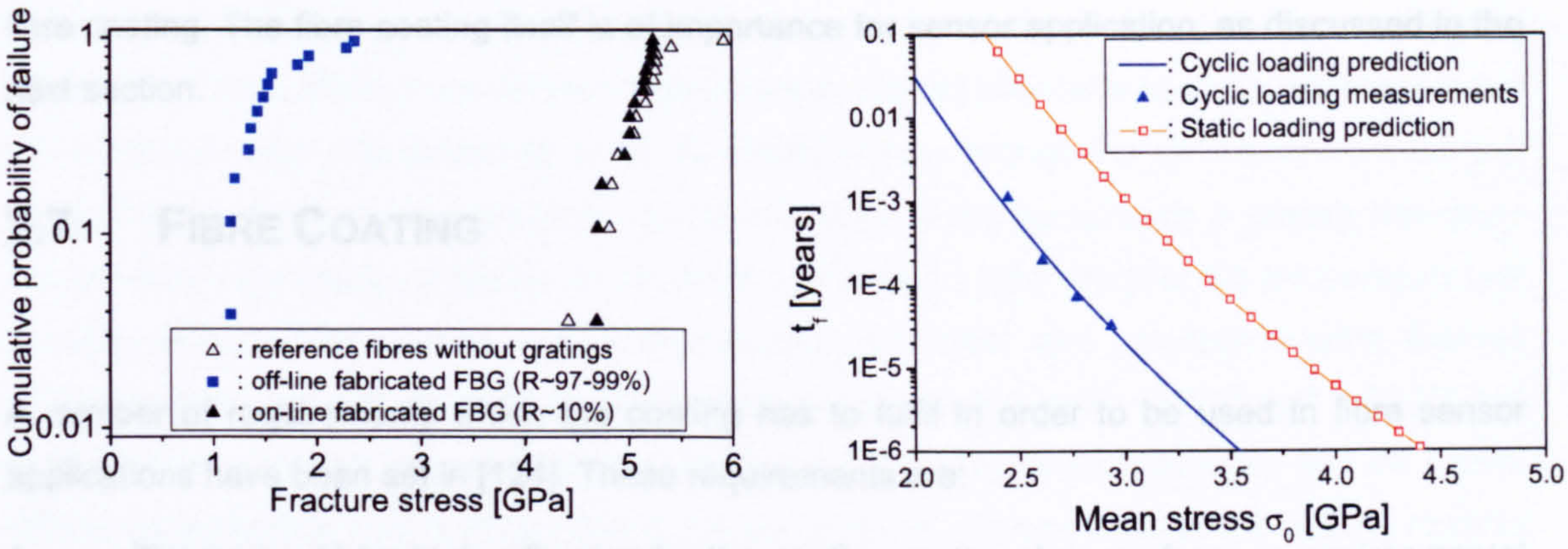

Figure 2.10: a) Typical fracture stress distribution for off-line and on-line fabricated FBGS. b) Measured lifetime under cyclic loading, as well as static and cyclic loading predictions [112].

The analysis of the tensile tests has given the results for static lifetime of the fibre. Mauron *et al.* [118] predicted a lifetime of about 50 years at 2 % constant static strain for draw-tower gratings. Furthermore, from the known relation of static to cyclic loading, predictions can be made on the cyclic fatigue of the gratings. The relation between lifetime under static tensile testing with constant stress σ_0, and lifetime under sinusoidal cyclic tensile testing with mean stress σ_0, amplitude modulation κ, and period T_P, can be written as

$$\frac{t_{f_{cylcic}}}{t_{f_{static}}} = \left\{ \int_0^{T_P} \left[1 + \kappa \sin\left(\frac{2\pi}{T_P} \tau \right) \right]^n \frac{d\tau}{T_P} \right\}^{-1} \tag{2.25}$$

Here $t_{fcyclic}$ and $t_{fstatic}$ are the lifetimes under cyclic and pure static loading, respectively. This model predicts reduced lifetime for sinusoidal modulation of the applied strain. A modulation depth of 10 % reduces fibre lifetime by 60 % for standard fibres. Experimental verification of the predicted behaviour for draw-tower gratings has been shown in [118].

In summary, FBGs fabricated on a draw tower have outstanding mechanical performance. Their mechanical strength and static and cyclic lifetime can be compared with standard telecom fibres. Put side by side with electrical strain gauges, FBGs posses higher maximum loading capacity and several orders of magnitude higher strength. In automotive and aerospace applications with maximum strain levels up to 1 % , high load frequencies and high number of load cycles, FBGs are superior to electrical strain gauges. Not only for their good mechanical performance offer draw-tower gratings the best choice for sensor gratings. The draw-tower technology offers the possibility for mass production and therefore a high low cost potential of the fabricated gratings. Furthermore, this fabrication process offers almost free choice of the

fibre coating. The fibre coating itself is of importance for sensor application, as discussed in the next section.

2.7 FIBRE COATING

A number of requirements which the coating has to fulfil in order to be used in fibre sensor applications have been set in [124]. These requirements are:

1. There should be high adhesion for the coating on the glass-surface, as environmental forces have to be transferred through the coating. As has been shown in push-out experiments, not only are there great differences in the adhesion between polyimide and acrylate coatings but also disparities between two differing polyimide coatings [125]. Moreover, the coating has to transfer the forces without creeping or slipping.

2. The fibre strength has to be warranted even in humid and harsh environments. The coating also affects the stress corrosion of the optical fibre and the optical attenuation (microbending losses).

3. The required temperature range extends the range of telecom applications. Typical coatings for standard telecom applications can be used between –50 to +85 °C. This range is not sufficient for many sensor applications e.g. in aerospace systems.

4. The material properties of the coating (Young's modulus, thermal expansion coefficient, coating thickness) have to be chosen individually for each application. For example, when bonding FBG sensors on the surface of structures, it is important to make sure that the modulus of the fibre coating is sufficiently high to transfer the strain being measured into the core of the fibre sensor over a certain bonding length. This procedure is comparable to the processing by electrical strain gauges. Another example for the application of FBGs is their structural integration into modern fibre-reinforced composites. It has been shown that by the use of an appropriate coating, stress concentrations in the fibre-matrix interface can be minimised and the sensor response affected.

5. The change in the material properties due to temperature change and humidity has a negative impact on the sensor function. It has been shown that the thermal stress produced within the fibre by the coating can produce a strong non-linearity in the temperature response of the FBG with acrylate coating at negative temperatures. Taking into account the change in Young's modulus due to the glass transition of the coating, a substantial agreement between theory and practice has been found [126]. An appropriate fibre coating must not show this effect. Another reason for non-linear temperature behaviour is believed to be the water

absorption of the coating. Previoius work of the author showed the hysteresis in the temperature response of some FBGs from different suppliers with distinct polyimide coatings, whereas some FBGs did not show this behaviour at all. As FBGS written through the UV transparent coating have become commercially available, the temperature response of such a grating has been studied within the scope of this thesis. As seen in Figure 2.11 the result of the temperature test is disappointing. The grating shows dramatically non-linear and non-reproducible thermal characteristics. Two temperature cycles from room temperature over – 20 °C and + 80 °C and back to room temperature have been carried out. For every cycle hysteresis can be found. Effects as hysteresis and nonlinearities in the temperature response due to the coating have to be avoided for FBGs in sensor applications.

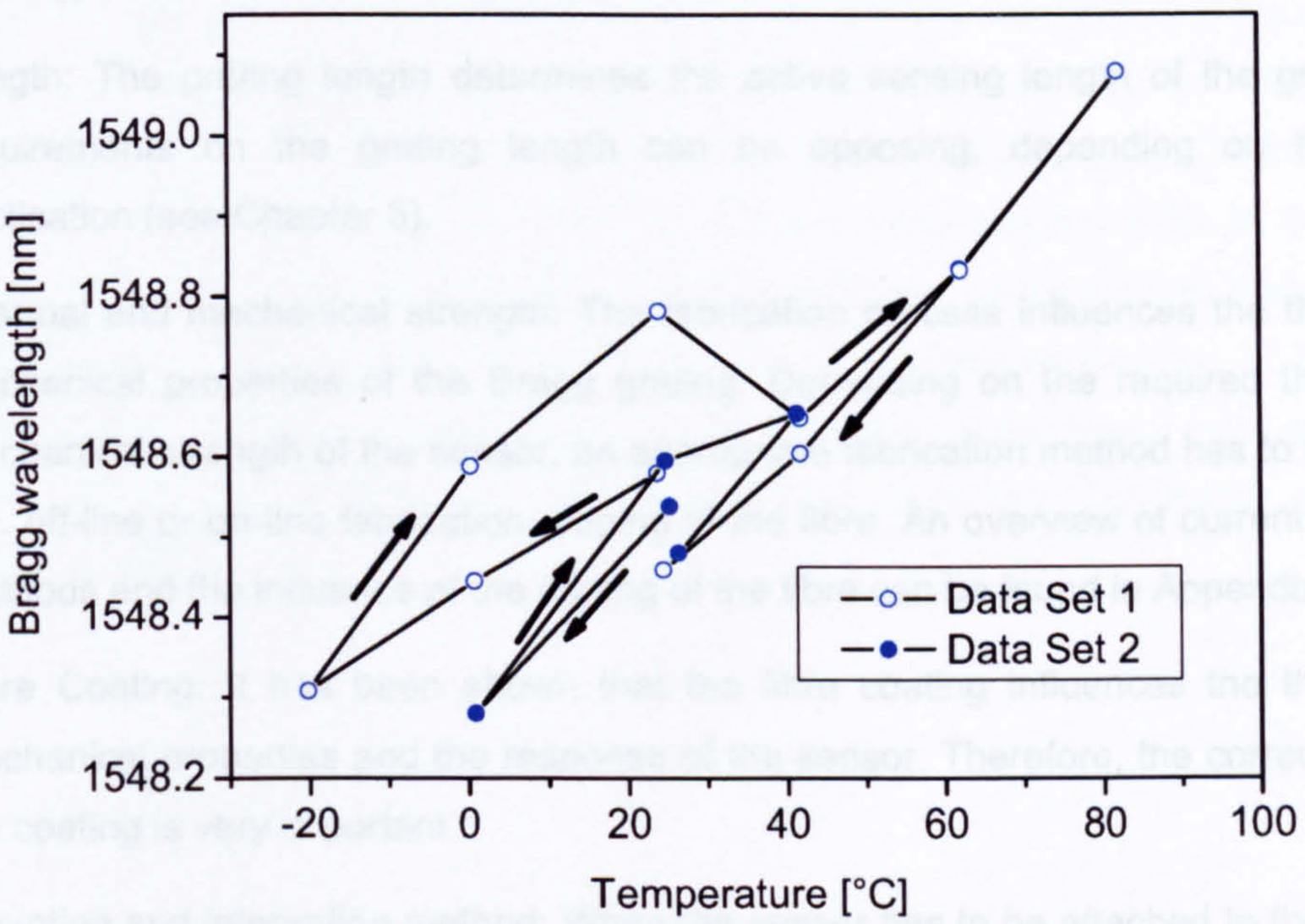

Figure 2.11: Temperature response of a FBG written through UV transparent coating.

Compared to the above described requirements set for coatings in strain-sensing applications, polyimide and *Ormocer*® are the materials with the greatest advantages. *Ormocer* (organically modified ceramics) is a polymer-based material which was developed by the *Fraunhofer Institute for Silicate Research (ISC)* in Wuerzburg (Germany) at the beginning of the 1990s. Compared to polyimide, it has a higher adhesion on glass and - as a main advantage – it can be UV-cured. This is a valuable benefit for the on-line fabrication of Bragg gratings on the draw-tower. It has been reported that using Bragg gratings with a special *Ormocer* coating, the effect of water absorption and the corresponding hysteresis in the temperature response can be dramatically decreased. FBGS available on the market with their index modulation written through UV transparent coating show high nonlinearities in their thermal response. A coating optimised for UV transparency seems not to be suited for high performance sensing applications.

2.8 CONCLUSIONS

This chapter has introduced the fibre Bragg grating as an innovative fibre optic sensor. After a short introduction into the theoretical and technological background of fiber Bragg gratings, their physical properties have been discussed with respect to sensing applications. The most important parameters which have to be considered before using the fibre Bragg grating as a strain and temperature sensor have been made out. These are:

- Reflectivity: Depends on the fibre optic interrogation unit and the optical network topology.
- Length: The grating length determines the active sensing length of the grating. The requirements on the grating length can be opposing, depending on the sensor application (see Chapter 5).
- Thermal and mechanical strength: The fabrication process influences the thermal and mechanical properties of the Bragg grating. Depending on the required thermal and mechanical strength of the sensor, an appropriate fabrication method has to be chosen, e.g. off-line or on-line fabrication, doping of the fibre. An overview of current fabrication methods and the influence of the doping of the fibre can be found in Appendix A.
- Fibre Coating: It has been shown that the fibre coating influences the thermal and mechanical properties and the response of the sensor. Therefore, the correct choice of the coating is very important.
- Mounting and integration method: When the sensor has to be attached to the structure, either by surface mounting or structural integration, care has to be taken to ensure correct strain and temperature transfer from the structure under investigation to the Bragg grating sensor.

3 FBG SENSORS FOR LOAD MONITORING

The continuous monitoring of structural loads plays an important role in HUMS. The knowledge of structural loads is also an important parameter in the characterisation of the structure during the design and development phase. Measuring structural loads is therefore a basic engineering need, particularly in aerospace. The chapter gives an overview of the standard load measurement techniques in today's applications. The fibre optic Bragg grating is introduced as an alternative sensor element that is capable to fulfil the same requirements as conventional methods, but provides additional advantages. A practical sensor layout utilising a backing patch for strain and temperature sensors is proposed. The strain transfer function of the backing material is studied in detail using an FE model. The proposed sensor layout has been build up and an experimental validation of the modelling results is presented. Concluding remarks are given in the final section.

3.1 BACKGROUND

Monitoring of structural loads allows the end-user to gain knowledge of the usage of the structure. This knowledge is important in all stages of the aircraft life. The design phase of the aircraft requires the maximum loads to be defined in order to fulfil the structural requirements. Before an aircraft goes into service all design criteria have to be validated using one aircraft for verification. This is done during a major airframe fatigue test, where all possible load scenarios that may occur during the aircraft life are simulated and structural responses are measured. Only if the aircraft passes this test, i.e. the design criteria are validated, will it receive airworthiness. The requirements on such a load monitoring system and the load monitoring state-of-art are described in section 3.1.1.

A major question throughout the further life of the aircraft is the actual amount of life consumed. Flight hours determined and being conventionally used as the parameter to characterise the amount of structural life spent are usually based on a loading spectrum defined during the design phase. However, the real loading spectrum might differ significantly from the spectrum

assumed during the design phase, as the aircraft is upgraded (e.g. new weapon systems, cargo instead of passengers) [11]. An answer to this point may be achieved by monitoring the actual loads directly or using flight parameters imposed on the aircraft using an in-flight monitoring system.

3.1.1 In-flight Monitoring and Structural Testing

Load monitoring of a structure or machine allows a measure of the structures or machines usage. Knowing the fatigue behaviour of the structural components this information can be combined with the actually measured loads in order to provide a measure of the fatigue life usage. From this many other information can be gained subsequently. In aircraft engineering this information can help for example to more effectively layout the inspection scheme of the structure [10, 12, 33, 127-129], to improve the design of the structure for forthcoming next generation aircrafts [11, 20], or to provide feedback on aircraft load spectra to the Regulatory Authority such as the Federal Aviation Authority (FAA) [130].

Loads play the major role in describing the operational environment of an aircraft. The structure is subject to a variety of loads. These are of course mechanical or aerodynamic loads resulting from flight manoeuvres and gusts but also loads resulting from environmental conditions, hazards or human error in general. The challenge associated with loads in the determination of the fatigue life of the structure is that loads cannot be predicted accurately. All the aforementioned loads vary significantly in their level, sequence and frequency of occurrence, depending on the actual usage of the aircraft. A possible solution to account for the negative effects of an uncertainty in the actual loads is to increase the monitoring effort [11]. An in-flight monitoring system has become an integral part of many structures, mainly fighter aircrafts [131, 132]. Today most of the systems are based on monitoring strain or flight parameter sequences which are then used to derive an operational load sequence for the aircraft part under consideration. For the physical background of the stress-strain relations, see Appendix B.

Initial work on in-flight monitoring was performed by bonding strain gauges to selected areas in the aircraft and measuring strain sequences (see Figure 3.1). The use of strain gauges directly correlates with the established techniques being used in major fatigue or static tests during the design phase. The requirements on the in-flight monitoring sensors in an operational environment are considerably higher than those compared to a laboratory environment. The development of improved bonding techniques, advanced electronics and signal processing tools as well as improved sensors, enabled the installation of in-flight systems. Strains are usually measured and stored in a data acquisition unit. Within a next step, the strains are then converted to stresses and a detailed fatigue life evaluation for the last flight and the overall flight history of the aircraft can be performed. However, as no sensor can assure 100 % reliability and

the complexity of a systems increases with the number of its components, the overall reliability of the monitoring system goes down. Furthermore, any extra sensor means more weight for the aircraft as not only the sensor but also the interrogation system including all the wiring has to be installed on-board the aircraft. This is a major drawback particularly for electrical strain gages.

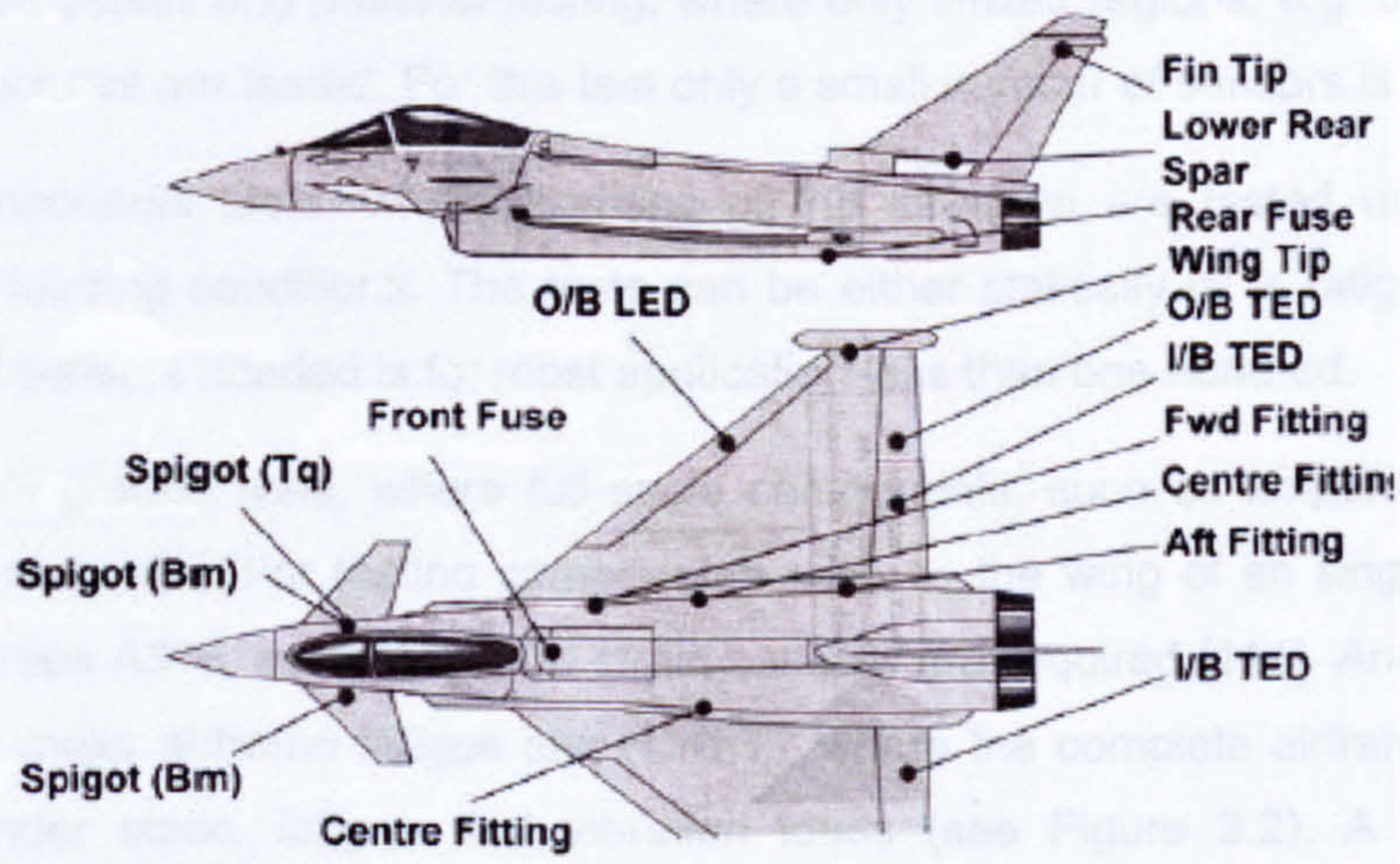

Figure 3.1: Strain gauge installation on a Eurofighter Typhoon aircraft [12].

Due to the above mentioned drawbacks of the strain gauge based monitoring system, an alternative system based on flight parameters has been established. Flight parameters are obtained from sensors already built into the aircraft. These sensors measure for example speed, altitude, acceleration, air data, pressure, and many other parameters. Flight parameter systems have proven airworthiness and are thus widely accepted. As for the strain gauge, the information obtained from flight parameters is used to calculate loads. However, the flight parameter approach relies on the accuracy of calibration data, in which the relation between structural loads and the flight parameter has been obtained. Thus, the optimum result which can be achieved using a flight parameter system is a load sequence that is identical to a load sequence measured with strain gauges. From this point of view, a flight parameter system clearly is not an optimal solution.

Before any structure goes into service it has to be certified by the relevant authorities. To get the admission several structural tests have to be passed in order to demonstrate the appropriate design and functionality of the structure. This is true for all kind of structures, especially within aerospace application, where failure of the structure could have catastrophic consequences. Structural testing is also required within the manufacturing phase of an aircraft in order to validate the predicted loads used during the design phase of newly developed or modified aircraft structures. The load spectra used for structural testing are also used to set-up

a maintenance schedule to monitor the fatigue life consumption of the structure. Load monitoring plays an important role during the test and qualification phase of the structure. Several types of structural tests can be identified which are usually performed to develop and/or certify aerospace structures. These are [133]:

- *Specimen details and material testing*, where only limited regions, e.g. critical locations of real structures are tested. For this test only a small number of sensors is required.

- *Sub-components tests*, where portions of the structure are tested under simple or combined loading conditions. The tests can be either statically or in fatigue cycles. The number of sensors needed is for most application less than one hundred.

- *Full scale ground tests*, where full scale components, such as empennages, wing or fuselage are tested. For testing components such as the wing of an single-aisle aircraft like the Airbus A318, more than 800 strain sensors are required [114]. Another important test is the major airframe fatigue test (MAFT), where the complete airframe is tested on ground under static, fatigue and vibration loads (see Figure 3.2). A load spectrum representative of the assumed real life is applied to the structure. The number of sensor installations increases with the size of the aircraft. For example in order to equip a modern large aircraft such as the Airbus A340/600 a number of 2000 up to 3000 strain sensors is required. Figure 3.2 schematically shows a Tornado aircraft prepared for the MAFT. The structure is equipped with all the necessary devices to launch the required loads into the structure.

- *Structural flight test*, where components or the whole airframe is tested in flight under loads coming from specific points of flight envelope. Component tests are usually performed on a specific aircraft specifically prepared and instrumented. The number of sensors for flight testing is reduced compared to ground testing. Yet, still several hundred sensors can be required for large scale testing.

Present instrumentation for large scale structural loads testing is based on electrical strain gauges. For specimen details testing other methods such as the photoelastic technique or holographic interferometry can be applied. These methods are briefly presented in section 3.2.

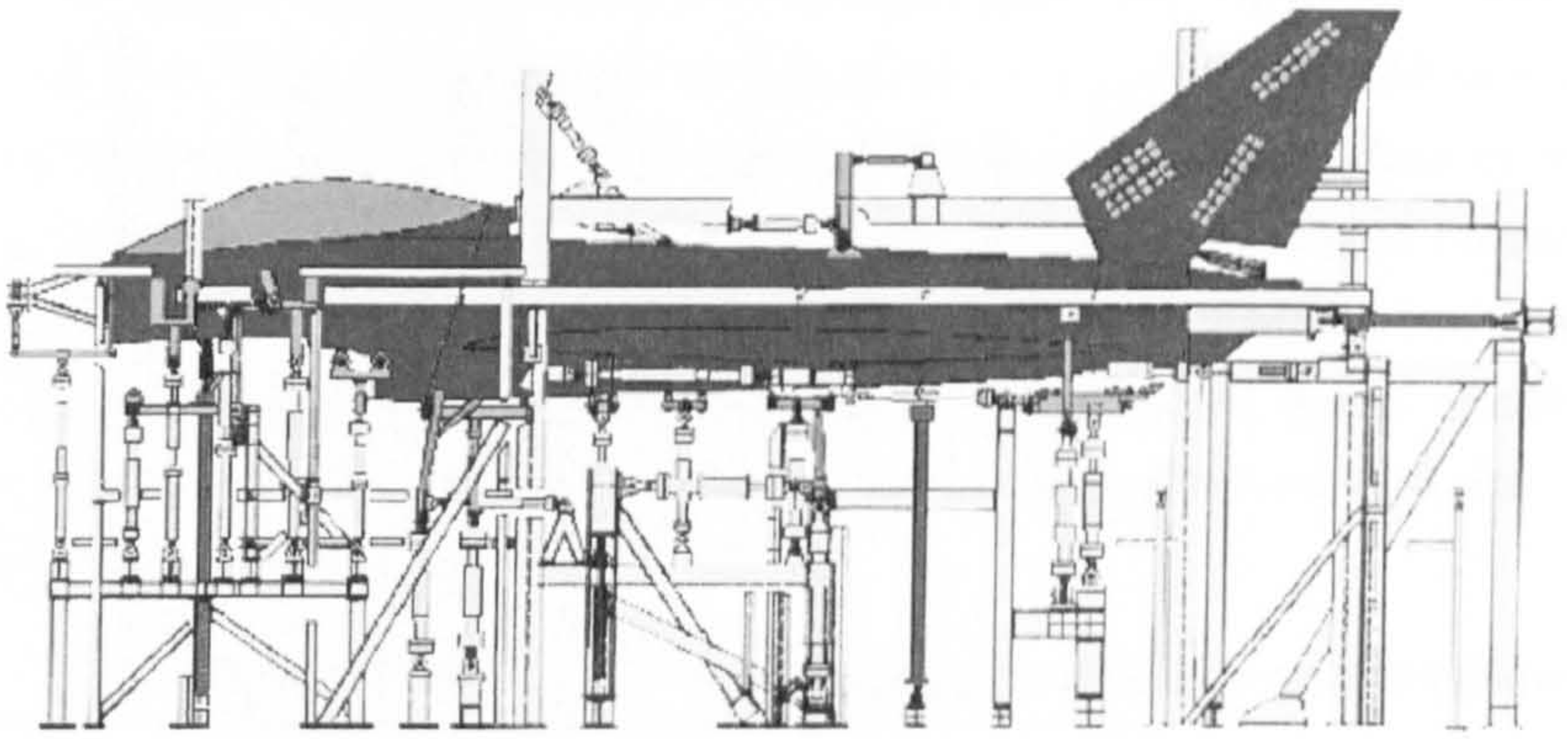

Figure 3.2: Major Airframe Fatigue Test (MAFT) for a Tornado aircraft.

3.2 Conventional Methods

In this section an overview of common methods for measuring strain is given. Their suitability for implementation into a load monitoring system especially into an in-flight monitoring system is examined. Special emphasis is on the electrical strain gauge, since it is the most widely used sensor in aerospace and automotive applications.

3.2.1 Overview

The photoelastic or photostress method is one of the major techniques used in experimental strain analysis. It uses the effect that for photoelastic materials, any elastic deformation of the material changes its optical properties, namely the refractive index. This change in the refractive index will also influence the state-of-polarisation if polarised light is used to illuminate the material. Optical instruments such as a polariscope can measure how much the state-of-polarisation is changed due to the presence of a stress field acting on the photoelastic material. From these measurements the strain field can be derived. Although the photoelastic method is limited to photoelastic materials, the deployment of photoelastic coatings being bonded on the structural component assures that virtually any test part regardless of its shape, size or material composition can be examined. In practice, a thin sheet of photoelastic material is attached to the surface of the structure under investigation. When the structure is loaded, the photoelastic coating will be deformed, as is the surface of the structure, and a strain field will be developed inside the coating. This strain field can then be observed using an appropriate optical

instrument, such as the polariscope. One of the advantages of the photoelastic method is that it provides a full-field strain distribution of the structure. It is non-destructive and can directly measure the strains on the surface of the structure. However, as the surface of the structure has to be accessible and even be modified, e.g. a photoelastic layer has to be bonded to the structure, this method will not work for in-flight monitoring of complex structures. In addition, the optical instrument that takes the measurement can be thought of as a kind of camera, which means that there must be no objects between camera and structure, and the size of the structure must be covered by the camera.

Another important method is holographic interferometry. Holography is a technique to record and reconstruct optical wavefronts. This can be used to compare wavefronts of one object recorded before and after the object has been loaded. The deformation of the structure due to the loading will change the wavefront and the corresponding strain field can be calculated. The holographic method requires the illumination of the structure with coherent light. Static and dynamic displacement measurements can be taken for any surface that reflects enough light to produce interferometric changes in the recorded wavefront. The method shows the same advantages as the photoelastic method being a non-destructive method and providing a whole-field displacement measurement. In contrast to the photoelastic approach no additional coatings are needed. But as for the photoelastic technique no object is allowed between interferometric measurement devices and the structure under investigation and the size of the structure is limited to the viewing area of the camera device.

3.2.2 Electrical Strain Gauges – Principle of Operation

The electrical resistance strain gauge (ESG) is a metallic or non-metallic resistance element, whose resistance varies in proportion to the amount of strain. Three kinds of resistance type strain gauge are popular for today's experimental strain analysis. These are [134, 135]:

- *Foil strain gauges.* Foil gauges are produced by etching or cutting the desired gauge pattern into a thin sheet of metal foil of an appropriate alloy. In practice, most often a several micrometer thick foil resistor of Cu-Ni or Ni-Cr alloy is used. These gauges feature accurate size and uniform characteristic through photo-etching technology. Together with a versatility in producing different strain gauge configurations, this makes the foil strain gauge the most popular tool used for strain measuring in general.

- *Wire strain gauges.* These gauges use a resistor wire, typically of 13-25 micrometers in thickness, for the resistance element. Although most of the strain gauges used are foil strain gauges, the wire strain gauges is used for special application, e.g. measurements at very high temperature or as extra long size concrete measurement gauges.

- *Semiconductor strain gauges.* Semiconductor gauges differ in many aspects from the metallic foil and wire strain gauge. Their resistance element is formed by monocrystal such as silicon. The most important difference is their increased sensitivity with a gauge factor 10 to 50 times higher compared to metal gauges. This makes them suitable for detection of micro strains as well as of manufacturing high sensitivity transducers. Transducers are used to translate the mechanical quantity to be measure, e.g. pressure, force, acceleration, into a surface strain of an elastic member. Strain gauges mounted on that member then provide an electrical output proportional to the applied force. Semiconductor gauges are however largely affected by temperatures and show high non-linearity. Their applications are therefore limited.

The basic principle of operation for metallic ESG is the change of electrical resistance with change in strain, found as [136]

$$\frac{\Delta R_{el}}{R_{el_0}} = k \cdot \varepsilon \qquad (3.1))$$

where ΔR_{el} is the resistance change and R_{el0} is the initial resistance of the conductor. The strain sensitivity k is also known as the gauge factor.

It is found that the gauge factor k is produced by two factors k_1 and k_2: the change in specific resistance of the conductor material and the change in the dimensions of the conductor. By definition,

$$k = k_1 + k_2 = \frac{d\rho_{sp}/\rho_{sp}}{\varepsilon} + (1+2\nu) \qquad (3.2)$$

where ρ_{sp} is the specific resistance and ν is Poisson's ratio of the conductor material. The gauge factor is approximately 2 in general purpose strain gauges.

Strain gauge structure

The typical layout of the basic ESG configuration is depicted in Figure 3.3. The resistance element is formed into a grid of a Cu-Ni alloy foil. It is placed on a carrier matrix of plastic or other material. This is the representative structure of a strain gauge which is ready for bonding on the surface of a measuring object. For surface bonding an adhesive is used normally.

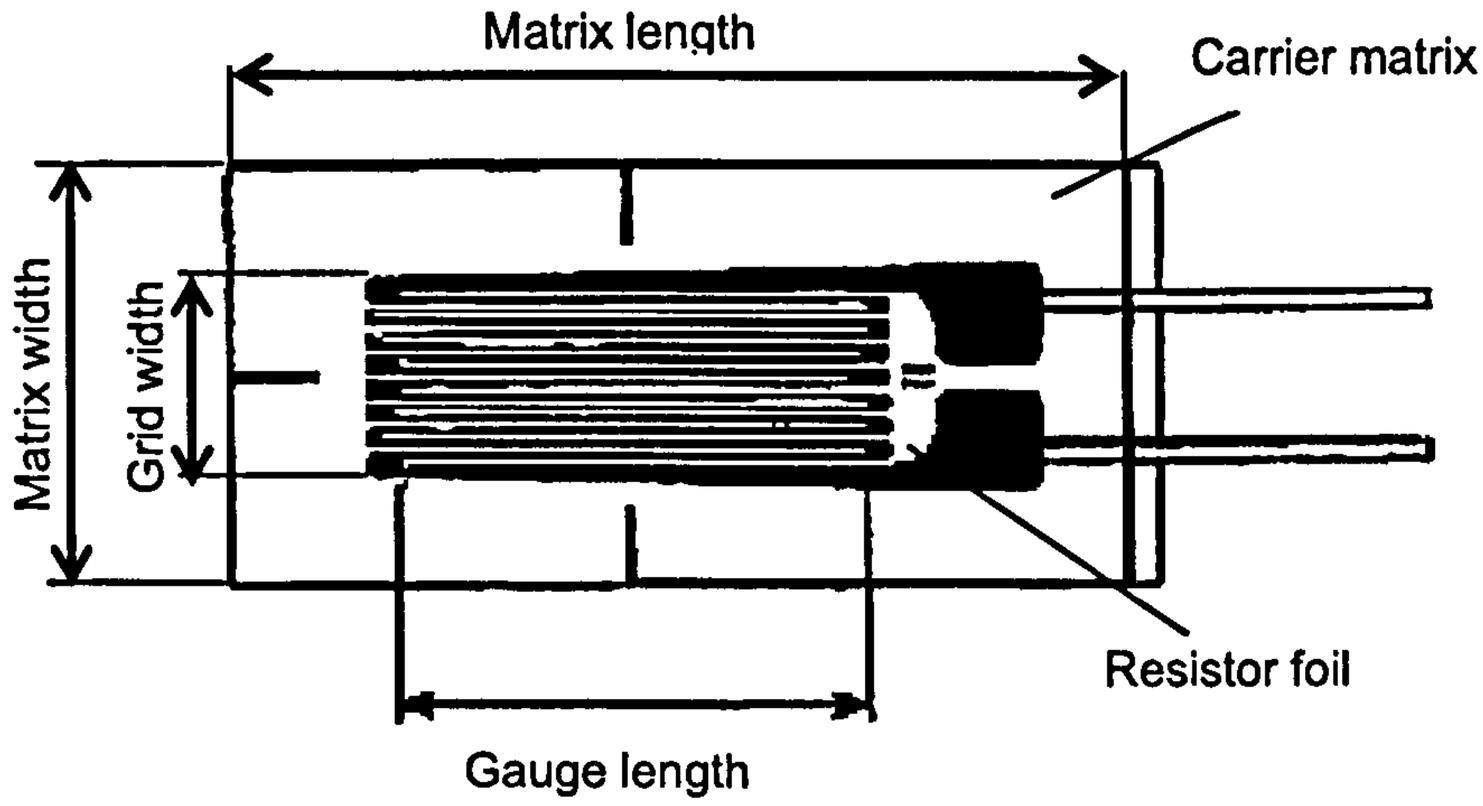

Figure 3.3: Typical strain gauge structure.

Strain gauge circuitry

The output of an ESG is a change in resistance as a function of applied strain. For a gage factor around 2 these resistance changes will be in the order of hundreds to a few thousand parts per million for strain levels normally encountered in experimental strain analysis. Resistance changes of this magnitude are much too low for direct indication in circuits of the ohmmeter type. For efficient measurement of small resistance changes a bridge circuitry, normally referred to as the Wheatstone bridge, is employed. Its output is usually amplified to such a degree as enough for indication and recording. The basic strain gauge bridge circuit is illustrated in Figure 3.4.

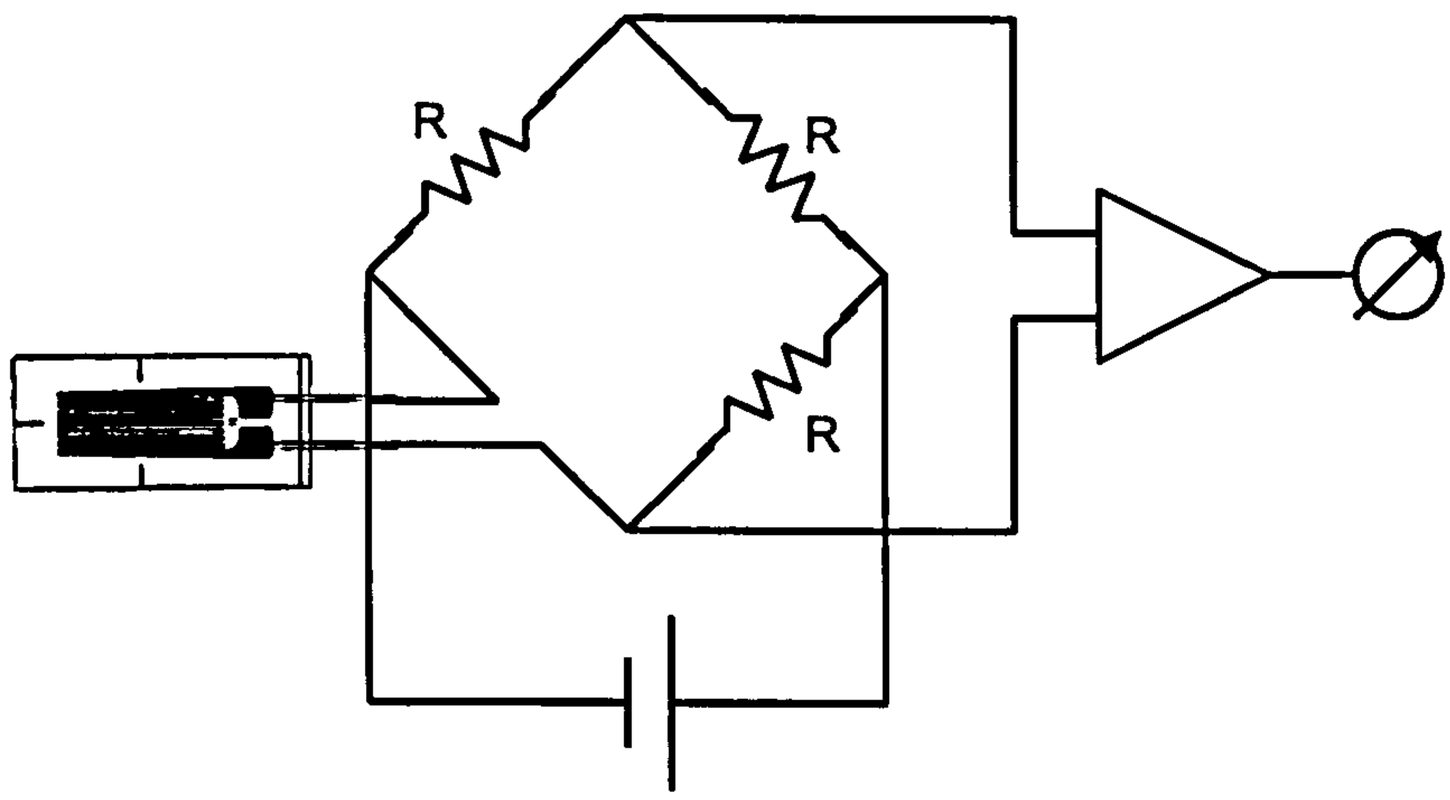

Figure 3.4: Basis strain gauge bridge circuit (Wheatstone bridge).

Strain gauge backing patch

Standard strain gauges consist essentially of the sensing grid in combination with a plastic material that makes up the carrier or matrix. That portion of the matrix which is underneath the grid is called the backing. Most foil gages have an additional top layer of insulation bonded over the grid and backing. This top layer is often called the overlay or encapsulating layer. The backing serves several important functions [137]:

- it provides a means of handling the foil pattern during installation;
- the backing presents a readily bondable surface for adhering the gauge to the test specimen;
- it also provides electrical insulation between the metal foil and the test object.

The important characteristics of the backing material are defined in terms of its shear modulus, creep, flexibility, and elongation capability. The shear modulus must be sufficiently high to transfer the structural strain faithfully to the sensing grid.

Generally, a carrier matrix uses polyimide or some other organic material. Polyimide has proven to be a tough and flexible carrier, and can be contoured to fit small radii. In addition, the high peel strength of the foil on the polyimide backing makes these gauges less sensitive to mechanical damage during installation.

Strain gauge bonding

It is very important to employ proper adhesive and bonding procedures to achieve strain measurements by using bonded ESG. The selection of a proper adhesive is strongly dependent on the carrier material, operating and curing temperatures, and the maximum strain to be measured. Ideally, the bonding adhesive for strain gauges would: form a strong permanent bond; be simple to mix and use in the field; have sufficient handling time to install a large number of sensors; possess sufficient strength and ductility for highest strains and operate properly from cryogenic to highest temperatures. In practice several compromises are necessary in selecting the appropriate adhesive. Since certain operating characteristics are more important than others in a given case, a large number of adhesive systems has been developed. The most commonly used bonding agents are cyanoacrylate adhesives, epoxy adhesives and ceramic-based adhesives.

For aerospace applications, cyanoacrylate adhesives are most widely used for bonding strain gauges. This is because they are suited for a large temperature range from cryogenic temperatures up to a few hundred degrees Celsius. Furthermore, during installation of the strain

gauges in the aircraft no thermal curing is allowed. Cyanoacrylates which cure at room temperature are therefore especially suited.

Strain gauge errors

Highly precise measurements can be achieved by using metal foil strain gauges. In practice, however, gauge performance is dependent on a number of external factors. Table 3.1 gives an overview of the parameters that should be considered to achieve high accuracy. A profound discussion of the relevant parameters can be found in [135, 136].

Table 3.1: Overview of common sources for strain gauge read-out error

Parameter	Possible reason for malfunction
Application	Strain gauge not suited for specific application, incorrect bonding or alignment of ESG, bad soldering points, bad insulation
Temperature	No temperature compensation, unisotropic temperature distribution, rapid change of temperature
Leadwire	Capacity and resistance of leadwire, insufficient insulation and shielding,
Limits	Violation of the mechanical or thermal limits, Violation of the duration limit (fatigue)
Environment	Not correctly considered pressure, humidity, chemicals, electric and magnetic interference, radiation
Structure	Faults, anisotropic characteristics

Temperature is the most serious and prominent source of error in static strain measurements using ESG. Temperature fluctuations will cause changes in the gauge resistance. This purely temperature induced resistance change causes an apparent strain. There are three basic methods of compensation or error correction available. The first option involves the simultaneous recording of both ESG output and gauge temperature with an additional temperature sensor. The second method is the use of a temperature compensating bridge circuit. The most attractive compensation method for general use involves self-temperature-compensated (S-T-C) gauges. S-T-C gauges display zero apparent strain when mounted on the corresponding type of material under test. However, S-T-C gauges are not perfectly compensated for a wide range of temperatures, due to the nonlinear behaviour of the thermal expansion coefficient and the temperature coefficient of resistance. The apparent strain is small only for a small range of temperature.

3.2.3 ELECTRICAL STRAIN GAUGES - CONFIGURATIONS

The basic set-up for ESG is a monoaxial configuration, where the sensing direction is parallel to its grid. In case the direction of principal stress is known, a monoaxial gauge bonded along that direction is enough to perform the measurement. However, for more complicated measurements other configurations are desirable. ESG are produced in a variety of different configurations. Figure 3.5 shows representative arrangements for biaxial and triaxial configurations.

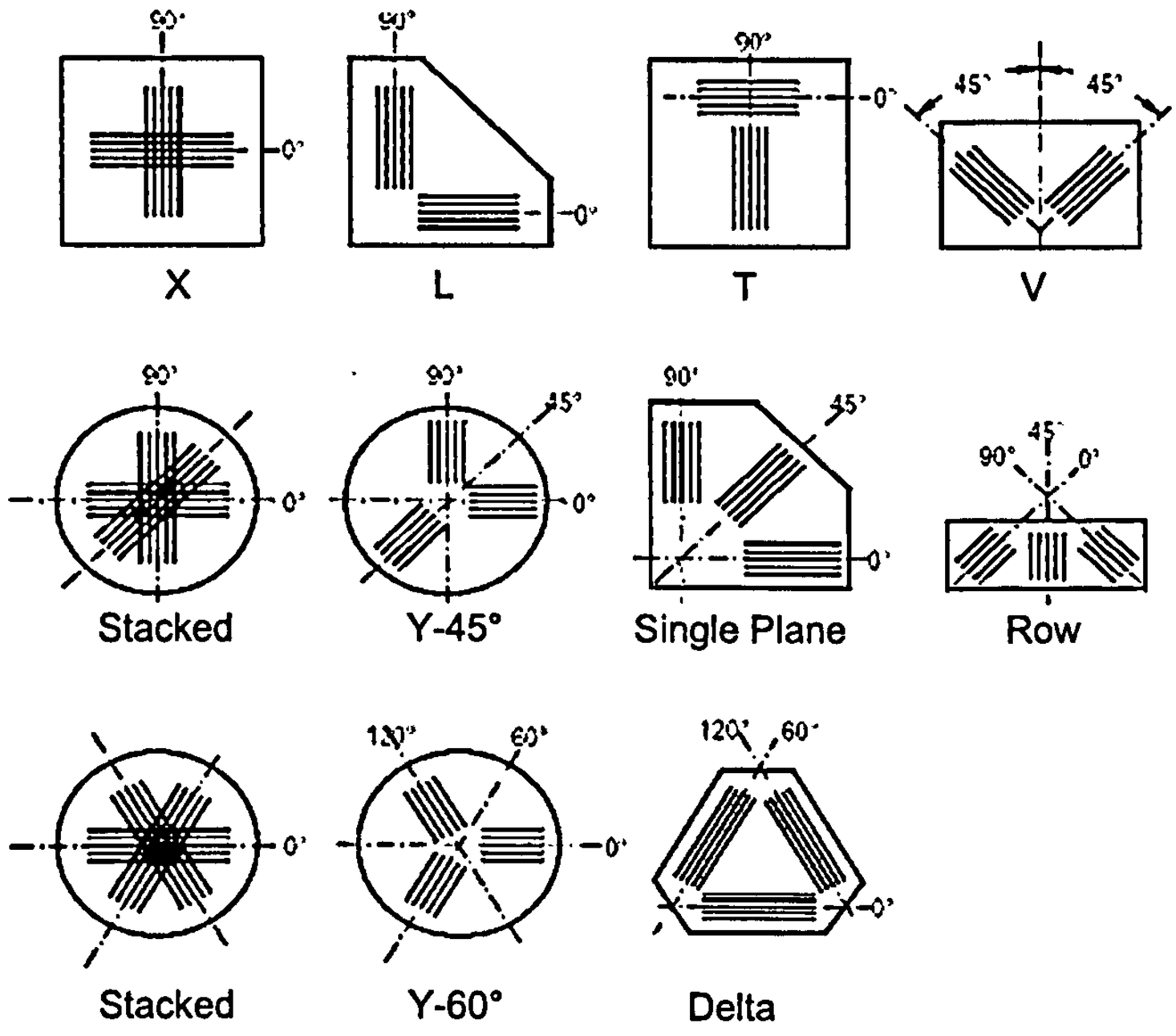

Figure 3.5: Example strain gauge configurations [136].

To obtain the complete state of strain on a structural surface. It is necessary to define the direction and magnitude of the principal strains. For the general case where the state of stress is unknown, this requires three separate readings at specific angles to each other. The most popular arrangements are the 60° delta or equiangular rosette and the 45° rectangular rosette. For both types analytical solutions to find the principal stresses from the measured strains along the axis of the rosette can be found. The advantage of the delta rosette is that the three readings are somewhat better defined or separated than for the 45° rosette.

3.3 IMPLEMENTATION OF THE BRAGG GRATING SENSOR

Fibre optic sensors are well known for measuring strain [138]. With respect to what has been said in the previous section, the ability of the fibre optic Bragg grating sensor to serve as a load monitoring sensor is discussed in this section. The fibre Bragg grating sensor has been introduced in Section 2.5 as a sensing element for both strain and temperature. As the FBGS is often called the fibre optic analogue of the electrical strain gauge, it is interesting to compare both techniques.

In general, the use of fibre optic strain sensors can give several advantages in comparison with conventional strain gauges, these are:

a) Lower weight of cabling (ρ_{glass}= 2.6 g / cm^3 versus ρ_{Cu} = 8.4 g / cm^3);

b) No electromagnetic interference;

c) More stable and higher strength than their metallic counterpart;

d) Embeddable into composite materials without altering the host structure;

The FBGS offers additional unique benefits even compared to other fibre optic sensors:

a) Superior multiplexing capabilities: more than 3000 sensors distributed in only four fibres have been realised [139].

b) High spatial resolution: a sensor distribution of five gratings within 5 mm fibre length, i.e. grating length of 1 mm and spacing of 1 mm has been fabricated by the IPHT, Jena, Germany [140].

c) Self calibration: as the Bragg-wavelength is an absolute not a relative measure.

d) Capability of mass production and therefore low cost potential.

These advantages make the fibre Bragg grating very attractive for both ground and flight testing, and an alternative to the existing electrical strain gauges, provided their performance is comparable to that of ESG. It could also help to install load monitoring systems on-board the aircrafts to overcome the limitations of a flight parameter based monitoring system.

Although the advantages of fibre optical sensors are significant, they still suffer from some drawbacks, which so far have obstructed their wide-spread use in real world applications, these are:

a) Handling of optical fibres is different to that of electrical cables. Special training is needed to gain experience of fibre sensor installation.

b) Fibre optic sensors and interrogation systems are still more expensive than their electrical counterpart. Especially for FBG sensors costs are ten times the costs for ESG [141].

c) Compared to ESG, fibre optic sensors are less mature. Fibre optic sensors are still restricted to fewer applications, which means not as much experience as with other sensors has been achieved.

d) Connecting optical fibres, especially single mode fibres as those required for FBG sensors, requires proper handling in order not to pollute the fibre optical interface.

3.3.1 FBGS INTERROGATION SYSTEMS

As for an ESG where the measurement of small changes in resistance is essential, the same is true for the wavelength measurements needed to interrogate the fibre Bragg grating. The resolution and accuracy of the strain measurements depend on the performance of the fibre optic interrogation system.

Requirements

A number of requirements on a load monitoring system have been listed in [142, 143]. These include:

a) number of sensors: 10 to 1000

b) interrogation frequency: 1 Hz to 1 kHz

c) accuracy: 1 % of maximum

d) maximum strain level: ± 2000 up to ± 3500 µstrain

e) temperature range (sensor) -54 to +100°C

f) airworthiness of system in terms of temperature, vibration, pressure, shock, etc.

These requirements can be translated into optical needs, depending on the wavelength of the system. The basic choice one has to make is the selection of the wavelength region. Two major regions have been established at 800 nm and 1550 nm. The above mentioned requirements translate into the respective wavelength regions as 10 pm accuracy and ± 1 nm optical bandwidth per sensor at 800 nm or 20 pm accuracy and ± 2 nm bandwidth at 1550 nm. The advantage for 800 nm systems is that less optical bandwidth is required and certain optical components, e.g. CCD (Charge Coupled Device) arrays are much cheaper than in the 1550 nm region. The big advantage for 1550 nm systems is they are compatible to telecommunication

applications. In telecommunication, 1550 nm are most attractive, because of the minimum optical attenuation in this wavelength region. This means all components used, profit from the emerging technologies and increasing prices of the large telecommunication market. Nowadays, most Bragg grating interrogation systems are settled in the 1550 nm region.

Concepts

A major advantage of FBGS over other strain measurement systems is its multiplexing capability. The number of measuring locations can easily be increased by networking of gratings in a serial or parallel layout or the combination of both. Several techniques are known to monitor a multitude of gratings by a single interrogation system in order to reduce the cost per sensing point:

- *Wavelength division multiplexing (WDM).* For every grating in the network an individual slice of the available optical spectrum is reserved. The Bragg wavelength of any grating remains within its slice, even at maximum strain and temperature shift. Therefore the number of gratings is limited by the operating conditions and the spectral width of light source and detection opto-electronics.

- *Time division multiplexing (TDM).* Another approach to identify the reflection of a specific grating is by the time, a light pulse takes to travel from the source to this grating and back to the detector. The run-time differs according to the distance between grating and interrogation system. If every grating is placed at a unique distance, all the reflections of all the gratings arrive at different times at the detector. A drawback to this technology is the demand for high time resolution of the detector and the need for fast signal processing. Furthermore, a minimum distance between gratings is required [144].

- *Spatial division multiplexing (SDM).* In some applications, the monitoring of all the gratings at a time or within a short period of time is not a necessity. In this case, the gratings can be addressed sequentially. A set of fibres, each containing single gratings or groups of serially multiplexed gratings, are joined at an optical fibre switch, that connects one fibre after another to the interrogation system.

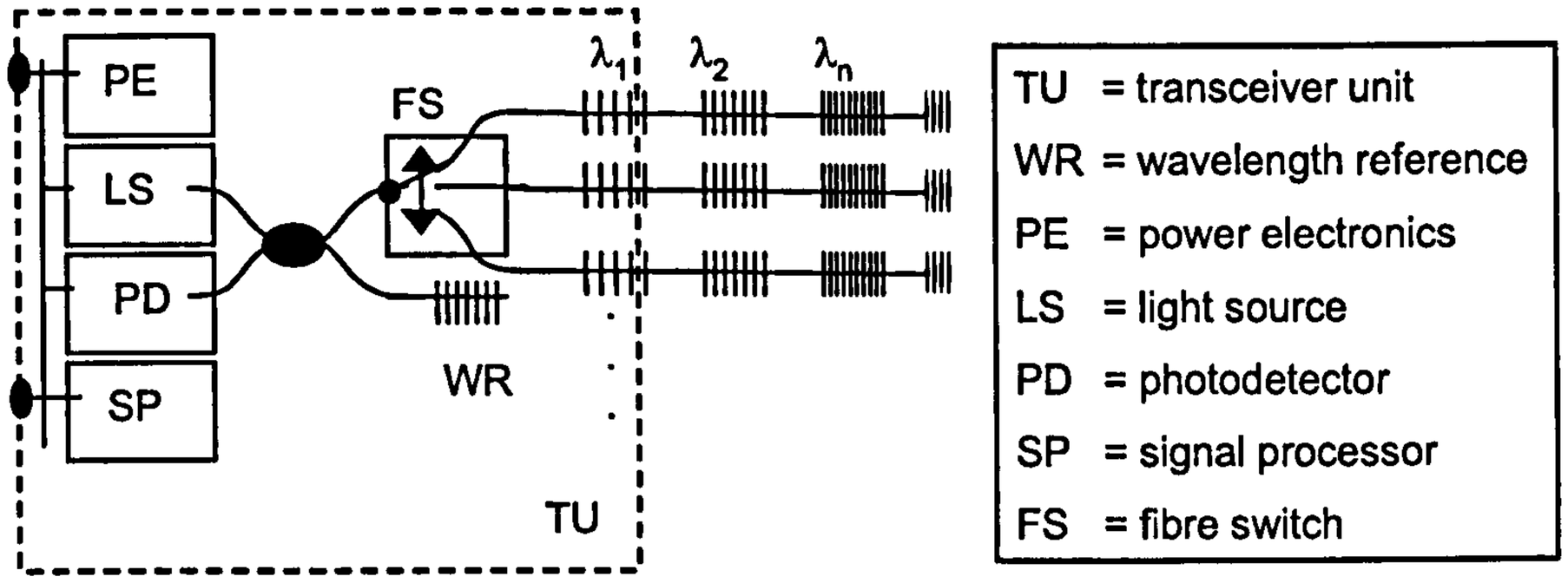

Figure 3.6: FBG sensor system consisting of a network of Bragg gratings (see page 49 for details).

A major component of the FBGS-system is the transceiver unit. The general concept of a transceiver unit is shown in Figure 3.6. The FBGS network shown is multiplexed by WDM at λ_1, λ_2, ..., λ_n and by SDM using a fibre switch (FS). The transceiver unit (TU) comprises a light source (LS), a photodetector (PD), a signal processor (SP), power electronics (PE) and the fibre switch. A wavelength reference (WR), e.g. a grating or a absorption cell, can be used for absolute wavelength measurements. The duty of the transceiver unit is, among others, the determination of the Bragg wavelength at adequate accuracy. Many different techniques have been published to perform this task [16, 17, 47, 112, 145]:

- *Ratiometric detection using passive filters.* This simple method is applicable only if the light spectrum consists of a single Bragg reflex at a time. If WDM is used in the sensor network, a dispersive element is needed to split the spectrum into single signals for an equivalent number of detection sub-units. A sub-unit incorporates two photo-detectors and a passive filter placed in front of one of them. The intensity of light measured by this detector is attenuated by the filter according to the wavelength. Consequently, the ratio of intensities at detector one and two is a wavelength representation and is independent of the absolute intensity of the light source and the degree of reflection at the Bragg grating.

- *Wavelength scanning using tuneable filters.* A different approach is the use of narrow bandpass filters with the ability of tuning the transmissive wavelength. Placed in front of a photo-detector, the filter scans the entire relevant spectrum. If the transmissive wavelength is equivalent to a Bragg reflex, the detector is illuminated and the wavelength can be derived from the adjustment of the filter. This method is well suited for WDM. Examples of the described filters are Fabry-Perot, acousto-optic and fibre Bragg grating filters.

- *Spectrometric detection.* Spectrometric detection features the simultaneous analysis of a wide spectrum and is therefore a preferred solution for WDM. The light emitted from the fibre end-face is projected to a CCD line array via a holographic grating acting as dispersion element. Consequently, every detector element can be illuminated by a specific wavelength only. And in reverse, the wavelength can be derived from the location of the illuminated element.

- *Interferometric detection.* In the interferometer the light returned from the fibre is split into two beams. Each of them is directed along a separate path before being recombined. The optical path of one beam is slightly longer than that of the other one which leads to an optical phase difference (OPD) at the recombination point. In case the OPD is a multiple of the Bragg wavelength, a maximum of optical power is seen by a photo detector placed at the output of the interferometer. By altering the OPD, the entire relevant spectrum can be scanned.

- *Wavelength scanning using a tuneable source.* Instead of using a broadband source and a tuneable filter, a tuneable narrow bandwidth source can be employed. The benefit as a much higher spectral power density, which allows the use of low reflective gratings or interrogation of remote fibre sensors.

Two fundamentally different concepts can be identified: broadband interrogation and tuneable laser based system. The broadband interrogation uses a broadband light source, e.g. LED or SLED, to couple light into the sensing fibre. Determining the reflected wavelength of the Bragg grating can be carried out using passive filter technologies or tuning filters. Concepts based on broadband light sources offer high interrogation frequencies and sufficient wavelength resolution. Furthermore, if the wavelength detection is done without tuneable filters, no moving parts are required which promises good life time performance. Systems based on tuneable lasers however, are favourable in terms of optical resolution. The spectral power density is much higher which means, also for very low reflective gratings high optical resolution can be achieved. The problem is a high interrogation frequency combined with a broad tuning range. Lasers that provide both are much more expensive than comparable systems based on broadband light sources. Yet, if high resolution is required and a complete spectral characterisation rather than just determining the reflected peak wavelength is desired, a tuneable laser is indispensable.

3.3.2 Strain Sensor

In Chapter 2 the sensor function of the FBGS has been defined as as

$$\frac{\Delta\lambda_B}{\lambda_{B_0}} = \left[1 - P^{eff}\right] \cdot \varepsilon_z^{s,m} + \left[\left(1 - P^{eff}\right) \cdot \alpha^s + \frac{1}{n_0}\frac{dn}{dT}\right] \cdot \Delta T \qquad (3.3)$$

where the structural strain ε_z^s is separated into its thermal $\alpha^s \cdot \Delta T$ and mechanical $\varepsilon_z^{s,m}$ strain components. Also, n is the refractive index of the fibre, α^s is the thermal expansion coefficient of the structure, and $(1\text{-}p^{eff})$ is the strain sensitivity of the FBGS comparable to the gauge factor k of the ESG.

FBGS bonding

To guarantee the strain-sensing function of the fibre-optic sensor, it has to be ensured that the surface of a structure being measured is able to transmit its dilation to the sensing fibre. Depending on the exact mounting or integration technique used, one has to investigate how the structure strain is transferred into the core of the fibre, in particular the material parameter (e.g. Young's modulus) and the geometry of the fibre coating can be used as an optimisation parameter. From a calibration perspective, it is desirable to find techniques where Equation (3.3) still holds, i.e. only the structure strain in the axial direction of the FBG sensor should be transferred.

At the *DaimlerChrysler* research laboratories a technique for bonding FBG sensors on the surface of structures was developed and presented in [32, 112]. This technique can be used to mount bare fibres on the surface of the structure. A mounting tool was developed to accurately bond the fibre onto the structure. After a careful selection of the adhesive, it is spread in a thin layer on the surface being measured. Subsequently the sensor is stamped onto the surface in the right direction. The mounting equipment guarantees the manageability of the fibre sensor, the mounting in the desired direction, and, in particular, a reproducible distribution of the glue between sensor and structure. The distribution was studied by examining several samples under a microscope and implemented in an FE model. As for ESG, the application of cyanoacrylate glues is often desirable because of their ease of processing and their optimised characteristics for strain sensor applications. It is essential that the glue does not surround the whole fibre, else birefringence effects could destroy the simple wavelength-strain relation (3.3).

Using a backing patch for bonding the fibre to the structure is known from the ESG and for FBGS from the literature [35]. In expansion to the direct bonding method, the use of backing patches was studied in more detail within the scope of this thesis and is presented in the following paragraph.

FBGS backing patch

In contrast to the electrical strain gauge the fibre can be bonded directly onto the structure, as no electrical insulation is necessary. However, a backing patch could be advantageous, in making the bonding procedure more practical. If the fibre is already placed on a backing patch, this patch could be simply glued to the surface and no additional care has to be taken concerning the surrounding of fibre by the glue. In addition, a backing could be used to prearrange three gratings to provide an optical rosette and to hold the sensor array together. A backing patch could also hold an additional sensor for temperature compensation, which can then be mounted in close distance to the strain sensor.

Polyimide is the material widely used for backing electrical foil strain gauges. It is therefore a logical choice to investigate the use of polyimide as a backing material for FBGS. The same requirements in terms of its shear modulus, creep, flexibility and elongation capability as for the ESG hold, see Section 3.2.2. Before presenting the results of the study on the backing patch, further developments on temperature compensation and fibre optic rosette configuration will be presented in the following paragraphs.

3.3.3 Temperature Compensation

Some applications require separate strain and a temperature sensor systems to obtain both the strain profile of the structure and its temperature profile. Also, knowledge of the temperature at the strain sensor location can help to overcome the temperature-strain cross-sensitivity, shown in Equation (3.3). As for the temperature compensation of ESG, several solutions to that problem exist [17, 30]. For a Bragg grating strain sensor network, the use of Bragg gratings to additionally measure temperature is an obvious choice. A temperature Bragg grating sensor requires a special setup to protect the sensor from the variety of environmental influences. For example, the sensor should be protected from structural strains and stresses, which would lead to a misinterpretation of the temperature sensor signal. Various setup technologies were studied to obtain a sensor with a reproducible and adjustable (over a certain range) temperature characteristic curve by choosing an appropriate composition of materials. Best performance was achieved when the whole setup was based on quartz glass with high mechanical stiffness. For this purpose, a Bragg grating sensor was mounted on a 40mm-long semi-quartz shell, which was first carefully cleaned, and then the fibre was glued onto the plate using the mounting technique as described in [32]. Covered with a second semi-quartz shell, the whole construction was enclosed in a metal tube, with special care taken to lower the mechanical strain transfer from the metal to the quartz shell. Finally, the ingress and egress of the fibre were sealed with silica glue. A picture of the housed sensor is shown in Figure 3.7. Gratings fabricated online at the draw-tower by the *IPHT* in Jena (Germany) with a special UV-curable coating (*Ormocer*®)

were used. The temperature response of these specially fabricated sensors has to be determined before they can be installed for the respective application. They are then ready for use as single temperature sensors or as temperature references for Bragg grating strain sensors. The remaining strain sensitivity of the temperature sensor fabricated using the above process reduces to 2-3% of the initial strain sensitivity.

Figure 3.7: Strain isolated fibre optic temperature sensor.

With the usage of a backing patch to mount the fibre optic strain sensor, it could be profitable to mount the temperature sensors on the backing patch, too. A special version of the above described strain isolated sensor adapted to installation on the backing patch, requires the modification of the sensor build-up procedure. Figure 3.8 shows how a combined strain-temperature sensor placed on a backing patch could look like. To the right the strain sensor is glued onto the backing material using a cyanoacrylate adhesive. The strain isolated temperature sensor is placed to the left. The fibre was glued into the semi quartz shell to be in perfect contact with the quartz. Strain isolation from the structure was achieved by mounting the quartz shell in an appropriate way onto the backing patch. In this case, only punctual gluing of one end of the quartz shell ensures no strain can be coupled from the structure over backing patch and quartz shell into the fibre. The sensing region of the fibre is in the middle of shell, away from the edge of the shell, where strains could be transferred from the bonding.

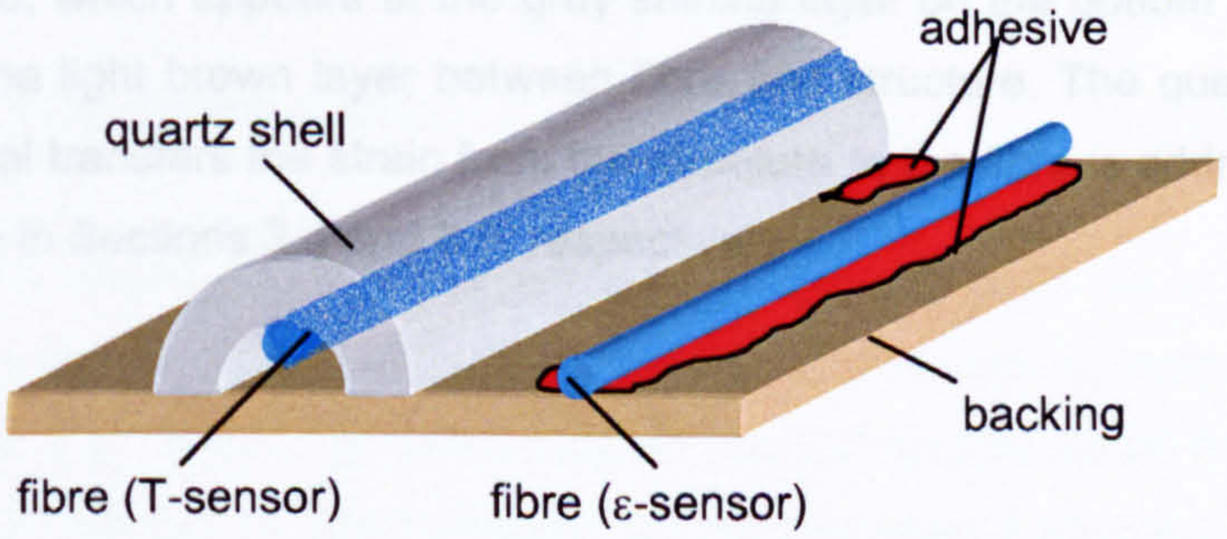

Figure 3.8: Combination of a fibre optic strain and temperature sensor on a single backing patch.

The use of a buffer material to fill the gap between quartz and backing patch could help to keep out moisture and contaminants. The buffer material should be of extremely low modulus for not transmitting any stress from the patch to the enclosed grating. Using a thermal coupling gel ensures the grating senses the correct temperature of the structure.

The big advantage of the proposed temperature sensor compared to other sensors presented in the literature is that the temperature sensor does not necessarily mean a dead end in the fibre optic network. Most temperature sensors suggested in the literature require the grating to be located at the tip of a fibre [146]. This means, one of the greatest advantages of the FBGS, the high multiplexing capability is sacrificed. Mounting the fibre in the proposed way on the quartz shell does not require a loose end of the fibre. Even if the fibre is subjected to strain, e.g. by fixing both ends of the fibre to the structure, the stiffness of the quartz as the carrier material minimises the corresponding strain levels. Data of both sensors, the strain isolated temperature sensor and the strain senor bonded a backing patch is shown in Figure 3.9. Figure 3.9a confirms the strain independent behaviour of the temperature sensors, with a strain isolation better than -14 dB. For a description of the experimental set-up see section 3.5.2. Figure 3.9b shows the temperature sensitivity for both sensors. The strain sensor has a higher sensitivity as it is bonded onto the aluminium structure. Most of the wavelength shift is the thermally induced strain of the structure. The temperature sensor is only slightly influenced by the thermal expansion of the quartz shell, as the fibre itself has similar thermal expansion as the quartz. Using Equation (2.18) and the parameters given in Section 2.5.5, the expected temperature sensitivities can be obtained as $24*10^{-6}$ 1/K for the strain sensor and $7.7*10^{-6}$ 1/K for the temperature sensor. The experimental results give $23*10^{-6}$ 1/K and $7.5*10^{-6}$ 1/K for the strain and temperature sensor, respectively. These results agree very well with the predicted values.

Figure 3.10 shows a photograph of the prototype strain-temperature sensor pad. The temperature sensor is shown on the left. The quartz shell and the bonded temperature sensor can be identified. The distribution of the glue (dark brown) at the fibre-quartz interface can be seen. On the right hand side the strain sensor is depicted. The pad was mounted on an aluminium structure, which appears at the grey shining layer on the bottom of the picture. The backing patch is the light brown layer between fibre and structure. The question of how good the backing material transfers the strain from the structure to the fibre is addressed theoretically and experimentally in Sections 3.4 and 3.5, respectively.

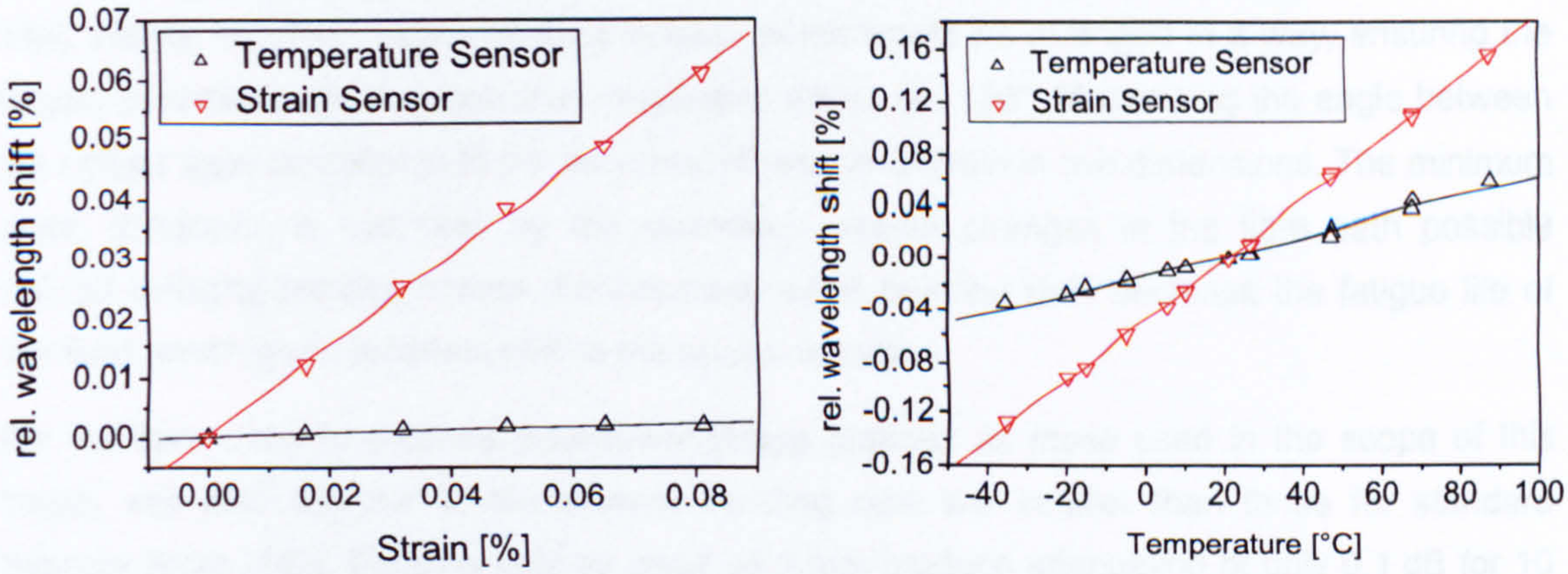

Figure 3.9: *Plot of relative wavelength shift of the strain isolated temperature and the strain sensitive sensor: a) plotted versus actual strain level as recorded using an ESG; b) plotted versus actual temperature.*

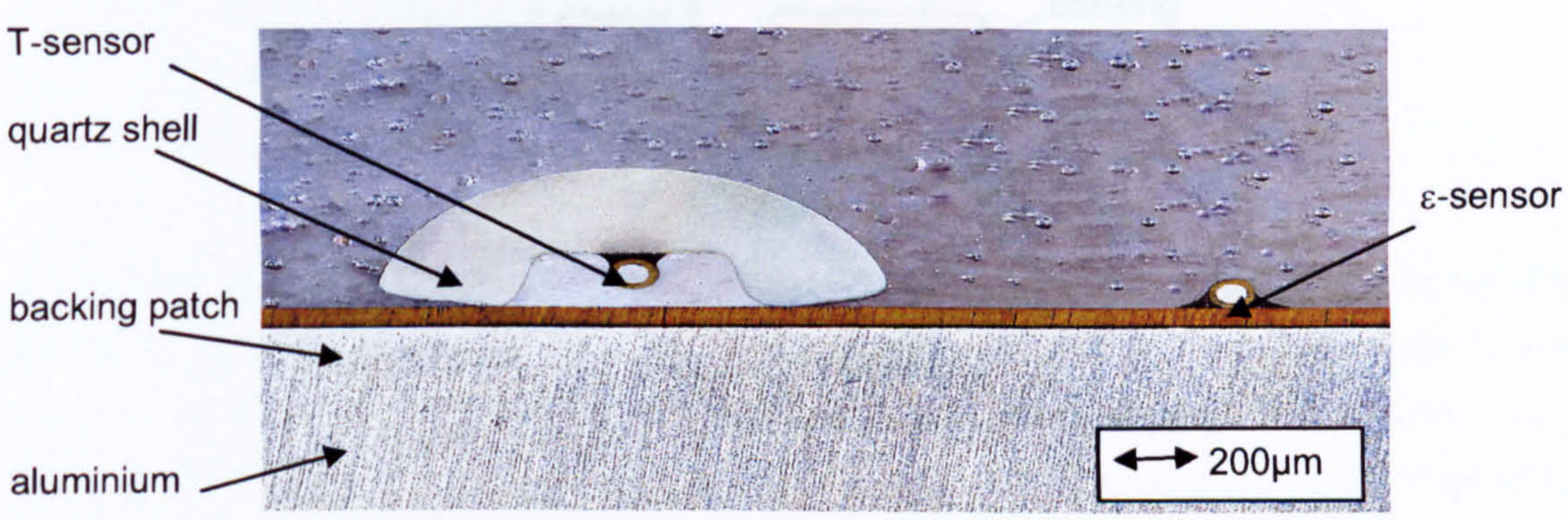

Figure 3.10: *Photograph of the prototype for a combined strain-temperature sensor pad.*

3.3.4 Rosette Type Configuration

The aforementioned combined strain-temperature sensor pad could be extended to a strain-temperature rosette by adding two more strain sensors on the backing patch. A possible layout is shown in Figure 3.11. Again the advantage of such a rosette would be the possibility of multiplexing several rosettes or other sensors, as the proposed temperature sensor does not produce a dead end of the fibre.

Several basic design parameters have been defined to build-up a fibre optic rosette [34, 64, 146]: Ideally, the three strain sensors in each patch would be arranged in a way, ensuring the largest possible angle between their respective axes., i.e. 120°. Maximising the angle between the sensor axes contributes to the accuracy of resolving strain in two dimensions. The minimum patch dimension is restricted by the maximum angular changes in the fibre path possible without inducing bending losses. Furthermore, small bending radii decrease the fatigue life of the fibre, which gives a certain limit to the minimum radius.

For the fibre used to produce draw-tower Bragg gratings as those used in the scope of this thesis, see also Chapter 2, the allowed bending radii are smaller than those for standard telecom fibres [102]. Bending radii as small as 1 mm produce attenuation of only 0.1 dB for 10 windings. In addition, encapsulating the sensor pad will not only prevent the fibres from moisture penetration, it could also stop the decrease in fatigue life due to small bending radii, as it can take over some of the bending induced loads of the fibre.

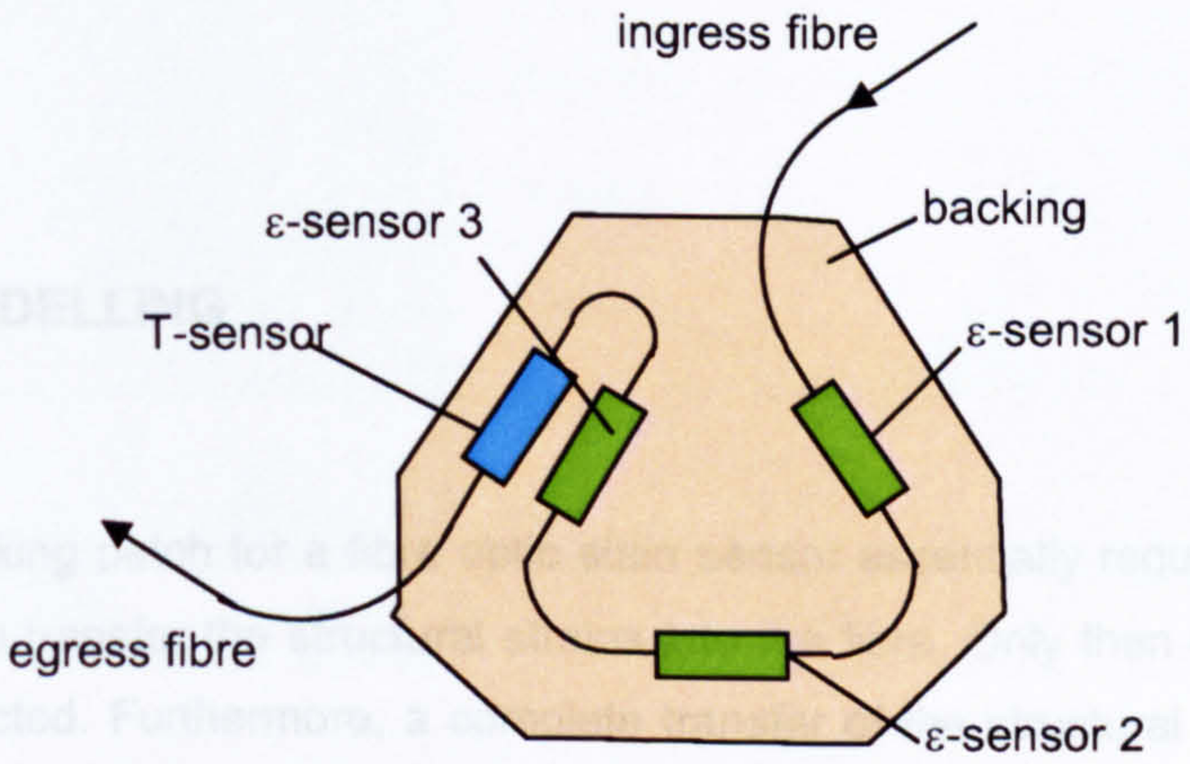

Figure 3.11: Proposed layout of a fibre optic rosette with temperature compensation and multiplexing capability.

Figure 3.12 shows a photograph of the encapsulated rosette with an ingress and egress fibre terminated by FC/APC connectors.

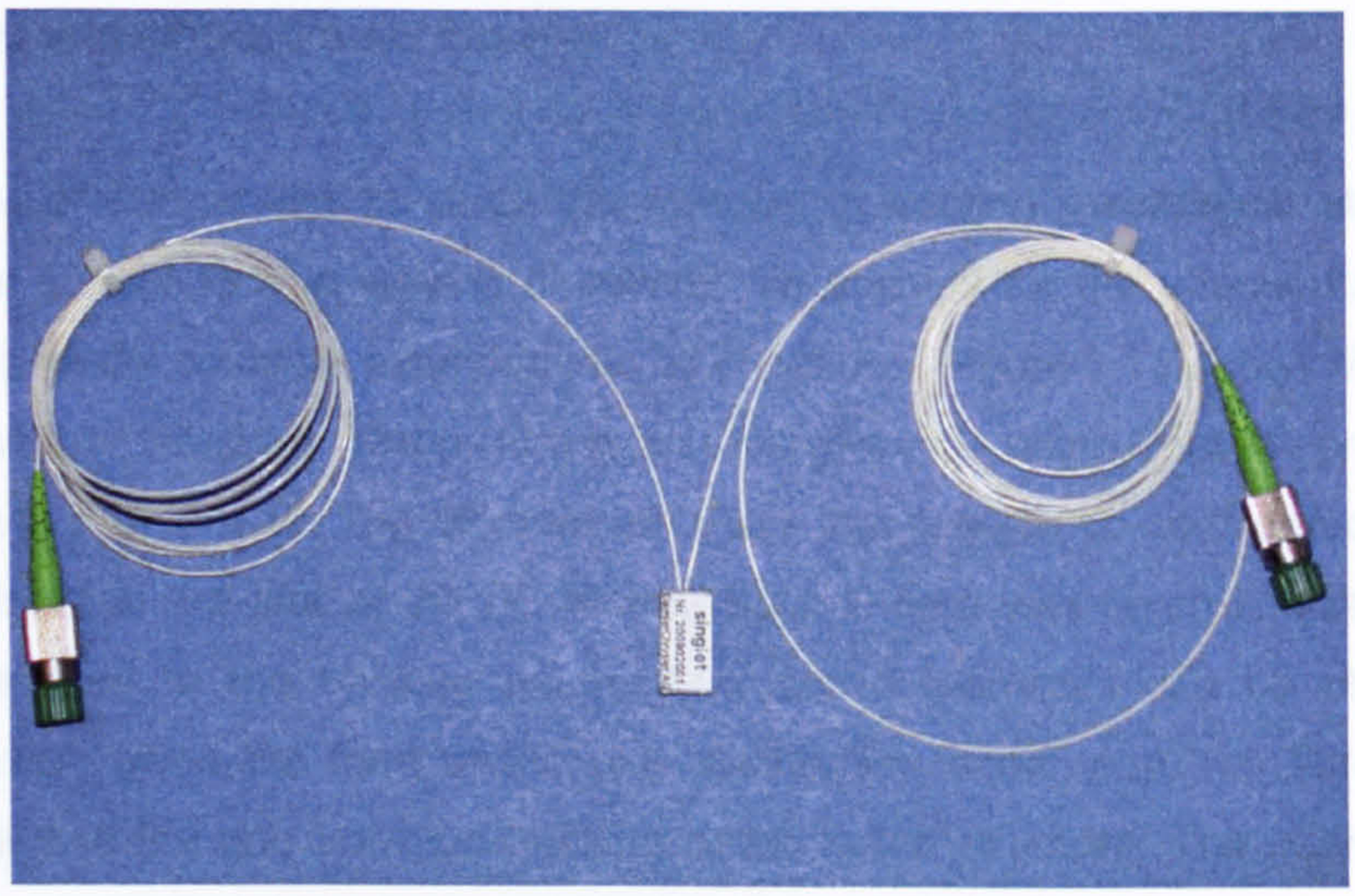

Figure 3.12: Photograph of the prototype of an encapsulated fibre optic rosette with two connecting fibres.

3.4 FE Modelling

The proposed backing patch for a fibre optic stain sensor essentially requires the ability of the backing material to transfer the structural strains into the fibre. Only then can a correct sensor response be expected. Furthermore, a complete transfer of the structural strain is required for Equation (3.3) to hold. If this equation no longer holds, a correction factor to the strain-sensitivity $(1-p^{eff})$ must be added. It can be assumed that the thickness and the modulus of the backing material play the important role. A stiff and thin material is expected to transfer strains much better than a soft and thick material. To study the influence of the material parameters, a FE (Finite Element) model was implemented and the material parameters were used as variables for a comparative study.

The aim of the FE simulations was to study the strain and stress response of the fibre under defined loading of the structure. The thickness and the modulus of the backing material could be variated in the model. In a joined research project, the model was implemented at the *IVW* (*Institute for Composite Materials*) at Kaiserslautern, Germany [147]. There, the commercial software ANSYS was used to create a parametric model of the sensor pad and to calculate the stress and strain along selected paths. The results of the study are presented in this section.

3.4.1 Modelling of the Strain Sensor

It was the aim of the project to study the transfer of varying mechanical strains from the structure to the sensor fibre in varying directions. To account for the effects due to Poisson's ratio, the basic model could be extended into all directions. Figure 3.13 shows the modelling of the complete sensor structure. The picture is an enlarged view taken from the prototype sensor pad, as shown in Figure 3.10. The different materials that have to be considered are displayed in different colours in the plot of the FE model. Special care was taken to exactly model the bonding of the fibre to the backing patch. A so-called meniscus can be observed in the photograph, which gives the form of the glue distribution underneath the fibre. The second bonding interface is the one from the backing patch to the structure. The geometry of all the layers was taken from the photograph and implemented in the FE model.

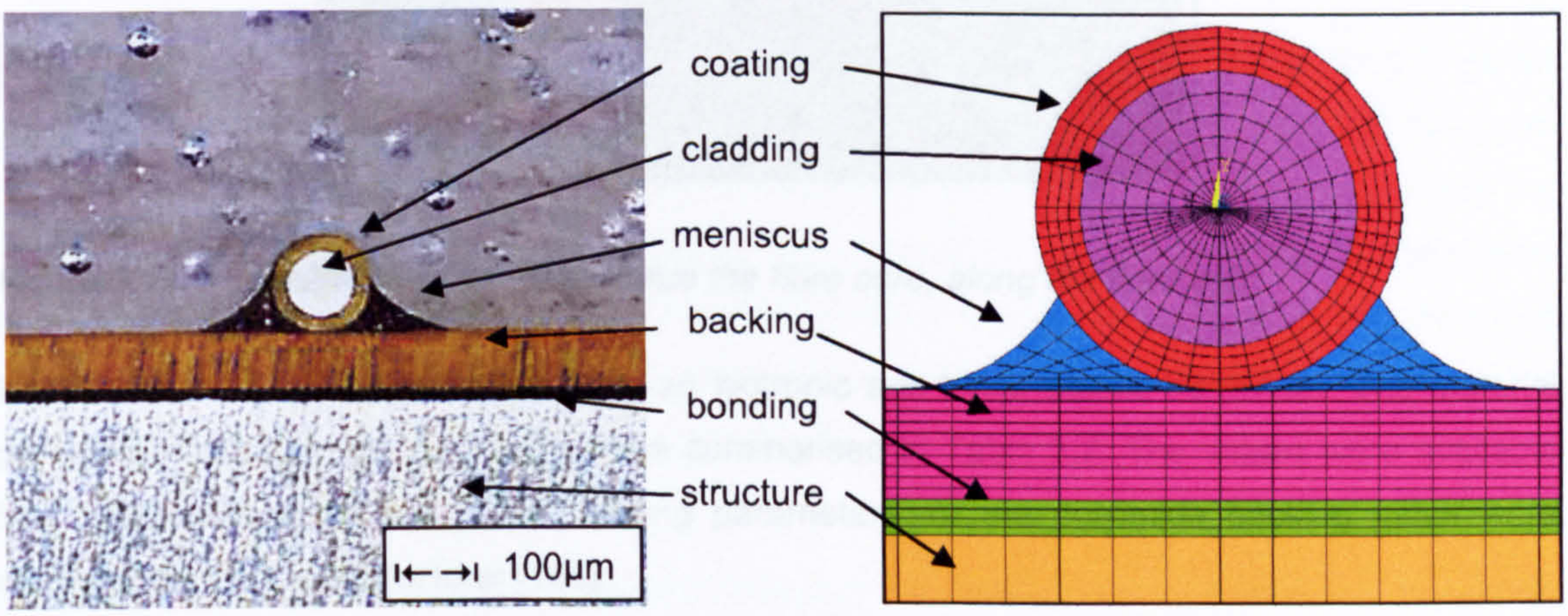

Figure 3.13: Photograph of the strain sensor on the backing patch and the derived FE model.

To define the geometry of the model, a Cartesian coordinate system was applied. The origin is in the centre of the fibre core. The axes Figure 3.14 are defined as follows:

- x-axis: transverse to the fibre
- y-axis: direction orthogonal to x-axis
- z-axis: parallel to the fibre axis

The basic model of the structure has a length of 5 mm along the z-axis. The core of the fibre has a diameter of 6 µm, the cladding's diameter is 125 µm and the coating has a thickness of 20 µm. The thickness of the interface from the patch to the structure is 16 µm.

The transfer of the strain was studied along different paths. The most important path shown in Figure 3.14 was considered in the presentation of the results. This path starts in the origin of the

coordinate system and extends from z = 0 to z = 5000 µm. It is essential for the response of the grating to determine the strain along this axis. As has been shown in [112], for the set-up under consideration the strains along the x-and y-axis are completely determined by Poisson's ratio of the fibre.

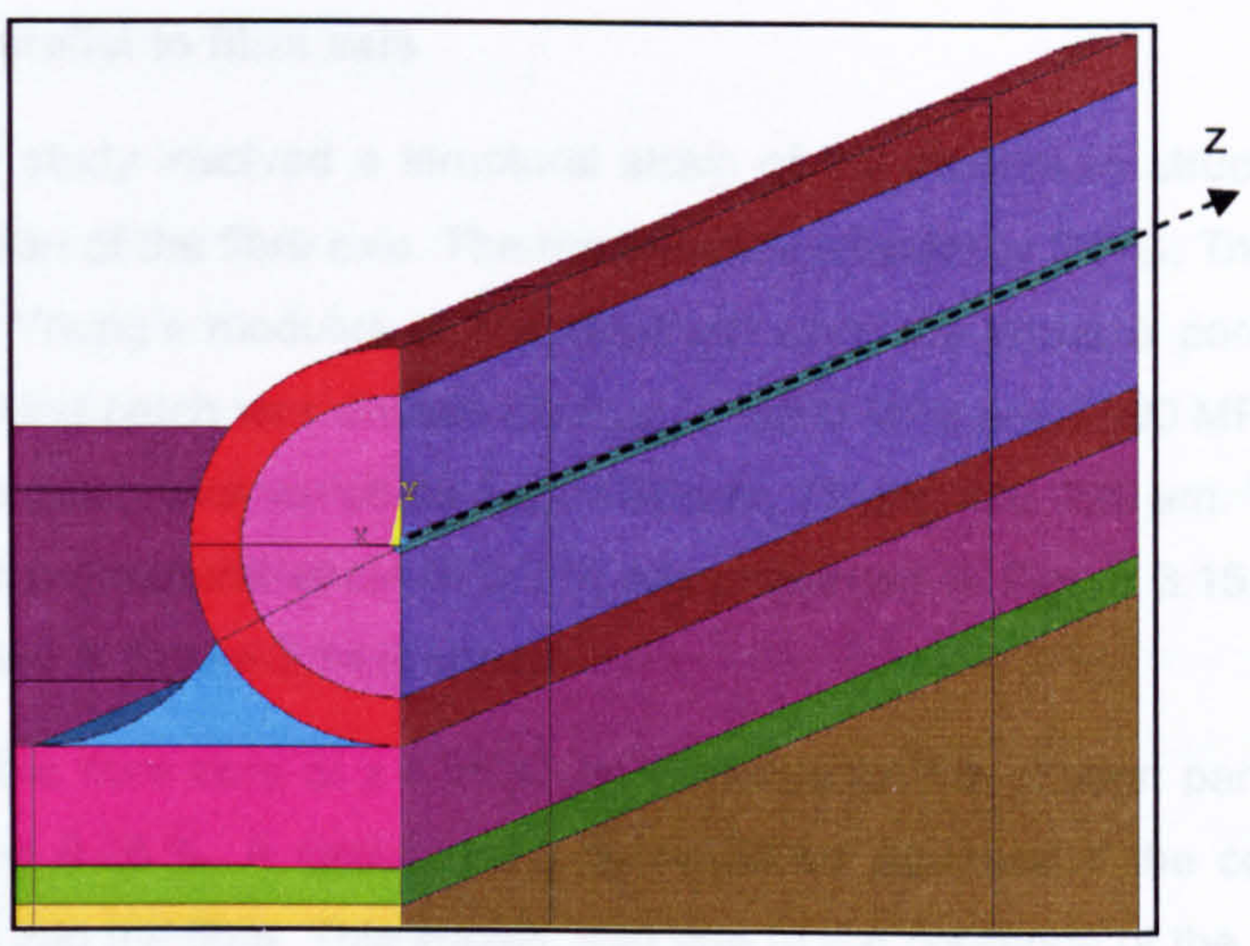

Figure 3.14: Definition of the path inside the fibre core, along the fibre axis.

It was assumed that all materials have an isotropic and linear elastic behaviour. The material parameters used for the calculations are summarised in Table 3.2. The values were available from previous calculations [112], missing parameters for the polyimide backing patch were obtained from the manufacturer [148].

Table 3.2: Overview of material parameters used for the FE modelling.

Component	$E_x=E_y=E_z$ [Mpa]	$G_{xy}=G_{yz}=G_{xz}$ [Mpa]	$\nu_{xy}=\nu_{yz}=\nu_{xz}$ [1]	$\alpha_x=\alpha_y=\alpha_z$ [10^{-6} K^{-1}]
Fibre core	73,000	31,200	0.17	1.34
Fibre cladding	73,000	31,200	0.17	1.34
Coating	3,000	1,110	0.35	20
Meniscus	3,451	1,280	0.35	54
Backing patch	E_{patch}	$E_{patch}/[2(1+\nu_{patch})]$	0.34	20
Bonding	3,451	1,280	0.35	54
Aluminium	70,000	26,000	0.35	23.5

where E is Young's modulus, G is the shear modulus, ν is Poisson's ration and α is the coefficient of thermal expansion.

Three different parametric variations were studied for two different directions of the structural strain and one for a variation of the temperature.

3.4.2 PARAMETRIC STUDY - STRAIN

Structural strain parallel to fibre axis

The first parameter study involved a structural strain of the aluminium structure of $\varepsilon_z = 0.3$ % parallel to the direction of the fibre axis. The temperature was set to 23 °C. The thickness of the backing patch and Young's modulus of the structure were the variable parameters. Young's modulus of the backing patch was chosen as $E_{patch} = 2000$ MPa and 3000 MPa. For each case the thickness of the patch was varied as $t_{patch} = 50$ µm, 75 µm, and 125 µm. The results of the parameter study for a structural strain of 0.3 % are presented in Figure 3.15, where the strain along the path defined in Figure 3.14 is shown.

The strain level in the fibre core at z = 2500 µm depends on the chosen parameters. It varies between 0.26 % and 0.28 %. A strain of 0.3 % would be assumed if the complete structural strain is transferred into the fibre. This shows, that due to the presence of the backing patch the strain has not been completely transferred. The degree to which the strain is transferred depends on the thickness and Young's modulus of the backing. An increase of the thickness obstructs the strain transfer, the same can be noticed if the modulus of the backing material is decreased. It can be concluded that for optimum strain transfer a thin and stiff backing patch is advantageous.

Looking at the strain levels for all the points between z = 2000 µm and z = 3000 µm reveals an almost constant strain level. Therefore, it can be concluded that the maximum possible strain has been transferred into the fibre. Any further elongation of the sensor fibre and the length of bonding would not affect the result. A bonding length of 2000 µm is enough to transfer to the optimum strain level – depending on the chosen parameters – from the structure inside the fibre core.

Structural strain perpendicular to fibre axis

The second parameter study involved a structural strain of 0.3 % perpendicular to the direction of the fibre axis. Figure 3.16 displays the results of the related parameter study. A structural strain of 0.3 % orthogonal to the fibre axis causes a strain parallel to the fibre inside the fibre core at z = 2500 µm between -0.09 % and -0.1 %. This is simply the structural strain that occurs inside the structure because of the contraction of the material. Only this strain component is then transferred into the fibre core. It is easy to calculate the structural strain along the fibre axis

by multiplying the orthogonal strain with Poisson's ratio. This calculation leads to a strain of 0.105 %. As the same restrictions of the transfer from the structure to the fibre as for the parallel strain are assumed, this is what one would expect.

3.4.3 PARAMETRIC STUDY - TEMPERATURE

The third parameter study involved only a change in temperature, but no mechanical strains. However, due to the mismatch of the thermal expansion coefficients of the various components, thermally induced strain are assumed to be observable. The influence of the thermally induced strains was studied at +80 °C and -40°C. Starting at a reference temperature of 23 °C, this means an increase in temperature of 57 °C and a decrease of 63 °C, respectively. Young's modulus of the backing patch was kept constant at 3,000 MPa. The thickness of the patch was varied as t_{patch} = 50 µm, 75 µm, and 125 µm. Figure 3.17 displays the results of the parameter study for different temperatures. The strain level along the same path as for the previous parameter studies was examined.

An increase in temperature results in thermally induced strains for all of the components. The dominating component is the aluminium structure, it is a high coefficient of thermal expansion and a high modulus. For this component, the thermally induced strain can be calculated from the thermal expansion coefficient and the temperature change. A thermally induced strain of ε_{therm} = 0.13 % is found. The simulation shows at z = 2500 µm a strain in the fibre core of ε_z = 0.12 %. This is consistent with the assumption that the structural strain of the aluminium is transferred into the fibre core, with some restrictions due to the imperfect strain transfer through the backing patch; which means, the fibre whose thermal expansion is much less than that for the other components does not take over the complete structural strain of the aluminium.

For a decrease in temperature the thermally induced strains in all components would have negative signs. The change to be expected for the aluminium structure is ε_{therm} = -0.15 %. The result of the simulation gives at z = 2500 µm a strain in the fibre core of ε_z = -0.13 %. Again this can be explained if an imperfect transfer of the strain in the aluminium structure through the backing patch is assumed.

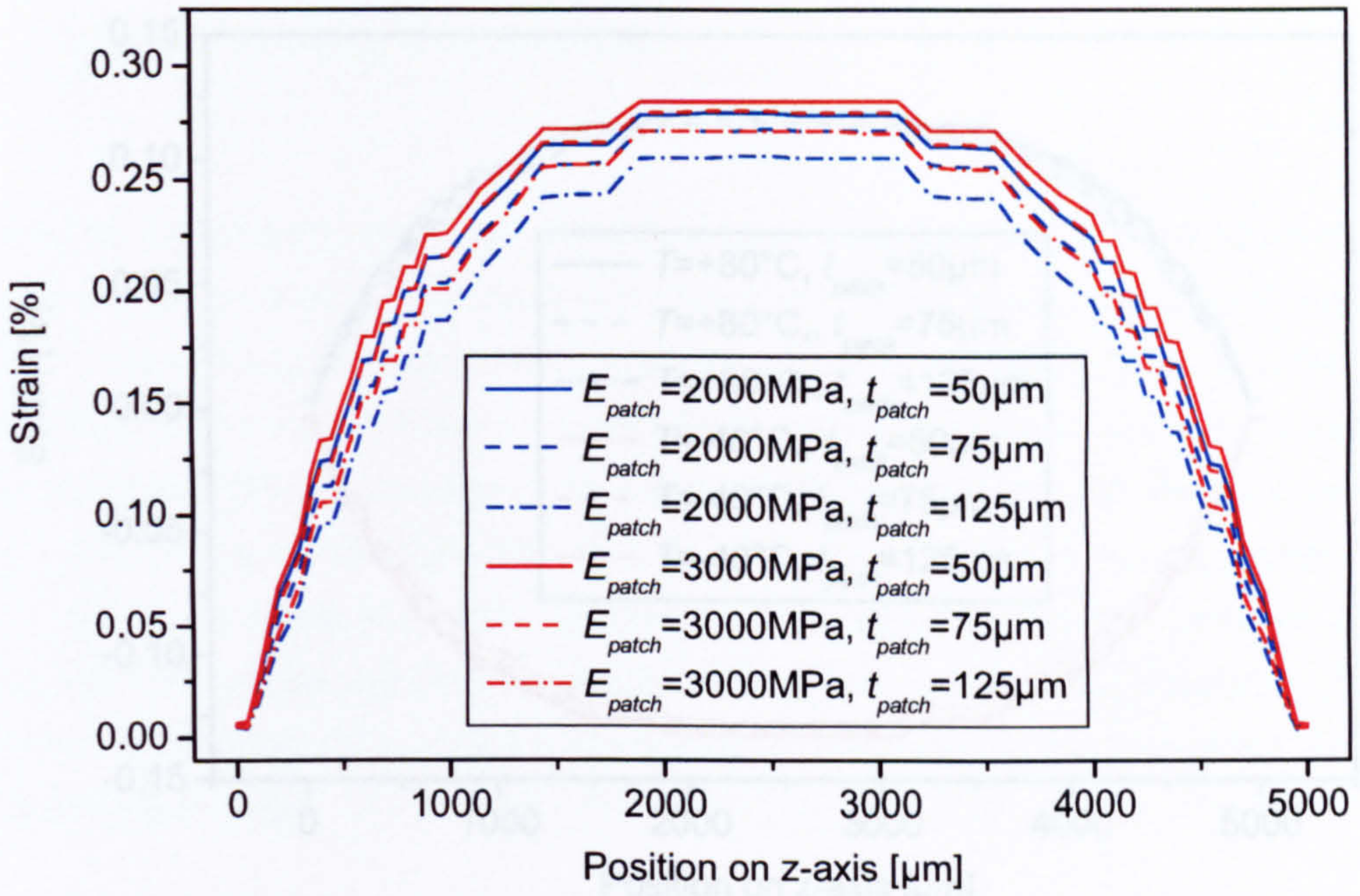

Figure 3.15: Parameter study for a structural load of 0.3% parallel to the fibre axis.

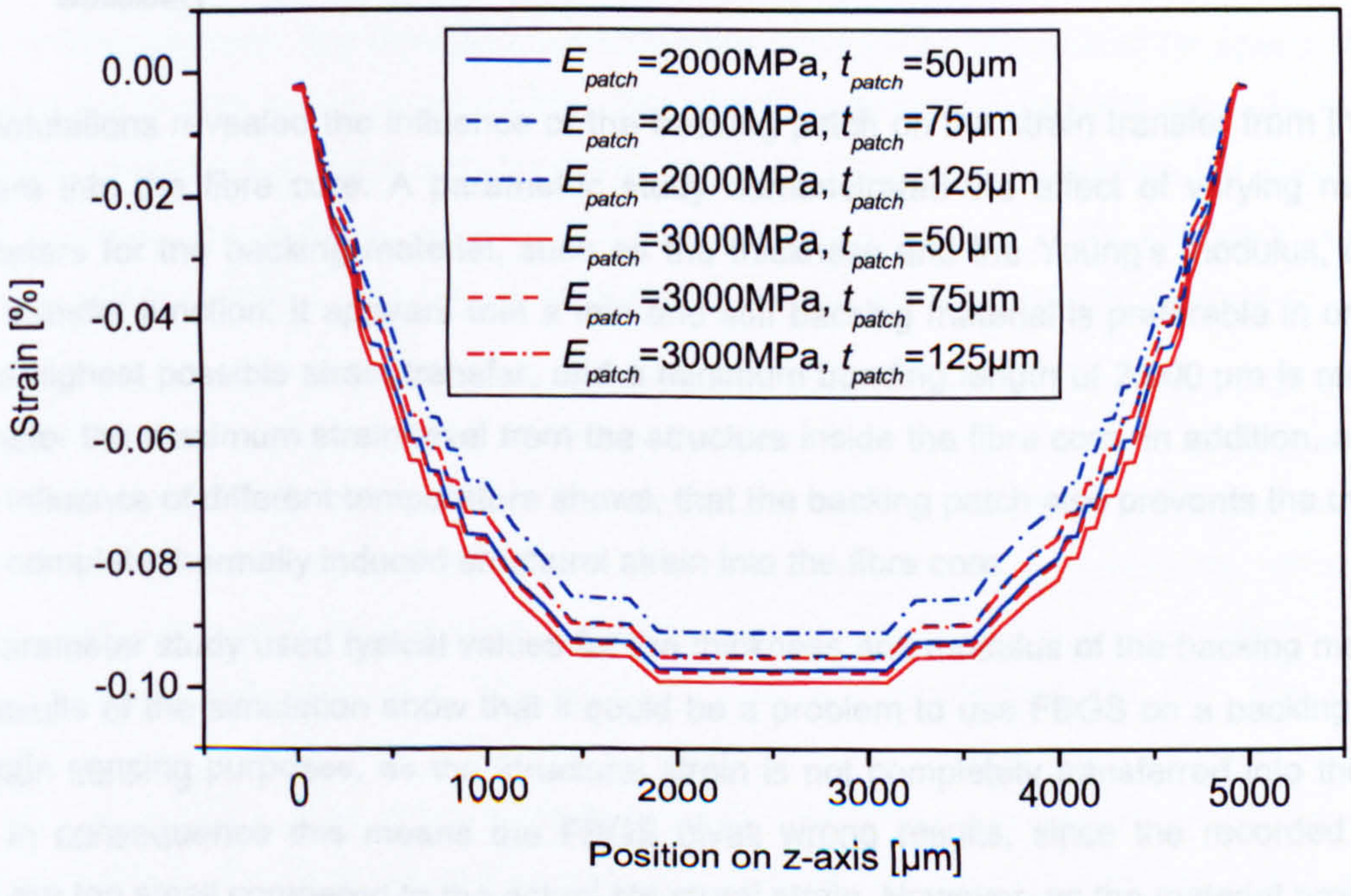

Figure 3.16: Parameter study for a structural load of 0.3% perpendicular to the fibre axis.

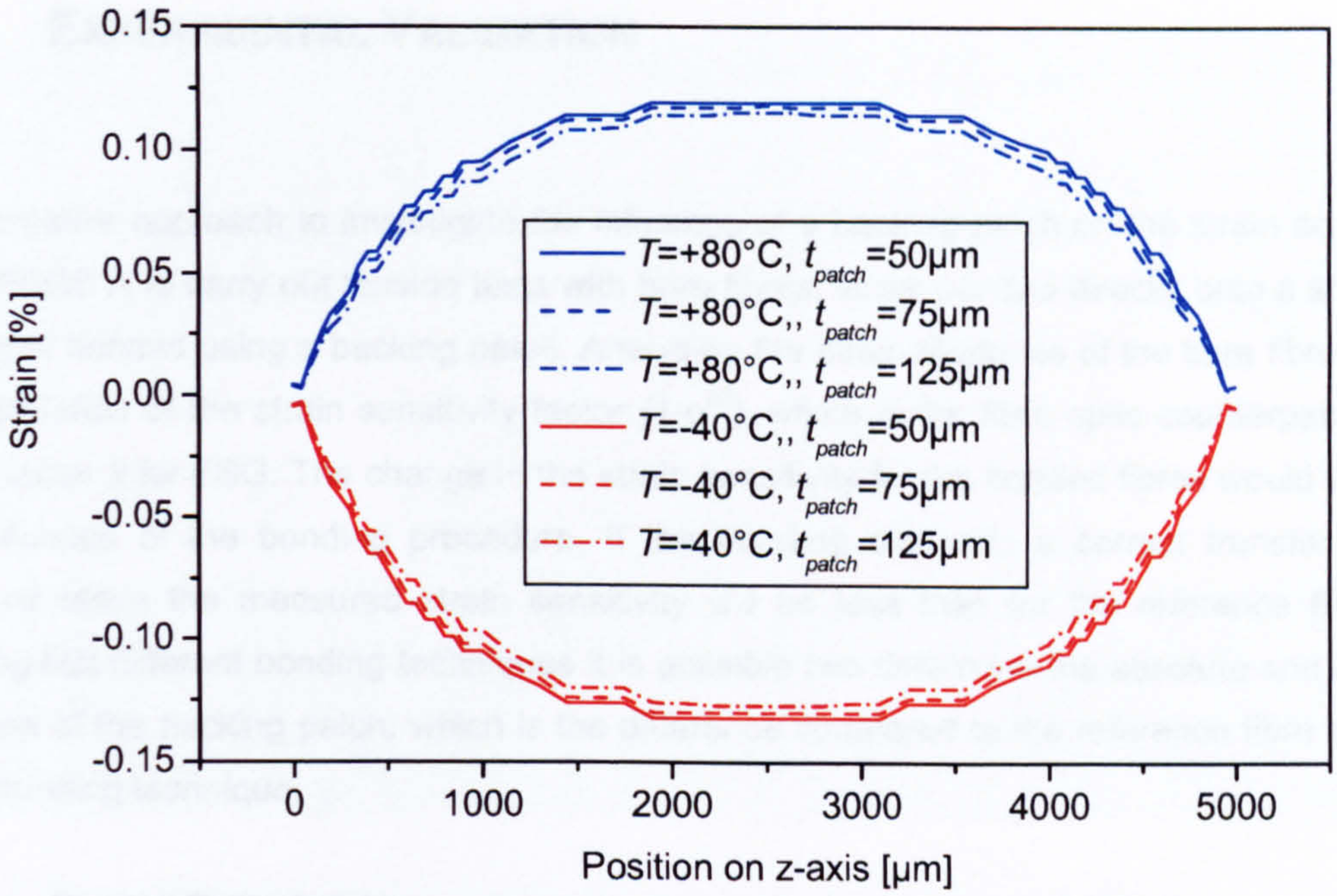

Figure 3.17: Parameter study for two different temperatures, E_{patch} = 3,000 MPa.

3.4.4 SUMMARY

The simulations revealed the influence of the backing patch on the strain transfer from the test structure into the fibre core. A parametric study demonstrated the effect of varying material parameters for the backing material, such as the thickness and the Young's modulus, on the strain transfer function. It appears that a thin and stiff backing material is preferable in order to ensure highest possible strain transfer, and a minimum bonding length of 2,000 µm is required to transfer the maximum strain level from the structure inside the fibre core. In addition, a study of the influence of different temperature shows, that the backing patch also prevents the transfer of the complete thermally induced structural strain into the fibre core.

The parameter study used typical values for the thickness and modulus of the backing material. The results of the simulation show that it could be a problem to use FBGS on a backing patch for strain sensing purposes, as the structural strain is not completely transferred into the fibre core. In consequence this means the FBGS gives wrong results, since the recorded strain levels are too small compared to the actual structural strain. However, as the material properties within this study are not exactly known, an experimental study could help to estimate the influence of the backing patch in practical applications. The results of the experimental study are presented in the following section.

3.5 EXPERIMENTAL VALIDATION

An alternative approach to investigate the influence of a backing patch on the strain sensitivity of the FBGS is to carry out tension tests with bare fibres, fibres bonded directly onto a structure and fibres bonded using a backing patch. Analysing the strain response of the bare fibre allows the calculation of the strain sensitivity factor $(1-p^{eff})$, which is the fibre optic counterpart to the gauge factor k for ESG. The change in the strain sensitivity for the bonded fibres would indicate any influence of the bonding procedure. If the bonding obstructs a correct transfer of the structural strain the measured strain sensitivity will be less than for the reference fibre. By studying two different bonding techniques it is possible two determine the absolute and relative influence of the backing patch, which is the difference compared to the reference fibre and the direct bonding technique.

3.5.1 SAMPLE PREPARATION

Two fibre Bragg gratings were chosen for strain sensitivity testing. Firstly, a tensile test was carried out to obtain the strain sensitivity for the bare fibres. Then both sensors were mounted on the same tensile test specimen. This specimen is an aluminium structure widely used for fatigue and tensile test. The fibre optic sensors were mounted on one side of the specimen; one was mounted directly on the structure the other one got a polyimide backing patch. To compare the results of the fibre gratings with the actual strain, an ESG was mounted on the reverse side of the specimen. As all the sensors were mounted at the same part of the specimen, identical results could be expected, provided all sensors display the correct structural strain level.

Figure 3.18 shows the prepared specimen with two bonded FBGS. The Bragg gratings used were fabricated by the *IPHT* Jena, Germany in draw-tower technology. The grating length is 5 mm and the reflectivity is about 15 %. An *Ormocer®* coating with 50 µm thickness was used. The first grating was mounted directly on the structure using a cyanoacrylate adhesive. A backing patch was used for the second grating. The backing patch is a polyimide patch from *CMC Klebetechnik* in Germany. The product name is *Kaptonträger Typ HN*. The material parameters as given by the manufacturer are: thickness = 125 µm, Young's modulus = 2,500 MPa. This corresponds to a rather thick backing compared to the parameters of the simulation. The second grating was mounted on the backing patch in a first step. A cyanoacrylate adhesive was used for the bonding. Then in a second step the patch was attached to the structure. Again a cyanoacrylate adhesive was used. This is the same adhesive the ESG was bonded onto the reverse side of the specimen.

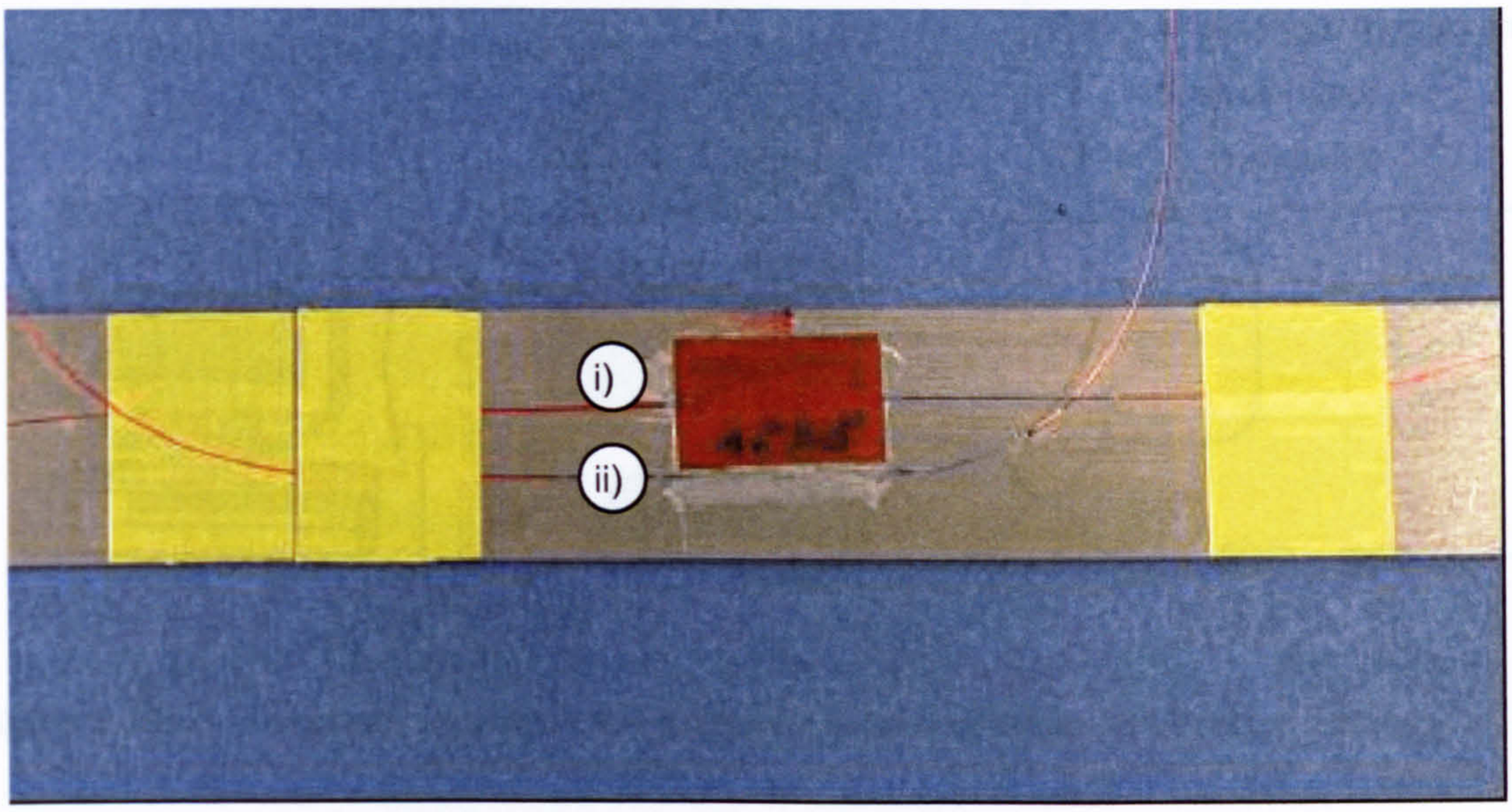

Figure 3.18: Photograph of the tensile test specimen with two bonded FBGS. i) FBGS bonded using a backing patch ii) FBGS bonded directly onto the structure.

3.5.2 Experimental Set-Up

FBGS Interrogation System

A system based on a tunable laser (TL) , Radians Innova Intun 1500, was available for interrogating the Bragg grating sensors and measuring the response from the sensors in reflection with a photodetector (PD). The wavelength measurement (WM) was carried out using a fiber-optic ring interferometer in combination with an absorption cell (multi-wavelength reference). All the components were packaged in a compact unit. The entire set-up was computer-controlled, and the Bragg wavelength was calculated from the measured spectrum using numerical methods. The system configuration for measuring the strain sensitivity of Bragg gratings ($\lambda_1, \lambda_2, \ldots \lambda_n$) used a spectral width of 60nm with a reproducible accuracy of about 0.2 pm for the determination of the Bragg wavelength. This was optimised for FBGS with a full width of half maximum (FWHM) < 150 pm and a reflectivity of ~15 %, as for the present draw-tower gratings. The optical resolution corresponds to a strain resolution of ~0.3 µm/m or a temperature resolution of ~0.02 K. The measurement frequency of the system was limited by the laser scan speed (max. 25 nm/s) to ~0.4 Hz for each array of sensors in one fiber.

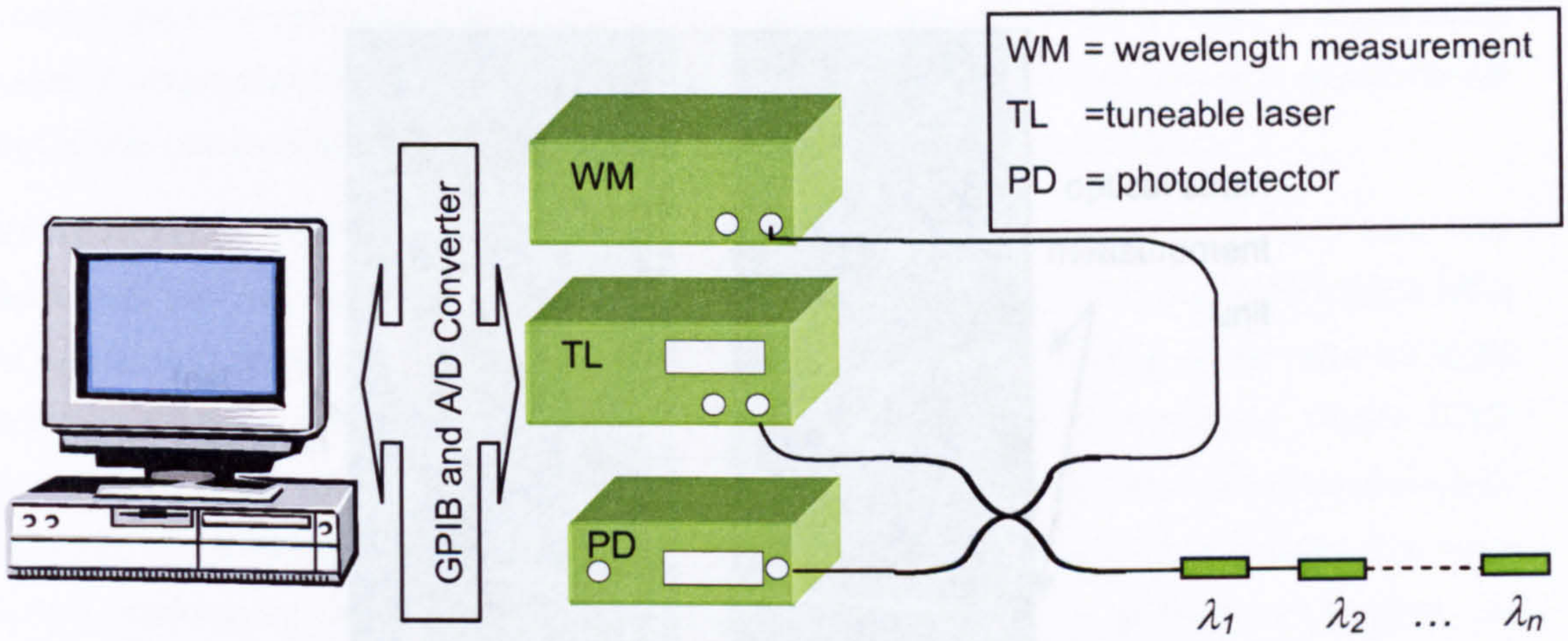

Figure 3.19: Schematic layout of the FBGS interrogation system (see text for details).

For conducting the tension test a *ZWICK* test machine 144, and the measurement software *ZWICK* Z2004, V1.21 was available. The machine with an inserted test specimen is shown in Figure 3.20. The experimental challenge in determining the strain sensitivity is the measurement of the corresponding strain level. ESG cannot be mounted on optical fibre, therefore another technique is required. The *ZWICK* test machine was equipped with an optical strain measurement system, as shown in Figure 3.20. This system involves two light sources which illuminate reflection marks that have to be attached to the test specimen. The reflected light is focused on a differential photodiode. If the structure is strained the reflection marks move and the differential photodiode observes a change in reflected power. A control unit moves the light sources to keep the reflected power maximal. From the movement of the light sources, the strain of the structure can be calculated. This system was proven to work correctly, as for bulk test objects the performance could be compared with electrical strain gauges. The tests conducted for obtaining the strain sensitivities used the optical strain measurement unit for the bare optical fibres and electrical strain gauges for the aluminium bonded optical fibres.

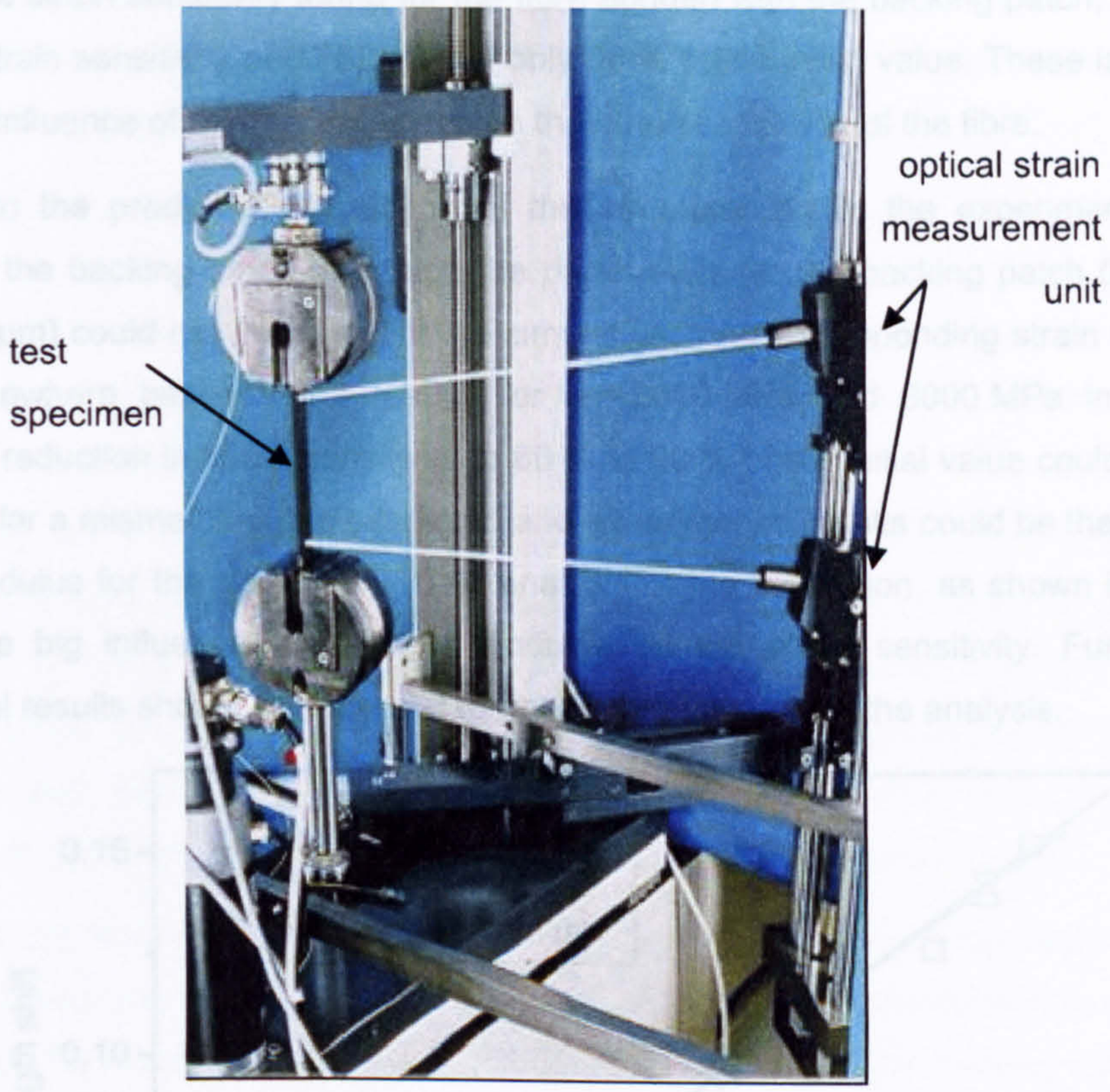

Figure 3.20: The ZWICK tension test machine 144.

3.5.3 RESULTS

The results of the tension tests for the bare and bonded fibres can be represented in a single graph to compare the difference in strain sensitivity. This graph is displayed in Figure 3.21. The relation of the shift in Bragg wavelength to the measured strain is plotted for the bare Ormocer-coated fibre, the fibre bonded onto the aluminium structure and the fibre with the backing patch bonded onto the aluminium. It appears there is no visible difference in the responses for the different fibres. To study the sensitivity more accurately, a linear fit was calculated for every fibre. The fit curves are also shown as straight lines in Figure 3.21. Again no visible difference can be made out. From the linear fit, the slope of the curve can be found. The slope corresponds to the strain sensitivity $(1-P^{eff})$. For better quality of the results, repeated measurements were conducted. The initial strain sensitivity $(1-P^{eff})$ for a bare fibre is found to be 0.789 ±0.007. The fibre that was directly bonded onto the structure shows a sensitivity of 0.781 where the same standard deviation as for the reference fibre is assumed. Within the error limits this is the same value. This is exactly what was expected for directly bonded fibres.

However, the strain sensitivity found for the fibre bonded with the backing patch, is significantly smaller. A strain sensitivity of 0.762 means only 96 % of the initial value. These is experimental proof of the influence of the backing patch on the strain sensitivity of the fibre.

Compared to the predicted attenuation of the structural strain, the experiment shows less influence of the backing patch. Although the parameters for the backing patch (E = 2500 MPa and t = 125 µm) could not be found for the simulations, the corresponding strain value must be placed somewhere between the results for E = 2000 MPa and 3000 MPa in Figure 3.15. Therefore a reduction in strain sensitivity to 86 % to 90 % of the initial value could be expected. The reason for a mismatch of the simulated and experimental results could be the uncertainty in Young's modulus for the simulations. The analysis of the simulation, as shown in Section 3.4, revealed the big influence of Young's modulus on the strain sensitivity. Furthermore, the experimental results should be repeated to get better statistics for the analysis.

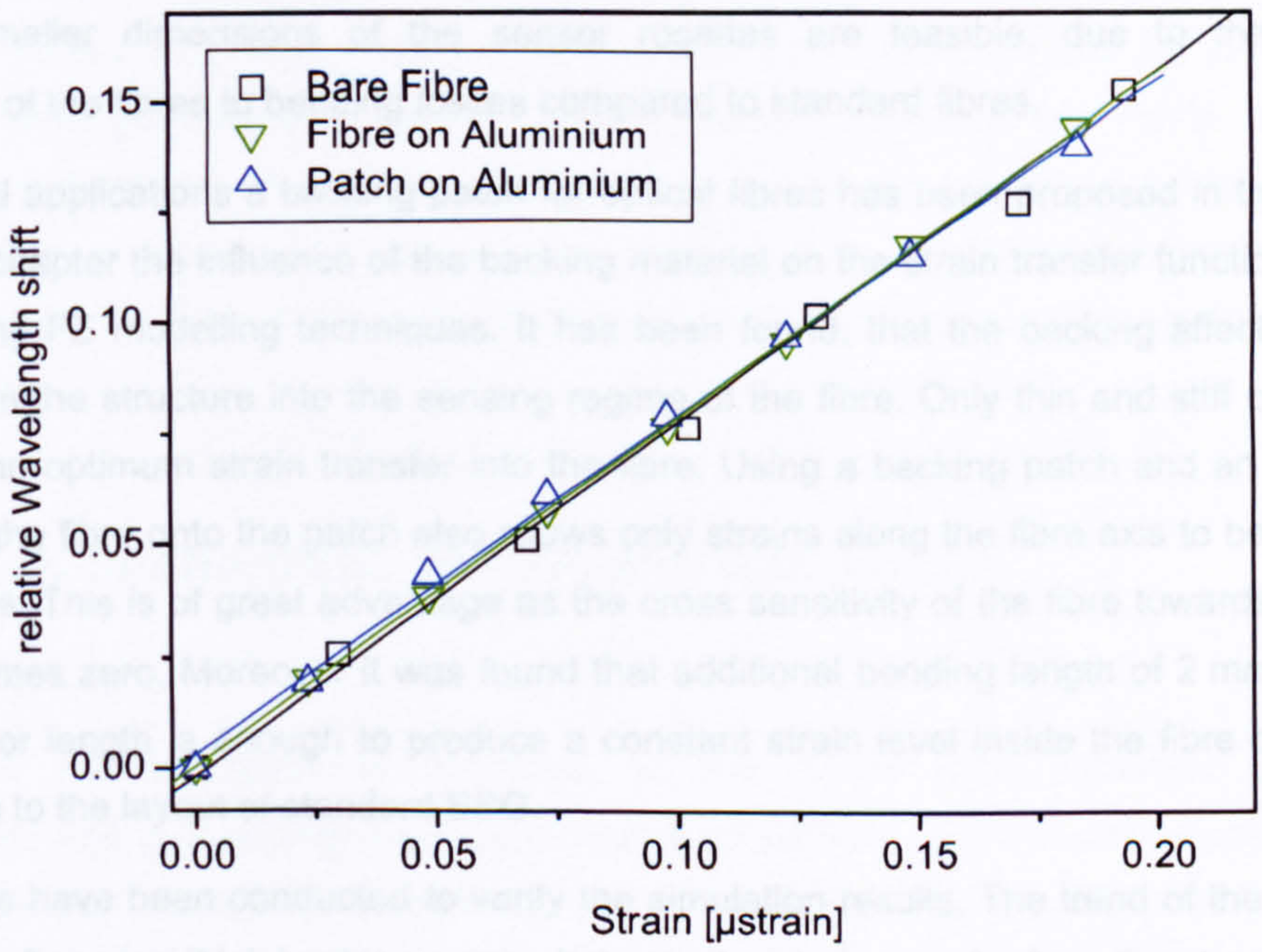

Figure 3.21: Bragg wavelength shift as a function of structural strain for different types of FBGS.

3.6 Conclusions

This chapter has shown the importance of a load monitoring system for the usage monitoring of structures. One of the favoured approaches in the literature towards a load monitoring system is based on the use of strain sensors. It has been reviewed that structural loads can easily be derived from strain measurements. The requirements on a load monitoring system for ground

and flight testing in aeronautic applications have been derived. Standard tools for strain measurements and the novel fibre optic Bragg gating sensor have been checked for their suitability to meet the desired properties.

It has been found that Bragg gratings provide unique advantages compared to standard techniques, like the electrical strain gauge. Yet, due to the good experience with ESG a load monitoring system based on FBGS could only profit if the positive characteristics of the ESG are adapted for the FBGS. Especially in terms of temperature compensation and bonding techniques the standard concepts for FBGS could be improved.

A new layout for a fibre optic temperature sensor has been proposed, which allows the development of fibre optic networks with several temperature sensors within a single fibre line. Furthermore, by using this concept for a temperature sensor a network of fibre optic rosettes with temperature compensation is possible. It has been highlighted that using draw-tower gratings, smaller dimensions of the sensor rosettes are feasible, due to the increased insensitivity of the fibres to bending losses compared to standard fibres.

For practical applications a backing patch for optical fibres has been proposed in the literature. Within this chapter the influence of the backing material on the strain transfer function has been studied using FE modelling techniques. It has been found, that the backing affects the strain transfer from the structure into the sensing regime of the fibre. Only thin and stiff coatings can guarantee an optimum strain transfer into the fibre. Using a backing patch and an appropriate bonding of the fibre onto the patch also allows only strains along the fibre axis to be transferred into the fibre. This is of great advantage as the cross sensitivity of the fibre towards orthogonal strain becomes zero. Moreover it was found that additional bonding length of 2 mm in addition to the sensor length is enough to produce a constant strain level inside the fibre core. This is comparable to the layout of standard ESG.

Experiments have been conducted to verify the simulation results. The trend of the simulations could be confirmed: a thick backing patch obstructs the strain transfer from the structure into the sensor fibre. However, the influence was not as big as predicted by the simulations. An explanation could be found as possibly inaccurate numbers for the material parameters were used for the simulations.

In summary, FBGS seem to be ideally suited to build up future load monitoring systems. The results presented within the chapter could help to find the optimal design for future FBG sensor networks.

4 STRUCTURAL HEALTH MONITORING USING GUIDED ULTRASONIC WAVES

This chapter presents an overview of recent methods for structural damage detection. Section 4.1 gives an introduction to non-destructive testing and evaluation techniques used for damage detection. A special focus is on their ability for an on-board automated testing system. Techniques based on guided ultrasonic waves, e.g. Lamb Waves, have the potential for a continuous damage detection system. Their physical properties are briefly reviewed in Section 4.2. A summary of currently used methods for the excitation and detection of Lamb waves is given in Section 4.3. Standard technology using the piezoelectric effect and, iln addition, optical methods for generation and detection of ultrasound are closer examined.

4.1 NON-DESTRUCTIVE TESTING AND EVALUATION

Maintenance and inspection of structures, is one of the most important concerns in transportation and civil engineering. Various kinds of defects can cause structural failure this includes: internal defects such as porosity, cracks, lamination, cavities, non-metallic inclusions and surface defects such as cracks, slivers, pinholes, corrosion for metallic structure. It appears cracks are the major cause of structural failure in aerospace and marine industries. For example for military aircrafts cracks contribute to 70 % of all types of damage [149]. Cracks are very hazardous flaws with regard to the loading capability of a material. Naturally the causes of crack creation, and therefore also the crack shape, are as varied as the materials. Cracks can be caused by material fatigue, mechanical stresses, corrosion, or a combination of these.

Various techniques have been developed for damage monitoring in structures over the last 40 years. This section reviews the most commonly used damage detection methods and introduces one of the most promising techniques based on Lamb waves.

4.1.1 INTRODUCTION

Non-destructive Testing (NDT) has been defined as "the branch of engineering concerned with all methods of detecting and evaluating flaws in materials" [150]. The essential feature of NDT is that the test process itself produces no deleterious effects on the material or structure under test. NDT technicians and engineers define and implement tests that locate and characterize material conditions and flaws that might otherwise cause planes to crash, reactors to fail, trains to derail, pipelines to burst, and a variety of less visible, but equally catastrophic events. These tests are performed in a manner that does not affect the future usefulness of the object or material. In other words, NDT allows parts and materials to be inspected and measured without damaging them, providing an excellent balance between quality control and cost-effectiveness.

Non-destructive Evaluation (NDE) is a term that is often used interchangeably with NDT. However, technically, NDE is used to describe measurements that are more quantitative in nature. For example, a NDE method would not only locate a defect, but it would also be used to estimate the size, shape, and orientation of defects. NDE may also be used to determine material properties such as fracture toughness, formability, and other physical characteristics.

The number of NDT/E methods that can be used to inspect components and make measurements is large and continues to grow, as researchers find new ways of applying physics and other scientific disciplines to develop better NDT techniques. Most common methods include: Visual inspection and enhanced visual inspection using penetrants and magnetic particle, Eddy current, Nuclear Magnetic Resonance, Microwave, Thermography, Optical interferometry, Radiography, Acoustic Inspection, Ultrasonic Inspection, Acoustic Emission, Load monitoring, and Modal Analysis. These methods are reviewed in Appendix C.

4.1.2 NDT/NDE FOR STRUCTURAL HEALTH MONITORING

Table 4.1 gives an overview of present NDT/E technologies under consideration for a future SHM system. Their ability to serve as an on-board damage detection system is evaluated and shown on the table. Most methods considered require a probe travelling or scanning to cover a large area must be disregarded for on-board systems since they need the direct intervention of humans to perform the inspection. Detection systems that can operate from a fixed location while achieving large area inspection are the prime candidates. In Table 4.1 a minus sign denotes there is no trend towards miniaturisation and structural integration of this technique. Only methods that are marked as high potentials can be considered for implementation of SHM systems. The technique that is especially interesting to be used in conjunction with the FBGS is the ultrasonic inspection using guided Lamb waves. Therefore, this technique is introduced in the following section.

Table 4.1: Overview present NDT/E technologies.

Method	Principle	on-board
electromagnetic waves		
10^2-10^7 Hz	Eddy current	-
10^6-10^8 Hz	Nuclear Magnetic Resonance	-
10^9-10^{11} Hz	Radar, Microwave	-
10^{13}-10^{15} Hz	Visual inspection	-
	Thermography	-
	Optical interferometry	-
	Penetrant	-
	Magnetic Particle	-
10^{15}-10^{20} Hz	Radiography	-
elastic waves		
10^1-10^4 Hz	Acoustic Inspection	-
10^5-10^8 Hz	Ultrasonic Inspection	+/-)*
	Acoustic Emission	+
vibrations		
10^0-10^2 Hz	Load monitoring	+)**
10^1-10^4 Hz	Modal Analysis	+

on-board:

+ technology shows high potential to be integrated into the structure or miniaturised

- no trend towards miniaturization or structural integration today

)* for ultrasonic inspection: guided wave methods show high potential, conventional scanning methods do not.

)** load monitoring is not a damage detection method; it has been included in this summary as it can be combined with other NDT/E techniques for applications in Health and Usage Monitoring Systems.

4.2 Guided Ultrasonic Waves

Wave packets propagating in bounded media, which are superpositions of various modes, are often called guided waves. There are various types of guided waves such as plate and surface waves. Lamb waves are guided ultrasonic waves in plate-like structures. They are governed by the same wave equations as bulk waves. This section gives an overview of the physical properties of guided ultrasonic waves and their applications to damage detection.

4.2.1 Elastic Waves

An elastic wave is a time-varying field of compressions and rarefactions that travels, or propagates, from one region of space to another [15]. Waves travelling in an unbounded bulk of elastic material are called bulk waves. These waves have a finite number of longitudinal and transversal components. Wave propagation in bounded media leads to guided waves. These exhibit an infinite number of modes resulting in a complex wave propagation mechanism.

For longitudinal waves the particle displacement is parallel to the direction of propagation. The wave function can be written as

$$y(x,t) = A\sin(\omega t - kx) \tag{4.1}$$

where $\omega = 2\pi f$ is the angular frequency of the wave, $k_{US} = 2\pi/\lambda_{US}$ is the wavenumber derived from the ultrasonic wavelength λ_{US}. and A is the amplitude. The longitudinal wave velocity c_L of the wave which relates angular frequency ω and wavenumber k can be found as

$$c_L = \frac{\omega}{k} = \sqrt{\frac{E}{\rho}} \tag{4.2}$$

with E being the Young's modulus, and ρ the density of the solid.

For transversal (or shear) waves the particle motion is perpendicular to the direction of propagation. Therefore, shear waves can be polarised horizontally and vertically leading to SH and SV components, respectively. The wave function for a shear wave can be given as

$$z(x,t) = A\sin(\omega t - kx) \tag{4.3}$$

In order to find a similar expression for the transversal wave velocity as in (4.2), it is helpful to introduce the Lamé constants λ and μ:

$$\lambda = \frac{\nu E}{(1-2\nu)(1+\nu)} \qquad \mu = \frac{E}{2(1+\nu)} \tag{4.4}$$

with E being the Young's modulus, and ν Poisson's ratio of the solid.

The wave velocities c_L and c_T for longitudinal and transversal wave, respectively, can be given by

$$c_L = \sqrt{\frac{\lambda+2\mu}{\rho}} \qquad c_T = \sqrt{\frac{\mu}{\rho}} \tag{4.5}$$

The two waves do not interfere, i.e. they propagate without interacting. For an infinite and isotropic medium the velocities depend only on the material constants not on the geometries. In a bounded medium the situation is more complicated. Depending on the geometries many different types of wave motion are possible. One possible solution of the wave equation for a wave subjected to boundary conditions states the presence of guided waves in the medium.

4.2.2 LAMB WAVES

Lamb waves are a type of elastic waves that are guided between the two parallel surfaces of a test object [14, 151]. For an object sufficiently thin to allow penetration to the opposite surface, e.g. a plate having a thickness of the order of a wavelength or so, surface waves degenerate into Lamb waves. Investigations on Lamb waves have been carried out continuously since their discovery and theoretical and experimental work has been performed for different purposes, ranging from seismology, to ship construction industry, to acoustic microscopy, and to non-destructive testing and acoustic sensors.

The mathematical setting for the analysis of Lamb waves is that of a solid medium bounded by two parallel planes a distance $2d$ apart. The coordinate system used is given in Figure 4.1. The direction of propagation is assumed to be along the z-axis.

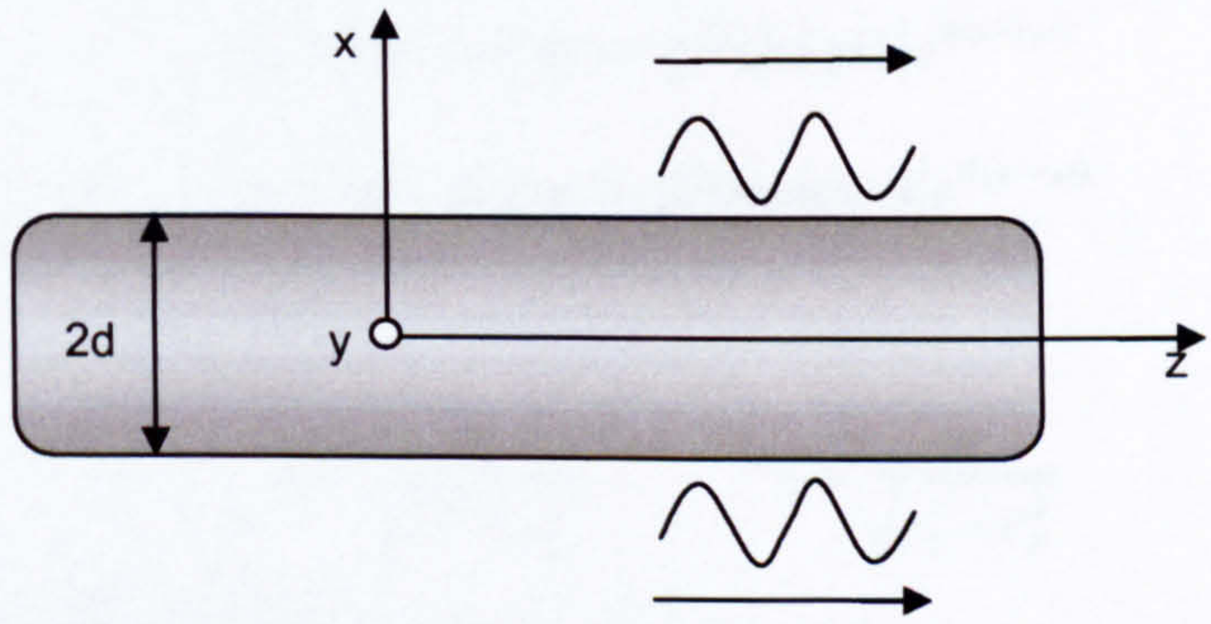

Figure 4.1: Coordinate system for Lamb waves in a plate.

There are two groups of Lamb waves, symmetric and antisymmetric, that satisfy the wave equation and boundary conditions, and which can propagate independently of the other. For the first group the in-plane displacement u is an even function of x, therefore the solutions are called symmetric. The other group is termed antisymmetric as the in-plane displacement is an odd function of x. A graphical representation of the modes is given in Figure 4.2. The particle displacement is shown in an array of vectors, which is like a "snapshot" of the particles at that moment.

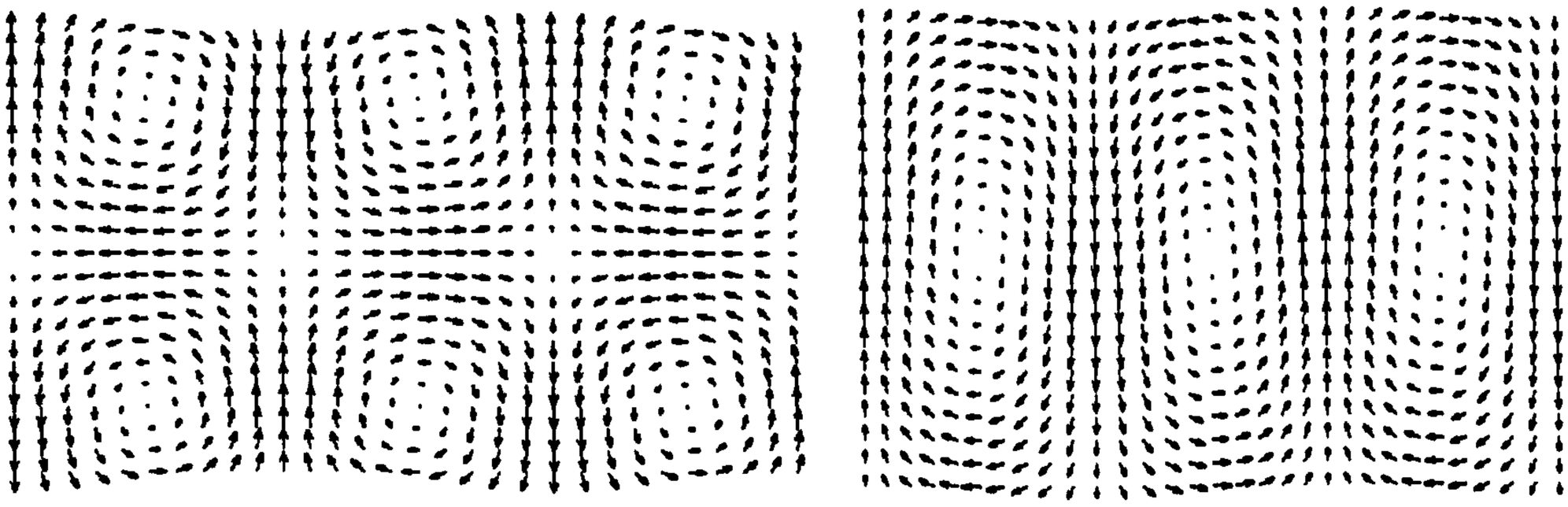

Symmetric mode Antisymmetric mode

Figure 4.2: Examples of Lamb wave modes [152].

For a plane wave travelling along the z-direction the longitudinal component of the displacement *u* and the transverse component *w* can be calculated. For symmetric modes these can be given as [153]

$$u = \{ikA\cos(px) + qB\cos(qx)\}e^{ik(z-c_p t)}$$
$$w = \{-pA\sin(px) - ikB\sin(qx)\}e^{ik(z-c_p t)} \tag{4.6}$$

whereas for asymmetric modes the displacements are given by

$$u = \{ikC\sin(px) - qD\sin(qx)\}e^{ik(z-c_p t)}$$
$$w = \{pC\cos(px) - ikD\cos(qx)\}e^{ik(z-c_p t)} \tag{4.7}$$

where

$$p = \frac{w}{\sqrt{c_L^2 - c_P^2}} \qquad q = \frac{w}{\sqrt{c_T^2 - c_P^2}} \tag{4.8}$$

A,B,C and D are arbitrary constants and c_p is the phase velocity of the Lamb mode in the above Equations. From the equations of the symmetrical mode one gets a homogeneous system of two equations for *A, B* (*C, D* antisymmetric). For these equations the determinant of the coefficient matrix must vanish in order to ensure non-trivial solutions. This means two characteristic equations have to be satisfied:

$$\frac{\tan(qd)}{\tan(pd)} = -\frac{4k^2 pq}{\left(q^2 - k^2\right)^2} \tag{4.9}$$

for the symmetric modes, and,

$$\frac{\tan(pd)}{\tan(qd)} = -\frac{4k^2pq}{\left(q^2-k^2\right)^2} \tag{4.10}$$

for the asymmetric modes.

For a given material and a given value of frequency ω, equations (4.9) and (4.10) can be solved numerically for the phase velocity c_P, which is a function of ω, i.e. the waves are dispersive. The velocity depends on the product *fd*, which is called the frequency-thickness product. The phase/group velocity is often represented as a function of the frequency-thickness product and is called a dispersion curve. Another interesting fact is that equations (4.9) and (4.10) may have any number of real solutions depending on the value of *fd*. The waveforms corresponding to the different solutions are termed modes. The number of modes increases with an increase of ωd. Below a certain threshold only two modes can propagate. These are called the fundamental symmetric S_0 and antisymmetric A_0 modes.

An example of a phase velocity dispersion curve for the first symmetric and antisymmetric modes using the material properties of an aluminium specimen also used in the present research are given in Figure 4.3. Multi-mode propagation complicates the analysis of Lamb wave signals, as each mode travels at a different velocity and incident and reflected signals interfere. The intention therefore is to restrict the allowed frequencies to a regime where only the fundamental modes propagate. For the example in Figure 4.3, this is true for a frequency-thickness product below 1.6 MHz.mm.

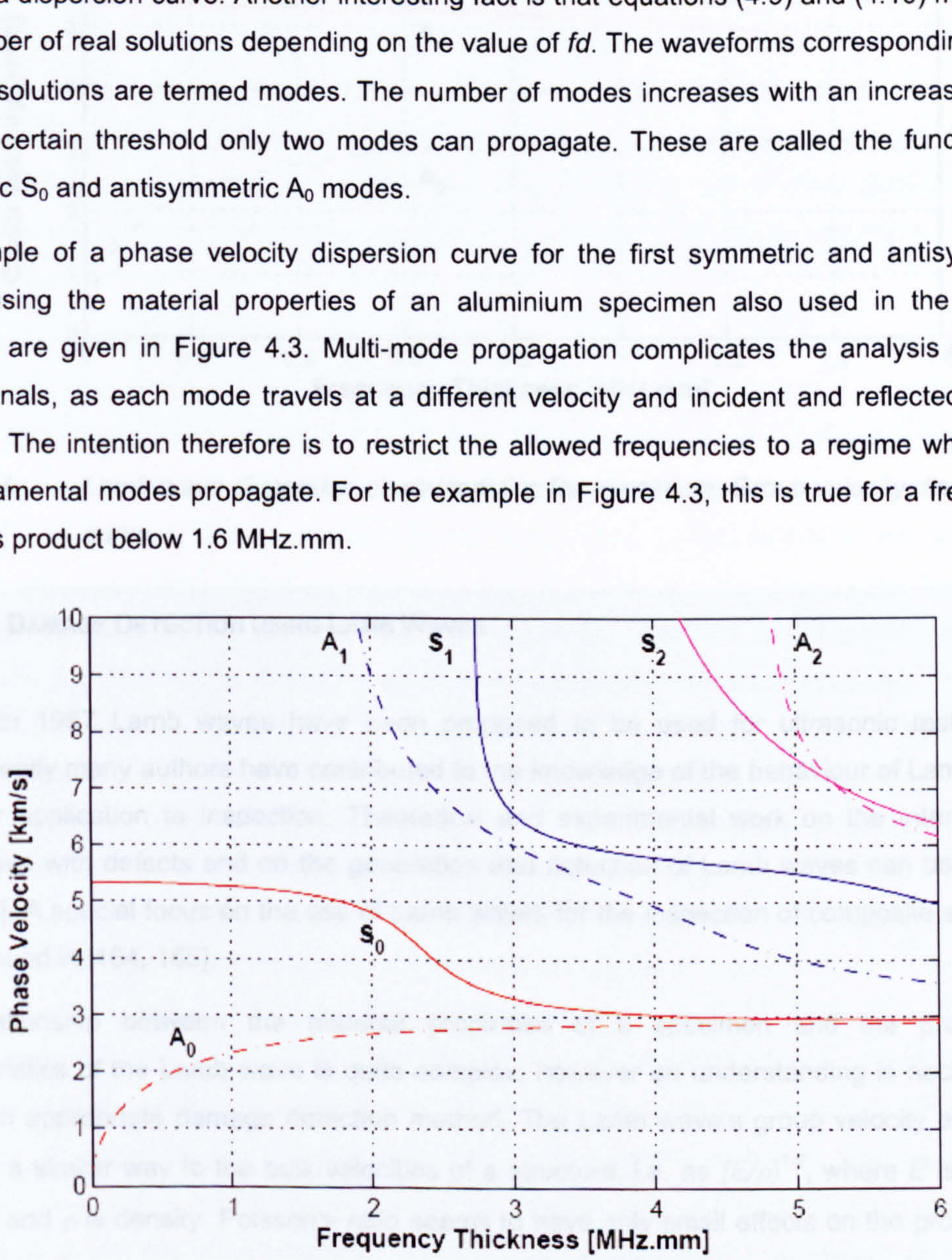

Figure 4.3: Lamb wave dispersion characteristics for aluminium: Phase velocity dispersion curve.

Another useful plot is the group velocity dispersion curve. The group velocity c_g can be derived from the phase velocity using

$$c_g = c_P + \frac{\partial c_P}{\partial k} k \tag{4.11}$$

An example of a group velocity dispersion curve, again using material properties of the present research can be seen in Figure 4.4.

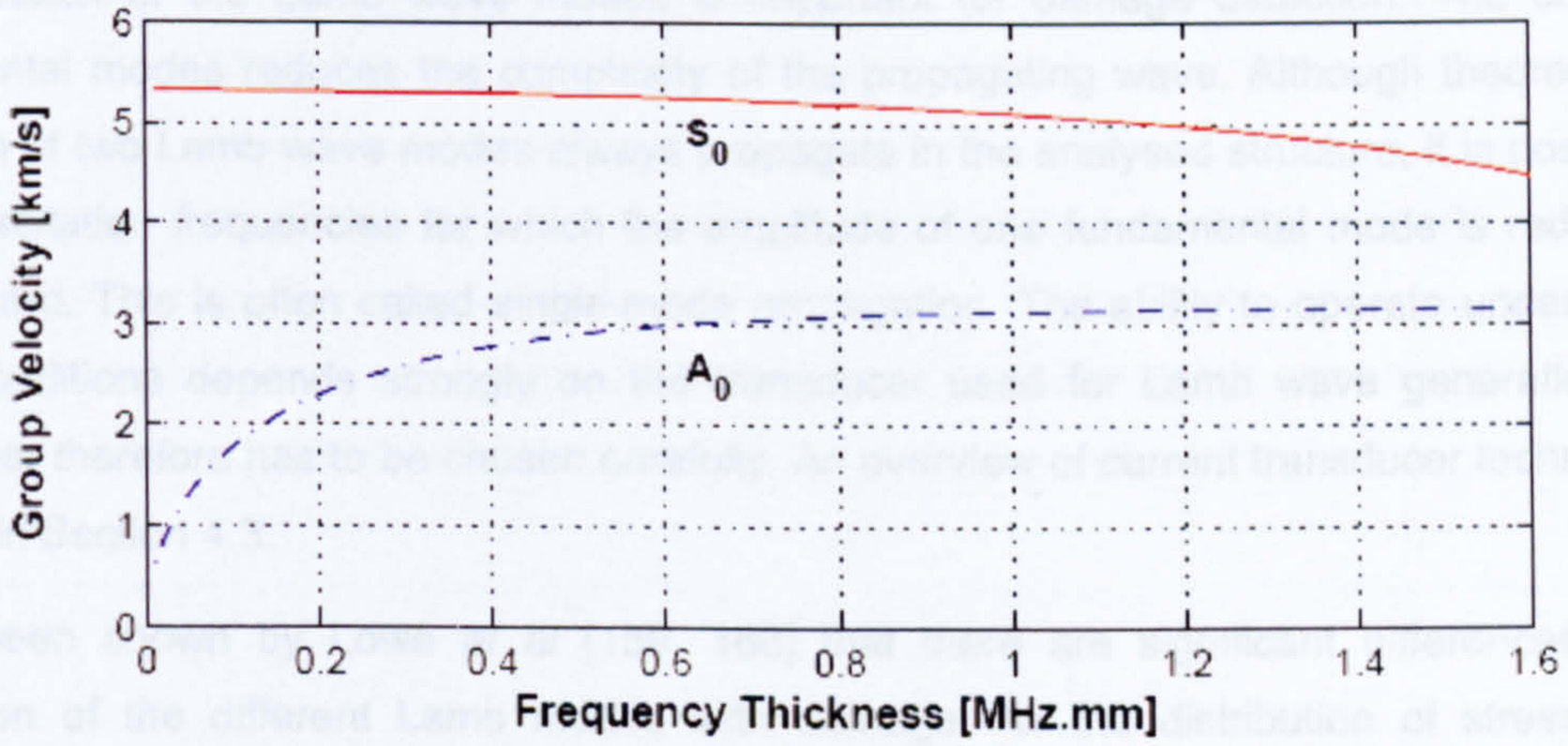

Figure 4.4: Lamb wave dispersion characteristics for aluminium: Group velocity dispersion curve.

4.2.3 Damage Detection using Lamb Waves

Already in 1957 Lamb waves have been proposed to be used for ultrasonic testing [13]. Subsequently many authors have contributed to the knowledge of the behaviour of Lamb waves and their application to inspection. Theoretical and experimental work on the interaction of Lamb wave with defects and on the generation and detection of Lamb waves can be found in [154-163]. A special focus on the use of Lamb waves for the inspection of composite structures can be found in [164, 165].

The relationship between the material properties of a specimen and the propagation characteristics of the Lamb wave is quite complex, however an understanding is necessary to design an appropriate damage detection method. The Lamb wave's group velocity essentially varies in a similar way to the bulk velocities of a structure, i.e. as $(E/\rho)^{1/2}$, where E is Young's modulus and ρ is density. Poisson's ratio seems to have only small effects on the propagation. This means, if a wave travels across an area of reduced stiffness, e.g. caused by the presence of a crack, it will slow down. The other effect that affects the propagation of the modes is

analogous to travelling acoustical waves. When reaching a region of dissimilar wave speed, part of the incident wave is reflected in proportion to the difference in the stiffness and density of the regions. By the time-of-flight , i.e. the interval between the launch of the wave and the return of its reflection, the distance of the inhomogeneity from the source can be computed. The two effects, change in velocity and reflection at defects can be used to predict the presence, location and size of damage. Often wave attenuation and mode conversion are also observed and used for damage detection.

The selection of the Lamb wave modes is important for damage detection. The choice of fundamental modes reduces the complexity of the propagating wave. Although theoretically a minimum of two Lamb wave modes always propagate in the analysed structure, it is possible to chose excitation frequencies for which the amplitude of one fundamental mode is reduced to almost zero. This is often called single-mode propagation. The ability to operate under single-mode conditions depends strongly on the transducer used for Lamb wave generation. The transducer therefore has to be chosen carefully. An overview of current transducer technologies is given in Section 4.3.

It has been shown by Lowe *et al* [159, 166] that there are significant differences in the interaction of the different Lamb modes with damage. As the distribution of stresses and displacements through the thickness of the plate differ, the nature of the modes needs to be understood in order to choose modes which are sensitive to defects. Ideally for long-range monitoring the S_0 mode is best exploited at low frequencies, i.e. below 1 MHz.mm, where it is practically non-dispersive. However, resolution requirements normally force higher frequencies and shorter wavelengths, so that a compromise is needed. Wilcox *et al.* [163] have shown that an optimum solution can be found for a particular mode at a particular frequency. In its field structure the S_0 mode is the simplest of the Lamb modes, as illustrated by the schematic mode shape presented in Figure 4.5a. The longitudinal and transversal displacements u and w are shown. For the S_0 mode the dominating displacement is the in-plane displacement in the direction of travel. The mode shapes vary very little with frequency; mainly at lower frequencies the magnitude of the displacement *w* diminishes with respect to *u*. The distribution of the stresses indicates the equal sensitivity of the mode to defects at different depths. Furthermore the relatively low amplitude of the transversal displacement w results in minimum leakage if the plate is immersed in a low velocity fluid [166]. The mode shapes of the A_0 mode are not as simple as for its symmetric counterpart, see Figure 4.5b. Whereas the S_0 mode is characterised just by its dominant displacement component in the direction of travel, the A_0 mode has significantly transversal out-of-plane displacement components. What complicates matters with the A_0 mode is that the mode shape depends on frequency. At lower frequencies the shapes of the displacement are simply those of bending the plate and the displacement *u* varies linearly through the depth of the plate and there is a large out-of-plane body motion (*w*). At higher

frequencies the through-thickness distributions are no longer linear [159]. The differences between the S_0 and A_0 mode become also obvious, when Figure 4.2 is considered. The particle motion in the mid-plane is dominated by the longitudinal displacements for the symmetric mode, while for the asymmetric mode the transversal displacements dominate.

The differing through-thickness distributions of the S_0 and A_0 mode become important when the position of the damage or the ultrasonic transducer can be positioned within different layers of the plate. It has been shown that Lamb wave modes which induce high shear stresses are the most sensitive to delamination in composite materials. As the A_0 mode induces more uniform shear stress distributions through the plate thickness than the S_0 does, it can be suggested that regardless of its through-thickness position a delamination can be expected when the A_0 mode is used for inspection. On the other hand, if the ultrasonic transducer is more sensitive to either the longitudinal or transversal displacement, it is important where the transducer is placed. If for example a transducer is most sensitive to a longitudinal displacement, it won't be able to record the A_0 mode if placed in the mid-plane of the structure.

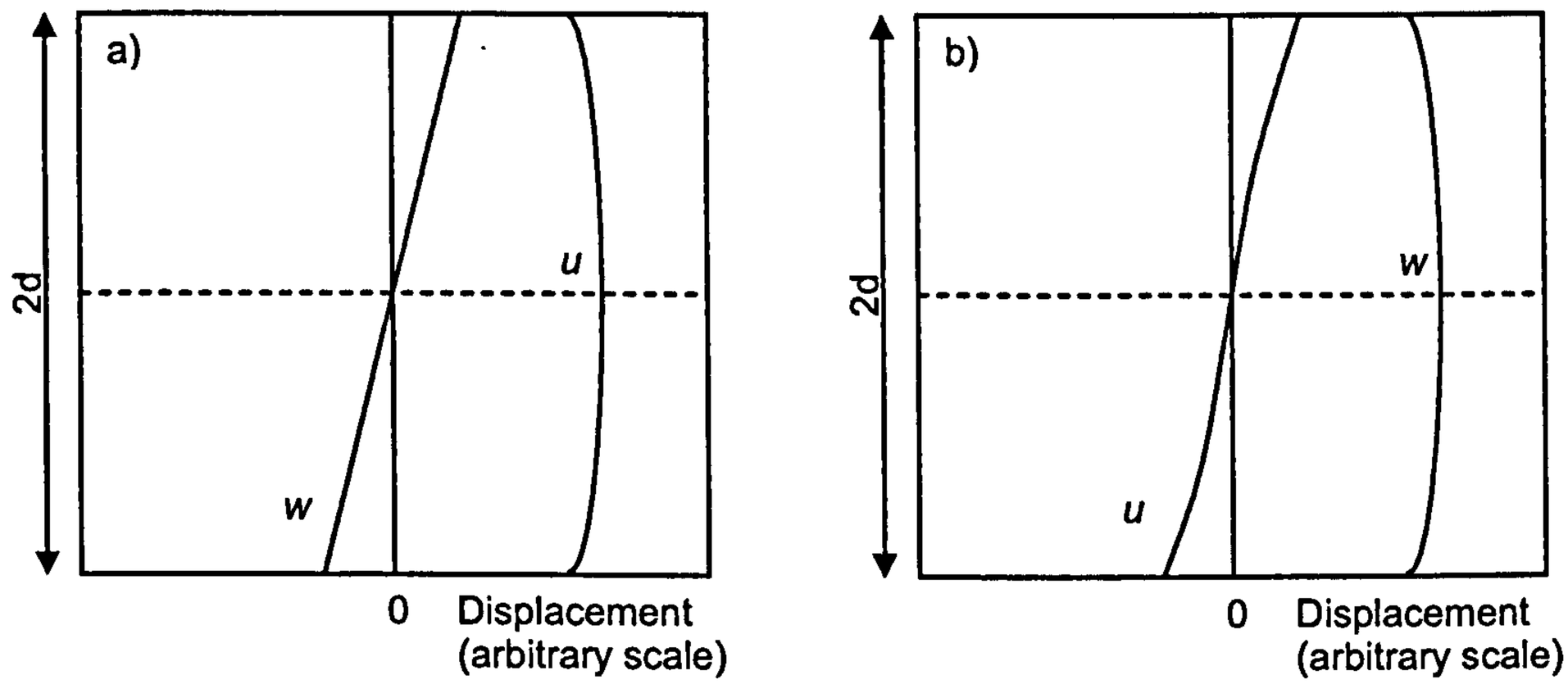

Figure 4.5: Displacement mode shapes at 1MHz.mm [159, 166]*: a) S_0 mode; b) A_0 mode.*

Further considerations include the attenuation of the Lamb modes. Percival and Birt [167] showed that the attenuation of the A_0 mode is up to eight times greater than the S_0 mode . This result implies that if the A_0 mode is used in a large area damage detection system, then significantly more sensors would be needed to overcome the same area for a given signal lever. Hence, the S_0 mode appears more attractive for larger area inspection since fewer transducers would be required, leading to simpler systems.

From the above presented specific properties of each Lamb mode it follows that for each application a suitable mode has to be chosen. Depending on the material of the test structure, its dimensions and the available ultrasonic transducers.

4.3 GENERATION AND DETECTION - TRANSDUCERS

In order to use Lamb waves for damage detection, it is necessary to launch and detect them. A variety of methods is known for Lamb wave excitation and detection. This section gives an overview of today's most common techniques. As the majority of ultrasonic transducers is based on the piezoelectric effect, this phenomenon is briefly reviewed in Appendix D. Different transducer techniques are described in the following paragraphs, where special emphasis is on the previous work on the use of fibre optical sensors for the detection of ultrasound.

4.3.1 PIEZO-BASED ULTRASONIC TRANSDUCERS

Piezo-based transducers are commonly used for the generation of ultrasound. There are many possibilities on how to form a transducer to effectively couple the Lamb wave into the plate [168]. Because of the inverse piezoelectric effect, the actuators can also be used as sensors tuned into a given wavelength. This is one of the reasons why piezo-based transducers have become so popular.

Wedge Transducers

One of the most robust and versatile means of actuation uses a wedge transducer (e.g. [169, 170]). Wedge transducers, also called angle-beam transducers, are commonly used to excite and detect Lamb waves in solid plates for NDE/NDT purposes. In this method, a piezoelectric patch is used in thickness mode to launch a longitudinal wave in the wedge material. Depending on the wedge angle, one can launch different Lamb modes at different wavelengths in the test structure. The incidence angle is determined by using Snell's law and the Lamb mode phase velocity from the dispersion diagrams. If the longitudinal velocity of the wedge material is c_L and the phase velocity of the structure is c_P then the appropriate geometrical condition on the wedge angle is $\sin\theta = c_L/c_P$. The only condition on the wedge material is that the bulk longitudinal wave should have a shorter wavelength than the Lamb mode for the transmission medium. Commercially available wedges can be found with variable angles which allow a range of Lamb wave modes to be selected.

Comb and Interdigital Transducers

An efficient method of coupling waves from a PZT patch into a structure is to use a comb [171] or an interdigital [161] design, which is a modern variation of the comb design. Comb

transducers and interdigital transducers are designed to excite modes with a specific wavelength which is controlled by the ridge spacing and the electrode finger spacing, respectively. The distance between the ridges or fingers, and the width of the ridges or fingers is taken as $\lambda_P/2$, where λ_P is the wavelength of the selected Lamb mode. Wilcox *et al* have demonstrated the use of a piezoelectric polymer film (PVDF) to transmit ultrasonic Lamb waves into metal plates [161]. This technique offers special advantages as it can be used in curved surfaces which would present problems to stiff piezoceramic materials. However, the acoustic amplitudes achieved with this technique are well below the levels for piezoceramic transducers [172].

Piezoelectric Patches

Conventional Lamb wave probes such as wedge and comb transducers are relatively too heavy and expensive to be considered for widespread deployment on a structure as part of a SHM system. A simple piezoelectric patch bonded to the surface of the structure can be used to initiate elastic waves. The shapes of the most common elements is depicted in Figure 4.6. Typical dimension are a few millimetres in length or diameter and only a few hundred microns in thickness. The operation of PZT patches is different to that of conventional ultrasonic probes [173]. PZT patches often use the planar mode in discs Figure 4.6a and the longitudinal mode in plates Figure 4.6c. This means Lamb wave excitation and sensing is achieved through in-plane strains of the patch, while conventional transducers excite through out-of-plane strains. PZT patches are strongly coupled with the structure and follow the structural dynamics. The properties of the coupling, such as damping and acoustic coupling strongly determine the pulse shape and and bandwidth issues of the transducer. The main advantages of PZT patches over conventional ultrasonic probes lies in their small size, lightweight, low profile and small cost. Furthermore, they are easy to bond to the structure and can even be embedded into composite materials.

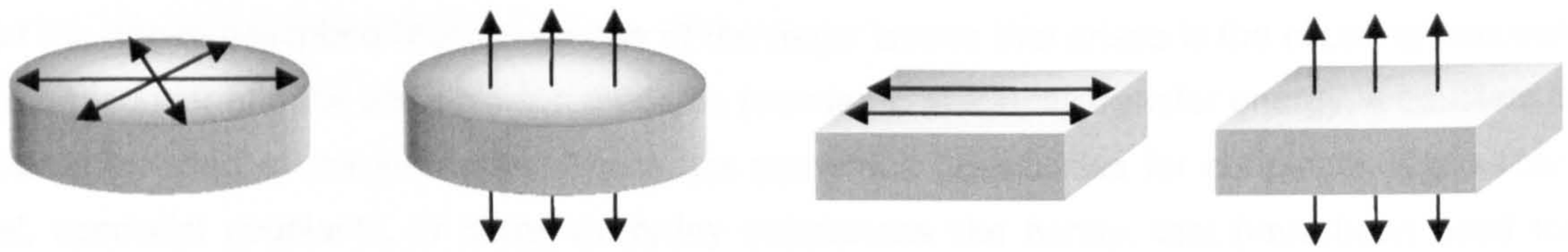

Figure 4.6: PZT elements and vibration modes: a) disc in planar mode; b) disc in thickness mode; c) plate in longitudinal mode; d) plate in thickness mode.

Smart Layers™

Few non-destructive tools are available to provide continuous monitoring, inspection and damage detection for SHM systems. In SHM applications a permanently attached device is required. *Acellent Technologies Inc.* has presented a versatile technique that can be built into or upon metal and composite structures [174-176]. The system is based on the *Smart Layers™* technology consisting of a network of piezoelectric patches embedded in a thin dielectric carrier film. This layer can either be surface mounted on existing structures or integrated into a composite structure during fabrication. An structurally integrated layer can provide built-in non-destructive assessment of the internal and external states of the structure.

Phased Arrays

Conventional transducers have a fixed focal region for the transmitted acoustical field. In order to focus on a defect mechanical movement of the transducer during an inspection is generally required. In order to reduce the efforts in moving the transducers, electronically driven array transducers generating ultrasound propagating in various directions are more and more often used [177, 178].

A phased array probe is a transducer made up of a large number of simple probes, or piezoelectric elements, individually connected and independently driven so that the signals they transmit or receive may be treated separately or combined as desired. Multiple piezoelectric elements are sometimes arranged in patterns in a common housing. These are usually linear or circular in shape. The elements can be pulsed simultaneous or in a certain pattern to each other. In phased array technique the angle and the focal length can be modified by applying appropriate delays on the signal emitted by each elementary transducer. Kress *et al* [179-181] and Giurgiutiu [173] have demonstrated the successful use of phased arrays in order to detect damage.

Air-coupled Transducers

For the above described techniques one of the major issues that arises is the coupling between the transducer and the transmission medium. In order to efficiently transfer energy, a couplant is usually inserted at the interfaces. There are numerous possibilities for couplants, e.g. silicon gel, specialist couplants, or some everyday substances like honey, that have been used for efficient coupling of ultrasound. However, the use of couplants is not always possible, as they might not be compatible with the industrial process or the couplant might cause permanent damage or contamination to the structure.

The problem when using air-coupled transducers [182] is that if the sound has to move between the test structure and the transducer, four solid-air interfaces have to be passed (from the transducer, to the air, to the structure, and then back again). At each interface only 1 % of the

sound energy is transmitted since air has a very low acoustic impedance. Thus, after four transitions very little sound is left. One solution to overcome this problem without introducing an additional couplant consists in generating very high sound levels and to use high-gain, low-noise amplification. Transducers for air-coupled NDT systems in current commercial applications are made of piezoelectric elements that are driven in the thickness mode. It is a distinct feature of air-coupled transducers to be able to efficiently generate Lamb waves which are otherwise rapidly dampened if water coupling is used.

4.3.2 Electromagnetic Acoustic Transducers (EMAT)

Besides piezoelectricity another physical effect can be used for generating and receiving ultrasonic waves: the electromagnetic acoustic effect. Electromagnetic Acoustic Transducers (EMAT) find attractive applications in many areas of ultrasonic NDT, especially because of their non-contact nature as compared to the conventional piezoelectric transducers [168, 183, 184]. The energy is transmitted by electromagnetic field from the transducer to the structure which avoids mechanical contact with the test surface. The conversion into or from acoustic energy takes place in the surface of the structure. this method thus requires no coupling medium avoiding a number of difficulties. When an EMAT is placed near an electrically conducting material ultrasonic waves are launched in the material through the reaction of induced eddy currents and static magnetic fields. This however, restricts their use to the examination of electrical conductors. EMATs are reciprocal devices, i.e. they can be used as receivers as well as transmitters of ultrasound.

4.3.3 Optical Generation of Ultrasound

The problems known from coupling the ultrasound generated within the transducer into the structure under test are solved by laser-generated ultrasound, which being a non-contact technique, does not need any couplant. In addition, optically generated ultrasound also has the following added advantages [168, 185, 186]:

- It provides broadband ultrasound (tens of MHz);
- Focusing the beam provides bigger spatial resolution and allows the generation of ultrasound in small samples (useful for acoustic microscopy);
- Combined with a non-contact optical detection technique it provides a completely remote system that can operate in corrosive, high temperature and radioactive environments;
- Flat spectra response (caused by the absence of resonant coupling conditions);
- It launches simultaneously bulk, surface and guided waves. It can therefore be used to detect volumetric, surface and subsurface defects;

- The optical beams can reach areas that are difficult to access, if optical fibres or mirrors are used to steer them;
- It offers good electromagnetic environment tolerance.
- It is good for calibratino purposes due to the excellent reproducability.

The limitations of the technique are:

- Safety issues, because of the high power laser radiation.
- The excited acoustical waves have relatively low amplitude.
- It is not completely non-destructive, as the surface of the structure is damaged.

In order to obtain ultrasound of sufficient amplitude to be readily detected, most work in optical generation has been carried out on the use of high-power pulse lasers. The two main regimes for high-power pulse laser generation of ultrasound are : (i) thermoelastic regime, and (ii) ablation regime. These regimes provide different sources of ultrasound, with differing characteristics.

In *Thermoelastic regime,* when the beam of a laser is directed onto a solid sample, the electromagnetic radiation interacts with electrons in the material close to the surface. Some of this incident radiation is absorbed by the sample, thereby heating its surface, whilst the remaining energy is reflected. Thermal conductivity distributes this heat through the sample causing temperature gradients which generate the stress and strain fields of the elastic waves by thermal expansion. The main temperature changes take place only within a few microns of the surface. In the first approximation we can consider this ultrasonic source as a centre of expansion with the principal stress components parallel to the surface and no perpendicular components. The amplitudes of the ultrasonic waves increase linearly with the applied power density.

In *Ablation regime,* focusing the laser beam can cause such an increase of the power density at the surface that it will start boiling and material to the depth of several micrometers will be vaporised, forming plasma. This removal of material produces a reactive stress predominantly normal to the surface. In this regime, the generation of compression and surface waves is enhanced with increasing power density, but shear waves will reach a maximum near the onset of plasma and then decrease.

As the ablation process is quite destructive and even the thermoelastic regime can cause damage to the sample, a low-power alternative for optical generation of ultrasound is required [187, 188]. Modulated low power CW (continuous wave) lasers can be used to generate ultrasound, however the amplitude of the waves is very small and therefore the thermal noise in the optical detectors dominates the received signal. As the thermal noise is totally random, the ultrasonic wave can be separated from the noisy signal using a pseudorandom modulation

scheme of the optical beam. The optical ultrasound bandwidth provided in this way depends on the pulse rise time and is often not as large as that generated by high-power pulse laser.

Using fibre optic technology a laser phased array for the generation of ultrasound can be achieved, Yang *et al* [189] have presented results from the application of a phased optical fibre array to transmit pulsed laser light to the surface of a test structure. The results indicate that the wave modes, beam width and directivity of the generated ultrasound can be controlled using the phased optical fibre array. A further development on the use of fibre optic arrays is the embedding of the optical fibres. Swift *et al* [190, 191] reported the excitation of ultrasound in carbon composite plates. By adjusting the elements of the array, the direction of the generated ultrasonic beam could be controlled.

4.3.4 Optical Detection of Ultrasound

Combining the advantages of the optical generation of ultrasound with optical detection systems a complete optical inspection tool for materials can be achieved. Two fundamentally different options exist: non-contact detection using remote laser-beams or fibre optic sensor bonded onto or embedded into the material .

Non-contact methods

Optical detection systems for ultrasound deploy most often methods that measure laser light reflected back from the surface of the test structure [192]. The optical methods can be divided into noninterferometric and interferometric techniques [193]. For interferometric methods the light undergoes phase or frequency modulation caused by any transient ultrasonic displacement at the surface of the sample. Most common two-beam interferometers, such as a Michelson or Mach-Zehnder one, is used for the detection of ultrasound. In this devices the laser beam is divided into two beams. One beam propagates to a sample surface where there is an ultrasonic signal and the reference beam travels to a mirror. The two beams are then combined through a beam mixer. The interferometer translates any phase or frequency shift of the light into an shift in optical amplitude, which can be easily detected using a photodetector. Interferometers are commercially available and in use for vibration analysis. It has been shown that these kind of laser vibrometers can be successfully used to detect Lamb waves and subsequently any damage information that is encoded into the ultrasonic signals [194, 195].

Optical fibres have also been tested for detecting ultrasound. Pierce *et al* [186] reported a Michelson interferometer probe which was sensitive to the out-of-plane displacements related to the ultrasonic displacement field. The ultrasonic field out-of-plane displacements change the optical path of light in the interferometric sensing arm, as it is reflected from the surface of the sample. This system requires a highly reflective surface and the use of short focal Graded

Refractive Index (GRIN) lenses can improve its sensitivity through effective re-collection of the scattered light.

Contact methods

Optical fibre sensors can be bonded or embedded in a material to detect ultrasound. Fibre optic devices can be found as point-to point scanning devices (Fabry-Perot and FBGS) or multipoint scanning devices (Mach-Zehnder and Polarimetric).

A point-to-point scanning device is said to be found when the sensor dimension is small compared to the acoustical wavelength to be detected. Dorighi [61, 196-198] described the implementation of an intrinsic Fabry-Perot sensor to detect the small high frequency strains associated with ultrasound. The primary advantage of the fibre Fabry-Perot interferometer over a two beam interferometer is that only one fibre length per sensor needs to be embedded, whereas two beam interferometers require a fibre length for each beam of the interferometer. The Fabry-Perot sensor has been successfully applied to structurally integrated cure monitoring of epoxy [197] .

Another point-to-point sensor is the fibre Bragg grating. The detection of ultrasound is based on the variation of the FBGS reflectivity spectra, as the strain field of the ultrasound waves modifies some properties of the grating, such as the spatial period and the effective refractive index. The changes in the reflectivity spectrum caused by ultrasound will be mainly a shift proportional to its strain field and will be modulated at the same frequency as that of the ultrasound. A detailed description of the implementation of a FBG ultrasonic sensor and an appropriate interrogation system is presented in Chapter 5.

A multipoint scanning device is the Mach-Zehnder interferometer. The Mach-Zehnder type of interferometric system [87] measures the change in phase of the light propagating through an optical fibre that is bonded to the sample plate. The pressure field of the acoustic wave acting on the fibre produces this phase modulation by changing the fibre's refractive index. This system is also referred to as a wavefront integration technique [97] because the light in the embedded or bonded optic fibre is modulated by a finite portion of the ultrasonic wavefront rather than by only one point of it. This means that by using only one detection transducer with one acoustic source a large area can be covered, in contrast to the aforementioned point-to-point scanning devices.

The polarimetric type of ultrasound detection measures the changes in the polarimetric state of light propagating through an optical fibre which has been either embedded into or bonded onto the plate to be tested. Thursby *et al* [83, 84] have described the directional properties of the sensor and its ability to detect a hole produced in a test structure. They also showed how the

relative sizes of the detected signal amplitudes from the source PZT and from the hole vary according to the alignment of the source with the sensor axis.

4.4 Conclusions

This chapter has discussed present NDT/E technologies and their potential for future applications in Health and Usage Monitoring systems. It turned out that ultrasonic inspection using guided waves shows high potential for implementation in future on-board damage detection systems. Therefore, guided ultrasonic waves and their application for damage detection have been investigated in detail. From the number of generators and detectors for ultrasound, fibre optic technologies offer a number of advantages compared to their (piezo-)electric counterparts. As the FBG sensor shows good performance for load monitoring systems, as shown in Chapter 3, the question is if this sensor could be also used for sensing guided ultrasonic waves. In consequence, this would enable a multifunctional Health and Usage Monitoring System based on only one type of sensor, the fibre Bragg grating. The implementation of a FBG sensor based ultrasound detection system is presented in the following chapter.

5 FBG SENSORS FOR ULTRASONIC SENSING

This chapter presents a novel approach towards damage detection based on Lamb waves and fibre optic Bragg grating sensors. This includes theoretical and experimental results with FBG ultrasonic sensors in Section 5.1. The critical feature of the Bragg grating is the grating length to acoustical wavelength ratio. A simulation of the sensor response under the influence of ultrasound was also carried out. The results of this study are presented in Section 0. The performance of structurally embedded sensors in CFRP composites is presented in Section 5.3.

5.1 IMPLEMENTATION OF THE FBG ULTRASONIC SENSOR

The major reason that makes an ultrasonic detection scheme using FBG sensors so attractive is their multifunctionality (e.g. strain, ultrasound, temperature, pressure). As Chapter 3 has shown, FBG sensors have high potential to serve as strain sensors in future load monitoring systems. this chapter demonstrates that FBG sensors are feasible for ultrasonic sensing, which means they can be employed for the detection of guided ultrasonic waves, such as Lamb waves, Rayleigh waves, longitudinal waves and vertically polarised shear waves and the corresponding damage identification schemes. The advantages of such a dual system have been highlighted already in Chapter 3. This section presents the results of the work carried out within the scope of this thesis.

As shown in the previous section fibre optics is particularly attractive for ultrasonic sensing as the sensors offer broadband detection capability. Despite the fact that research on Bragg grating sensors has soared, only few publications deal with Bragg gratings as ultrasonic sensors. Fisher *et al* [199-201] have demonstrated the feasibility of short fibre Bragg gratings to measure MHz acoustic fields and temperature simultaneously. An application can be thought of for medical examinations. Another demonstration of a FBGS to measure ultrasonic pressure waves was carried out by Fomitchov *et al* [25]. They proposed applications for measuring ultrasound in liquids and solids. An underwater acoustic sensor with fibre Bragg gratings has been examined by Takahashi *et al* [202, 203]. They made use of a tuneable laser source for the

interrogation of the Bragg grating. Liu *et al* [204] also used a tuneable laser source for the detection of seismic signals up to 1.7 kHz using FBG sensors. More recently, two studies on Bragg gratings for the detection of Acoustic Emission have been presented [205, 206]. Yet, their frequency range is much less than needed for Lamb wave inspection. Theoretical considerations on the use of FBGS for ultrasonic sensing have been presented by Coppola *et al* [207]. Their study discusses some aspects as the influence of the ultrasonic strain field on the Bragg grating, but do not discuss any consequences for an interrogation scheme. The literature survey shows the growing importance of a FBGS-based sensing technique. However, the application of FBGS for the detection of ultrasonic Lamb waves with respect to the detection of damage, has not been demonstrated yet and is introduced in this chapter.

5.1.1 Theory of Ultrasonic Sensing Using FBGS

The basic idea of the proposed interrogation method is to use a low noise, narrow line-width laser diode and a high sensitivity detector. If the wavelength of the laser is set to a certain part of the grating spectrum, any shift of the spectrum will as a consequence modulate the reflected optical power. The use of a tuneable laser source allows the interrogation of several gratings within a single fibre line.

The sensor function of the FBGS has been defined in Chapter 2. The relation of the Bragg wavelength to the structural strain and temperature can be written as

$$\frac{\Delta\lambda_B}{\lambda_{B_0}} = \left[1 - P^{eff}\right] \cdot \varepsilon_z^{s,m} + \left[\left(1 - P^{eff}\right) \cdot \alpha^s + \frac{1}{n_0}\frac{dn}{dT}\right] \cdot \Delta T \qquad (5.1)$$

where the structural strain ε_z^s is separated into its thermal $\alpha^s \cdot \Delta T$ and mechanical $\varepsilon_z^{s,m}$ strain components. n is the refractive index of the fibre, α^s is the thermal expansion coefficient of the structure, and $(1\text{-}P^{eff})$ is the strain sensitivity of the FBGS. In case of ultrasonic detection the influence of temperature can be neglected, as the time scale for changes in temperature is much larger than that of the dynamic strain field.

A typical Bragg grating reflection spectrum is shown in Figure 5.1. The optical power reflected by the fibre grating $P_{r,\,opt}$ depends on the wavelength λ. It can be given as a function of the incoming optical power $P_{in,\,opt}$ and the wavelength-dependent reflection $R(\lambda)$:

$$P_{r,opt}(\lambda) = P_{in,opt} \cdot R(\lambda) \qquad (5.2)$$

$R(\lambda)$ describes the entire grating spectrum and is a non-linear function of λ, see Section 2.3.1.

The interrogation method concentrates on the part of the spectrum where the function is assumed to be linear. This is assumed to be true for 20 to 80 % of the gratings' maximum reflectivity R_{max}. The corresponding wavelength range is marked as $\delta\lambda$. For this part of the spectrum, on both sides of the main peak, the slope is constant with a value presented as $dR/d\lambda$. For experiments that only include reflection spectra it is useful to normalise the reflectivity of the grating with the main peak giving by definition a reflection of 1.

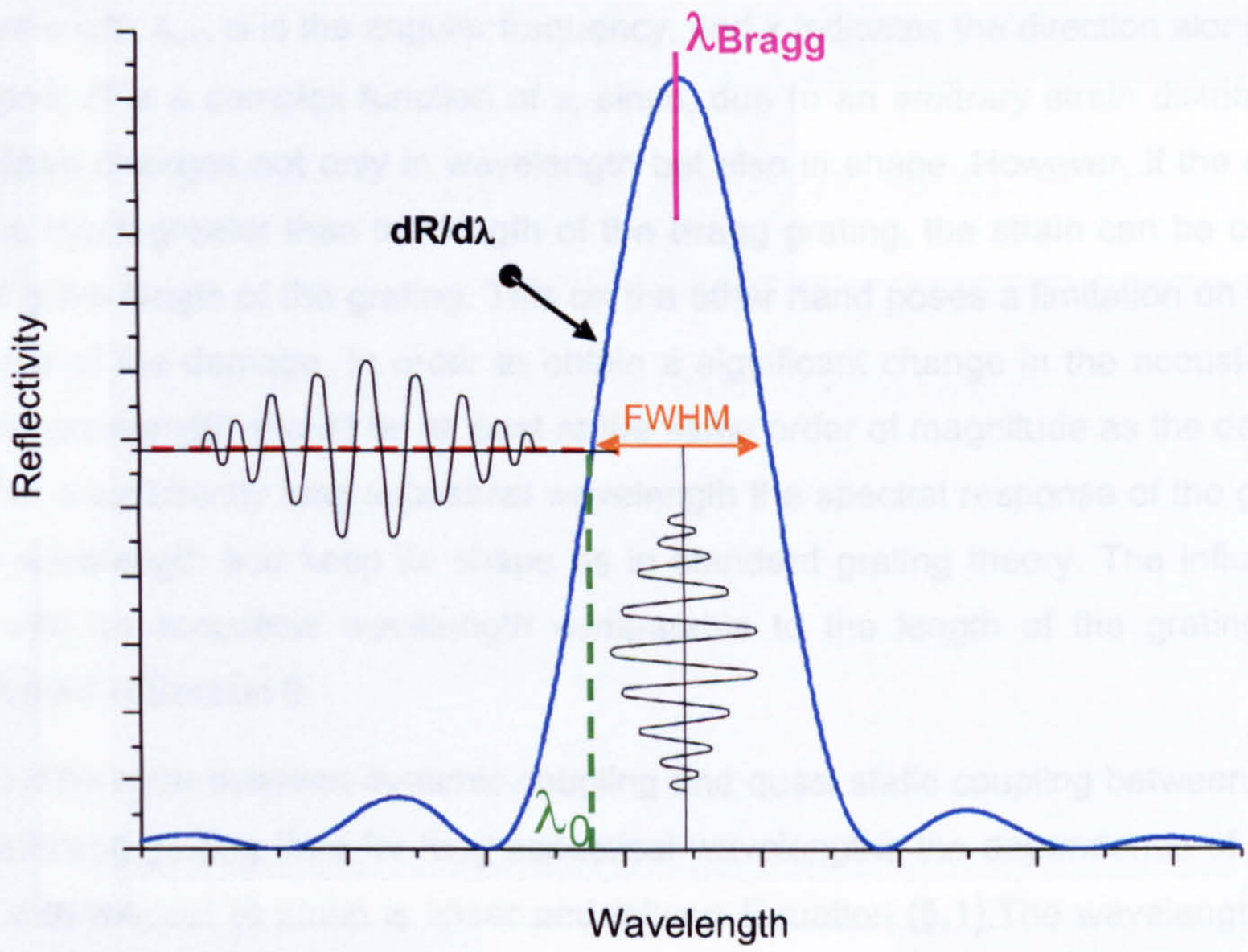

Figure 5.1: Relevant parameters to describe the grating spectrum.

While the input wavelength is kept constant, as a first step the laser should be tuned to any point in the spectrum where the linear approximation holds. Yet, in order to achieve the maximum range in both directions, the laser should be set to the wavelength at FWHM (Full Width at Half Maximum). This results in a linear relation of the shift of the optical spectrum and the reflected power amplitude. With the laser being fixed at the wavelength λ_0 (see Figure 5.1), the time-varying reflection of the grating can be given as a function of the time-varying wavelength of the main peak $\lambda(t)$ and initial reflection R_0:

$$R(\lambda(t)) = \frac{dR}{d\lambda}\lambda(t) + R_0 \tag{5.3}$$

The acoustical wave travelling through the material is described as a series of expansions and compressions, yielding a time-dependent strain field $\varepsilon(t)$. The next step is to find an equation that represents R as a function of the strain $\varepsilon(t)$. As a first assumption, the strain field is modelled here by a longitudinal strain wave propagating along the fibre axis. In addition, the time dependence is assumed to be sinusoidal.

$$\varepsilon(t) = A_{US}\cos(k_s x - \omega t) \tag{5.4}$$

Here A_{US} is the amplitude of the acoustic wave, $k_{US} = 2\pi/\lambda_{US}$ is the wave number to the acoustic wavelength λ_{US}, ω is the angular frequency, and x indicates the direction along the fibre axis. In general, R is a complex function of ε, since, due to an arbitrary strain distribution, the grating spectrum changes not only in wavelength but also in shape. However, if the acoustical wavelength is much greater than the length of the Bragg grating, the strain can be considered constant along the length of the grating. This on the other hand poses a limitation on the actual detectable size of the damage. In order to obtain a significant change in the acoustical wave, the acoustical wavelength should be at least at the same order of magnitude as the defects size or smaller. For a sufficiently long acoustical wavelength the spectral response of the grating will shift only in wavelength and keep its shape as in standard grating theory. The influence of a strain field with an acoustical wavelength comparable to the length of the grating or even smaller is studied in Section 0.

If there is no difference between dynamic coupling and quasi static coupling between the strain field and the Bragg grating then for long acoustical wavelengths the dependence of the Bragg wavelength with respect to strain is linear and follows Equation (5.1).The wavelength shift will be modulated with the same frequency as the acoustic wave. From (5.3) and (5.4), the reflection as a function of strain can be written as follows:

$$R(\varepsilon(t)) = \frac{dR}{d\lambda}\frac{d\lambda}{d\varepsilon}\varepsilon(t) + R_0 \tag{5.5}$$

This can be simplified to

$$R(t) = R_0 + \frac{dR}{d\varepsilon}\cdot\varepsilon(t) \tag{5.6}$$

with

$$\frac{dR}{d\varepsilon} = \frac{dR}{d\lambda}\cdot\frac{d\lambda}{d\varepsilon} \tag{5.7}$$

Both terms on the right-hand side in Equation (5.7) can be obtained from calibration experiments, as described below. The first term $dR/d\lambda$ is different for each grating. Its value is a

function of the grating reflectivity and the grating's bandwidth, both depend on the length and the strength of the grating. The second term $d\lambda/d\varepsilon$ depends on material parameters and corresponds to $(1-P^{eff})$ in Equation (5.1).

For the measurements, the results are not obtained in terms of reflection but rather in terms of reflected optical power. The optical power $P_{r,opt}$ in Equation (5.2) is converted to an electrical voltage $U(t)$ by means of the photo receiver. The equation that relates the measured electrical voltage to the strain field seen by the fibre grating can be described by:

$$\varepsilon(t)=\left[U(t)\cdot\frac{R_0}{U_0}-R_0\right]\cdot\left(\frac{dR}{d\varepsilon}\right)^{-1} \tag{5.8}$$

The time-dependent voltage can be expressed in terms of a DC and AC component:

$$U(t)=U_0+\Delta U(t) \tag{5.9}$$

Finally the acoustical strain is given as a function of the measured voltage:

$$\varepsilon(t)=\left[\Delta U(t)\cdot\frac{R_0}{U_0}\right]\cdot\left(\frac{dR}{d\varepsilon}\right)^{-1} \tag{5.10}$$

where by definition the strain at $t = 0$ and $U = U_0$ is zero.

Using Equation (5.10), it is possible to determine the acoustic strain levels from the fibre-optic signal, provided that the calibration has been carried out carefully. The next section presents the results of the calibration experiments where the grating parameters were obtained. First the optical set-up is explained, followed by a description of the experiments.

5.1.2 Interrogation System

The idea of a combined system based on fibre Bragg gratings is very attractive. Yet, the demands on the optical interrogation system are stringent, because high absolute accuracy and ultra-fast interrogation have to be implemented in a single system. An approach including a tuneable laser source will be able to meet these requirements. This approach enables a dual loads and damage monitoring system, where the fibre optical systems runs in a scanning mode to record the load levels for the time the structure is in service. During maintenance however, when the structure is out of service, the system can be driven in the acousto-ultrasonic mode in

order to detect any structural damage. The loads sensing part of the system has been explained in Section 3.5.2.

The optical interrogation system is based on a tuneable laser (TL), shown in Figure 5.2. An external cavity laser (ECL) is used because of its extremely narrow linewidth (below 100 kHz) and its wide tuning range of about 100 nm in the 1500 nm region. The gratings are interrogated in reflection, their signal being detected by a photo receiver (PD). Any oscilloscope or PC-based system can be used to acquire the data. This set-up enables the interrogation of several Bragg gratings (FBGS λ_1 to λ_n) within a single optical fibre by means of wavelength division multiplexing (WDM). Each grating can be measured within a certain time, before the laser scans to the next wavelength, which is the wavelength of the corresponding grating at FWHM. In the intended application, where damage detection is carried out in certain inspection intervals, an interrogation sequentially in time is adequate. In conclusion, this permits monitoring of a large area of a structure with only one optical fibre and one ultrasonic actuator. For a detailed discussion of the lay-out of such a system see Section 7.2.7.

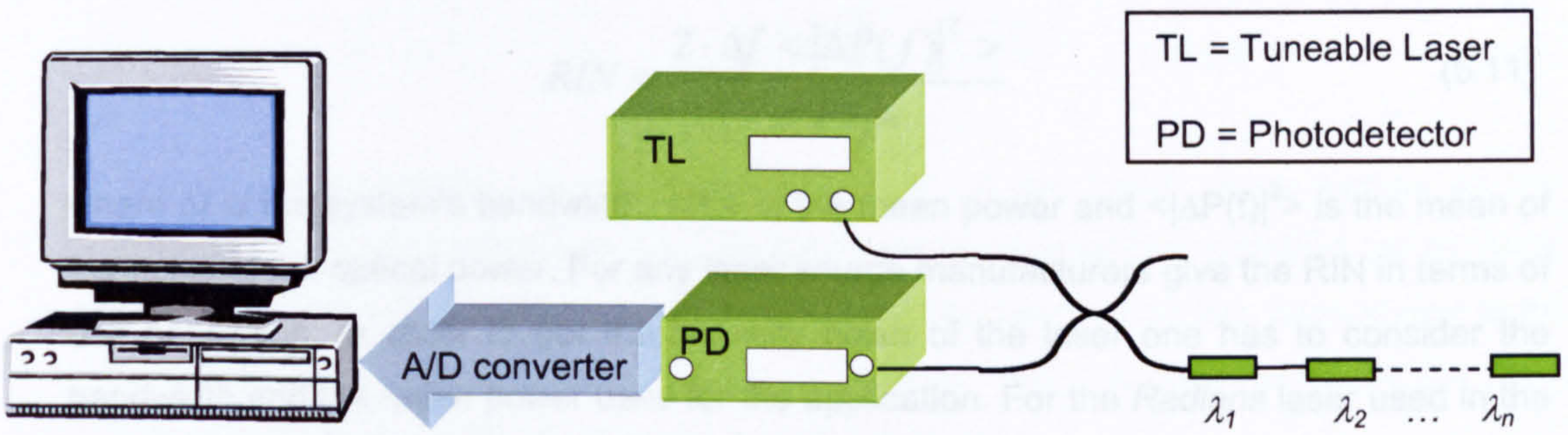

Figure 5.2: Measurement set-up for acousto-ultrasonic sensing. System operates in WDM mode.

System requirements

The requirements for the system bandwidth are determined by the expected acoustical frequencies. Lamb wave propagation is typically characterized by the frequency-thickness product. It is an objective to have a low frequency-thickness product, since only then will two modes of Lamb waves propagate, which simplifies signal interpretation. A low frequency-thickness product is commonly seen as <1 MHz mm. Most structures have a thickness > 1 mm, resulting in an upper limit for the acoustic frequency of 1 MHz. Standard optical receivers easily cover the required bandwidth; the same is true for a standard oscilloscope or any another A/D converter.

The required resolution in terms of voltage strongly depends on the respective test conditions and is determined by the expected acoustical strain field. The acoustical wave amplitude at the detector depends on numerous parameters e.g. transducer properties, material of the structure, location of the sensor with respect to transducer, mounting techniques, and the resulting acoustical coupling of both transducer and receiver. It has been found that a typical order of magnitude for strains related to ultrasonic Lamb waves is in the μstrain range. Equation (5.10) translates this into a requirement for the detectable voltage.

System limits

The major limits that are set for the resolution of the optical interrogation system contribute from two devices: the laser and the photo-receiver.

- *Laser noise.* Two noise sources can be identified for a laser diode: Intensity (AM) and Phase (FM) noise [208]. The intensity noise is usually addressed by defining the relative intensity noise (RIN) by relating the noise of the optical power to the mean power as [208],

$$RIN = \frac{2 \cdot \Delta f < |\Delta P(f)|^2 >}{< P^2 >} \tag{5.11}$$

where Δf is the system's bandwidth, $<P^2>$ is the mean power and $<|\Delta P(f)|^2>$ is the mean of the noise of the optical power. For any laser source manufacturers give the RIN in terms of unit bandwidth. In order to get the intensity noise of the laser one has to consider the bandwidth and the mean power used for the application. For the *Radians* laser used in the present work, the intensity noise is given as RIN/Δf <160 dB/Hz. The mean power of the laser is 1 mW and the system bandwidth is less than 1 MHz. It follows from (5.11) that the mean power of the optical noise is less than 10 nW.

The frequency noise of the laser has two main contributions which are referred to as white frequency noise and 1/f noise. White frequency noise adds a Lorentzian shaped spectrum and 1/f noise a Gaussian spectrum to the laser spectrum [208]. This means the laser oscillates not only at a single wavelength, but the spectrum is of definite width. This width is given by the manufacturer as the linewidth of the laser. The linewidth of the Radians laser is smaller than 100 kHz. This corresponds to a linewidth of 0.8 fm at 1550 nm. For optical devices the minimum distance for separation of two spectral lines corresponds to the FWHM [209]. Therefore, the minimum detectable wavelength shift of the Bragg grating corresponds to the linewidth of the laser. This minimum wavelength can be translated into a minimum detectable strain of 0.6 nanostrain.

- *Photoreceiver noise.* Every electro-optical system is limited by noise, which arises from physical processes in the electro-optic components. The level of noise in relation to the

signal is given by the signal-to-noise-ratio (SNR). In photodetection the noise determines the minimal incident power which can be detected. A detailed analysis of the noise components can be found for example in [210, 211]. The signal-to-noise-ratio (SNR) can be written as the ratio of the total mean square signal current to the total mean noise current. The squared total mean noise current is the sum of the squares of the individual noise sources: signal shot noise, dark current shot noise, and thermal noise. The equivalent optical power related with detector noise currents can be calculated using the response (in units Amps/Watts) of the photodiode. The minimum detectable signal current is assumed to be that for which the total signal current equals the total noise current (SNR=1). In terms of power, this is the noise-equivalent-power (NEP). The NEP is usually quoted for unity bandwidth in units of W/√Hz. Usually, the manufacturer gives the NEP in the specifications of the photoreceiver. This is usually the sum of thermal, electrical, and dark current shot noise. The photoreceivers used within the present work have a NEP < 5pW/√Hz. If a system bandwidth of 1 MHz is assumed, the NEP is

$$\sqrt{<|\Delta P(f)|^2>} \qquad \leq 5\frac{pW}{\sqrt{Hz}} \cdot \sqrt{1MHz} \qquad \leq 5nW \tag{5.12}$$

From the experiments the mean optical power of the Lamb wave signals at the photoreceiver could be determined. The minimum signal level that occurred corresponds to 0.8 µW. This can be compared to the power of the noise, which has been shown to be dominated by the relative intensity noise of the laser. With the obtained values the SNR of the FBGS interrogation system can be estimated as

$$SNR \geq \frac{800\,nW}{10\,nW} = 19\,dB \tag{5.13}$$

An experimental procedure to determine the SNR of the interrogation system is presented In Section 6.5. This procedure was applied to get the SNR of the optical interrogation system for single shot measurements: an SNR of 14 dB was found. The experimental SNR is less than what could be expected from the theoretical estimations. Yet, for the experiments other noise sources than optical ones could also contribute to the SNR, e.g. electrical noise or mechanical vibrations. In Section 5.1.4 the SNR for the FBGS and the PZT are compared. As they show the same level of SNR, it is likely that it can be concluded that other noise sources than from the optical interrogation system dominate the Lamb wave detection.

5.1.3 Calibration of the Sensor

Equation (5.10) gives the key parameter for increasing the sensitivity of the system: $dR/d\varepsilon$. In order to achieve a maximum sensitivity, it should have the highest possible value, hence, both values $dR/d\lambda$ and $d\lambda/d\varepsilon$, (see Equation (5.7)), should be maximised. Whereas the first parameter can be adjusted over a wider range by appropriate grating parameters, e.g. length, strength, the second one is a material constant and varies only slightly for different types of fibre. Bragg gratings from different manufacturers have been studied by *DaimlerChrysler* over the last few years [112]. The variation in the strain sensitivity is marginal and it can assumed to be a constant within the measurement uncertainties. The value which is used in this work is $d\lambda/d\varepsilon$ = 1.2 pm/µstrain for a grating at 1540 nm. To study the variation of $dR/d\lambda$ with the grating parameters, several different types of gratings from one manufacturer were acquired. Grating specifications varied in reflectivity (10 %, 50 %, 90 %) and length (1 mm, 5mm).

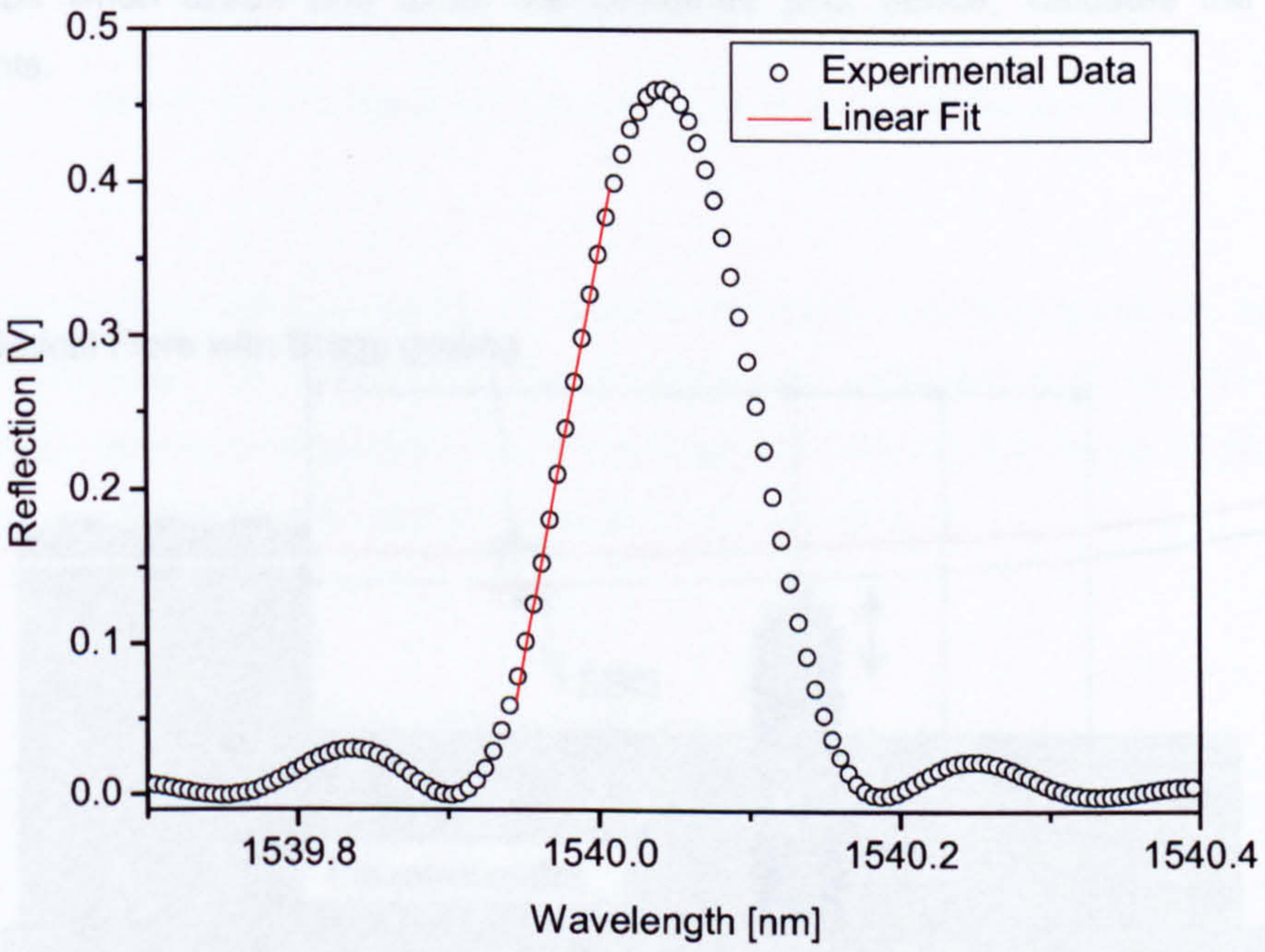

Figure 5.3: Measured grating spectrum and linear fit between 20 and 80% of the peak value.

For each grating, the reflection spectrum was measured. A high-resolution interrogation system as described in the chapter on load monitoring was used. Figure 5.3 shows a typical result. A linear fit gives the desired value of the spectrum's slope and also, the wavelength range where the linear approximation holds can be obtained. As stated above, the grating length should be as short as possible, since it has to be much shorter than the acoustical wavelength. The gratings that have been chosen as possible ultrasonic sensing elements have a length of 1 mm.

To validate the resulting value for $dR/d\varepsilon$, a simple experiment has been carried out where both strain and the change in reflected power were measured. This involved a cantilever on which an electrical strain gauge (ESG) and a fibre grating have been mounted. The layout is schematically presented in Figure 5.4. By deflecting the cantilever, a strain is introduced in both the ESG and the grating. In order to accurately control the deflection of the cantilever, a piezotranslator was used. The grating and the ESG are glued to opposite sides of the cantilever, leading to a different sign of the respective strain values. In addition, the expected strain levels could also be calculated using standard beam bending theory. Figure 5.5 sets out the result of the experiments. In this graph the starting point where the laser is set to 50 % of maximum reflection is marked as FWHM. The range where the grating response is linear with strain can be clearly identified. The deviation from the linear fit at higher strain levels can be attributed to a thermal drift of the sensor during the time of measurements. The numerical value for the sensitivity $dR/d\varepsilon$ is obtained by a fitting routine. The result is within 5% of the theoretically derived value when $dR/d\lambda$ and $d\lambda/d\varepsilon$ are combined and, hence, validates the theoretical developments.

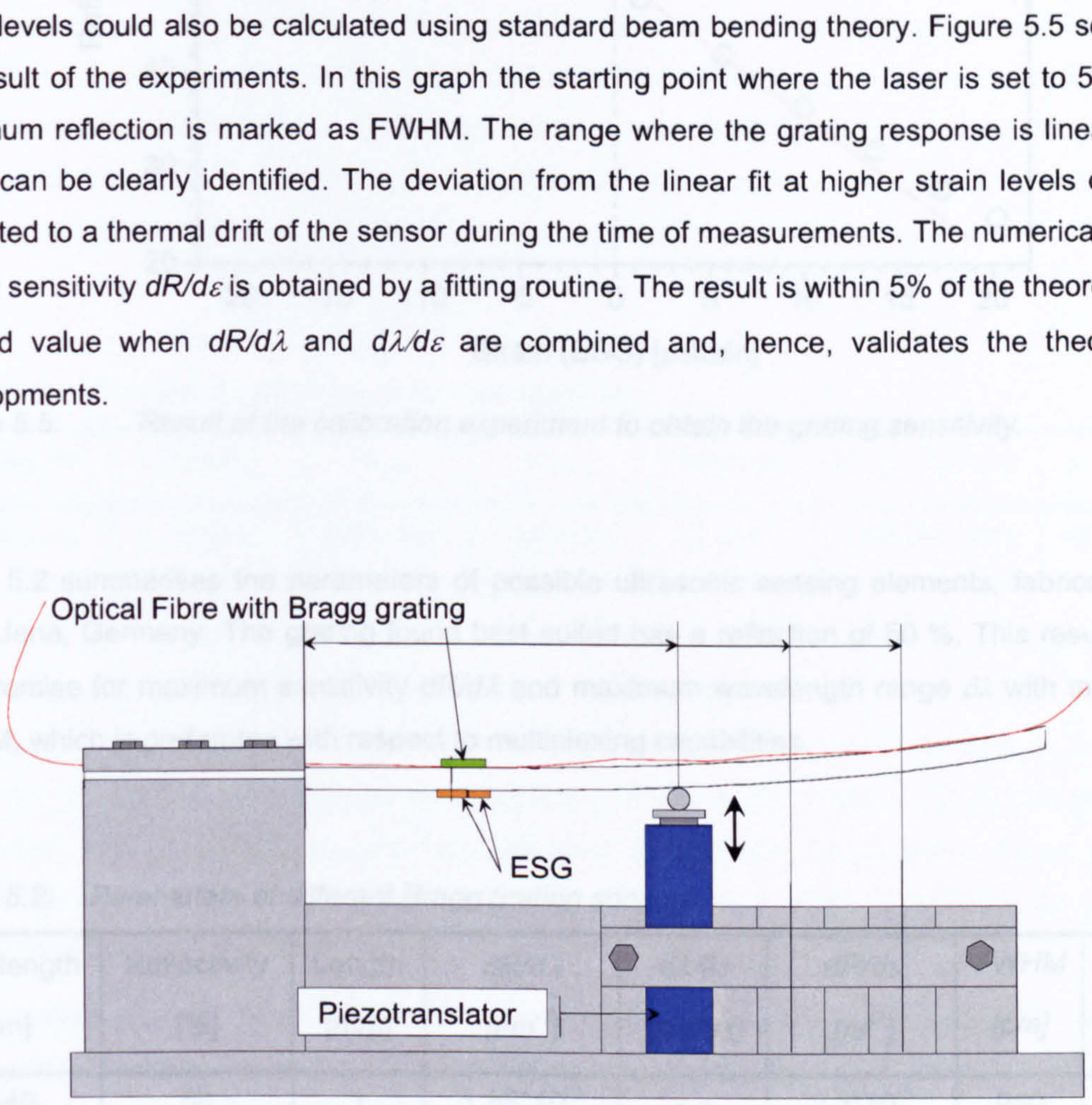

Figure 5.4: Cantilever experiment for calibration of the FBG ultrasonic sensor.

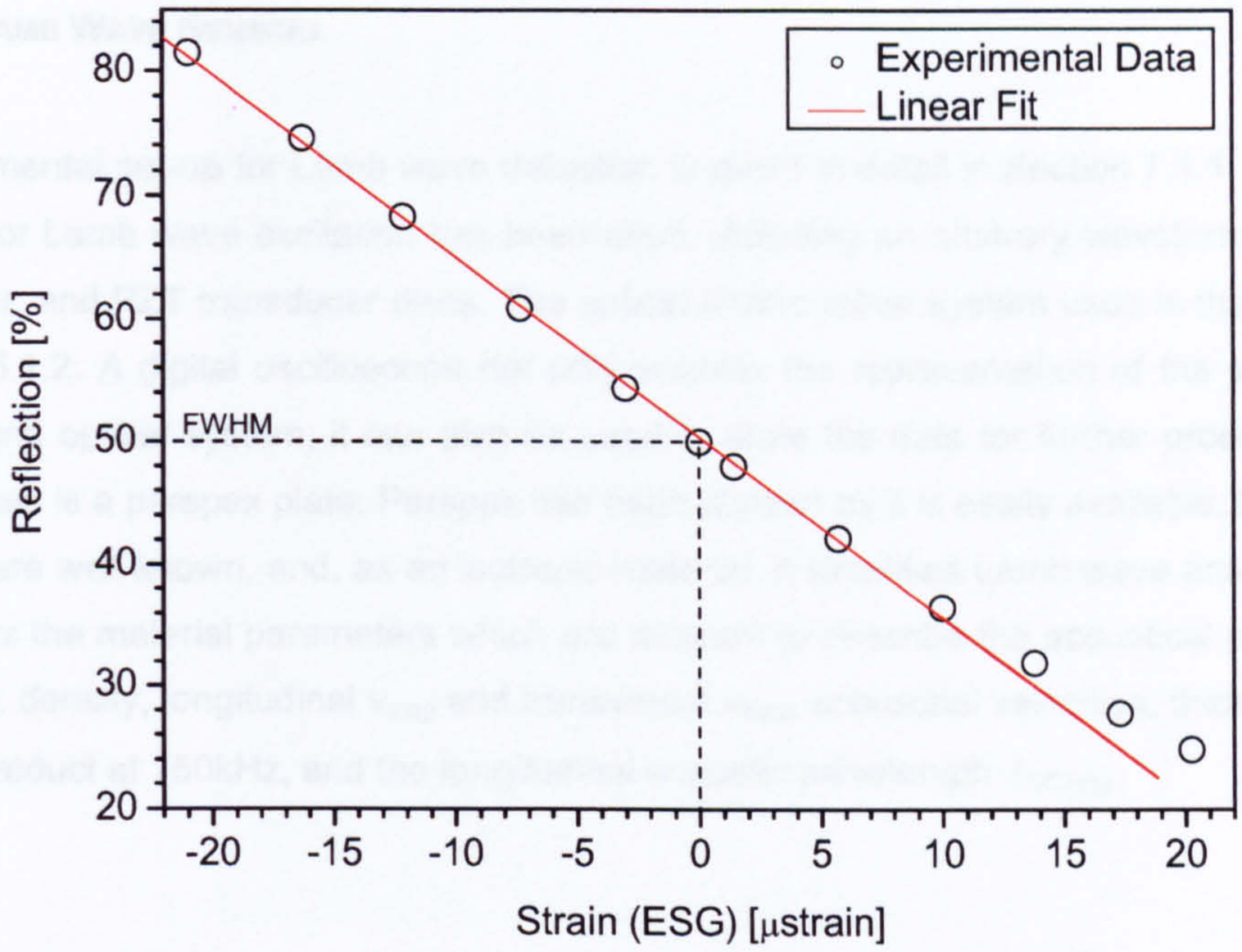

Figure 5.5: Result of the calibration experiment to obtain the grating sensitivity.

Table 5.2 summarises the parameters of possible ultrasonic sensing elements, fabricated by *IPHT* Jena, Germany. The grating found best suited has a reflection of 50 %. This results in a compromise for maximum sensitivity $dR/d\lambda$ and maximum wavelength range $\delta\lambda$ with minimum FWHM, which is preferable with respect to multiplexing capabilities.

Table 5.2: Parameters of different Bragg grating sensors.

Wavelength [nm]	Reflectivity [%]	Length [mm]	$dR/d\lambda$ [pm^{-1}]	$d\lambda/d\varepsilon$ [$pm/\mu\varepsilon$]	$dR/d\varepsilon$ [$\mu\varepsilon^{-1}$]	*FWHM* [pm]	$\delta\lambda$ [pm]
1540	50	1	$1.88*10^{-3}$	1.2	$2.3*10^{-3}$	950	300
1540	10	5	$1.13*10^{-2}$	1.2	$1.4*10^{-2}$	130	50
1540	90	1	$2.23*10^{-3}$	1.2	$2.7*10^{-3}$	1380	300
1548	99	5	non-linear	-	non-linear	3000	-

5.1.4 LAMB WAVE SENSING

The experimental set-up for Lamb wave detection is given in detail in Section 7.1.1. A standard technique for Lamb wave excitation has been used, including an arbitrary waveform generator, RF amplifier, and PZT transducer discs. The optical interrogation system used is that described in section 5.1.2. A digital oscilloscope not only enables the representation of the signals from both PZT and optical system, it can also be used to store the data for further processing. The test specimen is a perspex plate. Perspex has been chosen as it is easily available, the material properties are well known, and, as an isotropic material, it simplifies Lamb wave analysis. Table 5.3 presents the material parameters which are relevant to describe the acoustical properties of the sample: density, longitudinal v_{long} and transversal v_{trans} acoustical velocities, thickness of the plate, FT product at 150kHz, and the longitudinal acoustic wavelength $\lambda_{US,long}$.

Table 5.3: Acoustical properties of the test specimen.

Material	Density	v_{long}	v_{trans}	Thickness	FT @ 150kHz	$\lambda_{US,long}$
perspex	1.18 g/cm³	2.67 km/s	1.12 km/s	3 mm	450 kHz mm	18 mm

The $\lambda_{US,long}$ is several times greater than the grating length, and the FT product is smaller 1 MHz mm, thus fulfilling the requirements defined in Sections 5.1.1 and 5.1.2. Furthermore, for this small frequency-thickness product, the first symmetrical Lamb wave mode is non-dispersive, which allows a straightforward signal interpretation, which is sufficient for a simple validation experiment at this stage.

The distribution of the different types of actuators and sensors is shown Figure 5.6. The lines along which the acoustic wave travels are marked with a dotted line, the distances are given in mm. In contrast to the FBGS, a PZT can be used as both an actuator or sensing element. Both PZT and Bragg grating (FBGS) have been surface mounted. A mounting technique for the fibre grating with an optimal strain-transfer from the structure to the fibre has been presented in Chapter 2.

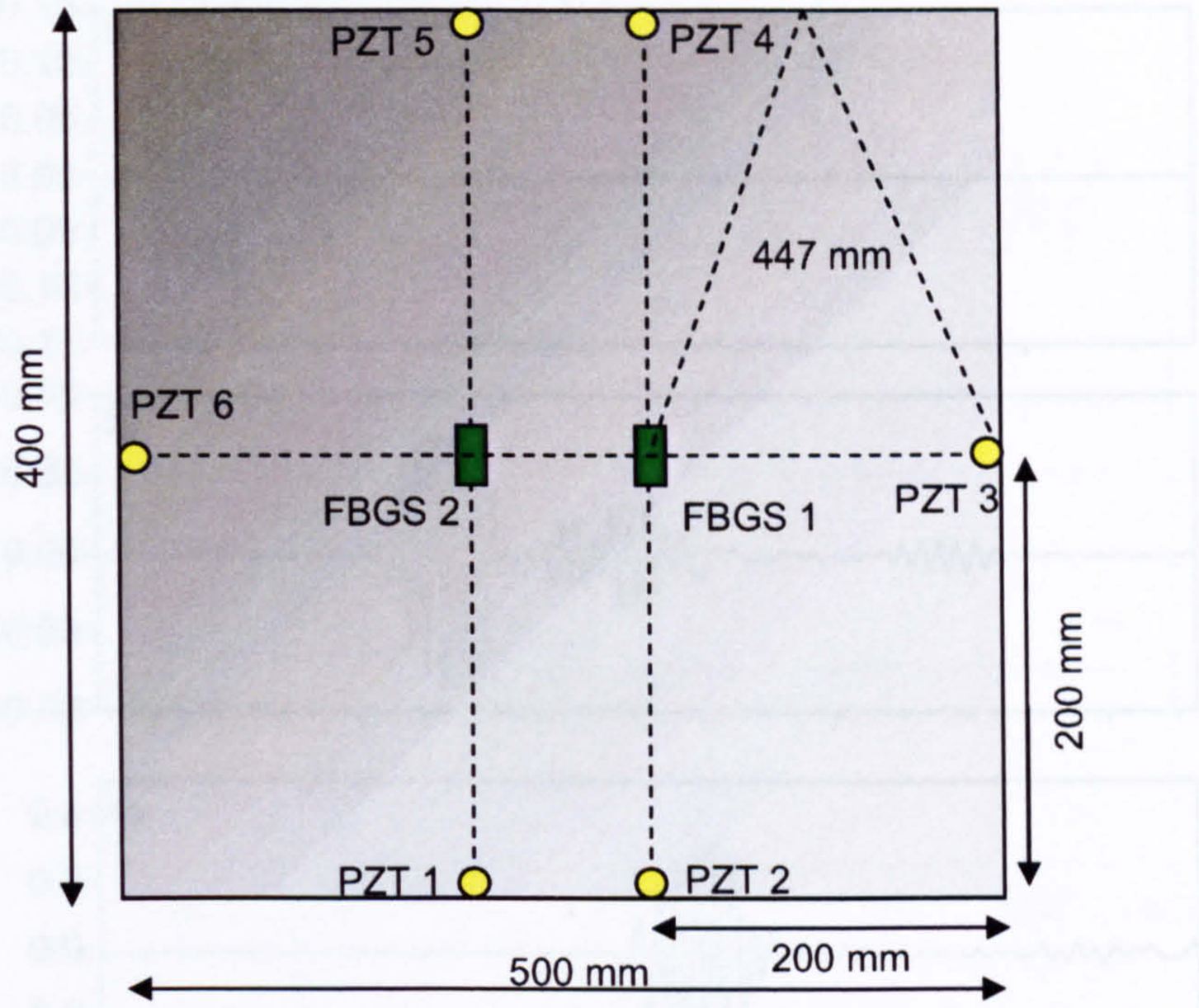

Figure 5.6: Dimensions of the Perspex plate and location of PZT and receivers FBGS.

Figure 5.7 shows the actuator signal and corresponding receiver signals from both PZT and FBGS. The actuator signal is a 5 cycle sine tone burst at 150 kHz. In this experiment PZT 2 acts as the transducer, PZT 4 and FBGS 1 are the receivers. The evaluation of both sensor signals reveals that the acoustic wave is dominated by the fundamental symmetric mode. The corresponding time matches the distance-velocity quotient for the velocity. On closer inspection the FBGS response shows several smaller signals besides the dominating symmetric mode at 100 µs. A possible explanation for the signals around 150 µs is the interference of the antisymmetric mode with reflections of the symmetric one. At 300 µs the back reflection of the symmetric mode from the opposite edge of the plate can be observed. Using Equation (5.10) the related strains in the optical fibre can be found. With the calibration parameters given in Table 5.2, a strain level of ±4 µstrain was obtained, which is in good agreement with the assumptions made in Section 5.1.1. The signal-to-noise ratio is 13dB for both the PZT and FBG sensor for a single shot measurement and 26 dB for a 128 times averaged signal, which is presented in Figure 5.7.

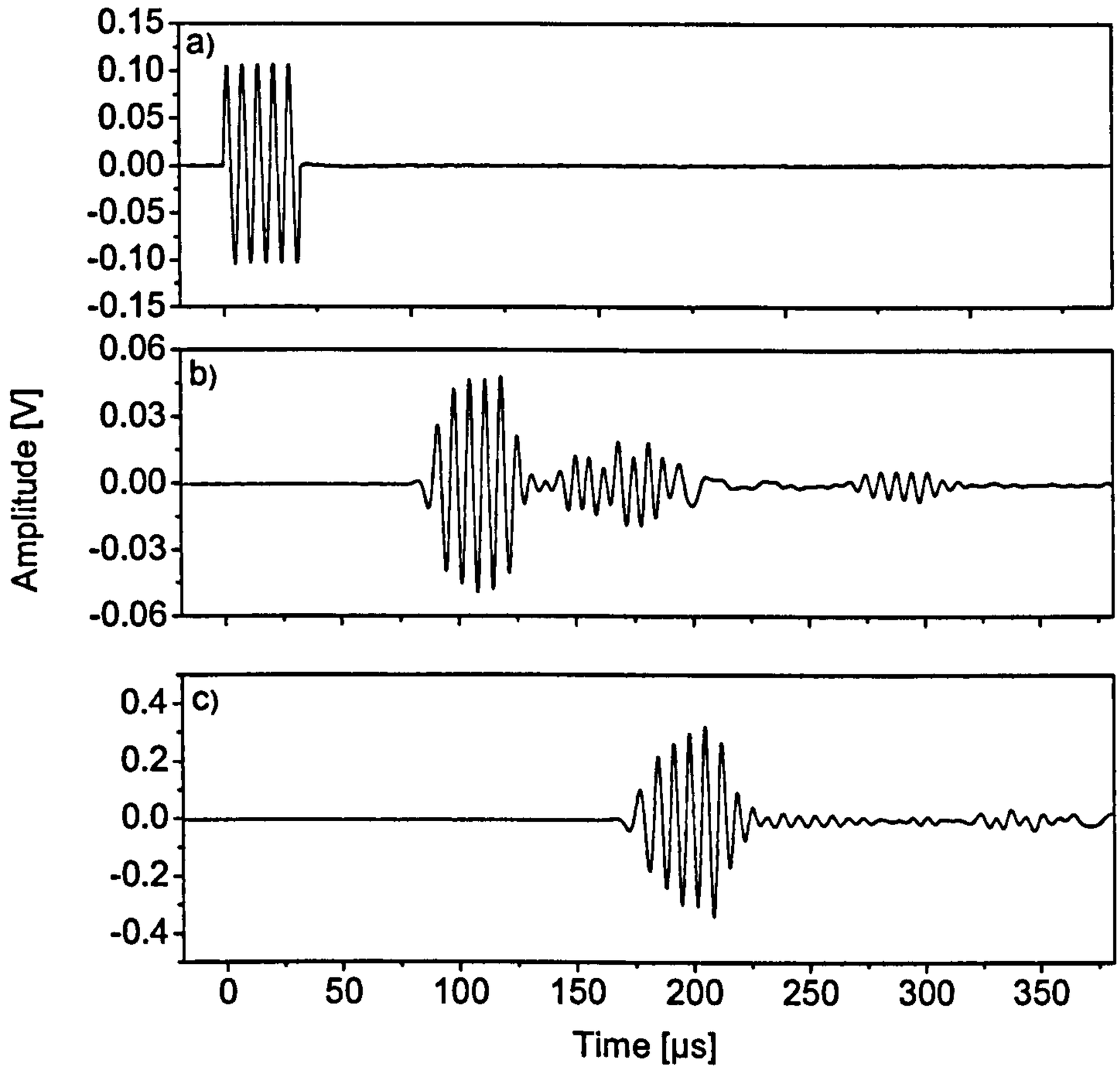

Figure 5.7: Lamb wave response on Perspex plate (see Figure 5.6) using FBGS and PZT: a) Excitation signal (PZT2); b) FBGS signal (FBGS1); c) PZT signal (PZT4).

As illustrated in Figure 5.8 the Bragg grating exhibits high directivity. The upper part shows the response of FBGS 1 when the acoustic wave is launched perpendicular to the fibre by PZT 3. The lower part refers to the parallel case, when the actuator is PZT 2. For both experiments, the grating interacts at 100 µs with the symmetric mode. However, the amplitude in the perpendicular case is hundredfold less than for the parallel one. This can be interpreted as follows: It is known from Section 2.5.5 that the grating is most sensitive to strain along the fibre axis. In addition the mounting technique of the fibre ensures maximum transfer of strains parallel to the fibre axis. The other parts of the signal refer to interferences between different modes and reflections from the sample edges. The directivity of the FBGS becomes important when their ability for damage location is studied in Chapter 7.

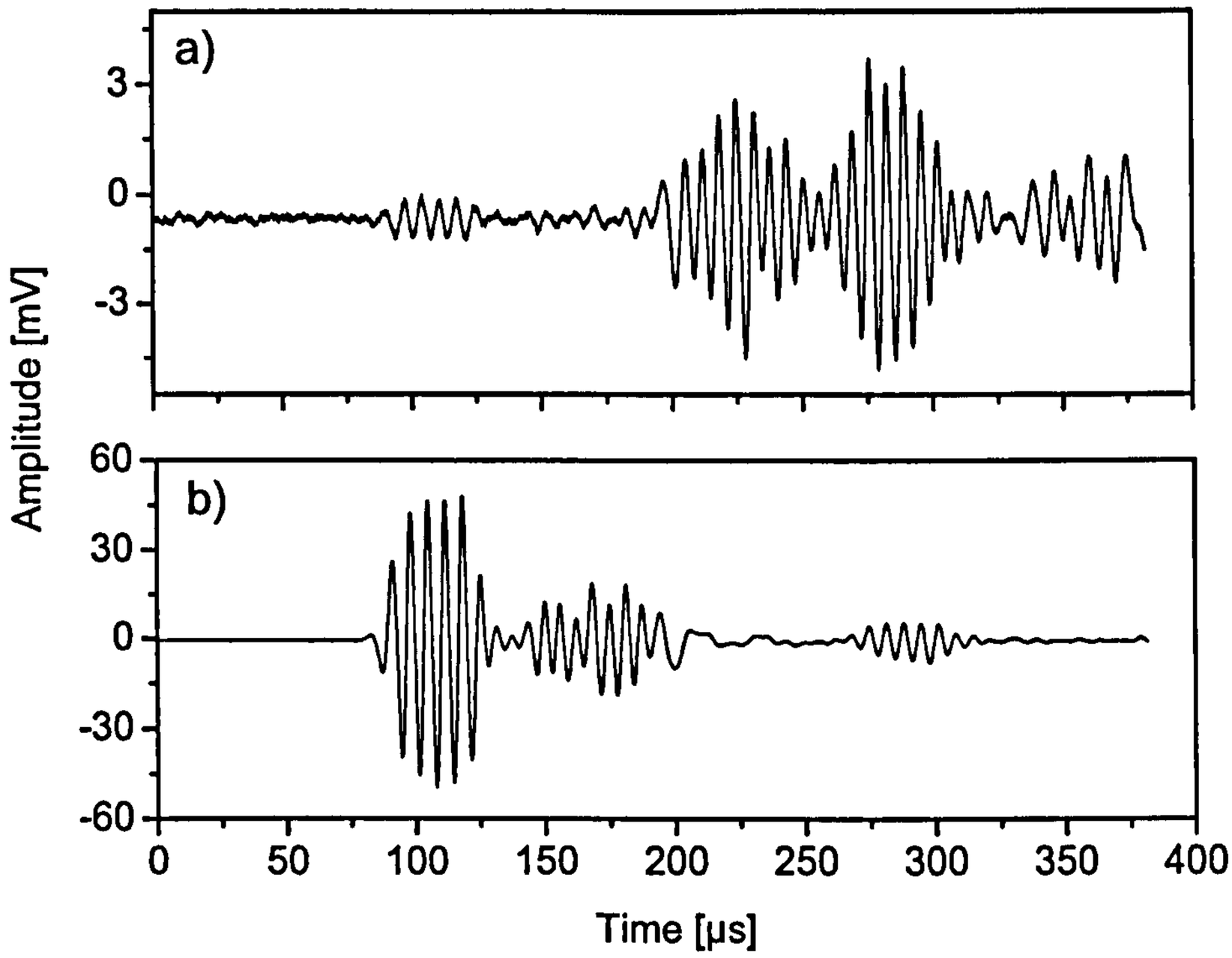

Figure 5.8: *FBGS signal for different orientation of the transducers with respect to fibre axis:*
a) FBGS perpendicular to the direction of acoustical propagation;
b) FBGS parallel to the direction of acoustical propagation.

Table 5.4 gives an overview of the state-of-the-art FBG ultrasound detection systems that have been published within the last few years. The table reveals the unique approach followed within the presented work. So far, no attempt had been made to sense ultrasonic Lamb waves using FBG sensors. Although it is difficult to compare the individual systems, as they have been designed for different purposes, it appears they cover a large range of acoustical frequencies from 1.7 KHz to 2.3 MHz. As the performance of the presented systems is not discussed in the publications a direct comparison of the achieved SNR or sensitivity is not possible. therefore, the table also includes one system that uses a Mach-Zehnder interferometric sensor to detect Lamb waves. The results of this system in terms of detected acoustical frequency and SNR compare very well to that of the present work.

Table 5.4: Published values for FBG ultrasound detection systems.

Reference	Sensor	Acoust. frequency	SNR	Application
[204]	FBG	1.7 kHz	-	seismic signals
[205]	FBG	100 kHz	-	acoustic emission
[202, 203]	FBG	35 kHz	-	underwater hydrophone
[199, 201]	FBG	1.9 MHz	-	underwater hydrophone
[25]	FBG	2.3 MHz	-	underwater hydrophone
[87, 212]	Mach-Zehnder	230 kHz	13 dB	Lamb wave
this work	FBG	460 kHz	13 dB	Lamb wave

5.2 Simulation of the FBG Sensor Response

The spectral response of the Bragg grating to an ultrasonic wave strongly depends on the amplitude and the wavelength of the acoustical wave. For the initial considerations and experiments the acoustical wavelength was considered to be relatively long compared to the grating length. This initial assumption allows to calculate the response of the grating as for a constant strain field, i.e. the complete spectrum shifts according to Equation (5.1) and the shape of the grating remains unchanged. However, if the acoustical amplitude becomes smaller, the assumption of a constant strain level over the complete length of the grating no longer holds. The grating will interact with a non-linear variation of the strain along its length. The influence of the strain field on the shape and position of the grating spectrum taking into account the geometrical and elasto-optic effects are non-linear. The corresponding mathematical equations cannot be solved analytically. Therefore, a numerical analysis is required to study the influence of ultrasound on the spectral response of the FBGS. A commercially available software was available to carry out the analysis. The "Fiber Optical Grating Simulation for Bragg Grating *FOGS – BG*" by *Apollo Photonics Inc.* was chosen because it allows for scanning of the grating variables which enables the user to optimise the grating performance by varying a parameter in a defined range.

To study the influence of the acoustical wavelength on the response of the grating, the acoustical strain was modelled according to

$$\varepsilon(z,t) = A_{US} \cdot \sin\left(2\pi \cdot \frac{z}{\lambda_{US}} - \omega t\right) \tag{5.14}$$

where A_{us} is the amplitude and λ_{US} is the wavelength of the acoustical wave. Here, $z \in [0,L]$ is the location along the fibre axis and $\omega t \in [0,2\pi]$ is introduced as a phaseshift to model the time dependency of the wave.

The strain field along the fibre axis for different ratios of λ_{US}/L is illustrated in Figure 5.9. For $\lambda_{US} >> L$ the strain is constant along the length of the fibre, and the complete spectrum will shift according to Equation (5.1). If the ratio is 2, then half a wavelength fits into the length of the grating. This means that the complete grating is stressed, yet the strain level varies with the position z along the fibre axis, as a consequence the grating period varies along the fibre axis, too. It is known from grating theory that such a chirp influences the spectral form of the grating. The spectrum broadens and the peak reflection decreases [16, 17]. For a ratio smaller than 1, part of the grating is subjected to a compression field, the other part to an expansion field. Only numerical analysis can determine the influence on the grating spectrum.

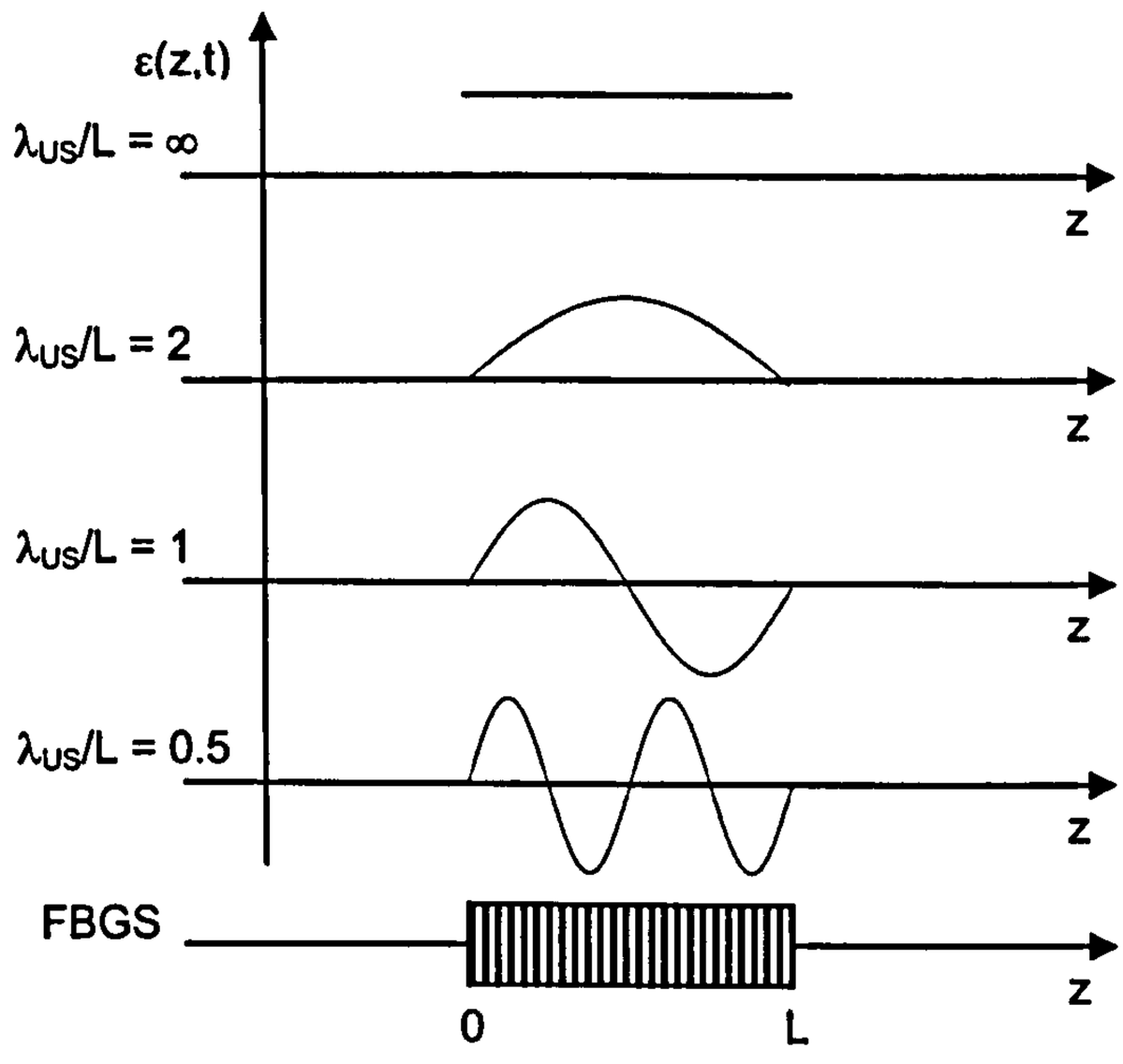

Figure 5.9: Presentation of different acoustical wavelength to grating length ratios.

In case $\lambda_{US} >> L$ the strain field will shift the complete spectrum according to Equation (5.1). The results of the software simulation when A_{US} is 50 µstrain and λ_{US} is 20 mm is shown in Figure 5.10. The acoustical amplitude was chosen relatively high compared to the experimentally values of 4 µstrain for better visualisation of the Bragg wavelength variation.

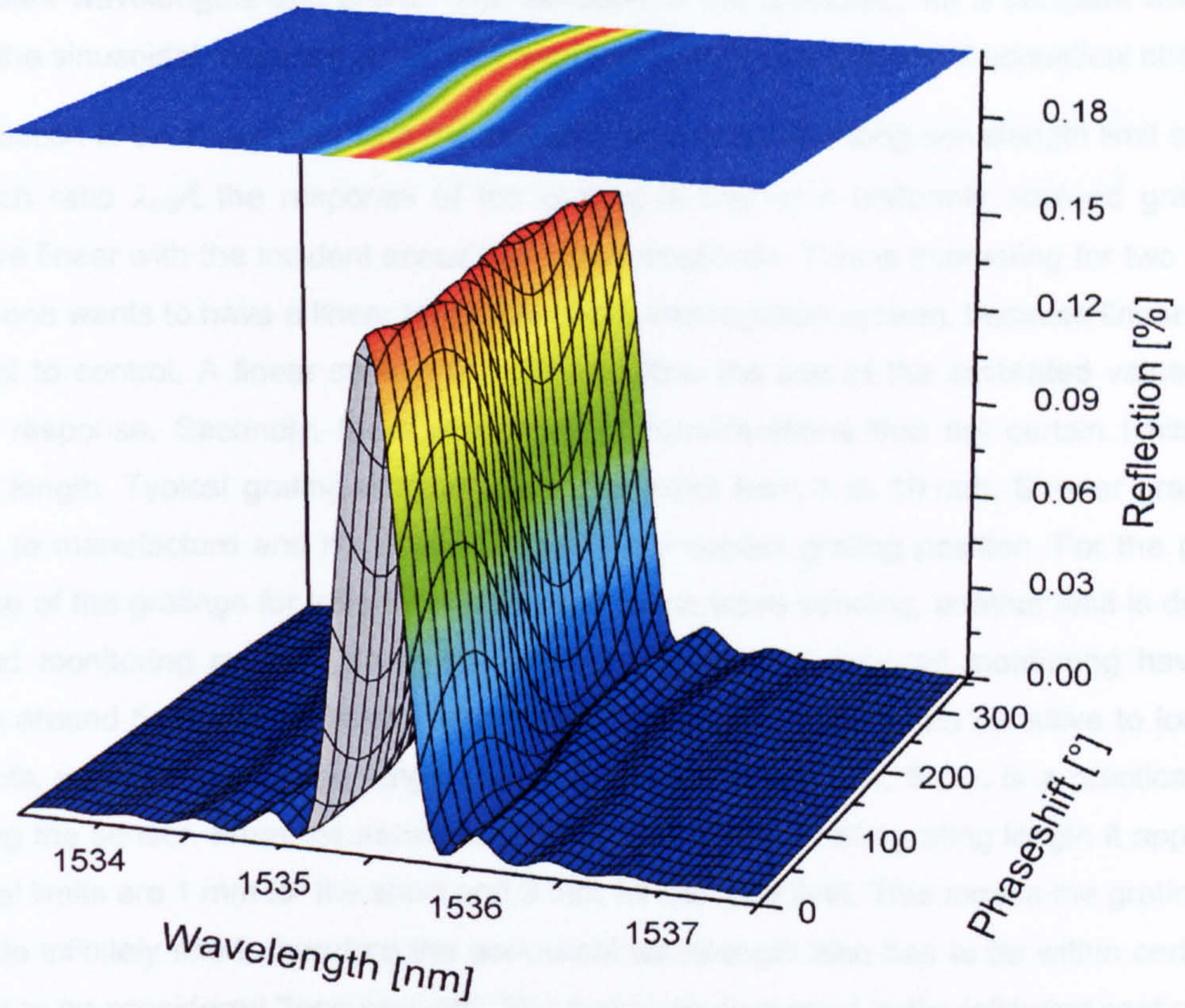

Figure 5.10: Response of the grating spectrum to a uniform time-varying strain field.

The parameters for the grating used during for the simulation were obtained by fitting the spectral response of a measured grating to the theoretical curve. The grating's parameter which are the same for all the presented simulations are:

- modulation of the refractive index: $n_{AC} = n_{DC} = 1.2*10^{-4}$
- grating length $L = 2.12$ mm
- grating period: $\Lambda = 530.655$ nm
- Bragg-wavelength: $\lambda_B = 1534.97$ nm
- sensitivity ($dR/d\lambda$): $S_{(20\%-80\%)} = 5.8*10^{-2}$ %/pm
- laser wavelength: $\lambda_0 = 1535.15$ nm

With the proposed interrogation method, where the laser is set to the wavelength at the FWHM, the response of the interrogation system to the ultrasonic wave can be studied using the simulation software. As the laser is fixed at one wavelength the response of the interrogation system is linear with the reflectivity at this specific wavelength. The reflectivity at a given wavelength can be obtained from Figure 5.10. The mesh of the contour plot gives the reflectivity

at constant wavelengths and phase. The variation of the reflectivity for a constant wavelength shows the sinusoidal response of the interrogation system to a sinusoidal acoustical strain field.

The question to be answered using the simulations is where the long wavelength limit starts, i.e. for which ratio λ_{US}/L the response of the grating is that of a uniformly strained grating and therefore linear with the incident acoustical strain amplitude. This is interesting for two reasons. Firstly, one wants to have a linear response of the interrogation system, because linear systems are best to control. A linear system would also allow the use of the calibrated values for the sensor response. Secondly, there are practical considerations that set certain limits on the grating length. Typical grating lengths are in the order from 1 to 10 mm. Shorter gratings are difficult to manufacture and it's difficult to mark the correct grating position. For the proposed dual use of the gratings for load monitoring and Lamb wave sensing, another limit is defined by the load monitoring system. Strain gauges commonly used for load monitoring have gauge lengths around 5 mm. If the length is too short, the strain gauge is too sensitive to local strain gradients, which longer gauge lengths tend to cancel. In addition, 5 mm is a practical limit for handling the sensor. From the above mentioned conditions on the grating length it appears that practical limits are 1 mm for the short and 5 mm for the long limit. This means the grating cannot be made infinitely short, therefore the acoustical wavelength also has to be within certain limits in order to be considered "long enough". The limits are discussed in the following section.

5.2.1 Parameter Study

In order to find out the limit for the ratio λ_{US}/L, the influence of the acoustical wavelength and amplitude on the grating spectrum was studied. The numerical software was used to directly simulate the output of the tuneable laser-based interrogation system.

Acoustical wavelength

The first parameter to be studied was the acoustical wavelength. As mentioned in the previous section, it is expected that for shorter wavelengths the response of the grating is no longer linear, and a deviation from the response for long wavelength signals appears. Figure 5.11 sets out the result of the study. The modulation depth of the reflection spectrum at the laser wavelength was calculated. For $\lambda_{US} >> L$ the amplitude has its maximum. This amplitude is used as a reference, for all other amplitudes at different λ_{US}/L. As the length of the grating was determined, the acoustical wavelength was varied for the simulations. The range of the wavelength was set from 1 mm to 100 mm. For an aluminium specimen, where $v_P \approx 5000$ m/s, this corresponds to a frequency range from 50 kHz to 5 MHz, which is the typical range for ultrasonic testing. The simulation was carried out at two different amplitudes of the acoustical strain. For simulation one, the amplitude was 50 µstrain and for simulation two it was 5 µstrain.

Due to the normalisation to the maximum amplitude both results can be plotted in a single figure. It appears that the response of the grating does not depend on the strain amplitude, but only on the ratio of the wavelength to grating length. The decrease in modulation depth with decreasing λ_{US}/L could be fitted to an asymptotic function: $y = a\text{-}bc^x$, the fit parameters are given in Figure 5.11.

From Figure 5.11 the limit for the minimum allowable wavelength to grating length ratio can be defined. If the limit is set to be 3 dB (50 %) of the maximum modulation depth, the minimum ratio is 1.2. This means that the acoustical wavelength should have at least 1.2 times the grating length. A more strict definition of the minimum ratio sets the decrease in amplitude to 0.2 dB (95 %). Then the minimum acoustical wavelength is 4 times the grating length. For a typical application when the structure under consideration is an aluminium plate with a velocity of 5000 m/s for the symmetric Lamb mode, and the grating length is 1 mm, the minimum acoustical wavelength is 1.2 mm or 4 mm, for a 3 dB and 0.2 dB limit, respectively. In terms of frequency this corresponds to a maximum frequency of 4.2 MHz or 1.3 MHz. As has been shown in Figure 4.3 the maximum frequency that allows only the two fundamental modes to travel is 1.6 MHz. For practical applications this means that a FBGS of 1 mm grating length can be used for Lamb wave detection for almost the complete frequency range of interest. Section 5.2.2 presents the results of the experiments, which were carried out in order to verify the results of the numerical simulations.

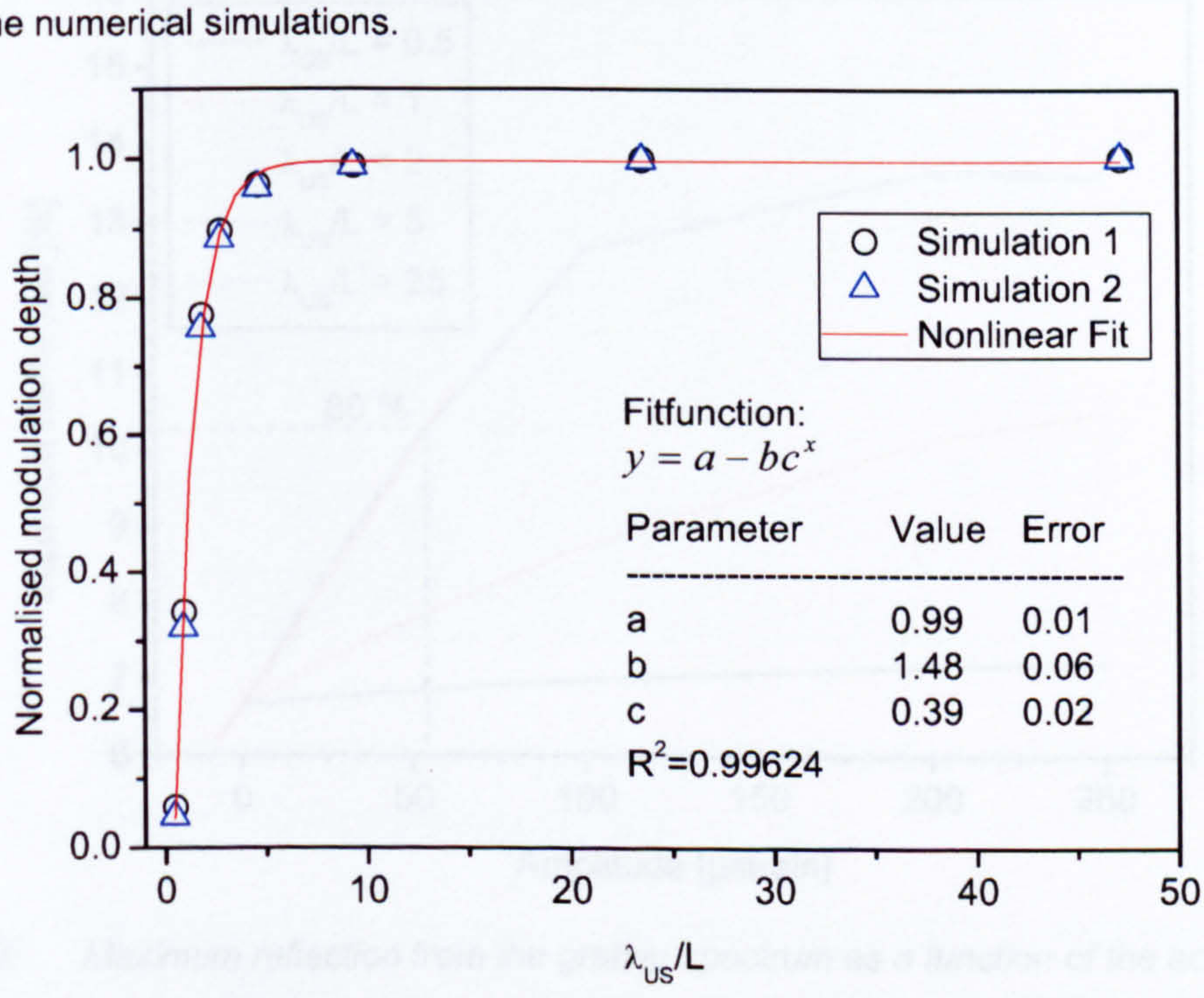

Figure 5.11: Normalised modulation depth as a function of λ_{US}/L.

Acoustical amplitude

The second parameter that was studied is the acoustical amplitude. Figure 5.12 presents the results of the simulations. The maximum reflection of the grating spectrum was calculated with increasing strain amplitude. For $\lambda_{US} >> L$ a linear increase in the maximum reflection according to the calibration data could be expected. For the grating under consideration this means applying a strain amplitude of 50 µstrain would increase the reflection from 6.7 % to 10.2 %. Figure 5.12 shows that this is exactly what was found using the simulations. The limit of $\lambda_{US} >> L$ holds for the plots of $\lambda_{US}/L = 5$ and $\lambda_{US}/L = 25$. For any ratio that is smaller than that, a non-linear behaviour of the grating leads to significantly decreased levels of the maximum reflection. The simulation also reveals the limit for the linear region as defined in Section 5.1.1. The maximum increase in amplitude relative to the starting reflection, which was 50 % as the laser is set to the wavelength of the FWHM is 80 %. For the simulation this means the linear region ends at about 10.8 %, as indicated in the plot. the red line shows the region of the constant slope between 6.7 % and 10.8 %. For higher strain amplitudes the response deviates from that slope. The maximum reflection that can observed is of course the maximum reflection of the grating, which is 13.4 % at the peak wavelength. If the strain amplitude is increased further, the maximum reflection decreases again, as the spectral peak was passed.

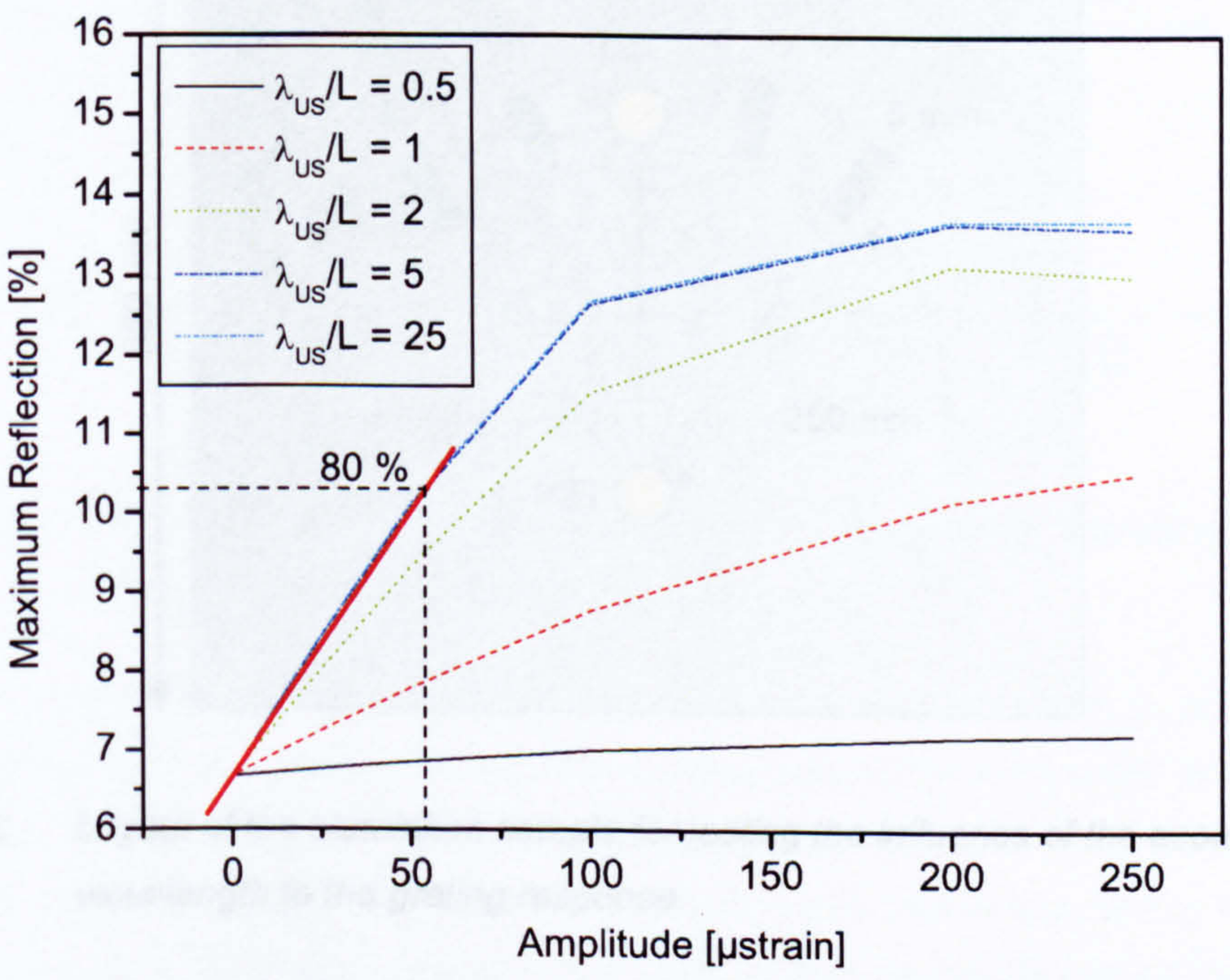

Figure 5.12: Maximum reflection from the grating spectrum as a function of the acoustical amplitude for different λ_{US}/L.

The results of the simulations show that the main parameter which influences the grating response is the acoustical wavelength. Further studies that considered the change in the

spectral shape such as the FWHM showed that even for very small ratios of λ_{US}/L no change in the FWHM could be observed. The minimum detectable change in the FWHM is 1 pm, which is the highest resolution of the software. The study showed that for acoustical wavelengths and acoustical strain levels which are typical for Lamb wave testing the proposed interrogation system in combination with grating lengths for the FBGS around 1 mm ensures linear relation of the observed sensor signal with the applied acoustical amplitude.

5.2.2 Experimental Validation

As presented in the previous section, the results from the numerical simulations predict a strong decrease in modulation depth when the wavelength to grating length ratio goes down. The experiments were carried out to study the response of FBGS with individual grating lengths to the incident acoustical waves. The experimental set-up is described in detail in Section 7.1.1.The layout of the experiment is depicted in Figure 5.13.

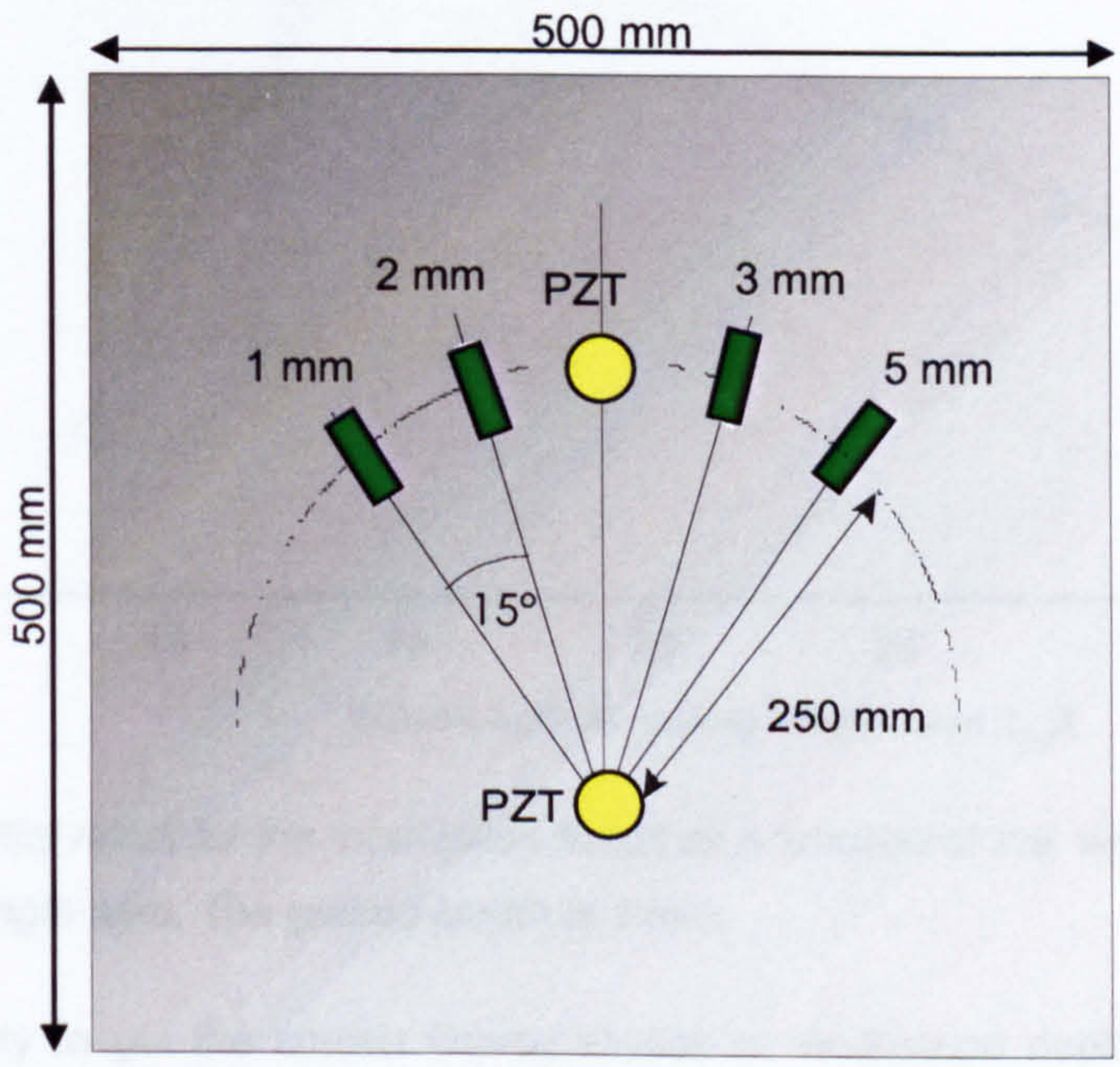

Figure 5.13: Layout of the aluminium sample for testing the influence of the acoustical wavelength to the grating response.

The gratings were glued onto the surface of a rectangular 500 x 500 x 1 mm aluminium sample. A *PI Ceramic* PZT PIC255 was used to launch the Lamb waves. For reference measurements an additional PZT was available. A disk transducer was used to launch a radial symmetric acoustical wave field. For the choice of the PZT material see Section 7.1. All gratings were placed at equal distance from the PZT transducer in order to ensure same acoustical amplitude.

As the gratings had four different lengths, i.e. 1 mm, 2 mm, 3 mm and 5 mm, a different modulation depth for each grating could be expected at the same acoustical frequency.

Figure 5.14 shows the result of the measurements for a FBGS with a grating length of 1 mm. Although there is a strong increase in modulation depth with increasing acoustical wavelength, this number decreases again after a maximum modulation depth was reached at a wavelength of 18 mm. This does not agree with the predictions from the simulations which suggested a constant modulation depth for higher wavelengths. The analysis of the experiment revealed that the recorded modulation depth represents the frequency characteristics of the PZT transducer. As explained in detail in Section 7.1, the resonance spectrum of the PZT is responsible for the obtained modulation depth characteristics.

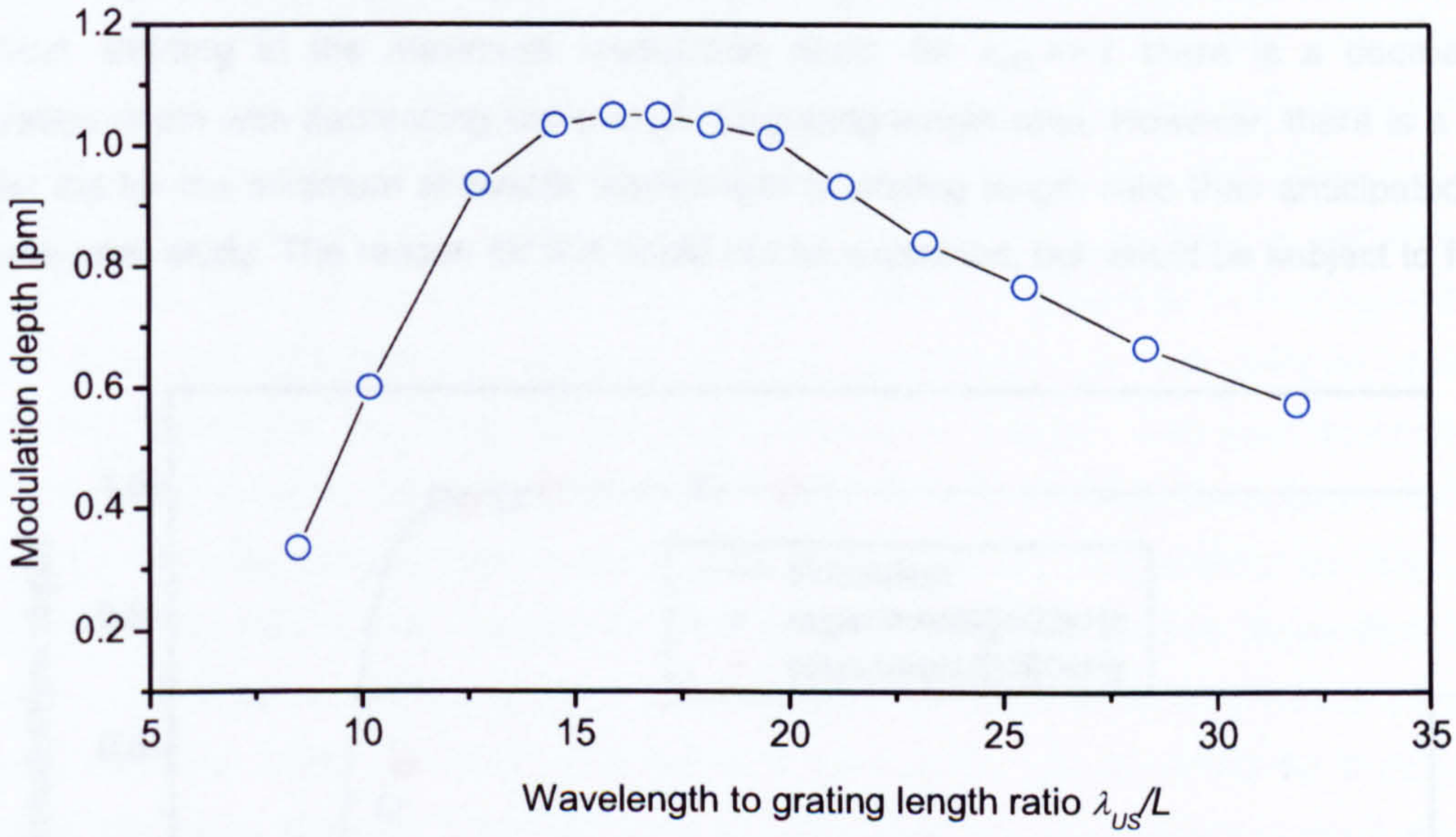

Figure 5.14: Initial result for the modulation depth as a function of the wavelength-to-grating-length ratio. The grating length is 1 mm.

The only possibility to get the correct characteristics of modulation depth is to compare the modulation depths for all gratings at equal acoustical wavelengths. In order to compare the results of the simulation with the experiment the following assumption has to be made. For $\lambda_{US} >> L$ the modulation depth has its maximum, which in this case is true for the 1 mm grating. If all results are normalised to the value of the 1 mm grating, all results can be compared with the simulation. Table 5.5 presents the measured values for the modulation depth at different acoustical frequencies.

Table 5.5: Calculation of the relative modulation depth.

Grating	Mod. depth [pm] @260kHz	Rel. Mod. Depth @260kHz	Mod. depth [pm] @400kHz	Rel. Mod. Depth @400kHz
1 mm	0.38	1	0.41	1
2 mm	0.38	1	0.40	0.98
3 mm	0.37	0.97	0.40	0.98
5 mm	0.22	0.55	0.21	0.51

The results of the experiment together with the results from the numerical simulations are shown in Figure 5.15. A good agreement of the experimental and simulated results can be observed. Starting at the maximum modulation depth for $\lambda_{US} >> L$ there is a decrease in modulation depth with decreasing wavelength-to-grating-length ratio. However, there is a much sharper cut for the minimum allowable wavelength to grating length ratio than anticipated from the parameter study. The reason for this could not be explained, but would be subject to further work.

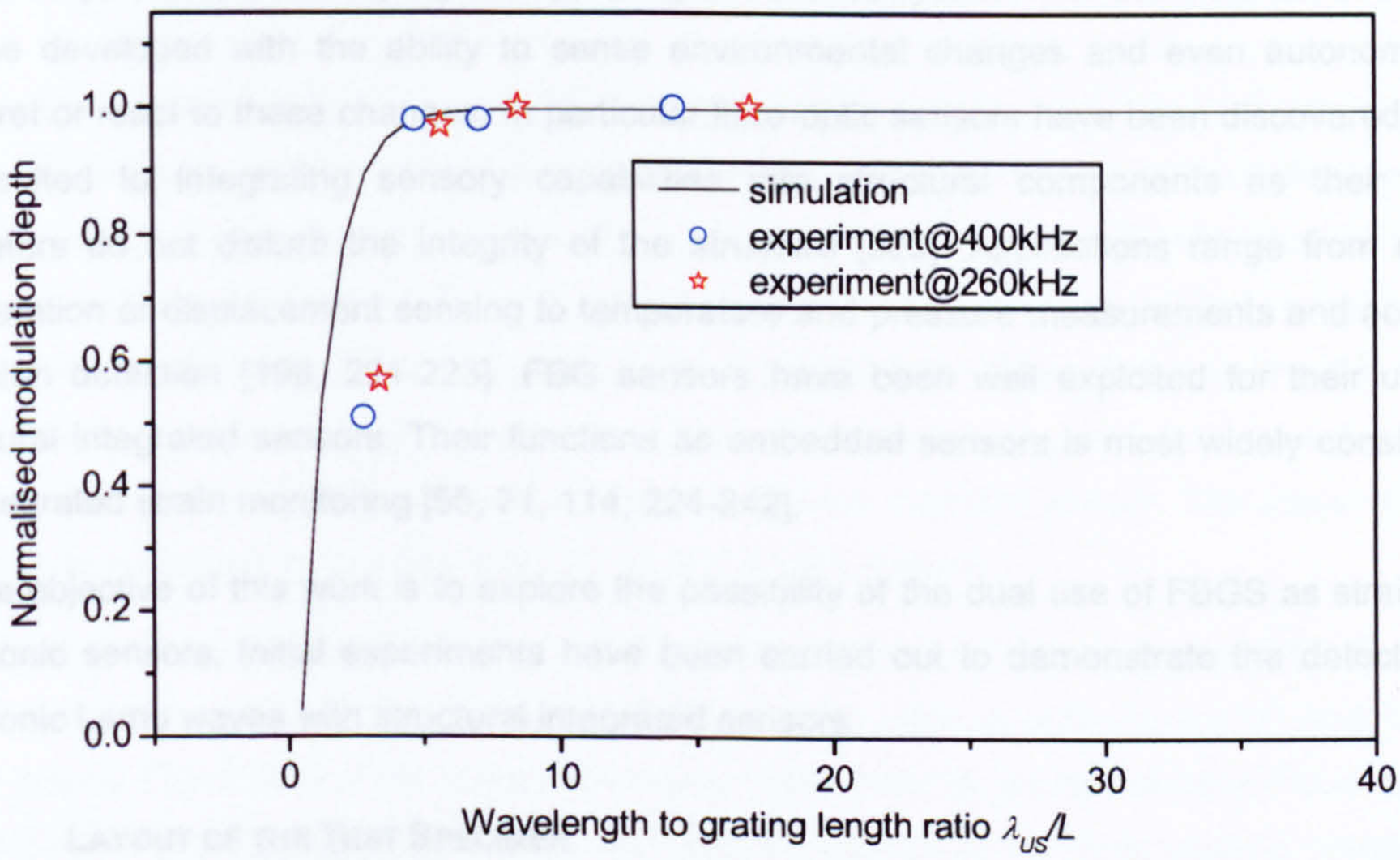

Figure 5.15: Modulation depth as a function of the wavelength-to-grating-length ratio. Results from the numerical simulations and the experiments on an aluminium sample.

5.3 Structural Integrated Sensors

The use of composites as engineering materials for aeronautic, automotive, and naval structures has considerably increased over the last ten years due to several advantages they offer over other conventional metallic materials [213]. These advantages include high strength-to-weight ratios, good fatigue resistance, good corrosion resistance, and flexibility to tailor the mechanical properties according to loading and kinematic boundary conditions. Yet, the extensive use of composite materials as primary structural members in applications such as civil aircraft or automotives has been delayed due to the fact that the reliability of components needs to be demonstrated, since the presence of damage may degrade severely their mechanical properties. In the maintenance of transportation and civil structures, the ability to evaluate the integrity of the structure without removing individual structural components has therefore become an important technological task [165, 214, 215]. As part of this trend, multifunctional structures have aroused keen interest among the engineering and scientific community. Multifunctional structures, also called smart structures, integrate sensors or actuators into structural components to extend the structure's capabilities in comparison to pure conventional structures [59, 128, 216-219]. By incorporating a "nervous system" into the material, structures can be developed with the ability to sense environmental changes and even autonomously interpret or react to these changes. In particular fibre-optic sensors have been discovered to be well suited to integrating sensory capabilities into structural components as their small diameters do not disturb the integrity of the structure [220]. Applications range from strain, acceleration or displacement sensing to temperature and pressure measurements and acoustic emission detection [198, 221-223]. FBG sensors have been well exploited for their use as structural integrated sensors. Their functions as embedded sensors is most widely considered for integrated strain monitoring [55, 71, 114, 224-242].

As the objective of this work is to explore the possibility of the dual use of FBGS as strain and ultrasonic sensors, initial experiments have been carried out to demonstrate the detection of ultrasonic Lamb waves with structural integrated sensors.

5.3.1 Layout of the Test Specimen

A CFRP (carbon fibre reinforced plastic) test structure was built up in order to measure the response of embedded FBGS under the influence of ultrasound.

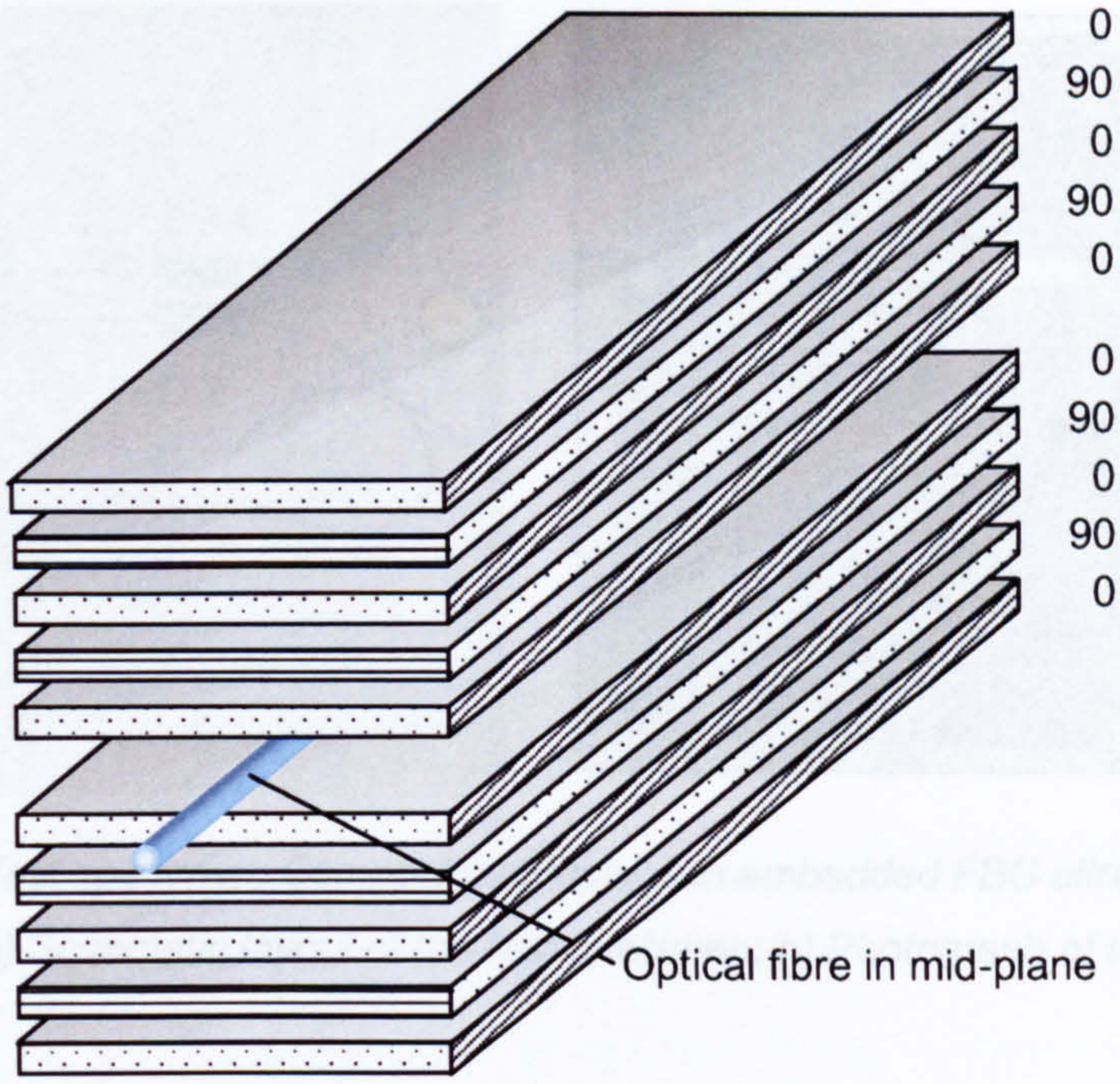

Figure 5.16: Layout of the composite sample with embedded FBGS. Layer orientation $(0/90/0/90/0)^2$.

A simple 300 x 300 x 1 mm structure for the composite sample was chosen. The sensors were integrated in the specimens using a laboratory technique. In order to protect the optical fibres at the ingress/egress locations sleeving PTFE was used The sensors were embedded parallel to the surrounding reinforcement fibres in order to avoid the formation of resin-rich pockets. The arrangement of the unidirectional prepreg layers in a $(0/90/0/90/0)^2$ lay-up is presented in Figure 5.16. The lay-up was chosen in way that a fibre integrated in the mid-plane has the same orientation to the surrounding carbon fibres as a surface mounted sensor. The specimen was cured in an autoclave for two hours at 170° C and 4 bar pressure.

A schematic diagram and a photograph of the test specimen are given in Figure 5.17. Two PZT patches were mounted on the surface of the composite plate in order to launch and receive Lamb waves. One FBGS (FBG 1) was embedded in the material, as illustrated in Figure 5.16. A second FBGS (FBG 2) was surface mounted on the specimen at the same position of the plate. Figure 5.17 shows an off set between the two sensors, but only for better visualisation. This layout was used to sense the Lamb waves launched by PZT 1 with three sensors: one surface PZT, one surface FBGS, and one embedded FBGS. The signals were then analysed and compared.

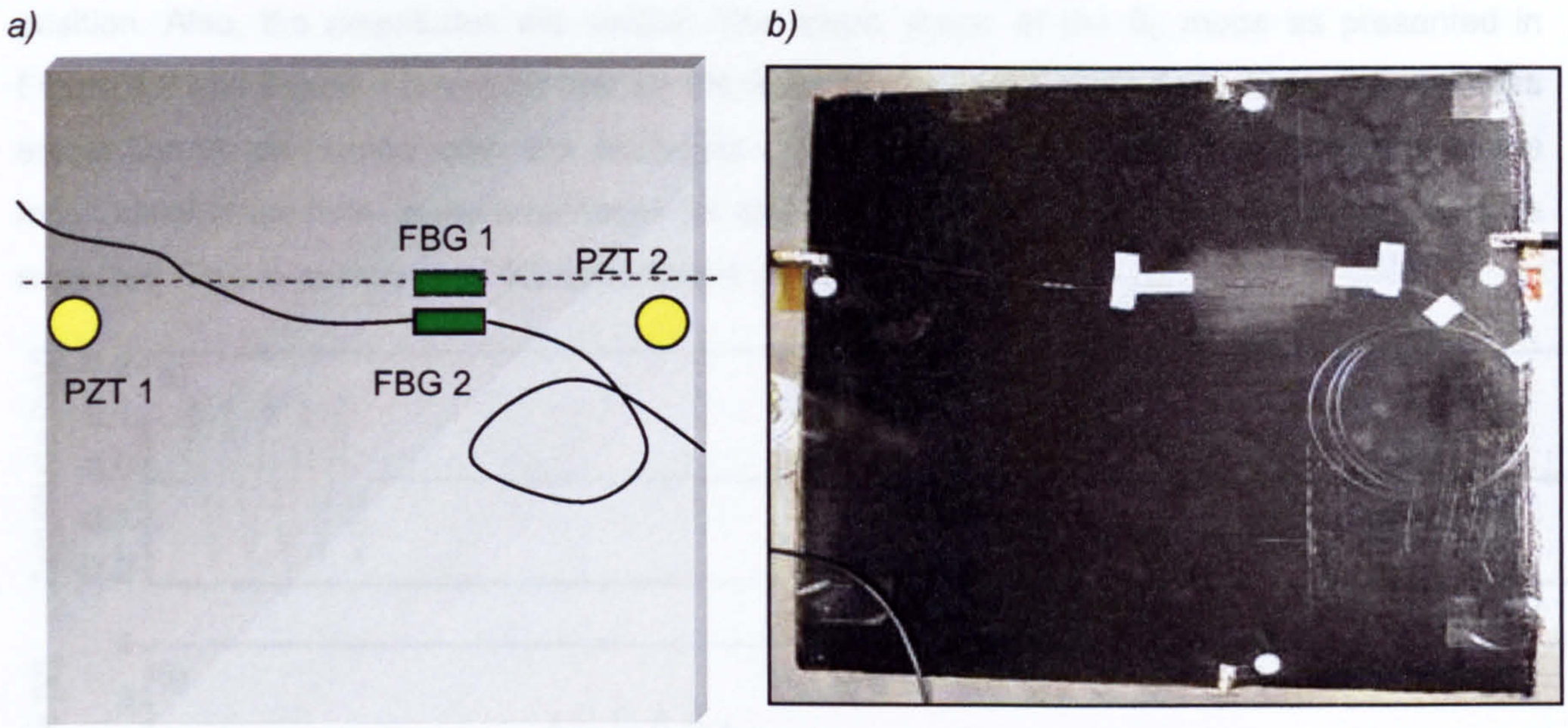

Figure 5.17: Test specimen: Composite sample with embedded FBG ultrasonic sensors: a) Schematic layout of the test specimen; b) Photograph of the test specimen.

5.3.2 Experimental Results

The same experimental set-up as described in Section 7.1 was used for Lamb wave testing. using piezoelectric generation and fibreoptic detection of ultrasound. The response of the sensors was studied at two different frequencies, i.e. 70 and 230 kHz. At 70 kHz the antisymmetric A_0 mode dominates the signal, whereas at 230 kHz the symmetric S_0 mode is more apparent. The excitation signal was a 5-cycle toneburst signal, travelling along the optical fibre axes.

S_0-mode

The signals recorded on the composite plate are shown in Figure 5.18. They have been averaged 64 times using the oscilloscope. It is interesting to compare the results for the surface mounted sensors and for the surface mounted and embedded FBGS. The excitation signal used is shown in Figure 5.18a. Figure 5.18b and c present the signals for the surface mounted PZT and FBGS, respectively. The incident Lamb mode arrives at first at the FBGS before it reaches the PZT. From the time-of-flight (TOF) and the known distance the velocity of the S_0 mode was determined as 6750 m/s. For all sensors the incident wave is clearly visible. At 150 µs the PZT receives the reflection of the wave, for the FBGS these happens already at 125 µs.

Both, the embedded and the surface mounted sensors in Figure 5.18c and d, respectively, clearly detect the S_0 mode. The time is identical as the sensors are located at the same

position. Also, the amplitudes are similar. The mode shape of the S_0 mode as presented in Figure 4.2 and Figure 4.5 reveals that for the S_0 mode the longitudinal displacement amplitudes are uniformly distributed over the thickness of the plate. As the FBGS is sensitive to the longitudinal strain field, same amplitudes for embedded and surface-mounted sensors could be expected. This is exactly what the experiment shows.

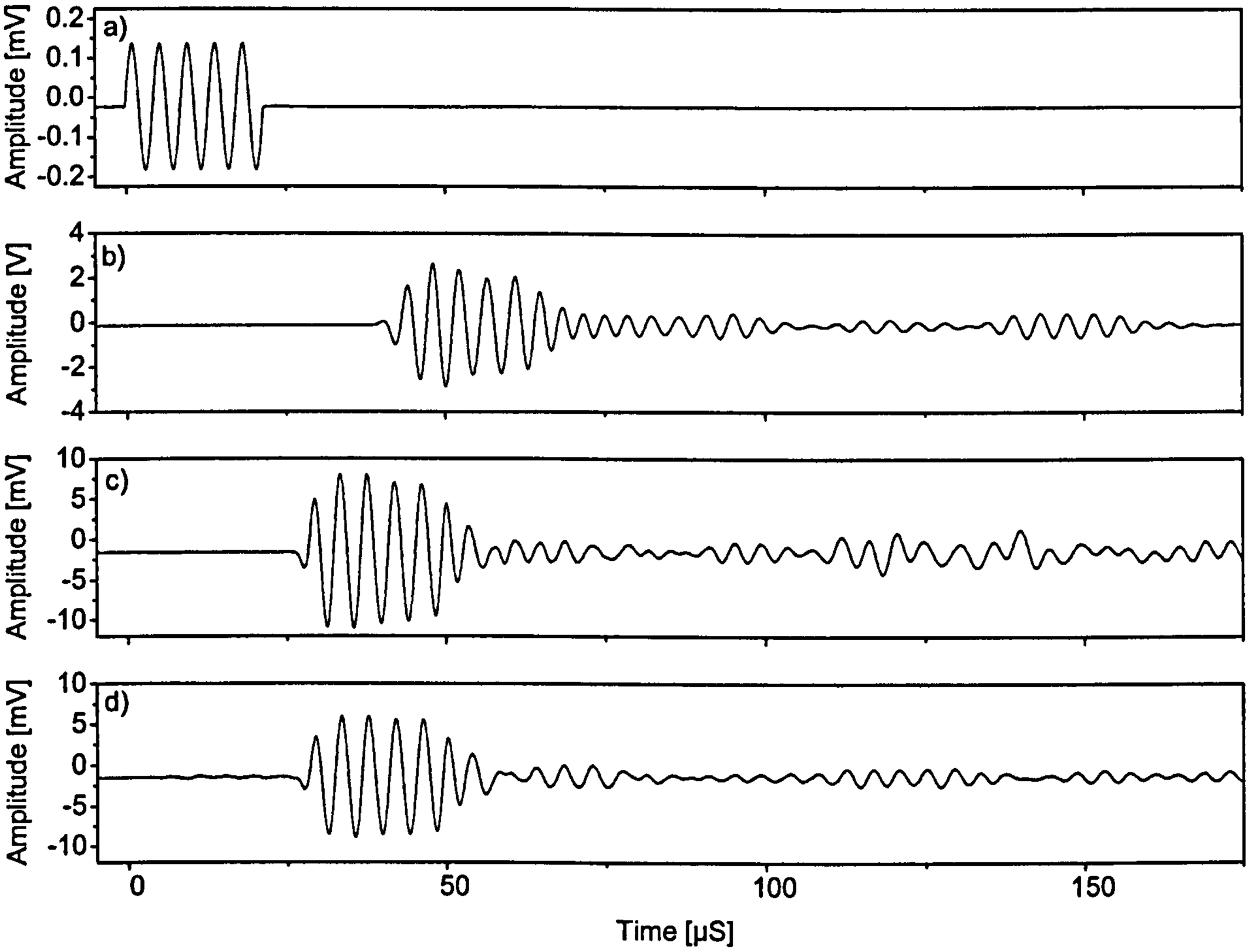

Figure 5.18: Lamb wave response recorded on the composite sample using the symmetric Lamb wave at 230 kHz: a) Excitation signal; b) surface mounted PZT sensor; c) surface mounted FBG sensor; d) embedded FBG sensor.

A_0-mode

The same measurements as for the S_0 mode were repeated at 70 kHz for the A_0 mode. The recorded signal responses are presented in Figure 5.19. For the A_0 mode the Lamb wave velocity could be determined from the TOF to be 1400 m/s. The signals show a dominant A_0 mode at 70 kHz, yet a distorted S_0 mode can be identified in advance of the A_0 signal. The surface mounted sensors recorded both modes, whereas for the embedded FBGS no signal can be assigned to the A_0 mode. This fundamental difference compared to the S_0 mode, can be

explained if the mode shape of the A_0 mode, shown in Figure 4.5 is considered. It appears that in contrast to the S_0 mode the amplitude of the longitudinal displacement strongly depends on the position along the thickness of the plate. The amplitude becomes zero for the mid-plane of the plate. For the embedded FBGS this means it is not able to detect the A_0 mode, as no longitudinal strain field is present to which the sensor is sensitive. The difference in the recorded signals for the S_0 and A_0 mode completely agree with the prediction from Lamb wave theory as presented in Section 4.2.2. Furthermore, the lack of any signal for the embedded sensor when no longitudinal strain field is present, proves the initial assumption from Section 5.1.1 correct, i.e. the response of the FBGS is determined by the interaction of the fibre with the longitudinal displacement of the ultrasonic field.

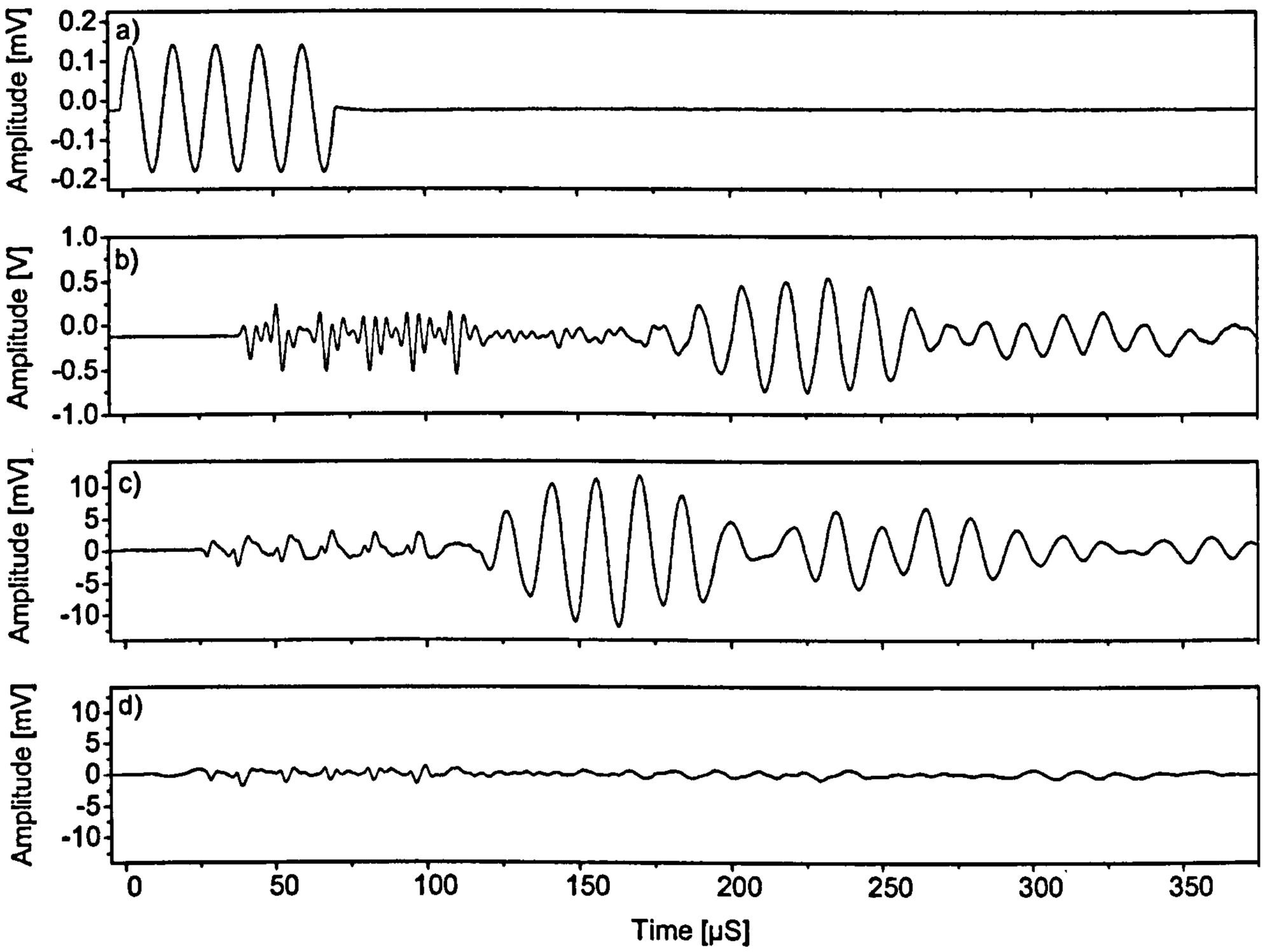

Figure 5.19: Lamb wave response recorded on the composite sample using the antisymmetric Lamb wave at 70 kHz: a) Excitation signal; b) surface mounted PZT sensor; c) surface mounted FBG sensor; d) embedded FBG sensor.

5.4 CONCLUSIONS

This chapter has introduced a novel approach for the detection of ultrasonic Lamb waves using FBGS. The theoretical background and the practical implementation of a FBG sensor based system has been studied.

The interrogation system deployed a tuneable laser that allows an amplitude modulated measurement of the Lamb wave signal. The optical specifications of the interrogation system were analysed and the theoretical limit for the SNR was found. Yet, experimental testing revealed that the practical limit is much smaller. The sensor transfer function has been obtained and the critical parameters for high quality measurements have been identified. Different commercially available gratings have been studied in order to identify the best combination of the parameters. The grating found to be best suited is a compromise for maximum sensitivity and maximum wavelength range with minimum FWHM, which is preferable with respect to multiplexing capabilities.

Initial tests have been carried out to record Lamb wave signals using FBGS, which are unprecedented in the literature. In addition, PZT transducers have been available as a reference. The comparison of the results showed that the signals recorded using FBGS have the same SNR as those from the PZT. This means that the proposed fibre optic system can compete with its conventional counterpart in terms of resolution.

The high directivity of the fibre optic sensor has been demonstrated. This can be used to implement a novel damage location scheme, as shown in Section 7.2.

Numerical simulations have been performed to study the influence of the ratio of the fibre grating length and the acoustical wavelength on the sensor signal. The results from the numerical simulations predicted a strong decrease in modulation depth when the wavelength to grating length ratio goes down. This behaviour has been experimentally validated. This results can be used to calculate the maximum allowable ultrasonic frequency for Lamb wave inspection for a FBGS with a given grating length, or to calculate the maximum grating length for any given ultrasonic frequency.

As a further step towards the implementation of smart structures, initial experiments using structural integrated FBGS for the detection of Lamb waves for the first time revealed the different sensitivities of the embedded sensor to different Lamb wave modes. This phenomenon could be explained using the mode shapes of the Lamb wave modes. Furthermore, it could be shown that the FBG ultrasonic sensor can be treated as sensor being sensitive to the longitudinal and not to the transversal strain field of the ultrasonic waves.

6 SIGNAL PROCESSING FOR DAMAGE IDENTIFICATION

This chapter describes mathematical tools used for damage identification. The basic idea of the damage identification algorithms is to recognise the difference in the signals related to damage and translate this information into a diagnosis of location and severity of damage. The first objective and first level of the overall problem of damage identification is damage detection. Higher levels of the identification include severity and classification of damage, location of damage and finally, prediction of the remaining service life of the structure [243, 244]. Apart from lifetime prediction, which is the subject of Chapter 8, all other damage identification issues are covered in this chapter. A variety of novel mathematical tools are examined to effectively solve the damage identification problem.

The tools used for feature extraction are briefly introduced and their results are illustrated using a simple waveform. The methods are demonstrated using the excitation signal for the ultrasonic waves. Its properties are presented in the first section. The following two sections describe the tools used for feature extraction and data reduction in time and frequency domain, respectively. Then the concept of the Hilbert transform is introduced which will help to identify the different packages within the sample record. Wavelet analysis has been used for denoising of the signals, for feature extraction, for compression of the data, and for time-frequency analysis. The basic concepts of wavelet analysis are described in the corresponding section. Finally, Genetic Algorithms are introduced and their properties are briefly reviewed. Genetic Algorithms have been applied to the damage location problem.

6.1 BURST SIGNAL

Signal processing methods presented in this chapter are illustrated using a broadband-frequency signal shown in Figure 6.1.

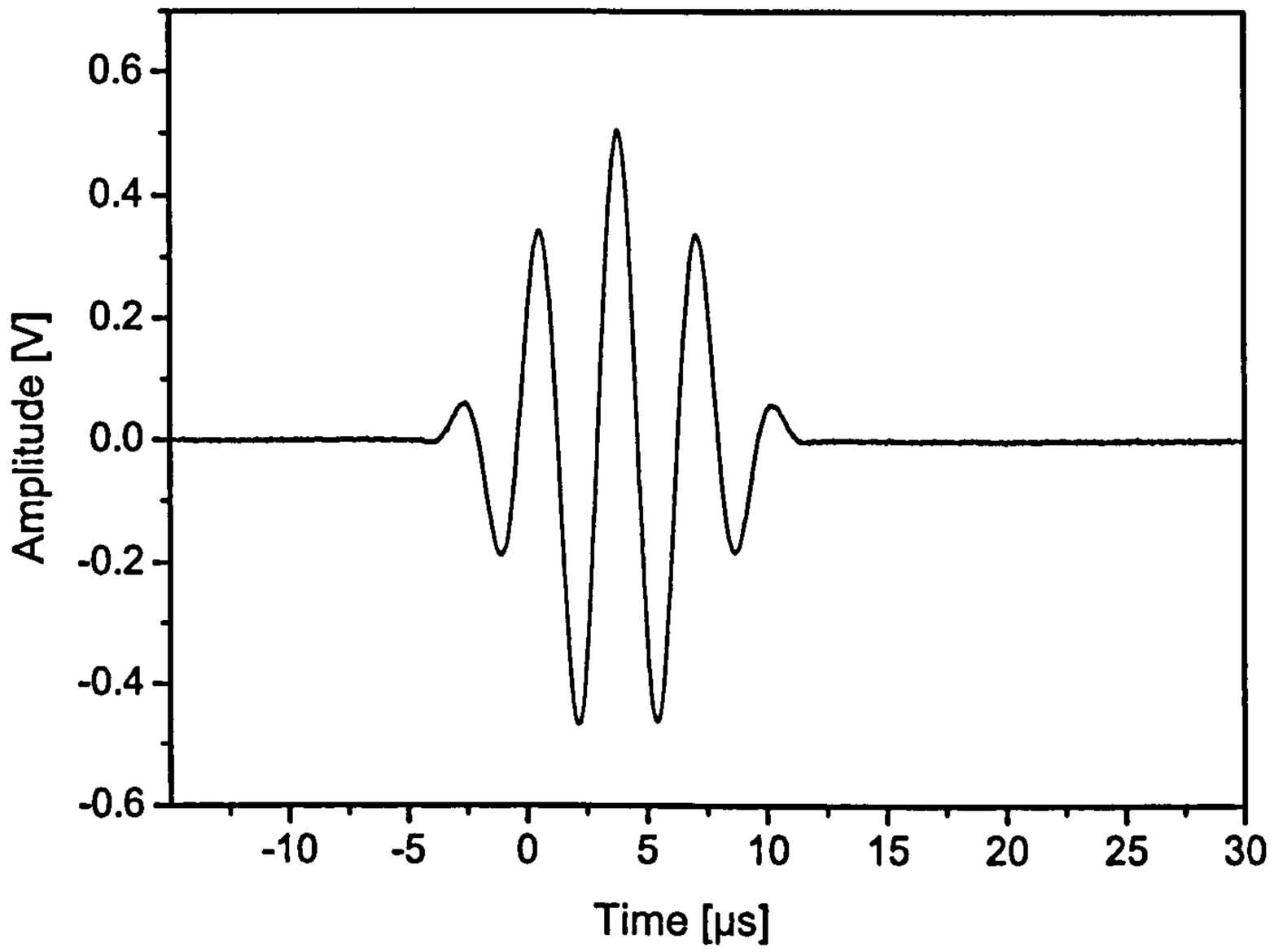

Figure 6.1: Tone burst signal used to launch the ultrasonic Lamb waves. Carrier frequency equal to 300 kHz.

A burst signal has been chosen because it is localised in time and can easily be identified within the sample record, as long as dispersion effects can be neglected. Burst signals also present the most common approach for Lamb wave analysis and have been used previously in various studies [87, 154-156, 158, 160]. The use of burst signals allows the measurement of the time it has taken for a signal to travel from the sender to the receiver and to calculate either the velocity of the wave, in the case where the distance the signal travelled is known or vice versa, i.e. the distance the signal travelled assuming the velocity of the wave is known. A window function has been applied to the initial tone burst signal in order to minimise spillover frequencies. Also, the number of cycles of the carrier wave is a compromise between a very small number that makes the signal shorter in time domain and a larger number that would give a more narrowband signal in frequency domain. Kessler [164] argues that an appropriate number of cycles can be determined by the maximum number of waves that can be sent in the time it takes for the lead wave to travel to the sensor. Wilcox [245] offers a detailed analysis for the optimum number of cycles. However, to keep things simple, the signal chosen here is a 4.5 cycle sine signal, windowed by a Hanning window. The Hanning window which is one period of a sine squared function gives a gradual transition of the discontinuity and is one of the most common used time windows in signal analysis [246]. An integer number has been avoided because of the symmetry of the signal in time domain, which makes peak of the signal easier to detect visually.

Kehlenbach [43, 247] suggested the use of chirped signals instead of burst signals to avoid ambiguities in signal identification for dispersive wave forms. He showed that for composite materials better resolution in damage location and size determination can be obtained if chirp signals instead of burst signals are used. However, for the experiments carried out within this thesis dispersion was negligible, and therefore the more common burst signals have been used.

6.2 Time Domain Analysis

Guided ultrasonic waves used for damage detection in Chapter 7 are continuous electrical signals generated by piezoceramic transducers and sensed by fibre Bragg gratings. Such a signal is referred to as a time-history [246]. A sample record is defined as the time-history representing a single measurement over a finite length of time. In general Lamb wave responses represent non-stationary data, due to the fact that burst signals are used for excitation. Burst signals are localised in time and can be easily identified within a sample record. Yet, the launch of different ultrasonic modes with different velocities and the presence of reflections from the structures boundaries cause the time-history to consist of many single burst signals, called packages. If there is no change in the condition of the structure, the time-history will be the same at any time the signal is recorded. This is because all sample records are initiated by a trigger event, which ensures the basic properties of the signal do not vary with time. If however, due to the presence of damage, the sample record at a given time is different to that recorded at a previous time, this difference has to be recognised and analysed. This approach is often called pattern recognition in damage detection. Reference data representing "no damage" (or "normal") condition serves as a template. The difference between patterns representing current monitored conditions and the template indicate possible damage of the structure. This section describes the parameters that have been used for feature extraction and data reduction in the time domain. The first part of this section introduces the concept of a discrete time series and related mathematical implications.

6.2.1 Discrete Time Series

Most experimental measurements are carried out digitally, i.e. a typical function $x(t)$ of the process to be measured is acquired by an analogue-to-digital (A/D) converter. The A/D converter samples the signal $x(t)$ at a series of regularly spaced times, as depicted in Figure 6.2. If the sampling interval is Δt, where Δt is constant then the discrete value of $x(t)$ at time $t = n \Delta t$ is written as x_n, and this sequence for $n = 0, 1, 2, 3, \ldots, N$ is called a *discrete time series [248].*

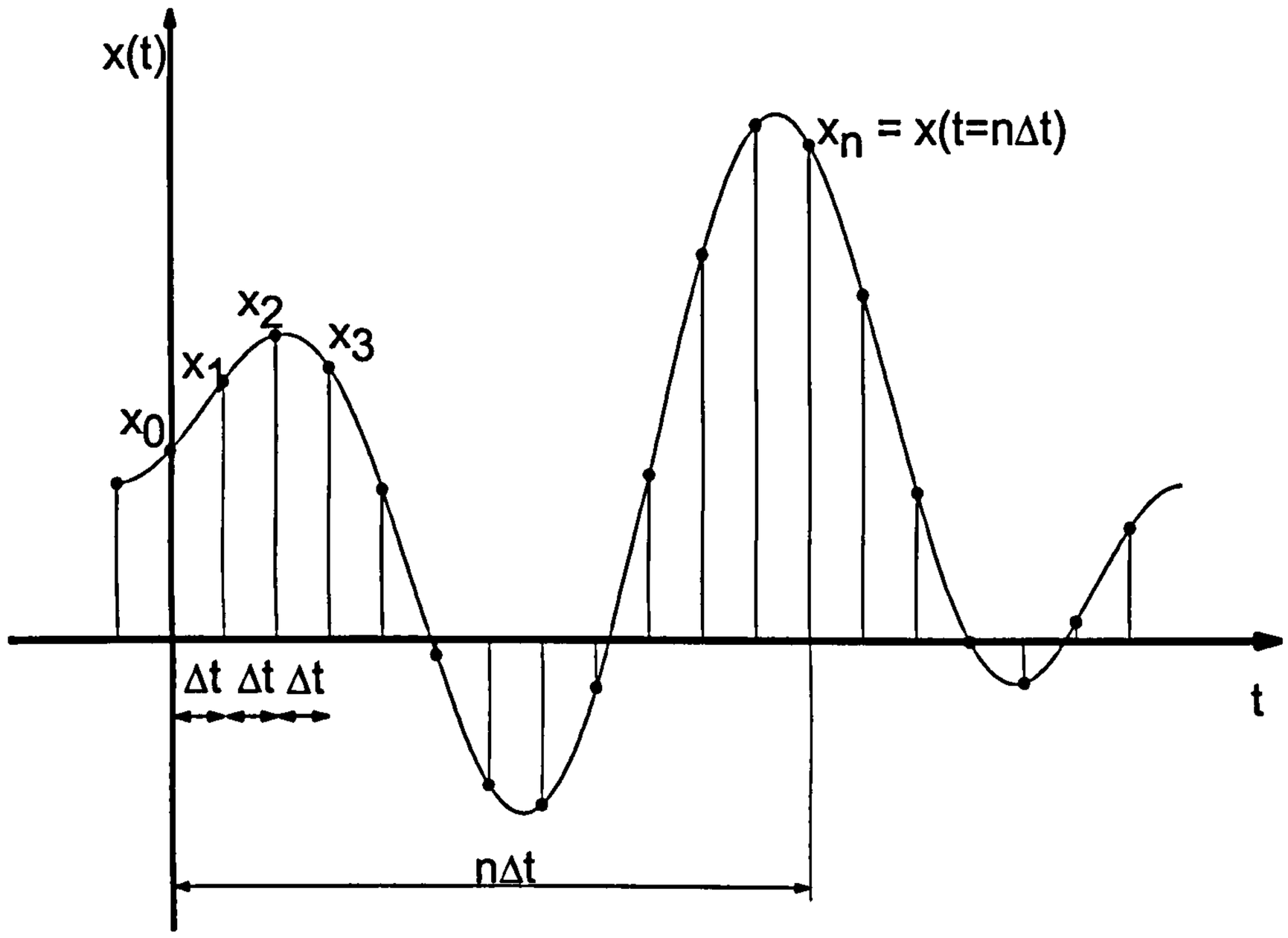

Figure 6.2: Sampling a continuous function of time at regular intervals.

The basic mathematical principles used for signal processing can be applied to both continuous/analogue or discrete/digital signals. Yet, the appearance of mathematical equations depends on whether analogue equations or digital algorithms have to be applied.

The major difference between analogue and digital equations, is that the integral over the continuous variable t is transferred into a sum over the sampling intervals Δt. This is represented mathematically as

$$\int_0^T x(t)dt \quad \Leftrightarrow \quad \sum_{n=0}^{N} x(n\Delta t) \tag{6.1}$$

The integral of the continuous function is from 0 to T, whereas the sum over the sampled signal is from 0 to N, i.e. $N\Delta t = T$. This is the basic principle, which has to be adapted to any individual function in the time domain. By analogy, a similar expression can be found in frequency domain.

6.2.2 TIME DOMAIN PARAMETERS

In general, signals acquired from sensors are in the time domain. The simplest parameters which describe time domain properties of signals and which have been used for damage feature extraction are:

- *Maximum Value* x_{max}
- *Minimum Value* x_{min}
- *Mean Value* defined as

$$\bar{x} = \frac{1}{T}\int_0^T x(t)dt \tag{6.2}$$

- *Root Mean Square (RMS)* defined as

$$x_{RMS} = \sqrt{\frac{1}{T}\int_0^T x^2(t)dt} \tag{6.3}$$

These parameters describe extreme and mean properties of the signal. In particular the RMS is used to indicate the average energy. Often statistical moments are important parameters to describe the deviation of a signal from the mean. The mean and the mean-square values are called the first and the second statistical moment respectively. The variance can be introduced as the difference between the mean square and the square of the mean value. Higher statistical moments are more sensitive to deviations in the data. The normalised fourth moment is called the kurtosis [249, 250].

- *Kurtosis*, defined as

$$K_r = \frac{\int_0^T (x(t)-\bar{x})^4 dt}{x_{RMS}^4} \tag{6.4}$$

Kurtosis is often used to analyse the spikiness of the data.

Examples

The time domain analysis has been applied to the burst signal shown in Figure 6.1. The results are summarised in Table 6.1. Here, the mean value is not equal to zero, as the signal is not symmetrical.

Table 6.1: Time domain analysis applied to basic tone burst signal.

Parameter	Result

Maximum value	0.5 V
Minimum value	-0.47 V
Mean value	$6.5*10^{-5}$V
Root mean square	0.14 V
Kurtosis	7.12

6.3 Frequency Domain Analysis

This section describes parameters that have been used for feature extraction and data reduction in the frequency domain. The first part of this section reviews the general concepts of frequency analysis.

6.3.1 Fourier Transform

Frequency domain descriptions of time-dependent signals, such as vibrations and ultrasound, are generally of great engineering value. The Fourier Transform (FT) plays a major role in both theoretical definitions used to describe signal properties and algorithms used for signal processing.

The Fourier Transform pair can be defined as

$$\mathcal{F}\{x(t)\} = X(f) = \int_0^T x(t)\, e^{-i2\pi f t}\, dt \tag{6.5}$$

$$\mathcal{F}^{-1}\{X(f)\} = x(t) = \int_0^T X(f)\, e^{i2\pi f t}\, df \tag{6.6}$$

where the former is the forward transform of x(t) whereas the latter is known as the inverse transform.

Discrete Fourier Transform

When the signal $x(t)$ is digitised, i.e. $x(t) = x(n\Delta t)$ the Discrete Fourier Transform (DFT) and the inverse DFT can be introduced as

$$X(m) = \Delta t \sum_{n=0}^{N-1} x(n\Delta t) e^{-i2\pi\, m\Delta f\, n\Delta t} \tag{6.7}$$

$$x(n) = \Delta t \sum_{m=0}^{N-1} X(m\Delta f) e^{i2\pi\, m\Delta f\, n\Delta t} \tag{6.8}$$

respectively.

These transformations give the spectrum values $X(m)$ at the N discrete frequencies $m\Delta f$ and give the time series $x(n)$ at the N discrete time points $n\Delta t$. An efficient way of calculating the DFT makes use of the Fast Fourier Transformation (FFT) [251]. The FFT algorithm calculates the spectra of blocks of data. The advantage of FFT is that it reduces the number of operations to obtain the result, but still has the same properties as the DFT [252].

Various parameters can be used to compare two different spectra. The arithmetic and geometric mean of the spectrum defined as

$$A_m = 20\log\left(\frac{1}{N}\sum_{i=1}^{N}\frac{A_i}{10^{-5}}\right) \tag{6.9}$$

$$G_m = \frac{1}{N}\sum_{i=1}^{N} 20\log\left(\frac{A_i}{\sqrt{2}10^{-5}}\right)^2 \tag{6.10}$$

respectively, describe the difference in the amplitude of the spectral components A_i.

Example

Figure 6.3 shows the amplitude spectrum of the basic tone burst signal of Figure 6.1 as a result of the Fourier transformation. The main frequency component is at 300 kHz which is the carrier frequency of the signal. As a tone burst signal rather than a continuous wave is used, the spectrum extends over a certain range in frequency domain.

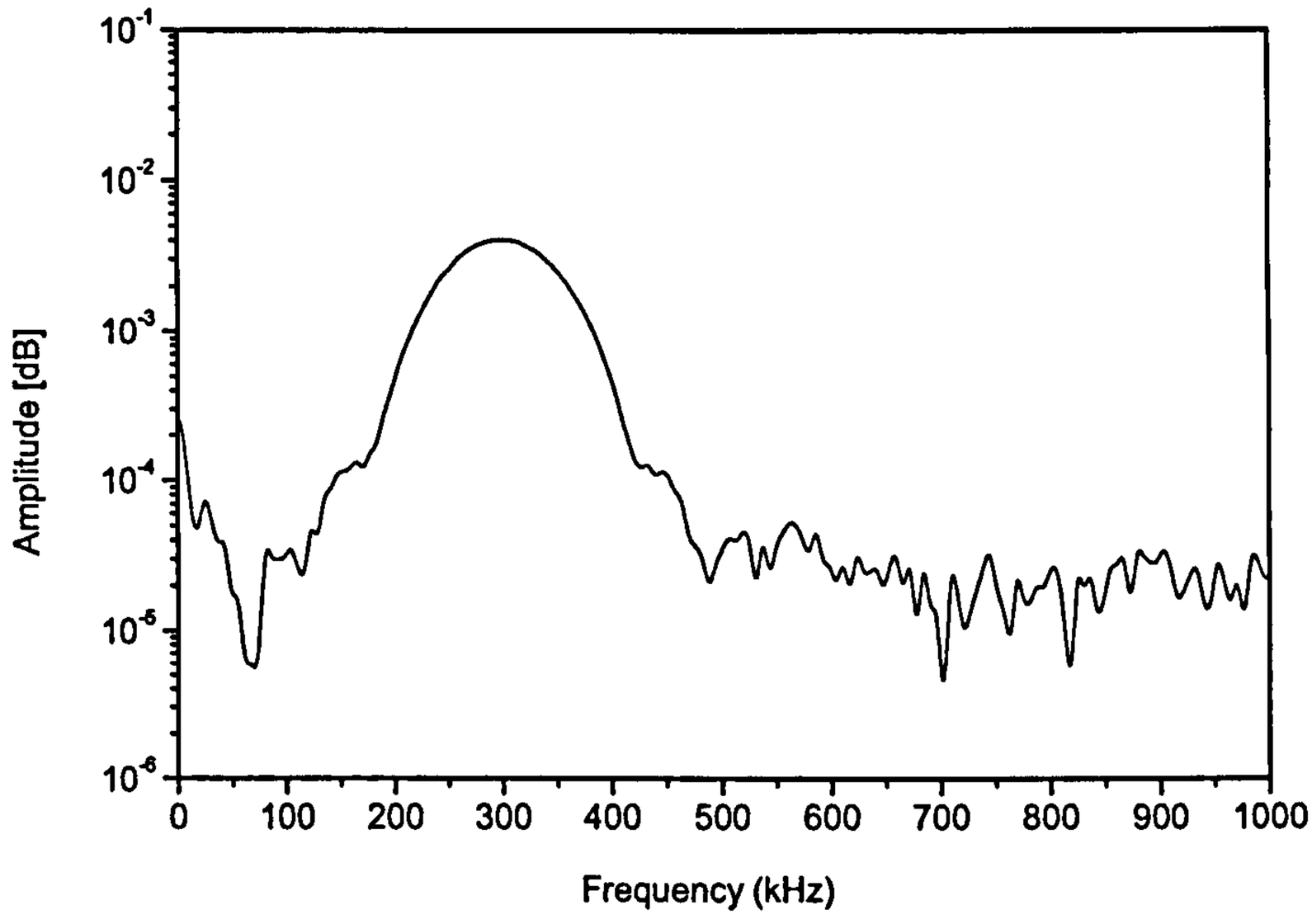

Figure 6.3: Frequency spectrum of the basic tone burst signal. Carrier frequency is 300 kHz.

6.4 HILBERT TRANSFORM

The Hilbert Transform (HT) $\mathcal{H}$ relates the real and the imaginary component of the Fourier transform of a signal. It can be applied to calculate the envelope of any analytical signal. The envelope of a signal provides a tool to identify the maximum and position of each wave package within the sample record even for dispersive media.

The concept of th Hilbert transform can be applied to any causal signal. A causal signal is a signal that is equal to zero for negative time values. It can be shown that for any causal signal the real and imaginary part of the Fourier transform are related by

$$A_R(f) = A_I(f) * \frac{1}{\pi f} \tag{6.11}$$

where $A_I(f)$ and $A_R(f)$ are the imaginary and real part of the Fourier transform, respectively.

The relation between $A_I(f)$ and $A_R(f)$ can be expressed in a more general way as

$$\mathcal{H}\{G(f)\}=\tilde{G}(f)=\frac{1}{\pi}\int_{-\infty}^{\infty}G(\phi)\frac{1}{f-\phi}d\phi \tag{6.12}$$

Equation (6.12) is in fact the definition of the Hilbert transform in the frequency domain. This can be expressed in the time domain as

$$\mathcal{H}\{a(t)\}=\tilde{a}(t)=\frac{1}{\pi}\int_{-\infty}^{\infty}a(\tau)\frac{1}{t-\tau}d\tau=\frac{1}{\pi}a(t)*\frac{1}{t} \tag{6.13}$$

where * denotes the convolution and the standard definition of the convolution has been used being

$$g(t)=f(t)*h(t)=\int_{-\infty}^{\infty}f(\tau)h(t-\tau)\,d\tau \tag{6.14}$$

The HT concept can be applied to analytical signals. An analytical signal is a complex time signal whose imaginary part is the Hilbert transform of the real part.

If

$$\tilde{a}(t)=\mathcal{H}\{a(t)\} \tag{6.15}$$

then

$$\hat{a}(t)=a(t)+i\tilde{a}(t) \tag{6.16}$$

and *â(t)* is called an analytical signal.

The physical background of the analytical signal is as follows. Real and imaginary parts of the analytical function can often be related to the two forms of energy always associated with a vibration oscillation; the potential and kinetic energy. Therefore for a complex signal when its real part (the square of it) represents the potential energy, then (the square of) the imaginary part would represent kinetic energy.

The amplitude of the analytical signal is known as the envelope function. For narrowband signals the envelope can be defined as

$$A(t) = \sqrt{a(t)^2 + \tilde{a}(t)^2} \tag{6.17}$$

Physically, the square of the amplitude function represents the total energy at any time. Referring to guided ultrasonic waves, the envelope represents one package. It is known from the wave theory that this package travels with the group velocity of the wave.

Example

In order to demonstrate how the envelope function works, equation (6.17) has been applied to the burst signal shown in Figure 6.1. The result is given in Figure 6.4. For better visualisation of how the envelope encloses the original signal both the positive value for the root and the negative value have been drawn. What becomes obvious by this representation is how the envelope helps to identify the maximum amplitude of the peak and its position in the signal. This becomes even more useful if the analysed signal suffers from dispersion.

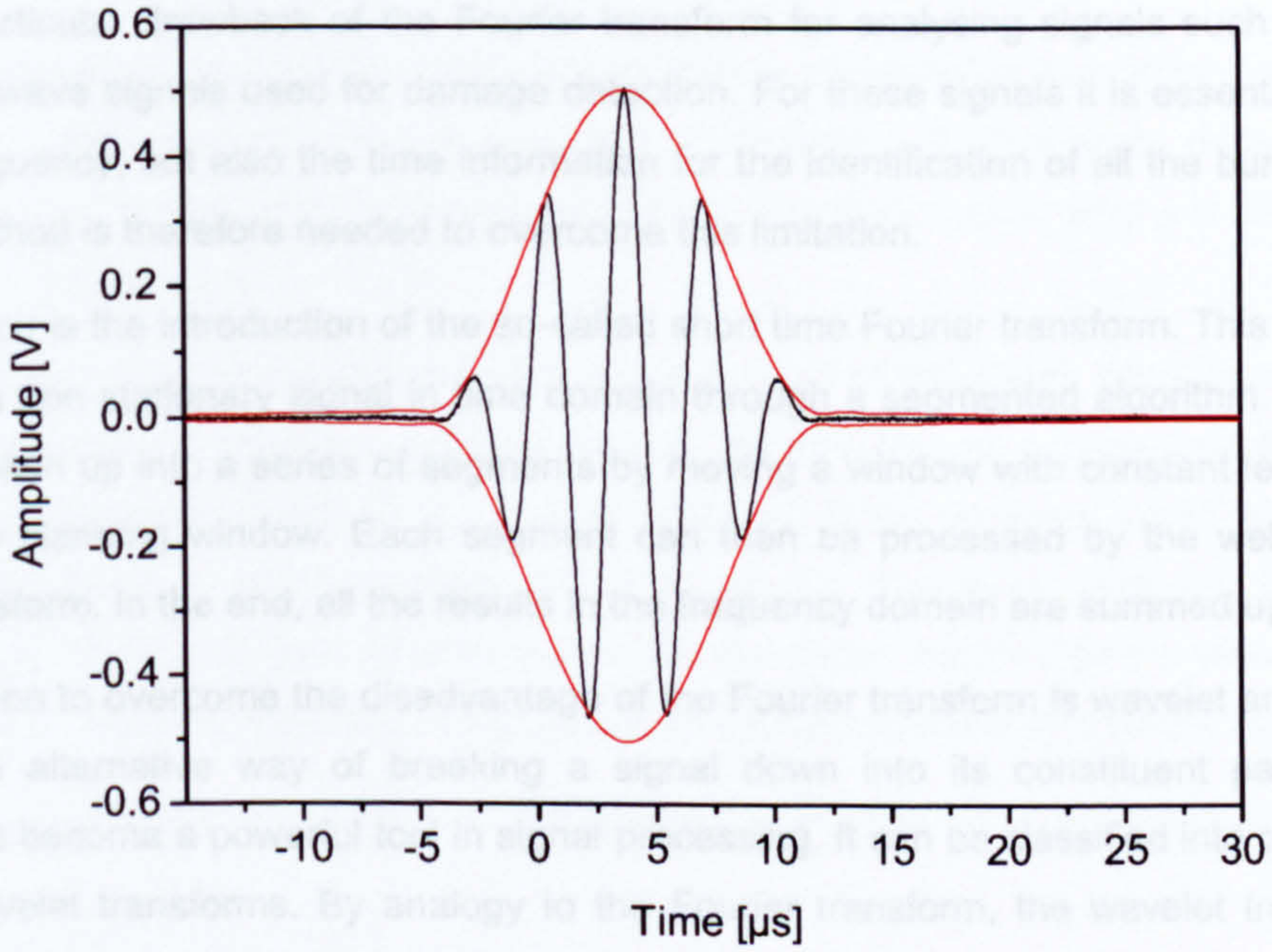

Figure 6.4: Envelope of the basic tone burst signal. The black line is the original signal, the red line is the positive and negative envelope signal.

6.5 WAVELET ANALYSIS

This section introduces the basic concepts of the wavelet analysis. The continuous and the discrete wavelet transform as tools for analysing non-stationary data are introduced. Examples of applications relevant to damage identification conclude the section.

6.5.1 INTRODUCTION

In signal processing a major interest is the frequency composition of *x(t)* which is often approached by the Fourier transform (6.3.1) in order to get the spectrum of the process of interest. A disadvantage of Fourier analysis is that frequency information can only be extracted for the complete duration of a signal *x(t)* or for stationary signals. Since the integral in the Fourier transform extends over all time, the information it provides arises from an average over the whole length of the signal. Any local oscillations which represent a particular feature will contribute to the calculated spectrum, but the information about its location in time will be lost.

This is a particular drawback of the Fourier transform for analysing signals such as the tone burst Lamb wave signals used for damage detection. For these signals it is essential to get not only the frequency, but also the time information for the identification of all the burst signals. A different method is therefore needed to overcome this limitation.

One approach is the introduction of the so-called short time Fourier transform. This is a process to analyse a non-stationary signal in time domain through a segmented algorithm. The original signal is broken up into a series of segments by moving a window with constant length in time, such as the Hanning window. Each segment can then be processed by the well-known fast Fourier transform. In the end, all the results in the frequency domain are summed up.

Another option to overcome the disadvantage of the Fourier transform is wavelet analysis which provides an alternative way of breaking a signal down into its constituent parts. Wavelet analysis has become a powerful tool in signal processing. It can be classified into continuous or discrete wavelet transforms. By analogy to the Fourier transform, the wavelet transform is a linear transformation that decomposes a given function *x(t)* into a superposition of elementary functions.

A wavelet is a function $\psi(t)$ of the real argument *t*. This function oscillates as a wave, but is also localised in time, thus the name wavelet. It is represented mathematically as

$$\psi_{a,b}(t)=\psi\left(\frac{t-b}{a}\right) \tag{6.18}$$

where b is a translation parameter indicating the locality, a is a dilation or scale parameter.

6.5.2 Continuous Wavelet Transform

Continuous wavelets provide a powerful tool for time-scale analysis.

The continuous wavelet transform is defined as [253]

$$W_\psi[x(t)]=W_\psi(a,b)=\frac{1}{\sqrt{a}}\int_{-\infty}^{+\infty}x(t)\,\psi^*\left(\frac{t-b}{a}\right)dt \tag{6.19}$$

where b is a translation parameter indicating the locality, a is a dilation or scale parameter, $\psi(t)$ is an analysing wavelet and ψ^* indicates the complex conjugate of ψ.

It has been shown that any signal of finite energy can be represented as a linear combination of wavelets. The time decomposition is obtained by translation b. The scale decomposition is found by dilating the chosen analysing wavelet. Thus, the dilation parameter a is responsible for the frequency segmentation.

For any wavelet acting as the analysing wavelet a number of conditions have been set. It must satisfy the admissibility condition, which is required for obtaining an inverse wavelet transform. The analysing wavelet must be a window function. Most wavelets used also fulfil the progressivity condition, which ensures that the wavelet transform does not produce any interference in the time domain. In other words, the conditions imposed on the wavelet ensure it has a time and frequency localisation and possesses some regularity and smoothness.

An example of an analysing wavelet for the continuous wavelet transform is the Morlet wavelet defined by

$$\psi(t)=e^{i2\pi f_0|t|}e^{-\frac{|t|^2}{2}} \tag{6.20}$$

The Fourier spectrum of the Morlet wavelet is a shifted Gaussian function,

$$\Psi(f)=\sqrt{2}\pi e^{-2\pi^2(f-f_0)^2} \tag{6.21}$$

The Morlet wavelet is the most widely used basic function in the continuous wavelet transform analysis. For the continuous wavelet transforms presented in this thesis the Morlet wavelet has been chosen as the analysing wavelet.

In contrast to the Fourier transformation, which extracts periodic infinite waves from the analysed function, the wavelet transform analyses a function only locally at windows defined by the wavelet. For any wavelet $\psi(t)$ the centre t_c and the width $2\Delta t_c$ of the window can be calculated. The centre and the width of the window of the wavelet transform (6.19) are given by $b + a\, t_c$ and $2a\, \Delta t_c$, respectively. This property is called time localisation in signal processing [254]. The wavelet transform obtains good resolution in time domain at high frequencies since the window narrows for small values of the scale parameter a.

It is one of the basic properties of the wavelet that it is localised in both time and frequency domain. If the centre and width of the frequency window of the wavelet are defined as f_c and $2\Delta f_c$, respectively, then the centre of the window of the wavelet transform is at f_c/a and the width is equal to $2\Delta f_c/a$. Accordingly, the wavelet transform has good resolution in frequency domain at low frequencies, as the frequency window tightens for large values of the dilation term a. It follows that the wavelet transform offers the time-scale analysis through a two dimensional time-scale window with a flexible window size. Flexible window size and flexible resolution is the main advantage of wavelet analysis compared to time-frequency analysis.

The square of the modulus of the continuous wavelet transform can be interpreted as an energy distribution over the (a, b) time-scale plane [244]. The energy of the signal is mainly concentrated on the time-scale plane around the so-called ridge of the wavelet transform. The ridge of the wavelet transform is a set of points (a, b) for which the transform behaves like the analytical signal. For linear systems, the ridge can be approximately given by the local maxima of the amplitude of the transform. Wavelet ridges can be used to determine signal instantaneous characteristics, which in turn can be used for damage identification.

For the wavelet transform the two dimensional time-frequency window has constant area. However, in contrast to the short time Fourier transform for the wavelet the length of the window is flexible and changes with the change of frequency. These properties are presented graphically in Figure 6.5.

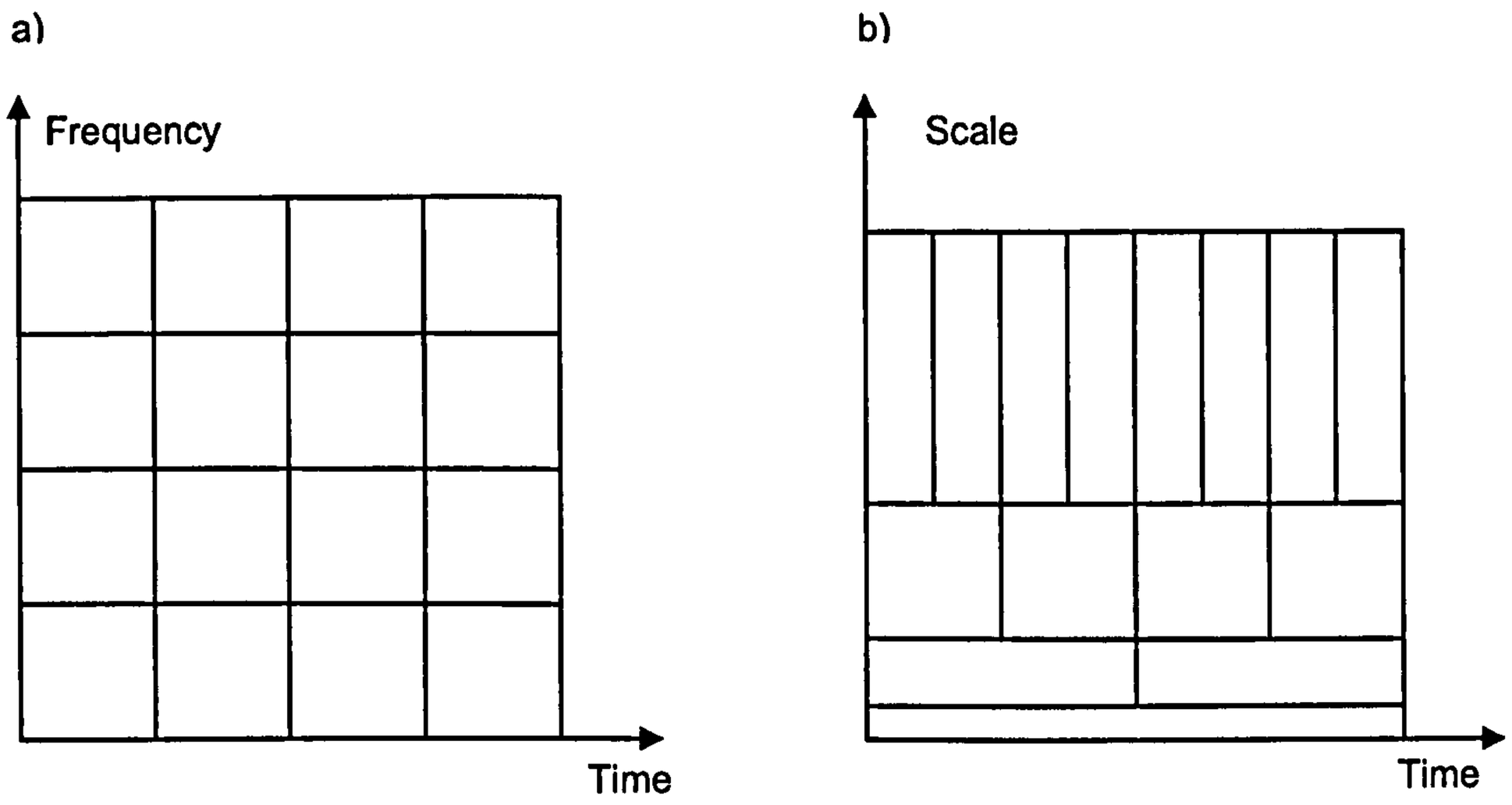

Figure 6.5: Time-frequency window: a) Short time Fourier transform; b) Wavelet transform. [254].

Giurgiutiu and Yu have presented a study that compares short time Fourier and wavelet transform for structural health monitoring [255]. They conclude that the major advantages of the wavelet transform is its size-adjustable window. This ensures that if the local area of the signal has a high frequency, the window length will be shorter, for low frequencies it will be longer, see also Figure 6.5. The problem with the short time Fourier transform is to find the optimal window length. Missing the optimal length will result in severe background noise in the high frequency area. Another advantage of the wavelet transform is that it can extract the coefficients at a certain frequency of interest, which is useful for monitoring some critical frequency components to the performance of the structure. More advantages of the wavelet analysis come from the discrete wavelet transform, which allows the denoising of the signal. Short time Fourier transform offers no possibilities for such an application. Although Giurgiutiu and Yu found many reasons why wavelet analysis is advantageous compared to Fourier transform, they don't give any advice on which method to use. One of the reasons for this is that in their mind short time Fourier transform is easier to understand and use. In consequence, the authors might fear any potential user is distracted by the complexity of the mathematical background of the wavelet analysis.

However, as the advantages of the wavelet analysis are obvious, wavelet analysis has been used for the damage identification analysis in this thesis, whereas short time Fourier transform has not been considered any further.

6.5.3 Discrete Wavelet Transform

The continuous wavelet analysis transforms a one-dimensional time signal into a two-dimensional continuous time-scale domain. This representation however is highly redundant. Thus a logical extension of the continuous analysis is a discretisation of the time *b* and scale *a* parameters by discrete samples of the dyadic time-scale grid given by [253]

$$a = 2^{-m} \qquad b = n2^{-m} \tag{6.22}$$

where *m* and *n* are integers. This concept leads to the discrete wavelet transform (DWT). The continuous wavelet transform in Equation (6.19) becomes

$$W_{\psi}(m,n) = \int_{-\infty}^{+\infty} x(t)\psi^{*}_{m,n}(t)dt \tag{6.23}$$

where $\psi_{m,n}(t)$ are translated and dilated analysing wavelets given by

$$\psi_{m,n}(t) = 2^{m/2}\psi\left(2^{m}t - n\right) \tag{6.24}$$

In theory, there is an infinite number of analysing wavelets for reasons of computational efficiency however, only a small subset of these is used. The most common used analysing wavelets that give an accurate decomposition and can be used for highly efficient numerical computing are orthogonal wavelets. If the functions $\psi_{m,n}(t)$ are orthonormal, the discrete wavelet transform leads to the orthogonal wavelet transform. Orthogonal wavelets are special cases of discrete wavelets. They are concise and decompose functions without any redundancy. Discrete wavelets are often associated with the dilation equation and scaling functions. The basic scaling function $\phi(t)$ can be defined as

$$\phi(t) = \sum_{k=0}^{N-1} c_k \phi(2t - k) \tag{6.25}$$

where the values of c_k are wavelet coefficients. These coefficients must satisfy certain conditions, which are discussed in detail in [256]. The scaling functions shown in Equation (6.25) are then used to construct the corresponding wavelets $\psi(t)$, where

$$\psi(t) = \sum_{k=0}^{N-1} (-1)^{k} c_k \phi(2t + k - N + 1) \tag{6.26}$$

Any arbitrary signal $x(t)$ can be then represented as a weighted sum of wavelet functions following the expansion

$$x(t) = \sum_{i}^{\infty}\sum_{k}^{\infty} c_{i,k}\psi(2^i t - k) \tag{6.27}$$

The discrete wavelet transform gives the span of the analysed signal at different resolutions according to wavelet scales. Wavelet functions can be constructed in a way that they form a family of orthogonal bases. Various orthogonal bases are used in practice. The current study utilises the 8th order Daubechies wavelets [257]. In order to perform a discrete wavelet transform, the range of variable t in (6.27) is often limited to a unit interval ($0 \le t < 1$) using the so-called circular wavelet transform [256]. The approach is similar to the Fast Fourier Transform (FFT) analysis and wraps wavelet functions around the unit interval. Within this approach, the wavelet decomposition of $x(t)$ can be represented in the interval $0 \le t < 1$ [256] which is analysed as

$$x(t) = a_0\varphi(t) + a_1\psi(t) + \begin{vmatrix} a_2 & a_2 \begin{vmatrix} \psi(2t) \\ \psi(2t-1) \end{vmatrix} \end{vmatrix} + \begin{vmatrix} a_4 & a_5 & a_6 & a_7 \begin{vmatrix} \psi(4t) \\ \psi(4t-1) \\ \psi(4t-2) \\ \psi(4t-3) \end{vmatrix} \end{vmatrix} + \ldots \tag{6.28}$$

where the coefficients $a_0, a_1, a_2, a_3, \ldots$ give the amplitudes of all the contributing wrapped wavelets. This equation shows that the analysed signal $x(t)$ can be represented as a sum of so-called wavelet levels given by

$$x_m(t) = \begin{cases} a_0\varphi(t) & for \quad m = -1 \\ \sum_n a_{2^m+n}\psi(2^m t - n) & for \quad m = 0,1,2,3.. \end{cases} \tag{6.29}$$

All levels are in fact reconstructed signals from the appropriate wavelet coefficients a_k. The sum of all levels recreates the original signal, i.e.

$$x(t) = \sum_m x_m(t) \tag{6.30}$$

The levels are usually numbered upwards from either –1 or 0. Each of the levels displays a different frequency band of the analysed signal and gives the contribution to the whole signal energy. Higher levels correspond to high frequencies whereas lower levels exhibit low

frequencies of the signal. Because dilation wavelets are compact in the sense that they have a definite beginning and ending in the time domain, they cannot also be compact in the frequency domain so that their Fourier transforms extend over an infinite frequency range. The predominant frequency range for level *m* is centred at

$$f = \frac{2^m}{\Delta \cdot N} \qquad [Hz] \tag{6.31}$$

where Δ is the sampling interval in [s], *N* is the number of samples and *m* is the wavelet level.

It is obvious that with increasing wavelet level the corresponding centre frequency also increases. This feature allows the wavelet transform to be effectively used in frequency analysis.

An example how wavelet decomposition and signal reconstruction works is given in Appendix E.

6.5.4 Applications

Denoising

As has been shown in the previous section, the DWT decomposes a signal into its wavelet levels, where each level corresponds to a centre frequency. Moreover, using the inverse DWT in order to eliminate certain frequency ranges just by setting their coefficients to zero, the DWT can be used for effective signal filtering. Orthogonal wavelet analysis has been found as perfectly suited for denoising processes. The higher the wavelet level gets, the more it contains noise. By omitting these higher levels during inverse wavelet transform, the noise will be absent in the reconstructed signal. Smart thresholding procedures have to be applied to the wavelet coefficients to remove the noise from the data. It has been shown that one possible solution is a threshold of two standard deviation for denoising [258, 259]. Often the attenuation of wavelet coefficients yields better denoising than coefficient selection. This requires the amplitude of all noisy coefficients that are above the threshold to be decreased by a certain level. This procedure is often referred to as soft thresholding.

The procedure of denoising falls into three steps: wavelet transform of the signal, thresholding of wavelet coefficients and inverse wavelet transform [260]. A threshold is used to set all coefficients smaller than threshold to zero. The so-called optimal threshold value *T*, established from *N* wavelet coefficients is given by

$$T = \sigma\sqrt{2\ln N} \tag{6.32}$$

where σ is the noise standard deviation. It can be shown that a robust estimation of the noise standard deviation can be calculated from the median of the highest level wavelet coefficients. These coefficients are approximately Gaussian random variables of variance σ^2. The median is used here rather than the averaged value since it can isolate outliers of potentially high amplitudes. To obtain the median *Med*, the middle coefficient a_p of the noise level has to be taken. Yielding an estimation for the standard deviation σ of

$$\sigma = \frac{1}{0.6745} Med \tag{6.33}$$

Figure 6.6 shows the denoising of the fibre optical data. The upper part gives the original, noisy signal. The signal represents a recorded Lamb wave signal, using a fibre Bragg grating sensor, bonded onto an aluminium plate. The clear signal has been reconstructed using the above described process and the 8th order Daubechie wavelet is presented below the original signal. The noise has been obtained by subtracting the filtered data from the original data. The orthogonal wavelet transform has been used to denoise the recorded Lamb wave data for both FBG and PZT sensors.

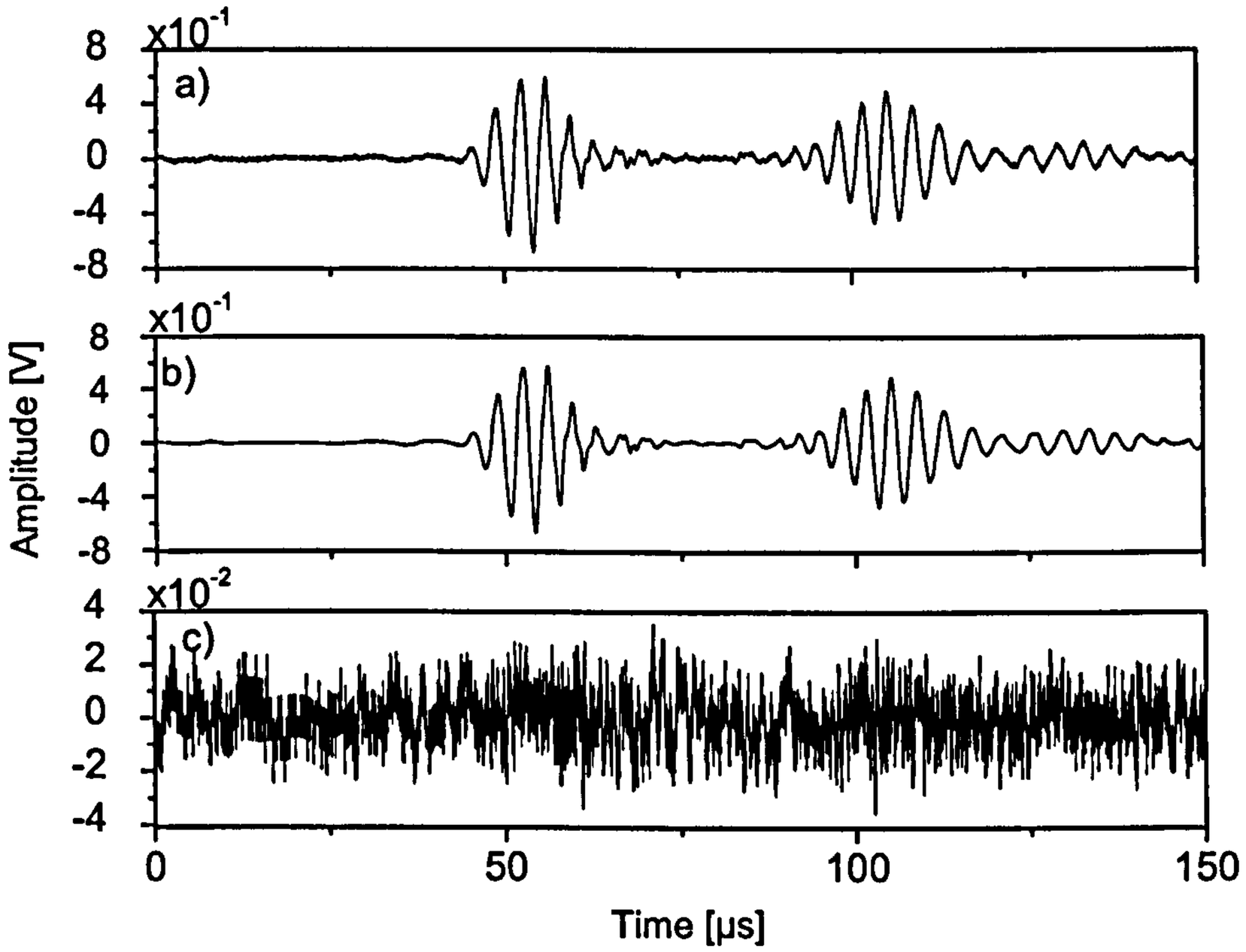

Figure 6.6: Denoising of fibre optic signal using orthogonal wavelet transform: a) Original signal; b) Reconstructed clear signal; c) Reconstructed noise.

Signal-to-Noise Ratio

Wavelet analysis can also be used to determine the signal-to-noise ratio (SNR) of the sampled signal. To do so, the denoised signal has to be obtained using one of the above described procedures. As a result the wavelet transformed signal has been separated into its coefficients representing the signal and the noise. Both parts of the signal can then be reconstructed to represent either signal or noise. Calculating either the mean square value or peak to peak amplitudes of both of the signals, the SNR can be found.

$$SNR = 10\log\frac{RMS_{Signal}}{RMS_{Noise}} \tag{6.34}$$

The SNR for the fibre optical data in Figure 6.6 using the threshold (6.32) has been found to be 14 dB.

Compression and feature extraction

A wavelet algorithm of compression and feature selection is based on a linear decomposition of a given function according to the wavelet synthesis formula given by Equation (6.29). In general, the aim of compression is to reduce the amount of information for effective storage, transmission and processing of the data. The main idea of wavelet based compression is to keep a small number of coefficients which represent the major energy of the signal. Due to the local nature of the wavelet decomposition, wavelet coefficients have an ability to pack energy of the data in a more efficient manner than other transformations [244].

Wavelet-based compression consists of four major steps: choice of the orthogonal basis, thresholding of wavelet coefficients, quantisation and encoding [244]. Thresholding truncates the wavelet coefficients according to their amplitude. Only a small number of coefficients which represent the major energy of the signal are kept. The remaining coefficients are set to zero. The smaller the number of wavelet coefficients kept, the higher the compression ratio.

With respect to the analysis of Lamb wave signals use can be made of the fact that the major energy of the signal is related to the carrier frequency of the signal. This knowledge which is accessible before starting the wavelet compression is known in the literature as a priori knowledge of features [261]. Making use of Equation (6.31), which relates the signal frequency to the wavelet level, it appears that most information can be found in the wavelet level corresponding to the carrier frequency.

Figure 6.7 gives the orthogonal wavelet decomposition of a Lamb wave signal. The signal has been gained from the difference of two signals. The first signal is the reference signal, the

second one the signal after damage has been introduced to the structure. The feature in the differential signal that represents the damage is a tone burst signal similar to the basic tone burst signal. This signal is due to the reflection of the original signal at the damage. Figure 6.7 gives the differential signal and three different wavelet levels. The signal created by the damage can be observed in all the displayed levels. All necessary information to detect the feature present in level 8, is even more apparent than in the original signal. For further analysis of the damage, e.g. severity or location of damage other tools as presented within this chapter can be applied to the differential signal. Another advantage of the wavelet decomposition is that there is significant data reduction if only level 8 is considered. This level is represented by 256 wavelet coefficients compared to the original data given by 10 000 samples.

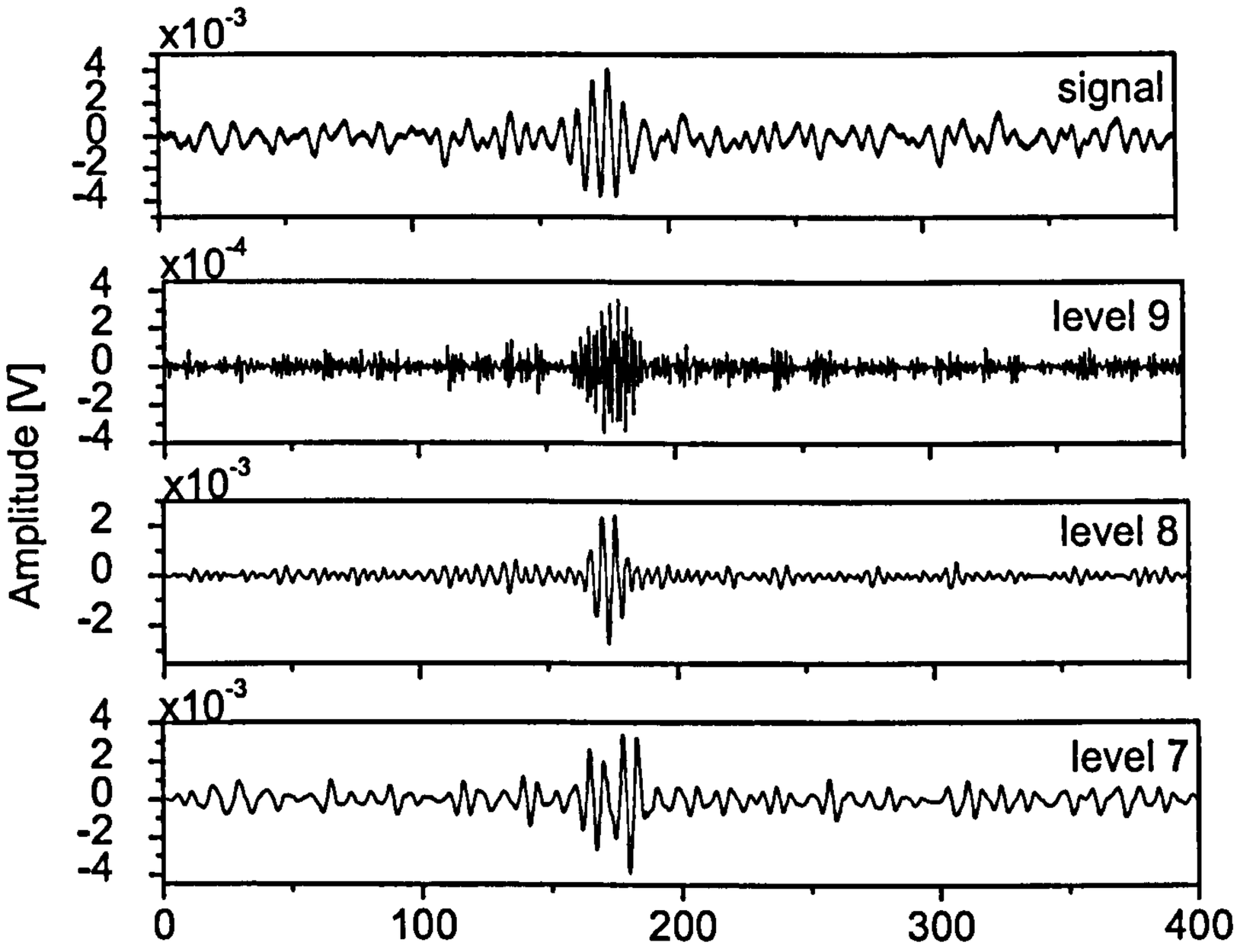

Figure 6.7: Orthogonal wavelet transform of a Lamb wave signal representing the occurrence of damage (hole 15 mm diameter).

Time-scale analysis

The continuous wavelet transform has been applied to the burst signal in Figure 6.1. The result is given in Figure 6.8. The graphs have been plotted as a time-scale spectrum. As has been explained in Section 6.5.2, the scale is closely related to the frequency, the information is therefore the same as in a time-frequency diagram. In this example a scale of 2.3 refers to a

frequency of 300 kHz. Thus Figure 6.8a indicates the amplitude peak and its location in time and frequency. The ridge in Figure 6.8b reveals the varying nature of the natural frequency of the basic tone burst signal.

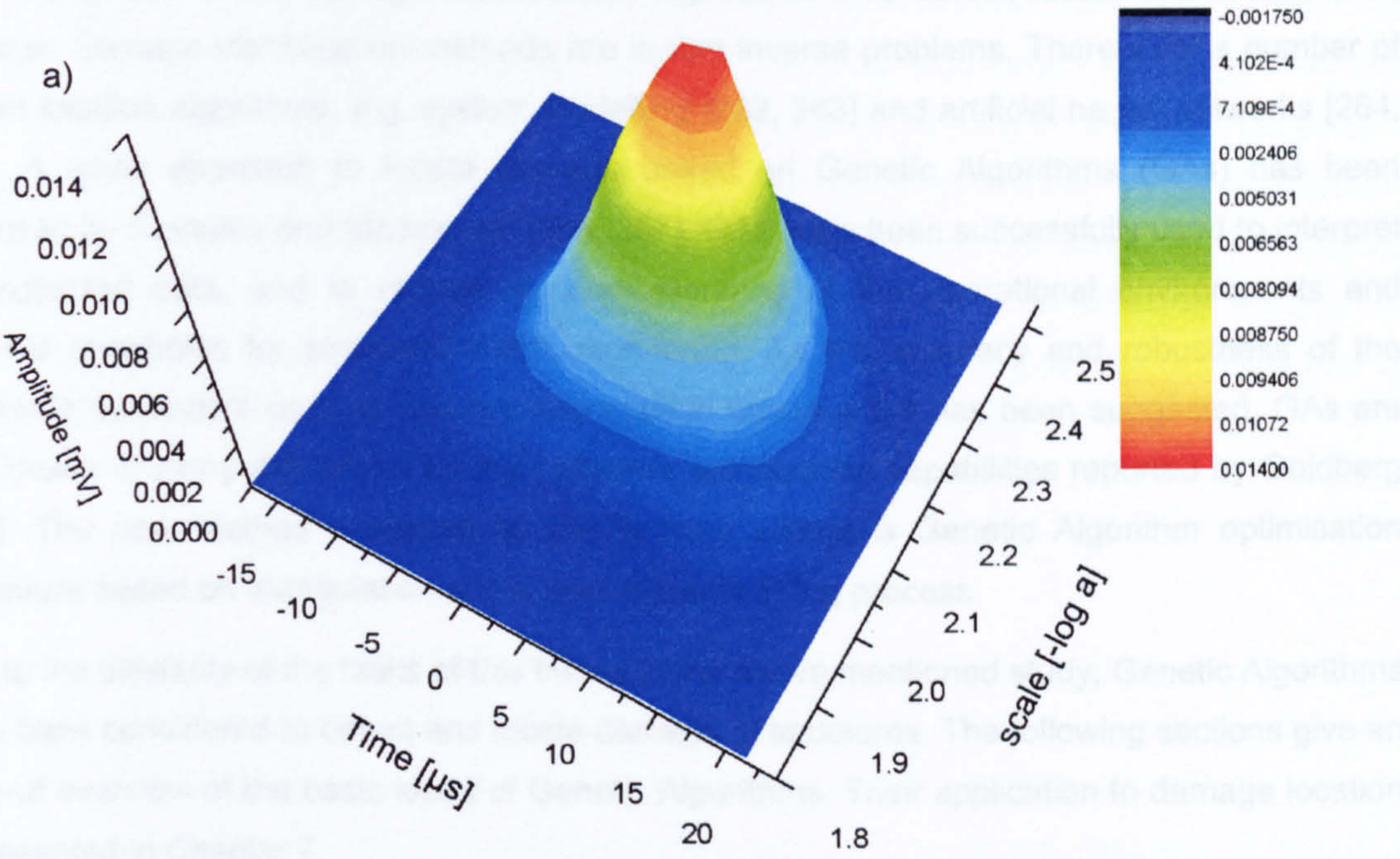

Figure 6.8: Continuous wavelet transform of basic tone burst signal: a) 3-D plot; b) Contour plot and ridge.

6.6 GENETIC ALGORITHMS

The overall task of the damage identification algorithms is to detect, locate and characterise damage. Damage identification methods are in fact inverse problems. There exist a number of impact location algorithms, e.g. system modelling [262, 263] and artificial neural networks [264, 265]. A novel approach to locate damage based on Genetic Algorithms (GAs) has been proposed by Coverley and Staszewski [266, 267]. GAs have been successfully used to interpret the collected data, and to require an understanding of the operational environments and material thresholds for structural health monitoring. As the accuracy and robustness of the system is dependent on how well the optimisation codes a GA has been suggested. GAs are well known in many disciplines for their efficient optimisation capabilities reported by Goldberg [268]. The new method proposed by the authors utilises a Genetic Algorithm optimisation procedure based on triangulation and a least squares fitting process.

Due to the similarity of the tasks of this thesis to the above mentioned study, Genetic Algorithms have been considered to detect and locate damage in structures. The following sections give an general overview of the basic ideas of Genetic Algorithms. Their application to damage location is presented in Chapter 7.

6.6.1 INTRODUCTION

Genetic Algorithms are a means by which machines can emulate the mechanisms of natural selection. It is an optimisation tool suitable for searching high dimensional spaces for the best solution. The algorithms are simple, robust and general, which means there is no knowledge of the search space assumed. GAs have been developed which perform optimisation with techniques modelled on biological genetics and natural selection. These operate by maintaining and modifying the characteristics of a population of individuals (solutions) over a large number of generations. This process is designed to produce successive populations having an increasing number of individuals with the desired properties. Like nature's solution, the process is probabilistic but not completely random. In fact, the rules of genetics retain desirable characteristics by maximising the probability of proliferation of those individuals who exhibit them.

Like other optimisation tools that find the maximum value of a function, a GA seeks continuous improvement of a population in order to derive the best solution. Yet, rather than producing optimal populations, genetics need only to produce individuals that are superior to other individuals in the population. Thus, by optimisation the GA might find a superior, but not necessarily an optimal solution. The element of mutation helps to overcome this stand-off

situation and may produce new individuals for the next round of optimisation. The mathematical foundations of GAs are based on the concept of a schema or similarity template. A deeper and more profound representation of the mathematics can be found in [268, 269].

GAs operate on a coding of the parameters, rather than the parameters themselves. The parameter space consists of individuals, which are coded as finite-length strings (genes) over some type of alphabet. The number of individuals in a population depends on several parameters including the size of each individual and the size of the solution space. Selection of an appropriate coding method is crucial to the success of the GA. The selection of the coding method however is not straightforward. There are two principles for effective coding, the principle of minimal alphabets and the principle of meaningful building blocks. Both are met by the most common coding techniques which are binary and integer coding.

Binary coding

In binary coding each individual consists of a number of (1,0) elements with each bit representing a gene. Each gene in the individual is given as its weight an appropriate power of two. The individual may be converted into its decimal equivalent by adding the weights over the 1's. Hence, for an individual that represents two values of a certain measure (1 0 0 1 0 1,0 0 1 0 1 1) would be the binary representation of 37 and 11. Here the first 6 genes represent the first value, the latter the second value. The generally accepted advantages of binary coding are the theoretical aspects are well developed and the binary coding reduces the size of the optimisation space. This can be of benefit in rationalising the performance of the GA in an effort toward improving it. A drawback of binary coding is that there is overhead associated with converting a floating point number to a binary string and back for each fitness function.

Integer coding

For integer coding each gene is an integer number. The individual consists of as many genes as are necessary for the representation of the optimisation problem. The same individual as in the example above would be (37 11). The primary advantage of integer number coding on the one side is its conceptual simplicity. On the other side it no longer requires the conversion between the binary strings and the floating point values for the variables being optimised, thus resulting in a good resolution and the elimination of computation overhead.

6.6.2 GENETIC OPTIMISATION

Given an initial population of individuals, a genetic algorithm produces a new population of individuals according to a set of genetic rules. These rules are devised so that the new generation tends to have individuals with superior performance compared to those in the previous generation. A measure for this performance is the fitness function. It ensures that successive generations of individuals are produced which tend to represent superior populations. GAs optimise the population rather than the single individual. That mostly contributes to the robustness of the method. Even if the genetic process inadvertently acts to lose a desirable characteristic in one individual, it may be safely retained in other members of the population. Genetic optimisation starts by generating, at random, an initial population of possible solutions. According to their individual fitness, high quality "parents" are selected to generate future off springs. The following simple genetic rules for GAs can be used.

Reproduction

Reproduction is an artificial version of natural selection. This process ensures that individuals are copied into the next generation according to their fitness. Copying individuals with respect to their fitness means that individuals with a higher value have a higher probability of contributing one or more offspring in the next generation. Figure 6.9 gives a graphical representation of this method. Once a individual has been selected for reproduction, an exact replica of the individual is made. It is then entered into a pool of individuals, a tentative new population, for further genetic operator action.

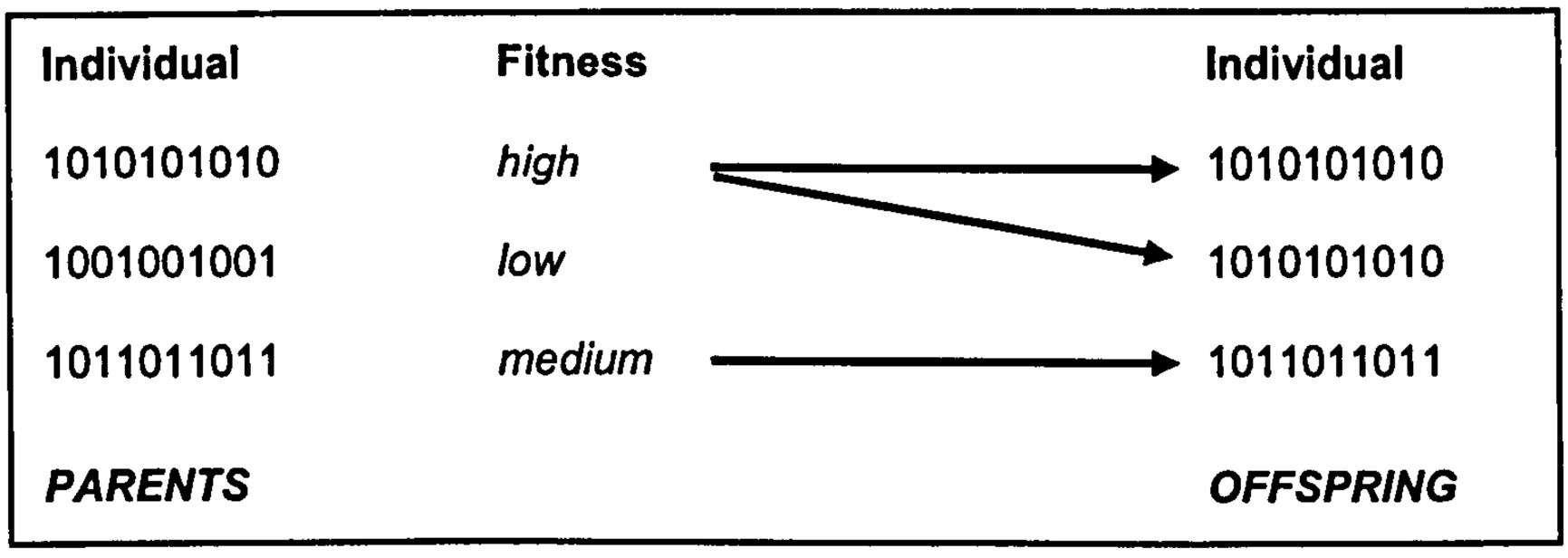

Figure 6.9: Reproduction.

Crossover

This is a method of combination between pairs of individuals in which the randomly chosen sub-strings from each individual are switched. Single point crossover involves cutting the individuals of the parents at a randomly chosen common point and exchanging the right-hand-side genes, as indicated in Figure 6.10.

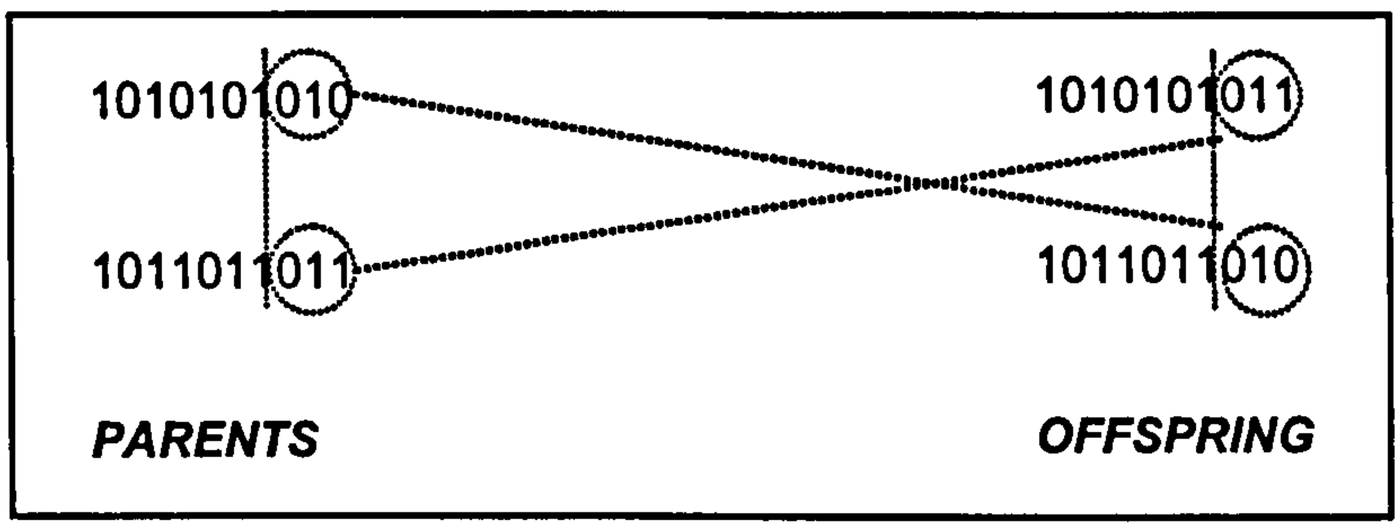

Figure 6.10: Crossover.

Mutation

Making alterations to the values of one or more genes in a individual is referred to as mutation. This can result in entirely new gene values being added to the gene pool. With these new gene values, the genetic algorithm may be able to arrive at better solutions than was previously possible, e.g. when the algorithm got stacked at a non optimal solution. However, to avoid losing too many of the fittest individuals, the mutation rate usually is kept small, in the order of one mutation per thousand bit. In binary coding mutation consists of inverting random bits of the genotypes as explained in Figure 6.11.

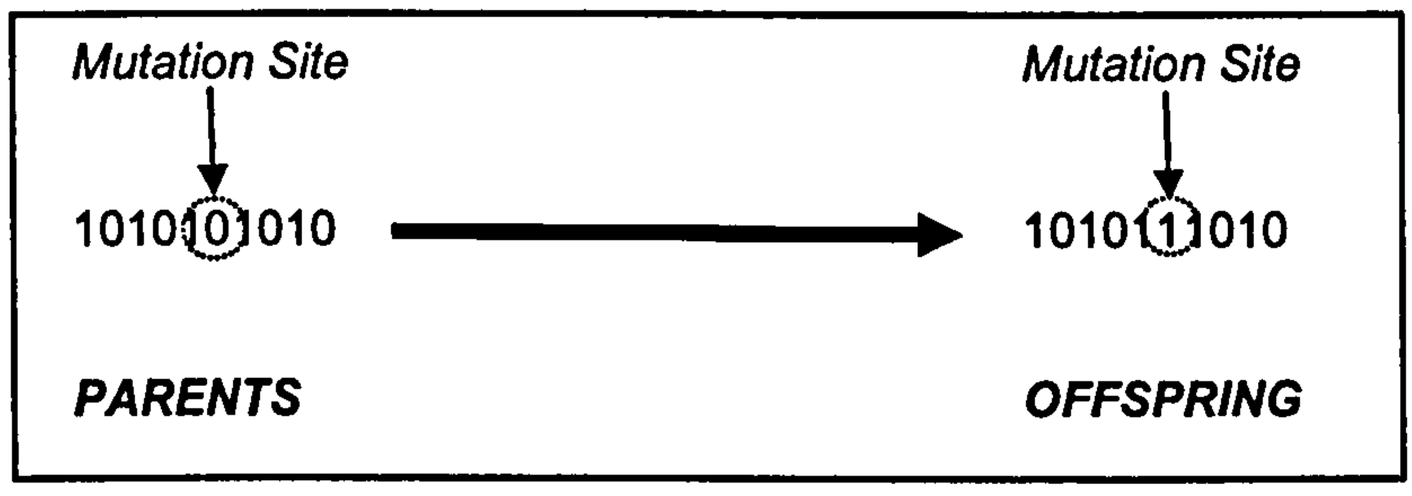

Figure 6.11: Mutation.

New Blood

To prevent a population from stagnating, new entirely random chosen individuals are chosen that form perturbations into the population. Again, the rate of creating entirely new individuals should be kept small.

Elite

In order to keep the best solutions in a population, they can be copied automatically into the next population. This process is called Elite. It avoids the loss of the fittest genetic material.

The above explained genetic rules form an iterative process through new generations. The GA ends after the termination criteria are satisfied or after a specified number of generations. The

last generation then contains a population that is dominated by the fittest individuals, as illustrated in Figure 6.12.

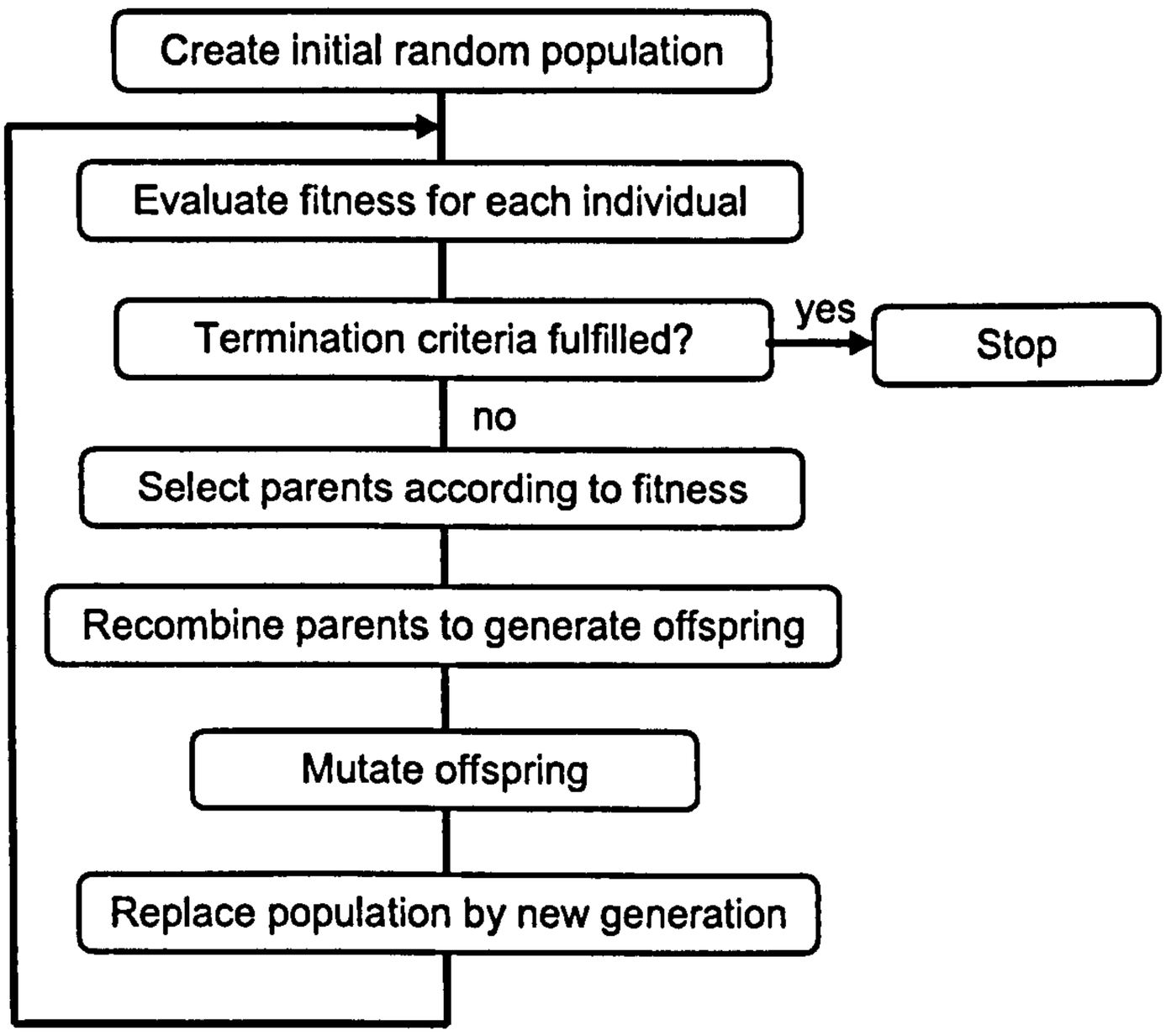

Figure 6.12: Basic Genetic Algorithm procedure [270].

7 EXPERIMENTAL IDENTIFICATION OF DAMAGE

The results from damage identification experiments are presented in this chapter. The Lamb wave based approach, as presented in Chapter 5, was applied to test a variety of structures. Fibre Bragg gratings were used to sense the Lamb wave responses. In addition, conventional piezoceramic transducers served as a reference for the fibre optic results. The experiments followed three different levels of damage identification, i.e. detection, location and severity of damage. Damage detection forms the first level of damage identification. The signal processing tools, presented in the previous chapter, were used to identify the presence of damage as reported in Section 7.1. Two different approaches were chosen depending on whether the location of the damage was known a priori or not. In case the damage position is unknown, the second level of the damage identification process has to be applied, i.e. location of the damage. This is presented in Section 7.2. The method followed here makes use of the directivity of the fibre Bragg grating sensor. A Genetic Algorithm was applied to calculate the location of the damage in metallic and plastic plates. The third level of damage identification, i.e. information about the severity of damage, is addressed in Section 7.3. Once the location of damage has been found, changes in Lamb wave responses can be related to the severity of damage. Finally, the influence of variable thermal conditions on the reliability of damage identification is studied in Section 7.4. The discussion of the results focuses on the comparison of fibre optic and piezoelectric sensor data.

7.1 DAMAGE DETECTION

Within the whole process of damage identification, damage detection forms the primary objective. It is therefore necessary to find robust and reliable measures to identify the presence of damage within recorded signals. Several aspects of damage detection were studied within the experiments. First of all, the feasibility of fibre Bragg grating (FBG) sensors for damage detection was investigated. The performance FBG sensors can be compared using conventional piezoceramic transducers (PZT) as a reference. As a second task different signal parameters were studied to find a reliable measure indicating the presence of damage.

7.1.1 Experimental Procedures

The experiments were carried out at three different locations. For the most part the testing took place at the DaimlerChrysler research laboratory in Ulm, Germany. Other tests were performed in the Department of Electronic and Electrical Engineering of the Strathclyde University in Glasgow, UK. Most of the evaluation work took place in the Department of Mechanical Engineering of the Sheffield University in Sheffield, UK. It is clear that different experimental conditions were experienced at the above locations. The basic experimental set-up which was common to all tests is shown in Figure 7.1.

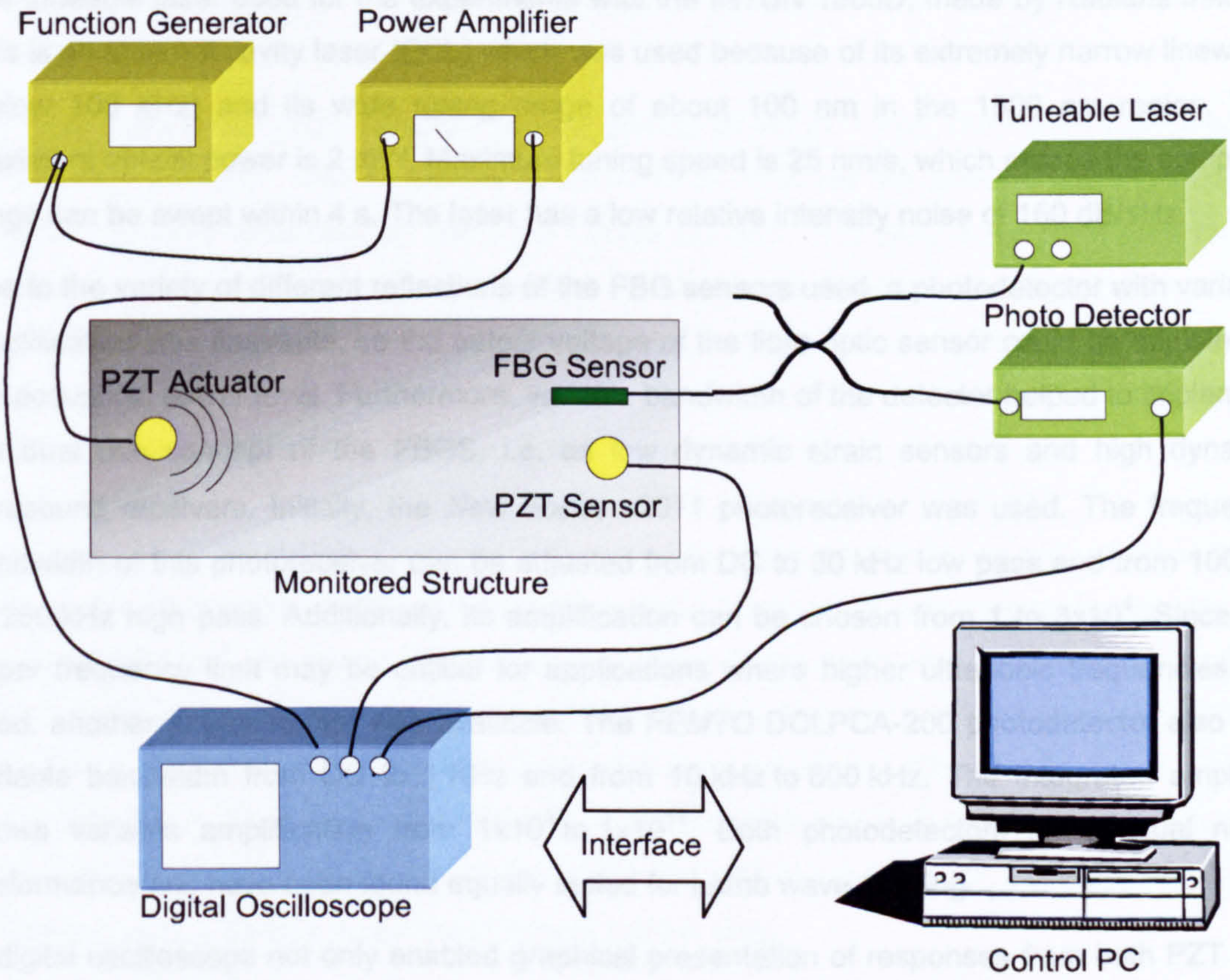

Figure 7.1: Schematic diagram of the basic experimental set-up.

Instrumentation

The *HP* (Hewlett Packard) 33120A and the *TTI* (*Thurby Thandar Instruments Ltd.*) TGA 1242 served as function generators. Both devices allow the generation of arbitrary signals. Both generators have a GPIB (General Purpose Interface Bus) interface, so that they can be controlled by a computer.

At all locations an *ENI* (Electronic Navigation Industries) power amplifier was available. They differed however in the amplification and the frequency range. The *ENI* 406L, used in Ulm, has an amplification of 40 dB and a frequency range from 150 kHz – 250 MHz; the maximum output power is 6 W. The *ENI* 2100L, used in Glasgow, has 50 dB amplification and a frequency range from 10 kHz - 12 MHz; the maximum output power is 100 W. It is clear that the 2100L is better suited for damage detection applications since frequencies range from kHz to MHz levels. Nevertheless, initial experiments were performed using the 406L amplifier which, at the time, was the only instrumentation available. For verification of the experimental results, the 2100L amplifier was sent to Ulm.

The tuneable laser used for the experiments was the INTUN 1500D, made by *Radians Innova*. This is an external cavity laser (ECL) which was used because of its extremely narrow linewidth (below 100 kHz) and its wide tuning range of about 100 nm in the 1500 nm region. The maximum optical power is 2 mW. Maximum tuning speed is 25 nm/s, which means the complete range can be swept within 4 s. The laser has a low relative intensity noise of 160 dB/√Hz.

Due to the variety of different reflections of the FBG sensors used, a photodetector with variable amplification was desirable, so the output voltage of the fibre optic sensor could be adjusted to the acoustical power level. Furthermore, variable bandwidth of the detector helped to implement the dual use concept of the FBGS, i.e. as low dynamic strain sensors and high dynamic ultrasound receivers. Initially, the *New Focus* v2011 photoreceiver was used. The frequency bandwidth of this photoreceiver can be adjusted from DC to 30 kHz low pass and from 100 Hz to 250 kHz high pass. Additionally, its amplification can be chosen from 1 to $3x10^4$. Since the upper frequency limit may be critical for applications where higher ultrasonic frequencies are used, another photodetector was available. The *FEMTO* DCLPCA-200 photodetector also has variable bandwidth from DC to 1 KHz and from 10 kHz to 600 kHz. The integrated amplifier allows variable amplification from $1x10^3$ to $1x10^{11}$. Both photodetectors have equal noise performance and have been found equally suited for Lamb wave sensing.

A digital oscilloscope not only enabled graphical presentation of responses from both PZT and optical sensors, but was also used to store the data for further processing. *Tektronix* oscilloscopes have been used at all locations. The TDS 3034B, available in Ulm, and the TDS 3014, available in Glasgow, only differ in their bandwidth; the bandwidth is 300 MHz and 100 MHz for both oscilloscopes, respectively. The 100 MHz bandwidth is sufficient for ultrasonic tests where maximum signal frequency is below 1 MHz. The further, common specifications of the oscilloscopes include 4 input channels, 2.5 GS/s sampling rate and interfaces for connection and data transmission to a computer.

A PC with an *Intel* Pentium II processor and *Microsoft* Windows operating system was used for data storage and further signal processing. The PC was also used to control instruments like

the tuneable laser, the function generator and the digital oscilloscope using a GPIB interface or a serial interface.

PZT discs, see Figure 4.6, were applied for the excitation of Lamb waves. Two different types of transducers were studied, i.e. the *Ferroperm* Pz29 with a diameter of 10 mm and a thickness of 0.4 mm and the *PI Ceramic* PIC255, with 10 mm diameter and 0.2 mm thickness. The acoustical properties of both transducers were examined experimentally. No significant difference in the performance of both PZTs was observed for a range of excitation frequencies. However, the PI Ceramic discs have wrapped-around electrodes, i.e. both electrodes are on the upper side of the disc, which makes the connection very easy. The PZTs were bonded on the plates using the *Polytec* EPO-TEK 301. This epoxy-based glue cures overnight and produces good quality bonds.

The FBG used for damage detection have a grating length of 1 mm. They were fabricated by *IPHT* Jena, Germany. Their reflectivity is about 15 %, whereas the spectral width is close to 500 pm. The FBG were bonded using the *Kyowa* CC-33A. This glue is recommended for the installation of electrical strain gauges. Good results for the FBG sensors bonding were also obtained.

7.1.2 Initial Experiments

There is currently no standard or even a best-practice advice available on how to proceed for damage detection when Lamb wave sensing is used. There are however some basic rules that should be followed. As already described in Chapter 4, the basic idea is to use a frequency region where only fundamental modes exist. Furthermore, the mode and the frequency chosen should be such that dispersion is kept to a minimum to avoid any difficulties in signal analysis and interpretation. The first step therefore is to calculate the dispersion curves for the structure to be tested. This requires the knowledge of the material properties such as Young's modulus E, Poisson ratio ν, density ρ and the thickness t of the plate.

Dispersion curves give theoretical values for the phase and group velocity and the preferable frequency of the Lamb wave modes. However, due to insufficient knowledge of material properties and complex geometry of tested structures they are difficult to obtain in practice. Furthermore, dispersion curves give optimum frequencies for Lamb waves. These frequencies are not necessarily the optimum driving frequencies of the ultrasonic transducers. The performance of the piezoceramic transducers depends on their geometry and the related resonance and anti-resonance frequencies.

Material properties

Table 7.1 gives the properties of the materials used for damage identification. The velocity measurements were taken at 130 kHz for the Perspex and 300 kHz for the aluminium plates. A comfortable way was found to measure the group velocity by looking at the envelopes of the signals. The time difference between the envelope peaks from the excitation signal and the corresponding mode was taken as a measure for the time-of-flight. Knowing the distance from actuator and receiver, the group velocity can be obtained.

Table 7.1: Material properties of the test structures.

Parameter	Perspex	Aluminium
Young's modulus, E [GPa]	24	70
Poisson ratio ν	0.35	0.345
Density, ρ [kg/m^3]	1190	2700
Thickness, t [mm]	3	1
Longitudinal velocity [m/s]	2730	6320
Shear velocity [m/s]	1430	3130
Velocity S_0 (Calculated) [m/s]	2300	5300
Velocity S_0 (Experimental) [m/s]	2100	5000
Velocity A_0 (Calculated) [m/s]	1400	2700
Velocity A_0 (Experimental) [m/s]	1600	2900

Although generally good correlation between measured and calculated velocities has been obtained, an offset of about 10% could be observed, as presented in Table 7.1. The reason for this is most likely insufficient knowledge of material properties. As the properties have not been available from manufacturers, the properties found in standard literature [15] have been taken instead.

Frequency selection

The optimum frequency of excitation is influenced by the frequency characteristics of the actuator, receiver and structure. In order to choose the best frequency, the amplitude of Lamb wave responses as a function of frequency has been obtained experimentally, as shown in Figure 7.2.

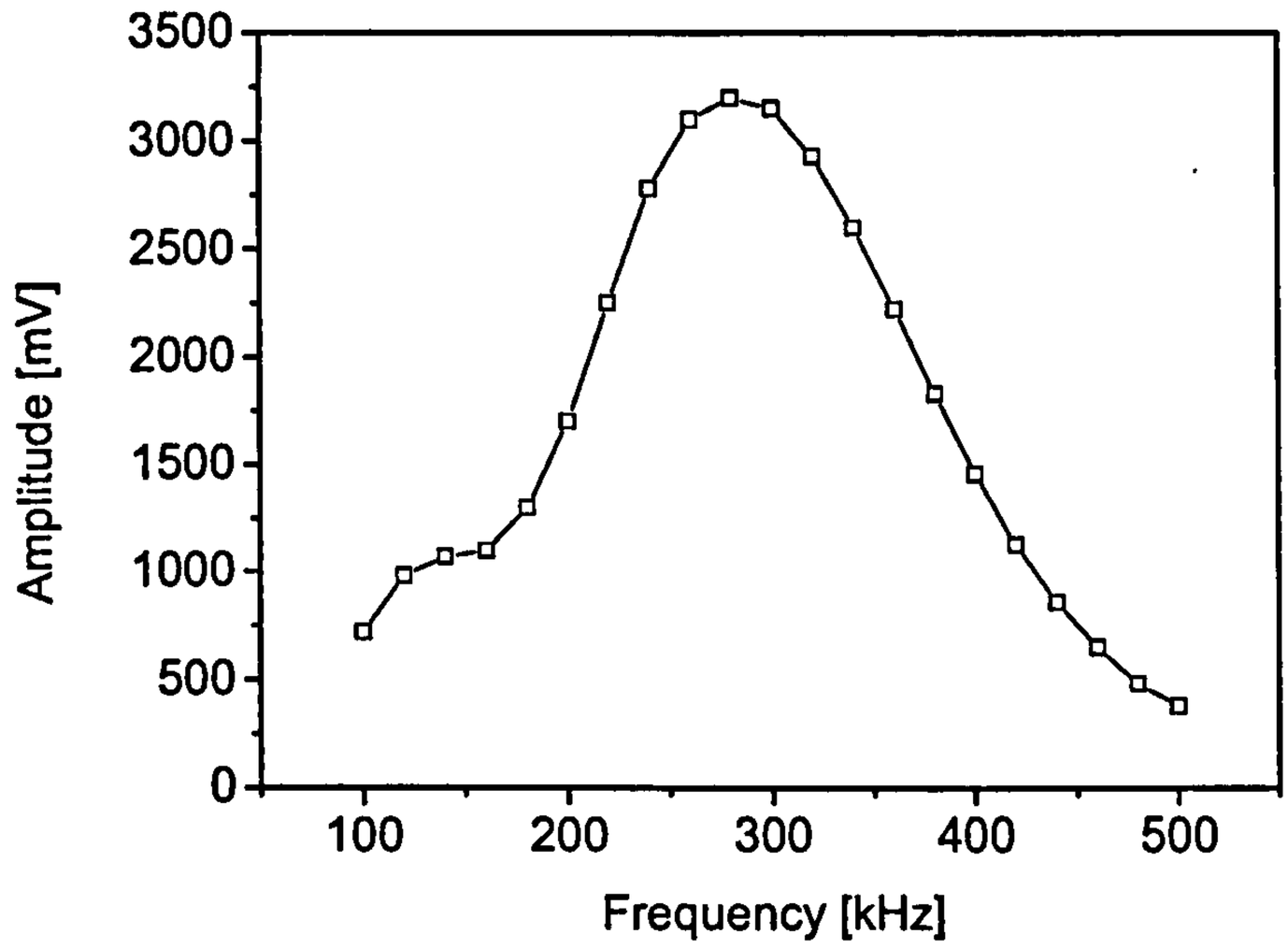

Figure 7.2: Maximum amplitudes of the S_0-Lamb wave mode in aluminium.

Here, a peak around 290 kHz can be identified. This dominant effect is the resonance frequency of the PZT bonded on the aluminium plate. It is well known that the best dynamic performance is achieved when the excitation frequency is chosen as one of the resonance frequencies of the transducer. For disc shaped transducers the radial mode of the piezoceramic generates the S_0 mode which is dominated by a longitudinal wave travelling in the plate [271, 272]. From the amplitude-frequency characteristics the optimum frequency for S_0 Lamb wave sensing in aluminium and Perspex plates have been found to be 290 kHz and 130 kHz respectively. This probably indicates the influence of the acoustical coupling between the PZT and different structures.

The attenuation characteristics of the material also influence the frequency characteristics of the Lamb waves. It is well known that the attenuation curve is proportional to *1/f* [273]. This explains the higher amplitudes on the lower frequency part of the spectrum in Figure 7.2. It has been shown in Chapter 5 that the response of the grating at this frequency range is independent of the frequency. However, within the experimental set-up a high pass filter at about 100 kHz has been used to cut low frequencies.

7.1.3 Experimental Approach using a Priori Knowledge about Damage Location

For the analysis of Lamb wave responses two fundamentally different approaches can be applied, depending on different damage conditions. The first approach is used when the location where the damage will occur is known a priori. Another approach has to be chosen if there is no knowledge or indication where on the structure damage can appear.

Several circumstances can be thought of when explicit knowledge of damage location exists. For example, it is well known that fatigue cracks start to grow at points of high stress concentration, e.g. close to rivets or holes [274, 275]. These high risk areas could be monitored in particular. The same is true for repaired damage. One method of repairing fatigue cracks in aircraft structures is to bond a patch of composite material [276-279]. This will slow down the fatigue process, although it will not completely stop it. Again, the task is to monitor such an area and see if any changes occur which would indicate growth of the crack. The second level here would be to gain precise knowledge of how much the crack grows. This subject will be covered in section 7.3. A third case where the location of damage is known in advance is the presence of so-called hot spots. This means that, from experience with the same kind of structure in other applications, points with high probability of failure are known, which in consequence have to be monitored in detail.

If there is knowledge about possible damage locations, the placement of transducers is simplified. A good choice is to position acoustical sender and receiver so that damage occurs along a straight line between both transducers (Figure 7.3). This line can be referred to as the primary acoustical path. In Chapter 4 different aspects of how damage will change wave propagation have been explained. If damage occurs on the primary acoustical path, the signal amplitude and velocity will change mainly because the acoustical properties of the material along the path have been altered by the damage. Any acoustical path, e.g. edge reflections in Figure 7.3, that will not pass the damage should remain unchanged. The distance between PZT and FBG transducers used in the experiments was 30 cm. The hole was placed in the middle.

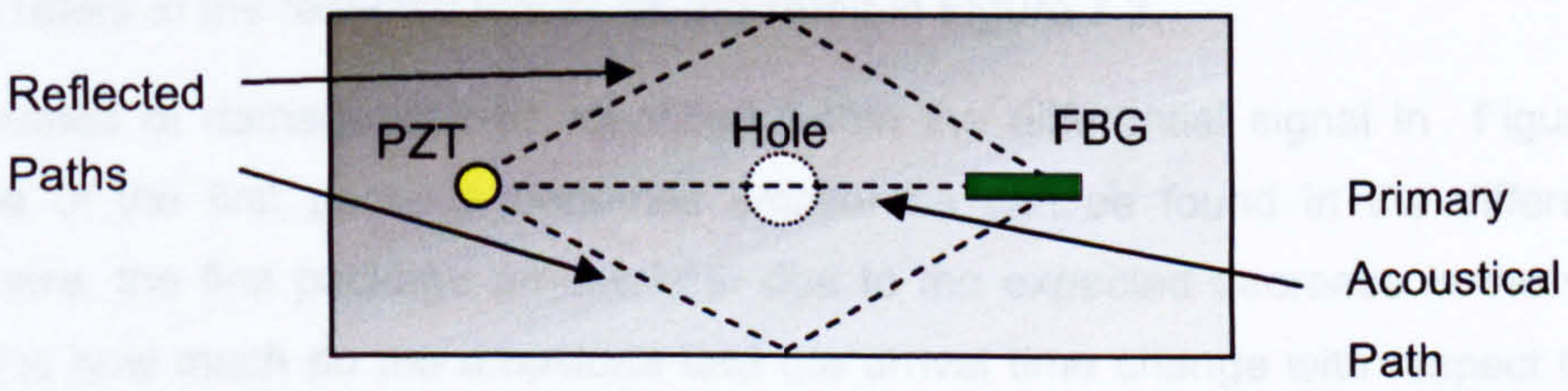

Figure 7.3: Transducer locations for damage detection with a priori *knowledge of damage location.*

The PZT actuator was used to generate the ultrasonic Lamb waves. The waves propagated along the dotted lines from the actuator to the FBG sensor. The line that crosses the indicated hole is the primary acoustical path. The reference (initial) condition has not involved any damage in the plate. To simulate damage a hole of 12 mm diameter was drilled into the test structure. Figure 7.4 gives two Lamb wave responses for the reference and damage conditions.

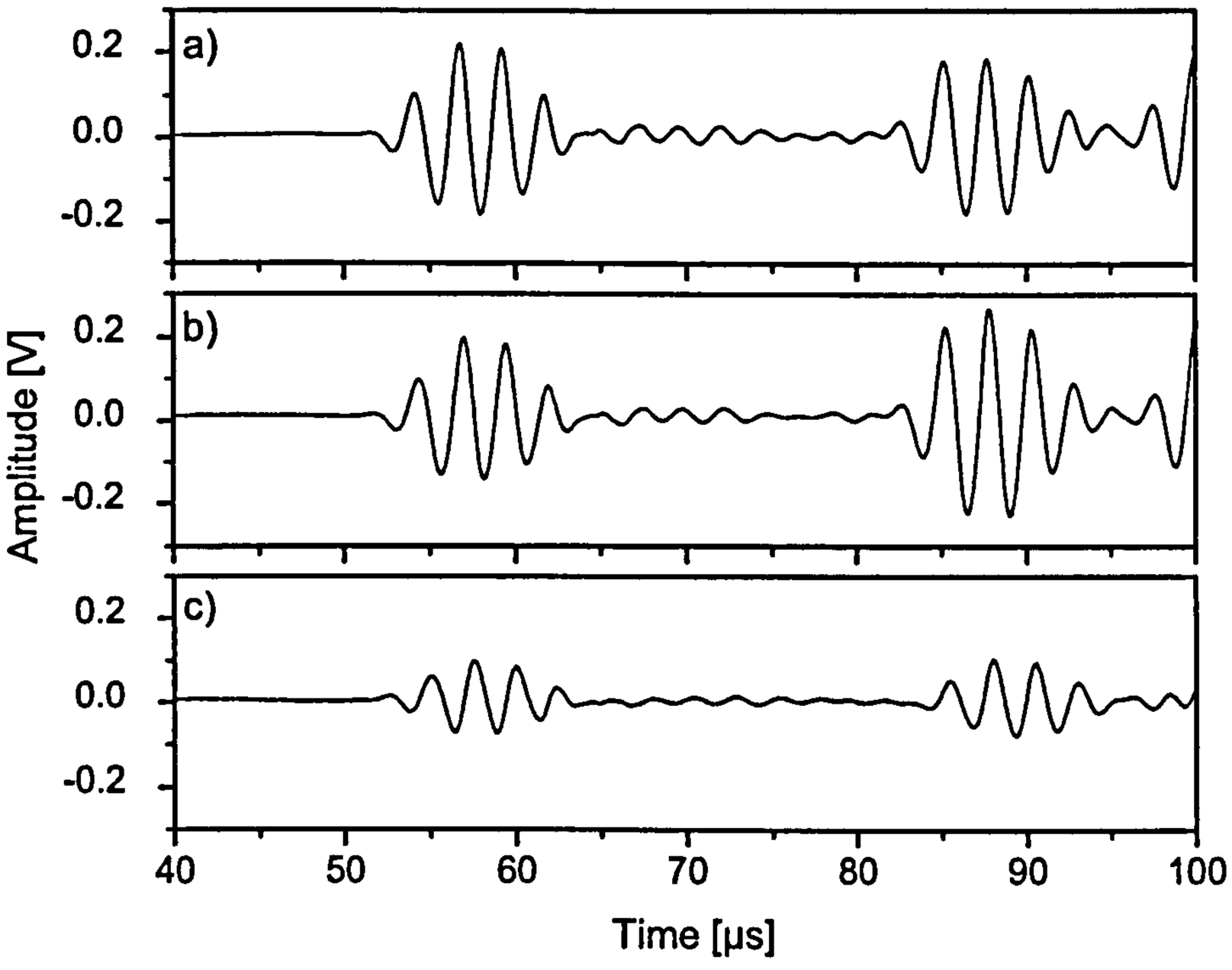

Figure 7.4: Lamb wave responses for the experiment with a priori *knowledge of damage location: a) reference condition; b) damage condition; c) differential signal.*

Two different packages of burst signals can seen in Figure 7.4. Identification of the packages can be achieved by measuring the time-of-flight and then see which distance the wave must have travelled. The corresponding path can be found from the geometry of the test structure. Here the first package is the S_0 mode travelling along the primary acoustical path. The second package refers to the reflected waves as indicated in Figure 7.3.

The presence of damage can be identified within the differential signal in Figure 7.4c. The amplitude of the first package becomes smaller as can be found in the differential signal. Furthermore, the first package arrives later due to the expected decrease in the velocity. The question is how much do the amplitude and the arrival time change with respect to severity of damage. This question will be addressed in Section 7.3.

7.1.4 Experimental Approach when Damage Location is Unknown

In the previous section examples have been given for damage events where the position is known in advance. The more general case however is the one without any a priori knowledge of damage location. This includes damage induced by impact, because the statistical nature of impacts makes it impossible to predict where the impact might occur. Furthermore, it is not always possible to predict where fatigue cracks will initiate.

Therefore, a different experimental approach has to be used when possible damage locations are not known in advance, i.e. damage is not on the primary acoustic path. Hence, damage detection can not rely on the analysis of the first package. Instead the presence of damage will be indicated by an additional wave package within the Lamb wave response. This package is the reflection of the Lamb wave from the damage. The assumption here is that damage can reflect ultrasonic waves. Damage was simulated here by drilling holes into the test structure. The radial symmetry and the different acoustical properties of structural material and air ensure the hole reflects the incoming Lamb wave.

The layout of the experiment to detect damage in case its location is unknown is shown in Figure 7.5. In this case the hole had been drilled off the primary acoustical path. The plate was dimensioned big enough, so that no reflection from the edge could influence the acoustical signal. The hole diameter was 12 mm as in the previous experiment. For better visualisation of the reflected wave, the orientation of the fibre sensor was adapted to the reflected signal. The distance between the PZT and the FBG sensor was 30 cm and the length of the acoustical path including PZT actuator, hole and FBG sensor was 70 cm.

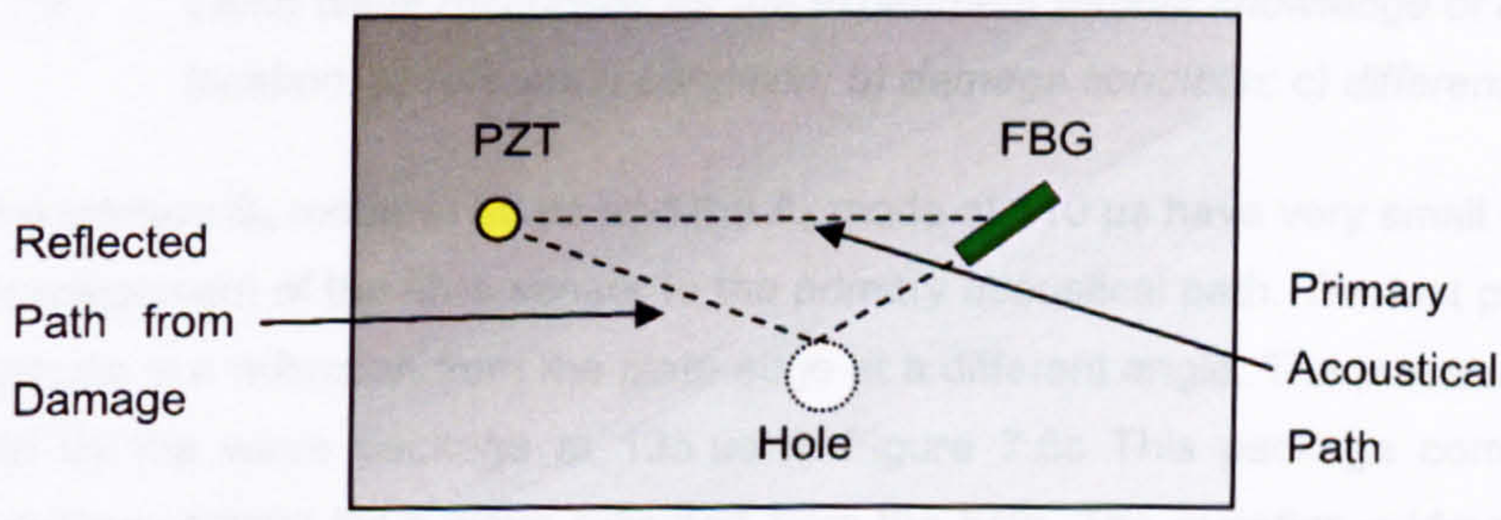

Figure 7.5: Transducer locations for damage detection when damage location is unknown.

Again the signals for the reference and the damage conditions were recorded. This time the differential signal, i.e. the difference between the damage and reference condition, was calculated, so the reflected signal becomes apparent. Figure 7.6 presents the results.

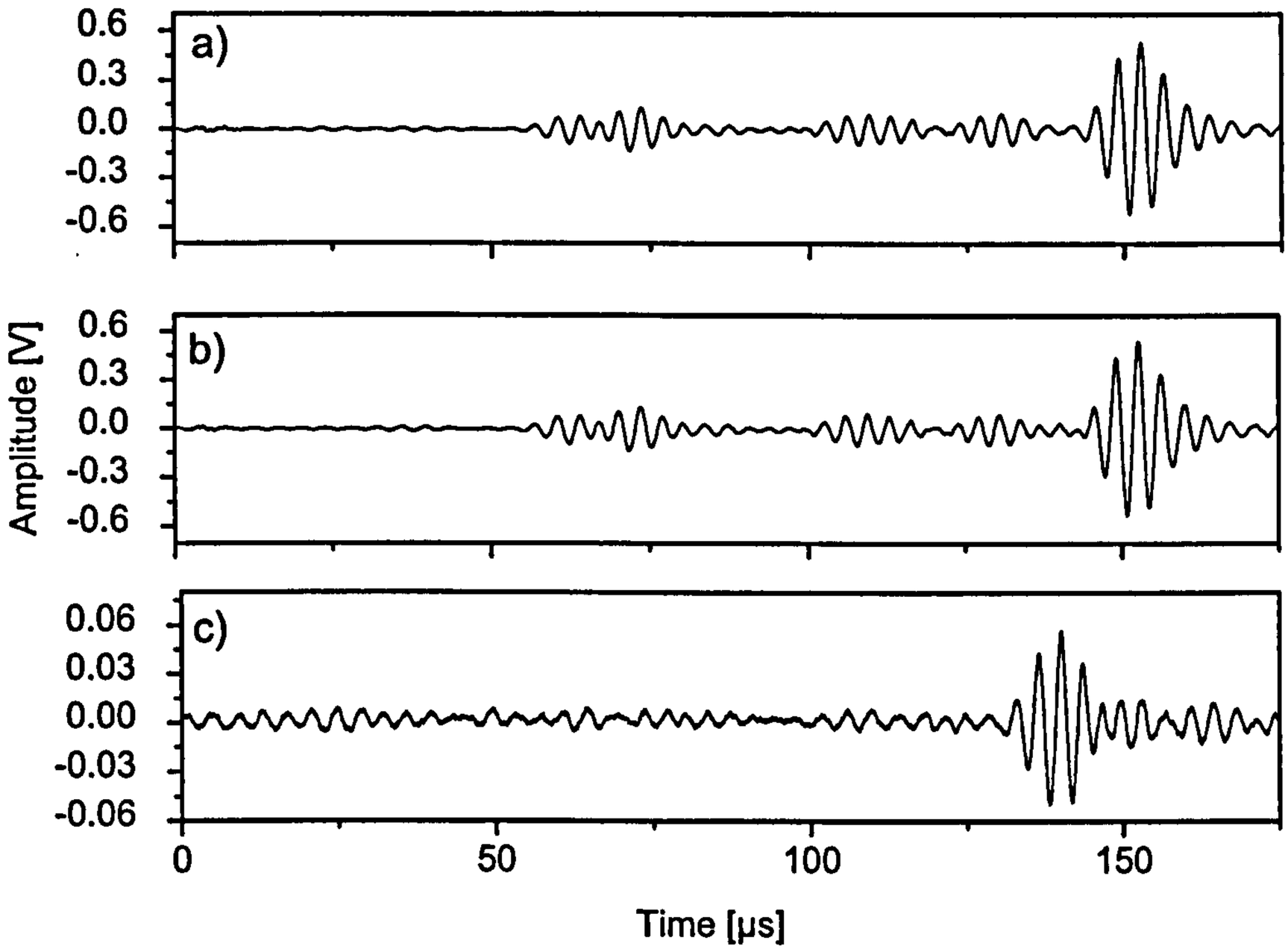

Figure 7.6: Lamb wave responses for the experiment without knowledge of damage location: a) reference condition; b) damage condition; c) differential signal.

Here, the primary S_0 mode at 60 µs and the A_0 mode at 110 µs have very small amplitudes, due to the misalignment of the fibre sensor to the primary acoustical path. The last package with the big amplitude is a reflection from the plate edge at a different angle. The presence of damage is indicated by the wave package at 135 µs in Figure 7.6c This package corresponds to the expected time-of-flight for a wave reflected from the hole. The question addressed in the next section is how to use differential signals for damage location.

7.2 Damage Location

7.2.1 Sensor Layout

In Chapter 3 the concept of fibre based strain rosettes has been introduced. For any loads where principal load directions are unknown, or for multi-axial load cases, the rosette configuration allows one to determine the principal directions and the principal strains. By analogy the rosette type sensor configuration can be used to determine the direction of acoustical strain fields. Optical Bragg grating sensors are well suited for rosette applications, as explained in Chapter 3. This is due to high inherent directivity. In addition, an appropriate

mounting technique can eliminate any strain cross-sensitivity. Strain rosettes can be used for detection of principal directions. For any strain sensor that is not adjusted to the principal direction, the strains along the principal direction can be found by applying the theory of elasticity. For an isotropic structure the equation to describe the sensitivity of the strain sensor with respect to the angle of the principal axis has been defined in Equation (B.5) see also [280]:

$$\varepsilon_z = \varepsilon_1 \cos^2 \alpha + \varepsilon_2 \sin^2 \alpha \tag{7.35}$$

Here ε_z is the strain along the sensor axis, ε_1, ε_2 are the principal strains and α is the angle measured from the direction of ε_1; the geometry is shown in Figure 7.7. The strain sensor in Figure 7.7 is a fibre Bragg grating and the principal axis of strain by the direction of the acoustical Lamb wave field. The Lamb wave can be assumed to be cetected in the far field, as the distance from the ultrasonic source to the sensor is much larger than the acoustical wavelength. In consequence, the Lamb wave far field can be assumed to be a plane wave, and ε_2 in Equation (7.35) is equal to zero.

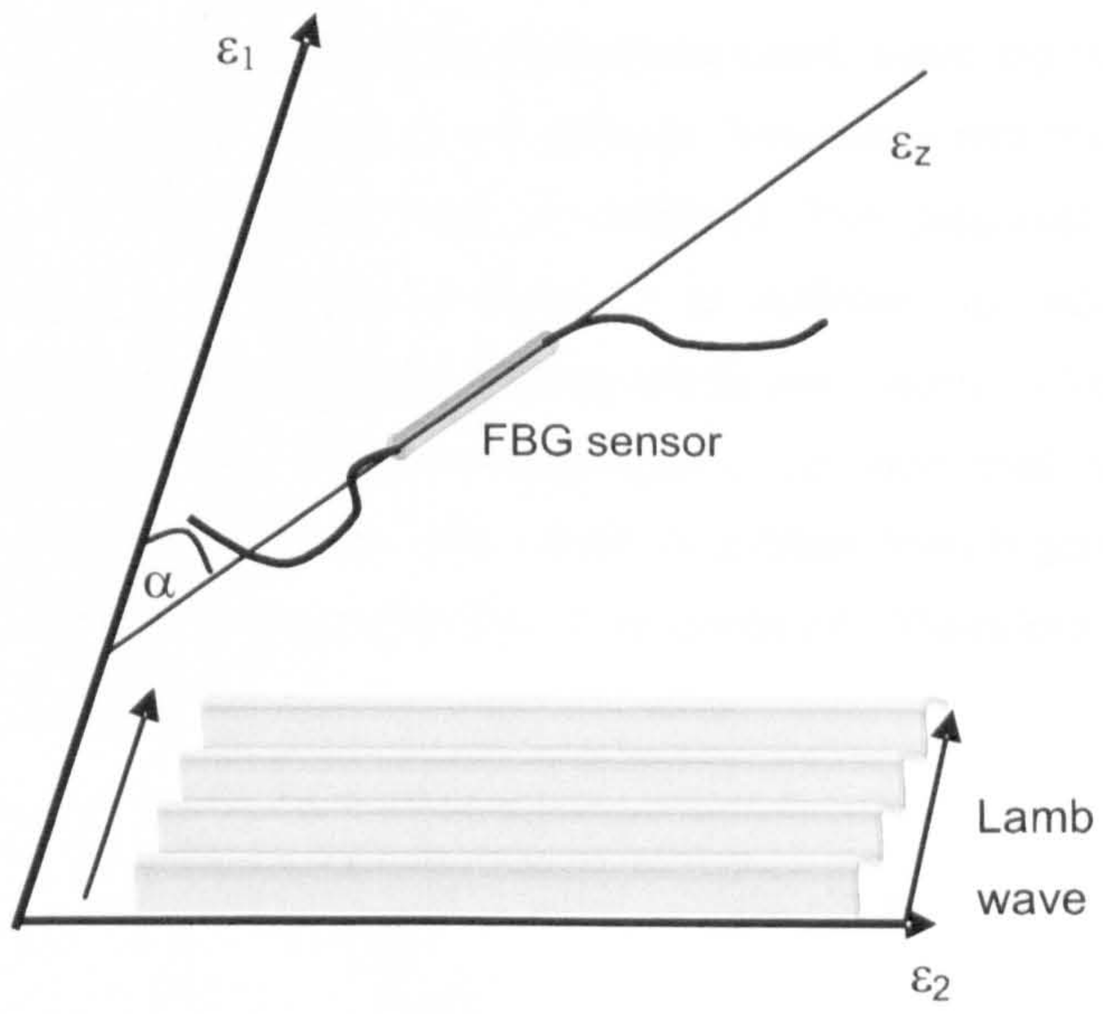

Figure 7.7: Definition of coordinates for the interaction of the Bragg grating with the ultrasonic wave.

For a rosette configuration Equation (7.35) is true for every sensor when α is adapted as $\alpha + \beta$ and $\alpha + 2\beta$ for gratings 2 and 3, respectively. Here, β is the angle of the rosette configuration. A 120° rosette set-up has been chosen for ultrasonic source location. The layout of the fibre Bragg grating rosette is shown in Figure 7.8a. An example of the reflection spectra of three gratings forming a rosette is displayed Figure 7.8b.

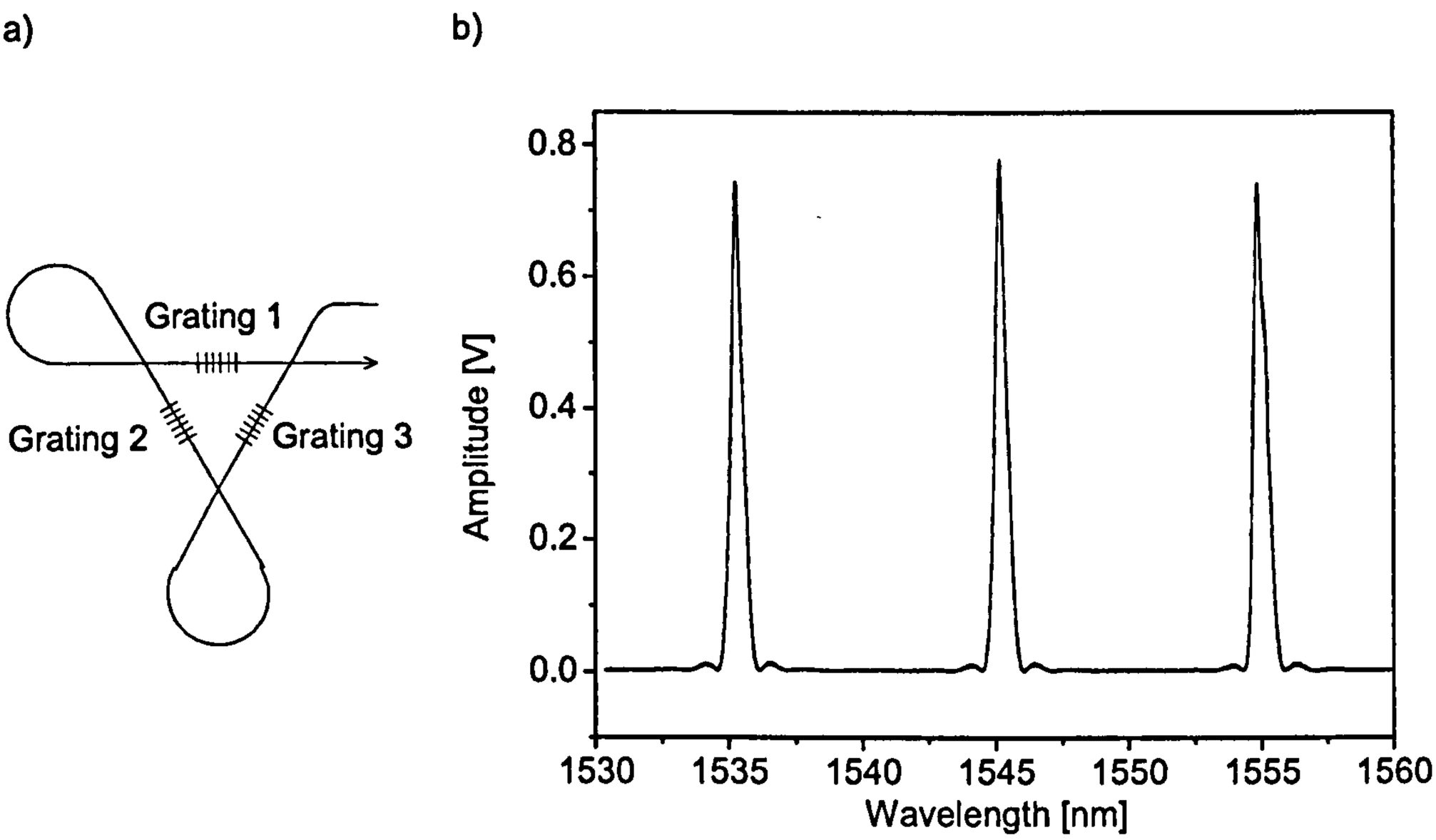

Figure 7.8: a) Layout of the Bragg grating rosette; b) Corresponding reflection spectra.

The Bragg grating can detect damage in the differential Lamb wave signal, as demonstrated in Section 7.1. From the differential signal, the amplitude, frequency and the time of arrival of the acoustical wave at the sensor location can be obtained. The proposed rosette interrogation technique only requires the amplitude analysis. It is sufficient to record the peak-to-peak amplitude of the signal for each individual grating within the rosette. The 120° set-up has the advantage that it enables a normalised measurement, i.e. one that is independent of the magnitude of the transmitted acoustical strain field. It is clear from trigonometric relations that for a 120° set-up the sum of the amplitudes A_i is constant. Therefore it is practical to use normalised amplitudes, as defined by

$$\hat{A}_i = \frac{3}{2}\frac{A_i}{\sum_k^3 A_k} \qquad i = 1,2,3 \tag{7.36}$$

Here *I* is the grating number and the factor 3/2 is obtained from the trigonometric relations.

From the normalised amplitudes one is able to calculate the direction of the incoming acoustical strain field, by using the inverse of Equation (7.35) when the strain is replaced by the normalised amplitudes. One direction, however, is not sufficient to locate the source. A second rosette placed at a suitable distance from the first one is therefore required to give another direction to the source. Combining this information by calculating the intersection of the two directions will finally point out the location of the ultrasonic source.

The advantage of the proposed source location scheme is that there are no absolute signal values needed. As stated above, by using normalised amplitudes the technique accounts for varying amplitudes of the transmitted signal. Possible reasons for alteration in the signal amplitude are changes in the bonding between PZT transducer and the structure. Ageing effects and thermal or mechanical stresses may weaken that interface, so time-varying signal amplitudes would be the consequence. In addition, the rosette technique does not require any measurement in the time domain. As explained in [247] the exact determination of arrival time of a Lamb wave signal is rather difficult because of Lamb waves dispersion. This drawback is overcome with the amplitude related interrogation technique presented in the next section.

7.2.2 Genetic Algorithm

A Genetic Algorithm (GA) was chosen for analysing the location tests. The problem when analysing the measured data for one rosette is the periodicity of the sinusoidal amplitude function. For each amplitude there are four corresponding angles giving a total of twelve angles for a rosette consisting of three gratings. Yet, only one angle α_{R1} will coincide for each of the gratings. The task is to find this angle as this will give the direction to the acoustic source for the first rosette as shown in Figure 7.9. After analysing data from two rosettes one ends up with two directions but four angles, as $\alpha_{R1,2} + 180°$ would also represent the desired direction (see Figure 7.9). The final task is then to find two angles for which the corresponding straight lines intersect, as shown in Figure 7.9. Calculating the x, y coordinates of the intersection *I* will give the location of the acoustic source. The idea is to optimise all these parameters. A GA procedure is used, as described below

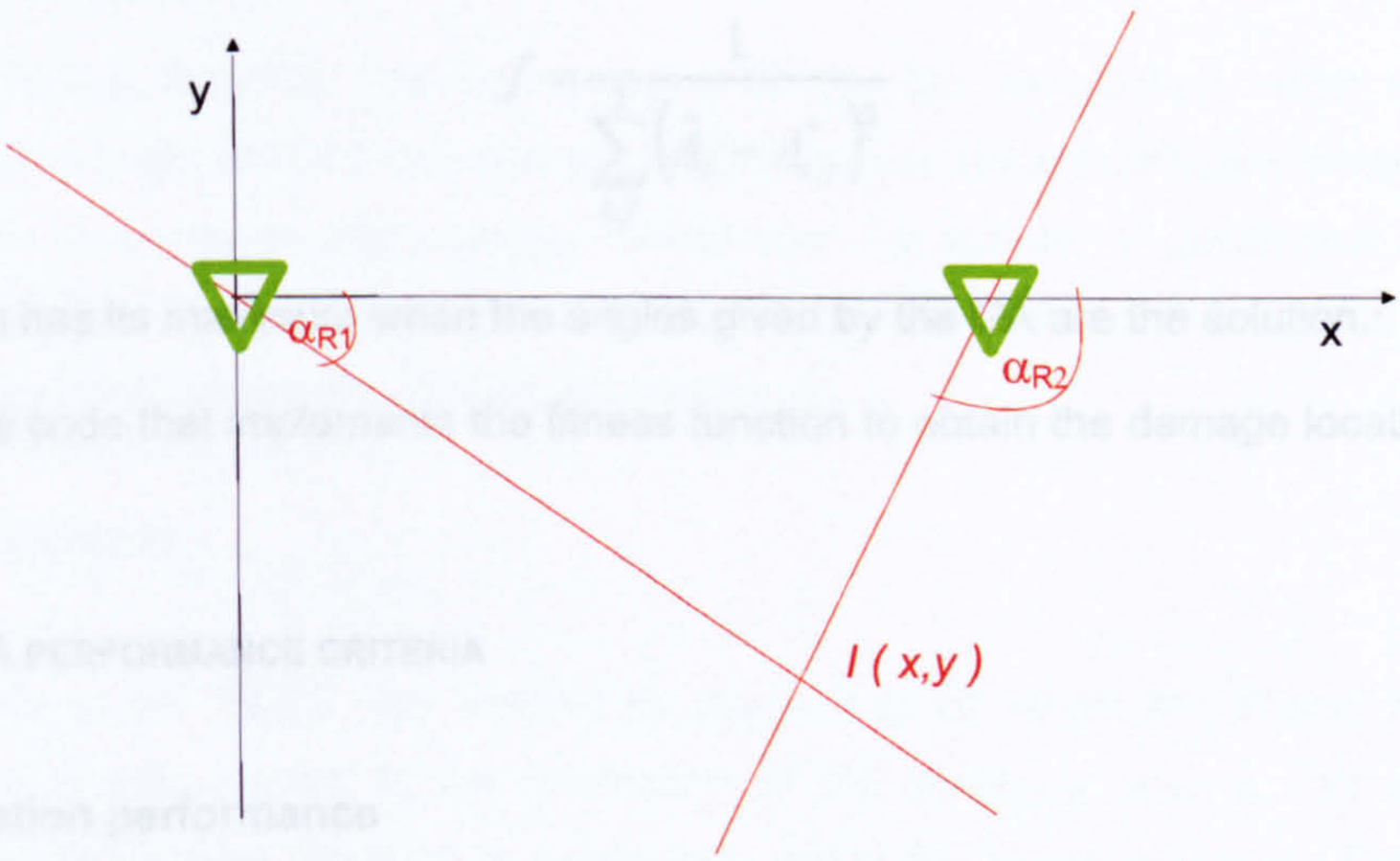

Figure 7.9: Possible solutions to the location problem.

Possible solutions are represented by two angles, each for one of the fibre rosettes. Therefore, a chromosome for the algorithm could be represented as (α_{R1}, α_{R2}). In integer coding each of the angle is an individual and is represented by one gene, which is an integer number. Maximum integer number then is 360. For binary coding each angle or individual should be represented by 9 genes. Nine genes (1,0) can give a maximum integer number equal to 511. As in this case an integer between 0 and 360 is needed, the software will map the numbers between 360 and 511 into the set 0-360.

The idea is to put all these conditions on the possible solutions into the fitness function of the GA. The role of the GA is to create sets of angles, which could be a solution to the localisation problem. For any pair of angles depicted by the GA the corresponding amplitude for each of the three gratings per rosette has to be found. These amplitudes A^{*}_{ij} (i = 1, 2, 3 j = 1,2) can be calculated as

$$A_{ij}^{*} = a_2 \sin^2\left(\pi\frac{\alpha_{Rj} - a_1}{180} - \pi\frac{\beta_i}{180}\right) \tag{7.37}$$

where the indices i, j denote sensor and rosette respectively. For the 120° rosette $\beta_1 = 0°$, $\beta_2=60°$, and $\beta_3=120°$, $a_{1,2}$ are the fit parameters from the sinusoidal fit (Equation (7.42)) and α_{Rj} are the angles depicted by the GA..

The fitness function *f* depends on the difference between the calculated amplitudes A^{*}_{ij} and the measured amplitudes $\hat{A}_i$. It can be represented as:

$$f = \frac{1}{\sum_{i,j}^{2}\left(\hat{A}_i - A_{i,j}^{*}\right)^2} \tag{7.38}$$

This function has its maximum when the angles given by the GA are the solution.

The software code that implements the fitness function to obtain the damage location is given in Appendix H.

7.2.3 GA PERFORMANCE CRITERIA

Source location performance

A measure of performance is required, to indicate the location accuracy, offered by the GA. This can be estimated using the root mean square error (RMSE) defined as

$$RMSE(x) = \sqrt{\frac{\sum_{n=1}^{N}(\hat{x}_n - x_n)^2}{N}} \tag{7.39}$$

where for a given total of N samples, x_n is the actual coordinate and $\hat{x}_n$ is the predicted coordinate. Alternatively, the relative percentage error RMS_{rel} can be found as

$$RMSE_{rel}(x) = \sqrt{\frac{\sum_{n=1}^{N}\left(\frac{\hat{x}_n - x_n}{x_n}\right)^2}{N}} \times 100\% \tag{7.40}$$

The error as a proportion of the analysed plate area is given as

$$E_{PA} = \frac{RMSE(x) \times RMSE(y)}{(x_p \times y_p)} \times 100\ \% \tag{7.41}$$

where x_P and y_P are the dimensions of the area covered by the sensors.

Fitness performance

The performance of the genetic algorithm can be assessed by the quality of the fitness function. A good fitness function assures a quick convergence to the solution. The mean and average fitness of the GA are observed as a function of the number of generations completed.

Parameter performance

As for the fitness function, the performance of the GA parameters, such as number of chromosomes per generation, mutation probability, needs some qualitative assessment. Again the behaviour of the mean and average fitness over the number of generation is considered. Good choice of parameters would give the fittest chromosomes earlier, i.e. for a lower number of generations, than comparatively worse parameters.

7.2.4 DIRECTIVITY

The directivity of the FBGS was studied by measuring the strain amplitudes of each of the rosette gratings with respect to the orientation of the ultrasonic source. The amplitude was determined by measuring the peak-to-peak value of the Bragg grating signal. The experimental data were then fitted to the expected cosine-squared function, defined as

$$\hat{A}(\alpha) = a_2 \sin^2\left(\pi \frac{\alpha - a_1}{180}\right) \tag{7.42}$$

where $a_{1,2}$ are the fit parameters.

The first test studied the response of the grating on an aluminium plate when different Lamb wave modes were used. Although for reasons explained before, the S_0 mode is preferred throughout this thesis, the directivity of the grating was studied for both A_0 and S_0 modes, in case there is any difference in how the grating behaves for different modes. A second experiment was performed for a Perspex plate.

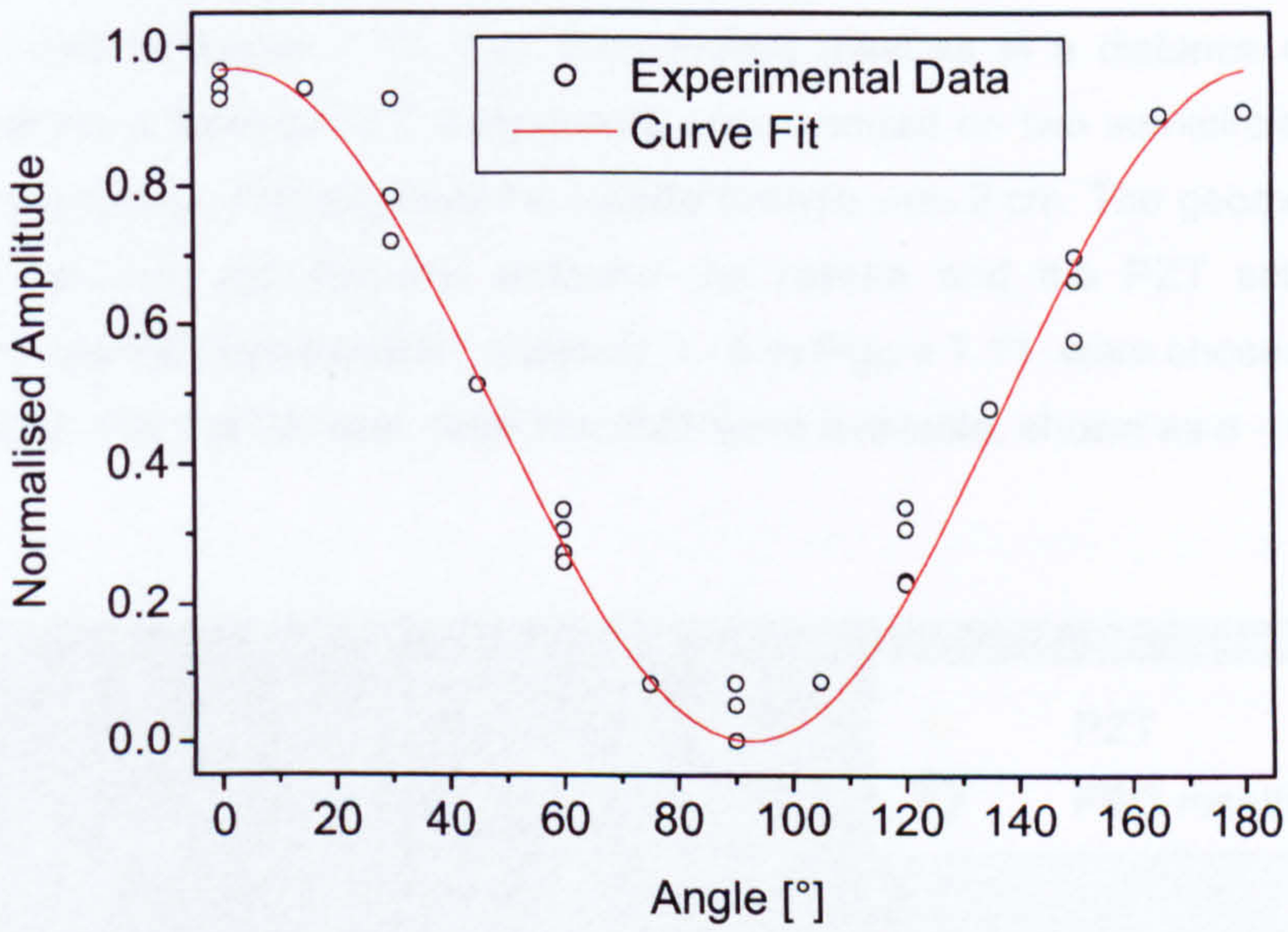

Figure 7.10: Grating directional characteristics on an aluminium plate.

The result of the A_0 mode (at 70 kHz) for an aluminium plate is shown in Figure 7.10. Clearly the experimental results confirm the predicted directivity function. The results of the various experiments have been gathered in Table 7.2.

Table 7.2: Directivity curves for FBGS rosettes.

	a_1	a_2
Theory	90	1
S_0 for an aluminium plate	90.2	0.92
A_0 for an aluminium plate	92.5	0.96
S_0 for a Perspex plate	87.7	0.93

The fit parameters for all gratings are in good agreement; 5% differences have been observed. Within the experimental uncertainty, this is the predicted function, see equation (7.35). Experimental errors are mainly due to low signal to noise ratio (< 0 dB) for the peak-to-peak amplitude around 90°.

7.2.5 Location of Ultrasonic Sources

The next step towards a damage location test is the localisation of ultrasonic sources. Locating an ultrasonic source means the acoustical signal sent by a transducer is received and identified. The experiment was performed on aluminium and Perspex plates. The layout of the test structures is shown in Figure 7.11. Two fibre grating rosettes at a distance of 50 cm were mounted on the plate. Several PZT transducers were bonded on two semicircles, to study the directivity of the gratings. The length of the rosette triangle was 2 cm. The geometrical off-set is negligible compared to the distance between the rosette and the PZT actuator. For the aluminium plate five PZT transducers , numbers 1 - 5 in Figure 7.11, were chosen for testing the location technique. For the Perspex plate four PZT were available, shown as a – d.

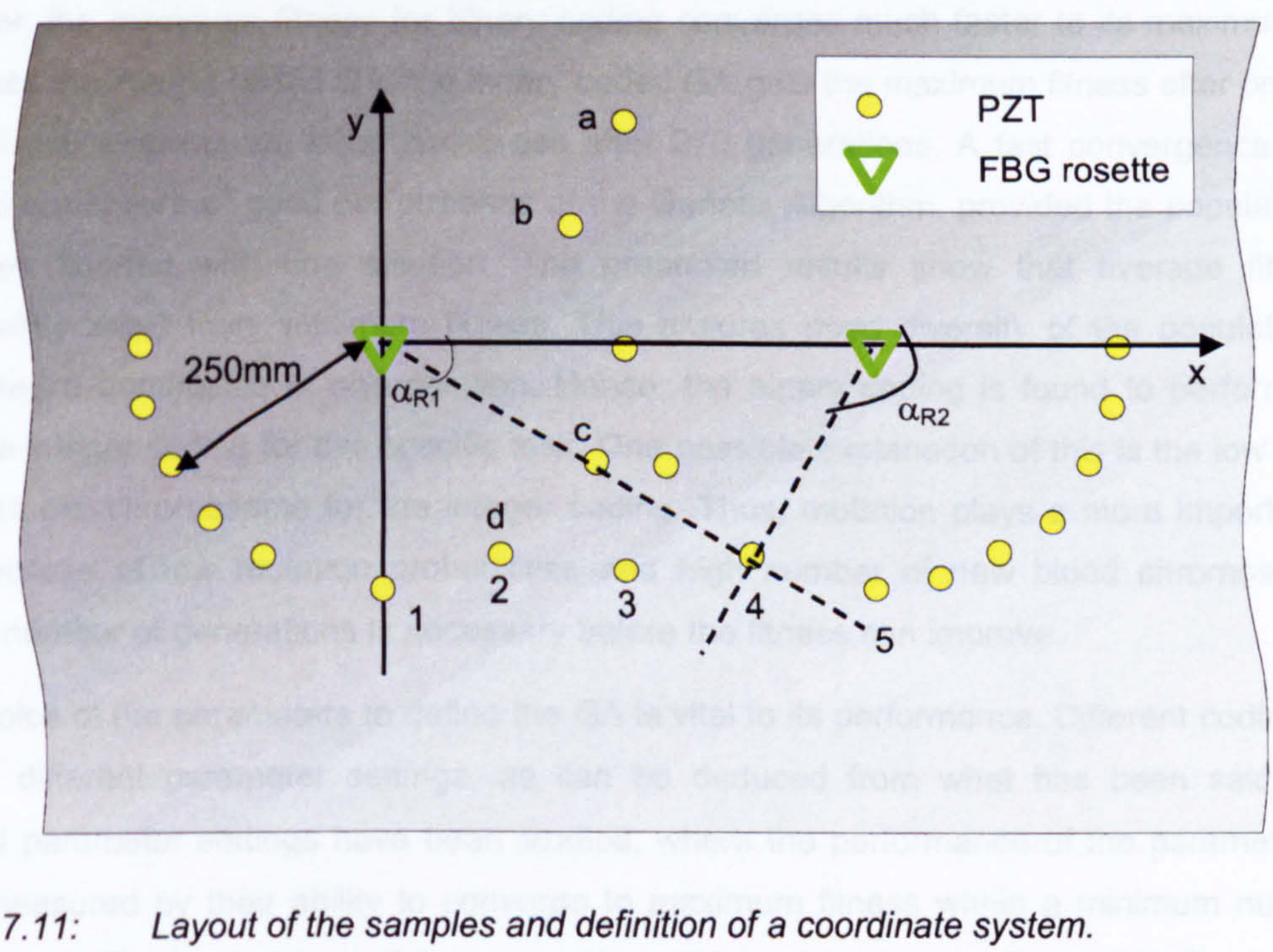

Figure 7.11: Layout of the samples and definition of a coordinate system.

GA performance using integer and binary coding

Two options for the GA coding were studied to investigate the location performance. The mean and maximum fitness of the GA operation for both integer and binary coding are displayed as functions of generations in Figure 7.12. Here, good convergence to the optimal solutions can be observed.

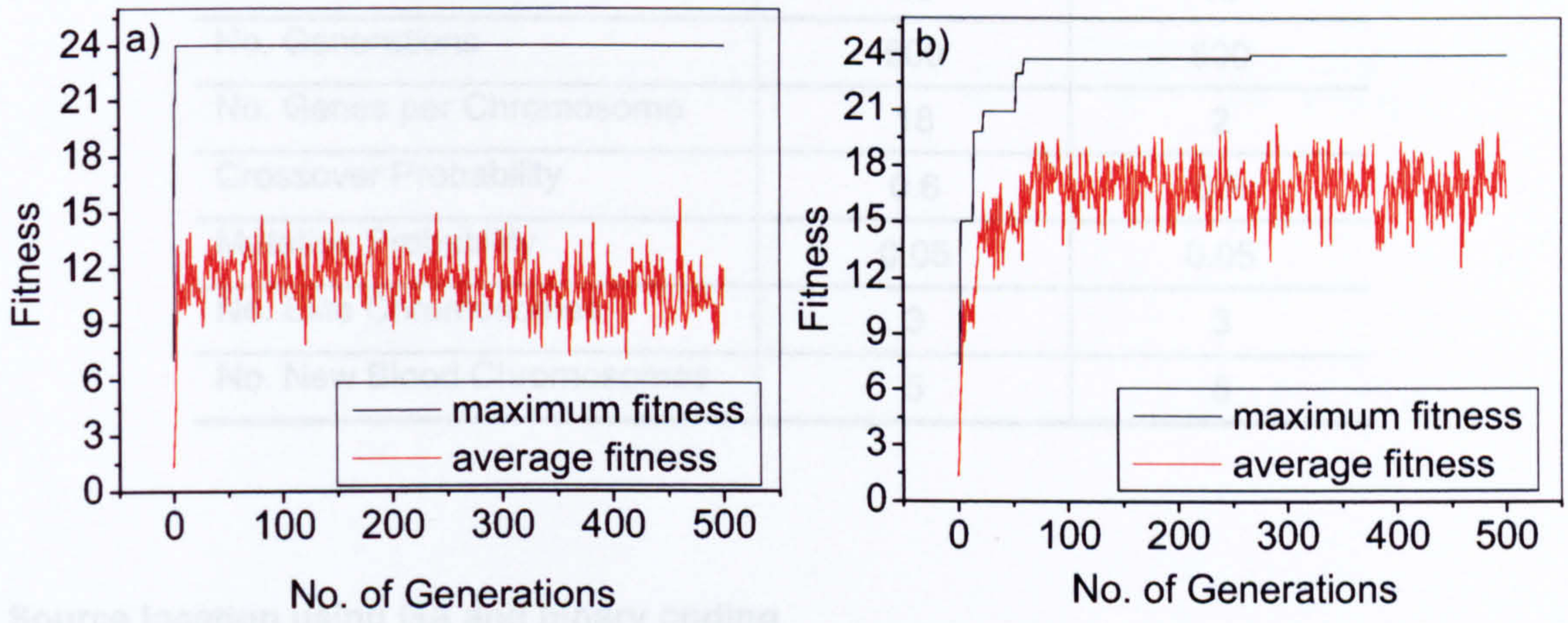

Figure 7.12: Mean and maximum fitness of the GA operation: a) binary; b) integer coding.

Both codings result in the same maximum fitness values corresponding to the same solution. However, the maximum fitness for binary coding converges much faster to its maximum value than does the integer coded GA; the binary coded GA gets the maximum fitness after only three generations, whereas the latter converges after 270 generations. A fast convergence can be seen as a measure of good performance of the Genetic Algorithm, provided the population has not been flooded with one solution. The presented results show that average fitness is siginifcantly lower than maximum fitness. This ensures good diversity of the population and therefore no dominance of one solution. Hence, the binary coding is found to perform better than the integer coding for this specific task. One possible explanation of this is the low number of genes per chromosome for the integer coding. Thus, mutation plays a more important role and because of low mutation probabilities and high number of new blood chromosomes a certain number of generations is necessary before the fitness can improve.

The choice of the parameters to define the GA is vital to its performance. Different coding types require different parameter settings, as can be deduced from what has been said above. Several parameter settings have been studied, where the performance of the parameters has been measured by their ability to converge to maximum fitness within a minimum number of generations. The best choice of the parameters obtained is given in Table 7.3. The results of the performance tests for the two types of coding clearly shows that binary coding should be

preferred. Binary coding has therefore been applied to get the results presented in the next sections.

Table 7.3: Best choice of GA parameters used for location studies.

Parameter	Binary Coding	Integer Coding
No. Chromosomes per Pop.	40	16
No. Generations	500	500
No. Genes per Chromosome	18	2
Crossover Probability	0.6	0.8
Mutation Probability	0.05	0.05
No. Elite Chromosomes	3	3
No. New Blood Chromosomes	5	8

Source location using GA and binary coding

Despite the small number of experiments the results shown in Figure 7.13 and Figure 7.14 clearly show the capability of the proposed interrogation scheme of detecting the position of the source of an ultrasonic wave. An overview of the achieved performance and the errors is given in Table 7.4. It is not understood why the error in the y-coordinate is significantly higher than for the x-coordinate on the aluminium and why it is the other way round for the Perspex plate. In general, the signal to noise ratio in the calibration experiment could be improved, which would also decrease the errors in the location algorithm. However, that would affect x- and y-coordinates for both experiments to the same degree.

Table 7.4: Performance of the source location algorithm.

Parameter	Aluminium	Perspex
RMS error for x-coordinate	2.5 cm	4.0 cm
RMS error for y-coordinate	6.5 cm	1.9 cm
rel. RMS error for x-coordinate	9.2 %	20.2 %
rel. RMS error for y-coordinate	27.8 %	7.6 %
rel. error for plate area	0.7 %	0.3 %

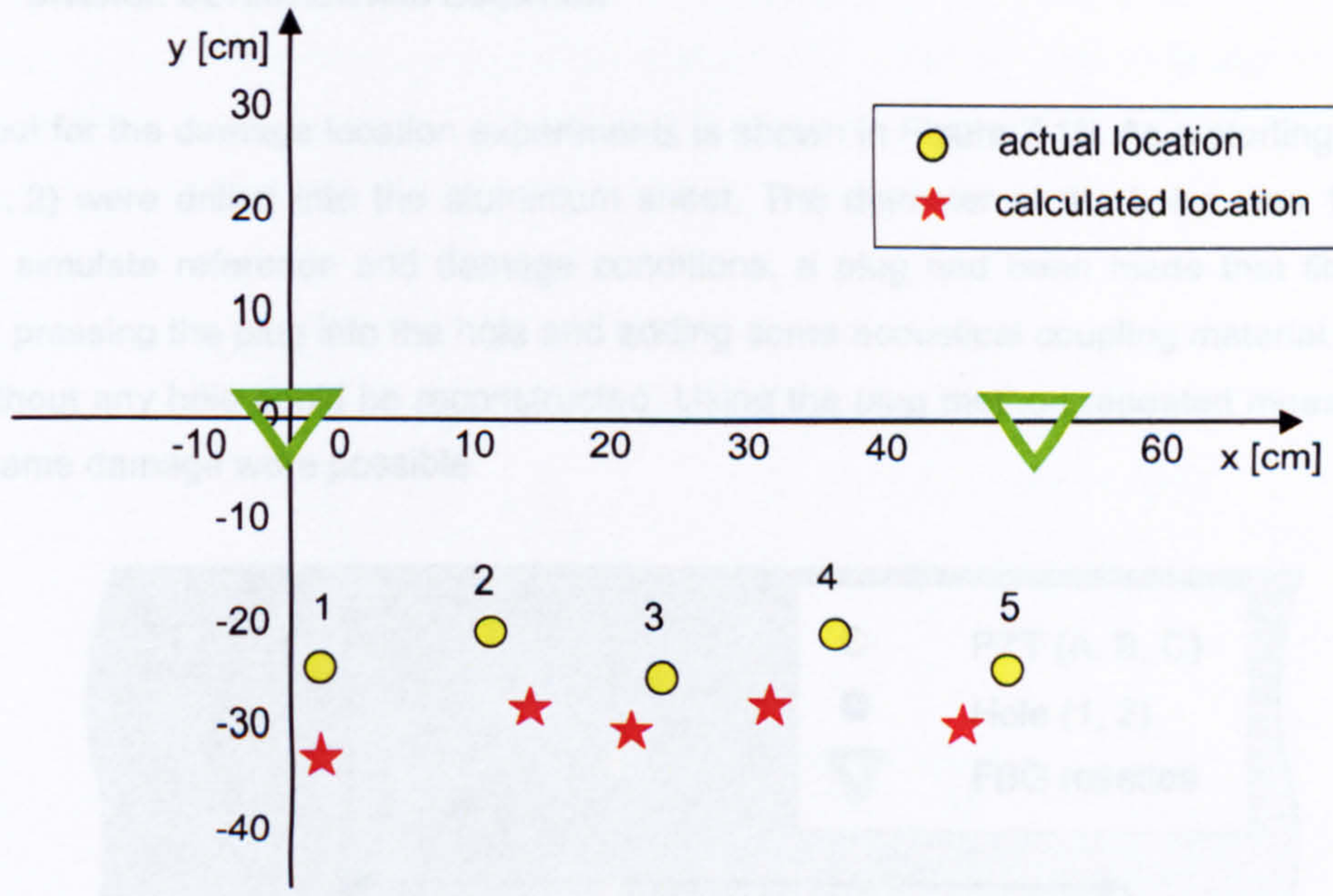

Figure 7.13: *Actual and calculated acoustic source location on aluminium plate.*

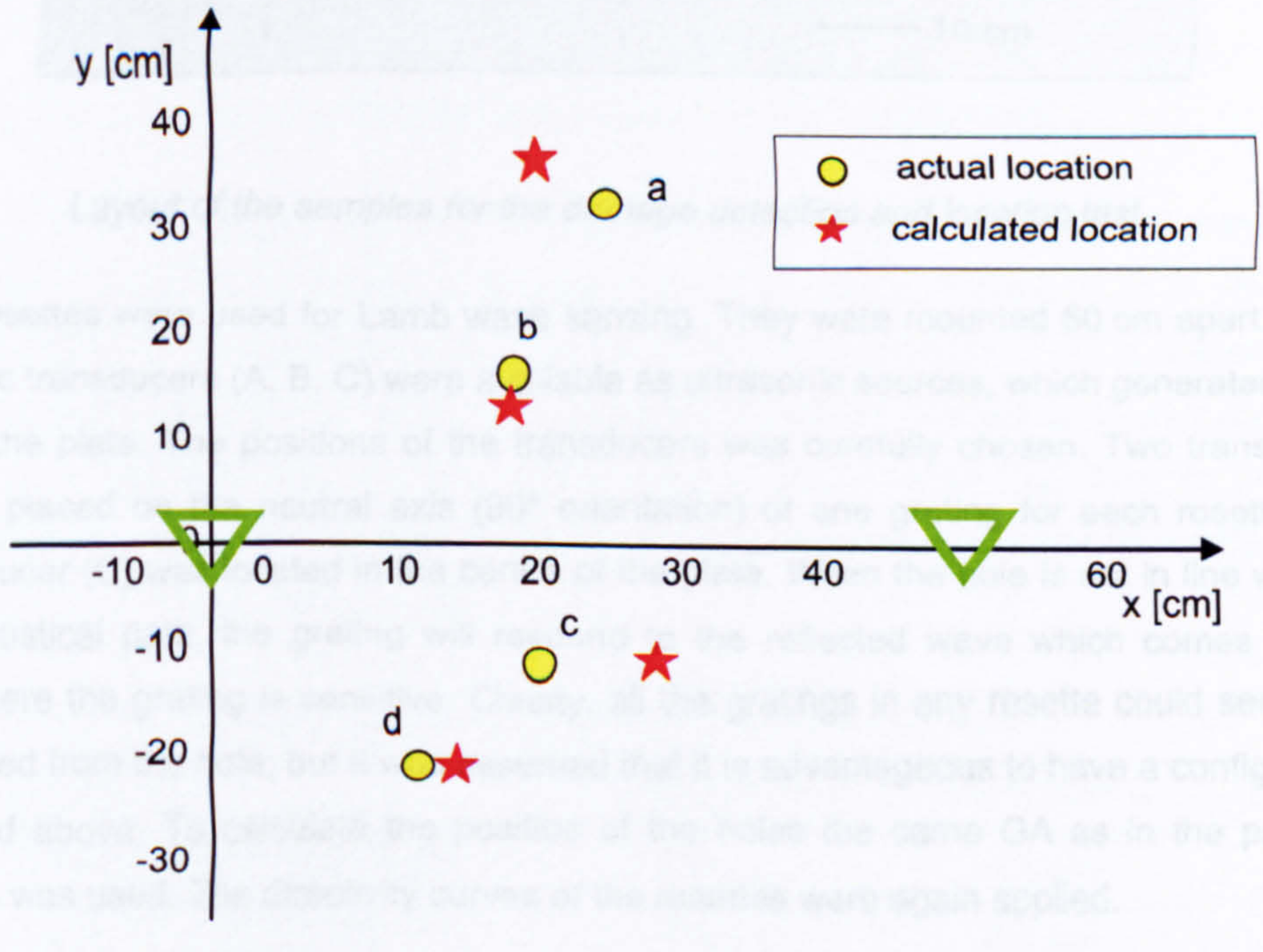

Figure 7.14: *Actual and calculated acoustic source location on Perspex plate.*

7.2.6 Damage Detection and Location

The layout for the damage location experiments is shown in Figure 7.15. As a starting point two holes (1, 2) were drilled into the aluminium sheet. The diameter of the holes was 12 mm. In order to simulate reference and damage conditions, a plug had been made that fits into the hole. By pressing the plug into the hole and adding some acoustical coupling material, the initial state without any hole could be reconstructed. Using the plug method repeated measurements for the same damage were possible.

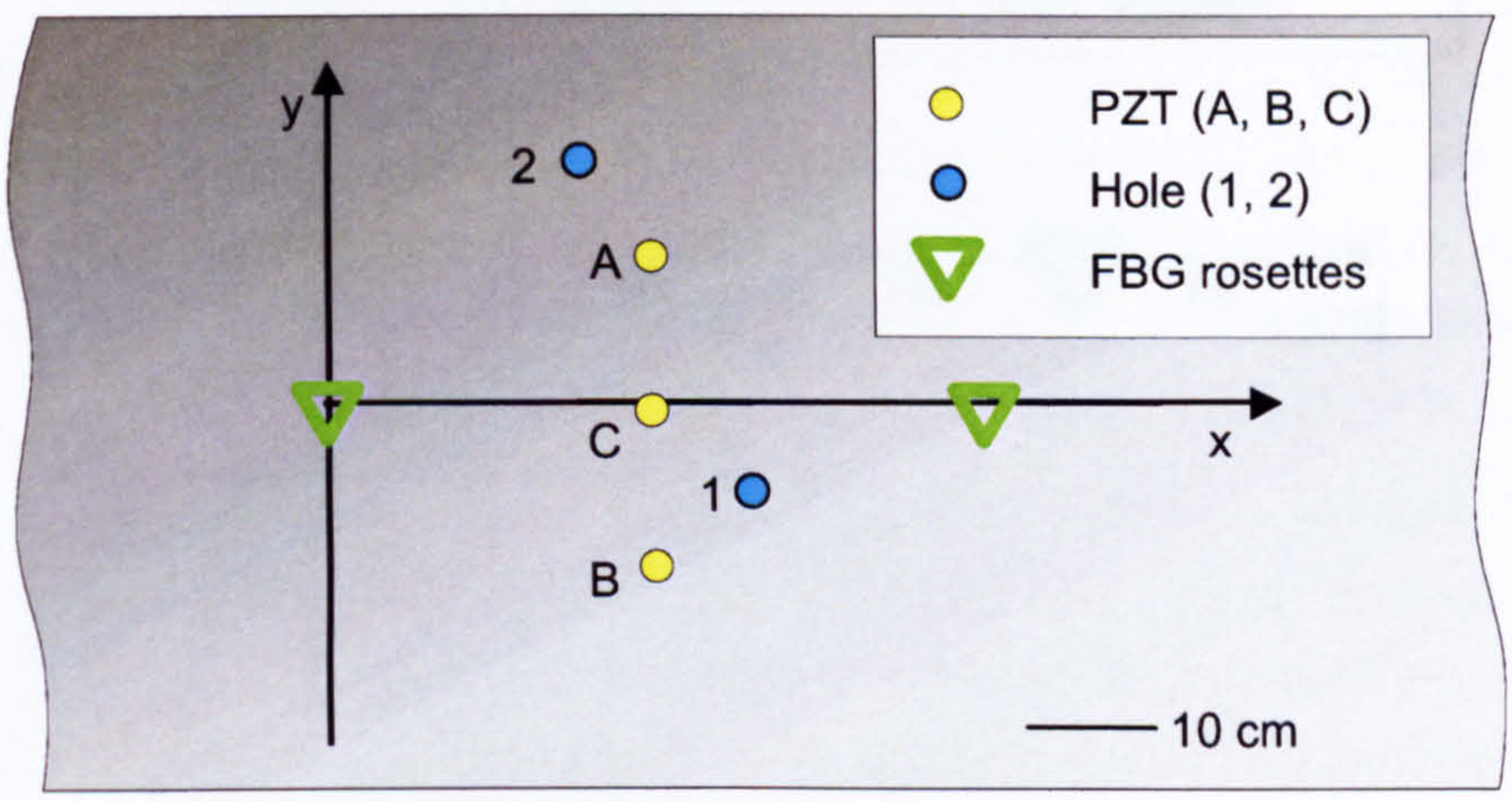

Figure 7.15: Layout of the samples for the damage detection and location test.

Two FBG rosettes were used for Lamb wave sensing. They were mounted 50 cm apart. Three piezoceramic transducers (A, B, C) were available as ultrasonic sources, which generated Lamb waves into the plate. The positions of the transducers was carefully chosen. Two transducers (A, B) were placed on the neutral axis (90° orientation) of one grating for each rosette. The other transducer (C) was located in the centre of the plate. When the hole is not in line with the primary acoustical path, the grating will respond to the reflected wave which comes from a direction where the grating is sensitive. Clearly, all the gratings in any rosette could sense the wave reflected from the hole, but it was assumed that it is advantageous to have a configuration as described above. To calculate the position of the holes the same GA as in the previous experiments was used. The directivity curves of the rosettes were again applied.

The experimental results shown in Figure 7.16 demonstrate how damage detection and location using FBGS work. The graph gives the actual and calculated locations when different transducers have been chosen as ultrasonic sources. The locations obtained by the proposed method are shown and prove to be remarkably accurate provided that the optimum position of the PZTs relative to the Bragg grating rosettes is used. The letters next to the stars indicate

which PZT source was used to obtain that particular location. It is clear that, in order to obtain the most accurate results, the case to be avoided is that in which the source is aligned along the axis of one of the Bragg gratings. In this case the signal obtained directly from the PZT is so large that it becomes difficult to recover the signal from the hole accurately.

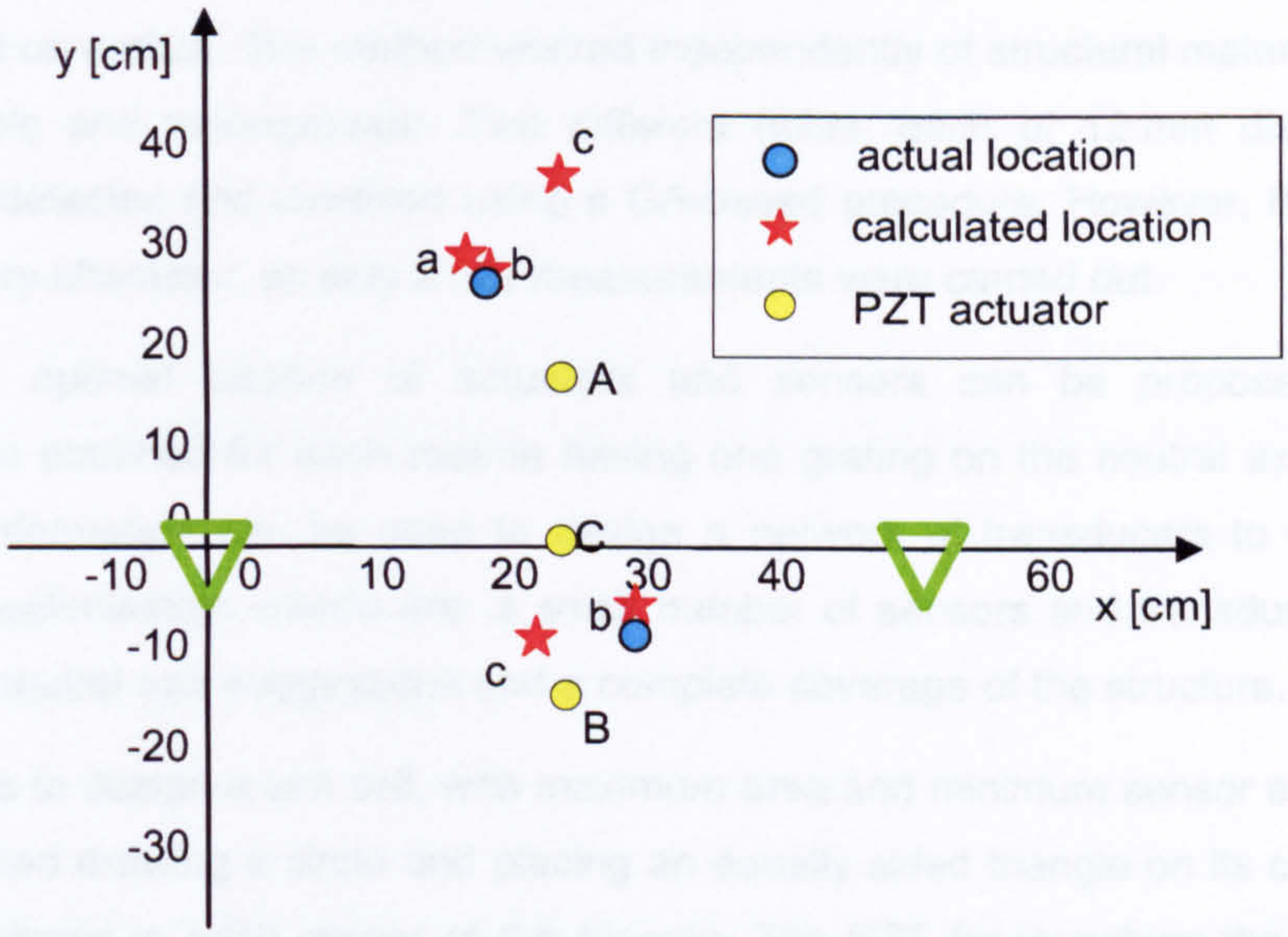

Figure 7.16: Actual and calculated damage location on an aluminium plate.

Table 7.5 gives the performance parameters of the location algorithm. Here, all transducers produce good results. The qualitative conclusions of interpretation of Figure 7.16 is verified by the smaller errors for transducers A and B compared to transducer C. It is interesting to compare the relative RMS errors for the hole location experiments with the source location tests (Table 7.4). The rel. RMS error for the x- and y-coordinates is even less than for the initial source location experiments on aluminium. However, more experiments would be needed to get better statistics for the damage detection results.

Table 7.5: Performance of the damage detection and location algorithm.

Parameter	Transducer A, B	Transducer C
RMS error for x-coordinate	1.0 cm	6.5 cm
RMS error for y-coordinate	2.9 cm	5.5 cm
rel. RMS error for x-coordinate	4.3 %	26.9 %
rel. RMS error for y-coordinate	19.9 %	22.9 %
rel. error on plate	0.1 %	1.4 %

7.2.7 Discussion

The proposed method for damage detection and localisation using the directivity of the FBGS was proven to work correctly. Various experiments on different materials and at different laboratories indicate that the changes due to a simulated damage can not only be detected but also be localised on a plate. The method worked independently of structural materials, provided they are isotropic and homogenous. Two different holes, each of 12 mm diameter, could successfully be detected and localised using a GA-based procedure. However, the results still have a preliminary character, as only a few measurements were carried out.

It appears that optimal location of actuators and sensors can be proposed. The best performance was obtained for each rosette having one grating on the neutral axis of the PZT actuator. This information can be used to design a network of transducers to monitor large structures. The optimisation criteria are: a small number of sensors and transducers, a layout that follows the neutral axis suggestions and a complete coverage of the structure.

The basic idea is to design a unit cell, with maximum area and minimum sensor effort. This cell can be constructed drawing a circle and placing an equally sided triangle on its circumference. One rosette is placed in each corner of the triangle. The PZT for launching the ultrasound is placed in the centre of the circle. This ensures for each rosette the PZT is neutral to one grating. The concept is depicted in Figure 7.17, where the solid lines give the unit cell.

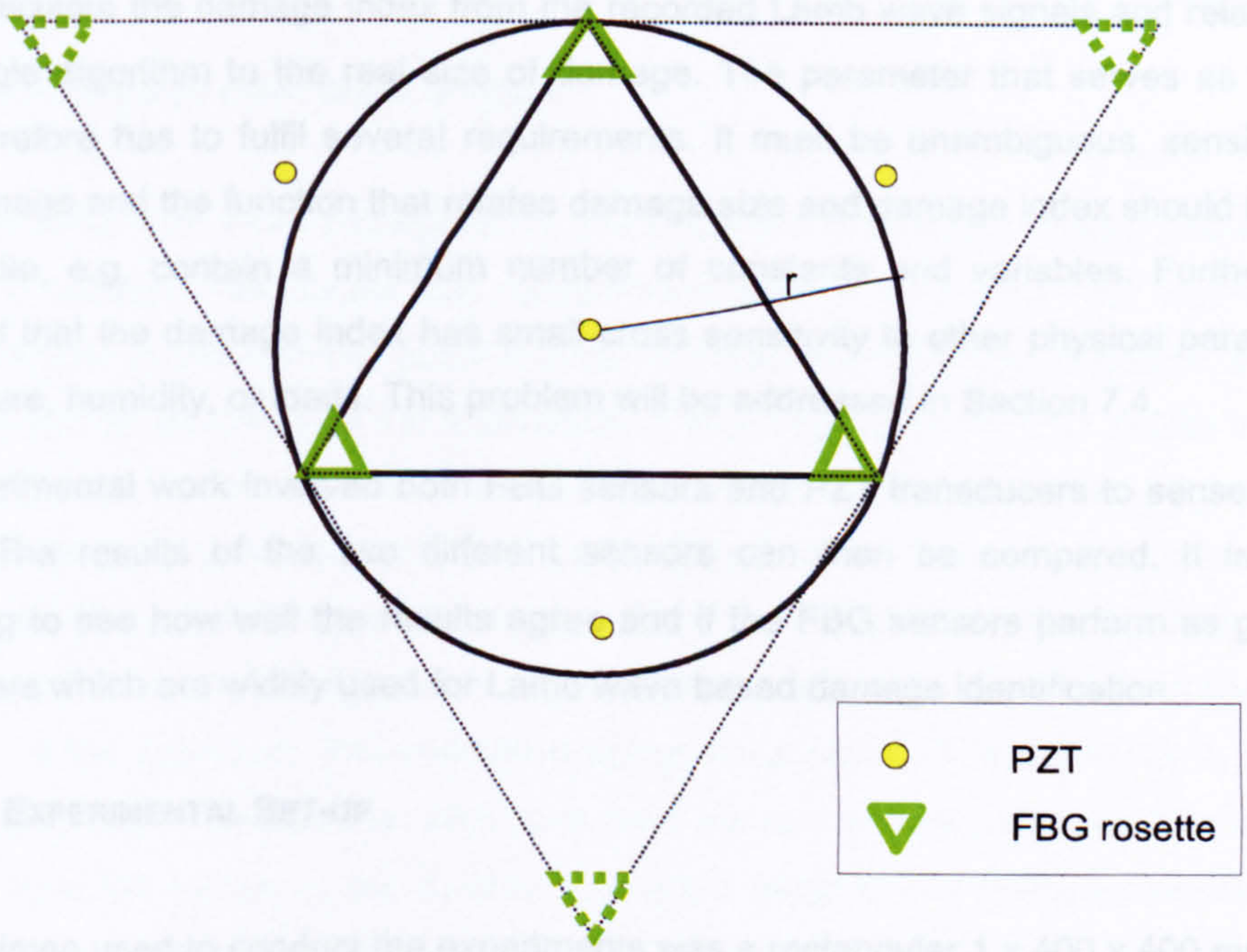

Figure 7.17: Proposed layout for the monitoring of large structures.

The maximum area which can be covered by the unit cell depends on the structural material, acoustical power launched by the PZT and performance of the optical measurement system. From the optical system the minimum signal-to-noise-ratio (SNR) is given. The attenuation of the structure determines the maximum length that a signal is allowed to travel before the launched acoustical power becomes too weak to produce a sufficient SNR at the optical system. This maximum length will give the radius of the initial circle, on which the basic equilateral triangle is placed. If the area to be monitored is larger than the unit cell, the unit cell can be extended in all directions. An example for a an extension is shown in Figure 7.17. The dotted lines represent the extended monitoring system. For the current system the maximum radius of the unit cell that has been tested is about 50 cm. However, further knowledge of the materials attenuation is needed to estimate the overall maximum area that could be monitored.

7.3 Severity of Damage

This section gives the results of the experiments carried out to study the severity of damage. Several signal processing tools were applied to the Lamb wave signals in order to find a parameter that corresponds to the severity of damage. This parameter can be referred to as the damage index. The basic idea is that for future applications the damage identification system is able to calculate the damage index from the recorded Lamb wave signals and relate this index by a simple algorithm to the real size of damage. The parameter that serves as the damage index therefore has to fulfil several requirements. It must be unambiguous, sensitive to even small damage and the function that relates damage size and damage index should be as simple as possible, e.g. contain a minimum number of constants and variables. Furthermore, it is requested that the damage index has small cross sensitivity to other physical parameters, e.g. temperature, humidity, or loads. This problem will be addressed in Section 7.4.

The experimental work involved both FBG sensors and PZT transducers to sense Lamb wave signals. The results of the two different sensors can then be compared. It is particularly interesting to see how well the results agree and if the FBG sensors perform as good as PZT transducers which are widely used for Lamb wave based damage identification.

7.3.1 Experimental Set-up

The specimen used to conduct the experiments was a rectangular 1 x 400 x 400 mm aluminium plate. The plate and the positions of the sensors are shown in Figure 7.18. The material properties can be found in Table 7.1.

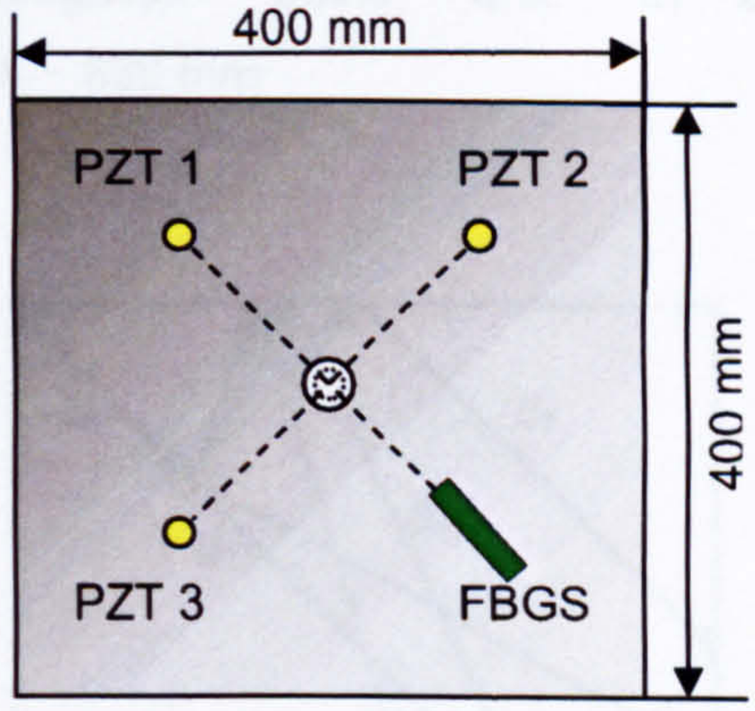

Figure 7.18: Layout of the experiment to determine the severity of damage.

The experimental procedure involved the same excitation signal as presented in Chapter 6. Two different driving frequencies were used to investigate whether the frequency affects damage identification. The frequencies were adapted to the propagation characteristics of the S_0 mode at 260 kHz and 460 kHz. The smaller frequency is less dispersive whereas the higher one gives smaller acoustical wavelengths. Smaller wavelengths are advantageous because there is less interference of the waves on the plate due to shorter wave packages and the ratio of damage size and wavelength is bigger for constant damage size, thus giving higher sensitivity to damage.

7.3.2 Analysis of Lamb Wave Signals

The understanding of wave propagation in the specimen is important before any experimental tests are performed. The signals may contain reflections of the waves from boundaries of the plate and mode conversions can occur in order to satisfy the boundary conditions; even multiple reflections can be observed as the attenuation in aluminium is small. This makes interpretation of the Lamb wave signals difficult for complex specimens. The test specimen (Figure 7.18) used in the current study produced variety of Lamb wave reflections resulting in a complex Lamb wave signal. The possible wave propagation paths for the plate are illustrated in Figure 7.19; the total number of acoustical paths is higher. These additional paths can be found due to the symmetry of the specimen. The shortest distance is named d_1. The distances d_2 and d_3 have equal length, they represent the reflections from the lateral face, whereas d_4 and d_5 are the reflection from the corner, d_4 and d_5 also have same lengths. The multiple reflections given by d_6 and d_7 come again from the lateral faces. Distance d_7 has the same length as d_4 and d_5. Obviously, owing to the symmetry the distances are the same for FBGS and PZT. The

distances of wave propagation paths are: $d_1 \sim 280$ mm; $d_2 = d_3 \sim 450$ mm; $d_4 = d_5 = d_7 \sim 570$ mm and $\sim$ $d_6 \sim 630$ mm

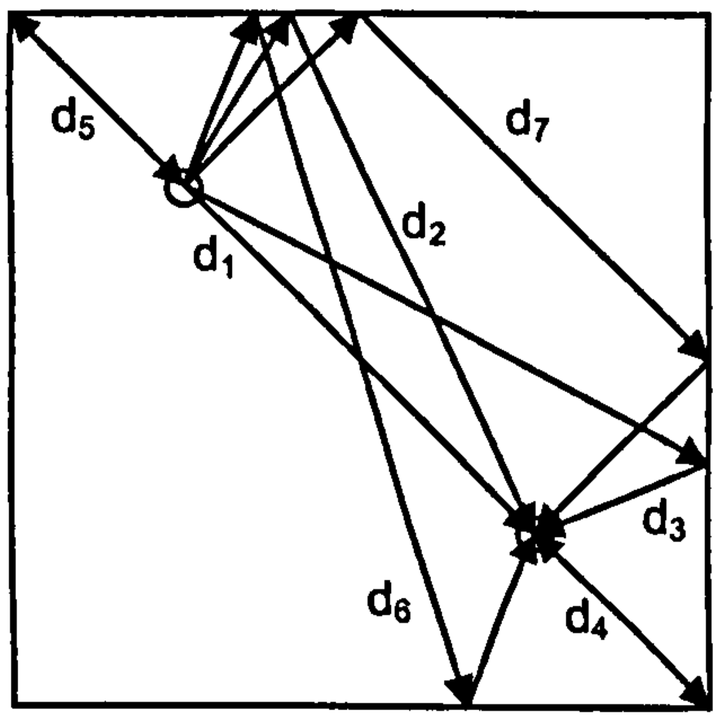

Figure 7.19: Possible paths of propagation on test specimen. Note: Due to symmetry the total number of paths is 12.

Some of the waves interfere at the sensor location due to the existence of propagation paths of equal length. This means if the symmetry is not perfect e.g. due to minor misalignments when bonding the sensors, it can be expected that not all responses look the same. Thus, for different driving frequencies and therefore different acoustical wavelengths the interference patterns will be different.

The reference Lamb wave responses acquired using the FBGS at two different frequencies are shown in Figure 7.20. The first package arrives at the FBGS after a time-of-flight (TOF) of 57 µs, the second one after 90 µs and the third one after 104 µs. There are packages at 120 µs for the 260 kHz signal and at 135 µs for the 460 kHz which do not have a counterpart in the other frequency signal.

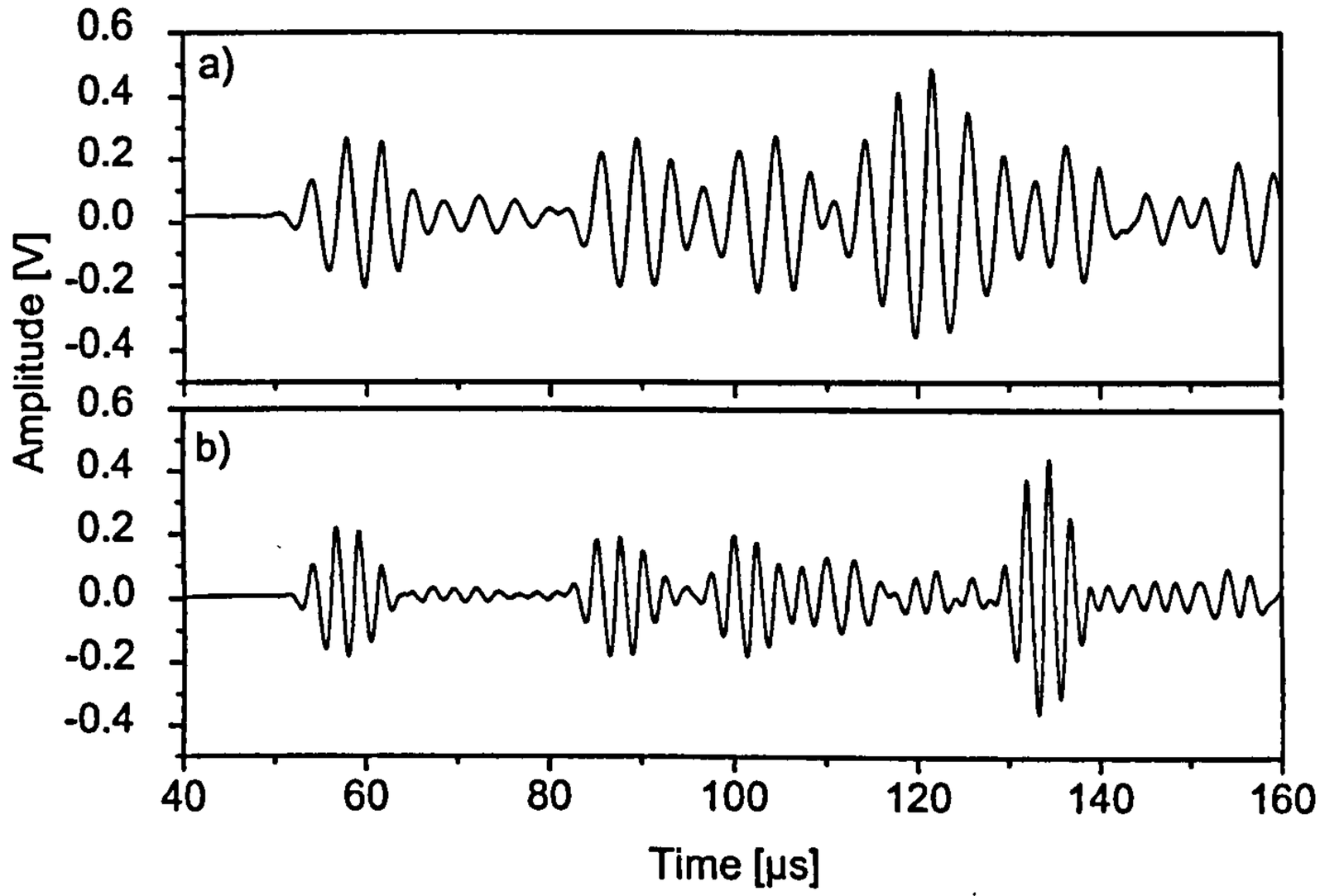

Figure 7.20: Lamb wave response of an undamaged aluminium plate sensed using FBG sensors at two different frequencies: a) 260 kHz; b) 460 kHz.

The time-of-flight and the velocity of the S_0 mode can be used to calculate the distance the corresponding wave package travelled. As there is no mode conversion on symmetric boundaries [281], the corresponding time-of-flight for the distances given in Figure 7.19 can be calculated. This allows one to identify different wave packages and their propagation paths. The results are summarised in Table 7.6. It appears that the first package is clearly identified as the incident S_0 mode travelling along d_1. The second package is identified as the mode reflected on the lateral faces of the plate. The third package is hard to identify. This is likely since six different acoustical paths interfere at the receiver. This pattern will be different for different frequencies as the corresponding acoustical length of the package also changes and also the phase of the wave is changed. The same reasons that explain the difficulties in identifying the third package hold for the fourth package.

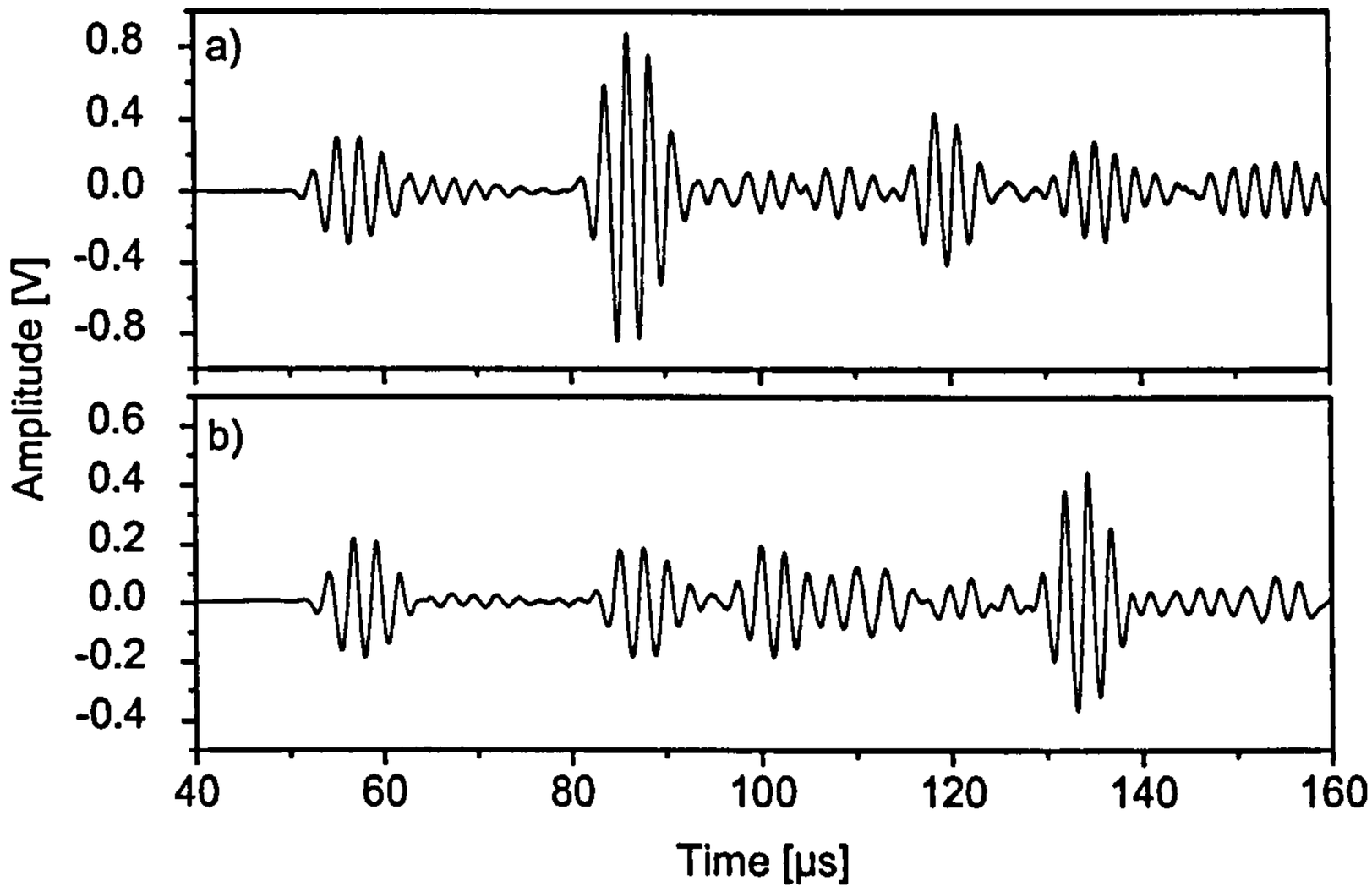

Figure 7.21: Lamb wave response of an undamaged aluminium plate sensed at 460 kHz: a) PZT; b) FBGS.

Figure 7.21 presents Lamb wave signals from the undamaged plate sensed using a PZT and a FBGS receiver. The excitation signal had a frequency of 460 kHz. Again the different wave packages can be identified and their time-of-flight can be calculated. The time-of-flight from the recorded signals can be compared to the time-of-flights that correspond to possible acoustical paths. The result together with the result for a 260 kHz signal recorded using a PZT transducer is given in Table 7.6. It appears that the first two packages are clearly identified as the incident S_0 mode travelling along d_1, and as the mode reflected on the lateral faces of the plate, respectively. However, the amplitude of the second package is different for PZT and FBGS. It is much higher for the PZT. As four acoustical paths arrive at the same time, the second package is an interference signal. The amplitude for the PZT must be higher as the FBGS has a high directivity. This means only the waves along the fibre axis fully contribute to the response signal. In contrast the PZT contains all waves. The third and fourth packages are hard to identify for all analysed signals. This is likely since several acoustical paths interfere at the receiver. If the symmetry of the plate is disturbed and if not all the PZT and FBGS are perfectly symmetrically bonded, each sensor will see an individual interference pattern. Furthermore, this pattern will be different for different frequencies as the corresponding acoustical length of the package also changes and also the phase of the wave is changed. Not only will geometrical disruptions of the symmetry influence the interference pattern. The structure itself might not be perfectly symmetric regarding its physical properties. For example, rolled aluminium sheets tend to lose their isotropy.

Table 7.6: Identification of the Lamb wave modes.

FBG at 260 kHz	FBG at 460 kHz	PZT at 260 kHz	PZT at 460 kHz	Acoustical path
57 µs	57 µs	57 µs	57 µs	d_1 = 56 µs
90 µs	90 µs	86 µs	86 µs	d_2, d_3 = 89 µs
104 µs	104 µs	105 µs	117 µs	d_4, d_5, d_7 = 113µs
120 µs	135 µs	124 µs	134 µs	d_6 = 127 µs

It can be concluded that for analysing the Lamb wave data independently of the receiver or the frequency used, only the first two packages within the signal should be considered.

7.3.3 Damage Index vs. Damage Size

The aluminium plate was used to study the influence of damage severity on Lamb wave responses. Damage was introduced into the plate by drilling a hole into the centre of the plate. In order to obtain different severity of damage, the hole diameter was increased in steps from 0 to 26.8 mm. For each step the Lamb wave signals were recorded for two different frequencies and with two different receivers as explained in the previous section.

Several signal processing tools as presented in Chapter 6 were used. Some of these tools analyse the entire signal whilst others concentrate on the individual wave packages. Lamb wave responses from one experiment are used to study different signal processing tools; the best methods will then be applied to other experiments with other receivers and different frequencies.

Original signal and its envelope

The experiment that employed the FBGS at 460 kHz serves as the reference for the damage index. Figure 7.22 shows the signals and their envelopes for different severities of damage. The wave packages within the signal can be identified using Table 7.6. The first important thing to notice is the decreasing amplitude of the first package with increasing damage severity (hole diameter). The second alteration in the response signals is the change of shape in the third package and between the third and fourth package. This can be easily explained following the discussion given in Section 7.3.2: The first package passes the damage; parts of the signal will be reflected, thus this energy is missing in the transmitted signal. The amplitude of the signal therefore decreases. After the third package arrives there are many waves interfering at the position of the FBGS. Therefore, small changes in the propagation of the waves will alter the interference pattern of Lamb wave responses. The relation of the amplitude of the first package to the damage size will be studied in more detail later in this section.

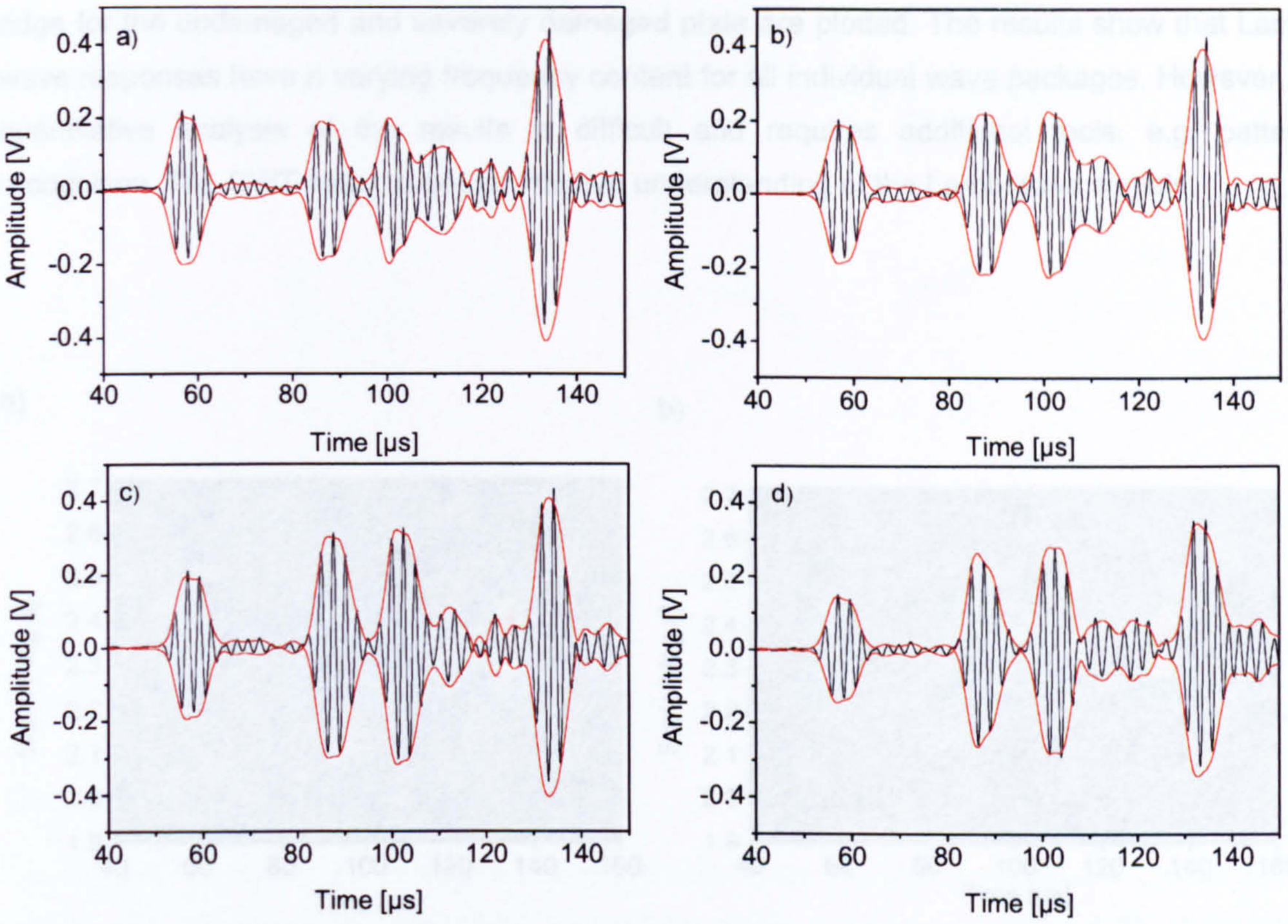

Figure 7.22: Series of Lamb wave signals sensed with FBG sensor at 460 kHz for different hole diameters: a) 0.8 mm; b) 6 mm; c) 14 mm; d) 26.8 mm.

Continuous wavelet transform

The concept of the continuous wavelet transform (CWT) for time frequency analysis has been introduced in Section 6.5. The results of the CWT analysis for the Lamb wave responses presented in Figure 7.22 are shown in Figure 7.23. Here, the contour plots represent the frequency composition of the signal over time. The colour of the plots corresponds to the amplitude of the frequency component. The four packages defining the individual Lamb waves can be easily identified. The parameter that is plotted on the left axis is the scale parameter *a*, that relates to frequency. The main frequency components appear around 460 kHz, which is the carrier frequency of the excitation signal. There is a change in the contour plots with increasing size of the damage. The decreasing amplitude of the first package and the increasing amplitudes of the second and third can be identified. However, other tools such as image processing are required to extract more information in order to obtain a damage index from the contour plots. An alternative approach would be to concentrate on the ridge of the wavelet. The CWT ridge is a smooth curve that approximates the local maxima of the transform. The ridge is indicated as a black solid line in Figure 7.23. A closer view is given in Figure 7.24 where the

ridge for the undamaged and severely damaged plate are plotted. The results show that Lamb wave responses have a varying frequency content for all individual wave packages. However, a quantitative analysis of the results is difficult and requires additional tools, e.g. pattern recognition. The CWT helps to get an intuitive understanding of the Lamb wave signals.

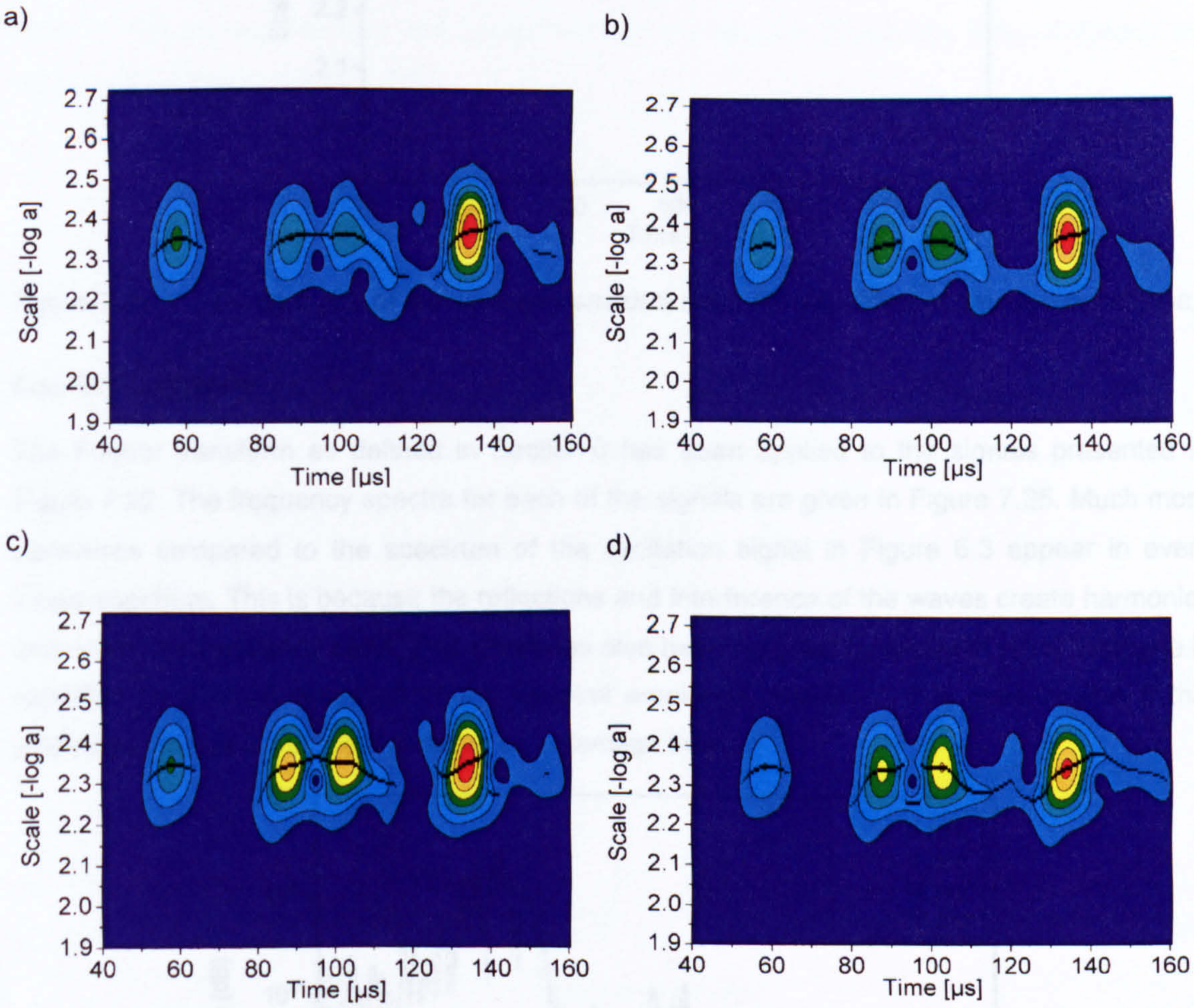

Figure 7.23: Series of CWT of the Lamb wave signals sensed with FBG sensor at 460 kHz for different hole diameters: a) 0.8 mm; b) 6 mm; c) 14 mm; d) 26.8 mm.

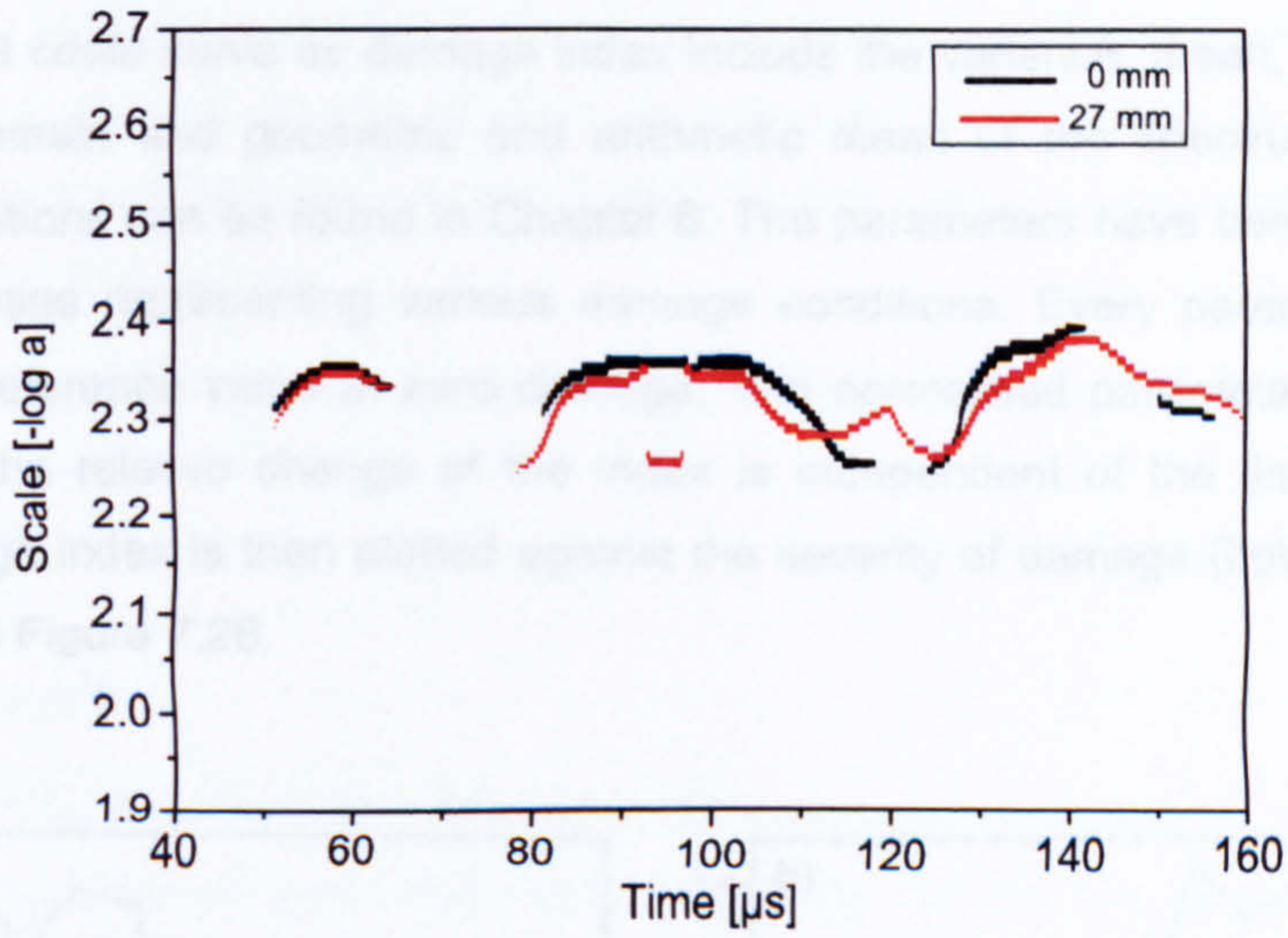

Figure 7.24: Contour plot of the wavelet transform ridge for two different damage conditions.

Fourier Transform

The Fourier transform as defined in Section 0 has been applied to the signals presented in Figure 7.22. The frequency spectra for each of the signals are given in Figure 7.25. Much more harmonics compared to the spectrum of the excitation signal in Figure 6.3 appear in every single spectrum. This is because the reflections and interference of the waves create harmonics and widen the frequency band. This effect has also been reported by Mallet in [194]. Damage is exhibited by a small reduction of the spectral amplitude. However, it is questionable if this amplitude change is sufficient to serve as a damage index.

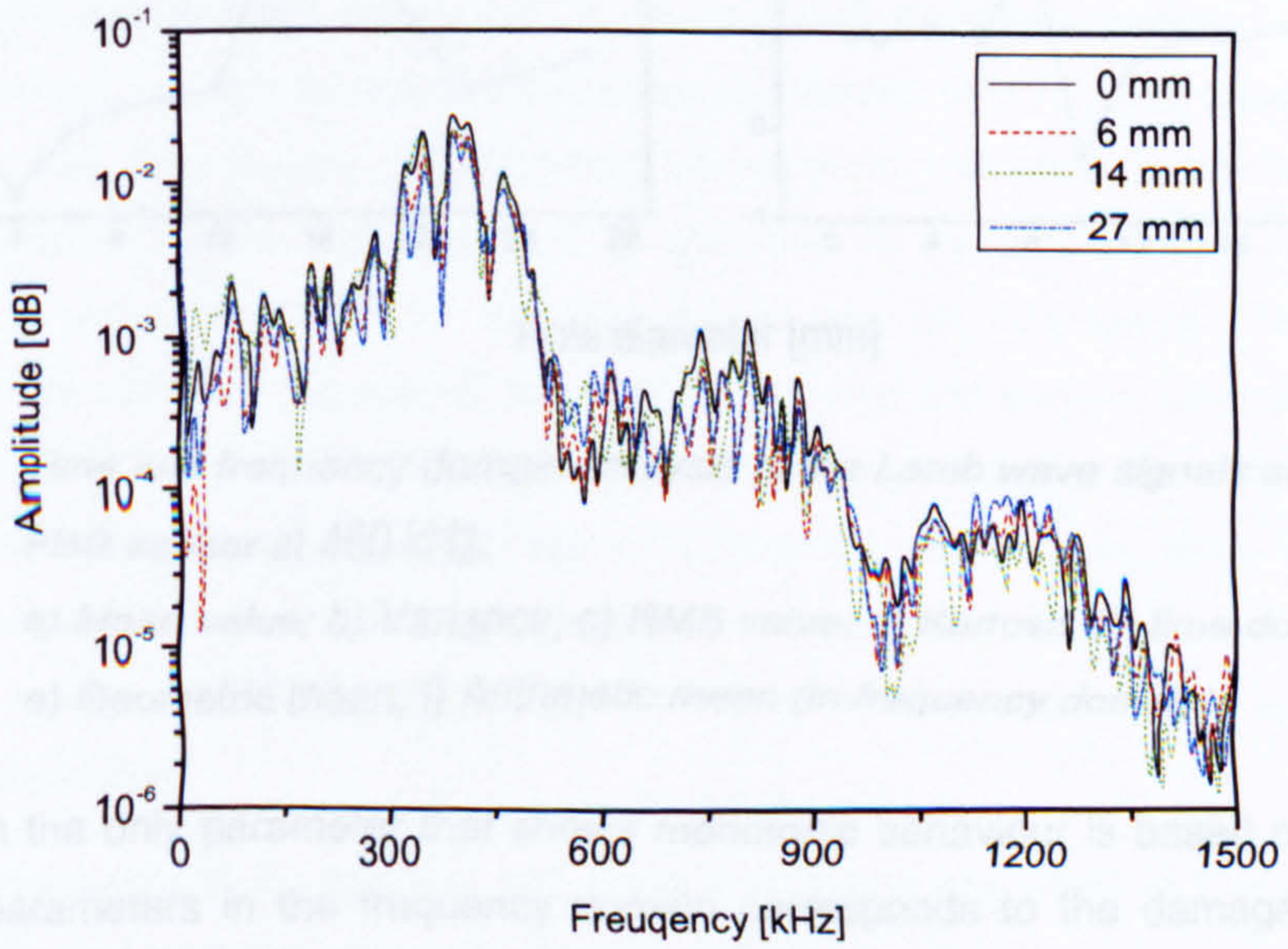

Figure 7.25: Frequency spectrum for the Lamb wave signals for different damage conditions.

Time and Frequency Domain Parameters

The parameters that could serve as damage index include the variance, mean, RMS value and Kurtosis in time domain and geometric and arithmetic mean of the spectrum in frequency domain. Their definitions can be found in Chapter 6. The parameters have been calculated for Lamb wave responses representing various damage conditions. Every parameter has been normalised to the reference value at zero damage. The normalised parameters can act as a damage index as the relative change of the index is independent of the time or frequency domain. The damage index is then plotted against the severity of damage (hole diameter); the results are shown in Figure 7.26.

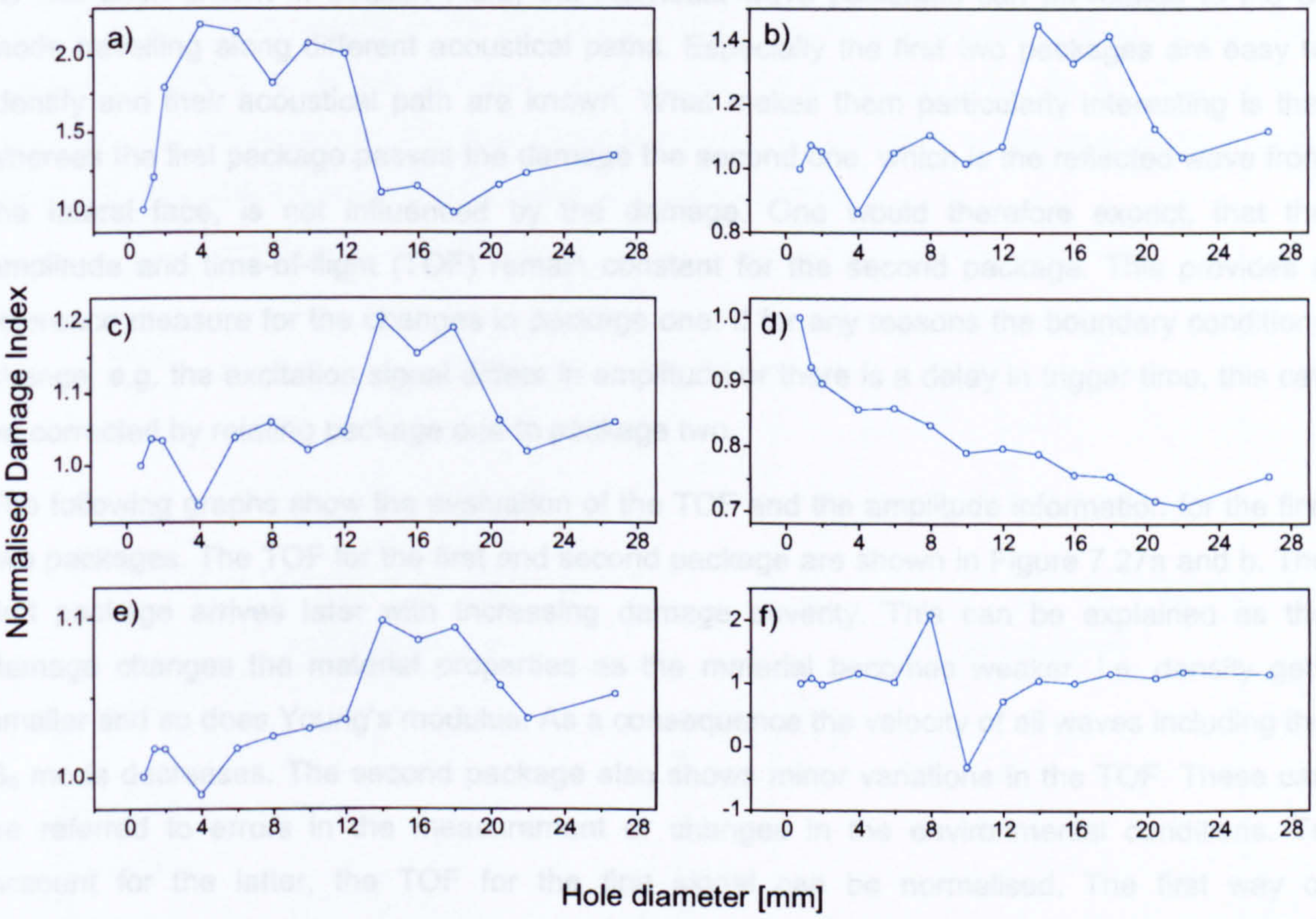

Figure 7.26: Time and frequency domain analysis of the Lamb wave signals sensed with FBG sensor at 460 kHz:
a) Mean value; b) Variance; c) RMS value; d) Kurtosis (in time domain)
e) Geometric mean; f) Arithmetic mean (in frequency domain).

In time domain the only parameter that shows monotonic behaviour is based on the Kurtosis. None of the parameters in the frequency domain corresponds to the damage severity. The damage index based on the Kurtosis was also investigated for the PZT sensors. In case of the PZT Kurtosis and all the other parameters show no correlation with damage size. This shows

that none of the parameters obtained from the time history of the Lamb wave signal meets the requirements earlier set for the damage index. The reason for this can be found in the complex wave propagation on the test specimen. With so many waves reflecting and interfering, the signals recorded with the FBGS also becomes complicated. And the environmental effects can not be separated from the damage.

An alternative approach for an appropriate damage index is to concentrate on the individual wave packages of the signal.

Wave package analysis

As has been shown in Section 7.3.2, the individual wave packages can be related to the S_0 mode travelling along different acoustical paths. Especially the first two packages are easy to identify and their acoustical path are known. What makes them particularly interesting is that whereas the first package passes the damage the second one, which is the reflected wave from the lateral face, is not influenced by the damage. One would therefore expect, that the amplitude and time-of-flight (TOF) remain constant for the second package. This provides a reference measure for the changes in package one. If for any reasons the boundary conditions change, e.g. the excitation signal differs in amplitude or there is a delay in trigger time, this can be corrected by relating package one to package two.

The following graphs show the evaluation of the TOF and the amplitude information for the first two packages. The TOF for the first and second package are shown in Figure 7.27a and b. The first package arrives later with increasing damage severity. This can be explained as the damage changes the material properties as the material becomes weaker, i.e. density gets smaller and so does Young's modulus. As a consequence the velocity of all waves including the S_0 mode decreases. The second package also shows minor variations in the TOF. These can be referred to errors in the measurement or changes in the environmental conditions. To account for the latter, the TOF for the first signal can be normalised. The first way of normalisation is to calculate the ratio of the TOF for the first and second wave package. These are referred to as TOF 1 and TOF 2. The second possibility is to take the difference of TOF 2 and TOF 1. Both results are shown in Figure 7.27c and d respectively. Both measures show good monotonic behaviour with damage severity. However, due to the ripples on the function the resolution is not optimal. Before analysing the result quantitatively the amplitude of the packages is considered.

The amplitude information for the first and second package are given in Figure 7.28a and b respectively. The first package shows decreasing amplitude with increasing damage. As the first package passes the damage, a part of the signal will be reflected at the metal – air interface, in

consequence this energy is missing in the transmitted signal. The amplitude of the signal therefore decreases. The second package however should not be affected by the damage. The observed changes in amplitude must have other reasons, e.g. changes in the boundary conditions. These can occur as the plate had to be removed from the test bench and be transported to the workshop for drilling the hole. The mechanical loads might change the coupling of both PZT and FBGS on the plate and therefore the transmission characteristics of the Lamb wave. Again the idea is to account for these effects by normalising the amplitude of package one by package two. Two possible ways of normalisation are shown in Figure 7.28c and d: calculation of the ratio and the difference of the amplitudes for the first and second wave package referred to as ampl 1 and ampl 2, respectively. For both methods a good monotonic behaviour of the damage index with the actual severity of damage can be found. The damage index shows a linear relation to the damage size for hole diameters smaller than 15 mm. The resolution in the range of hole diameter is very good, the individual points for 0.8 mm, 1.4 mm and 2 mm can be separated. For hole diameters larger than 15 mm a saturation effect can be observed: the slope becomes smaller and then it gets saturated.

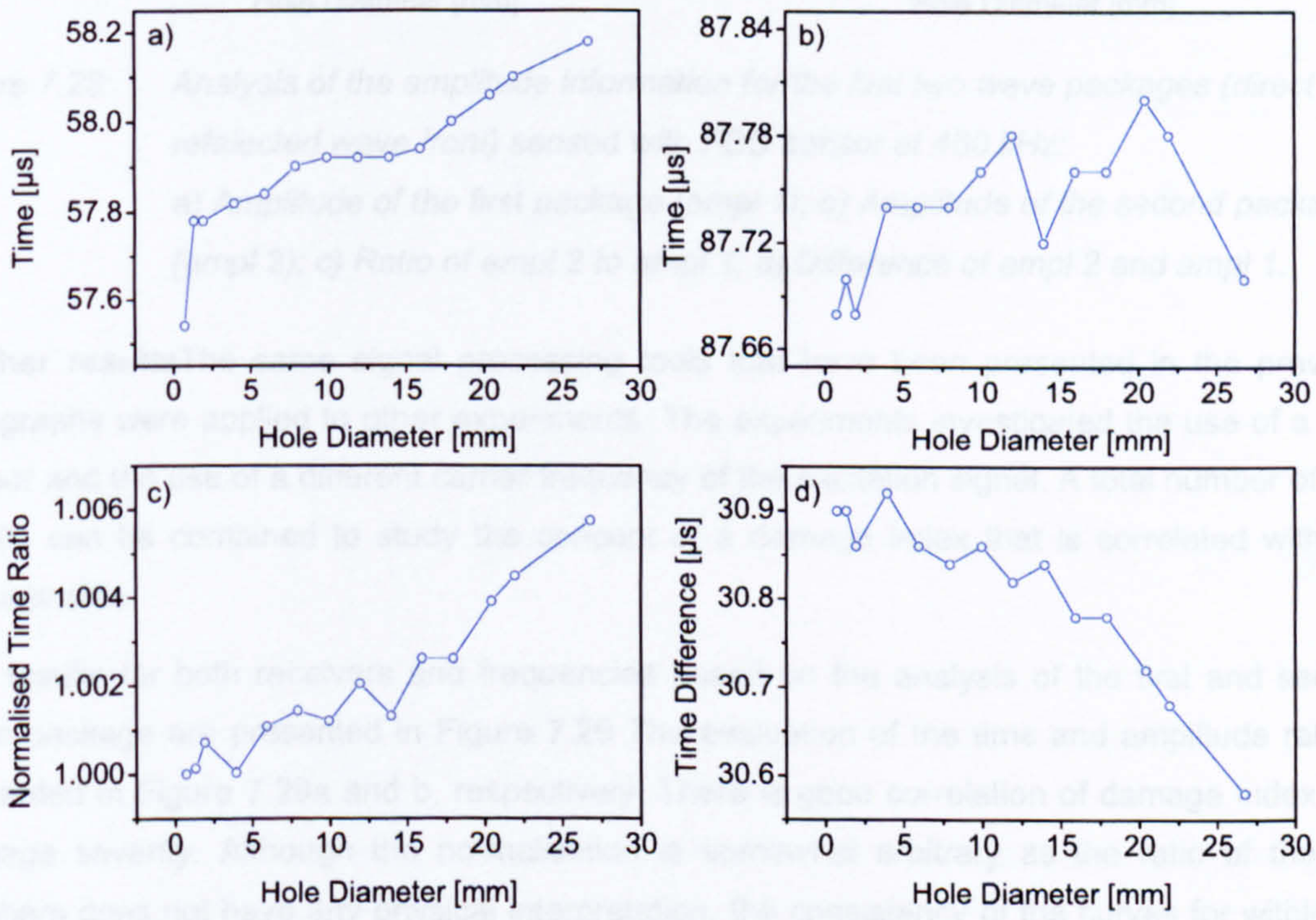

Figure 7.27: Analysis of the time-of-flight (TOF) information for the first two wave packages (direct and refelected wave front) sensed with FBG sensor at 460 kHz: a) TOF for the first package; b) TOF for the second package c) Ratio of TOF 2 to TOF 1; d) Difference of TOF 2 – TOF 1.

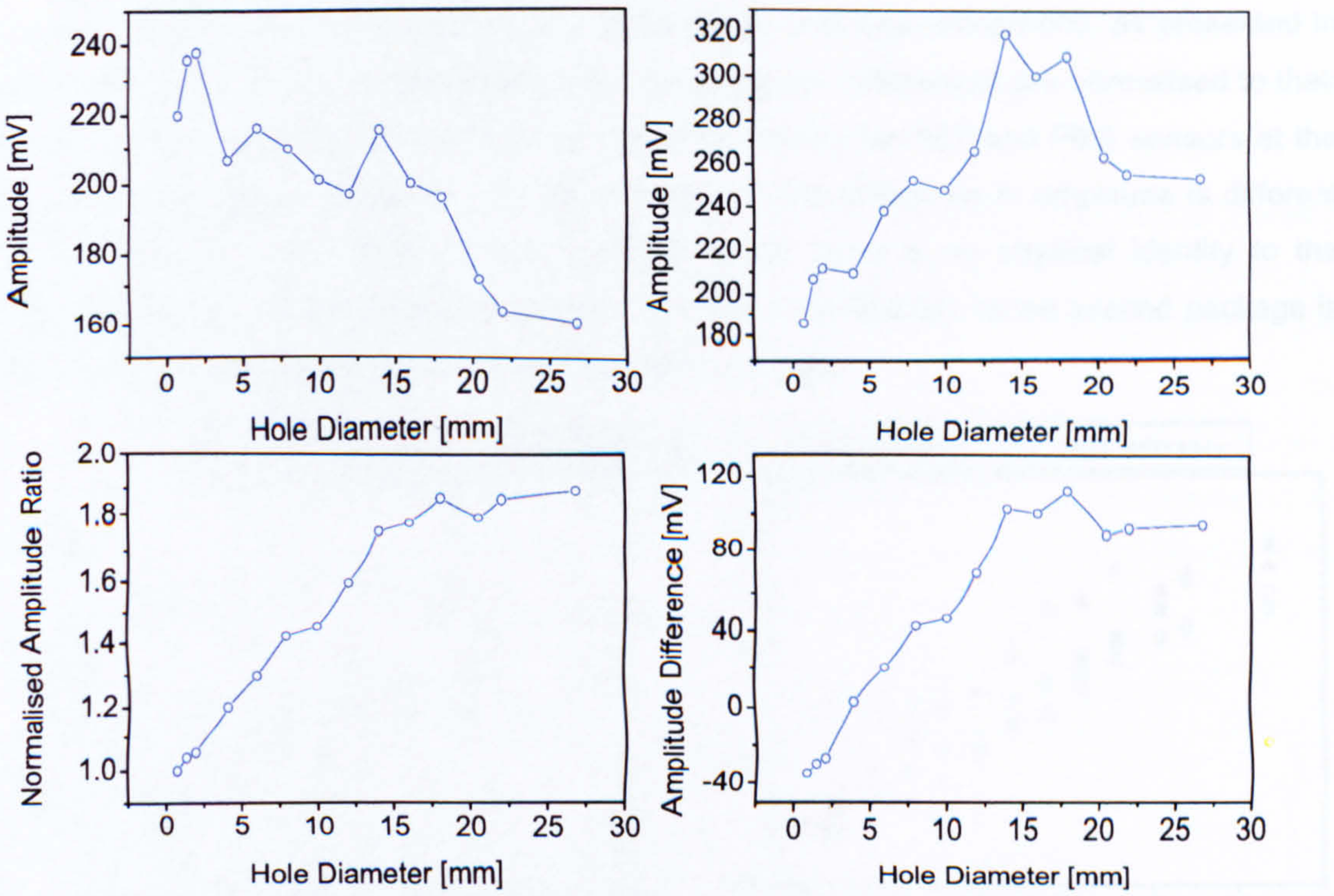

Figure 7.28: Analysis of the amplitude information for the first two wave packages (direct and refelected wave front) sensed with FBG sensor at 460 kHz:
a) Amplitude of the first package (ampl 1); b) Amplitude of the second package (ampl 2); c) Ratio of ampl 2 to ampl 1; d) Difference of ampl 2 and ampl 1.

Further results The same signal processing tools that have been presented in the previous paragraphs were applied to other experiments. The experiments investigated the use of a PZT sensor and the use of a different carrier frequency of the excitation signal. A total number of four results can be combined to study the concept of a damage index that is correlated with the damage size.

The results for both receivers and frequencies based on the analysis of the first and second wave package are presented in Figure 7.29 The evaluation of the time and amplitude ratio is presented in Figure 7.29a and b, respectively. There is good correlation of damage index and damage severity. Although the normalisation is somewhat arbitrary as the ratio of the two numbers does not have any physical interpretation, the consistency of the curves for within the amplitude and time analysis is obvious. For both receivers and at both frequencies there is a relation of damage index and damage size. For the same frequency the results for the PZT and FBG sensors agree very well. The different between amplitude and time is that for the amplitude the damage index changes about 50 to 100 %, whereas the index changes only about 0.5 to 0.8 % for the time analysis.

The picture is different for the analysis of the amplitude and time differences, as presented in Figure 7.29c and d. For this analysis the time and amplitude differences are normalised to their initial values. In case of the time difference again the results for PZT and FBG sensors at the same frequencies agree. However, the index based on the difference in amplitude is different for all the studies. The problem in the analysis is that there is no physical identity to the normalised damage indices of amplitude and time. The normalisation to the second package is somewhat arbitrary and might depend on the initial conditions.

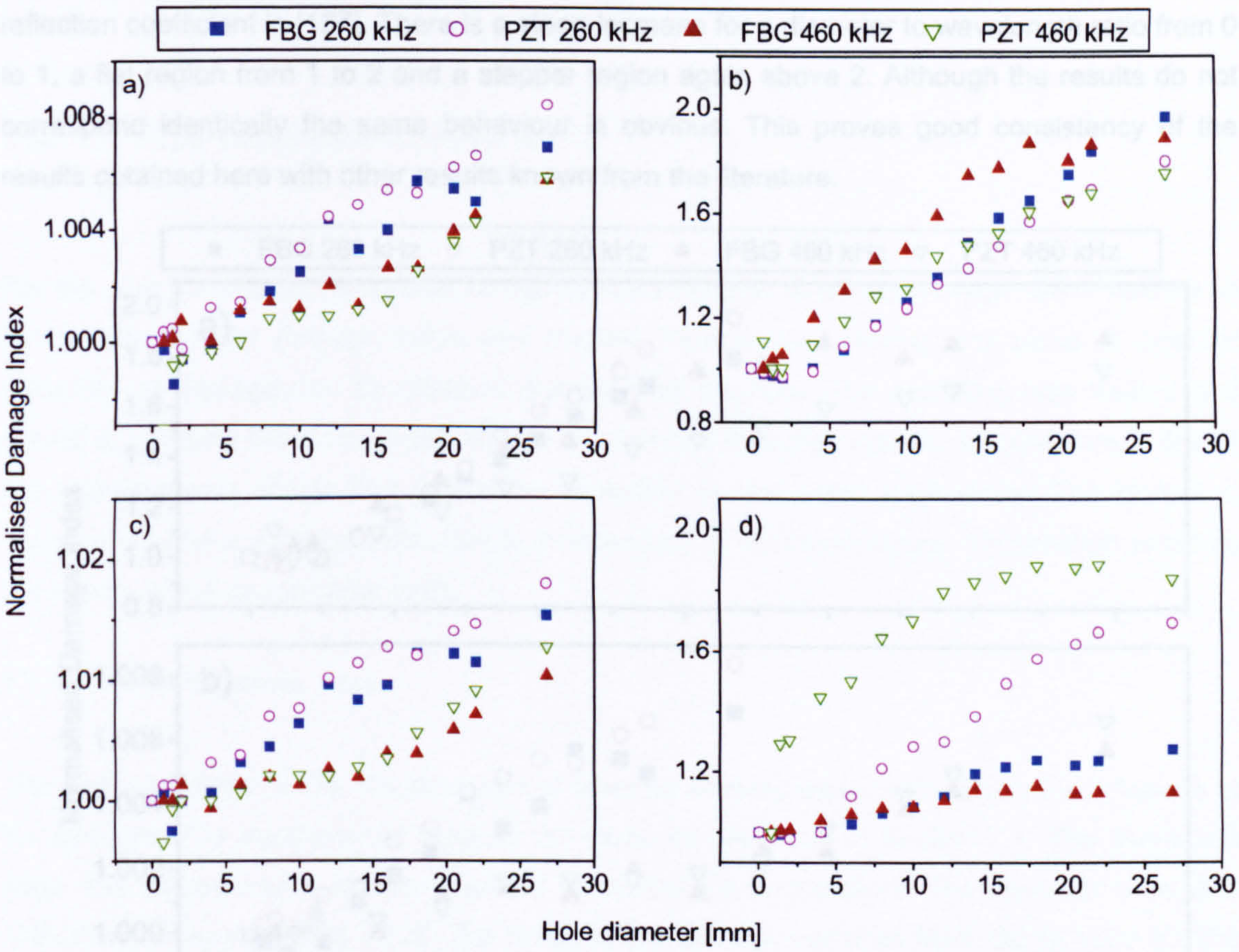

Figure 7.29: Damage Index obtained from wave package evaluation using different transducers and driving frequencies:
a) Time ratio; b) Amplitude ratio; c) Time difference, d) Amplitude difference.

It is problematic to find a mathematical model to describe the relation of damage index and damage size. The reason is because Lamb waves are guided waves and cannot be treated via standard scattering theory. No models are known from the literature that describe the influence of a hole on the amplitude and velocity of the Lamb wave. McKeon and Hinders present a theoretical approach to model the scattering of low order Lamb waves [282]. However, they do not discuss their result with respect to amplitude or velocity of the S_0 mode. A different approach

has been chosen be Diligent et al [157]. They present the results of modelling the reflections from a hole using FE analysis. The calculated the reflection coefficient of a hole with respect to the ratio of the diameter of the hole and the acoustical wavelength.

Figure 7.30 gives the results from this work in a presentation of damage index versus diameter to wavelength ratio. The amplitude analysis is shown in Figure 7.30a and the time analysis in Figure 7.30b. Both results can be compared to an analysis presented in [157]. The PZT and FBG sensors at 460 kHz for amplitude and time analysis show the same tendency as the reflection coefficient in [157]. There is a steep increase for a diameter to wavelength ratio from 0 to 1, a flat region from 1 to 2 and a stepper region again above 2. Although the results do not correspond identically the same behaviour is obvious. This proves good consistency of the results obtained here with other results known from the literature.

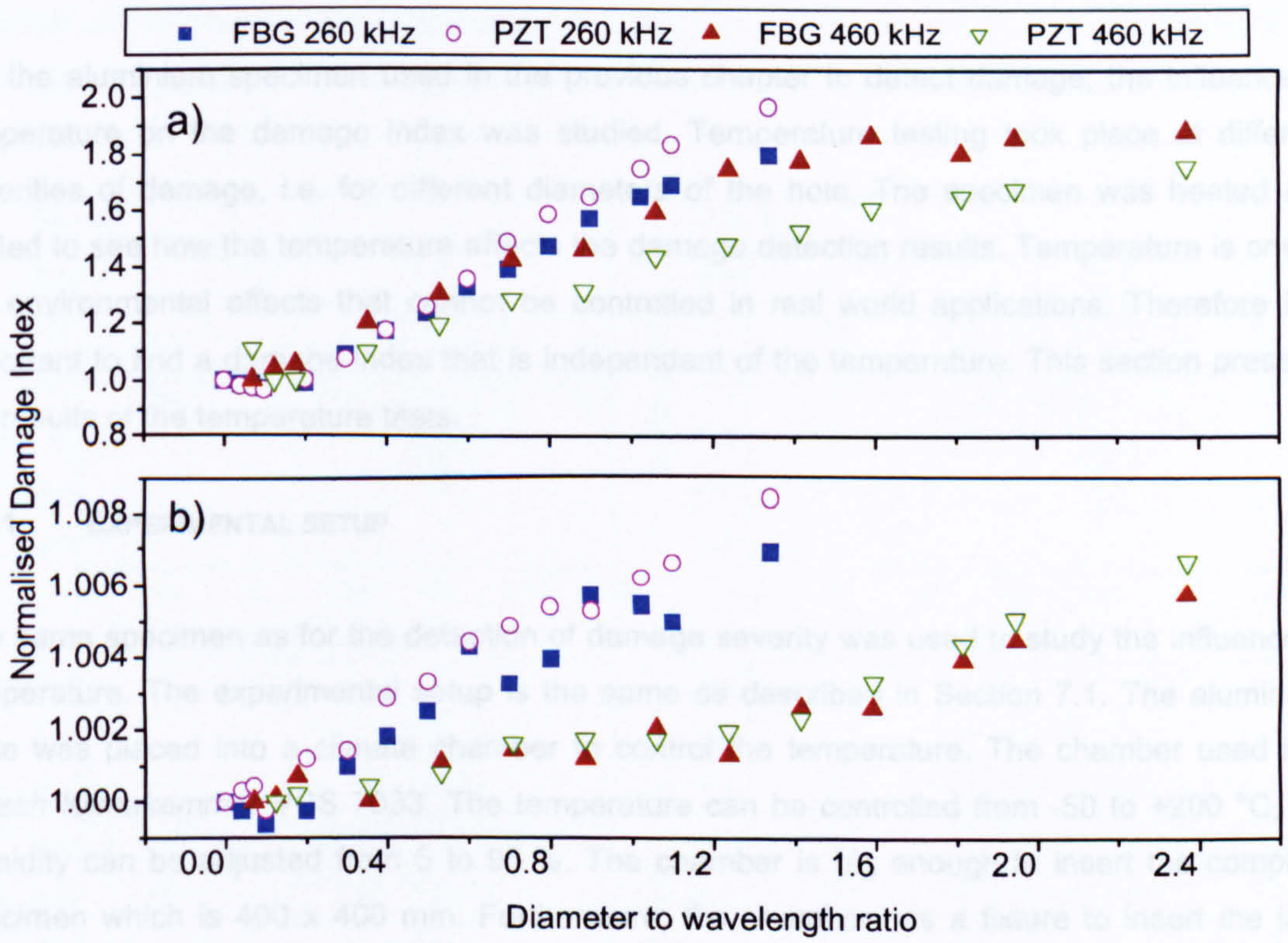

Figure 7.30: Damage Index obtained from wave package evaluation as a function of the diameter to wavelength ratio: a) Amplitude ratio; b) Time ratio.

It can be concluded that using the normalised amplitude and time changes of the first two packages a damage index can be defined. Both PZT and FBG sensors produce very similar results, which means the FBGS is as good as a PZT capable to determine the severity of damage. The difference at 260 and 460 kHz can not be explained, but they occur for both PZT and FBGS.

7.3.4 SUMMARY

This section showed that FBG and PZT sensors produce corresponding results for the severity of damage. The ratio of the time-of-flight and the amplitude of the first and second wave package within the Lamb wave response can be used as damage index that shows good monotonic behaviour with increasing damage severity. The best result using a FBG sensor shows that hole diameters as small as 0.8 mm can be identified.

7.4 TEMPERATURE EFFECTS

For the aluminium specimen used in the previous chapter to detect damage, the influence of temperature on the damage index was studied. Temperature testing took place at different severities of damage, i.e. for different diameters of the hole. The specimen was heated and cooled to see how the temperature affects the damage detection results. Temperature is one of the environmental effects that cannot be controlled in real world applications. Therefore it is important to find a damage index that is independent of the temperature. This section presents the results of the temperature tests.

7.4.1 EXPERIMENTAL SETUP

The same specimen as for the detection of damage severity was used to study the influence of temperature. The experimental setup is the same as described in Section 7.1. The aluminium plate was placed into a climate chamber to control the temperature. The chamber used is a *Vötsch Klimakammer* VCS 7033. The temperature can be controlled from -50 to +200 °C, the humidity can be adjusted from 5 to 95 %. The chamber is big enough to insert the complete specimen which is 400 x 400 mm. Furthermore, the chamber has a fixture to insert the lead wires and optical cables.

Starting point for the temperature cycle was at 25 °C. Temperature was increased step by step to 70 °C and was then cooled down to -20 °C, before the starting point was reached again. A loop has the advantage that any hysteresis in the specimen's behaviour becomes obvious. Before taking the measurement at each step the temperature was kept constant for about 15 min. The influence of temperature on the results obtained from both receivers, PZT and FBGS, was studied. The frequency of the excitation signal was kept constant at 260 kHz.

The temperature tests were carried out for the reference condition, at 0.8 mm, 12 mm and the maximum damage at 26.8 mm diameter of the hole.

7.4.2 RESULTS

To give an overview how temperature influences the Lamb wave propagation, the signals for the reference plate recorded with the FBGS are studied. The signal processing tools applied to the signals in Section 7.3 are used to analyse the thermal influence.

Original signal and its envelope

The Lamb wave responses as acquired at four different temperatures are displayed in Figure 7.31. Two things can be noticed immediately: The major changes happen to the fourth package. Its amplitude decreases with temperature and has a minimum at +70 °C. The amplitude of the first three packages is only slightly changed by temperature and the relative amplitude seems to be constant.

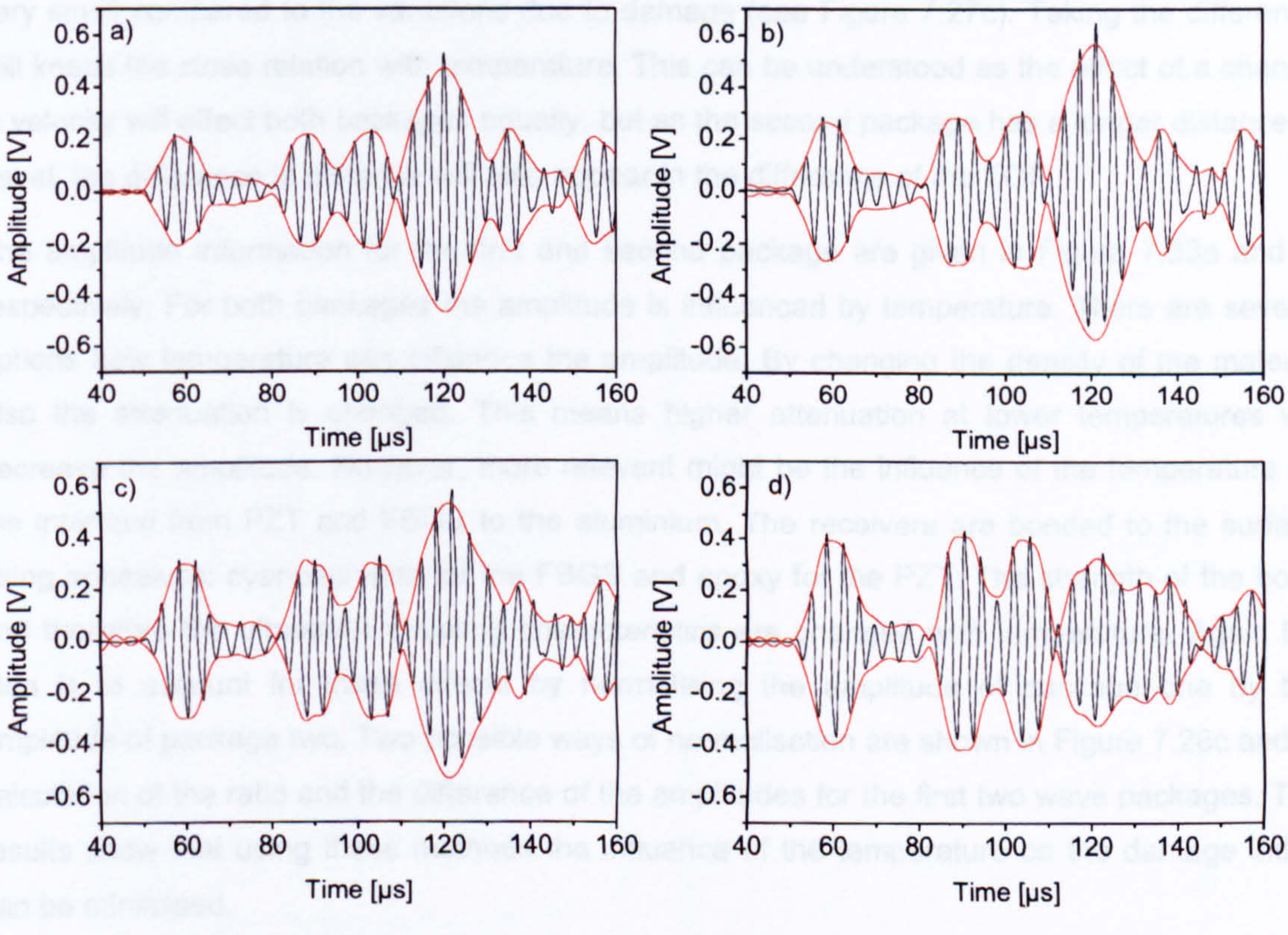

Figure 7.31: Series of Lamb wave signals at different temperatures sensed with FBG sensor at 260 kHz: a) -20 °C; b) +10 °C; c) +40 °C, d) +70 °C.

More results can be found in Appendix I.

Wave package analysis

The best results for the damage index in the previous chapter were obtained when only the first two packages of the Lamb wave signal were considered. It is therefore logical to concentrate on these packages for the temperature test. and check the damage index on its cross sensitivity to temperature.

The results of the TOF evaluation are given in Figure 7.32. The TOF for the first and second packages are shown in Figure 7.32a and b. The TOF for the first and second packages clearly depend on the temperature. Higher temperature gives later arrival times than lower temperature. It is also observed that the effect is completely reversible and no hysteresis occurs. This can be explained as temperature changes the material properties. If the material becomes warmer the density decreases as does the Young's modulus. As a consequence, the velocity of all waves, including the S_0 mode decreases. Again, for normalisation of the results, the ratio and the difference of the first two wave packages have been calculated. For the ratio any dependency of the temperature with damage index is lost. The variations in the signal are very small compared to the variations due to damage (see Figure 7.27c). Taking the difference still keeps the close relation with temperature. This can be understood as the effect of a change in velocity will effect both packages equally, but as the second package has a longer distance to travel, the difference in distance will also appear in the difference of the TOF.

The amplitude information for the first and second package are given in Figure 7.33a and b, respectively. For both packages the amplitude is influenced by temperature. There are several options how temperature can influence the amplitude. By changing the density of the material also the attenuation is changed. This means higher attenuation at lower temperatures will decrease the amplitude. However, more relevant might be the influence of the temperature on the interface from PZT and FBGS to the aluminium. The receivers are bonded to the surface using adhesives: cyanoacrylate for the FBGS and epoxy for the PZT. The strength of the bond and therefore the ultrasonic coupling characteristics are changed with temperature. Again the idea is to account for these effects by normalising the amplitude of package one by the amplitude of package two. Two possible ways of normalisation are shown in Figure 7.28c and d: calculation of the ratio and the difference of the amplitudes for the first two wave packages. The results show that using these methods the influence of the temperature on the damage index can be minimised.

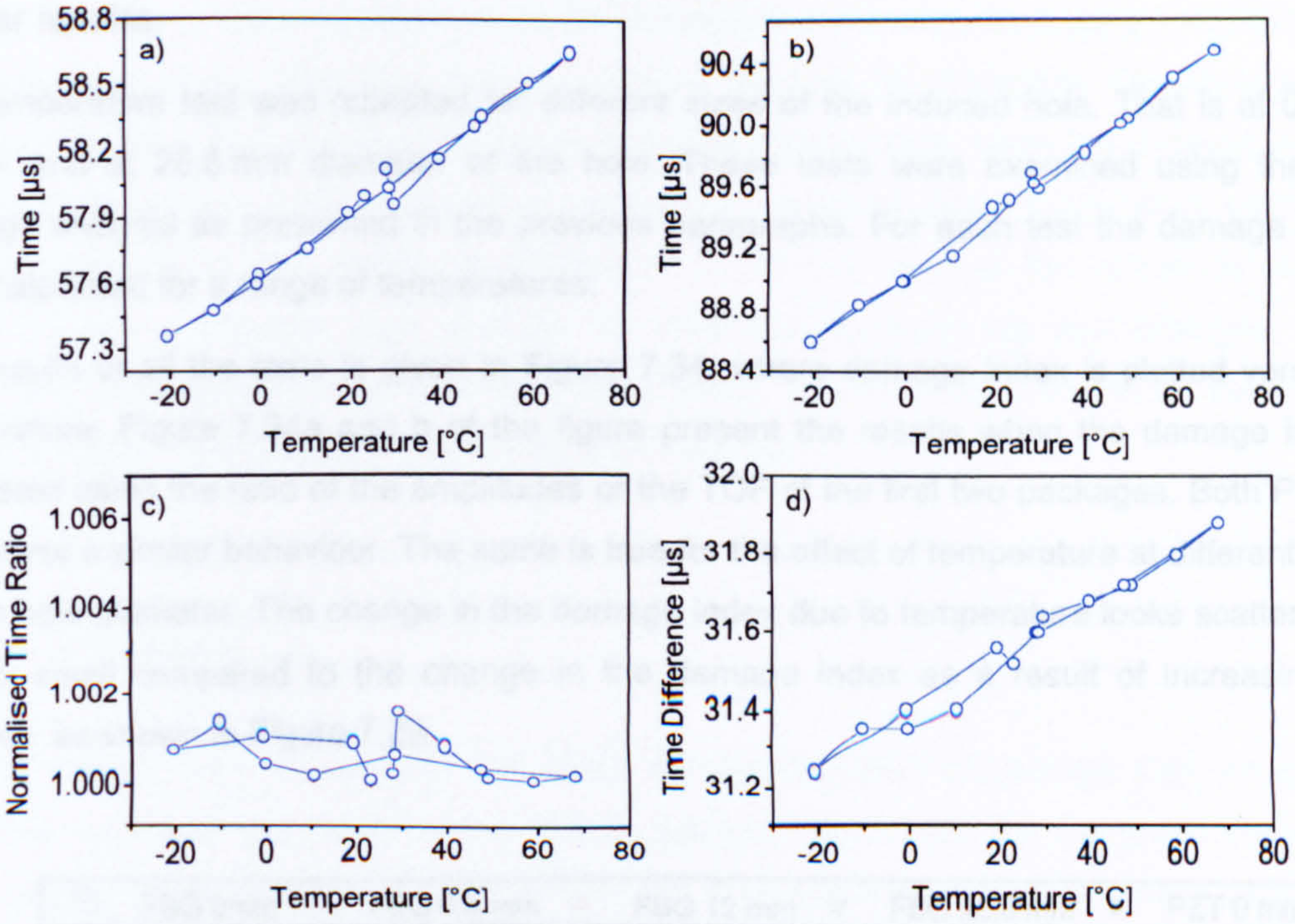

Figure 7.32: Analysis of the time-of-flight (TOF) information for the first two wave packages
a) TOF for the first package; b) TOF for the second package
c) Ratio of TOF 2 to TOF 1; d) Difference of TOF 2 – TOF 1

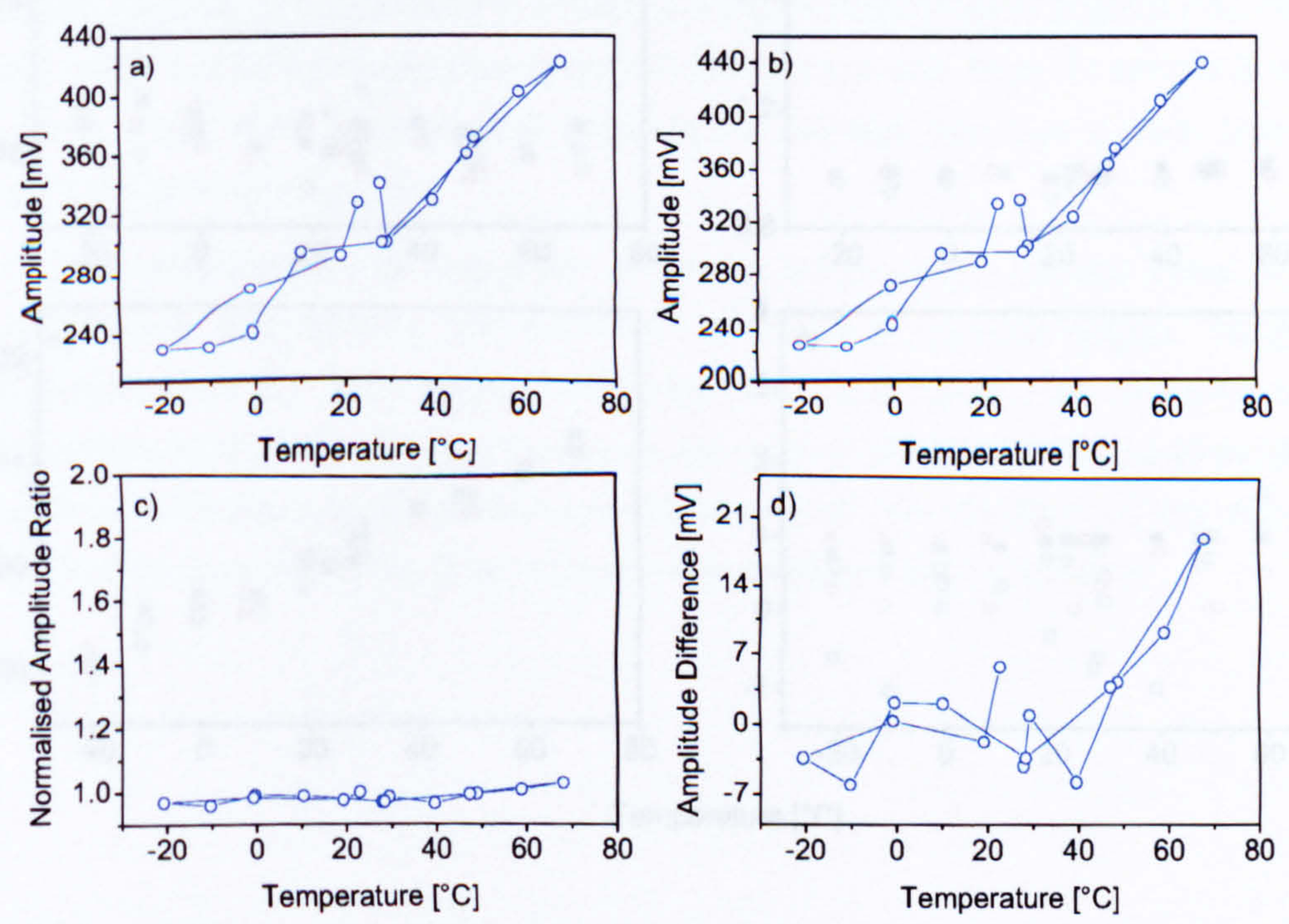

Figure 7.33: Analysis of the amplitude information for the first two wave packages
a) Amplitude of the first package (ampl 1); b) Amplitude of the second package (ampl2); c) Ratio of ampl 2 to ampl 1; d) Difference of ampl 2 and ampl 1

Further results

The temperature test was repeated for different sizes of the induced hole. That is at 0.8 mm, 12 mm and at 26.8 mm diameter of the hole. These tests were examined using the wave package analysis as presented in the previous paragraphs. For each test the damage indices were calculated for a range of temperatures.

The results of all the tests is given in Figure 7.34, where damage index is plotted versus the temperature. Figure 7.34a and b of the figure present the results when the damage index is calculated using the ratio of the amplitudes or the TOF of the first two packages. Both PZT and FBG show a similar behaviour. The same is true for the effect of temperature at different values for the hole diameter. The change in the damage index due to temperature looks scattered and is very small compared to the change in the damage index as a result of increasing hole diameter as shown in Figure 7.29.

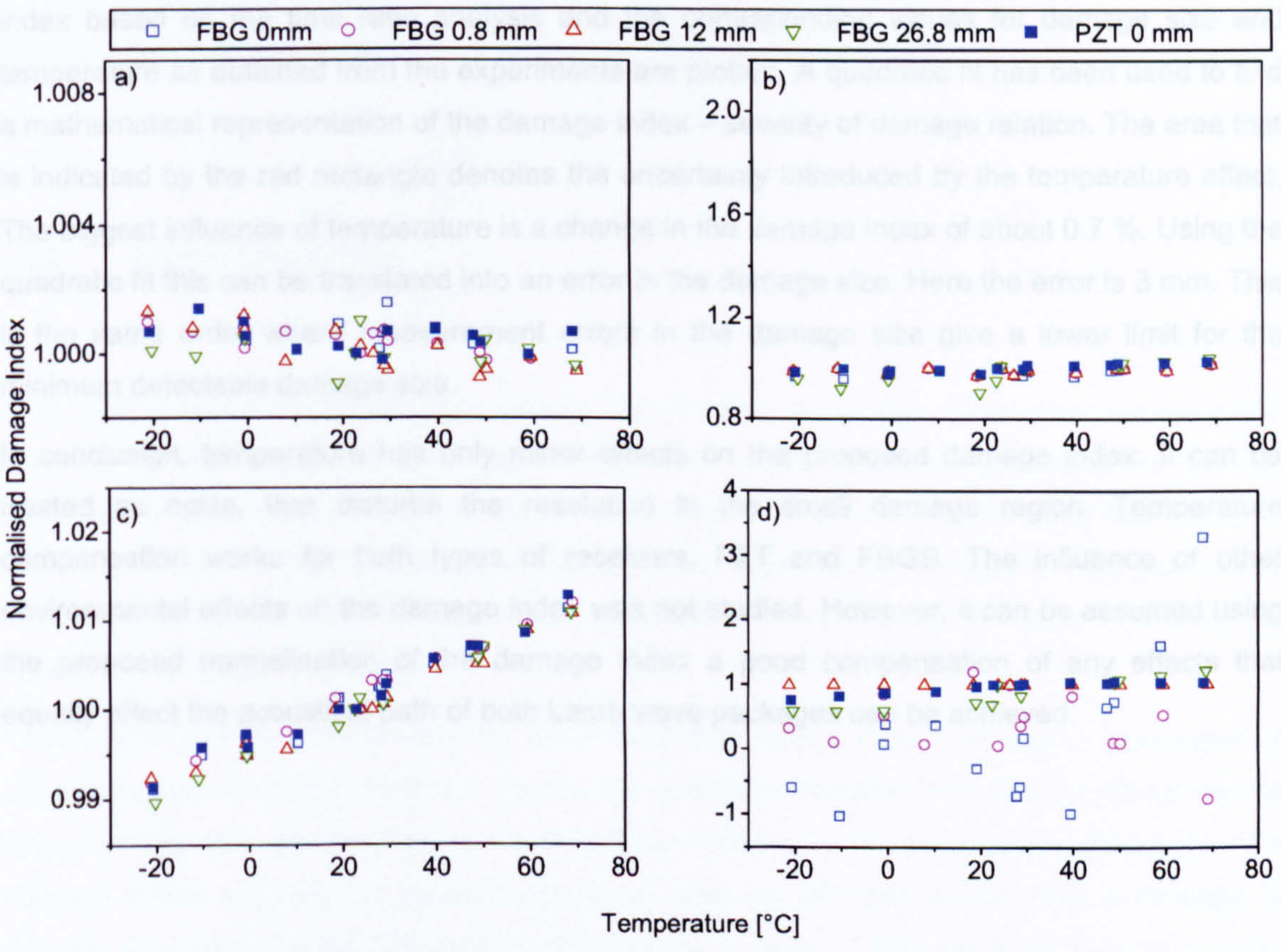

Figure 7.34: Influence of temperature on damage index:
a) Time ratio; b) Amplitude ratio; c) Time difference, d) Amplitude difference.

Figure 7.34c and d show the result when the damage index is calculated using the difference of the amplitudes or the TOF. The results is not as good as for the ratios. The damage index obtained from the TOF still strongly depends on the temperature, while the damage index for the amplitude analysis looks scattered and shows big variations. Again the problem comes from the normalisation of the amplitude difference. If, for example, at the reference state the difference has a negative sign whereas for other temperatures the sign changes, for the normalised index positive and negative values occur. Such a result can not be compared to others where no change in the sign of the index appears.

7.4.3 Discussion

To demonstrate how temperature can affect the determination of damage size, an example using the results for the FBGS at 260 kHz is given in Figure 7.35. For the graph the damage index based on the time ratio analysis and the corresponding values for damage size and temperature as obtained from the experiments are plotted. A quadratic fit has been used to find a mathematical representation of the damage index – severity of damage relation. The area that is indicated by the red rectangle denotes the uncertainty introduced by the temperature effect. The biggest influence of temperature is a change in the damage index of about 0.7 %. Using the quadratic fit this can be translated into an error in the damage size. Here the error is 3 mm. This is the same order where measurement errors in the damage size give a lower limit for the minimum detectable damage size.

In conclusion, temperature has only minor effects on the proposed damage index. It can be treated as noise, that disturbs the resolution in the small damage region. Temperature compensation works for both types of receivers, PZT and FBGS. The influence of other environmental effects on the damage index was not studied. However, it can be assumed using the proposed normalisation of the damage index a good compensation of any effects that equally effect the acoustical path of both Lamb wave packages can be achieved.

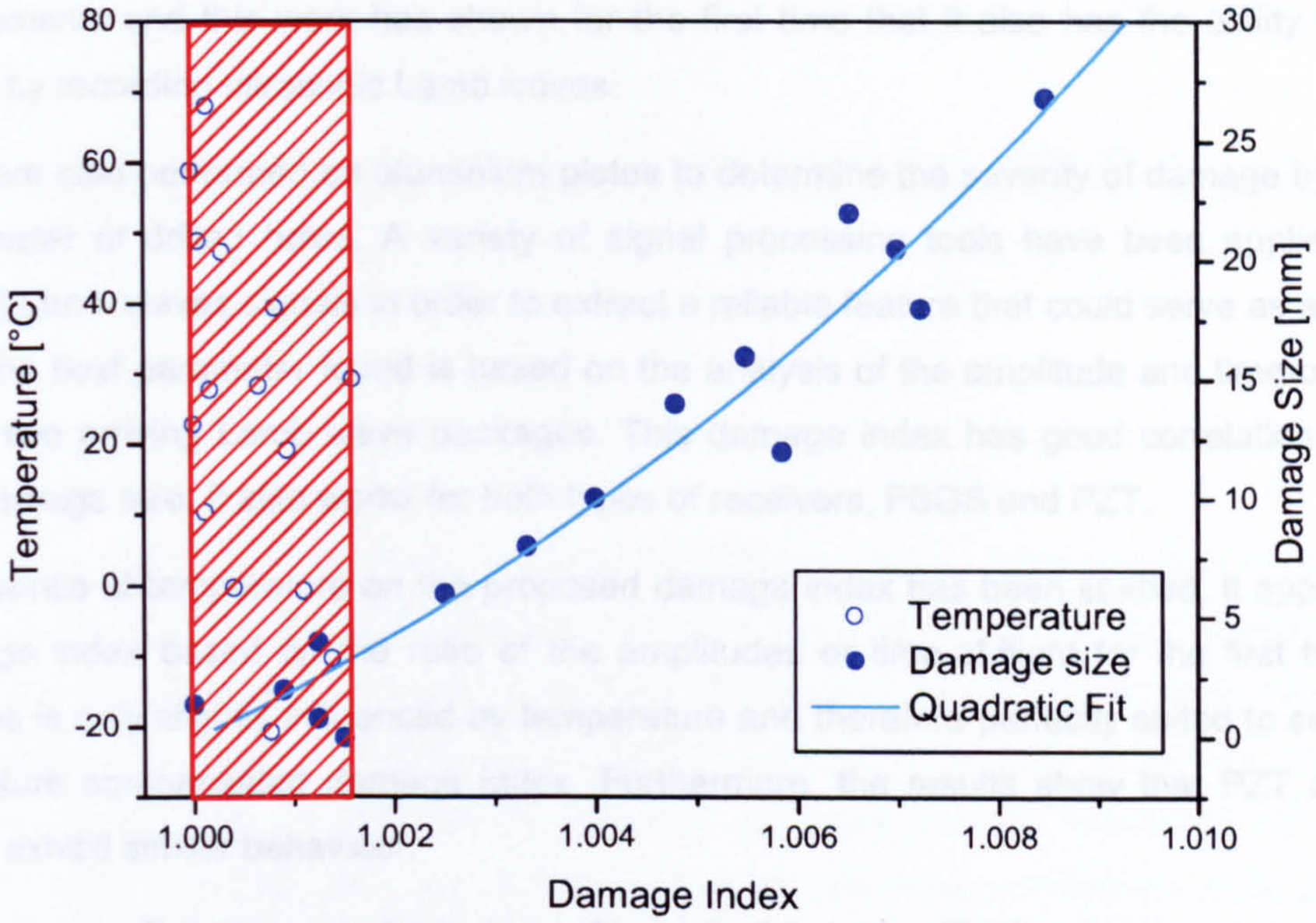

Figure 7.35: Influence of the temperature on the determination of damage size.

7.5 Conclusions

This chapter has explored the experimental identification of damage. Tests were carried out to address the three objectives of damage identification: detection of damage, location of damage and severity of damage. For the detection of damage, two different cases have been studied: with and without a priori knowledge of damage. The experiments showed that for both cases FBG sensors can be used to record the Lamb waves. The information found in the signals allows the detection of damage.

The directivity of the FBG sensor has been used to introduce a new concept of localisation of damage. By mounting the FBG in a rosette, the directivity characteristics of the gratings can be used to determine the direction of the incoming acoustic wave. It has been shown that this concept works not only for incident waves but also for reflected waves from a damage. A Genetic Algorithm has been applied to calculate the location of damage in an aluminium plate. This type of damage location is reserved for FBG sensors as a circular PZT transducer does not have the required directivity. Furthermore, this approach is useful if a dual strain and ultrasound monitoring sensor system has to be designed. The rosette is a common device for the strain

measurements and this work has shown for the first time that it also has the ability to locate damage by recording ultrasonic Lamb waves.

Tests were also performed on aluminium plates to determine the severity of damage by varying the diameter of drilled holes. A variety of signal processing tools have been applied to the recorded Lamb waves signals in order to extract a reliable feature that could serve as a damage index. The best parameter found is based on the analysis of the amplitude and time-of-flight of the first two arriving Lamb wave packages. This damage index has good correlation with the actual damage size. It also works for both types of receivers, FBGS and PZT.

The influence of temperature on the proposed damage index has been studied. It appears that a damage index based on the ratio of the amplitudes or time-of-flight for the first two wave packages is only slightly influenced by temperature and therefore perfectly suited to serve as a temperature compensated damage index. Furthermore, the results show that PZT and FBG sensors exhibit similar behaviour.

Fibre Bragg grating sensors have been found to be very effective for damage detection, damage location and determining the size of damage. For most of the tests they perform equally well as the more common piezoceramic transducers, but they offer superior performance for the proposed damage location scheme.

8 FATIGUE ANALYSIS USING FBG SENSORS

The previous chapter showed how a damage identification system based on fibre Bragg grating sensors could work. Methods for damage detection, damage localisation and determining the severity of damage were experimentally verified. This chapter describes a combined Health and Usage Monitoring System (HUMS) for the fatigue analysis of metallic structures. Initial tests have been carried out to demonstrate the dual load and damage monitoring on a simple aluminium plate. A fatigue test was carried out to study the crack propagation of the plate. The first section of this chapter gives an introduction to fatigue analysis. Basic concepts such as the safe-life and the fail-safe approach are explained and the relevant analysis tools based on load spectra and stress histories are presented. The experimental setup for the fatigue test is described in the second section. For load monitoring FBGS were used to record the load history of the test. For a comparative study electrical strain gages were also applied to record the loads. The results of the study are presented in the third section of this chapter. For fatigue analysis the crack growth was observed using a conventional method and Lamb wave analysis. FBGS and PZT were applied to record the Lamb wave signals. The same methods as presented in Chapter 6 were applied to determine a damage index that correlates with the damage or in this case the crack length. The results for both transducers are given in this chapter and their performance is compared. Final remarks on this initial test of a dual loads and damage monitoring system based on FBGS conclude the chapter.

8.1 BACKGROUND

The word fatigue in technical terms stands for damage and failure of materials under cyclic loads. It is an engineering task on the one hand to understand the basic principles of fatigue and on the other hand to find methods to measure and quantify the phenomenon. Research on fatigue involves many scientific disciplines and has been of interest to academic and industrial institutes for many years.

For the most general situation the progressing of fatigue can be classified in the following stages [275]:

a) Sub structural and micro structural changes which cause formation of permanent damage.
b) Creation of microscopic cracks (crack initiation).
c) Growth of microscopic cracks to form dominant cracks (crack propagation).
d) Stable propagation of the dominant crack.
e) Structural instability or complete fracture.

The exact definition of when the state of crack initiation occurs is one of the biggest impediments to the development of life prediction models. The state of crack initiation is needed to predict the total fatigue life of the structure which is defined as the sum of the number of cycles to initiate a fatigue crack and the number of cycles a crack propagates until it reaches final crack length.

The classical approach to fatigue design is called the *total-life or safe-life approach*. To obtain the total fatigue life the number of cycles necessary to produce a failure of an initially undamaged specimen is estimated under controlled amplitudes of cyclic stresses or strains. Both parts of the life time cycle, the one before crack initiation and the one until final failure contribute to the total life. It turns out that the crack initiation life dominates the total life, in fact it can be as high as 90 % of the total life. Therefore, the aim of the total-life approach is to design a structure that prevents crack initiation. In service the structure is then driven at load levels that are too low to initiate a crack. Structures designed in that way can traditionally be found in ground-vehicles.

In contrast, the *damage-tolerant or fail-safe approach* tolerates the existence of flaws or cracks in a structure, provided that they do not exceed a critical size. The structure therefore may contain an initial crack and the useful fatigue life is determined as the number of cycles that is required to propagate the crack from its initial size to a critical dimension. Various methods are available to determine that critical dimension for a specific structure. Crack propagation is characterised by empirical crack growth laws based on fracture mechanics. Different approaches to these empirical laws exist and can be used to determine the crack growth life. The defect-tolerant approach is often used in fatigue-critical applications, for example the aerospace industry.

The design of a structure will depend on which approach to fatigue life one will follow. It is essentially the microstructure of the material that will determine whether its more appropriate to prevent crack initiation and therefore favours a total-life approach or whether its designed to resist a crack propagation and so is suitable for the defect-tolerant approach.

In aeronautics the two different design philosophies co-exist. *Safe-life* is designed to achieve the required life time without any crack initiating. To determine the specific load spectra for a structure in service, tests have to be carried out in a first instance. This information on the loads will then be used to obtain the fatigue life of the structure under real life conditions. A safety factor might then be added to this life and the expected maximum life time of the structure can be specified. After its individual life the structure will be taken out of service, irrespective of whether a crack has developed or not. To guarantee the *safe-life* in any case, a large margin of safety is acknowledged during the design of the structure. However, this may contradict to the requirements of economy or performance. On the other hand the *fail-safe* or *damage-tolerant* concept would allow for cracks in a structure, provided there is enough remaining undamaged structure that could takeover the loads once carried by the now damaged part. This concept inherently requires an inspection scheme to monitor crack propagation. Should the crack arise to a critical dimension this has to be detected during inspection and appropriate measures, e.g. repair or replacement have to be taken, see also Section 0 for more details.

Regardless of which approach, safe-life or fail-safe, is taken, an inspection scheme is always desirable. It helps to avoid catastrophic failures due to any unforeseen damage either due to wrong design parameters or to unexpected structural events in service. For many structures in safety critical environments there exist detailed inspection schemes and regulations, for example the FAA regulations in the aircraft industry. These rules have to be obeyed whatever design philosophy the structure originally followed.

An in-depth discussion of the safe-life and fail-safe approach can be found in Appendix F.

8.1.1 Fatigue Analysis and Structural Health Monitoring

The benefits of a Structural Health Monitoring (SHM) system have already been discussed in the first chapter of this thesis. The motivation for a dual loads and damage monitoring system for fatigue analysis is reviewed in this section and the major benefits related to fatigue analysis are recalled.

A damage-tolerant approach requires the inspection of the structure at certain intervals. This is because cracks are tolerated in the material and the growth of the cracks must be monitored in order to prevent a crack growing to its critical dimension, which would result in catastrophic failure of the structure. The remaining life of the structure can be determined as the number of cycles that is required to propagate the crack from its current size to a critical dimension. Empirical crack growth laws are available to predict the remaining life of the structure if the current crack size is known and the future load spectra can be anticipated. The crucial point is that the load spectra are not always known to the required extension. Today, fatigue crack

growth analysis is based on past experience and projected to the future service. A corresponding inspection schedule is proposed and must be obeyed. During the inspection the structure is checked for existing cracks and their propagation since the previous inspection.

A structural health and usage monitoring system that is capable of monitoring loads and damage could help to improve the current inspection scheme and therefore give better knowledge of the life consumption so far and the remaining structural life. The load monitoring part of the system is designed to permanently update the anticipated load spectra. This allows an adaptation of the analysis to the actual service experience. The damage monitoring part gives the actual crack length independently of any inspection intervals, as the integrated system can explore the structure autonomously. The proposed SHM system for fatigue analysis could always update the remaining fatigue life, even from flight to flight.

The basic idea followed within this work is that a single sensor could be used for loads and damage monitoring. The previous chapters have shown that the fibre Bragg grating sensor is capable of sensing both the loads and the ultrasonic waves needed for damage detection. The fatigue test presented in this chapter combines all the experience with the individual monitoring task. An array of three Bragg gratings was used to monitor the loads that occur during the fatigue test and the Lamb wave signals after certain intervals in order to determine the crack length.

8.2 Experimental Procedure

At the Department of Mechanical Engineering at the University of Sheffield several tests were initiated to study damage detection and classification techniques using Lamb wave signals. Some of these tests involved different experimental techniques to record the data. Other tests focused on fatigue analysis of a metallic test specimen. In order to compare all experimental results a simple specimen was designed and manufactured. The specimens were used for testing the dual loads and damage monitoring system using FBG sensors at the DaimlerChrysler research laboratory in Ulm, Germany. The experimental setup and the test specimen are described in the following sections.

8.2.1 Instrumentation

The standard experimental setup for recording Lamb wave responses as presented in Chapter 7 was used to carry out the tests. Additional devices were necessary for recording the loads. A *HBM* (*Hottinger Baldwin Messtechnik*) strain recorder was used to interrogate the Electrical Strain Gages (ESG). The strain gage used was a *HBM* 6/120Y13. This strain gage is

thermally adapted to aluminium. The *HBM* strain recorder was connected via RS232 to a laptop in order to store the data for further signal processing. For recording the fibre optical strain signals a *Micron Optics* si425 was available. This device is capable of measuring 128 FBG sensors with a frequency of 250 Hz. This bandwidth is high enough for sampling the dynamic fatigue test loads. The machine used to run the fatigue test was an *Instron* 8800. The

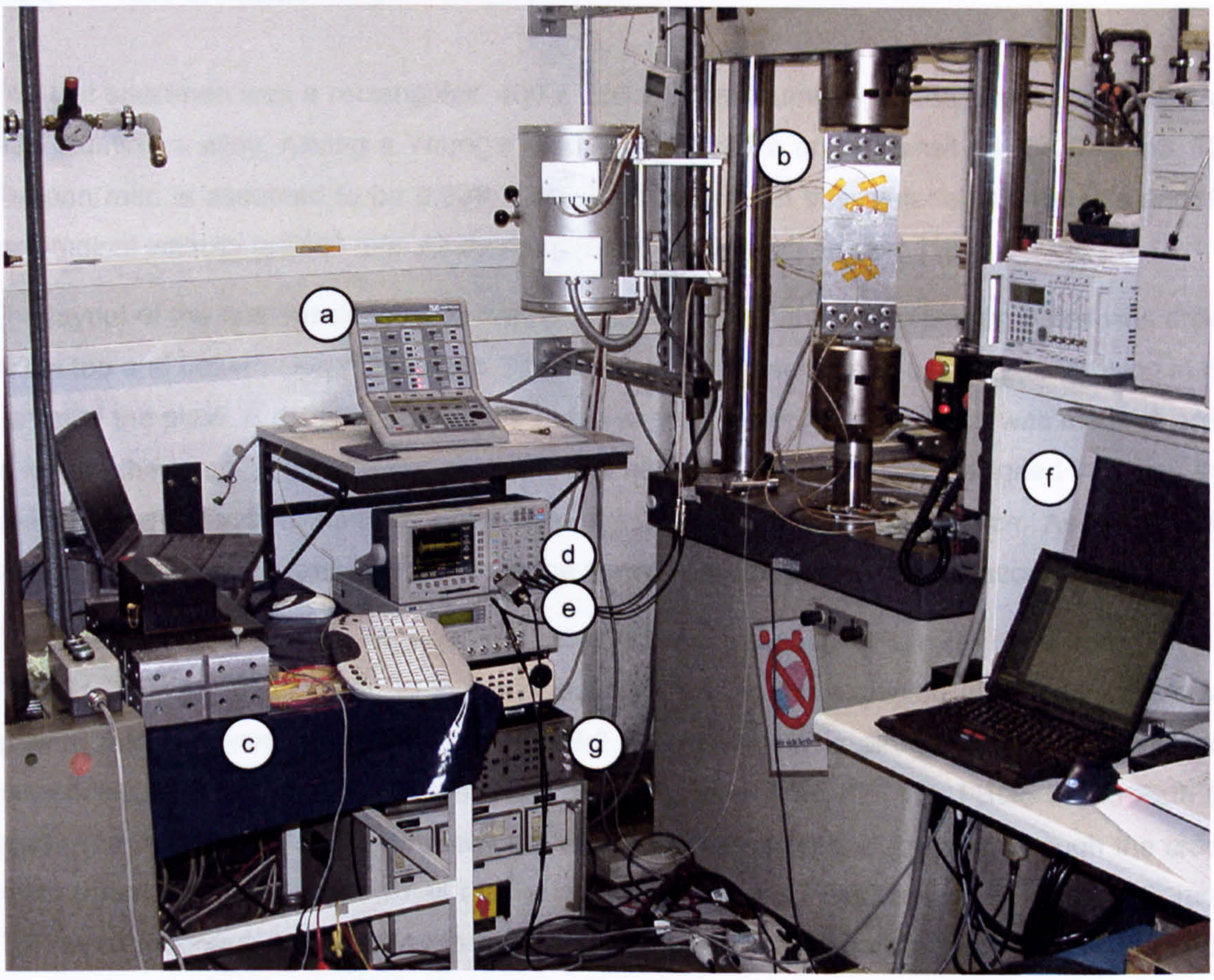

Figure 8.1: Experimental setup for the fatigue tests:
*a) Control panel of the fatigue test machine (*Instron *8800), b) Test specimen*
c) Fibre-optic control laptop and optoelectronic devices, d) Digital Oscilloscope
e) Signal Generator, f) Electrical strain gage control laptop and amplifier
g) Micron Optics *si425.*

parameters for the fatigue test were a static load of 20 kN, a dynamic load of ±9 kN and a cycling frequency of 10 Hz. A sine wave was used for dynamic loading of the specimen. Figure 8.1: Experimental setup for the fatigue tests:
a) Control panel of the fatigue test machine (Instron 8800), b) Test specimen
c) Fibre-optic control laptop and optoelectronic devices, d) Digital Oscilloscope
e) Signal Generator, f) Electrical strain gage control laptop and amplifier
g) *Micron Optics* si425.

shows a picture of the lab with all the devices installed.

8.2.2 TEST SPECIMEN

The test specimen was a rectangular 400 x 150 x 2 mm aluminium plate. The material was an NS4 aluminium alloy, having a Young's modulus of 71 GPa and a density of 2700 kg/m3. The Poisson ratio is assumed to be 0.338. The shear velocity in this material is 3100 m/s and the longitudinal velocity is 6300 m/s. All these parameters were taken from [194].

The layout of the test specimen is shown in Figure 8.2. A number of clamping holes was drilled at the top and bottom side of the plate. A small notch had been made using spark erosion in the centre of the plate. A detailed view of the notch is also presented. The notch was made in order to initiate the crack at the desired position. The layout of the notch was designed in a way that makes sure, the crack starts to grow perpendicular to the loading direction. As the starting position of the crack is known in advance the sensor positions were chosen accordingly.

Different acoustical paths were used for Lamb wave propagation. Path (a) goes from PZT I to FBGS 1. This is 45° direction to the principal load and to the expected direction of the crack growth. Path (b) involves PZT II and FBGS 2. The direction is along the principal load and perpendicular to the direction of the crack. Path (c) goes from PZT I to FBGS 2 and Path (d) goes from PZT II to FBGS 1. Whereas the acoustical paths (a) and (b) pass through the crack, paths (c) and (d) will bypass small cracks. In addition to the FBGS shown in Figure 8.2, more PZT were mounted on the reverse side of the plate at corresponding positions to the FBG sensors on the front side. This allowed the parallel recording of PZT and FBGS Lamb wave responses along identical acoustical paths, the only difference being the surface on which the transducers were mounted. As described in Chapter 7, an epoxy (*Epotek 306)* was used to bond the PZT transducer to the structure, whereas the FBGS were bonded using cyanoacrylate glue (*Kyowa CC-33A*). For the fatigue test the fibres were bonded directly onto the surface of the structure, no backing patch was used.

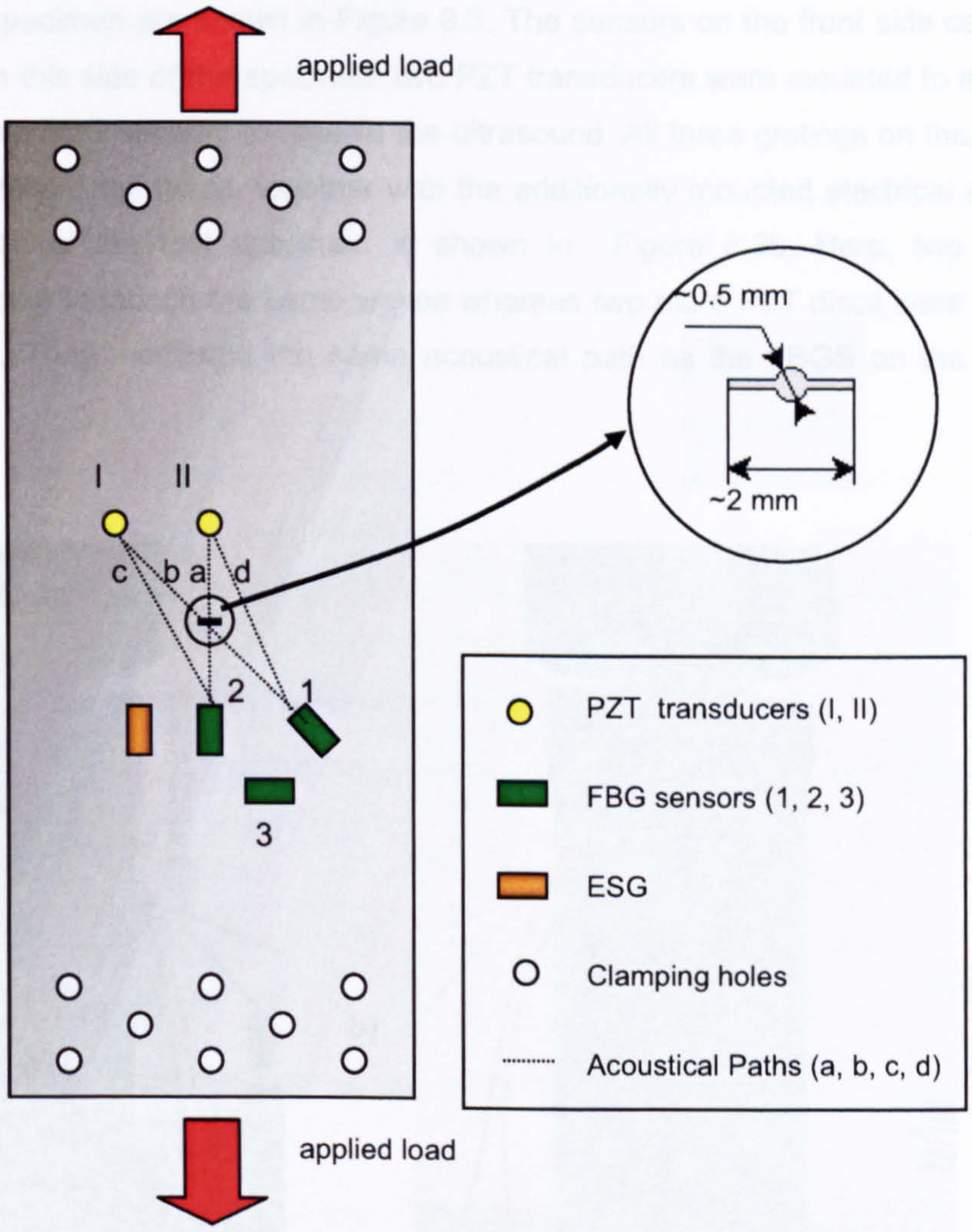

Figure 8.2: Layout of the test specimen and sensor positions.

As presented in Section 0 it is essential for the FBG sensor to have a suitable sensor length to be able to detect both, static and ultrasonic strain. The ultrasonic frequency chosen for the Lamb wave signals was 300 kHz, which for aluminium corresponds to a wavelength of 17 mm. Therefore, the FBG sensors used for the fatigue test had a grating length of 1 mm. The Bragg gratings were fabricated by *IPHT* Jena, Germany. Their reflectivity is about 15 %, their spectral width is about 500 pm. The FBG sensors installed could not only be used for detection of the ultrasonic Lamb waves, but could also be employed for measuring the strains related to the loading of the specimen. For a comparative study an electrical strain gage (ESG) was additionally mounted on the front side of the specimen. The same bonding technique as for the fibre was used.

Both sides of the test specimen are shown in Figure 8.3. The sensors on the front side can be seen in Figure 8.3a. On this side of the specimen two PZT transducers were mounted to excite the ultrasonic waves, two FBG sensors to receive the ultrasound. All three gratings on the front side could be used to record the loads, together with the additionally mounted electrical strain gage. The reverse side of the test specimen is shown in Figure 8.3b. Here, two PZT transducers were mounted to launch the Lamb waves whereas two more PZT discs were used as ultrasonic receivers. They monitored the same acoustical path as the FBGS on the front side.

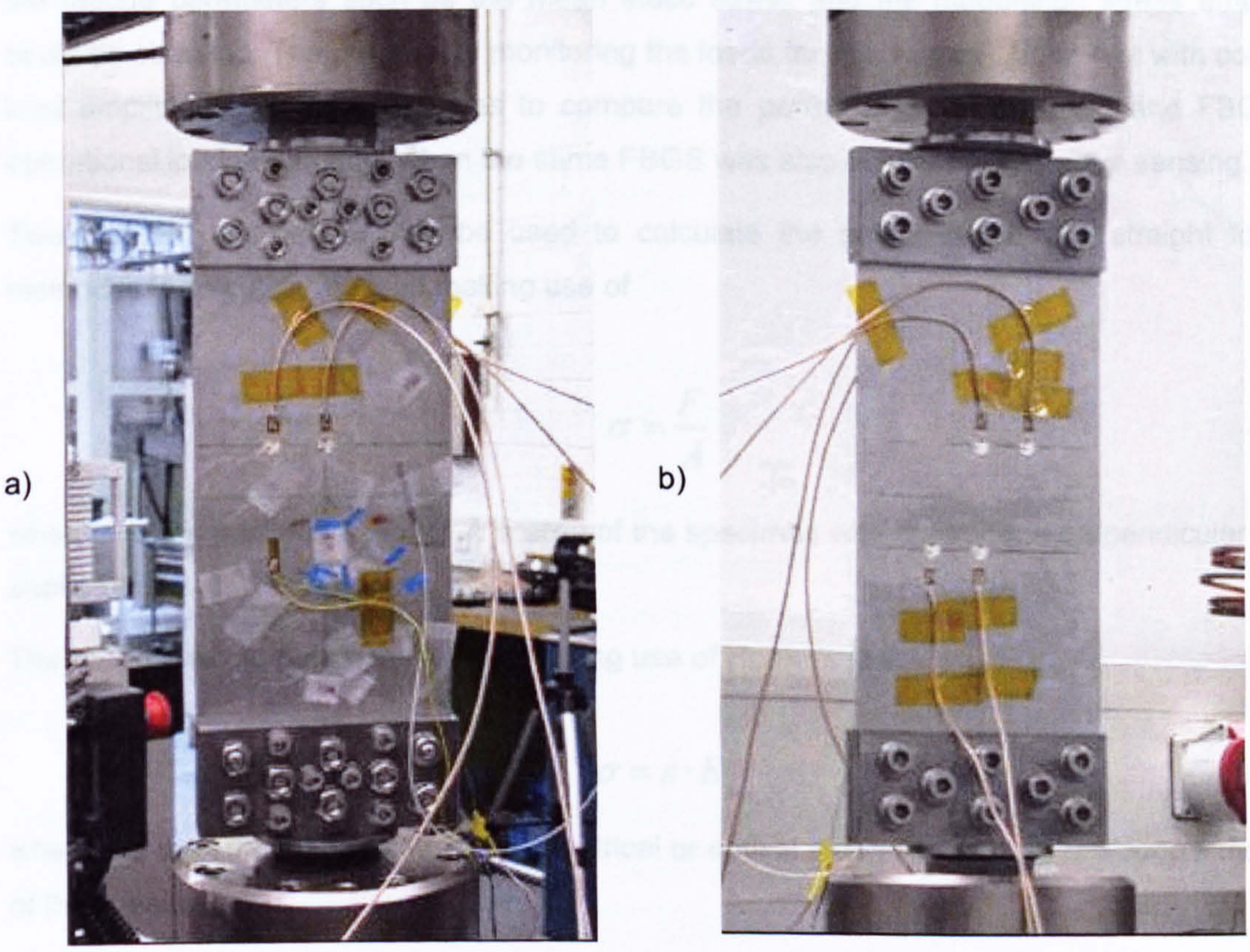

Figure 8.3: Photograph of the test specimen clamped into the test machine: a) Front side with FBGS installation; b) Reverse side with PZT installation.

8.3 LOAD MONITORING

The fatigue test was carried out in the following way. Before starting the test the reference condition was recorded for both the PZT and the FBG sensors. Then a dynamic load was applied. After a certain number of cycles the specimen was investigated for the presence of any fatigue cracks. If a crack was observed its length was documented and the dynamic loads were applied again. In this way a crack propagation curve was obtained. Additionally to crack monitoring the dynamic loads were recorded using both ESG and FBGS. From the loads history the fatigue parameters such as the mean static stress and the modulation stress amplitude could be obtained. The purpose of monitoring the loads for this simple fatigue test with constant load amplitude and frequency was to compare the performance of the ESG and FBGS for operational load monitoring, when the same FBGS was also used for Lamb wave sensing.

Two different approaches can be used to calculate the actual loads. The straight forward method is to calculate the load making use of

$$\sigma = \frac{F}{A} \tag{8.1}$$

where F is the applied force and A is area of the specimen with the surface perpendicular to the applied force.

The second way to obtain the load is making use of Hooke's law:

$$\sigma = \varepsilon \cdot E \tag{8.2}$$

where ε is the strain measured by the electrical or optical strain gage and E is Young's modulus of the specimen.

Figure 8.4 shows the recorded signals of the ESG and FBGS. The information of the strain gage signal was directly converted into a load using Equation (8.2). The result is shown on the right axis of Figure 8.4a. The FBGS in this experiment was not calibrated to any load, therefore no direct conversion of the Bragg wavelength into a corresponding load was possible. However, this measurement could be used to obtain calibrated loads from the FBGS for further load monitoring.

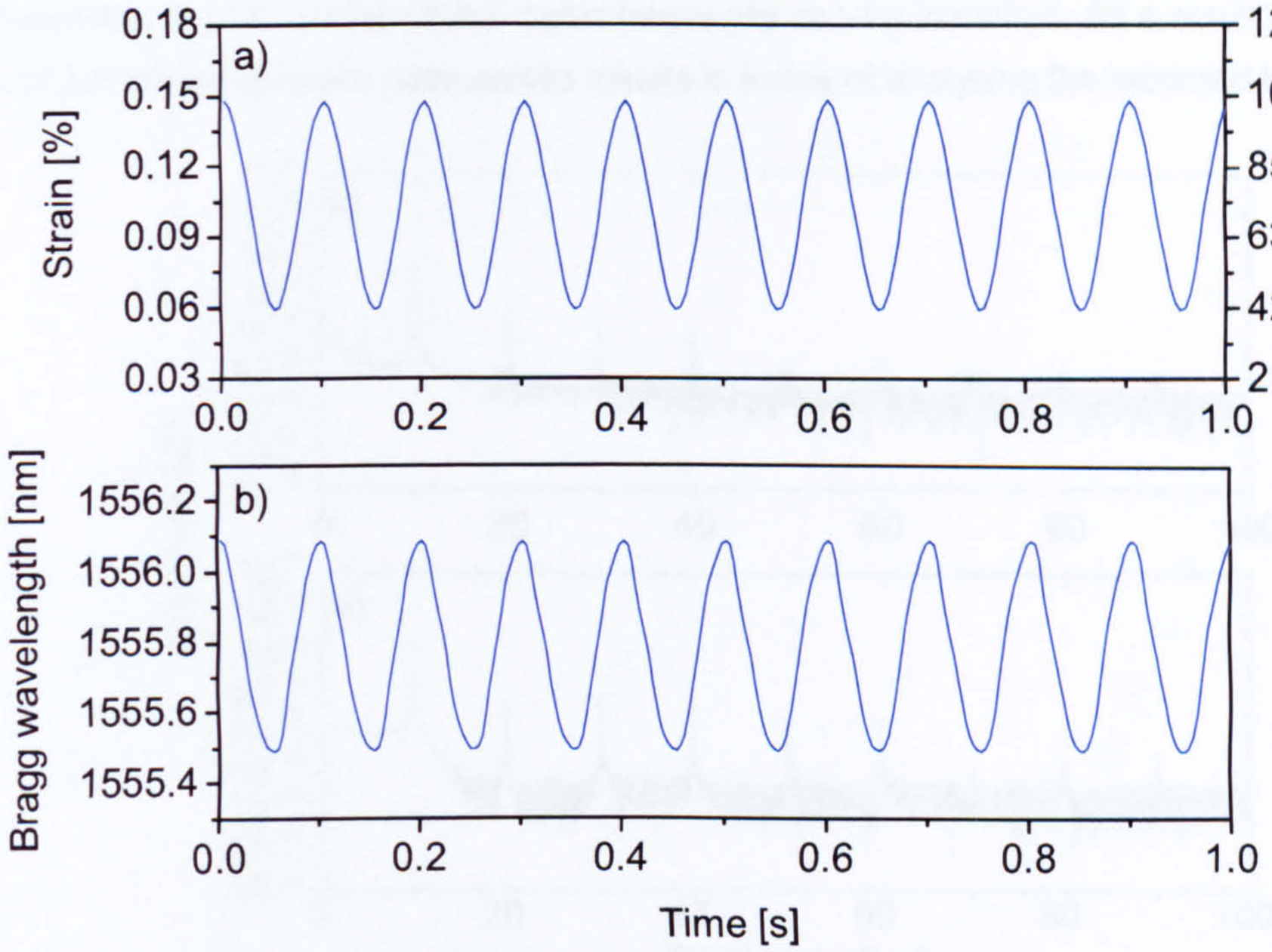

Figure 8.4: Sequence of the dynamic loading of the fatigue test specimen: a) Electrical Strain Gage; b) Fibre Bragg Grating Sensor.

The results from the recording of the load history using the ESG can be compared with the results from the force method. Table 8.1 shows the results for the mean static load and the load amplitude, as defined in Section 0. The experimental error in the results for both methods is assumed to be less then 5 %, which is standard error in practical applications of strain gages [136].

Table 8.1: Calculated load parameters using the strain and the force method.

Parameter	Strain method	Force method
Mean static load σ_m	73.5 MPa	67.5 MPa
Load amplitude σ_a	31.6 MPa	30.5 MPa

Both methods give slightly different results for the load parameters. This can be explained by a systematic error as the actual Young's modulus might differ from the specifications of the manufacturer. Within these error limits the results for both methods are in good agreement.

A further measure of the ability of the FBGS for load monitoring can be found when the frequency response of the load history is studied The spectra obtained by the ESG and FBGS are shown in Figure 8.5, respectively. The ESG spectrum was recorded with 200 Hz and the FBGS spectrum with 250 Hz sampling frequency. Both spectra show the 10 Hz dynamic load.

Furthermore, the harmonics of this basic frequency can be identified. As a result both methods of load monitoring produce comparable results in terms of analysing the recorded loads history.

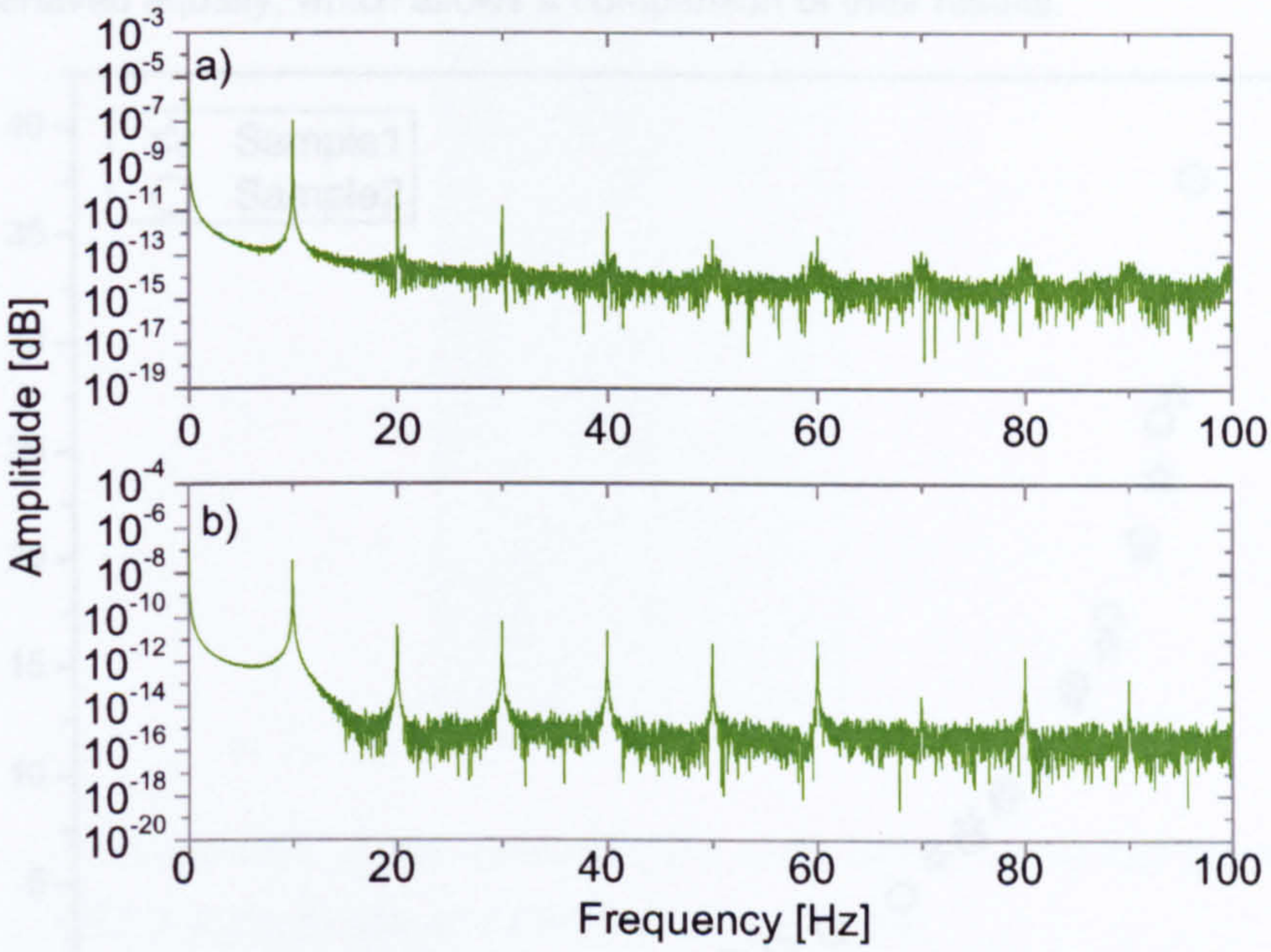

Figure 8.5: Frequency spectra of the recorded signals in Figure 8.4: a) Electrical Strain Gage; b) Fibre Bragg Grating Sensor.

8.4 Crack Growth and Damage Monitoring

The dynamic fatigue test aimed to establish a damage index for the Lamb wave analysis that correlates with the actual crack length. Two specimens were available for the initial tests.

8.4.1 Crack propagation curves

For both specimens that were available for the fatigue test the test conditions, e.g. the sensor installation and the fatigue parameters were identical. To see how good the experimental conditions could be reproduced, the crack propagation curves as obtained by visual inspection, are plotted in the same diagram. The crack length was determined using a lens and a meter. Figure 8.6 shows both crack propagation curves. For the first specimen no data has been gathered between 150 000 and 230 000 cycles. This is because no crack was observed during the experiment, but as the evaluation shows this is related to an uncertainty in the visual inspection. As the curves perfectly agree for other regions, a crack must have occurred, but

remained undetected. The coincidence of the two curves shows that not only the experimental conditions were identical for both tests, but the specimens as well. Furthermore, both specimens behaved equally, which allows a comparison of their results.

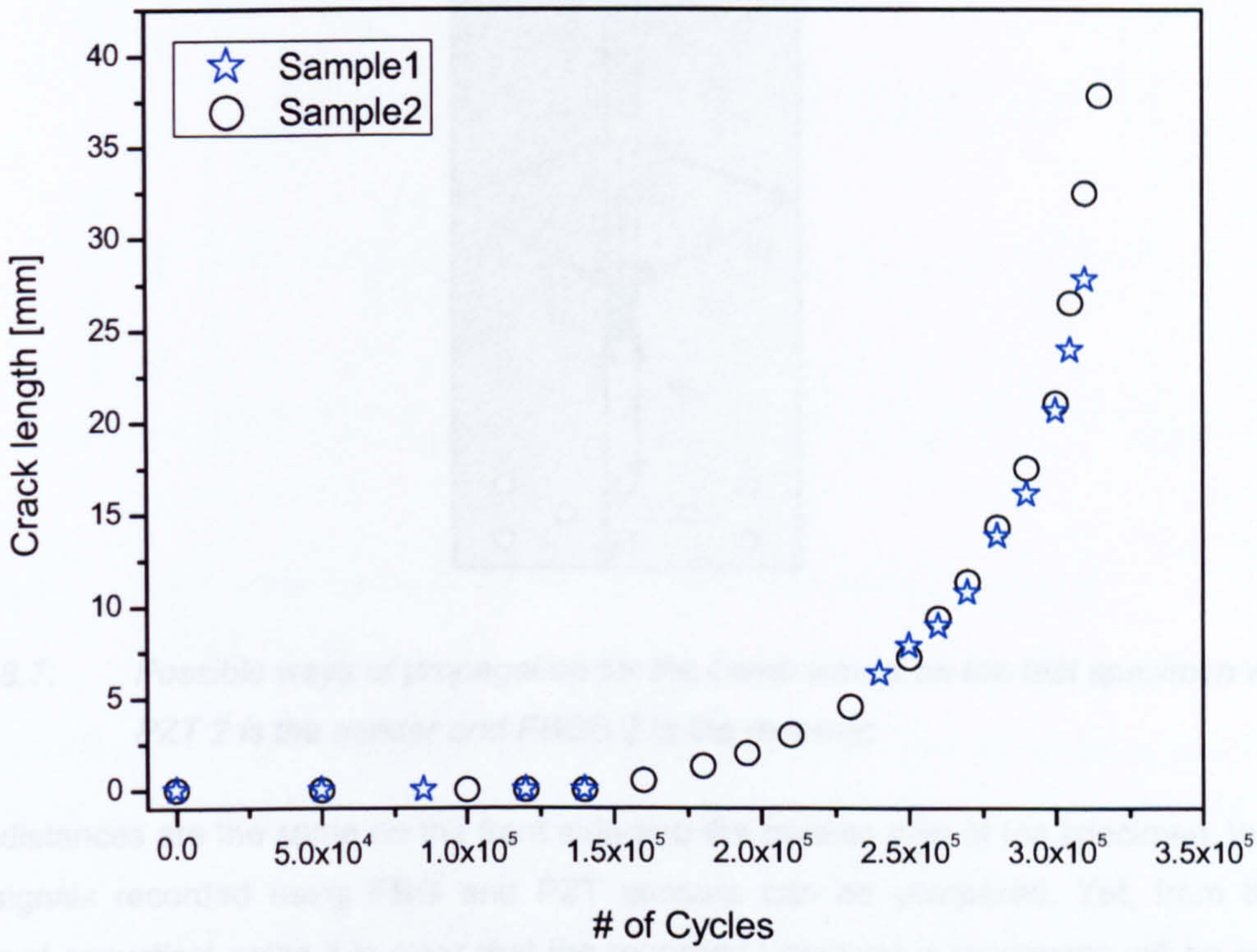

Figure 8.6: Crack propagation curve for both fatigue test specimens.

8.4.2 Analysis of the Lamb wave signals

The first step in analysing the Lamb wave data is to understand the Lamb wave propagation in the specimen. This allows the identification of each wave package within the recorded signal. According to what has been said in Chapter 7 the frequency of the Lamb wave was chosen to support the propagation of only the S_0 Lamb wave mode. The possible ways of propagation for the Lamb waves are displayed in Figure 8.7. The shortest distance is named d_1. This is the direct path from the source to the receiver, passing the notch and the expected crack. The distances d_2 and d_3 have equal length, they represent the reflections from the lateral face. The distances d_4 and d_5 are the reflection from the clamping holes, where multiple reflections can occur; d_4 and d_5 also have same lengths. The multiple reflections given by d_6 and d_7 come from the edges of the specimen. The distances for the different ways of propagation are the following: $d_1 \sim 60$ mm; $d_2 = d_3 = 160$ mm; $d_4 = d_5 = 300$ mm and $d_6 = d_7 = 400$ mm.

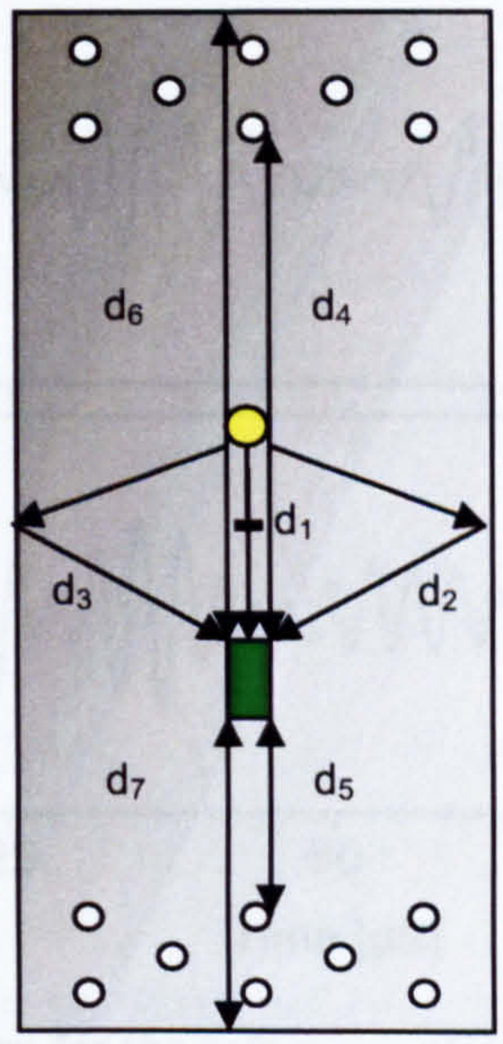

Figure 8.7: Possible ways of propagation for the Lamb waves on the test specimen when PZT 2 is the sender and FBGS 2 is the receiver.

As the distances are the same on the front side and the reverse side of the specimen, the Lamb wave signals recorded using FBG and PZT sensors can be compared. Yet, from the high number of acoustical paths it is clear that the recorded Lamb wave responses will be complex. In addition, due to the presence of propagation ways of equal length some of the waves interfere at the sensor location. This means if the symmetry is not perfect due to minor misalignments when mounting the sensors, it can be expected that not all the signals for PZT and FBG sensors are similar.

Figure 8.8 presents the Lamb wave signal of the plate in a no-damage condition recorded using a PZT and FBG receiver. The excitation signal had a frequency of 300 kHz. A 4.5 cycle tone burst signal was used, as for the experiments in Chapter 7. The individual wave packages can be identified and their time-of-flight (TOF) be calculated. The first package arrives at the PZT after the time-of-flight of 13 µs and slightly later at the FBGS after 16 µs. The second package arrives at approximately the same time for both sensors after 33 µs. Then there are different wave packages for each of the sensors. The third package for the FBGS arrives at 57 µs, and there is a smaller package at 77 µs. For the PZT the third package is at 61 µs whereas the fourth also arrives at 88 µs. The fourth package has a counterpart in the FBGS signal also at 88 µs.

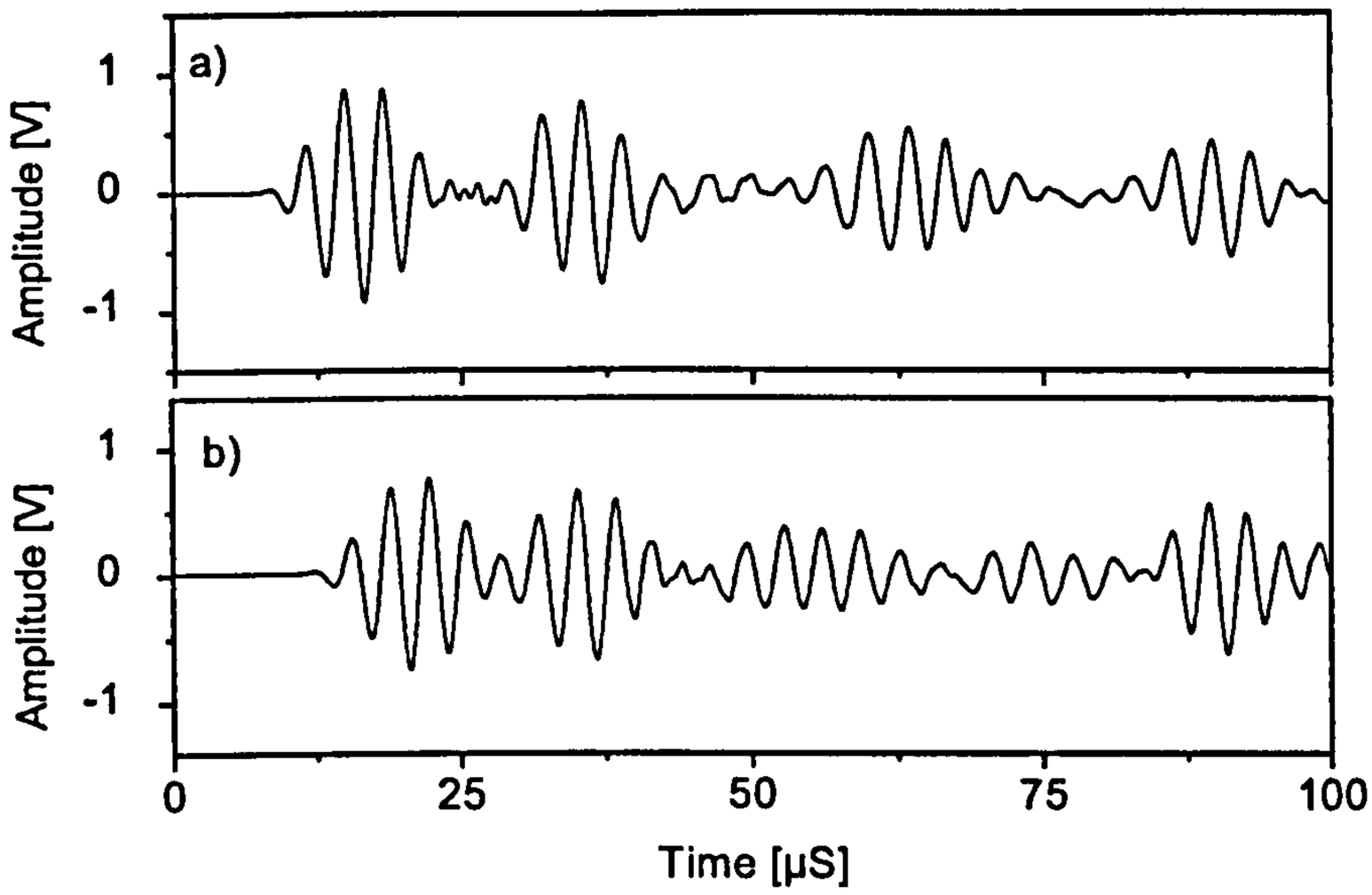

Figure 8.8: Lamb wave response for the reference state without any crack: a) PZT; b) FBGS.

The time-of-flight and the velocity of the S_0 mode (5000 m/s) can be used to calculate the distance the corresponding wave package travelled. As there is no mode conversion on the boundaries, the corresponding time-of-flight for the distances given in Figure 8.8 can be calculated. This allows the identification of the different packages and their propagation paths. The result is presented in Table 8.2. The first package is clearly identified as the incident S_0 Lamb wave mode travelling along path d_1. Furthermore, the second package is also identified for both receivers as the mode reflected on the edges of the plate. As two acoustical paths arrive at the same time, the second package is an interference signal. The third and fourth package are hard to identify for all signals. This is because there are several reflections from the clamping holes for each side of the plate. It is therefore understood that each sensor will give different signals, as the interference pattern for each sensor is different. It can be concluded that for analysing the Lamb wave data only the first two packages within the signal should be considered. The same is true when the second pair of ultrasonic transducers, PZT 1 and FBGS 1 is considered, as the analysis of the Lamb wave signals gives similar results.

Table 8.2: Identification of the Lamb wave packages.

FBGS	PZT	Acoustical path
16 µs	13 µs	d_1 = 12µs
34 µs	32 µs	d_2, d_3 = 32 µs
57 and 77 µs	61 µs	d_4, d_5 = 61 µs
88 µs	88 µs	d_6, d_7 = 80 µs

8.5 RESULTS

This section provides the results for both test specimens using FBG and PZT transducers. The evaluation of the Lamb wave signals follows the results presented in Chapter 7.3. There, a damage index based on the wave package analysis was introduced.

8.5.1 ANALYSIS OF SPECIMEN 1

Figure 8.9 shows a picture of the 30 mm crack taken after 310,000 cycles, when the specimen was removed from the fatigue test machine. As the detailed view of the crack reveals the crack started to grow at the desired locations at the edges of the initial notch. The direction of the crack propagation was perpendicular to the applied load. When calculating the crack length the size of the initial notch was neglected.

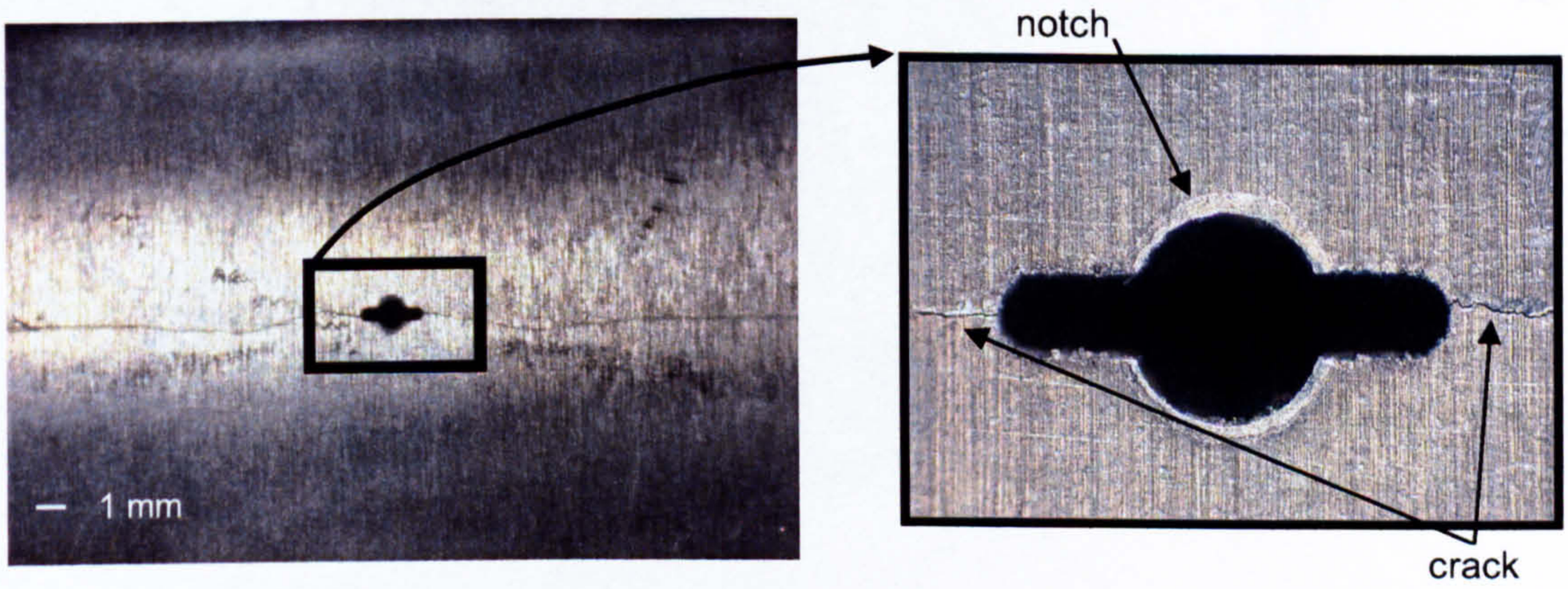

Figure 8.9: Photograph of specimen 1 and detailed view of the crack.

Analysis of the FBGS signals

A series of the recorded Lamb wave signals using the FBG sensors is presented in Figure 8.10. For this series, the acoustical path (a), as shown in Figure 8.2, has been evaluated. The graphs show the signals at distinctive points of the crack propagation curve. The first package decreases in amplitude with increasing number of cycles, whereas the second package is not much influenced. To see if this is a monotonic behaviour with the actual crack length, a detailed analysis of the signals using is necessary. A damage index based on the amplitude and time-of-flight of the first two packages is considered.

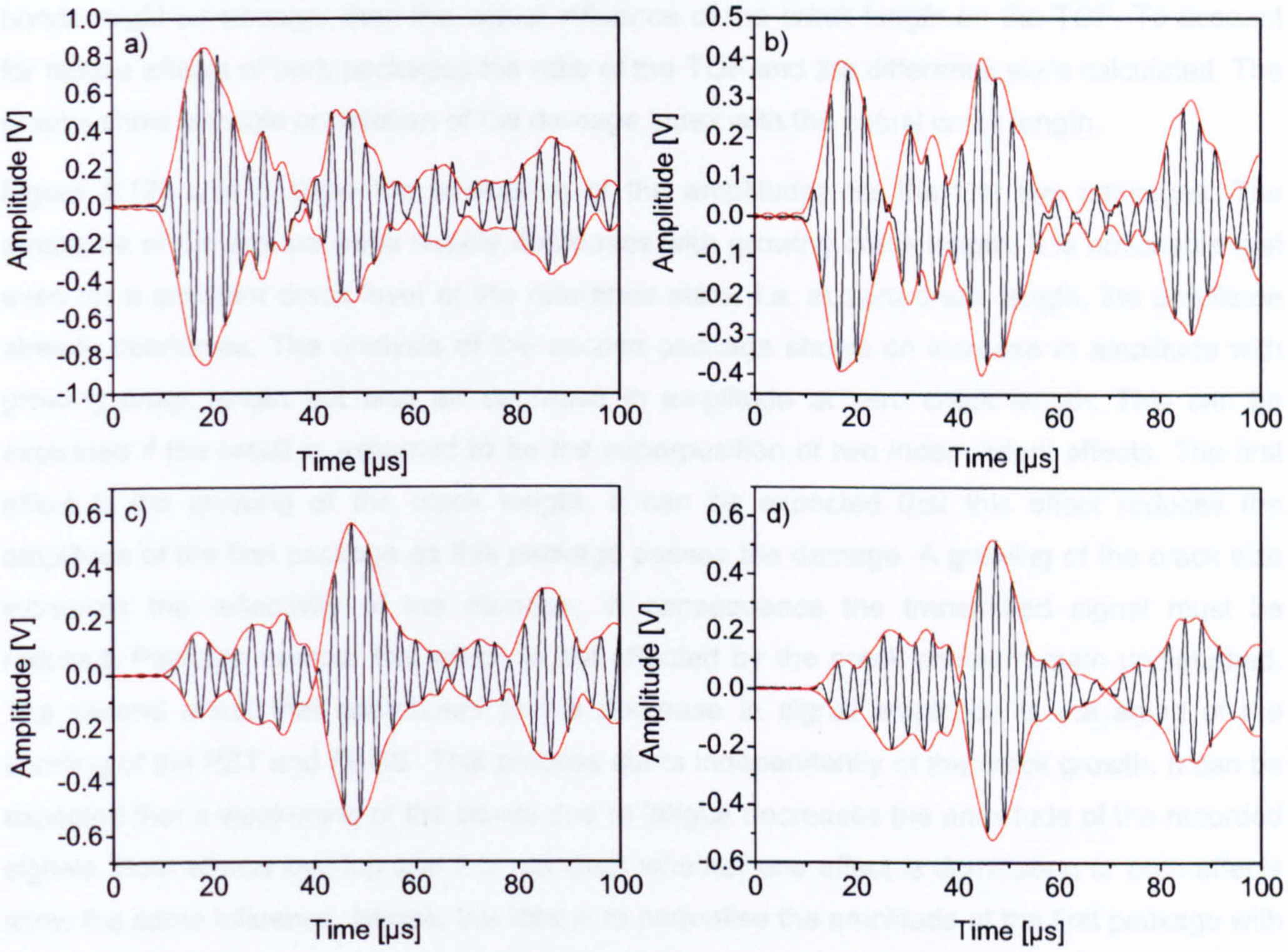

Figure 8.10: Lamb wave responses at different stages of the fatigue test: a) -0 cycles, crack length = 0 mm); b) 200,000 cycles, crack length = 2 mm; c) 300,000 cycles, crack = 21 mm; d) 310,000 cycles, crack = 32 mm.

Figure 8.11 presents the results of the time-of-flight (TOF) analysis for the first two packages.. The analysis of the TOF for the first package reveals a steadily growing delay in the arrival time with increasing crack length. There is however some deviation from this behaviour for small crack lengths below 5 mm. Looking at the second package a constant TOF can be found. Again for the starting region this observation doesn't hold. The delay of the first package and the constant TOF of the second package is expected theoretically. As the first package passes the damage, it will be slowed down by the increasing crack length, whereas the second, reflected package is not influenced by the crack. It is interesting to see that the deviation from the predicted behaviour in the starting region is equivalent for both packages. A possible explanation is that this deviation is due to aging effects of the bonding of PZT or FBG transducers. For the small crack length region up to 5 mm the structure was already subjected to 200,000 fatigue cycles. If this weakens the bonding of the actuators and receivers, a constant delay in the arrival of the signals could be expected. Furthermore, the effect of the aging of the

bonds might be stronger than the actual influence of the crack length on the TOF. To account for fatigue effects of both packages the ratio of the TOF and the difference were calculated. The graphs show a visible correlation of the damage index with the actual crack length.

Figure 8.12a and b show the evaluation of the amplitudes for the first two packages. The amplitude of the first package rapidly decreases with growing crack length. It is noticeable that even for a constant crack level at the reference state, i.e. at zero crack length, the amplitude already decreases. The analysis of the second package shows an increase in amplitude with growing crack length but also an decrease in amplitude at zero crack length. This can be explained if the result is assumed to be the superposition of two independent effects. The first effect is the growing of the crack length. It can be expected that this effect reduces the amplitude of the first package as this package passes the damage. A growing of the crack size increases the reflectivity of the damage, in consequence the transmitted signal must be reduced. Package number two which is not affected by the crack should remain undisturbed. The second effect that contributes to the decrease in signal amplitude is the aging of the bonding of the PZT and FBGS. This process starts independently of the crack growth. It can be expected that a weakening of the bonds due to fatigue decreases the amplitude of the recorded signals. Both effects overlap and it is not clear whether one effect is dominating or both effects show the same influence. Hence, the idea is to normalise the amplitude of the first package with respect to the second package. This should help to separate the aging effect from the effect of damage. The result of the normalisation is shown in Figure 8.11 c) and d). For the amplitude ratio there is visible correlation with the crack length for crack lengths larger than 10 mm. The amplitude difference still shows uncorrelated behaviour at zero crack length, there is however some correlation with the crack length even for lengths below 10 mm.

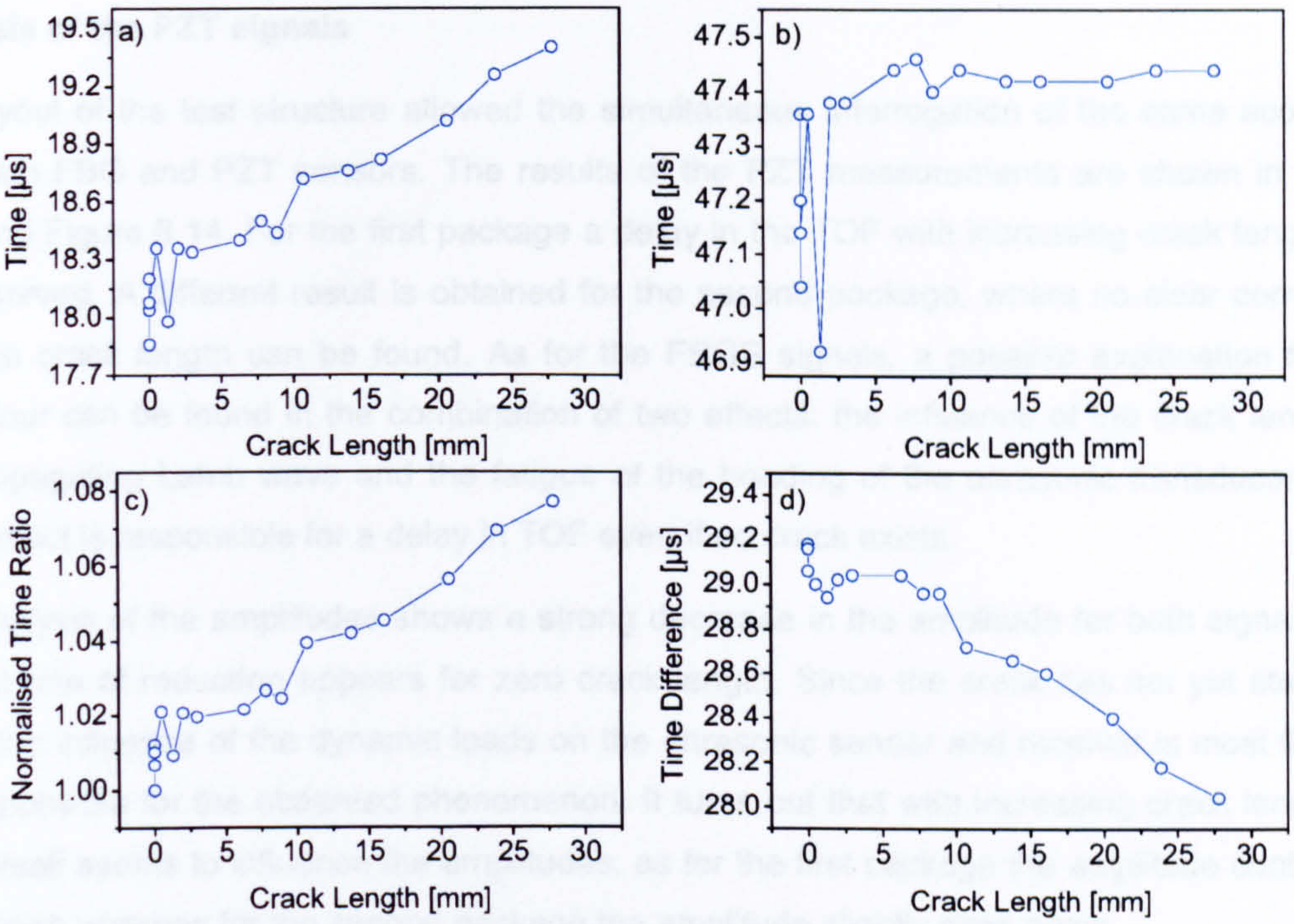

Figure 8.11: Analysis of the time-of-flight (TOF) information for the FBG sensors: a) TOF for the first package; b) TOF for the second package c) Ratio of TOF 2 to TOF 1; d) Difference of TOF 2 and TOF 1.

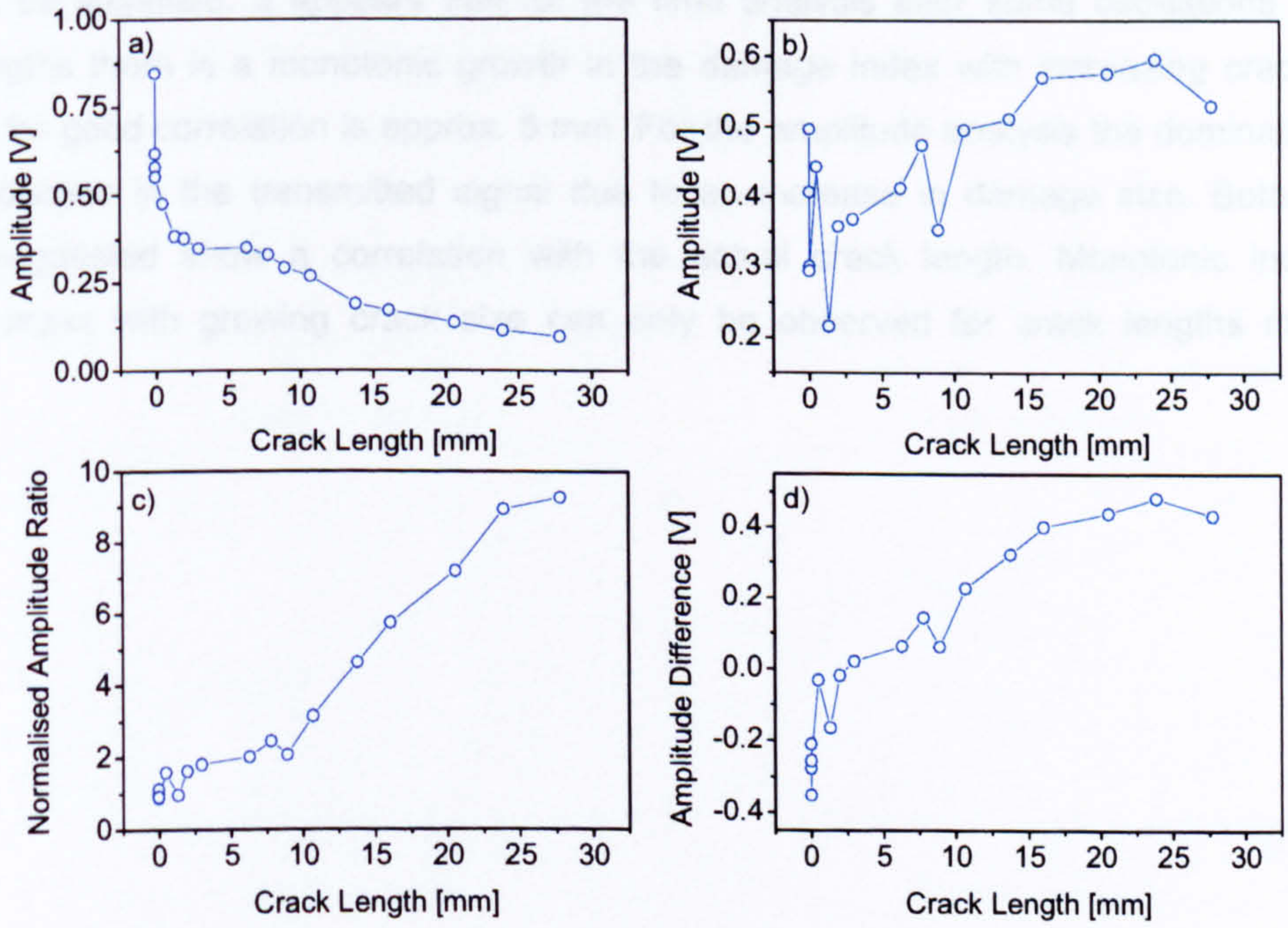

Figure 8.12: Analysis of the amplitude information for the FBG sensors: a) Amplitude of the first package (ampl 1); b) Amplitude of the second package (ampl 2); c) Ratio of ampl 2 to ampl 1; d) Difference of ampl 2 – ampl 1.

Analysis of the PZT signals

The layout of the test structure allowed the simultaneous interrogation of the same acoustical path with FBG and PZT sensors. The results of the PZT measurements are shown in Figure 8.13 and Figure 8.14. For the first package a delay in the TOF with increasing crack length can be observed. A different result is obtained for the second package, where no clear correlation with the crack length can be found. As for the FBGS signals, a possible explanation for this behaviour can be found in the combination of two effects: the influence of the crack length on the propagating Lamb wave and the fatigue of the bonding of the ultrasonic transducers. The latter effect is responsible for a delay in TOF even if no crack exists.

The analysis of the amplitudes shows a strong decrease in the amplitude for both signals. The highest rate of reduction appears for zero crack length. Since the crack has not yet started to grow, the influence of the dynamic loads on the ultrasonic sender and receiver is most likely to be responsible for the observed phenomenon. It turns out that with increasing crack length the crack itself seems to influence the amplitudes, as for the first package the amplitude continuous to diminish whereas for the second package the amplitude slightly rises again.

Comparing the results of the FBG and PZT sensor it appears that both transducers produce the same results. For both sensors the superposition of two effects, the aging of the bonding of the acoustical sender and receiver and the influence of the crack length on the amplitude and the TOF can be identified. It appears that for the time analysis after some oscillations for small crack lengths there is a monotonic growth in the damage index with increasing crack length. The limit for good correlation is approx. 5 mm. For the amplitude analysis the dominating effect is the reduction in the transmitted signal due to an increase in damage size. Both damage indices suggested show a correlation with the actual crack length. Monotonic increase in damage index with growing crack size can only be observed for crack lengths more than 10 mm.

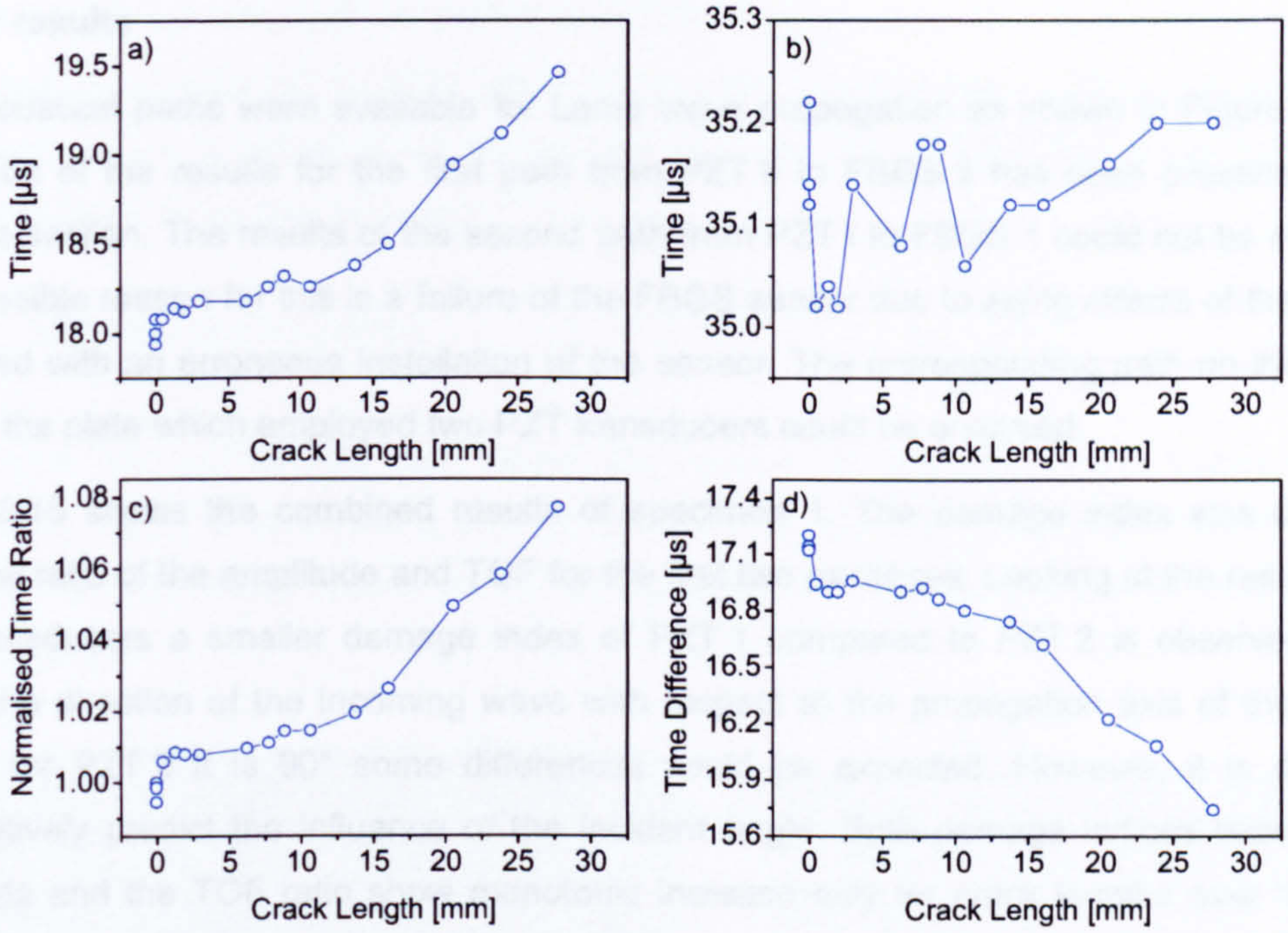

Figure 8.13: Analysis of the time-of-flight (TOF) information for the PZT receivers: a) TOF for the first package; b) TOF for the second package c) Ratio of TOF 2 to TOF 1; d) Difference of TOF 2 and TOF 1.

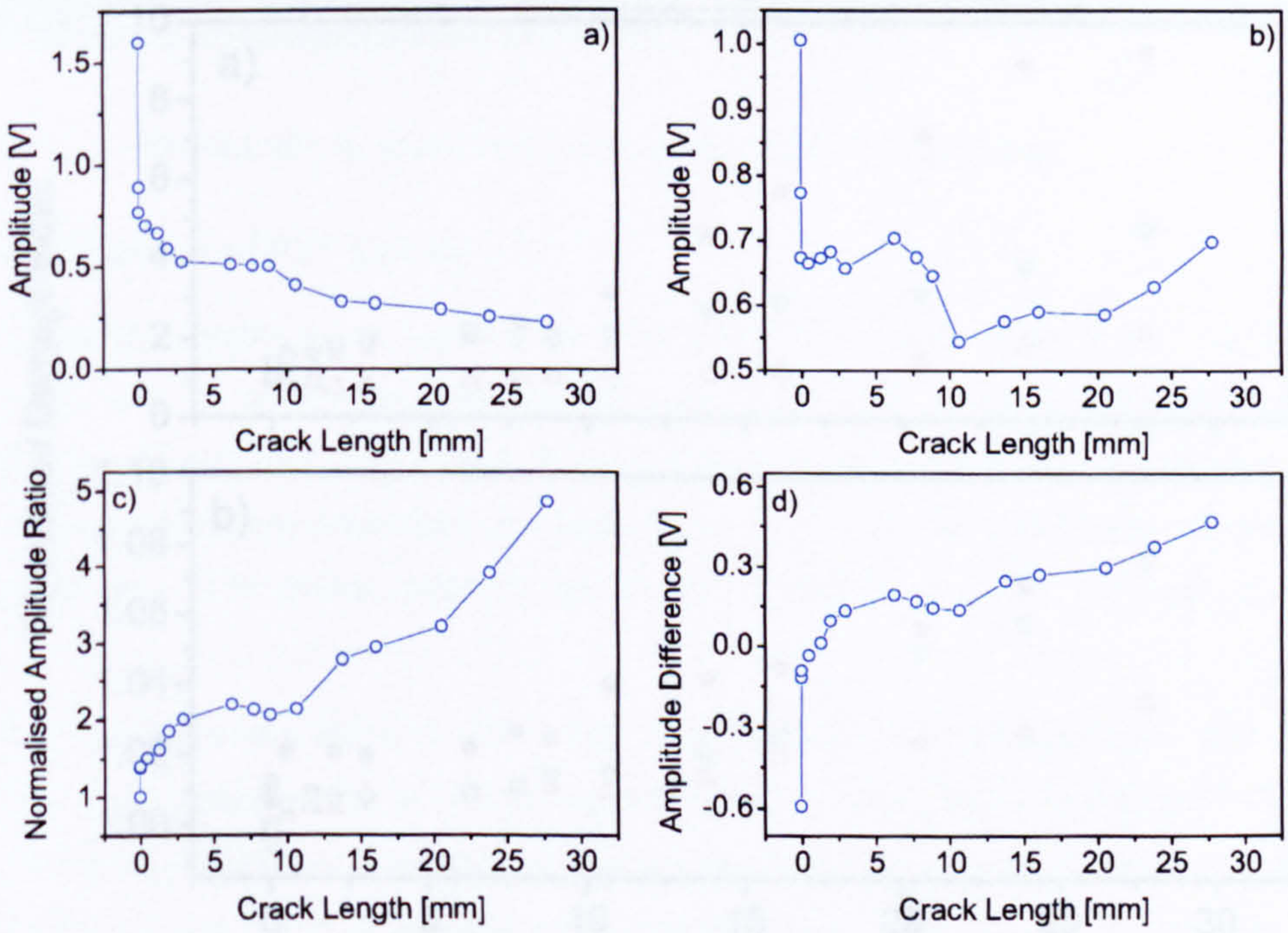

Figure 8.14: Analysis of the amplitude information for the PZT receivers: a) Amplitude of the first package (ampl 1); b) Amplitude of the second package (ampl 2); c) Ratio of ampl 2 to ampl 1; d) Difference of ampl 2 – ampl 1.

Further results

Two acoustical paths were available for Lamb wave propagation as shown in Figure 8.2. The evaluation of the results for the first path from PZT II to FBGS 2 has been presented in the previous section. The results of the second path from PZT I to FBGS 1 could not be evaluated. One possible reason for this is a failure of the FBGS sensor due to aging effects of the bonding combined with an erroneous installation of the sensor. The corresponding path on the reverse side on the plate which employed two PZT transducers could be analysed.

Figure 8.15 shows the combined results of specimen 1. The damage index was calculated using the ratio of the amplitude and TOF for the first two packages. Looking at the results of the PZT transducers a smaller damage index of PZT 1 compared to PZT 2 is observed. As for PZT 1 the direction of the incoming wave with respect to the propagation axis of the crack is 45°and for PZT 2 it is 90° some differences could be expected. However, it is difficult to quantitatively predict the influence of the incident angle. Both damage indices based on the amplitude and the TOF ratio show monotonic increase only for crack lengths over 10 mm. A possible explanation of this minimum detectable crack length is that only for crack lengths longer than 10 mm the effect of crack size dominates the aging effect of the bonding of the PZT and FBGS receivers.

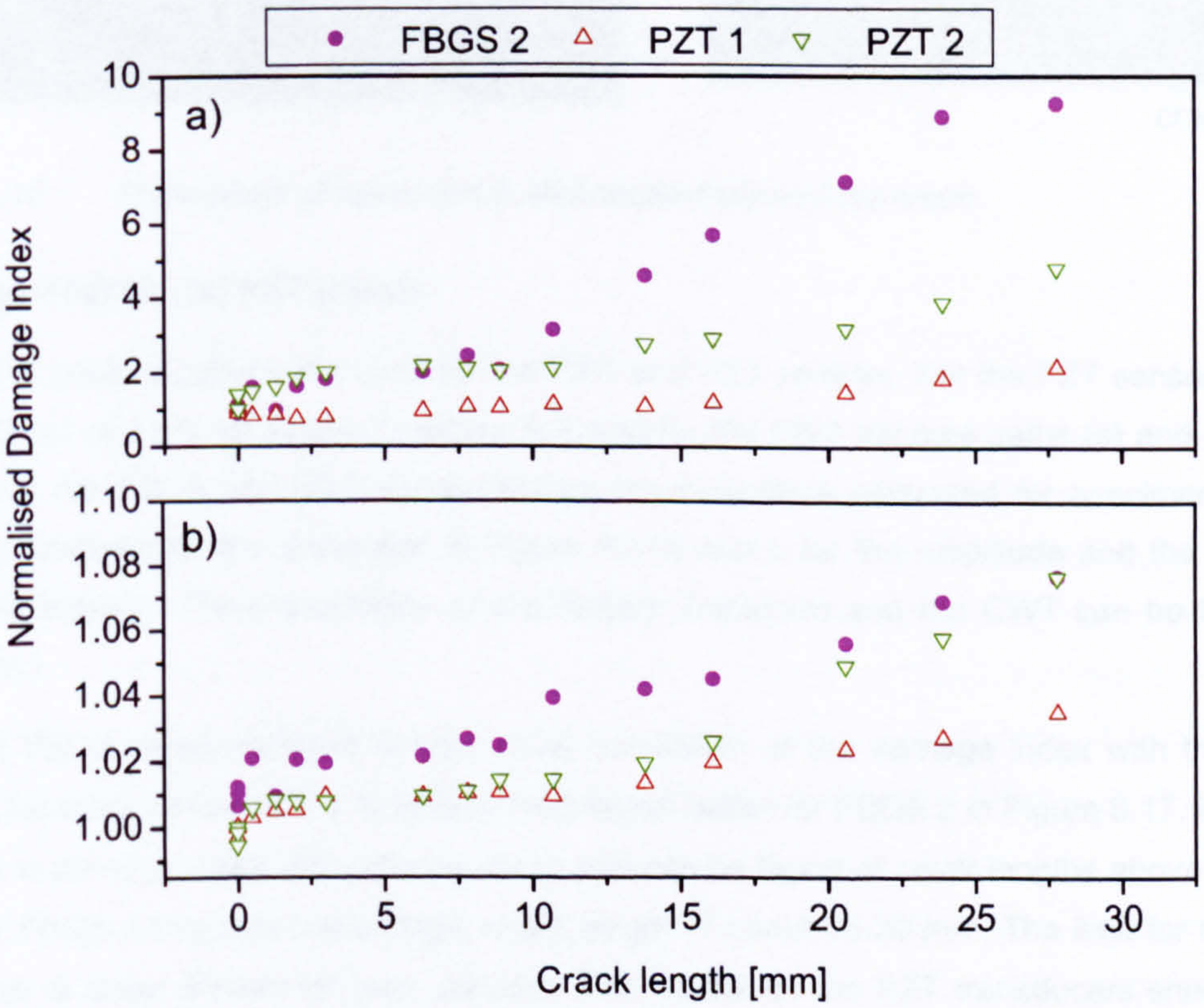

Figure 8.15: Damage Index for specimen 1 obtained from wave package evaluation as a function of crack length: a) Amplitude ratio; b) Time ratio.

In general good agreement of the FBGS and PZT ultrasonic receiver was observed. A damage index could be established for both types of receivers. The damage index shows good visible correlation with the actual crack length. However, a lower limit for the minimum detectable crack length was found to be approximately 10 mm.

8.5.2 ANALYSIS OF SPECIMEN 2

The fatigue test carried out to analyse the fatigue of specimen 1 was repeated using specimen 2. Figure 8.16 shows a photograph of the crack. The photograph reveals that the crack did not grow perpendicular to the load axis, but at an angle of 75° with respect to the loading direction.

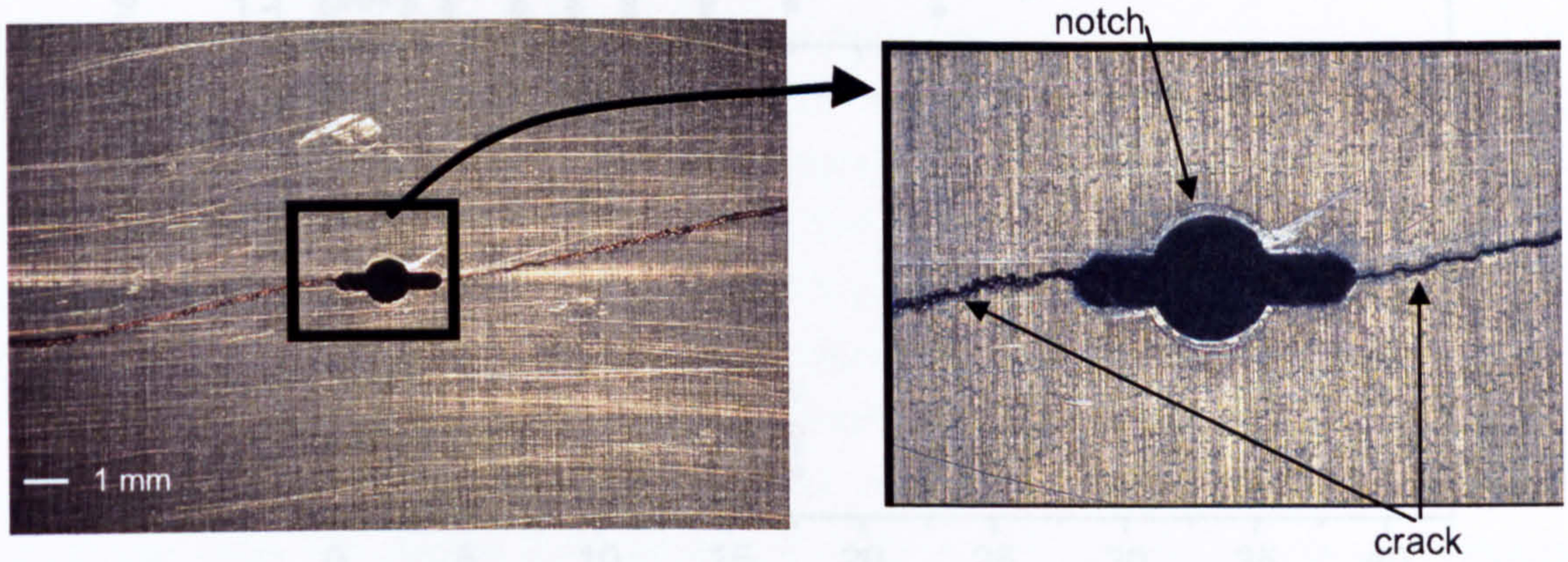

Figure 8.16: Photograph of specimen 2 and detailed view of the crack.

Analysis of FBGS and PZT signals

Different acoustical paths were used for the FBG and PZT sensors. For the PZT sensors these are paths (a) and (b), as shown in Figure 8.2, and for the FBG sensors paths (c) and (d). The analysis of the FBGS and PZT signals follows the evaluation presented for specimen 1. The results of evaluations are presented in Figure 8.17a and b for the amplitude and the time-of-flight, respectively. The presentation of the Hilbert Transform and the CWT can be found in Appendix J.

For both FBGS receivers there is only small correlation of the damage index with the crack length. The index based on the amplitude ratio works better for FBGS 2 in Figure 8.17. Here, an increase in damage index with growing crack size can be found at crack lengths above 15 mm. while for FBGS 1 this starts at a larger crack length of about 25-30 mm. The limit for the TOF evaluation is about 30 mm for both sensors. The results for the PZT transducers show better correlation to the crack length than the FBG sensors. The minimum crack length before a monotonic increase in damage index with increasing crack length can be observed, is smaller

than for the FBG sensors. This limit is found at about 15 mm crack length, only for PZT 2 there is a trend for the TOF evaluation that this limit is significantly lower at 5 mm. Furthermore, for PZT 1 and amplitude evaluation a saturation of the damage index above 35 mm crack length can be noticed.

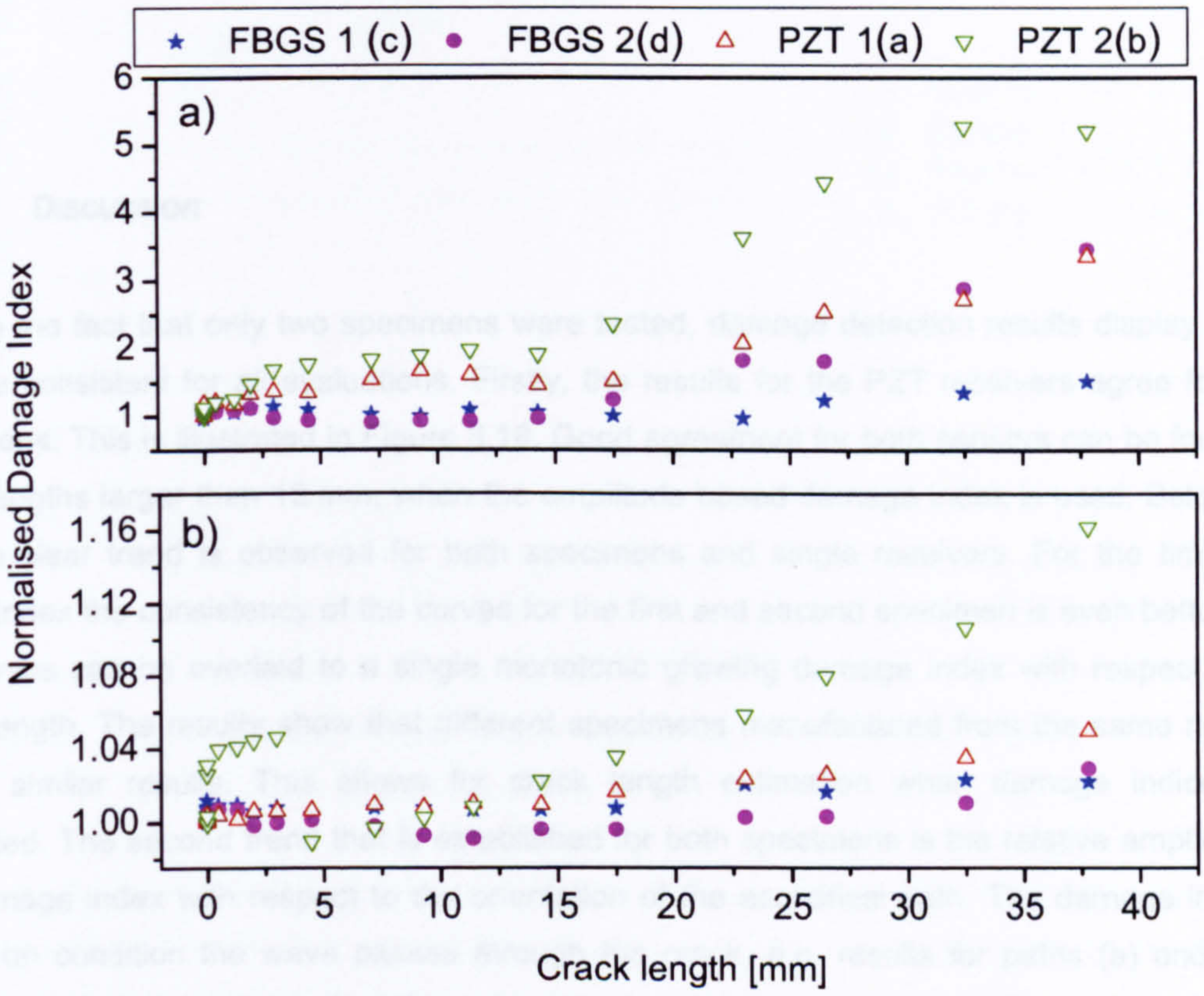

Figure 8.17: Damage Index for specimen 2 obtained from wave package evaluation as a function of the crack length: a) Amplitude ratio; b) Time ratio.

The results reflect the different acoustical arrangements for both types of sensors. The damage index for the PZT receiver starts much earlier to grow than the one for the corresponding FBGS. This can be understood, as the waves for the PZT transducers always pass through the crack, whereas for the FBG sensors, this is true only after a crack length of 30 mm.. As for the first specimen the damage index of the PZT also doesn't start to correlate with the crack length before a minimum crack length is reached. A possible explanation for a lower limit could be the domination of the aging effects in the low cycle and low crack length regime, as explained in Section 8.5.1.

As the two acoustical paths differ in their orientation to the crack direction a different damage index level is expected. The damage index for the path perpendicular to the crack is relatively higher than the one for the other path. Only for the time ratio based index and the FBGS receivers no such a difference can be observed.

From the amplitude and time signals for each individual receiver, the same conclusions as for specimen 1 can be drawn. A superposition of two effects takes place: the aging of the bonding of the acoustical sender and receiver and the influence of the crack length on the amplitude and the time-of-flight.

8.5.3 Discussion

Despite the fact that only two specimens were tested, damage detection results display trends that are consistent for all evaluations. Firstly, the results for the PZT receivers agree for both specimens. This is illustrated in Figure 8.18. Good agreement for both sensors can be found for crack lengths larger than 15 mm, when the amplitude based damage index is used. Below that limit no clear trend is observed for both specimens and single receivers. For the time ratio based index the consistency of the curves for the first and second specimen is even better. The two curves can be overlaid to a single monotonic growing damage index with respect to the crack length. The results show that different specimens manufactured from the same material exhibit similar results. This allows for crack length estimation when damage indices are calibrated. The second trend that is established for both specimens is the relative amplitude of the damage index with respect to the orientation of the acoustical path. The damage index is higher on condition the wave passes through the crack, e.g. results for paths (a) and (b) in Figure 8.2 will be better than that for paths (c) and (d) for small crack lengths. This means the positioning of the ultrasonic senders and receivers is important to get optimum damage indication levels.

Yet, what is also consistent to both specimens, is that there is no good correlation of damage index and crack length in the small crack length region. There is non-monotonic behaviour in the damage index which cannot be explained, but might be simply the effect of noise on the measurement. The study shows that it is important to understand the physics behind wave propagation and wave interaction with damage. Further theoretical and experimental investigations are required to quantitatively describe the influence of the angle of the incident wave on the damage index. In addition, a study of the influence of the aging effects of the ultrasonic sender and receiver would be necessary to distinguish between these effects and damage.

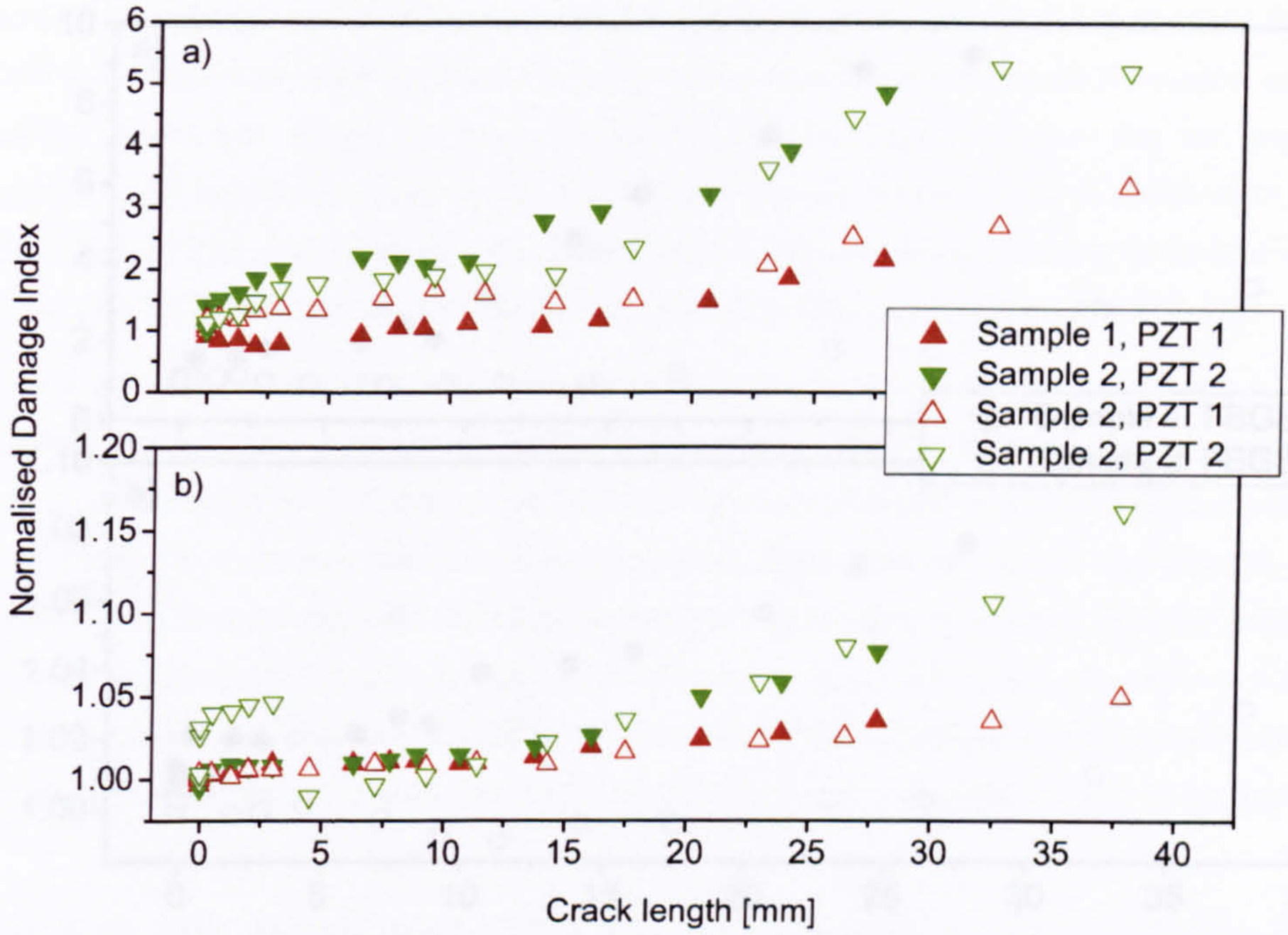

Figure 8.18: Damage index for specimens 1 and 2 and PZT receivers 1 and 2: a) Amplitude ratio; b) Time ratio.

Due to the failure of FBGS 1 on the first specimen, only one Bragg sensor can be compared for both specimens. The result is presented in Figure 8.19, where different values of the damage index can be observed for both specimens. The monotonic behaviour for specimen 1 and 2 can be observed after 10 and 30 mm, respectively. This can be explained when propagation paths are analysed. For specimen 1 the Lamb wave always passes the crack, whereas for specimen 2 the crack has to grow to about 30 mm before any interaction between Lamb wave and the fault can be expected. As for the PZT there is no unambiguous trend below the minimum crack length for which the correlation with the crack length starts. It is not clear whether the fluctuations in the damage index come from experimental errors or if they are related to other phenomena of the Lamb wave detection.

In conclusion, the results from the fatigue test show good consistency of the FBG and PZT receivers. This means, FBG sensors could be used in addition or instead of PZT transducers for the sensing of ultrasonic Lamb wave signals. Any signal processing tools that have been or will be established for PZT could be adapted for the analysis of FBGS signals. Furthermore, the proposed damage index based on the analysis of the first two Lamb wave packages showed good correlation with the actual crack length, if a minimum crack length is passed.

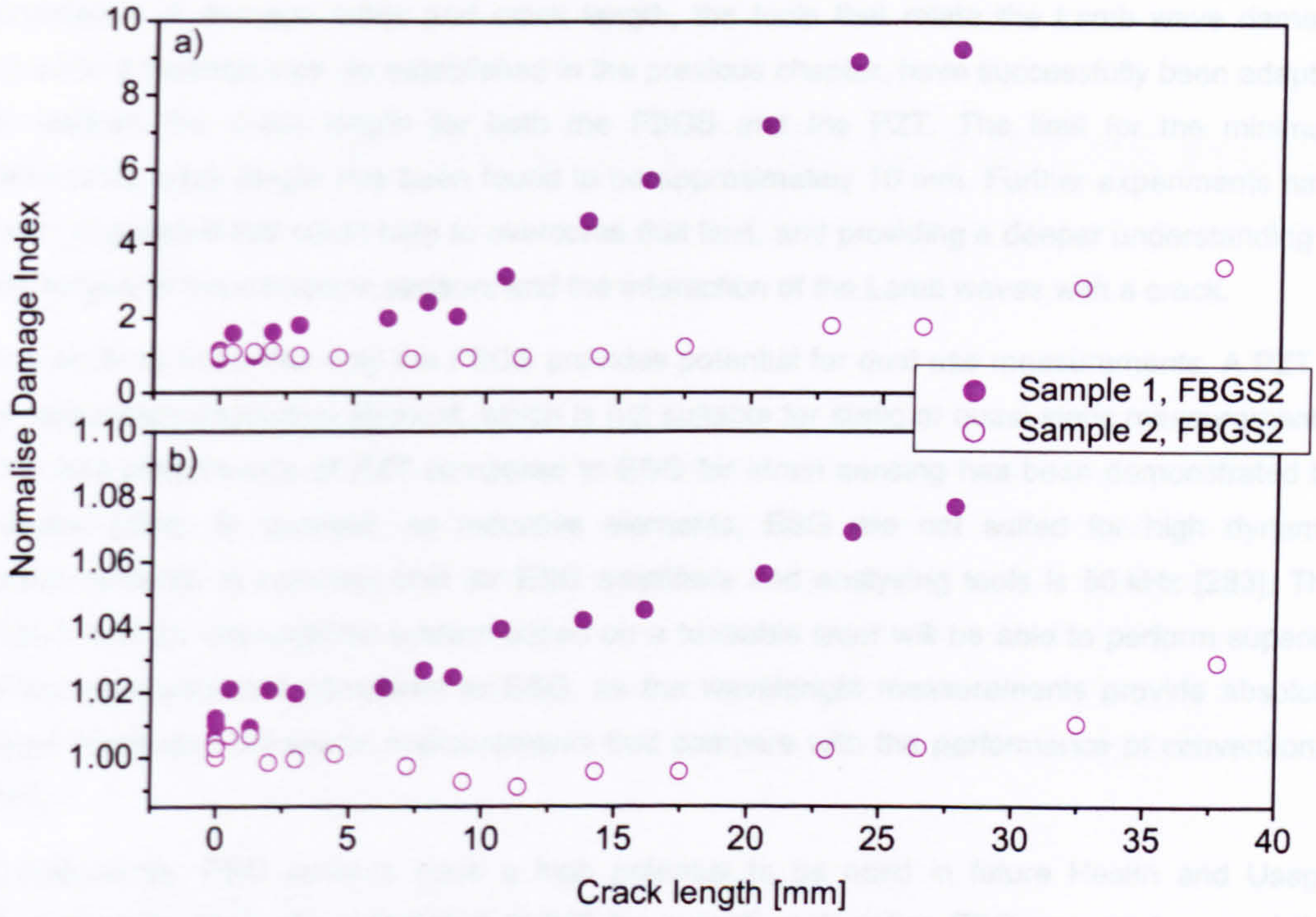

Figure 8.19: Damage index for specimens 1 and 2 and FBG sensor 2: a) Amplitude ratio; b) Time ratio.

8.6 Conclusions

This chapter has explored the application of Bragg grating sensors for fatigue analysis. The Bragg grating sensor offers the unique advantage of determining both essential parameters for a Health and Usage Monitoring System: loads and crack length. A test was conducted where the multifunctionality of Bragg grating sensors was used to gather the strains that occurred during the fatigue test, and for sensing ultrasonic Lamb waves in order to predict the crack length. Alternative sensors were available to compare the results of the FBG sensors with the conventional methods. An electrical strain gage was used for measuring the loads and a PZT transducer was used to sense the ultrasonic signals. The test demonstrated the feasibility of the Bragg grating sensor to be used a dual strain and ultrasonic sensor. The load monitoring experiment yielded similar results for the strain gage and the FBG sensors with respect to amplitude and frequency analysis. The same FBG sensors then produced consistent Lamb wave signals with the signals recorded by a conventional PZT. In order to demonstrate the

correlation of damage index and crack length, the tools that relate the Lamb wave damage index to a damage size, as established in the previous chapter, have successfully been adapted to indicate the crack length for both the FBGS and the PZT. The limit for the minimum detectable crack length has been found to be approximately 10 mm. Further experiments have been suggested that could help to overcome that limit, and providing a deeper understanding of the fatigue of the ultrasonic sensors and the interaction of the Lamb waves with a crack.

It is worth to note, that only the FBGS provides potential for dual use measurements. A PZT is an electrically capacitive element, which is not suitable for static or quasi-static measurements- The bad performance of PZT compared to ESG for strain sensing has been demonstrated by Kessler [164]. In contrast, as inductive elements, ESG are not suited for high dynamic measurements. A common limit for ESG amplifiers and analysing tools is 50 kHz [283]. The FBGS with an interrogation system based on a tuneable laser will be able to perform superior strain measurements compared to ESG, as the wavelength measurements provide absolute strain levels and ultrasonic measurements that compare with the performance of conventional PZT.

Consequently, FBG sensors have a high potential to be used in future Health and Usage Monitoring Systems. An automated HUMS for aircraft could utilise FBG sensors to record the load history on every flight. After each flight, the relevant parts of the structure could be monitored using the Lamb wave method. From these ultrasonic signals the position and severity of damage could be established. This combined load/damage information could lead to a prediction of the remaining fatigue life if the same load spectrum as on the previous flight is assumed. The load spectrum used for calculating the remaining life can be adapted after every flight. The advantage using FBGS in addition to other advantages of fibre optic sensors, is that only one sensor and also only one sensor interrogation system needs to be used to perform the dual loads and crack growth monitoring. Therefore saving installation weight, time and money, provided the fibre optic system compares to the conventional strain gage or ultrasonic systems with respect to weight, size and price. It should be noted, that there is still an ultrasonic sender required, to launch the ultrasonic Lamb waves that will be detected using the FBGS.

9 CONCLUSIONS AND FUTURE WORK

The work presented in this thesis has demonstrated the ability of fibre optic Bragg gratings to be used as either high precision strain sensors or broadband ultrasonic receivers. Motivation for a Structural Health and Usage Monitoring system based on multifunctional FBG sensors has been given. The requirements for the implementation and application of such a load monitoring and damage detection system have been discussed. This chapter draws conclusions from the analytical and experimental work presented in this thesis and presents recommendations for further experimentation in this field.

9.1 REVIEW OF THESIS

The thesis has investigated the use of fibre Bragg grating sensors for Structural Health and Usage Monitoring. Several fundamental areas on the interaction of FBG sensors with structural conditions have been addressed analytically and experimentally.

In chapter 2, the fibre Bragg grating was introduced as a multifunctional sensing element. The chapter provided an overview of the state of the art for Bragg gratings sensors. The requirements on the sensor and the fibre for industrial applications were discussed, and the use of draw-tower gratings was suggested.

Chapter 3 presented the motivations for monitoring the loads of engineering structures, especially for aerospace applications. Conventional techniques for load monitoring based on strain measurements were compared to the FBGS. Although the use of FBGS for experimental strain analysis has been extensively discussed in the literature, this work added new approaches towards the implementation of large area FBGS networks using fibre optical rosettes and temperature compensated strain sensors.

Chapter 4 provided an overview of current NDT/E technologies. An introduction into damage detection based on Lamb wave methods was given. The state-of-the-art for optical detection and generation of ultrasound was presented.

The first successful detection of Lamb waves using FBG sensors was described in Chapter 5. The theoretical approach that led to the development of an appropriate ultrasonic interrogation system for FBGS was introduced. Numerical simulations on the influence of the grating dimensions on its ability to detect ultrasonic strain fields and their experimental validation were presented. A simple fibre optic smart structure, i.e. a composite sample with embedded FBG sensors, was presented. For the first time embedded fibre sensors were used for Lamb wave detection.

Chapter 6 presented signal processing tools that could be applied to the Lamb wave signals for signal conditioning and signal analysis. The use of traditional techniques, such as frequency analysis and novel approaches, such as wavelet analysis were applied to a simple reference signal. The methods could then be transferred to more complex signals obtained from experimental data in the subsequent chapters.

FBG ultrasonic sensors have been applied to experimental identification of damage in Chapter 7. Three different tasks of damage identification were considered: detection of damage, localisation of damage and severity of damage. Experimental results on all three tasks were presented and compared to the results of conventional PZT receivers. As part of this experimental work, a reliable, temperature independent damage index was introduced and a novel detection scheme using fibre Bragg grating rosettes and a genetic algorithm for the localisation of damage was developed

In Chapter 8 the findings of the previous chapters culminated in a demonstrator on which the dual load monitoring and damage detection capabilities of the FBG sensors were demonstrated. The chapter presented the results of a simple fatigue test experiment on which the FBG sensors were used to measure the load parameters and the crack size.

9.2 Summary of Findings

This section gives a brief overview of the findings presented within this thesis. For further reading the list of publications that have been published during the presented work is given in Appendix K.

9.2.1 FBG Sensors for Load monitoring

The use of fibre Bragg grating rosettes for the evaluation of structural loading conditions is well known in the literature. The rosette normally needs to be prearranged on a backing patch for proper alignment of the sensors axes. In addition to the strain sensing gratings the mounting of

a temperature sensor has been proposed for compensating the thermal drift of the strain sensors. In this work a new, miniaturised build-up technique for the temperature sensor has been demonstrated which allows multiplexing of several strain and temperature sensors within a single fibre network. The use of a backing patch for FBG sensors has been investigated numerically and experimentally. It appears that thickness and Young's modulus of the backing material determine the characteristics of the strain transfer. Only thin and stiff materials will couple the strain from the structure to the fibre core. A decrease in strain transfer down to 86 % of the original value has been calculated depending on the material properties. A reduction to 96 % has been found experimentally, indicating that some parametric errors could be within the numerical simulations. The importance of the correct choice of the backing material has been highlighted.

9.2.2 FBG Sensors for Lamb Wave Sensing

An interrogation system for ultrasonic sensing using FBG sensors has been proposed. The system is based on a tuneable laser which can be driven in a scanning mode for high resolution spectral measurements or in a fixed-tuning mode in order to allow high dynamic ultrasonic measurements. The mathematical description of the sensor function has been derived. The optical interrogation system has been characterised and calibrated. It has been shown that the system can detect Lamb wave signals in plate like structures, and is competitive in its specifications with standard PZT technology. The SNR for single shot has been shown to be 13 dB on a Perspex plate and 15 dB on an aluminium plate, which agrees well with the findings for standard PZT. Two initial experiments have demonstrated the capability of the FBG sensor to detect Lamb waves either in a surface mounted or structural integrated configuration. However, it appears that if the FBG is integrated in the mid-plane of the plate, it is sensitive only to the symmetric Lamb mode.

Numerical simulations of the response of the FBG sensors to an ultrasonic strain field have shown the influence of the ratio of grating length to acoustical wavelength on the sensor function. The result indicates that the acoustical wavelength should be 4 times the grating length. As the fabrication limit for the minimum grating length is about 1 mm this means the acoustical wavelength should be more than 4 mm for the fibre optic sensor. The numerical findings have been validated experimentally.

9.2.3 FBG Sensors for Damage Identification

A novel approach for the localisation of damage has been proposed. This approach makes use of the directivity of the FBG. By mounting the FBG in a rosette, the directivity characteristics of

the gratings can be used to determine the direction of the incoming acoustic wave. Genetic Algorithms have been implemented to calculate the location of damage on an aluminium plate. It has been shown that this method is capable of detecting and locating a hole of 12 mm diameter within a monitored area of 50 x 50 cm. This type of damage location technique is reserved for FBG sensors as circular PZT do not possess the required directivity, which makes the corresponding procedure very complex.

Recent developments of signal processing tools have been applied to the recorded Lamb waves signals in order to extract a reliable feature that could serve as a damage index. The best parameter found is based on the analysis of the amplitude and time of flight of the first two arriving Lamb wave packages. This damage index has good correlation with the actual damage size. It turned out that the damage index based on the time and amplitude of the Lamb wave packages has minimum cross sensitivity due to temperature. It has been shown that the minimum resolvable damage size is 3 mm if the temperature effects are taken into account. It has been concluded that FBG sensors perform equally well as the more common piezoceramic transducers, but offer superior performance for the proposed damage location scheme.

9.2.4 Multifunctional FBG Sensors for Load monitoring and Damage Detection

A fatigue test of a simple metal plate has been conducted where Bragg grating sensors were used for recording the strains that occurred during the fatigue test and for recording ultrasonic Lamb waves in order to predict the crack length. The results indicated the feasibility of the Bragg grating sensor to be used as a multifunctional strain and ultrasonic sensor. The load monitoring experiment yielded similar results for the electrical strain gage and the FBGS with respect to amplitude and frequency analysis. The same FBGS then produced consistent Lamb wave signals with the signals recorded by a conventional PZT. Both receivers showed good correlation of damage index with actual crack length. The practical implementation of such measurements could be an accurate lifetime prediction of the structure based on the actual loads and crack lengths.

9.3 Future Work

This thesis has investigated some basic concepts for a dual use of FBGS for load monitoring and damage detection. Several topics have been covered in some detail, and in this section future work in these fields is proposed.

9.3.1 FBG Sensors for Load monitoring

The proposed layout of the temperature compensated rosette needs experimental validation, under superimposed mechanical and thermal loads. From this experiments error limits could be derived to determine the temperature and strain accuracy of the FBG sensor.

The strain transfer functions of the FE model need further experimental validation. In this work only one combination of backing thickness and Young's modulus could be tested. Further tests with different materials could help to find a practical solution for which the backing patch does not affect the calibrated strain sensitivity of a bare fibre.

9.3.2 FBG Sensors for Damage Identification

In the work described here, all damage identification tests were performed on simple plates made of isotropic materials such as Perspex and aluminium. The proposed damage index needs further investigation for anisotropic materials such as composites, in order to proof good correlation between damage index and severity of damage, e.g. crack length. As composites become more and more important in the aerospace and automotive industry, answers have to be found to see if the proposed damage index could be adapted to composite materials.

The damage index proposed in this work compares the signals of a wave that has interacted with the damage and a wave that has been reflected from a boundary and has not interacted with the damage. This detection scheme requires the presence of boundaries, which in practical applications might not always exist. Therefore, another approach that should be tested is to use two FBGS receivers. One that is located close to the ultrasonic source and detects the wave before it interacts with the damage and the second on further away from the source, which detects the wave after the interaction with the damage. Because of the multiplexing capabilities of the FBGS a second ultrasonic receiver could be easily added. The use of two receivers requires further analytical and experimental investigation.

9.3.3 Multifunctional FBG Sensors for Load monitoring and Damage Detection

One of the major advantages of FBG sensors in Structural Health and Usage Monitoring Systems is their multifunctionality. This work proposed an interrogation scheme based on a tuneable laser which could operate in two modes: scanning and locked onto a single wavelength. For the experiments carried out within this work, two different lasers were used, one for the scanning mode and one for the lock mode. The reason is that no laser was available that could be operated in a fast scanning mode and high stability wavelength lock mode. By the end of this work, a tuneable laser has become available that could be operated in both modes

[284, 285]. Based on this laser, a software controlled interrogation system could be build-up that could switch from load monitoring to damage detection by a simple mouse-click. This needs of course experimental validation.

The fibre sensors that were used in the fatigue test were directly bonded onto the surface of the material. As a backing patch was proposed for installation of fibre rosettes, the use of a backing patch for an ultrasonic FBGS should also be considered. However, to understand the effect of the backing material on the propagation and coupling of the Lamb waves, a numerical study, e.g. FE modelling or experimental investigations is required.

REFERENCES

[1] H. G. Natke and C. Campel, *Model-Based Diagnosis of Mechanical Systems*. Springer, 1997.

[2] S. W. Doebling, C. R. Farrar, M. B. Prime, and D. Shevitz, "Damage identification and health monitoring of structural and mechanical systems from changes in their vibration characteristics," Los Alamos National Lab., Tech. Report LA-13070, 1996.

[3] A. Ryther, *Vibration Based Inspection of Civil Engineering Structures*, PhD Thesis, Aalborg University, 1993.

[4] F.-K. Chang, *Structural Health Monitoring 2000: Proceedings of the 2nd International Workshop on Structural Health Monitoring 1999*. Technomic Publishing Company Inc., Stanford University, Stanford, CA, 2000.

[5] F.-K. Chang, *Structural Health Monitoring, the Demands and Challenges: Proceedings of the 3rd International Workshop on Structural Health Monitoring*. SRC Publications, Stanford University, Stanford, CA, 2001.

[6] F.-K. Chang, *Structural Health Monitoring 2003: Proceedings of the 4th International Workshop on Structural Health Monitoring*. DESTech Publications, Inc., Lancaster, 2003.

[7] D. L. Balageas, *Proceedings of the first European Workshop on Structural Health Monitoring 2002*. DEStech Publications, Lancaster, 2002.

[8] W. J. Staszewski, C. Boller, and G. R. Tomlinson, "Health Monitoring of Aerospace Structures: Smart Sensor Technologies and Signal Processing." Chichester: Jon Wiley & Sons Inc, 2004, pp. 288.

[9] P. D. Foote, "Structural Health Monitoring: Tales from Europe", in *Proceedings of the 2nd International Workshop on Structural Health Monitoring, Stanford, CA*, F.-K. Chang, Ed. Lancaster: Technomic Publishing Company, Inc., 2000.

[10] C. Boller, "Fundamentals on Damage Monitoring.," *AGARD Lecture Series*, vol. 205, pp. 4.1-4.15, 1996.

[11] C. Boller, "Next Generation Structural Health Monitoring and its Integration into Aircraft Design.," *International Journal of Systems Science*, vol. 31, pp. 1333-49, 2000.

[12] C. Boller, "Ways and options for aircraft structural health management.," *Smart Materials and Structures*, vol. 10, pp. 432-440, 2001.

[13] D. C. Worlton, "Ultrasonic Testing With Lamb Waves," *Non-Destr. Test.*, vol. 15, pp. 218–222, 1957.

[14] I. A. Viktorov, "Rayleigh and Lamb Waves - Physical Theory and Applications.," *Plenum Press, New York*, 1967.

[15] J. L. Rose, "Ultrasonic Waves in Solid Media.," *Cambridge University Press*, 1999.

[16] K. Othonos and K. Kalli, "Fiber Bragg Gratings; Fundamentals and Applications in Telecommunications and Sensing.," *Artech House Inc.*, 1999.

[17] R. Kashyap, "Fiber Bragg Gratings," *Academic Press, San Diego*, 1999.

[18] O. K. Hill, Y. Fujii, D. C. Johnson, and B. S. Kawasaki, "Photosensitivity in optical fiber waveguides: Application to reflection filter fabrication.," *Appl. Phys. Letters*, vol. 32, pp. 647-649, 1978.

[19] H. J. Schmidt and B. Schmidt-Brandecker, "Structure Design and Maintenance Benefits from Structural Health Monitoring", in *Proceedings of the 3rd International Workshop on Structural Health Monitoring, Stanford, CA*, F.-K. Chang, Ed. Stanford University, Stanford, CA: Technomic Publishing Company Inc., 2001.

[20] H. J. Schmidt, B. Schmidt-Brandecker, and G. Tober, "Design of Modern Aircraft Structure and the Role of NDT," presented at 7th European Conference on Non-Destructive Testing, Copenhagen, 1998.

[21] J. Telgkamp and H. J. Schmidt, "Benefits of the Application of Structural Health Monitoring (SHM) Systems on Civil Transport Aircraft", in *Proceedings of the 4th International Workshop on Structural Health Monitoring*, F.-K. Chang, Ed. Lancaster: DEStech Publications, Inc., 2003.

[22] P.-F. Gobin, M. Salvia, J.-C. Baboux, N. Godin, and Y. Jayet, "Global Approach of the Health Monitoring Concept", in *Proceedings of the First European Workshop on Structural Health Monitoring 2002*, D. L. Balageas, Ed. Lancaster: DEStech Publications, 2002.

[23] J. F. Huang, "Structural Health Monitoring for Reusable Launch Vehicles - An Integrated System and Process Approach", in *Proceedings of the 3rd International Workshop on Structural Health Monitoring, Stanford, CA*, F.-K. Chang, Ed. Stanford University, Stanford, CA: Technomic Publishing Company Inc., 2001.

[24] A. Cusano, P. Salvarezza, G. Breglio, A. Cutolo, A. Calabro, M. Giurdano, S. De Nicola, and L. Nicolais, "An Integrated Fiber Optic Sensing System for in Situ Characterization of the Curing Process of Thermoset Based Composites.," *Smart Structures and Materials 2001: Sensory Phenomena and Measurement Instrumentation for Smart Structures and Materials, Proc. SPIE*, vol. 4328, pp. 275-284, 2001.

[25] P. A. Fomitchov and S. Krishnaswamy, "Fiber Bragg Grating Ultrasound Sensor for Process Monitoring and NDE Applications," *Review of Progress in Quantitative Nondestructive Evaluation*, vol. 21, pp. 937-944, 2002.

[26] H. K. Kang, D. H. Kang, C. S. Hong, and C. G. Kim, "Simultaneous monitoring of strain and temperature during and after cure of unsymmetric composite laminate using fibre-optic sensors," *Smart Material and Structures*, vol. 12, pp. 29-35, 2003.

[27] J. S. Leng and A. Asundi, "Real-time cure monitoring of smart composite materials using extrinsic Fabry-Perot interferometer and fiber Bragg grating sensors," *Smart Material and Structures*, vol. 11, pp. 249-255, 2002.

[28] J. M. Menendez, P. Munoz-Esquer, F. Rodriguez-Lence, and J. A. Guemes, "Fiber Optic Sensors for Process Monitoring of Composite Aerospace Structures," presented at Smart Structures and Materials 2002: Smart Sensor Technology and Measurement Systems, San Diego, CA, USA, 2002.

[29] P. Ferdinand, V. Marty-Dewynter, L. Maurin, J. Boussoir, S. Rougeault, and S. Magne, "FBG-based smart composite applications", in *Proceedings of the First European Workshop on Structural Healt Monitoring 2002*, D. Balageas, Ed.: DEStech Publications, 2002.

[30] D. C. Betz, L. Staudigel, M. Trutzel, M. Schmuecker, E. Huelsmann, and U. Czernay, "Test of a Fiber Bragg Grating Sensor Network for Commercial Aircraft Structures," presented at 15th International Conference on Optical Fiber Sensors, Portland, USA, 2002.

[31] M. Trutzel, H. F. Siegling, D. Betz, R. Sangkohl, M. Holz, L. Staudigel, W. Martin, and O. Krumpholz, "Determination of Strain and Temperature Fields using Fiberoptic Bragg Grating Sensors.," *Sensor-Kongreß, Nürnberg*, 1999.

[32] M. Trutzel, K. Wauer, D. Betz, L. Staudigel, O. Krumpholz, H. C. Mühlmann, T. Müllert, and W. Gleine, "Smart Sensing of Aviation Structures with Fiber-optic Bragg Grating Sensors.," *Smart Structures and Materials 2000: Sensory Phenomena and Measurement Instrumentation for Smart Structures and Materials, Proc. SPIE*, vol. 3986, pp. 134-143, 2000.

[33] W. J. Staszewski, "Monitoring ON-line Integrated Technologies for Operational Reliability - MONITOR.," *Air & Space Europe*, vol. 2, 2000.

[34] N. Aldridge, P. D. Foote, and I. Read, "Operational Load Monitoring for Aircraft & Maritime Applications," *Strain*, vol. 36, pp. 123-126, 2000.

[35] P. D. Foote, "Optical Fibre Sensing Techniques for Health and Usage Monitoring.," *Paper presented at the RTO AVT Specialists Meeting on "Exploitation of Structural Loads/Health Data for Reduced Life Cycle Costs" held in Brussels, Belgium*, 1998.

[36] R. G. Duncan, B. A. Childers, D. K. Gifford, D. E. Pettit, A. W. Hickson, and T. L. Brown, "Distributed sensing technique for test article damage detection and monitoring," *Proceedings of SPIE*, vol. 5050, pp. 367-375, 2003.

[37] D. K. Gifford, B. A. Childers, R. G. Duncan, A. C. Jackson, S. Shaw, B. Schwienberg, and J. Mazza, "Structural integrity monitoring of aircraft panels using a distributed Bragg grating sensing technique," *Proceedings of SPIE*, vol. 5050, pp. 358-366, 2003.

[38] P. M. Nellen, A. Frank, and U. Sennhauser, "Fiber Optic Strain Gradient Sensing," presented at Test 2001, Nuremberg, 2001.

[39] I. McKenzie, R. Jones, W. K. Chiu, D. Booth, and S. Galea, "Monitoring of crack growth beneath a bonded repair using Bragg gratings.," *Proceedings of the SPIE - The International Society for Optical Engineering*, vol. 3242, pp. 272-83, 1997.

[40] S. C. Galea, N. Rajic, S. D. Moss, I. McKenzie, Y. L. Koh, and T.-H. Chiu, "In-Situ Health Monitoring of Composite Bonded Repairs", in *Proceedings of the 3rd International Workshop on Structural Health Monitoring, Stanford, CA*, F.-K. Chang, Ed. Stanford University, Stanford, CA: Technomic Publishing Company Inc., 2001.

[41] V. Dewynter-Marty, S. Rougeault, P. Ferdinand, D. Chauvel, E. Toppani, M. Leygonie, B. Jarret, and P. Fenaux, "Concrete strain measurements and crack detection with surface-mounted and embedded Bragg grating," *12th International Conference on Optical Fiber Sensors. Technical Digest. Postconference Edition, Washington, DC, USA*, pp. 600-603, 1997.

[42] M. Prabhugoud and K. Peters, "Efficient simulation of Bragg grating sensors for implementation to damage identification in composites," *Smart Materials and Structures*, vol. 12, pp. 914-924, 2003.

[43] M. Kehlenbach, *Integrierte Sensorik zur Schädigungserkennung in Faserverbundwerksoffen für die Luftfahrt*, PhD Thesis, Fachbereich Maschinenbau der Technischen Universität Darmstadt, 2003.

[44] J. Dakin and B. Culshaw, "Optical Fiber Sensors.," *Artech House, Inc.*, vol. I-IV, 1988.

[45] K. T. V. Grattan and B. T. Meggit, "Optical Fiber Sensor Technology.," *Chapman&Hall*, 1995.

[46] E. Udd, "Fiber Optic Sensors.," *Jon Wiley & Sons Inc., New York*, 1991.

[47] A. D. Kersey, M. A. Davis, H. J. Patrick, M. LebLanc, K. P. Koo, C. G. Askins, M. A. Putnam, and J. E. Friebele, "Fiber Grating Sensors," *Journal of Lightwave Technology*, vol. 15, pp. 1442-1463, 1997.

[48] Y.-J. Rao, "in-fibre Bragg grating sensors," *Meas. Sci. and Technol*, vol. 8, pp. 355-375, 1997.

[49] K. O. Hill and G. Meltz, "Fiber Bragg Grating Technology Fundamentals and Overview.," *Journal of Lightwave Technology*, vol. 15, pp. 1263-1276, 1997.

[50] W. J. Staszewski, C. Boller, and G. R. Tomlinson, "Health Monitoring of Aerospace Structures: Smart Sensor Technologies and Signal Processing." Chichester: Jon Wiley & Sons Inc, 2003, pp. 288.

[51] G. Grau, *Optische Nachrichtentechnik - Eine Einführung*. Springer-Verlag, Berlin Heidelberg, 1981.

[52] E. Voges and K. Petermann, *Optische Kommunikationstechnik*. Springer, Berlin, 2002.

[53] R. Szweda, "Fibre Bragg gratings win ground in telecommunications and sensors.," *Optics and Lasers Europe*, pp. 43-47, 2000.

[54] R. M. Measures, *Structural Monitoring with Fiber Optic Technology*. Academic Press, San Diego, California, 2001.

[55] C. S. Baldwin, T. J. Salter, J. Niemczuk, P. C. Chen, and J. S. Kiddy, "Structural monitoring of composite marine piles using multiplexed fiber Bragg grating sensors: In-field applications," presented at Smart Structures and Materials 2002: Smart Systems for Bridges, Structures and Highways, San Diego, CA, USA, 2002.

[56] V. Bhatia, C. A. Schmidt, K. A. Murphy, R. O. Claus, T. A. Tran, J. A. Greene, and M. S. Miller, "Optical fiber sensing technique for edge-induced and internal delamination detection in composites," *Smart Material and Structures*, vol. 4, pp. 164-169, 1995.

[57] E. Bocherens, S. Bourasseau, V. Dewynter-Marty, S. Py, M. Dupont, P. Ferdinand, and H. Berenger, "Damage detection in a radome sandwich material with embedded Fiber Optic Sensors.," *At 4th European Conferrence on Smart Structures and Materials, Harrogate, UK*, pp. July 1998, 1998.

[58] P. Castelli, R. Falciai, R. Galli, N. Mattiucci, N. Pallaro, and C. Trono, "Applications of FBG sensors for the monitoring of critical components of vehicles," presented at European Workshop on Smart Structures in Engineering and Technology, 2003.
[59] B. Culshaw and W. C. Michie, "Optical fiber sensors and their role in smart structures," *Proceedings of the SPIE - The International Society for Optical Engineering*, vol. 3211, pp. 432-43, 1997.
[60] S. D.I., S. Talabattula, and A. Selvarajan, "Analysis of fiber Bragg grating sensors in smart structures.," *Proceedings of SPIE - The International Society for Optical Engineering*, vol. 3241, pp. 289-298, 1997.
[61] J. Dorighi, S. Krishnaswamy, and J. Achenbach, "Response of an embedded fiber ultrasound sensor.," *J. Acoust. Soc. Am.*, vol. 101, pp. 257-263, 1997.
[62] J. A. J. Fells, M. J. Goodwin, C. J. Groves-Kirkby, D. C. J. Reid, J. E. Rule, and M. B. Snell, "Fibre Optic Sensing for Military Bridge Health and Load Monitoring.," *IEE Colloquium on Optical Techniques for Smart Structures an Structural Monitoring, London*, vol. 10/1-10/11, 1997.
[63] P. Ferdinand, S. Magne, V. Dewynter-Marty, S. Rougeault, and M. Bugaud, "Optical Fiber Bragg Grating Sensors Make Composite Structures Smart.," *At SAMPE Europe Conference'99, Paris, F*, 1999.
[64] P. D. Foote, "Optical fibre Bragg grating sensors for aerospace smart structures.," *IEE Colloquium on 'Optical Fibre Gratings and Their Applications.(Digest No.1995/017), London*, vol. 1995/017, pp. 14/1-14/6, 1995.
[65] E. J. Friebele, "Fiber Bragg grating strain sensors: present and future applications in smart structures.," *Optics & Photonics News*, vol. 9, pp. 33-37, 1998.
[66] E. J. Friebele and A. D. Kersey, "Fiberoptic sensors measure up for smart structures," *Laser Focus World*, pp. 165-171, 1994.
[67] E. Udd, *Fiber Optic Smart Structures*. Jon Wiley & Sons Inc., New York, 1995.
[68] G. Zhou and L. M. Sim, "Damage detection and assessment in fibre-reinforced composite structures with embedded fibre optic sensors - review," *Smart Materials and Strucutres*, vol. 11, pp. 925-939, 2002.
[69] D. C. Betz, M. N. Trutzel, L. Staudigel, M. Schmuecker, E. Huelsmann, U. Czernay, H. C. Muehlmann, and T. Muellert, "Fiber-Optic Smart Sensing of Aviation Structures." in *Proceedings of the 3rd International Workshop on Structural Health Monitoring, Stanford, CA*, F.-K. Chang, Ed. Stanford University, Stanford, CA: Technomic Publishing Company Inc., 2001.
[70] P. D. Foote, "Fibre Bragg grating strain sensors for aerospace smart structures," *Proceedings of the SPIE - The International Society for Optical Engineering*, vol. 2361, pp. 290-3, 1994.
[71] M. L. Dockney, I. J. Read, P. D. Foote, and R. P. Tatam, "Embedded optical fibre Bragg gratings for aerospace monitoring.," *IEE Colloquium on Optical Techniques for SMART Structures and Structural*, 1997.
[72] E. J. Friebele, C. G. Askins, A. B. Bosse, A. D. Kersey, H. J. Patrick, W. R. Pogue, M. A. Putnam, W. R. Simon, F. A. Tasker, W. S. Vincent, and S. T. Vohra, "Optical fiber sensors for spacecraft applications.," *Smart Materials and Structures*, vol. 8, pp. 813-838, 1999.
[73] J. R. Lee, C. Y. Ryu, B. Y. Koo, S. G. Kang, C. S. Hong, and C. G. Kim, "In-flight health monitoring of a subscale wing using a fiber Bragg grating sensor system," *Smart Material and Structures*, vol. 12, pp. 147-155, 2003.
[74] K. Wood, T. Brown, Rogowski, R., and B. Jensen, "Fiber optic sensors for health monitoring of morphing airframes: I. Chemical sensing using optical fibers with Bragg gratings.," *Smart Materials and Strucutres*, vol. 9, pp. 170-174, 2000.
[75] K. Wood, T. Brown, R. Rogowski, and B. Jensen, "Fiber optic sensors for health monitoring of morphing airframes: I. Bragg grating strain and temperature sensor.," *Smart Materials and Strucutres*, vol. 9, pp. 163-169, 2000.
[76] J. Hecht, "Understanding fiber optics.," *3rd edition, Prentice Hall, NJ*, 1998.
[77] M. Young, "Optik, Laser, Wellenleiter.," *Springer-Verlag, Berlin/Heidelberg*, 1997.

[78] M. Born and E. Wolf, "Principles of Optics," *Pergamon Press*, vol. Ed.5, pp. 544-554, 1975.

[79] K. S. Abedin, M. Hyodo, and N. Onodera, "154GHz polarisation-maintaining dispersion-managed actively modelocked fibre ring laser.," *Electronics Letters*, vol. 36, pp. 1185-1186, 2000.

[80] M. L. Lee, J. S. Park, W. J. Lee, S. H. Yun, Y. H. Lee, and B. Y. Kim, "A polarimetric current sensor using an orthogonally polarized dual-frequency fibre laser.," *Meas. Sci. and Technol*, vol. 9, pp. 952-959, 1998.

[81] T. Okoshi, "Polarization Phenomena in Optical Fibers.," *In Optical Fiber Sensors: Proceedings of the NATO Advanced Study Institute, Erice, Italy*, pp. 227-241, 1987.

[82] S. C. Rashleigh, "Origins and Control of Polarization Effects in Single-Mode Fibers.," *Journal of Lightwave Technology*, vol. LT-1, pp. 312-331, 1983.

[83] G. Thursby, F. Dong, Y. Yong, B. Sorazu, D. C. Betz, and B. Culshaw, "Fiber Optic Polarimetric Detection of Lamb Waves," presented at OFS 2002, 15th International Conference on Optical Fiber Sensors, Portland, Oregon, USA, 2002.

[84] G. Thursby, B. Sorazu, F. Dong, D. C. Betz, and B. Culshaw, "Damage Detection in Structural Materials using a Polarimetric Fibre Optic Sensor," presented at Smart Structures and Materials 2003: Sensory Phenomena and Measurement Instrumentation for Smart Structures and Materials, San Diego, CA, USA, 2003.

[85] N. G. Walker and G. R. Walker, "Polarisation control for coherent optical fibre systems," *Br Telecom Technol Journal*, vol. 5, pp. 63-76, 1987.

[86] D. K. Wilson, "Polarization control aids fiber component testing.," *Laser Focus World*, pp. 129-133, 1997.

[87] K. Atherton, F. Dong, G. Pierce, and B. Culshaw, "Mach-Zehnder optical fiber interferometers for the detection of ultrasound.," *Smart Structures and Materials 2000: Sensory Phenomena and Measurement Instrumentation for Smart Structures and Materials, Proc. SPIE*, vol. 3986, pp. 27-34, 2000.

[88] V. Bhatia, M. B. Sen, K. A. Murphy, A. Wang, R. O. Claus, M. E. Jones, J. L. Grace, and J. A. Greene, "Demodulation of wavelength-encoded optical fiber sensor signals using fiber modal interferometers," *Proceedings of the SPIE - The International Society for Optical Engineering*, vol. 2594, pp. 99-113, 1996.

[89] D. H. Kim, J. W. Park, H. K. Kang, C. S. Hong, and C. G. Kim, "Measuring dynamic strain of structures using a gold-deposited Fabry-Perot interferometer," *Smart Material and Structures*, vol. 12, pp. 1-5, 2003.

[90] S. F. Knowles, R. D. Pechstedt, and Y. Lu, "ASOC white light interferometry for sensing applications," presented at Sensor and Transducer Conference mtec'99, Birmingham, 1999.

[91] K. P. Koo, A. D. Kersey, and Fibre, "Laser sensor with ultrahigh strain resolution using interferometric interrogation.," *Electronics Letters*, vol. 31, pp. 1180-1182, 1995.

[92] P. Niewczas, L. Dziuda, G. Fusiek, A. J. Willshire, J. R. McDonald, G. Thursby, D. Harvey, and W. C. Michie, "Interrogation of Extrinsic Fabry-Perot Interferometric Sensors Using Arrayed Waveguide Grating Devices," presented at IEEE Instrumentation and Measurement Technology Conference, Anchorage, AK, USA, 2002.

[93] S. G. Pierce, W. R. Philp, A. Gachagan, A. McNab, G. Hayward, and B. Culshaw, "Surface-bonded and embedded optical fibers as ultrasonic sensors.," *Applied Optics*, vol. 35, pp. 5191-5197, 1996.

[94] J. Sirkis and H. W. Haslach, "Interferometric Strain Measurement by Arbitrarily Configured, Surface-Mounted, Optical Fibers," *Journal of Lightwave Technology*, vol. 8, pp. 1497-1503, 1990.

[95] J. S. Sirkis, "Unified approach to phase-strain-temperature models for smart structure interferometic optical fiber sensor:," *part 1 and 2. Optical Engineering*, vol. 32, pp. 752-773, 1993.

[96] M. Song, S. Yin, and P. B. Ruffin, "Fiber Bragg grating strain sensor demodulation with quadrature sampling of a Mach-Zehnder interferometer.," *Applied Optics*, vol. 39, pp. 1106-1111, 2000.

[97] B. Sorazu, G. Thursby, B. Culshaw, F. Dong, Y. Yong, and J. Yao, "Ultrasonic wavefront integration using optical fibre sensors," presented at Smart Structures and Materials 2003: Sensory Phenomena and Measurement Instrumentation for Smart Structures and Materials, San Diego, CA, USA, 2003.
[98] H. Tsuda, J. Takahashi, K. Urabe, and T. Ikeguchi, "Damage monitoring of carbon fiber-reinforced plastics with Michelson interferometric fiber-optic sensors.," *Journal of Materials Science*, vol. 34, pp. 4163-4172, 1999.
[99] W. H. Bragg and W. L. Bragg, *X rays and crystal structure*. Bell & Sons, London, 1915.
[100] T. Erdogan, "Fiber Grating Spectra.," *Journal of Lightwave Technology*, vol. 15, pp. 1277-1294, 1997.
[101] M. McCall, "On the Application of Coupled Mode Theory for Modeling Fiber Bragg Gratings.," *Journal of Lightwave Technology*, vol. 18, pp. 236-242, 2000.
[102] M. Riedel, "Untersuchung und Realisierung eines kompakten faseroptischen Systems zur Wellenlängenmessung.," *Diplomarbeit, Lehrstuhl Prof. Dr. K.J. Ebeling, Universität Ulm*, 1998.
[103] J. Hong, W. Huang, and T. Makino, "On the Transfer Matrix Method for Distributed-Feedback Waveguide Devices.," *Journal of Lightwave Technology*, vol. 10, pp. 1860-1868, 1992.
[104] J. Capmany and M. A. Muriel, "A New Transfer Matrix Formalism for the Analysis fo Fiber Ring Resonators: Compound Coupled Structures for FDMA Demultplexing.," *Journal of Lightwave Technology*, vol. 8, pp. 1904-1919, 1990.
[105] A. Cartaxo, B. Wedding, and W. Idler, "Influence of Fiber Nonlinearity on the Transfer Function: Theoretical and Experimental Analysis," *Journal of Lightwave Technology*, vol. 17, pp. 1806-1812, 1999.
[106] M. A. Muriel and A. Carballar, "Internal Field distributions in Fiber Bragg Gratings.," *IEEE Photonics Technology Letters*, vol. 9, pp. 955-957, 1997.
[107] Z. H. Wang, G.-D. Pang, and P. L. Chu, "Improved Roaurd's method for fiber and waveguide gratings," *Optics Communications*, vol. 177, pp. 245-250, 2000.
[108] L. A. Weller-Brophy and D. G. Hall, "Analysis of waveguide gratings: application of Rouard's method," *J. Opt. Soc. Am.*, vol. 2, pp. 863-871, 1985.
[109] L. A. Weller-Brophy and D. G. Hall, "Analysis of waveguide gratings: a comparison of the results of Rouard's method and coupled mode theory," *J. Opt. Soc. Am.*, vol. 4, pp. 60-65, 1987.
[110] L. A. Weller-Brophy and D. G. Hall, "Statistical analysis of waveguide gratings using Rouard's method," *Applied Optics*, vol. 27, pp. 963-966, 1988.
[111] ApolloPhotonics, *Fiber Optical Grating Simulation - Reference Manual*. Apollo Photonics Inc., Burlington, Ontario, 2003.
[112] M. Trutzel, *Dehnungsermittlung mit faseroptischen Bragg-Gitter-Sensoren*, PhD Thesis, Technische Universität Berlin, 2001.
[113] R. van Steenkiste and G. Springer, *Strain and Temperature Measurement with Fiber Optic Sensors*. Technomic Publishing Inc, Lancaster, Basel, 1997.
[114] D. Betz, L. Staudigel, M. N. Trutzel, and M. Kehlenbach, "Structural Monitoring Using Fiber-optic Bragg Grating Sensors," *Structural Health Monitoring: An International Journal*, vol. 2, pp. 145-152, 2003.
[115] M. Trutzel, D. Betz, M. Holz, L. Staudigel, O. Krumpholz, H. F. Siegling, R. Sangkohl, W. Martin, H. C. Mühlmann, T. Müllert, and H. Ahrendt, "Investigation of Fiberoptic Bragg Grating Sensors for Applications in the Aviation Industry.," *in 13th International Conference on Optical Fiber Sensors, Proceedings of SPIE*, vol. 3746, pp. 624-627, 1999.
[116] M. Trutzel, D. Betz, M. Holz, L. Staudigel, O. Krumpholz, H. F. Siegling, R. Sangkohl, W. Martin, H. C. Mühlmann, T. Müllert, and H. Ahrendt, "Strukturdiagnostik mit faseroptischen Bragg-Gitter-Sensoren.," *GESA Symposium „Anspruch und Tendenzen in der experimentellen Strukturmechanik", Warnemünde*, 1999.
[117] T. Erdogan, V. Mizrahi, P. J. Lemaire, and D. Monroe, "Decay of ultraviolet-induced fiber Bragg gratings.," *J.Appl.Phys.*, vol. 76, pp. 73-80, 1994.

[118] P. Mauron, *Reliability and lifetime of optical fibres and fibre Brag gratings for metrology and telecommunications*, Thesis for the degree of Doctor of Technical Sciences, Swiss Federal Institute of Technology Lausanne (EPFL), Lausanne, 2001.

[119] P. M. Nellen, P. Mauron, A. Frank, P. Pequignot, K. Bohnert, H. Brändle, and U. Sennhauser, "Mechanical and Optical Reliability of Fiber Bragg Grating Strain and Temperature Sensors at High Temperature.," presented at SPIE's International Symposium on Voice, Video and Data Communications, Conference on Optical Fiber Reliability and Testing, Boston, 1999.

[120] P. Mauron, P. M. Nellen, U. Sennhauser, M. N. Trutzel, D. Betz, V. Hagemann, and M. Rothardt, "Lifetime of Fibre Bragg Gratings Under Cyclic Fatigue.," *SPIE's International Symposium on Voice, Video and Data Communications, Program on Optical Fiber Devices and Systems, VV12: Conference on Optical Fiber reliability and Testing, Boston*, 1999.

[121] P. Mauron, P. M. Nellen, and U. Sennhauser, "Cyclic Loading of Optical Fibers," presented at Eurocable Conference, Delft, The Netherlands, 1999.

[122] V. Hagemann, M. Rothhardt, H.-R. Müller, M. N. Trutzel, L. Staudigel, and O. Krumpholz, "Mechanical resistance of draw-tower-Bragg-grating sensors," *Electronics Letters*, vol. 24, pp. 211-212, 1998.

[123] V. J. Hagemann, *Untersuchungen zum dynamischen Einzelpuls-Einschreiben von Faser-Bragg-Gittern und deren Anwendung*. dissertation.de, Berlin, 2001.

[124] D. C. Betz, M. N. Trutzel, H. F. Siegling, R. Sangkohl, M. Holz, L. Staudigel, W. Martin, and O. Krumpholz, "Fiberoptic Smart Sensing of Component Deformations in Adaptive Wings.," *International Council of the Aeronautical Sciences Conference (ICAS), Harrogate (UK)*, 2000.

[125] P. M. Nellen, A. Frank, P. Mauron, and U. Sennhauser, "Lifetime and reliability of embedded optical sensor fibers," presented at International Workshop on Fiber Optic Sensors for Construction Materials and Bridges, Newark, NJ, USA, 1998.

[126] D. C. Betz, *Physikalische Eigenschaften faseroptischer Bragg-Gitter Sensoren*, Diplomarbeit, Universität Karlsruhe (TH), Karlsruhe, 1999.

[127] C. Boller, "General Introduction.," *AGARD Lecture Series 205*, pp. 1.1-1.7, 1996.

[128] J. N. Kudva, M. J. Grage, and M. M. Roberts, "Aircraft Structural Health Monitoring and Other Smart Structures Technologies- Perspectives on Development of Future Smart Aircraft.," in *Proceedings of the 2nd International Workshop on Structural Health Monitoring, Stanford, CA*, F.-K. Chang, Ed. Lancaster: Technomic Publishing Co., Inc, 1999.

[129] J. N. Kudva, A. J. Lockyer, and C. B. Van Way, "Structural Health Monitoring of Aircraft Components.," *AGARD Lecture Series 205*, pp. 9.1-9.15, 1996.

[130] T. J. Barnes, "The FAA Operational Loads Monitoring Program-Achievements and Problems.," *ICAS 2000 Congress, 433, Harrogate*, 2000.

[131] M. Neumair, "Structural Health Monitoring, In-Service Experience, Benefit and Way Ahead", in *Proceedings of the first European Workshop on Structural Health Monitoring 2002*, D. L. Balageas, Ed. Lancaster: DEStech Publications, 2002.

[132] S. R. Hunt and I. G. Hebden, "Validation of the Eurofighter Typhoon Structural Health and Useage MonitoringSystem.," *Smart-Materials-and-Structures*, vol. 10, pp. 497-503, 2001.

[133] C. Voto, F. P. Camerlingo, S. Inserra, M. Iodice, and I. Rendina, "Fiber Optic Strain Sensors: Aerospace Applications and Requirements", in *Proceedings of the first European Workshop on Structural Health Monitoring 2002*, D. L. Balageas, Ed. Lancaster: DEStech Publications, 2002.

[134] Kyowa, "Strain Gage Installation Guide," http://www.kyowa-ei.co.jp, 2003.

[135] R. L. Hannah and S. E. Reed, *Strain Gage Users' Handbook*. Elsevier Applied Science, London and New York, 2000.

[136] K. Hoffmann, *Eine Einführung in die Technik des Messens mit Dehnungsmeßstreifen*. Hottinger Baldwin Messtechnik GmbH, Darmstadt, 1987.

[137] "Interactive Guide to Strain Measurement Technology," http://vishay.com/brands/measurements_group/guide/, 2003.

[138] B. Culshaw, "Measuring Strain Using Optical Fibres," *Strain 2000*, vol. 36, pp. 105-113, 2000.
[139] B. A. Childers, M. E. Froggatt, S. G. Allison, T. C. Moore, D. A. Hare, C. F. Batten, and D. C. Jegley, "Use of 3000 Bragg grating strain sensors distributed on four eight-meter optical fibers during static load tests of a composite structure," *Proceedings of the SPIE - The International Society for Optical*, vol. 4332, pp. 133-142, 2001.
[140] D. C. Betz, "Spezifikationen "Messkette" mit Faser Bragg Gittern," DaimlerChrysler Research and Technology, Ulm, Germany 2003.
[141] C. Chojetzki, "Personal Communication", IPHT Germany, 2003.
[142] T. Stolley, *Untersuchungen zur Applikation von Bragg-Gitter-Sensoren zur Ermittlung von statischen und dynamischen Lasten in Luftfahrzeugen*, Master Thesis, Fachhochschule Westküste, Heide/Holstein, Germany, 2003.
[143] P. D. Foote, M. Breidne, K. Levin, P. Papadopolous, I. Read, M. Signorazzi, L. K. Nilsson, R. Stubbe, and A. Claesson, "Operational Load Monitoring Using Optical Fibre Sensors", in *Health Monitoring of Aerospace Structures: Smart Sensor Technologies and Signal Processing*, W. J. Staszewski, C. Boller, and G. R. Tomlinson, Eds. Chichester: Jon Wiley & Sons Inc, 2003.
[144] D. C. Betz, M. N. Trutzel, M. Holz, F. Pabst, L. Staudigel, and O. Krumpholz, "Tunable Laser-Based Hybrid WDM/TDM Sensor System for the Interrogation of Low-Reflective Fiber Bragg Gratings.," *14th International Conference on Optical Fiber Sensors;*, 2000.
[145] A. D. Kersey, "A Review of Recent Developments in Fiber Optic Sensor Technology.," *Optical Fiber Technology 2*, pp. 291-317, 1996.
[146] P. Foote and I. Read, "Applications of optical fibre sensors in aerospace: the achievements and challenges," *Proceedings of SPIE - The International Society for Optical Engineering*, vol. 4074, pp. 246-261, 2000.
[147] Y. C. Roth, "FE-Analyse Lichtleitfaser. Kurzdokumentation," IVW, Institut für Verbundwerkstoffe GmbH, Kaiserslautern, Germany 2003.
[148] L. Staudigel, "Physikalische Daten von Kapton," DaimlerChrysler Research and Technology, Ulm, Germany 2003.
[149] M. Buderath, "Maintaining Ageing Military Aircraft Using the Tornado Fighter as an Example", in *Proceedings of the First European Workshop on Structural Healt Monitoring 2002*, D. L. Balageas, Ed. Paris: DEStech Publications, 2002.
[150] British-Institute-of-Non-Destructive-Testing, "What is Non-Destructive Testing," www.bindt.org/Mk1Site/Ndt.html, 2004.
[151] H. Lamb, "On waves in an elastic plate," *Proceedings of the Royal Society*, vol. 93 (PT series A), pp. 114-128, 1917.
[152] V. Giurgiutiu, J. Bao, and W. Zhao, "Active Sensor Wave Propagation Health Monitoring of Beam and Plate Structures.," *Smart Structures and Materials 1994, Smart Sensing, Processing, and Instrumentation, Orlando, USA, Newport Beach, CA, USA, 2001*, pp. 4-8, 2001.
[153] K. Worden, "Rayleigh and Lamb waves—basic principles," *Strain*, vol. 37, pp. 167–172, 2001.
[154] D. N. Alleyne and P. Cawley, "The interaction of Lamb waves with defects.," *IEEE Transactions on Ultrasonics, Ferroeletrics and Frequency Control*, vol. 39(3), pp. 381-397, 1992.
[155] D. N. Alleyne and P. Cawley, "Optimisation of Lamb wave inspection techniques.," *NDT&E International*, vol. 25, pp. 11-22, 1998.
[156] P. Cawley and D. N. Alleyne, "The use of Lamb waves for the long range inspection of large structures.," *Ultrasonics*, vol. 36, pp. 287-290, 1996.
[157] O. Diligent, M. J. S. Lowe, and P. Cawley, "Reflection and Scattering of the S0 Lamb Mode From Circular Defects in Plates," *Review of Progress in Quantitative Nondestructive Evaluation*, vol. 20, pp. 134-141, 2001.
[158] N. Guo and P. Cawley, "The interaction of Lamb waves with delaminations in composite laminates.," *J. Acoust. Soc. Am.*, vol. 94, pp. 2240-2246, 1993.

[159] M. J. S. Lowe, P. Cawley, J.-Y. Kao, and O. Diligent, "Low-frequency reflection characteristics of the fundamental asymmetric a0 Lamb wave from a rectangular notch in a plate," *J. Acoust. Soc. Am*, vol. 112, pp. 2612-2622, 2002.

[160] P. N. Marty, M. J. S. Lowe, and P. Cawley, "Finite Element Predictions of Guided Ultrasonic Wave Fields Generated by Piezoelectric Transducers," *Review of Progress in Quantitative Nondestructive Evaluation*, vol. 20, pp. 829-836, 2001.

[161] P. D. Wilcox, P. Cawley, and M. J. S. Lowe, "Acoustic fields from PVDF interdigital transducers.," *IEE Proc.-Sci. Meas. Technol*, vol. 145, pp. 250-259, 1998.

[162] P. D. Wilcox, M. J. S. Lowe, and P. Cawley, "A Signal Processing Technique to Remove the Effect of Dispersion From Guided Wave Signals," *Review of Progress in Quantitative Nondestructive Evaluation*, vol. 20, pp. 555-562, 2001.

[163] P. D. Wilcox, M. J. S. Lowe, and P. Cawley, "Long Range Lamb Wave Inspection: The Effect of Dispersion And Modal Selectivity", in *First half of the proceedings of the Twnty-Fifth Annual Symposium on Quantitative Nondestructive Evaluation*. New York: Plenum Press, 1999.

[164] S. S. Kessler, *Piezoelectric-Based In-Situ Damage Detection of Composite Materials for Structural Health Monitoring Systems*. PhD Thesis, Department of Aeronautics and Astronautics, Massachusetts Institute of Technology, Massachusetts, 2002.

[165] S. H. D. Valdés, *Structural Integrity Monitoring of CFRP Laminates using Piezoelectric Devices*. PhD Thesis, Department of Aeronautics, Imperial College London, 2000.

[166] M. J. S. Lowe and O. Diligent, "Low-frequency reflection characteristics of the s0 Lamb wave from a rectangular notch in a plate," *J. Acoust. Soc. Am*, vol. 111, pp. 64-74, 2002.

[167] W. J. Percival and E. A. Birt, "A study of Lamb wave propagation on carbon-fibre composites," *Insight*, vol. 39, 1997.

[168] M. G. Silk, *Ultrasonic Transducers for Nondestructive Testing*. Adam Hilger Ltd, Bristol, 1984.

[169] A. Chahbaz, V. Mustaphy, B. Hay, M. Brassard, and S. Dubois, "Corrosion detection in aircraft structure using guided Lamb waves," *The e-Journal of Nondestructive Testing 2(3): www.ndt.net/article/tektren2/tektren2.htm*, 1997.

[170] J. L. Rose, "A baseline and vision of ultrasonic guided wave inspection potential," *Journal of Pressure Vessel Technology*, vol. 124, pp. 273-282, 2002.

[171] J. J. Ditri, J. L. Rose, and A. Pilarski, "Generation of guided waves in hollow cylinders by wegde and comb transducers," *Review of Progress in Quantitative Nondestructive Evaluation*, vol. 12A, pp. 211-218, 1993.

[172] A. Gachagan, G. Hayward, A. McNab, P. Reynolds, S. G. Pierce, W. R. Philp, and B. Culshaw, "Generation and Reception of Ultrasonic Guided Waves in Composite Plates Using Conformable Piezoelectric Transmitters an Optical-Fiber Detectors.," *IEEE Transactions on Ultrasonics, Ferrolectrics, and Frequency Control*, vol. 46, pp. 71-81, 1999.

[173] V. Giurgiutiu, "Lamb Wave Generation with Piezoelectric Wafer Active Sensors for Structural Health Monitoring", in *Proceedings of SPIE*, vol. 5056, 2003.

[174] M. Lin, A. Kumar, X. Qing, and S. J. Beard, "Advances in utilization of structurally integrated sensor networks for health monitoring in commercial applications," presented at Smart Structures and Materials 2002: Smart Structures and Integrated Systems, San Diego, CA, USA, 2002.

[175] M. Lin, "Development of SMART Layer for Built-In Structural Diagnostics", in *Proceedings of the 2nd International Workshop on Structural Health Monitoring, Stanford, CA*, F.-K. Chang, Ed. Lancaster: Technomic Publishing Company, Inc., 2000.

[176] F.-K. Chang, "Smart layer: built-in diagnostic system for composite structures", in *Proceedings of the Fourth European Conference on Smart Structures and Materials, Second International Conference on Micromechanics, Intelligent Materials and Robotics, Harrogate, UK*, 1998.

[177] W. A. K. Deutsch, A. Cheng, and J. D. Achenbach., "Self-Focusing of Rayleigh Waves and Lamb Waves with a Linear Phased Array.," *Res. Nondestructive evaluation*, pp. 81-95, 1997.

[178] P. Blanquet, T. Demol, and C. Delebarre, "Application of array transducers to health monitoring of aeronautic structures", in *Proceedings of the 14th World Congress on Nondestructive Testing*, vol. 4. New Delhi, India, 1996.

[179] K.-P. Kress, "Integrated Imaging Ultrasound SWISS", in *Proceedings of the 4th International Workshop on Structural Health Monitoring, Stanford, CA*, F.-K. Chang, Ed. Lancaster: DEStech Publications, Inc., 2003.

[180] K.-P. Kress, H. J. Baderschneider, and G. Guse, "Imaging Ultrasonic Sensor System SWISS Completed 60.000 Simulated Flight Hours to Check Structural Integrity of Aircraft Subcomponent," *Proceedings of SPIE*, vol. 5046, pp. 284-290, 2003.

[181] K.-P. Kress, K. Dittrich, and G. Guse, "Smart Wide-area Imaging Sensor System (SWISS)," presented at Smart Structures and Materials 2001: Industrial and Commercial Applications of Smart Structures Technologies, Proceedings of SPIE, 2001.

[182] D. A. Hutchins, W. M. D. Wright, G. Hayward, and A. Gachagan, "Air-coupled piezoelectric detection of laser-generated ultrasound," *IEEE Transactions on Ultrasonics, Ferroeletrics and Frequency Control*, vol. 41, pp. 796-805, 1994.

[183] G. A. Alers and L. R. Burns, "EMAT designs for special applications," *Material Evaluation*, vol. 45, pp. 1184-1189, 1987.

[184] S. Aliouane, M. Hassam, A. Badidi Bouda, and A. Benchaala, "Electromagnetic Acoustic Transducers (EMATs) design evaluation of their performance", in *Proceedings of the 15th World Congress on Nondetrsuctive Testing, Rome, Italy. Paper No. 591: www.ndt.net/article/wcndt00/papers/idn591/idn591.htm*, 2000.

[185] B. Sorazu, G. Thursby, B. Culshaw, F. Dong, S. G. Pierce, Y. Yang, and D. C. Betz, "Optical Generation and Detection of Ultrasound," *Strain*, vol. 39, pp. 111-114, 2003.

[186] S. G. Pierce and B. Culshaw, "Applications of broadband laser-based ultrasound to materials testing.," *IOP Publishing Ltd, Health Monitoring, 4th ESSM and 2nd MIMR conference, Harrogate*, pp. 421-427, 1998.

[187] S. G. Pierce and B. Culshaw, "Laser generation of ultrasonic Lamb waves using low power optical sources.," *IEE Proc.-Sci. Meas. Technol*, vol. 145, pp. 244-249, 1998.

[188] S. G. Pierce and B. Culshaw, "Laser generation of ultrasound using a modulated continuous wave laser diode.," *Applied Physics Letters*, vol. 72, pp. 1030-1032, 1998.

[189] J. Yang, T. Sanderson, C. Ume, and J. Jarzynski, "Laser Phased Array Generated Ultrasound for Nondestructive Evalutaion of Ceramic Materials.," *Journal of Nondestructive Evaluation*, vol. 16, pp. 1-9, 1997.

[190] C. I. Swift, S. G. Pierce, and B. Culshaw, "Generation of an ultrasonic beam using embedded fibre optic delivery and low power laser sources.," *Smart Structures and Materials 2000: Sensory Phenomena and Measurement Instrumentation for Smart Structures and Materials, Proc. SPIE*, vol. 3986, pp. 20-26, 2000.

[191] C. I. Swift, S. G. Pierce, and B. Culshaw, "Laser generated ultrasound using directly coated fibre optic patchcords.," *Electronics Letters*, vol. 36, pp. 2113-2114, 2000.

[192] R. J. Dewhurst and Q. Shan, "Optical remote measurement of ultrasound.," *Meas. Sci. Technol.*, vol. 10, pp. 139-168, 1999.

[193] J. P. Monchalin, "Optical Detection of Ultrasound," *IEEE Transactions on Ultrasonics, Ferroeletrics and Frequency Control*, vol. 33, pp. 485-499, 1986.

[194] L. Mallet, *Laser Vibrometer Technique for Damage Detection in Metallic Structures Using Lamb Waves*, MSc Thesis, University of Sheffield, 2003.

[195] L. Mallet, B. C. Lee, W. J. Staszewski, and F. Scarpa, "Damage Detection in Metallic Structures Using Laser Acousto-Ultrasonics," *Proceedings of the 4th International Workshop on Structural Health Monitoring, Stanford, CA*, pp. 765-771, 2003.

[196] J. Dorighi, S. Krishnaswamy, and J. Achenbach, "Stabilized Fiber Optic Sensor for Ultrasound Detection.," *Review of Progress in Quantitative Nondestructive Evaluation, Plenum Press*, vol. 14, pp. 1135-1142, 1995.

[197] J. Dorighi, S. Krishnaswamy, and J. Achenbach, "A fiber optic ultrasonic system to monitor the cure of epoxy.," *Res. Nondestr. Eval 9, Spriger Verlag*, pp. 13-24, 1997.

[198] J. F. Dorighi, "Development, Characterization and Application of an Embedded Fiber Optic Ultrasound Sensor.," *Dissertation, Northwestern University, Evanston, Illinois*, 1996.
[199] N. E. Fisher, D. J. Webb, C. N. Pannell, D. A. Jackson, L. R. Gavrilov, J. W. Hand, L. Zhang, and I. Bennion, "Ultrasonic field and temperature sensor based on short in-fibre Bragg gratings.," *Electonic Letters*, vol. 34, pp. 1139-1140, 1998.
[200] M. W. Hathaway, N. E. Fisher, D. J. Webb, C. N. Pannell, D. A. Jackson, L. R. Gavrilov, J. W. Hand, L. Zhang, and I. Bennion, "Ultrasonic field and temperature sensor based on short in-fibre Bragg gratings.," presented at 3th International Conference on Optical Fiber Sensors, SPIE, Korea, 1999.
[201] S. F. O'Neill, M. W. Hathaway, N. E. Fisher, D. J. Webb, C. N. Pannell, D. A. Jackson, L. R. Gavrilov, J. W. Hand, L. Zhang, and I. Bennion, "High-frequency ultrasound detection using a fibre Bragg grating.," *IEE Colloquium on Optical Fibre Gratings (Ref. No.1999/023) London, UK*, pp. 16/1-16/6, 1999.
[202] N. Takahashi, S. Takahashi, and K. Tetsumura, "Fiber-Bragg-grating underwater acoustic sensor.," *In 13th International Conference on Optical Fiber Sensors, SPIE*, vol. 3746, pp. 565-568, 1999.
[203] N. Takahashi, K. Tetsumura, K. Imamura, and S. Takahashi, "Fiber-Bragg-grating WDM underwater acoustic sensor with directivity.," *Proceedings of the SPIE - The International Society for Optical Engineering*, vol. 3541, pp. 18-26, 1998.
[204] J. G. Liu, C. Schmidt-Hattenberger, and G. Borm, "Dynamic strain measurement with a fibre Bragg grating sensor system," *Measurement*, vol. 32, pp. 151-161, 2002.
[205] C. S. Baldwin and A. Vizzini, "Acoustic emission crack detection with FBG," *Proceedings of SPIE*, vol. 5050, pp. 133-143, 2003.
[206] I. Perez, H. L. Cui, and E. Udd, "Acoustic Emission Detection Using Fiber Bragg Gratings.," *Smart Structures and Materials 2001: Sensory Phenomena and Measurement Instrumentation for Smart Structures and Materials, Proc. SPIE*, vol. 4328, pp. 209-215, 2001.
[207] G. Coppola, A. Minardo, A. Cusano, G. Breglio, G. Zeni, A. Cutolo, A. Calabro, M. Giurdano, and L. Nicolais, "Analysis of Feasibility on the Use of Fiber Bragg Grating Sensors as Ultrasound Detectors.," *Smart Structures and Materials 2001: Sensory Phenomena and Measurement Instrumentation for Smart Structures and Materials, Proc. SPIE*, vol. 4328, pp. 224-232, 2001.
[208] K. Petermann, "Laser Diode Modulation And Noise.," *Kluwer Academic Publishers*, 1991.
[209] W. Demtröder, "Laserspektroskopie - Grundlagen und Techniken,," *4. Aufl., Springer-Verlag, Berlin Heidelberg 2000*, 2000.
[210] Andonovic and D. Uttamchandani, *Principles of modern optical systems*. Artech House Publishers, 1992.
[211] Derrickson, *Fiber Optic Test and Measurement*. Prentice Hall, 1998.
[212] S. G. Pierce, W. R. Philp, B. Culshaw, A. Gachagan, A. McNab, G. Hayward, and F. Lecuyer, "Surface-bonded optical fibre sensors for the inspection of CFRP plates using ultrasonic Lamb waves.," *Smart Mater. Struct.*, vol. 5, pp. 776-787, 1996.
[213] B. C. Hoskin and A. A. Baker, "Composite Materials for Aircraft Sructures.," *AIAA education Series, AIAA Inc. New York*, 1986.
[214] G. Mook, J. Pohl, and F. Michel, "Non-destructive characterization of smart CFRP structures," *Smart Materials and Structures*, vol. 12, pp. 997-1004, 2003.
[215] B. Culshaw, S. G. Pierce, and W. J. Staszewski, "Condition Monitoring in Composite Materials: An integrated System Approach.," *Proceedings of the Institution of Mechanical Engineers, Journal of System and Control Engineering*, vol. 212(3), pp. 189-202, 1998.
[216] C. Boller, "Smart Structures in Engineering and Technology - An Aerospace and Automotive Perspective," presented at European Workshop on Smart Structures in Engineering and Technology, 2003.
[217] B. Culshaw, *Smart Structures and Materials.* Artech House, Inc., Norwood, 1996.
[218] H. Janocha, *Adaptronics and Smart Structures*. Springer Verlag, Heidelberg, 1999.

[219] K. Johannessen, "Smart structures for sea, land and space.," *SPIE*, vol. 3099, pp. 300-304, 1997.
[220] S. R. Waite and G. N. Sage, "The failure of optical fibres embedded in composite mateials.," *Composites*, vol. 19, pp. 288 -494, 1988.
[221] H. J. Bang, D. H. Kima, H. K. Kang, C. S. Hong, and C. G. Kim "Optical fiber sensor systems for simultaneous monitoring of strain and damage in smart composites," *Proceedings of SPIE*, vol. 5050, pp. 43-51, 2003.
[222] I. Read, P. Foote, and S. Murray, "Optical fibre acoustic emission sensor for damage detection in carbon fibre composite structures," *Measurement Science & Technology*, vol. 13, pp. N5-N9, 2002.
[223] S. G. Pierce, B. Culshaw, K. Worden, and W. J. Staszewski, "Lamb wave sensing for composite materials evaluation.," *Smart Structures and Materials 1999: Sensory Phenomena and Measurement Instrumentation for Smart Structures and Materials, 1-4 March 1999, Newport Beach, CA, USA, Proc. SPIE - Int. Soc. Opt. Eng. (USA),*, vol. Band 3670, pp. 403-410, 1999.
[224] V. Dewynter-Marty, P. Ferdinand, H. Beranger, S. Bourasseau, M. Dupont, D. Balageas, E. Bocherens, and R. Carbone, "JournalEmbedded Fiber Bragg Grating sensors for industrial composite cure monitoring. of Intelligent Material Systems and Structures," *Journal of Intelligent Material Systems and Structures*, vol. 9, pp. 785-787, 1999.
[225] N. D. Dykes, M. J. O'Dwyer, S. W. James, R. P. Tatam, and P. E. Irving, "Mechanical and sensing performance of embedded in-fibre Bragg grating devices during impact testing of carbon fibre reinforced polymer composite.," *Workshop on Smart Systems Demonstrators: Concepts and Applications.*, 1998.
[226] A. Frank, *Dehnungs- und Temperaturmessung in Verbundwerkstoffen mit eingebetteten faseroptischen Bragg-Gitter-Sensoren*, Thesis for the degree of Doctor of Technical Sciences, Eidgenössische Technische Hochschule (ETHZ), Zürich, 2001.
[227] A. Frank, P. M. Nellen, R. Brönnimann, and U. Sennhauser, "Fiber Optic Bragg Grating Sensors Embedded in GFRP Rockbolts.," presented at Smart Structures and Materials 1999: Sensory Phenomena and Measurement Instrumentation for Smart Structures and Materials, 1999.
[228] E. J. Friebele, C. G. Askins, M. A. Putnam, J. Florio, Jr., A. A. Fosha, Jr., R. P. Donti, and C. D. Mosley, "Distributed strain sensing with fiber Bragg grating arrays embedded in CRTM composites.," *Proceedings of the SPIE - The International Society for Optical Engineering*, vol. 2361, pp. 338-41, 1994.
[229] J. A. Guemes, J. M. Pintado, M. Frovel, F. R-Lence, and J. M. Menendez, "Embedded Fibre Bragg Gratings for Damage Detection in Composites", in *Proceedings of the 4th International Workshop on Structural Health Monitoring*, F.-K. Chang, Ed. Lancaster: DEStech Publications, Inc., 2003.
[230] X. D. Jin, J. S. Sirkis, J. K. Chung, and V. S. Venkat, "Embedded in-line fiber etalon/Bragg grating hybrid sensor to measure strain and temperature in a composite beam.," *Journal of Intelligent Material Systems and Structures*, vol. 9, pp. 171-181, 1998.
[231] M. Kowalik, I. McKenzie, and S. C. Galea, "Detection of disbonds in secondary bonded structures using embedded Bragg grating optical fibre sensors.," presented at Proceedings of the SPIE 2000 Symposium on Smart Materials and MEMS, Melbourne, Australia, 2000.
[232] X. C. Li, F. Prinz, and J. Seim, "Thermal Behaviour of Metal Embedded Fiber Bragg Grating Sensor," *submitted to Journal of Smart Materials and Structures*, 2000.
[233] J. Matrat, K. Levin, and R. Jarlas, "Implementation of a Bragg Grating Strain Rosette Embedded in Composites.," *Smart Structures and Materials 2001: Sensory Phenomena and Measurement Instrumentation for Smart Structures and Materials, Proc. SPIE*, vol. 4328, pp. 168-179, 2001.
[234] J. Matrat, K. Levin, and R. Jarlås, "Effect of Debonding on Strain Measurement of Embedded Bragg Grating Sensors.," *Structural Health Monitoring: 2000, Technomic Publishing Company, Inc.,*, pp. 651-660, 1999.

[235] P. M. Nellen, A. Frank, R. Brönnimann, U. Meier, and U. Sennhauser, "Fiber Optical Bragg Grating Sensors Embedded in CFRP Wires.," presented at Smart Structures and Materials 1999: Sensory Phenomena and Measurement Instrumentation for Smart Structures and Materials, 1999.

[236] Y. Okabe, S. Yashiro, T. Kosaka, and N. Takeda, "Real-time detection of transverse cracks in CFRP composites using embedded fiber Bragg grating sensors.," *to be published in Smart Structures and Materials*.

[237] K. Peters, M. Studer, J. Botsis, A. Iocco, H. G. Limberger, and R. P. Salathe, "Measurement of stress concentrations using embedded optical fiber Bragg grating sensors.," *Proceedings of the SPIE - The International Society for Optical Engineering*, vol. 3670, pp. 195-206, 1999.

[238] M. Prabhugoud and K. Peters, "Efficient interpretation algorithm for embedded Bragg gratings for damage detection in composites," *Proceedings of SPIE*, vol. 5050, pp. 159-170, 2003.

[239] S. Sandlin and A. Hokkanen, "Reliability of metal embedded fibre optical BRagg gratings at elevated temperatures up to 600°C," 2003.

[240] N. Tanaka, Y. Okabe, and N. Takeda, "Temperature-compensated strain measurement using FBG sensors embedded in composite laminates," presented at Smart Structures and Materials 2002: Smart Sensor Technology and Measurement Systems, San Diego, CA, USA, 2002.

[241] N. Tanaka, Y. Okabe, and N. Takeda, "Temperature-compensated strain measurement using fibre Bragg grating sensors embedded in composite laminates," *Smart Materials and Structures*, vol. 12, pp. 940-946, 2003.

[242] L. Tang, X. Tao, and C.-I. Choy, "Effectiveness and optimization of fiber Bragg grating sensor as embedded strain sensor.," *Smart Materials and Structures*, vol. 8, pp. 154-160, 1999.

[243] K. Worden, W. J. Staszewski, and G. R. Tomlinson, "Smart Systems - The Role of Signal Processing", in *Proceedings of CEAS (Confederation of European Aerospace Societies) International Forum on Aeroelasticity and Structural Dynamics*. Rome, Italy, 1997.

[244] W. J. Staszewski, "Structural and Mechanical Damage Detection Using Wavelets.," *The Shock and Vibration Digest*, vol. 30, pp. 457-472, 1998.

[245] P. D. Wilcox, *Lamb Wave Inspection of Large Structures Using Permanently Attached Transducers*, PhD Thesis, Imperial College, London, 1998.

[246] C. M. Harris and A. G. Piersol, *Harris' Shock and Vibration Handbook*. McGraw-Hill, New York, 2002.

[247] M. Kehlenbach and S. Das, "Identifying Damage in Plates by Analyzing Lamb Wave Propagation Characteristics," presented at Smart Structures and Materials, San Diego, 2002.

[248] S. Mallat, *A Wavelet Tour of Signal Processing*. Academic Press, New York, 1998.

[249] C. Cempel, *Vibroacoustic Condition Monitoring*. Ellis Horwood, Chichester, 1991.

[250] R. A. Collacot, *Mechanical Fault Diagnosis and Condition Monitoring*. Chapman and Hall, London, 1977.

[251] J. W. Cooley and J. W. Tukey, "An algorithm for the machine calculation of complex Fourier series, Vol 19(90): page 291," *Mathematics of Computation*, vol. 19, pp. 291, 1965.

[252] E. O. Brigham, *The Fast Fourier Transformation*. Prentice Hall, Inc., Englewood Cliffs, N.J., 1974.

[253] W. J. Staszewski, "Advanced data pre-processing for damage identification based on pattern recognition.," *International Journal of Systems Science*, vol. 31, pp. 1381-1396, 2000.

[254] W. J. Staszewski, *Wavelets for Mechanical and Structural Damage Identification*. IMP PAN Press, Gdansk, 2001.

[255] V. Giurgiutiu and L. Yu, "Comparison of Short-Time Fourier Transform and Wavelet Transform of Transient and Tone Burst Wave Propagation Signals for Structural Healtm

Monitoring", in *Proceedings of the 4th International Workshop on Structural Health Monitoring*, F.-K. Chang, Ed. Lancaster: DEStech Publications, Inc., 2003.
[256] D. E. Newland, *An Introduction to Random Vibrations, Spectral & Wavelet Analysis*. Longman Scientific & Technical, Harlow, England, 1993.
[257] I. Daubechies, *Ten Lectures on Wavelets*. SIAM, Philadelphia, 1992.
[258] D. Donoho and I. Johnstone, "Ideal denoising in an orthonormal basis chosen from a library of bases," *C.R. Acad. Sci. Paris, Serie I*, vol. 319, pp. 317-322, 1994.
[259] D. Donoho and I. Johnstone, "Ideal spatial adaption via wavelet shrinkage," *Biometrika*, vol. 81, pp. 425-455, 1994.
[260] W. J. Staszewski, I. Read, and P. D. Foote, "Damage Detection in Composite Materials Using Optical Fibres - Recent Advantages in Signal Processing.," *SPIE's 7th International Symposium on Smart Structures and Materials Conference on Smart Structures and Integrated Systems, Newport Beach, CA*, 2000.
[261] W. J. Staszewski, "Wavelet Based Compression and Feature Selection for Vibration Analysis.," *Journal of Sound and Vibration*, vol. 211, pp. 735-760, 1998.
[262] R. Seydel and F.-K. Chang, "Impact identification of stiffened composite panels: I. system developments," *Smart Material and Structures*, vol. 10, pp. 354-369, 2001.
[263] R. Seydel and F.-K. Chang, "Impact identification of stiffened composite panels: II. implementation studies," *Smart Material and Structures*, vol. 10, pp. 370-379, 2001.
[264] W. J. Staszewski, K. Worden, G. R. Tomlinson, and A. Ball, "Optimal Sensor locations for impact detection on a composite panel." in *Proceedings of the 2nd International Workshop on Damage Assessment Using Advanced Signal Processing Procedures - DAMAS 97*. Sheffield, UK, 1997.
[265] K. Worden and W. J. Staszewski, "Impact Location and Quantification on a Composite Panel using Neural Networks and a Genetic Algorithm," *Strain 2000*, vol. 36, pp. 61-70, 2000.
[266] P. T. Coverley and W. J. Staszewski, "Impact Damage Location in Composite Structures Using Optimised Sensor Triangulation Procedure," *Smart. Mater. Struct*, 2002.
[267] P. T. Coverley and W. J. Staszewski, "Impact damage location in composite structures using genetic algorithms," *Proceedings of the First European Workshop on Structural Healt Monitoring 2002*, pp. 271-278, 2002.
[268] D. E. Goldberg, *Genetic Algorithms in Search, Optimisation, and Machine Learning*. Addison-Wesley, 1989.
[269] H.-P. Schwefel, *Evolution and Optimum Seeking*. John Wiley & Sons, New York, 1995.
[270] P. T. Coverley, *Impact Damage Location in Smart Composite Structures using Genetic Algorithms*, MSc Thesis, University of Sheffield, Sheffield, 2002.
[271] B. A. Auld, *Acoustic fields and waves in solids*. North-Holland, New York, 1990.
[272] D. Certon, N. Felix, I. Lacaze, F. Teston, and F. Patat, "Investigation of cross-coupling in 1-3 piezocomposite arrays," *IEEE Transactions on Ultrasonics, Ferroeletrics and Frequency Control*, vol. 48, pp. 58,92, 2001.
[273] J. Krautkrämer and H. Krautkrämer, "Werkstoffprüfung mit Ultraschall.," *Springer Verlag, Berlin Heidelberg*, 1986.
[274] D. Broek, *The practical use of fracture mechanics*. Kluwer Academic Publishers, Dordrecht, 1988.
[275] S. Suresh, *Fatigue of materials*. Cambridge University Press, Cambridge, 1998.
[276] B. Aktepe and A. Baker, "Sensor techniques to validate the stress intensity in cracked metallic panels repaired with bonded composite patches," *Proceedings of the12th International Conference on Composite Materials (ICCM12), Paris*, 1999.
[277] A. Baker, "Bonded Composite Repair of Metallic Aircraft Components -Overview of Australian Activities.," *AGARD-CP-550 Published 1995 Paper 1*, pp. 1-14, 1995.
[278] A. Baker, "Fatigue studies related to certification of composite crack patching for primary metallic aircraft structure," *Proceedings of FAA-NASA Symposium on Continued Airworthiness of Aircraft Structures Atlanta*, 1996.

[279] A. Baker, "Issues in the certification of bonded composite patch repairs for cracked metallic aircraft structures," *Proceedings of the 20th Symposium of the International Committee on Aeronautical Fatigue (ICAF),Seattle, USA*, 1999.
[280] S. P. Timoshenko and J. N. Goodier, "Theory of Elasticity.," *3rd edition, McGraw-Hill 1970*, 1987.
[281] O. Diligent, *Interaction Between Fundamental Lamb Modes And Defects in Plates*, PhD Thesis, Imperial College, London, 2003.
[282] J. C. P. McKeon and M. K. Hinders, "Lamb wave scattering from a through hole," *Journal of Sound and Vibration*, vol. 224, pp. 843-862, 1999.
[283] HBM, "MGCplus - Product Specifications S31.03.0," Hottinger Baldwin Messtechnik 2000.
[284] C. Duvall, "VCSELs may make metro networks dynamic," *WDM Solutions*, 2000.
[285] A. Lindstrom, "Widely Tunable Lasers Ready to Lock and Roll," *Photonics Spectra*, 2002.
[286] G. Meltz and W. W. Morey, "Bragg-Grating Formation and Germanosilicate Fiber Photosensitivity.," *SPIE*, vol. 1516, 1991.
[287] R. M. Atkins, V. Mizrahi, and T. Erdogan, "248 nm Induced vacuum uv spectral changes in optical fibre preform cores. Support for colour centre model of photosensitivity.," *Electronics Letters*, vol. 29, pp. 385-387, 1993.
[288] L. Dong, J. L. Archambault, L. Reekie, P. S. J. Russell, and D. N. Payne, "Photoinduced absorption change in germanosilicate preforms: evidence for the color-center model of photosensitivity.," *Applied Optics*, vol. 34, pp. 3436-3440, 1995.
[289] T. Erdogan and V. Mizrahi, "Characterization of UV-inuced birefringence in photosensitive Ge-doped silica optical fibers ." *J. Opt. Soc. Am. B*, vol. 11, pp. 2100-2105, 1994.
[290] R. Kashyap, "Photosensitive Optical Fibers: Devices and Applications," *Optical Fiber Technology*, vol. 1, pp. 17-34, 1994.
[291] P. J. Lemaire, R. M. Atkins, V. Mizrahi, and W. A. Reed, "High Pressure H2 Loading as a Technique for Achieving Ultrahigh UV Photosensitivity and Thermal Sensitivity in Ge02 Doped Optical Fibres.," *Electronics Letters*, vol. 29, pp. 1191-1193, 1993.
[292] D. S. Staradubov, V. Grubsky, J. Feinberg, B. Kobrin, and S. Juma, "Bragg grating fabrication in germanosilicate fibers by use of near-UV light: a new pathway for refractive-index changes.," *Optics Letters*, vol. 22, pp. 1086-1088, 1997.
[293] G. Meltz, W. W. Morey, and W. H. Glenn, "Formation of Bragg gratings in optical fibers by a transverse holographoc method.," *Optics Letters*, vol. 14, pp. 823-825, 1998.
[294] R. Feced, M. P. Roe-Edwards, S. E. Kanellopoulos, N. H. Taylor, and V. A. Handerek, "Mechanical strength degradation of UV exposed optical fibres.," *Electronics Letters*, vol. 33, pp. 157-158, 1997.
[295] C. G. Askins, M. A. Putnam, G. M. Williams, and E. J. Friebele, "Stepped-wavelength optical-fiber Bragg grating arrays fabricated in line on a draw tower.," *Optics Letters*, vol. 19, pp. 147-149, 1994.
[296] E. J. Friebele, C. G. Askins, M. A. Putnam, G. M. Williams, A. D. Kersey, A. A. Fosha, J. Florio, R. Donti, P., and R. G. Blosser, "Fabrication and application of low-cost optical fiber sensor arrays for industrial and commercial applications.," *Ind. and Commercial Applications of Smart Structures Technol., Smart Structures and Materials 1995, San Diego, USA, Proc., SPIE*, vol. 2447, pp. 305-311, 1995.
[297] L. Dong, J. L. Archambault, L. Reekie, P. S. J. Russell, and D. N. Payne, "Single Pulse Bragg Gratings written During Fibre Drawing.," *Electronic Letters*, vol. 29, pp. 1577-1578, 1993.
[298] http://www.sabeus.com.
[299] L. Chao, L. Reekie, and M. Ibsen, "Grating writing through fiber coating at 244 and 248 nm," *Electronics Letters*, vol. 35, pp. 924-926, 1999.
[300] A. S. Khan and X. Wang, *Strain measurements and stress analysis*. Prentice Hall, New Jersey, 2001.
[301] C. J. Hellier, *Handbook of non-destructive evaluation*. McGraw-Hill, 2001.

[302] G. Muravin, *Inspection, diagnostics and monitoring of construction materials and structures by the acoustic emission methods*. Minerva Press, London, 2000.
[303] T. Holyrod, *The Acoustic Emission and Ultrasonic Monitoring Handbook*. Coxmoor Publishing Company, Oxford, 2001.
[304] A. S. Buirks, J. R. E. Grenn, and P. McIntire, "Nondestructive testing Handbook. Vol.7, Ultrasonic Testing." Columbus: American Society of Nondestructive Testing Press, 1991.
[305] P. J. Shull, *Nondestructive evaluation: theory, techniques, and applications*. Marcel Dekker, Inc., New York, 2002.
[306] PI, "Fundamentals of Piezoelectricity and Piezo Actuators", in *MicroPositioning, NanoPositioning, NanoAutomation (PI catalog)*. Karlsruhe: PI (Physik Instrumente), 2001.
[307] APC, *Piezoelectric Ceramics: Principles and Applications*. American Piezo (APC) International, Ltd., 2003.

Appendix

Appendix A: Fibre Bragg Grating Sensors

Photosensitivity

In 1978 Hill and co-workers observed an increasing reflection of the light of an argon ion laser at 488 nm in a germanium-doped silica fibre [18]. The light coupled into the fibre interfered with the Fresnel reflected beam from the end of the fibre and formed a standing wave intensity pattern. The high-intensity points obviously altered the index of refraction and the so far unknown non-linear effect has been called photosensitivity. This effect describes the influence of ultraviolet light on the refractive index of photosensitive optical fibres. In contrary to the well known photo-elastic effect that occurs in ferroelectric materials due to the electro-optic effect, photosensitivity produces less intense index modulations [49].

Standard telecommunication fibres possess only relatively low photosensitivity, which can be increased by means of photosensitisation. This expression encompasses a number of methods that have been found useful to increase the photosensitivity of fibres. Doping of the fibre core proved to be a very effective method. As almost all fibres contain some kind of dopant used to generate the index profile of the fibre, this almost automatically leads to increased photosensitivity of commonly used fibres. Since germanium doped fibres are the most important photosensitive fibres, most studies that focused on the theory of photosensitivity focus on that material [286-290]. However, several other methods such as hydrogen loading [291], flame brushing, use of other writing wavelengths than the common 240 nm band [292] and use of other co-dopants have been successful [16, 17].

The effect of photosensitivity is still not fully understood. Not just one single effect can be made responsible for all the effects seen in the experiments. Three main contributions have been made out in germanosilicate optical fibres:

- Formation of colour centres (GeE')
- Densification and increase in tension
- Formation of GeH

The colour centre model predicts an increase in the population of GeE' centres, which are germanium oxygen vacancy defects in the glass matrix, after UV exposure. The resultant colour-centres are responsible for changes in the UV absorption spectra, which lead to a change in the refractive index directly through the Kramers-Kronig relationship. The densification model is based on changes in the fibres density that result in refractive index changes. Such a change in the materials density can be induced by the UV laser irradiation. In hydrogen loaded fibres one important effect of the hydrogen is the reaction with the Ge ion to form GeH, under the influence of UV radiation. The formation of GeH changes the band

structure in the UV region. As in the colour-centre model, these changes, in turn, influence the local refractive index as per the Kramers-Kronig model.

Due to different dominating photosensitive effects a classification of the different types of Bragg gratings has been established: Type I, Type IIa and Type II.

Type I gratings refer to gratings that are formed in normal photosensitive fibres under moderate intensities. They are the most utilised Bragg gratings in telecom and sensor applications. The qualitative form of the UV-induced change of the refractive index versus time for a type I grating is shown in Figure A.1.

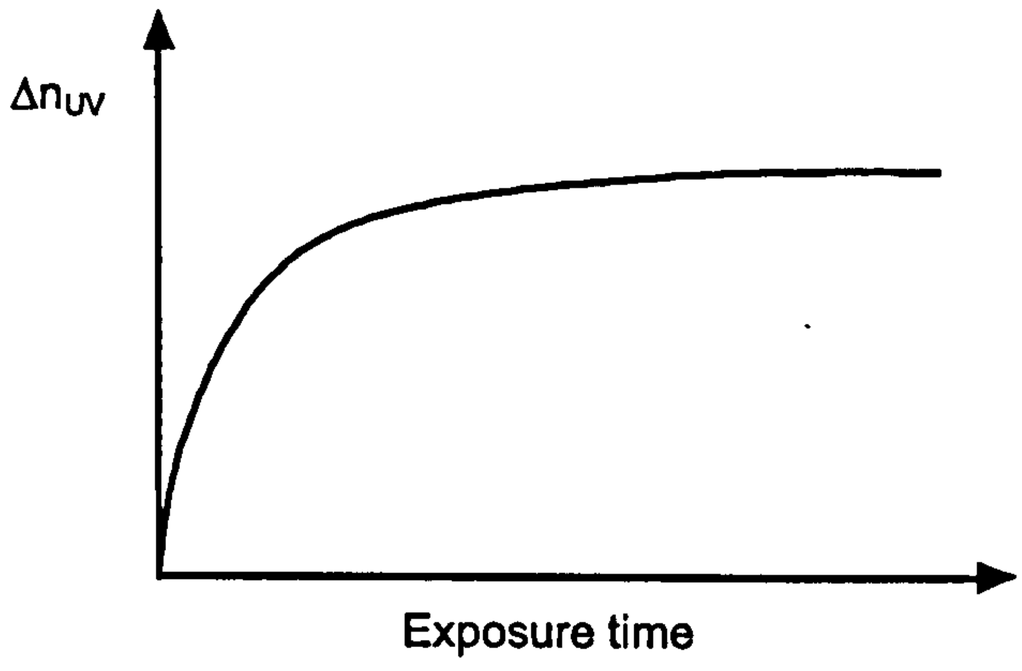

Figure A.1: UV-induced change of the refractive index versus time.

The high growth rate of the index change, and of the corresponding reflectivity of the grating, allows the formation of single pulse gratings. This will be important for the fabrication process, as discussed in the next section.

Type IIa gratings are inscribed through a significantly longer process than Type I gratings. Although the have the same spectral characteristics, Type IIa gratings have noticeable higher thermal decay limits. Their limitation is however associated with the time-consuming fabrication process.

Type II gratings are formed under very high, single-pulse fluence. They have different transmission and reflection characteristics. Wavelengths longer than the Bragg wavelength can pass the gratings, whereas shorter wavelengths are strongly coupled into the cladding. Thermal stability tests have shown that Type II gratings are extremely stable at high temperatures. And in contrast to Type IIa gratings, the fabrication process is conform with the on-line fabrication of the gratings [122].

Fabrication

The aforementioned discovery of photosensitivity took place when interference occurred between light coupled into a fibre and the reflected wave from the fibre end. The standing wave produced a modulation of the refractive index of the period

$$\Lambda = \frac{\lambda_{in}}{2n_{eff}} \tag{A.1}$$

where λ_{in} is the wavelength of the light coupled into the fibre and n_{eff} is the effective refractive index in the grating region. The so-formed grating then causes a reflection of incident light that meets the Bragg condition:

$$\lambda_B = 2n_{eff}\Lambda \tag{A.2}$$

It is obvious that this equation is only satisfied for the wavelength of the light used to produce the grating as depicted in Equation (A.2). This restriction has been overcome by a new fabrication process established by Meltz and his co-workers in 1989 [293]. They managed to inscribe the grating externally by side-exposing a photosensitive fibre to the interference pattern of a UV irradiation source. It is possible to side-write a grating into the fibre core, because the fibre cladding is transparent for UV light, whereas the core is not. There exist two major methods for side-writing Bragg gratings into fibres, the interferometric technique and the phase mask technique. A third method where the grating is written point-by-point has almost no practical importance, but is suitable for special purpose gratings . For commercial fabrication of Bragg gratings the use of the phase mask technique is the standard process. The advantages of this method lay in the excellent reproducibility, low demands on the coherence of the light source and the possibility to produce long and complex grating structures. The drawback however is that for every grating with a specific structure or wavelength one specific phase mask has to be provided. The interferometric method has the advantage that it is easy to change the grating period and therefore to produce any desired Bragg wavelength This is shown in Figure A.2. The UV laser beam is split into equal intensity beams that subsequently recombine after the reflection at two mirrors. The beams interfere at the region of the fibre core and produce a fringe pattern that subsequently creates the Bragg grating. The period of the grating follows from the period of the interference pattern, that depends on both the UV wavelength λ_{UV}, and the angle θ between the intersecting UV beams. The period of the grating is then given as

$$\Lambda = \frac{\lambda_{UV}}{2\sin\left(\frac{\theta}{2}\right)} \tag{A.3}$$

It can be shown that it is relatively simple to change the desired grating period by changing the angle between the intersecting beams. The interferometric technique however has stringent requirements on a stable mechanical set-up. Furthermore, a laser source with a good spatial and temporal coherence and stable wavelength and power output is required.

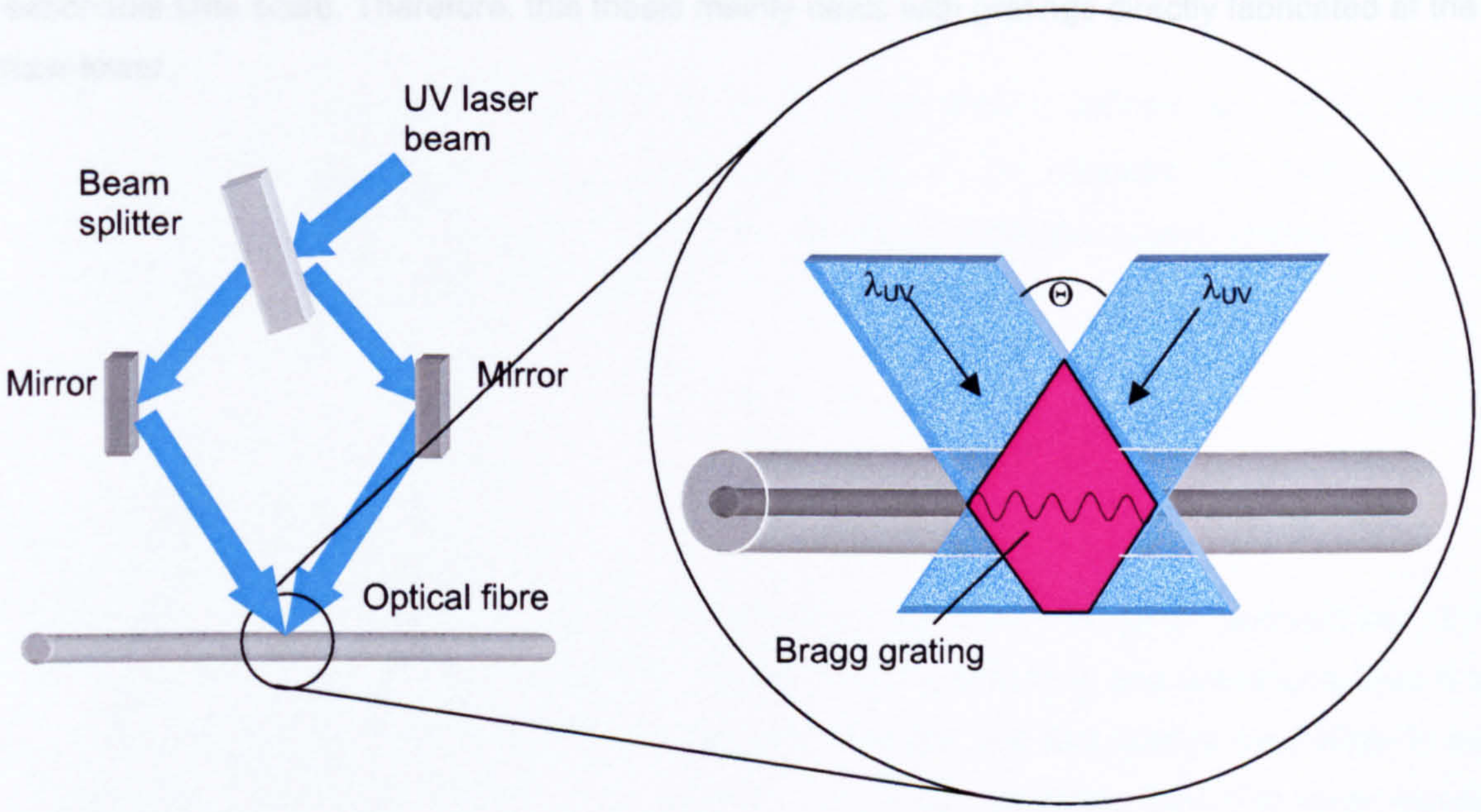

Figure A.2: Fabrication of fibre Bragg gratings – the interferometric technique.

The standard fabrication process requires the stripping of the UV absorbing polymer coating before the fibre can be exposed to the UV irradiation. Several investigations show that this process significantly weakens the fibre and reduces its mechanical strength [294] (see Section 2.6.2). Even if the fibre is recoated after the inscription process, the high mechanical strength is lost. Two methods have been established that avoid this drawback. The first technique is the inscription during fibre drawing [123, 295-297] and the second one the inscription through a special UV transparent polymer coating. FBGs fabricated directly through the polymer coating have become commercially available [298, 299]. Investigations that accompanied the current work showed poor thermal behaviour of this kind of gratings (see Section 2.7). It has to be stressed that for sensor applications other properties of the fibre grating are required than for telecom FBGs. Mechanical and thermal strength are vital for any structural monitoring. This is true not only for the grating itself but also for the coating of the

fibre. The draw-tower technique offers another advantage over other inscription methods as one has almost free choice of the fibre coating (see also Section 2.7). Because no recoating is required a coating with excellent adhesive properties can be chosen. For the inscription of the grating during the fibre drawing process only single shot gratings can be formed. This is because the fibre itself is in constant motion at the draw tower. Single pulse gratings can be fabricated due to the high growth rate of the grating reflectivity as presented in Figure A.1. Under controlled drawing and inscription conditions reflectivities up to 15-20 % can be achieved. Another big advantage of the draw-tower technique is its suitability for mass production. No other method offers the chance of writing many gratings in the same section of a fibre within a reasonable time scale. Therefore, this thesis mainly deals with gratings directly fabricated at the draw-tower.

Appendix B: Stress-Strain Relations

Structural loads are usually determined by observing the deformation of the structure under a specific load. The relation between the structural load and the deformation can be obtained from the stress-strain relations. Within certain stress limits the relation between structural load σ and structural strain ε_x is given by Hooke's law, which for unidirectional stress can be written as [280]

$$\varepsilon_x = \frac{\sigma_x}{E} \tag{B.1}$$

where E is Young's modulus or the modus of elasticity. The strain is defined as $\varepsilon = \Delta L/L_0$, where ΔL is the change in length and L_0 is the initial length of the structure. For isotropic and homogenous materials it appears that any uniaxial stress produces lateral strains ε_y and ε_z where the following relationship holds [280]

$$\varepsilon_y = \varepsilon_z = -\nu\frac{\sigma_x}{E} = -\nu\varepsilon_x \tag{B.2}$$

and ν is known as Poisson's ratio.

In case of monitoring the loads of mobile structures such as aircraft or automotives, the structural layout will always be such as the response of the structure to any operational load is a linear elastic deformation, i.e. equation (B.1) holds. However, the real load is most likely to be more complex than an uniaxial load and will result in a multiaxial stress field. For linear elastic deformations the principle of superposition can be employed, which means that two or more stress fields can be combined by direct superposition whereas the order of the combination does not affect the final stress field [300].

Similarly to the Hooke's law, given by Equation (B.1), the following linear relation for the shear stress τ_{xy} and the shear strain γ_{xy} can be found [280]

$$\gamma_{xy} = \frac{\tau_{xy}}{G} \qquad \text{with} \qquad G = \frac{E}{2(1+\nu)} \tag{B.3}$$

where G is the modulus of rigidity or modulus of elasticity in shear. The shear strains γ_{yz} and γ_{zx} are defined accordingly.

The aim of any load monitoring system is to provide knowledge about the actual operational loads of the structure. In a general three dimensional system this requires the knowledge of the three components of stress and the three components of shear stress. However, most practical

applications are referred to an experimental stress analysis in flat plate-like structures whose thickness is small compared with its other dimensions or to a free surface of a more complex three-dimensional body. For these special cases, there are no stresses in the direction perpendicular to the surface. This condition is known as the plane stress. It can be characterised as $\sigma_z = \tau_{xz} = \tau_{yz} = 0$. The equations to solve therefore reduce to a two-dimensional problem. The stress-strain relations become [280]

$$\begin{aligned} \sigma_x &= \frac{E}{1-\nu^2}\left(\varepsilon_x + \nu\varepsilon_y\right) \\ \sigma_y &= \frac{E}{1-\nu^2}\left(\varepsilon_y + \nu\varepsilon_x\right) \\ \sigma_z &= 0 \qquad\qquad \tau_{xy} = G\gamma_{xy} \end{aligned} \tag{B.4}$$

The task of building up a load monitoring system can therefore be done by implementing a strain monitoring system. Knowing the structural properties as Young's modulus, modulus of rigidity and Poisson's ratio, the stress field can be derived from the strain field using Equation (B.4).

Principal strain

Many engineering problems require the knowledge of the strain level associated with another coordinate system or the determination of the directions of maximum and minimum strain. The latter are also called the principal strains. Therefore it is necessary to find the equations of strain transformation from one coordinate system to another. If the initial system is the x-y system and the destination system is the x'-y' system then an angle α between the x and the x' axis can be defined. The following equations of strain transformation can be found as [300]

$$\begin{aligned} \varepsilon_{x'} &= \varepsilon_x \cos^2\alpha + \varepsilon_y \sin^2\alpha + \gamma_{xy}\sin\alpha\cos\alpha \\ \varepsilon_{y'} &= \varepsilon_x \sin^2\alpha + \varepsilon_y \cos^2\alpha - \gamma_{xy}\sin\alpha\cos\alpha \\ \gamma_{x'y'} &= 2\left(\varepsilon_x - \varepsilon_y\right)\sin\alpha\cos\alpha + \gamma_{xy}\left(\cos^2\alpha - \sin^2\alpha\right) \end{aligned} \tag{B.5}$$

Principal strains are generally indicated by indices 1 and 2. It can be shown that the principal strains, the principal angle α and the maximum shear strain can be obtained as [300]

$$\varepsilon_1 = \varepsilon_{\max} = \frac{\varepsilon_x + \varepsilon_y}{2} + \left[\left(\frac{\varepsilon_x - \varepsilon_y}{2}\right)^2 + \left(\frac{\gamma_{xy}}{2}\right)^2\right]^{1/2}$$

$$\varepsilon_2 = \varepsilon_{\min} = \frac{\varepsilon_x + \varepsilon_y}{2} - \left[\left(\frac{\varepsilon_x - \varepsilon_y}{2}\right)^2 + \left(\frac{\gamma_{xy}}{2}\right)^2\right]^{1/2} \qquad \text{(B.6)}$$

$$\tan 2\alpha = \frac{\gamma_{xy}}{\varepsilon_x - \varepsilon_y}$$

$$\gamma_{\max} = \varepsilon_1 - \varepsilon_2$$

Principal stresses from principal strains

Once the principal strains ε_1 and ε_2, Young's modulus E, and Poisson's ratio ν are known, the principal stresses σ_1 and σ_2 can be found by replacing the subscripts x and y in Equation (B.4) by 1 and 2:

$$\sigma_1 = \frac{E}{1-\nu^2}(\varepsilon_1 + \nu\varepsilon_2); \quad \sigma_2 = \frac{E}{1-\nu^2}(\varepsilon_2 + \nu\varepsilon_1) \qquad \text{(B.7)}$$

The directions of the principal stresses are the same as those of the principal strains. Determining the principal stresses from the strains requires the following properties of the structure under investigation:

- homogenous material without any discontinuities or faults;
- isotropic characteristics, i.e. Young's modulus and Poisson's ratio are independent of the direction;
- linear elastic behaviour, i.e. the Hooke's law holds.

Visual Inspection

Visual Inspection is the leading NDT/E method and it represents the highest percentage of the inspection procedures that is applied to aircrafts in service. Although it was the first inspection method used in the industry, it took a long time to be formally acknowledged. The method can be divided into to categories: direct visual and remote (indirect) visual. For direct visual testing the human eye may be assisted by measuring devices, auxiliary light sources, visual aids such as magnifiers, mirrors and cameras. Direct visual examination is conducted when access allows the eye to be within 610 mm of the surface to be examined, and at an angle not less than 30° to the surface to be examined [301]. Whenever the eye cannot obtain a direct view of the specimen test surface without an assisting device, a remote visual examination is required. It is defined as an inspection that uses one of the following three aiding devices: borescopes (endoscopes), fibrescopes and video technology. Borescopes have been originally developed to inspect the bores of rifles or cannons utilising a hollow tube, a mirror and a miniaturised light source. The introduction of optical fibres for optical image transmission allowed the formation of a flexible fibrescope in contrast to the rigid borescope. The development of video and photographic devices that can be mounted on the scopes and record the image produced established the latest category of remote visual testing.

Applications that are covered by Visual Inspection are manifold. The fundamental task is the detection of discontinuities on the surface of the materials. These can be inherent to the material, process-induced or service-induced. They can appear in form of corrosion, cracks, and many other ways. The advantage of visual inspection over other techniques is that it generally gives the clearest view of the test surface. The direct view will result in the processing of the full spectrum of light wavelengths that are available to the human eye and the brain to form an image. The information on the damage is directly available to the inspector through a change in colour, forming of shades and textures or any other visual attributes. Clearly, NDE by means of visual testing is restricted to the surface of the test structure. As it will not always be possible to have access to the inspection area even with the aid of remote imaging tools, visual testing is limited to the cases where access is can be gained. However, with emerging technology of video and photographs, e.g. digital imaging and storage as well as miniaturisation these limits are further put ahead. Another draw back is that the results of visual testing depend on the experience and skill of the inspector.

Penetrant Testing

Penetrant Testing is a method that is part of visual inspection. The basic principle on which Penetrant Testing is based is that of capillary action. Capillary action is a surface tension

phenomenon that permits liquids to be drawn into tight openings. Penetrant Testing is a widely used NDE method and can be applied to a variety of materials. For Penetrant Testing to object to be examined has to be carefully cleaned. Then a penetrant – a material that seeps into and out of a surface discontinuity - is applied. To be seen, the penetrant must be of different colour than the surface and it must be able to remove some of the penetrant, so that any profile of the discontinuity becomes visible.

Penetrant Testing has found applications in many industries including automotive and aerospace manufacturing and maintenance. The major advantage of the method is that it can be applied to almost every material. In addition, it is a relatively simple method and very economical. The major drawback is that it is restricted to the detection of surface discontinuities. Furthermore, the results strongly depend on the experience and skill of the inspector. Which is especially true because of the high demands on the surface cleanness. Moreover, the inspection area must be accessible to the inspector or to any visual aid tool.

Magnetic Particle Testing

Magnetic Particle Testing is another NDT/E method that belongs to the large group of visual inspection methods. It is used for detecting discontinuities on the surface or near the surface of components or structures. Magnetic Particle Testing is governed by the laws of magnetism and is therefore restricted to ferromagnetic materials. It is a relatively simple method, where the test object first has to be magnetised. Simultaneously, finely divided ferromagnetic particles are spread out over the surface. Any defects in the material will affect the magnetic field of the test specimen. Thus, the magnetic particles will be attracted to the edges of the defects. Looking at the distribution of the magnetic particles on the surface of the test specimen, surface and near surface defects will be outlined.

Applications of Magnetic Particle Testing are in any industry that deals with ferromagnetic materials, this is true for example for the automotive and aerospace industries. There are a number of advantages of magnetic particle testing. As penetrant testing it is a simple and economical method. But this method also works if the defect is filled with a foreign material and even for slightly subsurface defects. The greatest disadvantages have already been mentioned, its restriction to ferromagnetic materials and to surface or near-surface defects. Also, as for all visual inspection methods, the area of inspection must be accessible.

Acoustic Emission

Acoustic Emission (AE) testing is a method used to detect and locate faults in mechanically loaded structures and components [302, 303]. It provides comprehensive information on the origination of a discontinuity in a stressed component. The development of the discontinuities,

e.g. the growth of a crack , can also be monitored, when the component is subjected to an external stimulus such as a change in load, pressure, temperature, etc. Under mechanical loading the discontinuities in the component release energy. This energy travels in the form of high-frequency stress waves. These waves, analoguous to induced ultrasonic waves are received with the use of ultrasonic sensors. Analysis of the collected data comprises the characterisation of the received voltage according to their source location, voltage intensity and frequency analysis.

Acoustic emission has been attempted for a wide variety of applications. A widely used application is for example the testing and certification of metal pressure vessels or for fatigue crack detection in aerospace structures .

The strengths of acoustic emission are that it is useful for a variety of materials, it is a rather inexpensive technique and sensitive to small events. However, the results are very complex and very high data rates have to be recorded. The limitation of the method is its reduced repeatability.

Eddy Current

Eddy current testing is one of the oldest and most commonly used NDT/E methods. Being a mature, proven technology with a solid theoretical foundation, it is widely accepted in industries such as automotive, aeronautics and power generation, and it is an integral part of inspection and maintenance in these industries. Eddy Current is one of the NDT/E methods that is prescribed in the inspections and maintenance regulations for standard commercial aircrafts.

Eddy Current theory is based on the principles of electromagnetism, particularly the inductive behaviour of alternating current. The eddy current probe is an AC transformer that picks up an AC electromagnetic field that has been induced by an excitation coil. The eddy current probe consists of a pair of coils. The first one is the excitation coil that is driven by an AC signal, the other one is the pick up coil and it is connected to a voltmeter. During the test procedure, the excitation coil produces a primary magnetic field. In the presence of a ferromagnetic material this field will induce a current in the conductive material. These currents will travel in closed paths, generally circular due to the geometry of the excitation coil, thus the name eddy currents. Like all currents, the eddy currents themselves produce a magnetic field, this time called the secondary field, that opposes the primary field. What happens to the pick up coil is that both primary and secondary field overlap. For perfect conductors and couplings primary and secondary field are equal and therefore cancel each other. The magnitude of the voltage that is displayed at the voltmeter of the pick up coil strongly depends on the conductivity and magnetic permeability of the test material. Changes therein will affect the voltage. Conductivity variations

occur for example with material processing, hardness and temperature. Any inhomogeneity of the material due to cracks, flaws, porosities, etc. implies an apparent change in the overall conductivity compared to a defect free region. It is clear that the test specimen has to be a ferromagnetic material. This is true for metals and alloys, but also for low-conductivity materials such as graphite-epoxy composites, or steel-reinforced concrete.

What makes Eddy Current so attractive are the advantages it has as a noncontacting method: no couplants are required nor is a preparation of the structure necessary. This allows for automated high-speed inspection. Furthermore, the system cost is relatively low compared for example to radiographic methods. The probe size is small, the technique is light weight and portable. However, there are a number of disadvantages, so is the inspections method limited to conductors, only a surface or near-surface evaluation is possible, and the interpretation of the obtained test results are one of the most complex. Furthermore, it takes lots of time to monitor large surfaces.

Ultrasonic Inspection

Acoustical testing is one of the oldest methods to test the integrity of structures. When a solid object is struck this will set up a vibration at the natural frequency of the object. Any major disturbance of the structural homogeneity will distort that natural frequency and indicate that there is a problem (see also the paragraph on Vibration/Modal Analysis in this section). Yet, this approach in the region of acoustical frequencies being audible to the human ear takes relatively large disturbances to cause a detectable change in sound. This is because the size of the distortion and the acoustical wavelength need to be of the same order in magnitude for any interaction. Turning to smaller defects such as those important for NDE, as a consequence the acoustical wavelength has to decrease. The corresponding frequency range is known as ultrasound.

The basic concepts behind ultrasonic NDT/E are simple as described in [303, 304]. Ultrasonic waves can propagate in solids. As the waves travel, they interact with the material in a way that can be predicted from physical modelling. Looking at the transmitted or reflected waves knowledge can be gained about the constitution of the structure. For example, the thickness and the elasticity of the structure can be obtained, even the existence of flaws and cracks can be identified. The most popular ultrasonic method is the scanning of the test object.The use of guided ultrasonic waves also provides a suitable tool for structural inspections. However, as the approach is different to that of scanning inspections, guided waves are explained in Section 4.2.

Ultrasonic inspection requires the use of a transducer, to transform a voltage pulse into an ultrasonic pulse and vice versa. The transducer is placed onto the test object and transmits the pulse into it. The pulse travels through the object, responding to its geometry and mechanical

properties. The signal is then received by another transducer (pitch-catch method) or reflected back to the original transducer (pulse-echo method). Either way, the signal is transformed back into an electrical pulse, which can be observed and stored on devices such as oscilloscopes. An A-Scan measures the density of the test object at a single point, a B-scan refers to the variations along a single line, and a C-scan is a collection of B-scans forming a surface contour plot. C-scanning is a flexible and robust technique, and has become common practice in innumerable applications, especially in the aircraft industry, where ultrasonic NDT/E is used to detect cracks and fatigue damage of safety-critical parts.

The big advantage of the ultrasonic method is, that besides radiography it is the only method that can reveal substantial subsurface flaws in materials. But ultrasonic testing does not suffer from the safety hazards of radiography. Moreover, ultrasound has a high penetration depth, a high sensitivity and accuracy in detecting flaws, and allows automation and area scans. The drawback is that best results can only be achieved when a couplant is used to attach the transducers to the structure. Some non-contact or dry contact techniques have been developed, but suffer from limitations in sensitivity and accuracy. There is also a limit in detecting planar flaws parallel to the wavefront. Ultrasonic testing is time-consuming when large surfaces have to be investigated. In addition, access to the surface is required. Furthermore, implementation and data interpretation of the ultrasonic inspection requires highly skilled operators.

Nuclear Magnetic Resonance

Nuclear Magnetic Resonance (NMR) is a method to determine material properties such as the gyro magnetic ratio and to determine the distribution of certain elements in the test specimen. A strong homogenous magnetic field is used to align the nuclear spin due to their magnetic momentum. A short high frequency signal is used to flip the spin state of the nucleus. The frequency of that motion only depends on the gyro magnetic ratio and the strength of the static magnetic field. Using appropriate coils and powerful data processing units one can get tomographic pictures of the specimen. NMR is widely used in medicine and has also found its way into NDT. However, the method is relatively expensive and the equipment is bulky.

Microwave Testing

The microwave method uses high-frequency electromagnetic energy for the inspection and characterisation of materials. The microwave frequency region is generally taken to lie between a few hundred megahertz and a few hundred gigahertz, the corresponding wavelengths range from 100 cm to 1 mm. The operating frequency is chosen to maximise the interaction of the electromagnetic wave with dielectric layers, inclusions, surface flaws, cracks, etc. Microwave

inspection generally consists of measuring various properties of the electromagnetic waves scattered by, reflected from, or transmitted through a test specimen. The interaction of the wave with the material depends on the incident power level, the absorption factor of the material and the frequency of operation. The development of devices and signal processing tools for microwave inspection benefits from the importance of radar and microwave technology for example in military applications and traffic (speed) control.

Demonstrated and potential applications of microwave NDT/E include [305]: accurate measurements of thickness, detection of disbonds and delaminations, determination of fibre orientation in composites, and detection and sizing of cracks in metals. An important feature of microwave testing is that it is a non-contacting inspection method, which allows for inspection of difficult accessible areas or moving parts. The internal inspection of structures is restricted to dielectric materials, for conducting materials the inspection is limited to their surfaces. One of the big advantages of the technique is the big choice of different probes and sensors. It is therefore possible to find devices that fit best to a given inspection task. If the probes are arranged in arrays, relatively large areas of the specimen can be investigated by forming beams of the electromagnetic waves and analysing the propagation characteristics.

Thermography Testing

Thermography is a collective noun for both an active thermography, where external heating is used to induce temperature changes and the thermal response of the sample being monitored, and a passive thermography, where no external thermal source is required and the condition of the sample is obtained by its static thermal properties, e.g. hot-spots in electrical circuits. Active thermography is more relevant to NDT/E, as it is the intention to find damage which normally doesn't appear as a change in temperature itself, but as a modification of the thermal response. Despite the large number of different thermography methods, there are a some common features to all active thermography methods. For all methods a controlled heating of the specimen is required. The thermal energy has to be transported into and within the specimen. Commonly, an infrared camera is used to make images of the resulting structure surface temperature distribution. From these images the information about the material and structural properties of the sample have to be obtained. The most common way to introduce heat into a structure is by optical heating, for example by a pulsed laser beam. The temperature distribution on the surface is often imaged by fast infrared cameras triggered by the laser pulse, enabling high temporal resolution and high sensitivity.

Many defects of interest such as cracks or delaminations are very readily detected with active thermography. Thermography is used in all kind of applications ranging from vessel monitoring

to aircraft inspections. Several advantages make thermography attractive, such as being a non-contact inspection tool. Even large stand-off distances are possible. NDT/E using thermography is not restricted to the surface of the structure. Faults such as delaminations in composites that are not visible on the surface become detectable. This is because the delamination alters the thermal behaviour of the material and the temperature distribution on the surface is influenced by the properties of the whole material. Another strength of the technique is that studying the thermal properties (specific heat and thermal conductivity) of a material differs from other methods that focus on elastic or electrical properties. Thus, it will be more suitable to detect damages that rely to changes in thermal properties. A disadvantage however is that energy consumption is high in order to induce the thermal energy into the specimen and that a miniaturisation of the method is currently not feasible.

Optical Interferometry Testing

Optical interferometry in the NDT/E context comprises methods such us holographic interferometry, speckle interferometry and shearography. Interferometry is a means of detecting phase changes in an optical wave. To do so, coherent light that has travelled along two different optical paths is brought to interference. The image that is produced by an interferometric set-up is an interference pattern. Depending on the relative phase of the wave travelling along the two different paths, the interference can be either positive, then the two amplitudes add, it can be negative, then the amplitudes cancel or anything in between. The interferometer can be said to translate any phase modulation into an amplitude modulation. [78].

The holographic interferometry uses coherent light to illuminate the test object. The reflected light and a reference beam are recorded for example on a photographic film. Due to interference of both beams, a holographic interferogram develops. From this interferogram the three dimensional image of the object can be reconstructed. The recorded holographic interferogram prior to any damage serves as a reference against which later interferograms after the object deformation can be compared. Any object deformation will induce a phase shift between the reference and the current holographic interferogram. By interference of the two wavefronts of both holographic interferograms, the phase difference becomes a variation in brightness, which can easily be measured. This is the principle of holographic testing: Surface distortions are mapped to changes in optical irradiation and can then be quantified.

Another interferometric method is speckle interferometry. Here, an interference pattern is derived from interfering an image before and after the object has been damaged. The optical phase can be made sensitive to local in-plane or out-of-plane displacements. In consequence,

the information on any changes of the structure is encoded in the brightness of the interferometric image.

Both techniques suffer from the same drawback, as vibrations have to be eliminated and the geometrical distances have to be maintained between and during the measurements. A drawback that is overcome by shearography. This methods used a "shear optic" that enables a recording of the reflected light of the object from slightly different positions and brings them to interference. Compared to speckle interferometry this method gives rather displacement gradients than absolute displacements.

The obvious advantage of any interferometric technique is that it is non-contact. Since the measurements are being made with light, remote sensing of deformations is possible. Measurements can be made in hostile environments as long as there is any optical path available. As the sensitivity of the interferometer is related to the wavelength of the light, a high sensitivity can be achieved and measurements on the order of a fraction of a wavelength are possible. The potential draw-back is its restriction to surface displacements, no inner changes of the material can be measured. The area covered by the interferometric inspection is restricted to the illuminated area of the light source and the focus of the recording optics.

Radiography

Radiography, especially X-ray radiography, is one of the few NDT/E methods that can examine the interior of the test specimen and it is one of the methods that works on all materials. Since the discovery of the X-rays by Wilhelm Röntgen more than a hundred years ago, radiography has become a mature method in NDE.

X-rays are produced in a vacuum tube when high-speed electrons are attracted by an anode and collide with the anode material. The electrons are produced when a filament is heated to incandescence. The electrons leave the material and are accelerated in the electric field. When the electrons hit the anode two different effects take place: On the first hand, the characteristic X-rays with energies determined by the atoms of the anode. The colliding electrons eject orbital electrons from the anode atoms. These electron vacancies are promptly filled and X-rays with characteristic energy are emitted. The second effect, that usually dominates the X-ray production is the interaction of the electrons passing the anode with the electron structure of the atoms. Each interaction results in radiative loss in the form of bremsstrahlung. X-rays penetrate the test object almost without any deflection, but they get attenuated. Attenuation is proportional to the third power of the atomic number of the target material. If the X-rays that have passed the test object are recorded on a detector or photographic film, inhomogeneities of the material become visible. Using a sophisticated arrangement of several X-ray detectors, it is even

possible to get a three-dimensional image of the object. This method is called computer tomography.

Radiography has found many applications, especially for the inspection of welds and castings. But also in the aircraft industry it is used for initial and in-service inspections. The major strength of radiography is that it can give information not only of the surface but of the whole volume of the test object. The interpretation of the images obtained is often intuitively and the whole procedure is rather simple. Furthermore, a permanent recording is possible. The disadvantage of the technique is the related safety hazard, as X-rays are harmful to the human health. In addition, the equipment and the implementation is expensive. Radiography has its limitations in the detection of cracks, where for specific crack geometries a penetrant is needed to give sufficient contrast on the detector.

Vibration/Modal Analysis

The basic principle on which modal analysis is based is the existence of resonant frequency modes (eigenmodes) when a structure is excited by ambient energy, an external shaker, or embedded actuators. These resonant frequencies are linked to the acoustical properties of the structure. Any discontinuities within the structure will alter the acoustical properties and consequently the resonant frequency modes. From analytical models or response-history tables the corresponding location of the damage can be calculated. Modal analysis requires the excitation of the test object and the recording of the object response, e.g. by using strain gauges or accelerometers. From the response of the structure the resonant modes have to be calculated and then have to be compared to the undamaged modes.

Although this technique holds much potential for NDT/E, it currently suffers from some limitations. The problem is that the resonant modes strongly depend on the boundary conditions, e.g. geometrical dimensions of the object and loads. Any change in the boundary conditions, for example by thermal expansion, will therefore also change the resonant modes. More sophisticated approaches making use of non-linear effects (higher harmonics, distortions, modulation) have been used in this area. Limits regarding the detectable size of the damage make vibration/modal analysis a global technique being useful only for a large ratio of damage dimension to structure dimension [164].

Appendix D: Piezoelectricity

In 1880, Jacques and Pierre Curie discovered that a pressure applied to a quartz crystal creates an electrical charge in the crystal. Tension and compression generated voltages of opposite polarity, and in proportion to the applied force. Later they also verified that an electrical field applied to the crystal would lead to a deformation of the material. The crystal lengthened and shortened according to the polarity of the field, and in proportion to the strength of the field. These behaviours were labelled the piezoelectric effect and the inverse piezoelectric effect, respectively. The word *piezo* is derived from the Greek word *piezein*, which means to press or squeeze [306].

Since the piezo effect exhibited by natural materials such as quartz, tourmaline or Rochelle salt, is very small, polycrystalline ferroelectric ceramic materials such as barium titanate and lead (*plumbum*) zirconate titanate (PZT) with improved properties have been developed. PZT ceramics are available in many shapes and are the most widely used materials for actuator or sensor applications. The term PZT has become a synonym for any piezoelectric material.

Ferroelectric ceramics become piezoelectric when poled. At temperatures below the Curie temperature, PZT crystallites exhibit tetragonal or rhombohedric structure. Due to their permanent electrical and mechanical asymmetry, these types of unit cells exhibit spontaneous polarisation and deformation. Groups of unit cells with the same polarisation and deformation are called domains. Because of random distribution of the domain orientations in the ceramic material, a ferroelectric poling process is required to obtain any macroscopic anisotropy and the associated piezoelectric properties. If heated above the Curie temperature the PZT crystallite unit cell takes on cubic centrosymmetric structure. When cooled the domains reform, but with randomised orientations, and the material does not regain its macroscopic piezoelectric properties.

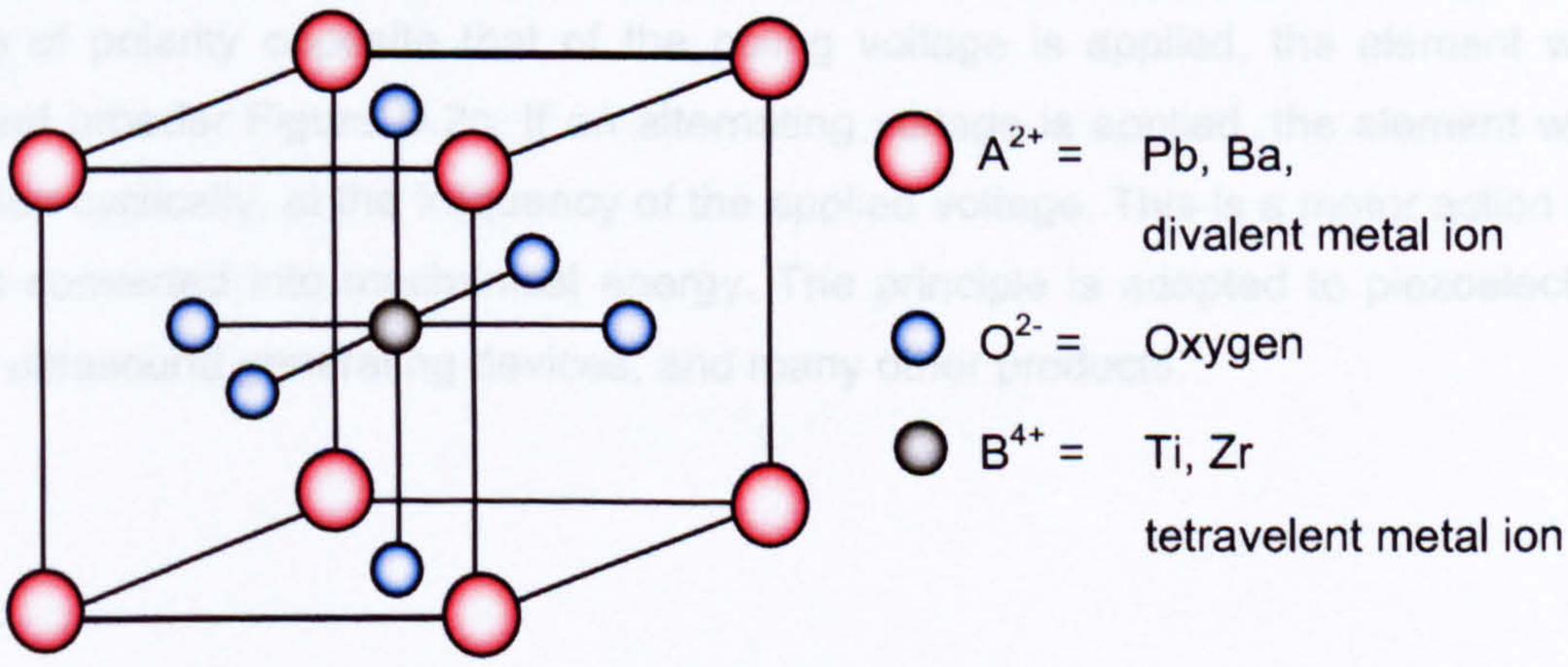

Figure D.1: Crystal structure of a traditional piezoelectric structure (Perovskite Crystal).

The asymmetric arrangement of the positive and negative ions imparts permanent electric dipole behaviour of the crystals. Before the poling treatment, the domains are randomly oriented in the piezoceramic material. During poling an intense electric field is applied to the material. Through this polarising treatment (poling), domains most nearly aligned with the electric field expand at the expense of domains that are not aligned with the field. The material expands along the axis of the field and contracts perpendicular to that axis as the domains line up. When the field is removed most of the dipoles are locked into a configuration of near alignment. The material now has a remanent polarisation, which can be degraded by exceeding the mechanical, thermal and electrical limits of the material. When a voltage is applied to the poled piezoelectric material, the ions in the unit cells are shifted and, additionally, the domains change their degree of alignment. The result is a corresponding change of the dimensions of the PZT material.

The piezoelectric effect is explained in Figure D.2 [307]. The disk of a piezoelectric material with antisymmetric unit cell is shown in Figure D.2a Mechanical compression or tension on a piezoelectric ceramic element changes the dipole moment, creating a voltage, Figure D.2b. Compression along the direction of polarization, or tension perpendicular to the direction of polarization, generates voltage of the same polarity as the poling voltage. Tension along the direction of polarization, or compression perpendicular to the direction of polarization, generates a voltage with polarity opposite that of the poling voltage. These actions are generator actions -- the ceramic element converts the mechanical energy of compression or tension into electrical energy. This behaviour is used in fuel-igniting devices, solid state batteries, force-sensing devices, and other products. Values for compressive stress and the voltage (or field strength) generated by applying stress to a piezoelectric ceramic element are linearly proportional up to a material-specific stress. The same is true for applied voltage and generated strain.

If a voltage of the same polarity as the poling voltage is applied to a ceramic element, in the direction of the poling voltage, the element will lengthen and its diameter will become smaller. If a voltage of polarity opposite that of the poling voltage is applied, the element will become shorter and broader Figure D.2c. If an alternating voltage is applied, the element will lengthen and shorten cyclically, at the frequency of the applied voltage. This is a motor action -- electrical energy is converted into mechanical energy. The principle is adapted to piezoelectric motors, sound or ultrasound generating devices, and many other products.

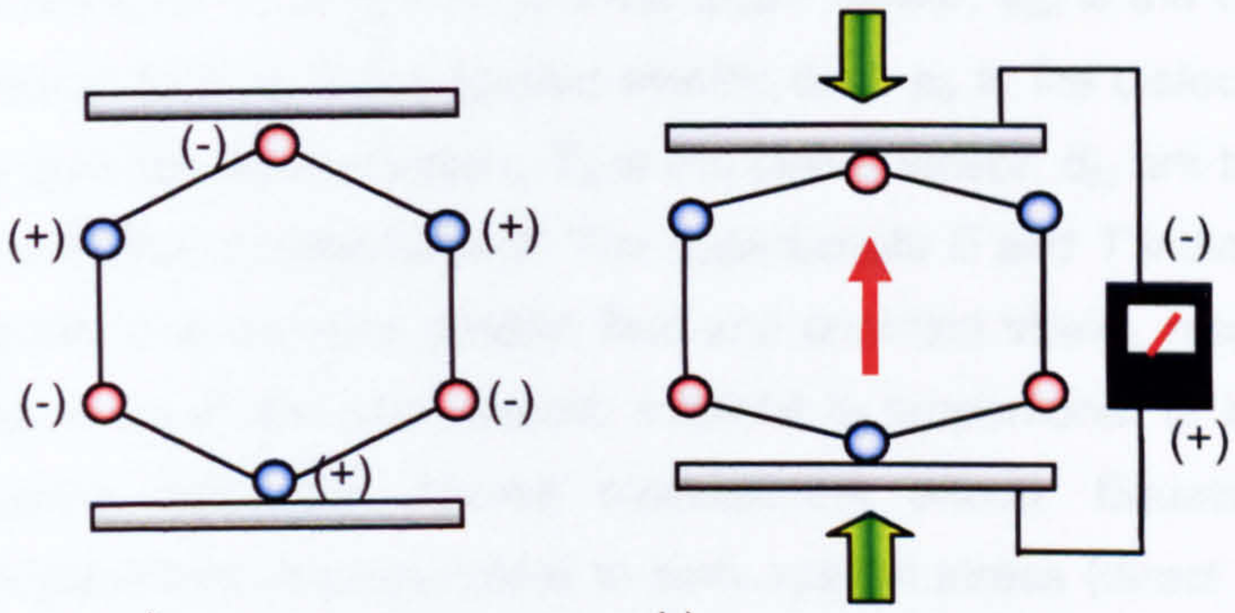

Figure D.2: Piezoelectricity: a) disk after polarisation; b) disk compressed: generation of voltage; c) applied voltage: deformation of disk [307].

Because of the anisotropic nature of piezoelectric materials, effects are dependent on direction. To identify directions, the axes termed 1,2, and 3, are introduced, see Figure D.3. The axes 4,5, and 6 identify rotations (shear deformation). The direction of polarization (3 axis) is established during the poling process by a strong electrical field between two electrodes.

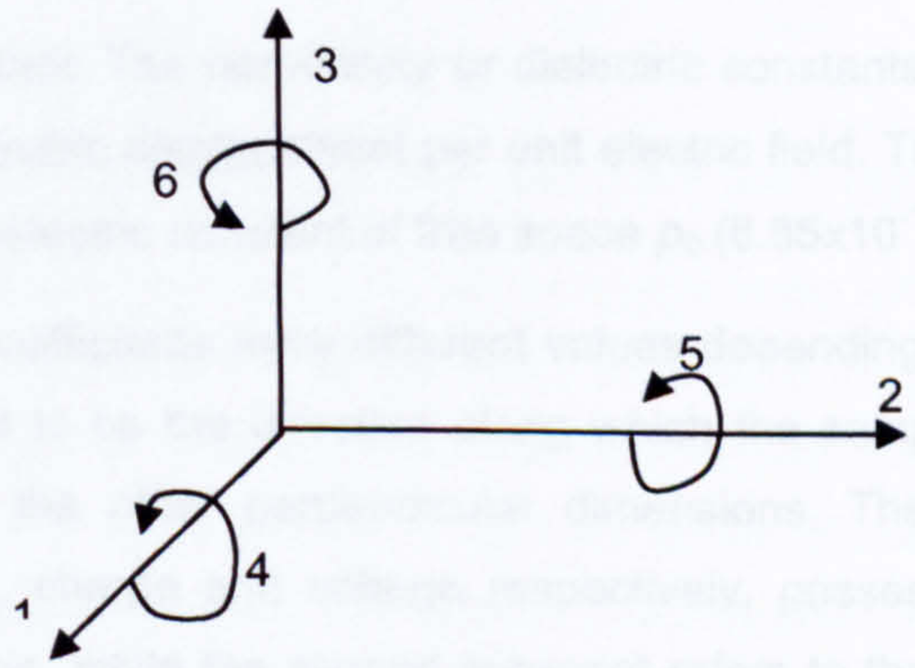

Figure D.3: Coordinate system introduced to describe the piezoelectric effect.

The fundamental equations relating the stress, strain, electric field, and displacement within a piezoelectric material [173] can be described by the following electromechanical equations known as constitutional equations:

$$\varepsilon_{ij} = s^{E}_{ijkl}\sigma_{kl} + d_{kij}E_k \tag{D.1}$$

and

$$D_i = d_{ikl}\sigma_{kl} + p^{T}_{ik}E_k \tag{D.2}$$

where $i,j,k,l = 1,2,3$, and, ε_{ij} is the strain tensor, s_{ijkl} is the compliance tensor measured at zero electric field, E_k is the applied electric field, p_{ik} is the dielectric constant (permittivity) measured at zero mechanical stress, T_{kl} is the stress tensor, d_{kij} are the piezoelectric constants, and D_i is the dielectric displacement. The superscripts E and T indicate that the values of constants are obtained at constant electric field and constant stress, respectively. Equation (D.1) states that the strain in the piezoelectric material is proportional to both applied stress and the applied electric field (the inverse piezoelectric effect). Equation (D.2) states that the electric displacement is proportional to both applied stress (direct piezoelectric effect) and the applied electric field. Piezoelectric materials are characterized by several coefficients:

- d_{ij}: The piezoelectric charge coefficient is the ratio of the electric charge generated per unit area to an applied force and is expressed in Coulomb/Newton (C/N).
- g_{ij}: The piezoelectric voltage coefficient is the ratio of the electric field produced to the mechanical stress applied and is expressed as Volt.meter/Newton (Vm/N)
- k_{ij}: Coupling coefficients. The coefficients are energy ratios describing the conversion from mechanical to electrical energy or vice versa. k^2 is the ratio of energy stored (mechanical or electrical) to energy (mechanical or electrical) applied.
- p_{ij}: Dielectric constant. The permittivity or dielectric constants for a piezoelectric ceramic material is the dielectric displacement per unit electric field. The relative permittivity is the ratio of p_{ij}: to the dielectric constant of free space p_0 (8.85×10^{-12} A s / V m).

In general the *d* and *g* coefficients have different values depending upon the orientation used. Direction *3* is considered to be the direction along which the sample has been polarised and directions *1* and *2* are the other perpendicular dimensions. The most widely used piezo-coefficients, d_{3n} and g_{3n}, charge and voltage respectively, possess two subscripts. The first refers to the electrical axis, while the second subscript refers to the mechanical axis. Because piezoelectric devices are thin, the electrodes are only applied to the top and bottom surfaces. Accordingly, the electrical axis is always *3*, as the charge or voltage is always transferred through the thickness ($n = 3$) of the element. The mechanical axis can be either *1*, *2*,or *3*, since the stress can be applied to any of these axes. Another important parameter is Young's modulus for each direction, describing the elastic response of the material.

Appendix E: Wavelet Analysis

This appendix explains how wavelet decomposition works. A sine wave with an added white noise has been decomposed into its wavelet components. The SNR is 6dB. Each component of the transform is called a level and the levels are numbered from 0 upwards. The number of levels depends on the number of data points that represent the signal to be decomposed. When the separate levels are added together, the original signal can be reconstructed, see Figure A.1.

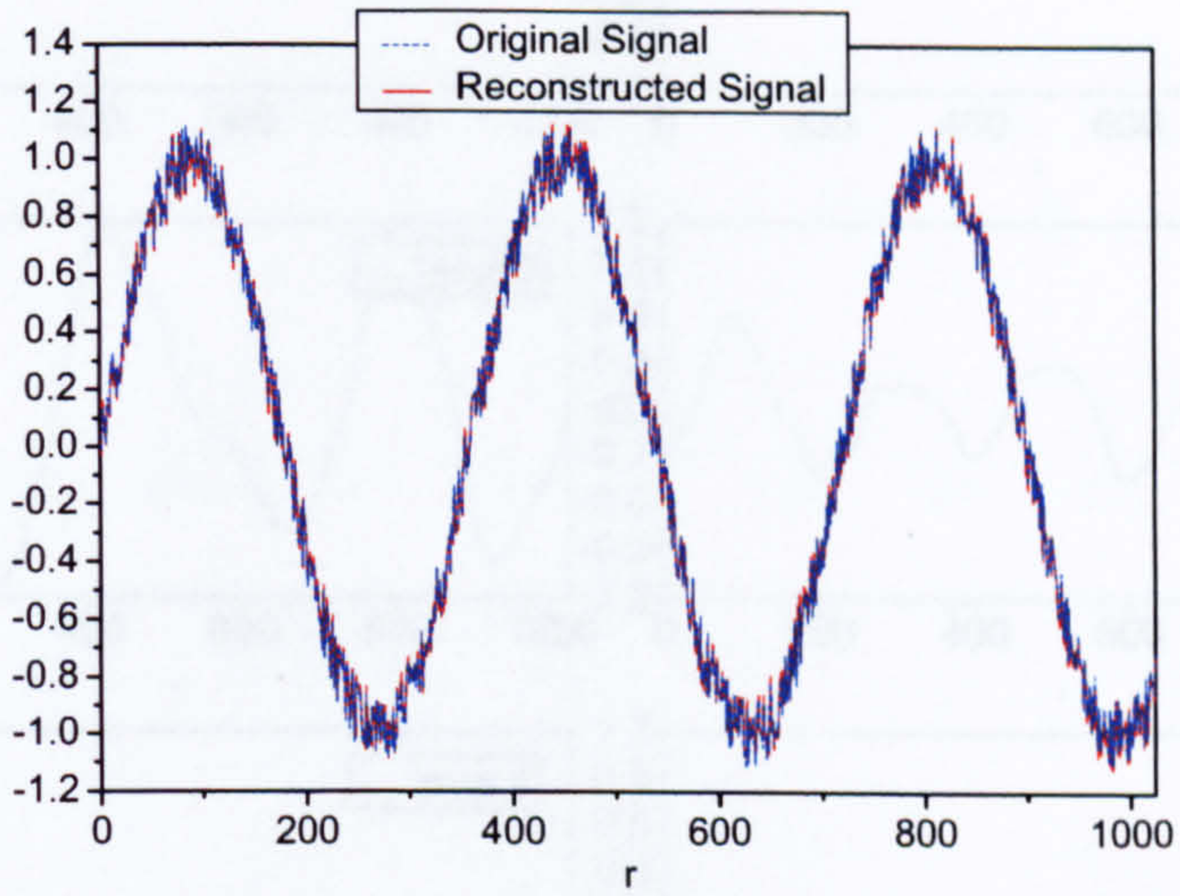

Figure A.1: Original signal and its reconstruction using the wavelet transform.

It is important for discrete wavelet analysis that the signal to be analysed has been sampled at equally spaced intervals, as described above. In the sine wave *f(r)* covers a range of *r* from 1 to 1024. The sequence length of *N* of the signal being analysed determines how many wavelet levels there are. For $N = 2^n$ there are $n + 2$ wavelet levels. However, the first level is only a constant and is not considered further. So, without that first level, for $N = 1024 = 2^{10}$ there are ten wavelet levels as shown in *Figure A.2*.

At each level *m* the analysing wavelet consists of a number of 2^m wavelets at equally spaced intervals along the horizontal axis. Every wavelet is displaced $N/2^m$ places with respect to its neighbour. Each of the analysing wavelets has the same shape. The position and spread of each wavelet along the horizontal axis is therefore determined by the structure of the wavelet transform and can not be altered. Only the vertical size of each wavelet needs to be adjusted to the analysed signal. The vertical sizes are specified by an appropriate term in an *N*-term series *a(r)*, $r = 1$ to *N*. The goal of the wavelet transform is to take the initial signal sequence *f(r)* and convert this into a new sequence of numbers *a(r)* where *r* is of [1 to N]. This sequence defines the vertical size of the wavelets at each of the set horizontal scales and positions in such way

that the addition of all the wavelets, taken together, faithfully reproduces the original signal (*Figure A.3*).

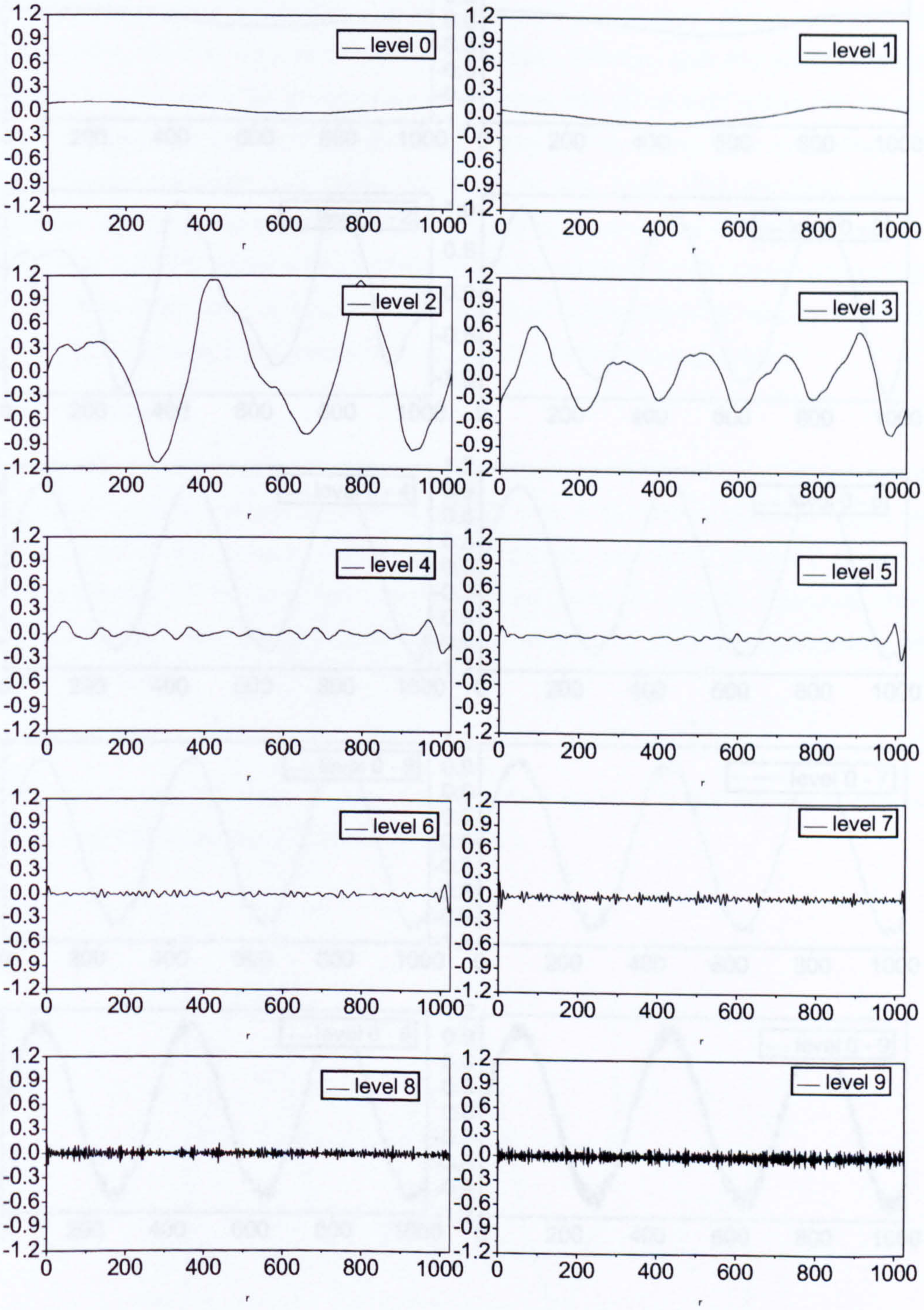

Figure A.2: Decomposition of a signal into its wavelet components.

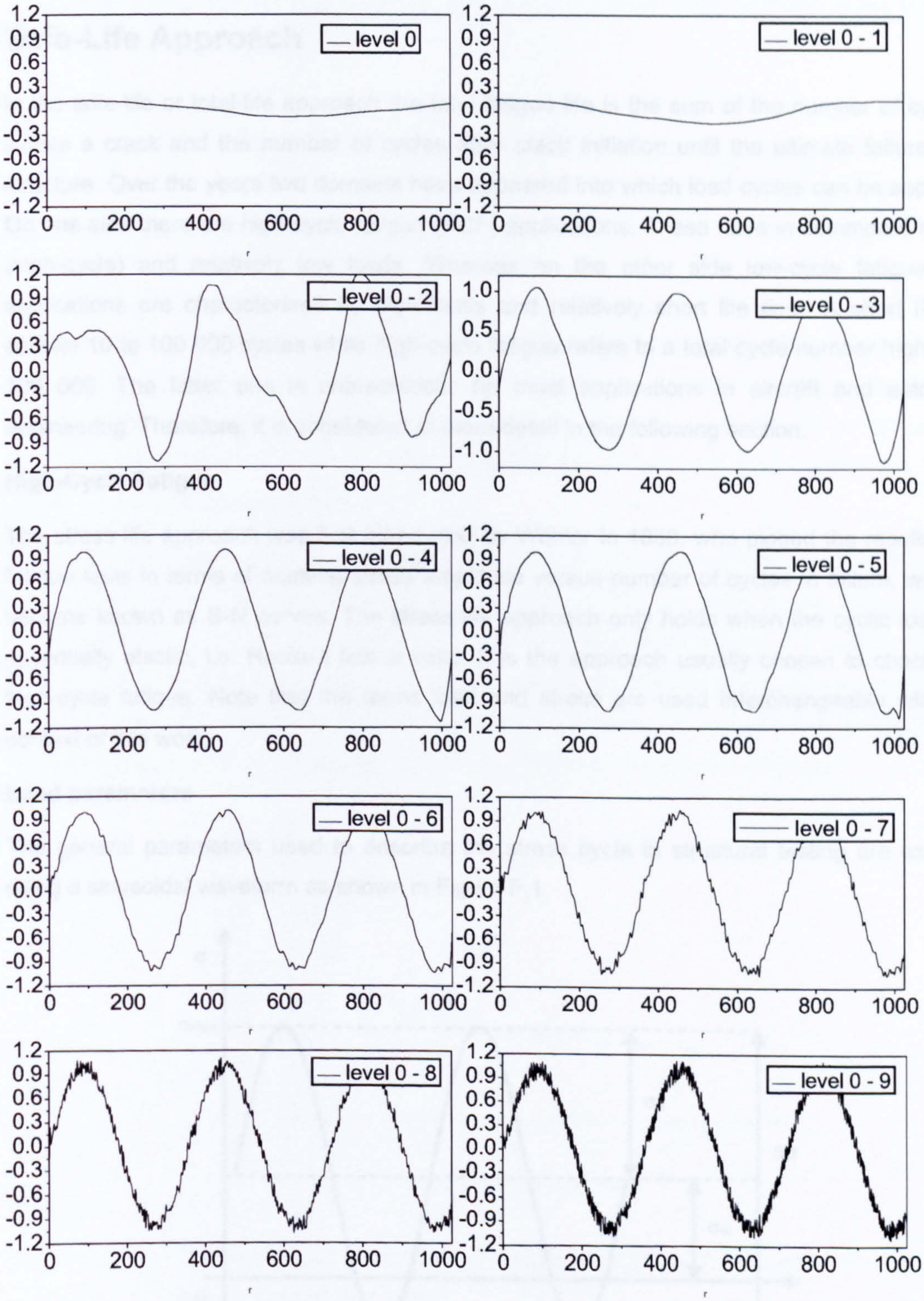

Figure A.3: Reconstruction of a waveform from its wavelet components.

Appendix F: Safe-Life and Fail-Safe Approaches

Safe-Life Approach

In the safe-life or total-life approach the total fatigue life is the sum of the number of cycles to initiate a crack and the number of cycles after crack initiation until the ultimate failure of the structure. Over the years two domains have appeared into which load cycles can be separated. On one side there are high-cycle fatigue (HCF) applications. These have in common a long life (high-cycle) and relatively low loads. Whereas on the other side low-cycle fatigue (LCF) applications are characterised by high loads and relatively short life time. A short life may contain 10 to 100 000 cycles while high-cycle fatigue refers to a total cycle number higher than 100 000. The latter one is characteristic for most applications in aircraft and automotive engineering. Therefore, it is considered in more detail in the following section.

High-Cycle Fatigue

The stress-life approach was first introduced by Wöhler in 1860, who plotted the results of his fatigue tests in terms of nominal stress amplitude versus number of cycles to failure, what has become known as S-N curves. The stress-life approach only holds when the cyclic loading is essentially elastic, i.e. Hooke's law is valid. It is the approach usually chosen to characterise high-cycle fatigue. Note that the terms load and stress are used interchangeable within the context of this work.

Load parameters

The general parameters used to describe the stress cycle in structural testing are explained using a sinusoidal waveform as shown in Figure F.1.

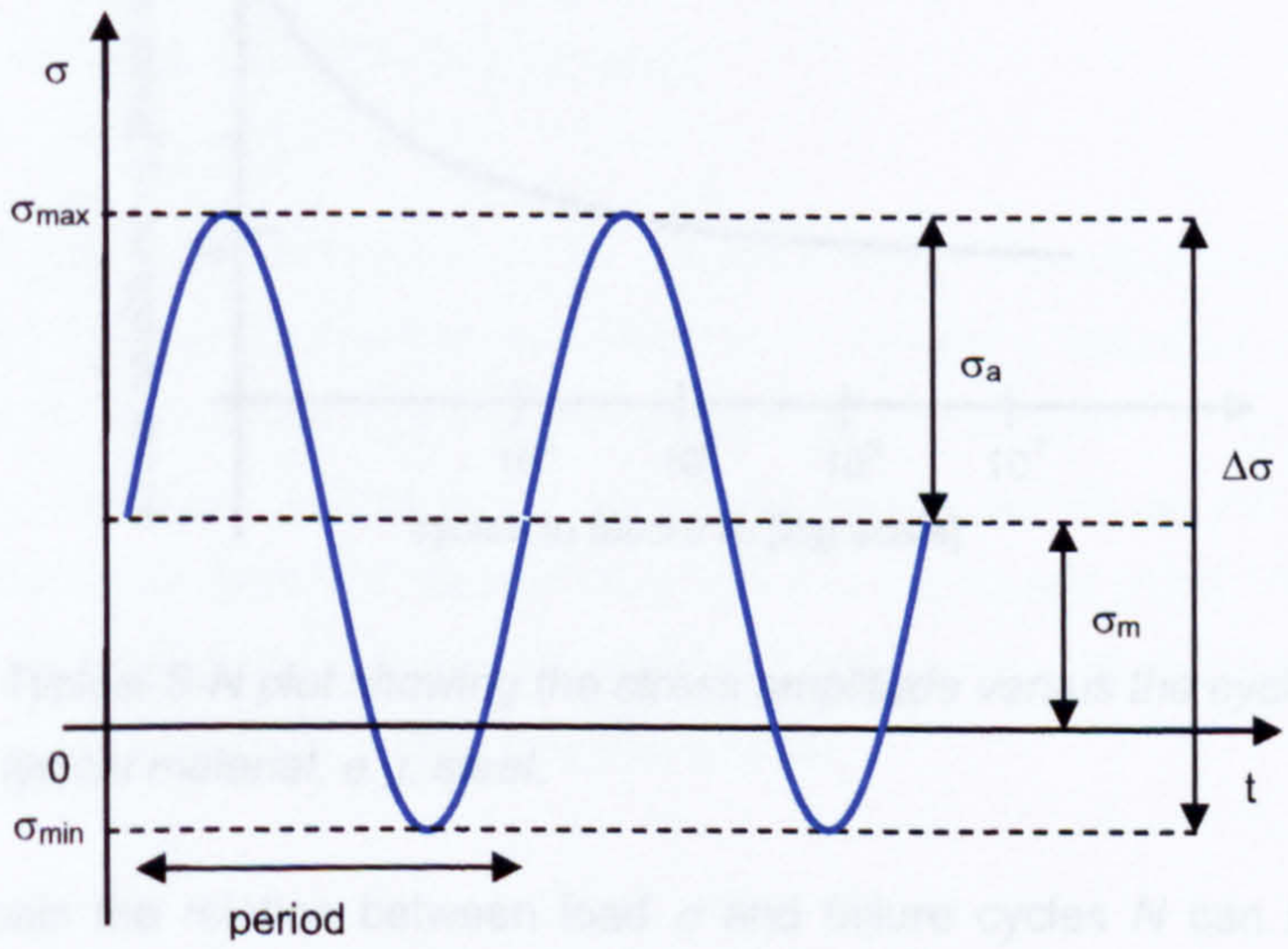

Figure F.1: Nomenclature for load parameters. Variation of stress σ with time t is shown.

The load consists of two main components, a mean static stress component σm and a modulation stress with the amplitude σa. Based on maximum and minimum stress these are defined as

$$\sigma_a = \frac{\sigma_{\max} - \sigma_{\min}}{2}, \quad \sigma_m = \frac{\sigma_{\max} + \sigma_{\min}}{2}, \quad \Delta\sigma = \sigma_{\max} - \sigma_{\min} \tag{F.1}$$

where the stress range $\Delta\sigma$ has also been defined.

It should be noted that although fatigue is related to cyclic load, the mean load is also of importance to the S-N curve. Different combinations of mean stress and stress amplitude will lead to different results for the total fatigue life. In general, any non-zero mean load will contribute to a reduced life. A common representation of non-zero load contribution can be found in the so-called Haigh diagrams.

The central diagram in the stress-life approach is the aforementioned S-N data plot. It plots the stress amplitude versus the number of cycles to failure. For an example see Figure F.2. For many materials, e.g. steel, this curve yields a constant level beyond about 10^6 cycles. This level is called the fatigue limit σ_e. Should the load amplitude not exceed that level the specimen will have an infinite life. That concept is referred to as the endurance limit. In practical terms infinite is anything beyond 10^7 to 10^8 cycles, which is the limit set in fatigue life analysis.

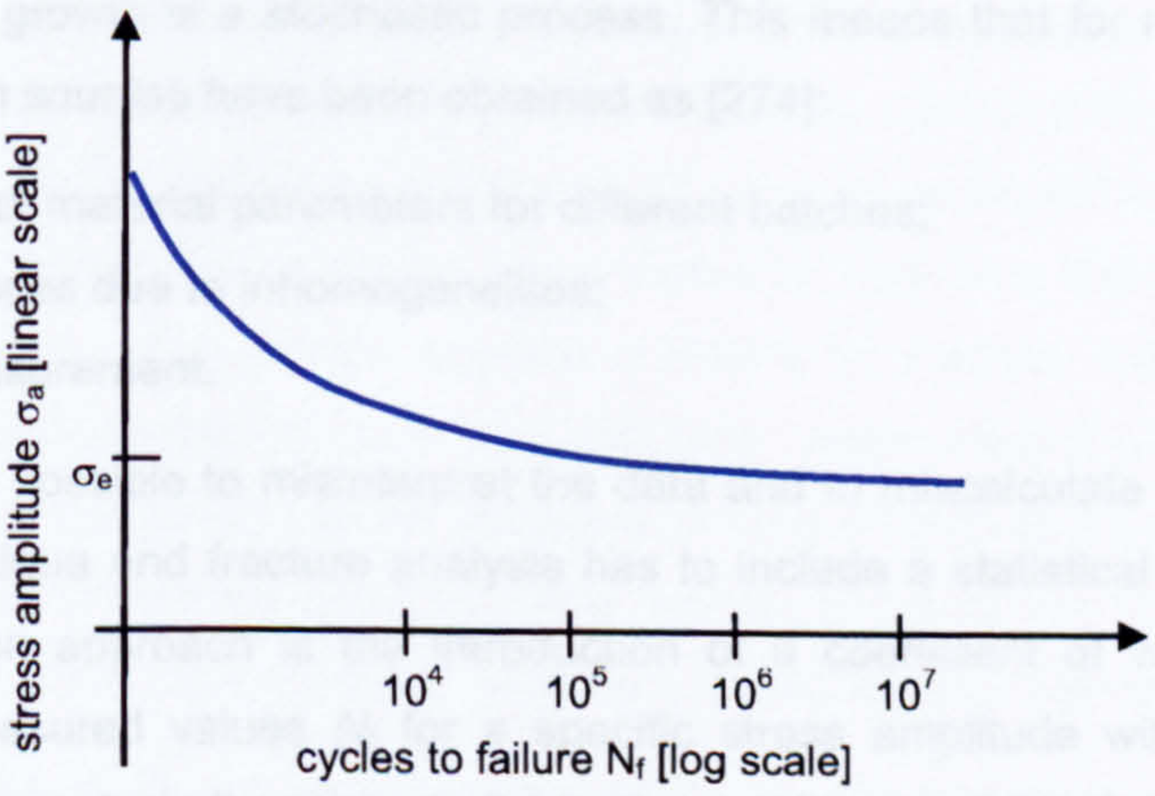

Figure F.2: Typical S-N plot showing the stress amplitude versus the cycles to failure for a typical material, e.g. steel.

On a log-log scale the relation between load σ and failure cycles N can be described as a straight line (see Figure F.3). The slope of the line can be derived between two points N and N_0.

$$b = -\frac{\log\sigma - \log\sigma_0}{\log N - \log N_0} \tag{F.2}$$

The function $N(\sigma)$ can be thus derived to be

$$N = N_0 \left(\frac{\sigma}{\sigma_0}\right)^{\frac{1}{b}} \tag{F.3}$$

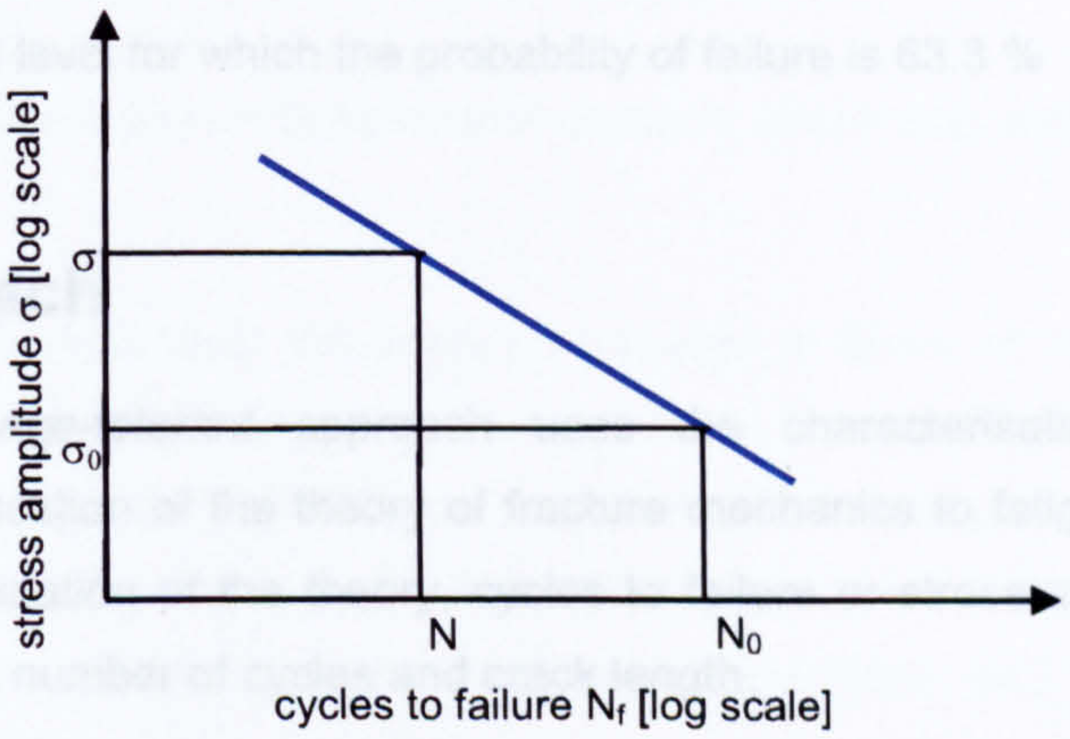

Figure F.3: Idealised form of the S-N curve.

Regardless of how accurate the inspection methods and the fatigue analysis parameters are, the process of crack growth is a stochastic process. This means that for real tests scatter will occur. The three main sources have been obtained as [274]:

a) Consistence of material parameters for different batches;
b) Local differences due to inhomogeneities;
c) Errors in measurement.

It is therefore always possible to misinterpret the data and to miscalculate the remaining life of the structure. The fatigue and fracture analysis has to include a statistical interpretation of the data. A very common approach is the introduction of a coefficient of variation. Due to the uncertainties the measured values N_f for a specific stress amplitude will follow a statistical distribution. In fatigue analysis the Weibull distribution is often used [274]. The statistical nature of the process is expressed by the presentation of a failure probability instead of using absolute values. Weibull defined the failure probability as follows:

$$P_F = 1 - P_s = 1 - \exp\left\{-\left(\frac{\sigma_F}{\sigma_0}\right)^{m_W}\right\} \tag{F.4}$$

where m_W is the Weibull modulus or Weibull parameter and σ_0 a reference strength.

The failure probability P_F gives the fraction of the number of specimens that will fail below a failure strength σ_F. Whereas P_S will represent the fraction that has higher failure strength than σ_F. For $\sigma_F = \sigma_0$ the fraction of the failed specimens is 63.3 %. This means the reference strength σ_0 is defined as the load level for which the probability of failure is 63.3 %

Fail-Safe Approach

The *fail-safe* or *damage-tolerant* approach uses the characterisation of fatigue crack propagation as an application of the theory of fracture mechanics to fatigue life. It implies that for an experimental validation of the theory, cycles to failure or stress amplitudes are not the important measures but number of cycles and crack length.

Damage-tolerant fatigue approaches are based on the assumption that every engineering structure is inherently damaged. Therefore, the useful fatigue life is the life that it takes for the existing crack to propagate from initial size to a critical dimension. The initial size can be either measured by any NDT method or defined by the resolution limit of the NDT method. The critical dimension though is not inherently known but will depend on the application and what is defined as its critical dimension. Crack propagation is only a suitable method if there is a stable regime of crack growth, that can be described mathematically and be accessed experimentally. This is true for most metallic materials but only to some extent for polymers and composite materials. The regime where stable crack growth conditions hold is for medium sized cracks where the crack propagation is independent of crack size. The time , respectively the number of cycles, for which a stable crack propagation can be assumed, is long enough to allow inspection of crack size at certain intervals. From the crack size and number of cycles the remaining life time can then be derived. This is the basis for many of today's inspection and maintenance regulations.

Considering the crack growth at a constant load amplitude, the rate of growth of a fatigue crack is expressed in terms of the crack length increment per cycle, da_c/dN. Under different loading conditions there will be different values of da_c/dN, which can be obtained experimentally. When the applied stress range is held constant, the rate of growth of a fatigue crack generally increases with increasing number of fatigue cycles. Figure F.4 schematically shows a typical fatigue crack growth curve.

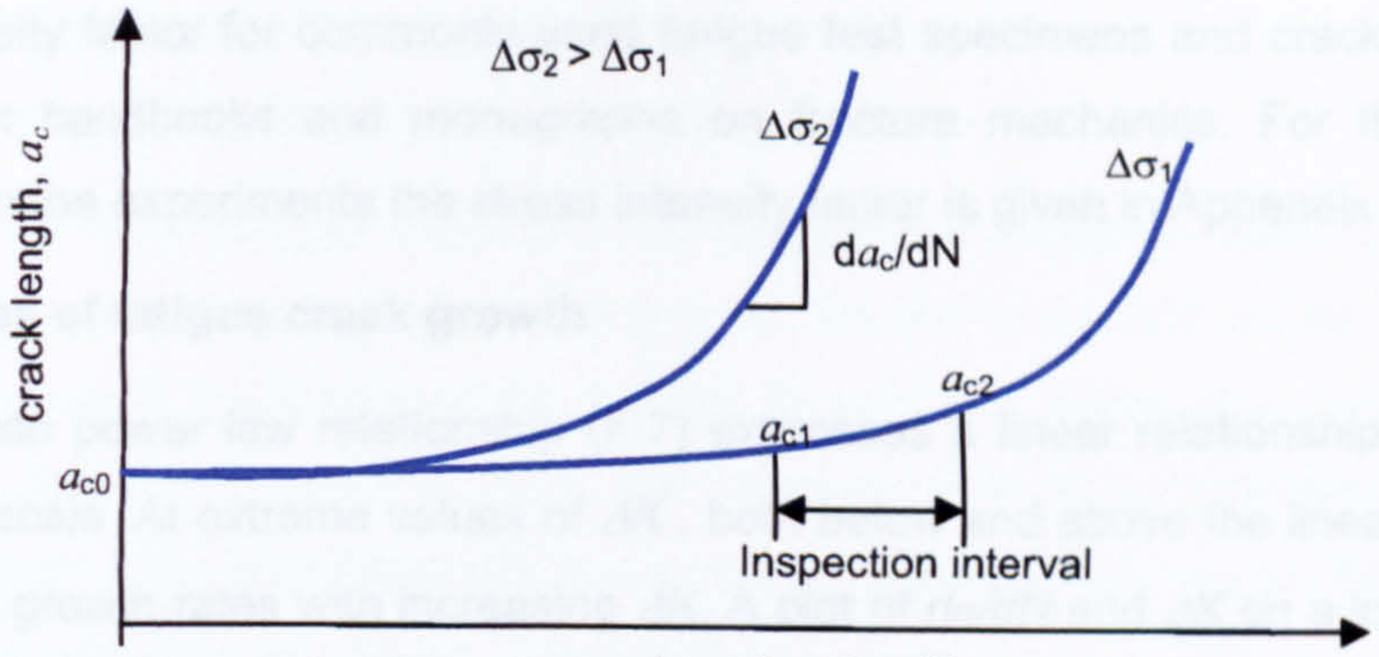

Figure F.4: Typical crack growth behaviour at constant stress amplitude for two different load levels.

Reliable methods for characterising the crack propagation in terms of an appropriate loading parameter are needed. The loading parameter enables a quantification of the materials behaviour during crack growth for different combinations of applied stresses, specimen geometry and crack geometry. For a cyclic variation of the applied loads, a method based on linear elastic fracture mechanics has been proposed by Paris and Erdogan [275], who suggested the relevant loading parameter to be the stress intensity factor *K*. The stress intensity factor can be derived from the applied fatigue load σ and the crack length a_c as

$$K = \mathrm{Y}\sigma\sqrt{\pi a_c} \tag{F.5}$$

where Y is a geometrical factor depending on the ratio of crack length to the width of the structure. The stress intensity factor range is the difference of maximum and minimum stress intensity factor which correspond to maximum and minimum fatigue stress, respectively. This can be expressed as

$$\Delta K = \mathrm{Y}\ \Delta\sigma\ \sqrt{\pi a_c} \tag{F.6}$$

Paris and Erdogan [275] showed that the fatigue crack growth increment da_c/dN is related to the stress intensity factor range by the power law relationship

$$\frac{da_c}{dN} = C(\Delta K)^m \tag{F.7}$$

where *C* and *m* are scaling constants. They are influenced by environment, temperature and most relevant to the load ratio *R*, that is the ratio of the minimum to maximum stress intensity factor K_{min}/K_{max}.

The stress intensity factor for commonly used fatigue test specimens and crack configurations can be found in handbooks and monographs on fracture mechanics. For the fatigue test specimen used in the experiments the stress intensity factor is given in Appendix G.

Different regimes of fatigue crack growth

The Paris/Erdogan power law relationship (F.7) expresses a linear relationship for da/dN and ΔK on a log-log scale. At extreme values of ΔK , both below and above the linear regime, there is a rise in crack growth rates with increasing ΔK. A plot of da/dN and ΔK on a log-log scale will for the most common metals and alloys look as schematically illustrated in Figure F.5.

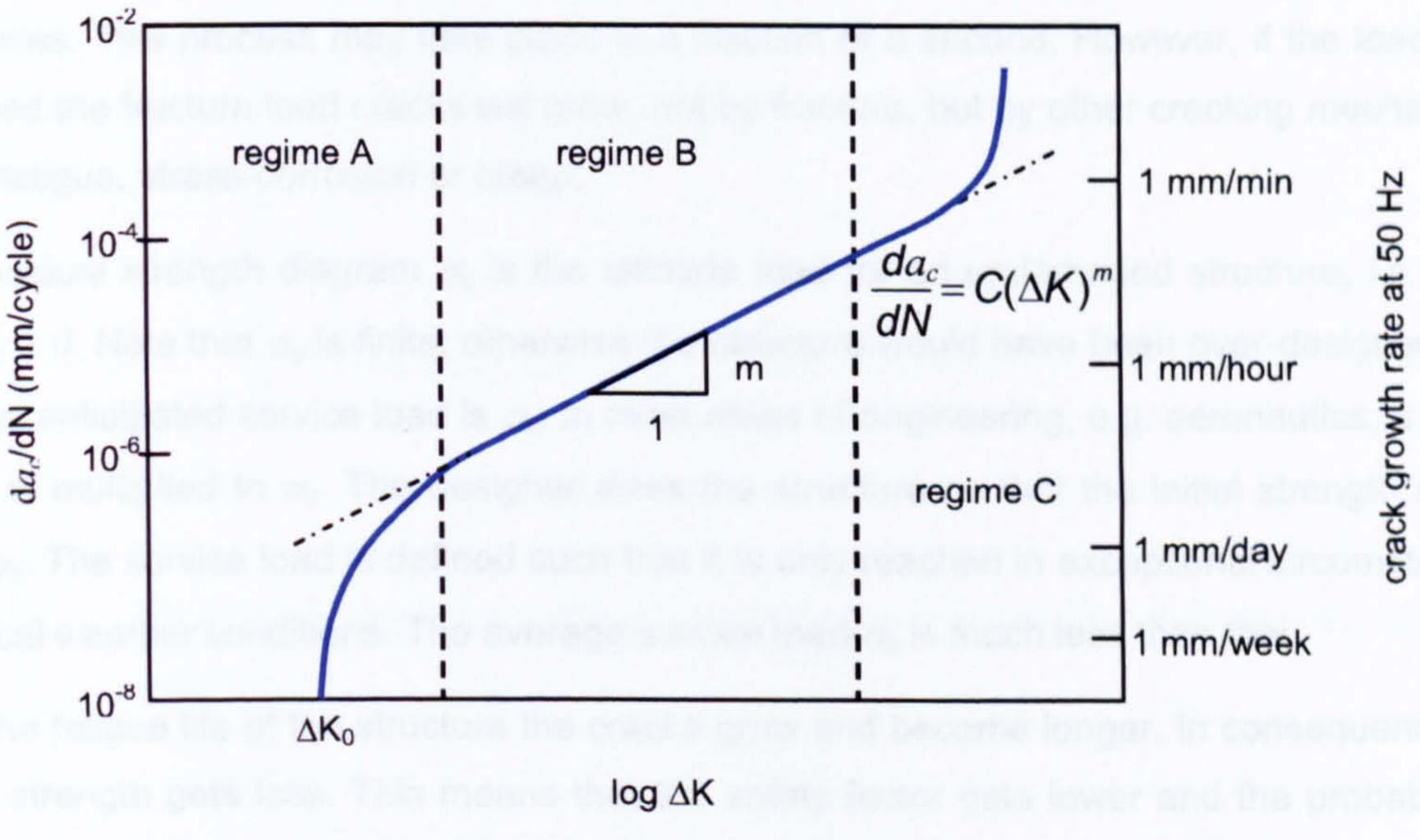

Figure F.5: Schematic illustration of the different regimes of stable fatigue crack propagation [275].

Three distinct regimes can be identified in Figure F.5. Regime A is characterised by the near-threshold fatigue crack growth. Below the threshold ΔK_0 , cracks either don't grow at all or at undetectable rates. Above that threshold there is a dramatic increase in da_c/dN with ΔK. Known as the Paris regime, the regime B exhibits a linear variation of *log* da_c/dN with log ΔK. In regime C a rapid increase of crack growth for high values of ΔK can be seen. This causes catastrophic failure at stress intensities beyond this point.

Crack Growth Analysis

In this section the important terms such as load spectra, structural strength, etc. are defined and related to the crack growth process.

According to Broek [274] the two objectives of damage tolerance analysis are:

a) Determination of the effect of cracks on the structural strength.
b) Determination of the crack growth as a function of time.

The effect of crack size on the structural strength can be explained using Figure F.6. The remaining strength under the presence of cracks is referred to as residual strength P_{res} . This strength is a function of crack size a. The general form of this relationship is presented in the residual strength diagram, Figure F.6. Here, the structural strength is expressed in terms of the load σ. The strength is the load the structure can carry before fracture occurs, this is the fracture load σ_{res}. For the structure in service, fracture takes place when a load $\sigma = \sigma_{res}$ arises. This eventually ends in a unstable fracture process where the structure finally breaks into two or more pieces. This process may take place in a fraction of a second. However, if the load does not exceed the fracture load cracks will grow, not by fracture, but by other cracking mechanisms such as fatigue, stress-corrosion or creep.

In the residual strength diagram σ_u is the ultimate load for an undamaged structure, i.e. crack length $a_c = 0$. Note that σ_u is finite, otherwise the structure would have been over-designed. The maximum anticipated service load is σ_s. In most areas of engineering, e.g. aeronautics, a safety factor f_s is multiplied to σ_s. The designer sizes the structure so that the initial strength equals $\sigma_u = f_s \sigma_s$. The service load is defined such that it is only reached in exceptional circumstances, e.g. critical weather conditions. The average service load σ_a is much less than that.

During the fatigue life of the structure the cracks grow and become longer. In consequence, the residual strength gets less. This means that the safety factor gets lower and the probability of failure increases. This could finally lead to a residual strength less than σ_s. Safety factor will be reduced to 1 and fracture already occurs at σ_s, the highest service load or even at the average load σ_a. This is what must be prevented. Therefore, a limit is introduced somewhere above σ_s. This limit gives the permissible residual strength σ_p. It is defined by multiplying a remaining safety factor f_r to the maximum service load $\sigma_p = f_r \sigma_s$. With the permissible load also the maximum permissible crack size a_{cp} has been defined implicitly. Provided the residual strength diagram is known and σ_p prescribed, a_{cp} follows from the diagram.

With the knowledge of the maximum permissible crack size the question arises when this crack size is reached in service. This can be deduced from the crack propagation curve. The shape of this curve is subject to the crack growth analysis. Starting from some initial crack length a_{c0}, which for example could be the smallest detectable crack length, the crack grows during time. The permissible crack length a_{cp} can be plotted on the curve and the life of the structure can be found using the diagram. Life of the structure which in this case is the life of safe operation, i.e. until a_{cp} is reached, is then the corresponding time H on the time axis. Since crack growth is not allowed beyond a_{cp}, the crack must be detected and repaired before the time H has expired. In

order to detect the crack in time, the time between two inspections must be less than *H*. Often, the inspection time is taken as *H/2*.

For both the residual strength and the crack growth diagram the relevant parameters and factors, e.g. safety factors and inspection times, are prescribed by rules and regulations. The manufacturer or operator of a structure has to ensure that these instructions are obeyed.

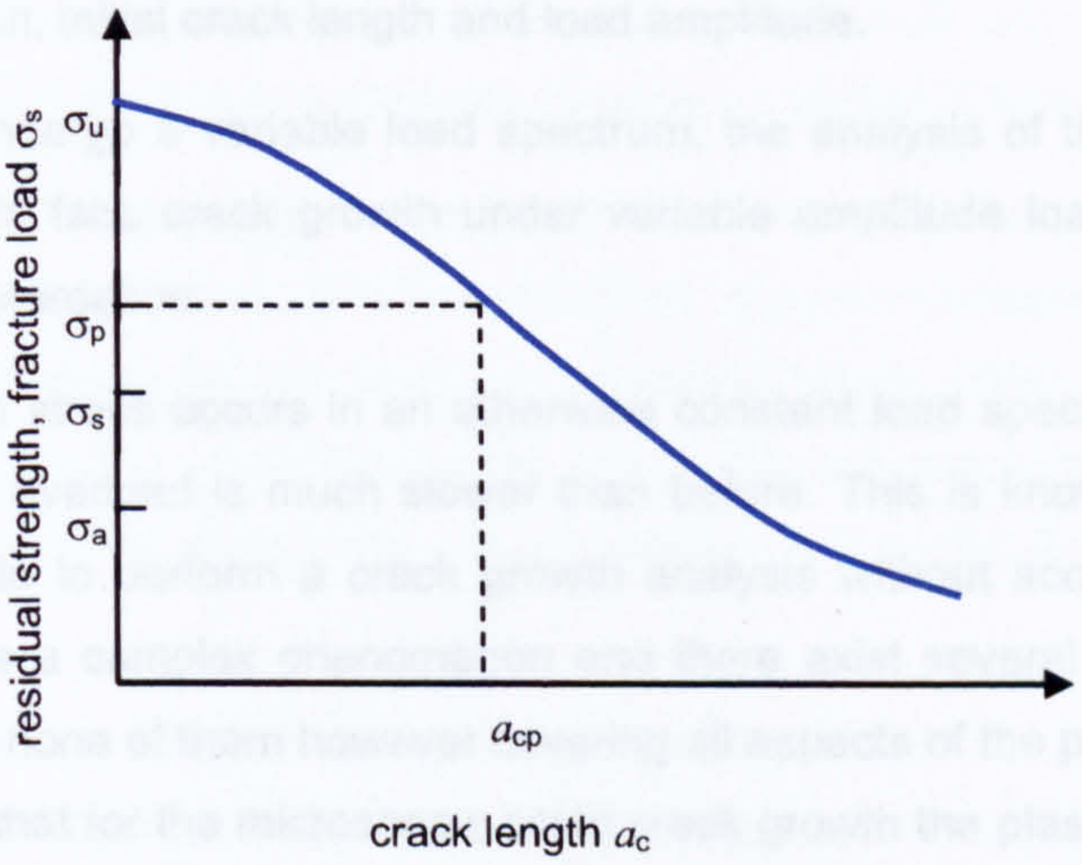

Figure F.6: Residual strength diagram. Effect of the presence of cracks to the structural strength.

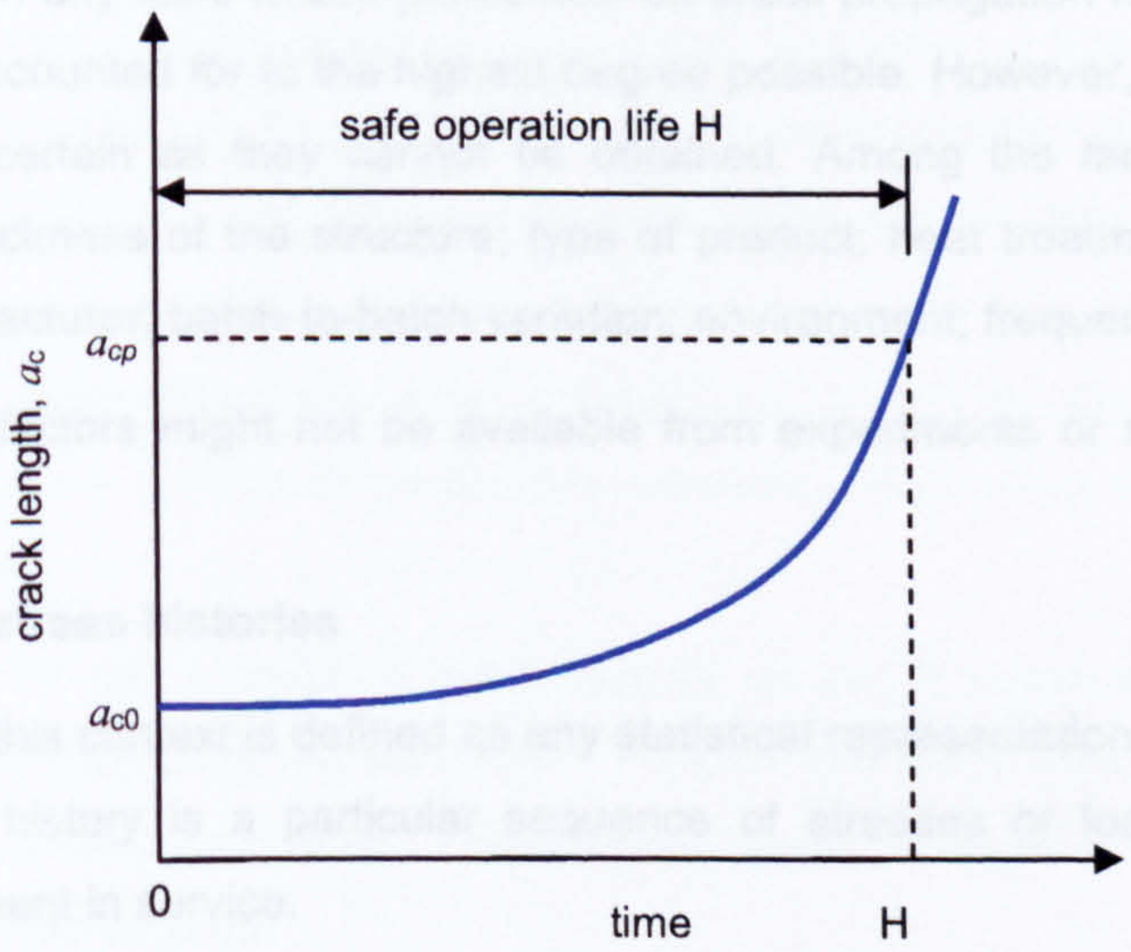

Figure F.7: Crack growth curve and the safe operation life.

Crack growth analysis concepts

In the case of constant amplitude loading the analysis of crack growth can be performed without a computer. A crack in the structure will grow at the rates indicated by the crack growth diagram. Analysis of the crack growth can be carried out manually, if the geometry factor for the structural configuration is known. The crack growth follows from an integration of the rates. The remaining lifetime can thus be calculated using the material's rate data obtained from the Paris/Erdogan equation, initial crack length and load amplitude.

As most structures undergo a variable load spectrum, the analysis of the crack growth is not that straightforward. In fact, crack growth under variable amplitude loading brings up a new phenomenon called retardation.

When one single high stress occurs in an otherwise constant load spectrum, the crack growth immediately after the overload is much slower than before. This is known as retardation. It is practically not possible to perform a crack growth analysis without accounting for retardation effects. Retardation is a complex phenomenon and there exist several mathematical-physical models to describe it, none of them however covering all aspects of the problem. The basic idea behind retardation is that for the microscopic scale crack growth the plastic zone near the crack tip is most important. The size and properties of that zone are dramatically changed when an overload occurs. In consequence the crack propagation after the overload event differs from the one before that event.

Retardation is not the only limit to crack growth analysis. There exist several factors that affect crack propagation. In any case where predictions on crack propagation have to be made these effects should be accounted for to the highest degree possible. However, the influence of many factors remains uncertain as they cannot be obtained. Among the factors that affect crack propagation are: thickness of the structure; type of product; heat treatment; cold deformation; temperature; manufacturer; batch-to-batch variation; environment; frequency [275].

As the data for all factors might not be available from experiments or manuals, estimation is often needed.

Load spectra and stress histories

A load spectrum in this context is defined as any statistical representation of loads and stresses.

A stress or loads history is a particular sequence of stresses or loads experienced by a structure or component in service.

For the fatigue analysis of materials the knowledge of the stress history is essential. Any prediction of the fatigue crack propagation rate or propagation time of a specific crack from starting time to the permissible size requires the input of crack propagation data, geometry

factors and stress history. The effects of stress history are significant as different load spectra lead to different shapes of the crack growth curve.

Most load spectra can be represented by exceedance diagrams. The representation by an exceedance diagram has many advantages for random and semi-random loads, not in the least for its simplicity. In most cases the stress history used in crack propagation analysis is a simplified version of the stress history anticipated to occur in service. Simplification is necessary because the actual stress cycles can not be known in advance and stress history must be derived as an interpretation of past load measurements on similar structures.

Load spectra have to be obtained before crack growth analysis can be performed. Two different kind of spectra are distinguished. On the one hand, the man-induced spectrum, where the spectrum can be calculated on the basis of anticipated usage. This is for example true for fighter aircrafts. On the other hand there is the nature-induced spectrum where the main loads are due to environmental influences, e.g. waves, winds, rough roads. Examples for that include commercial aircrafts.

In order to obtain the load spectrum, only indirect measurements are possible. Measurements such as strain gauge records are called indirect because strains are measured and have then to be transferred into loads. These measurements are very extensive and give rise to huge amounts of data. A smart data reduction is strongly needed in order to obtain a specific pattern or envelope of the data set. Two options exist, for example power density spectra can be calculated or exceedance diagrams can be established. Many counting methods for data reduction have been developed. Starting from simple peak count and mean-crossing peak count to range pair count and range-pair mean count. The latter is also known as the rainflow count and commonly known as the best method for the representation of fatigue. However, any method can be obtained as long as the spectrum allows the correct prediction of the crack growth.

The exceedance diagram shows how often a certain load level is exceeded. This is the number of times certain maxima, minima or ranges are exceeded, depending on the counting method that has been applied.

A typical spectrum for nature induced loads (waves, winds) is presented in Figure F.8a. The diagram is linear in the semi-log representation. It shows symmetry around a steady load, which in this diagram is around zero load. This diagram is an example of the general trend for commercial aircraft load spectra.

A man-introduced load spectrum produces a non-linear diagram in the semi-log scale (Figure F.8b). The steady load is not necessarily zero. This is an example for fighter aircraft.

As no load experience is available for new structures, fatigue crack growth analysis must be based on past experience and projected to the future service. Today, for some structures (e.g. military aircrafts with their mechanically induced loads) continuous monitoring is carried out in order to permanently update the anticipated load spectra. This allows an adaptation of the analysis to the actual service experience.

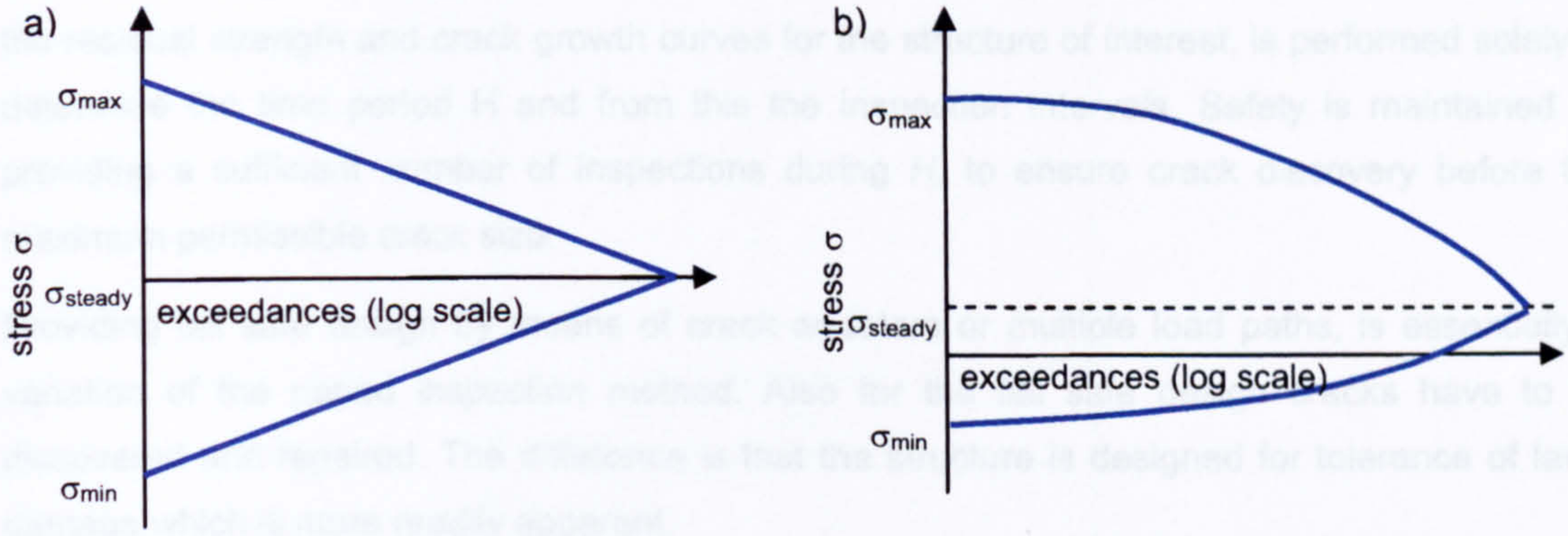

Figure F.8: Exceedance diagrams: a) weather induced loads: commercial aircraft; b) mechanical induced loads: fighter aircraft.

Fracture control

As has been outlined above, the analysis of fatigue crack growth allows the determination of the remaining residual strength of a material at a given crack size. Furthermore, the remaining structural life can be obtained, as the time that it takes for the present crack to grow to the maximum permissible crack size. This time period *H* to reach the maximum crack size is the essential information needed. As no crack is allowed to grow beyond that size, a repair or replacement is dictated by *H*. The following options are available for the implementation of fracture control [274]:

a) Periodic inspection: repair upon crack detection.
b) Fail safe design: repair upon occurrence of partial failure.
c) Durability / safe life design: replacement or retirement after time *H*.
d) Periodic proof testing: repair after failure in proof test.
e) Stripping: periodic removal of crack.

Damage tolerance requirements sometimes prescribe the fracture control procedure. For example military aircraft requirements prescribe methods (a) and (c). Commercial aircraft requirements prescribe method (a) and by their intent promote (b).

The control by periodic inspection requires the detection of the crack before it reaches the maximum permissible crack size. Any method that is known from non-destructive evaluation can be used. The most promising methods are discussed in Section 4.1. For every method there is a certain crack length a_{c0}, that gives the minimum detectable crack size. For any inspection before a_{c0}, the crack is unlikely to be discovered. This has to be taken into account when defining the requirements for the inspection intervals. Damage tolerance analysis, which gives the residual strength and crack growth curves for the structure of interest, is performed solely to determine the time period H and from this the inspection intervals. Safety is maintained by providing a sufficient number of inspections during H, to ensure crack discovery before the maximum permissible crack size.

Providing fail safe design by means of crack arresters or multiple load paths, is essentially a variation of the period inspection method. Also for the fail safe design cracks have to be discovered and repaired. The difference is that the structure is designed for tolerance of large damage which is more readily apparent.

If no inspections can or will be done, a small crack could be assumed to exist initially in the new structure. The time H for this crack to grow to maximum permissible size is then the available safe life. In that case the structure or component must be retired or replaced before the time H has passed. This is the durability or safe life design.

The proof testing approach is chosen when the permissible crack size is smaller than the detectable crack size. At certain test intervals the component (or part of it) is subjected to a proof stress. If the component passes the test, i.e. no fracture occurs, the whole structure is assumed to have a safe operational life for the forthcoming test interval.

Stripping is another option for fracture control for structures where the permissible crack size is so small that it defies detection. By stripping away a surface layer at certain test intervals, the crack size could artificially be decreased. For any crack growth curve this means to slow down the crack propagation. As a consequence, for the next test interval a safe operation life can be assumed.

Appendix G: Centre-Cracked Tension Specimen

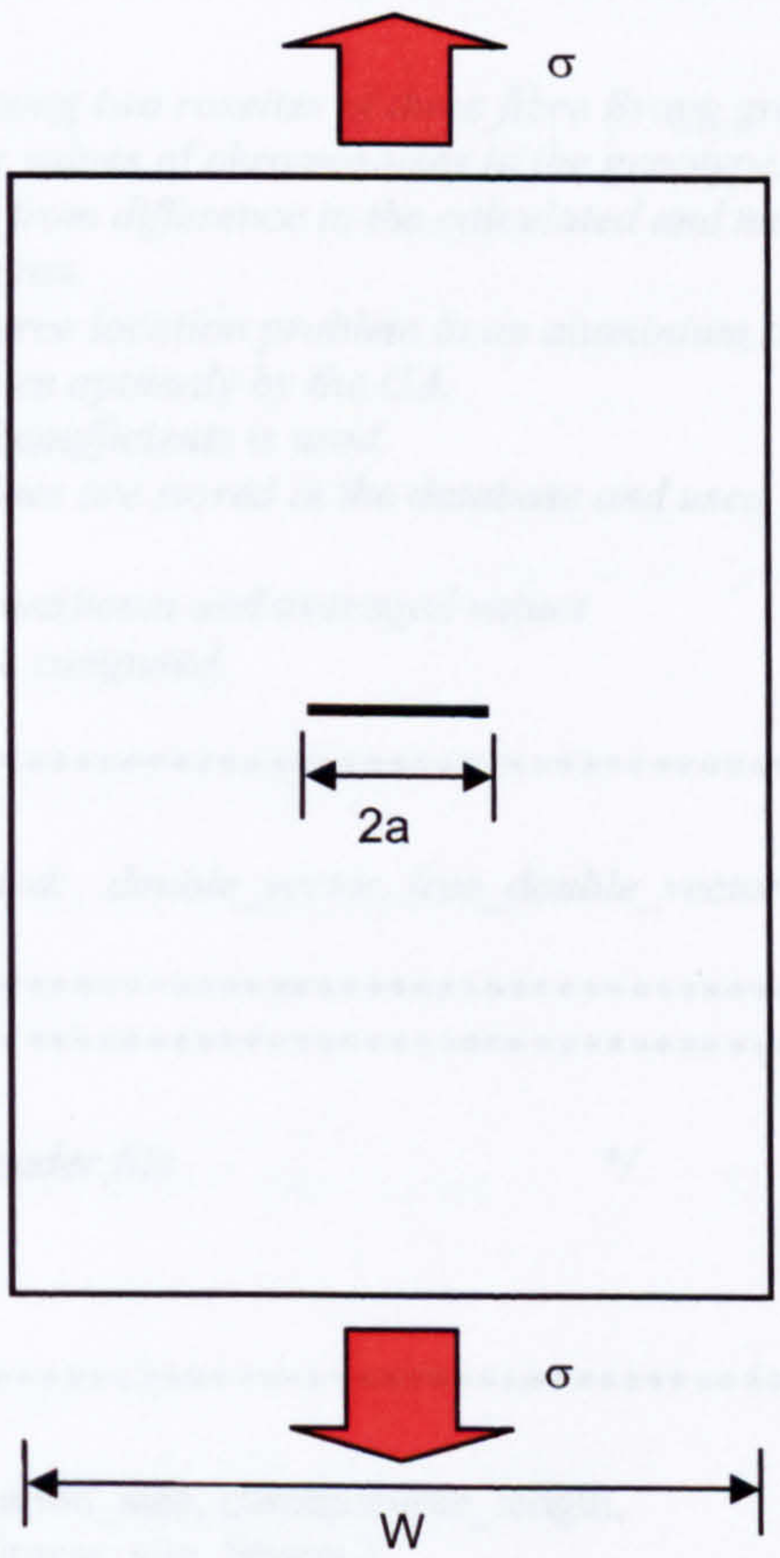

Figure G.1. Centre-cracked tension specimen.

The stress intensity factor for a centre crack length *2a* in a plate of width *W* which is subjected to remote tensile stress σ is

$$K = \sigma \sqrt{\pi a} \left(\sec \frac{\pi a}{W} \right)^{1/2} \qquad \text{(G.1)}$$

Appendix H: Source Code for Genetic Algorithm

```
*****************************************************************************

   For use in the location tests using two rosettes of three fibre Bragg gratings.
   This procedure returns fitness values of chromosomes in the genotype.
   The fitness values is obtained from difference in the calculated and measured
   amplitude of the grating response.
   The routine is used for the source location problem in an aluminium structure.
   - x and y coordinates are chosen optimaly by the GA.
   The integer coding of optimal coefficients is used.
   The phenotype and fitness values are stored in the database and used
   to save computation time.
   Finnaly, the total, minimum, maximum and averaged values
   of fitness in the population are computed.

*****************************************************************************

   Procedures and functions called:   double_vector, free_double_vector

*****************************************************************************
*****************************************************************************/

/*  Include genetic algorithm header file                    */

#include "header.h"

/*****************************************************************************/

void fitness( population, population_size, chromosome_length,
              min_fitness, max_fitness, ave_fitness )

 INDIVIDUAL   **population;      /* Array of pointers to individuals    */
 int          population_size;   /* Number of individuals per population */
 int          chromosome_length; /* Number of genes per chromosome      */
 double       *min_fitness;      /* Minimum fitness of the genotype     */
 double       *max_fitness;      /* Maximum fitness of the genotype     */
 double       *ave_fitness;      /* Averaged fitness of the genotype    */


 { /* Begin of procedure */

 char          system_command[256];   /* Character string used to execute compression
                                         software*/
 unsigned      *chromosome;           /* Chromosome from the population     */
 unsigned      *unsigned_vector();    /* Memory allocation routine          */
 unsigned      *free_unsigned_vector(); /* Memory deallocation routine      */
 int           angle11;               /* Source angle  Rosette1 Sensor1     */
 int           angle21;               /* Source angle  Rosette2 Sensor1     */
 int           angle12;               /* Source angle  Rosette1 Sensor2     */
 int           angle22;               /* Source angle  Rosette2 Sensor2     */
 int           angle13;               /* Source angle  Rosette1 Sensor3     */
 int           angle23;               /* Source angle  Rosette2 Sensor3     */
 int           sample;                /* Sample number */
 int           ind_counter;           /* Loop counter; individuals          */
```

```
int             gene_counter;           /* Loop counter: genes          */
float           s_dist;                 /* squared distance of calc. and meas. amplitude*/
float           x,y;                    /* Impact coordinates from the GA   */
float           m_ampl[20][6];          /* Measured amplitudes */
float           norm_ampl[20][6];       /* Normalized amplitudes*/
float           amplitude[370];         /* Fitted amplitudes from file      */
float           calc_ampl[6];           /* Calculated amplitudes*/
float           m1,m2;                  /* slope of the intersection lines*/
float           sum_ampl_1,sum_ampl_2;  /* sum of measured amplitudes/rosette*/
double          total_fitness;          /* Total fitness of the genotype    */
double          *double_vector();       /* Memory allocation routine        */
double          *free_double_vector()/**/;
FILE            *fp_input;              /* Pointer the "input.txt" file     */
FILE            *fp_file;               /* Pointer to the "generations" file  */

/* Allocate memory for chromosome vector                                    */

   chromosome = unsigned_vector( MAX_INTEGER );

/* Initialize total, minimum and maximum values of fitness                  */

  total_fitness = *max_fitness = 0.0;
  *min_fitness = 10000000.0;

/* Read calculated amplitudes for different angle values                    */

  sample = 4;

  fp_input = fopen( "ampl_360.dat", "r");
  for( gene_counter = 0; gene_counter <= 360; gene_counter++ )
  fscanf( fp_input, "%g\n", &amplitude[gene_counter] );
  fclose( fp_input );

/* Read measured amplitudes                                                 */

  fp_input = fopen( "m_ampl.dat", "r");
  for( gene_counter = 1; gene_counter <= 5; gene_counter++ )
  fscanf( fp_input, "%g %g %g %g %g %g \n", &m_ampl[gene_counter][1],
   &m_ampl[gene_counter][2], &m_ampl[gene_counter][3],
   &m_ampl[gene_counter][4], &m_ampl[gene_counter][5],
   &m_ampl[gene_counter][6]);
  fclose( fp_input );

/* Loop over chromosomes - begin                                            */

  for( ind_counter = 1; ind_counter <= population_size; ind_counter++ )
  {

/* Write to the "generation" file information about number of chromosomes  */
/* being produced                                                           */

   fp_file = fopen( "generations", "a");
   fprintf( fp_file, "     chromosome = %d\n", ind_counter );
   fclose( fp_file );
```

```
/*****************************************************************************/
/*  Extract the fitness value                                                */
/*****************************************************************************/

/*  Calculate possible angles from chromosomes                               */
/*  angle11 and angle21 are main angles, angle12 and angle22 derived         */

   angle11 = population[ind_counter]->chrom[1];

   if(angle11>360)
   angle11 = (int)((angle11 - 360)*(360.0/151.0));

   if (angle11 > 60)
   angle12 = angle11 - 60;
   else
   angle12 = angle11 + 300;

   if (angle11 > 120)
   angle13 = angle11 - 120;
   else
   angle13 = angle11 + 240;


   angle21 = population[ind_counter]->chrom[2];

   if(angle21>360)
   angle21 = (int)((angle21 - 360)*(360.0/151.0));

   if (angle21 > 60)
   angle22 = angle21 - 60;
   else
   angle22 = angle21 + 300;

   if (angle21 > 120)
   angle23 = angle21 - 120;
   else
   angle23 = angle21 + 240;

/*  normalize measured amplitudes          */

sum_ampl_1 = m_ampl[sample][1] + m_ampl[sample][2] +
m_ampl[sample][3];
norm_ampl[sample][1] = 1.5 *  m_ampl[sample][1] / sum_ampl_1;
norm_ampl[sample][2] = 1.5 *  m_ampl[sample][2] / sum_ampl_1;
norm_ampl[sample][3] = 1.5 *  m_ampl[sample][3] / sum_ampl_1;

   sum_ampl_2 = m_ampl[sample][4] + m_ampl[sample][5] +
        m_ampl[sample][6];

        norm_ampl[sample][4] = 1.5 *  m_ampl[sample][4] / sum_ampl_2;
   norm_ampl[sample][5] = 1.5 *  m_ampl[sample][5] / sum_ampl_2;
   norm_ampl[sample][6] = 1.5 *  m_ampl[sample][6] / sum_ampl_2;


/*  calculate amplitudes from angles       */
```

```
calc_ampl[1] = amplitude[angle11];
calc_ampl[2] = amplitude[angle12];
calc_ampl[3] = amplitude[angle13];
calc_ampl[4] = amplitude[angle21];
calc_ampl[5] = amplitude[angle22];
calc_ampl[6] = amplitude[angle23];

/*      calculate squared distance of calculated and measured amplitude
        needs to be a minimum for maximum fitness */
  s_dist  = pow( (double) (norm_ampl[sample][1] - calc_ampl[1]), 2.0 ) +
                          pow( (double) (norm_ampl[sample][2] - calc_ampl[2]), 2.0 ) +
                          pow( (double) (norm_ampl[sample][3] - calc_ampl[3]), 2.0 ) +
                          pow( (double) (norm_ampl[sample][4] - calc_ampl[4]), 2.0 ) +
                          pow( (double) (norm_ampl[sample][5] - calc_ampl[5]), 2.0 ) +
                          pow( (double) (norm_ampl[sample][6] - calc_ampl[6]), 2.0 );

/*      check for impossible solutions*/

        if (angle11 == angle21)
        s_dist =  10000000.0;


/*      calculate intersection of the two main angles angle11 and angle21          */
/*      lines have the form y1 = m1 * x and y2 = m2 * (x - 50), where x and y are given in centimeters,
        Origin (0,0) is at rosette 1 m1 = - tan(angle11), m2 = - tan (angle21)
        check where tangens function is infinite      */
        if (s_dist < 10000000.0)

        if (angle11 == 90  || angle11 == 270)          {
        x = 0.0;
        y = 50.0 * tan((double)((angle21 * M_PI)/180.0));
        }
        else if (angle21 == 90 || angle21 == 270) {
        x = 50.0;
        y = - 50.0 * tan((double)((angle11 * M_PI)/180.0));
        }
        else       {
        m1 = - tan((double)((angle11 * M_PI)/180.0));
        m2 = - tan((double)((angle21 * M_PI)/180.0));
        x = 50.0 * (m2 / (m2 - m1));
        y = m1 * x;
        }

        if  (s_dist == 10000000.0)   {
            x = 0.0;
            y = 0.0;
            }

/*  this  can never be a solution, so any output (0,0) indicates an error in the conditions   */


   if(s_dist == 0.0)
```

```
    s_dist = 10000000.0;

    population[ind_counter]->fitness = 1.0 / s_dist;

/*  Estimate minimum and maximum fitness values                    */

    if( population[ind_counter]->fitness > *max_fitness )
    {
     *max_fitness = population[ind_counter]->fitness;
     fp_input = fopen( "cor_ga.dat", "w");
     fprintf( fp_input, "%g %g\n", x, y );       /* changed here !*/
     fprintf( fp_input, "%d %d\n", angle11, angle12 );
     fprintf( fp_input, "%d %d\n", angle21, angle22 );
     fclose( fp_input );
    }

    if( population[ind_counter]->fitness < *min_fitness )
    *min_fitness = population[ind_counter]->fitness;

/*  Take the next chromosome from the population                   */
/*  Loop over chromosomes - end                                    */

   }

/*  Estimate averaged fitness value                                */

   for( ind_counter = 1; ind_counter <= population_size; ind_counter++ )
   total_fitness += population[ind_counter]->fitness;

    *ave_fitness = total_fitness / (float) population_size;

/*  Deallocate memory for vector chromosome                        */

   free_unsigned_vector( chromosome );

  } /*  End of procedure */

/************************************ End ************************************/
```

Appendix I:Additional Results for Temperature Analysis

Original Waveform and Envelope (see Chapter 7.4)

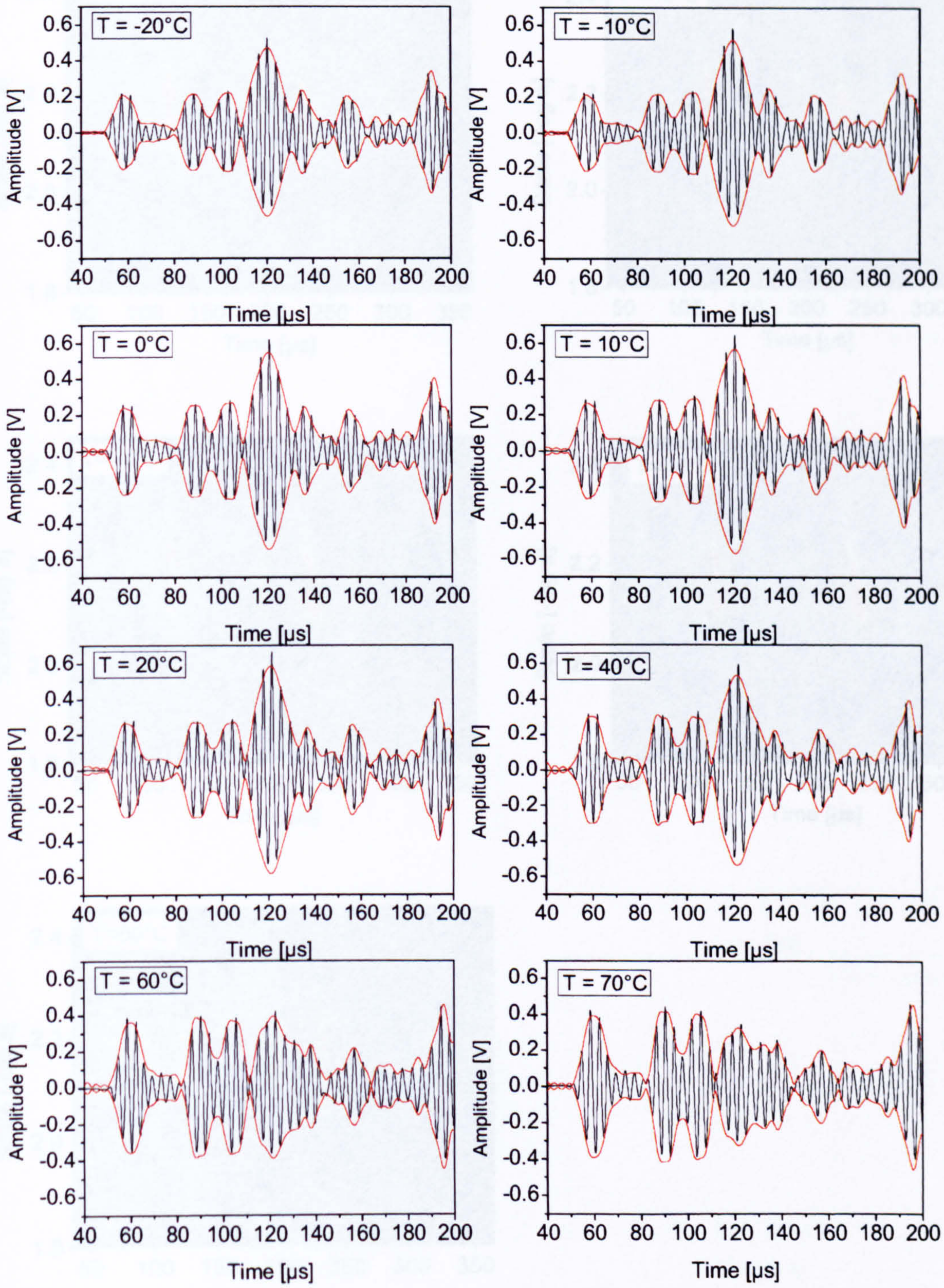

Figure I.2.: Series of Lamb wave signals at different temperatures.

Continuous wavelet transform

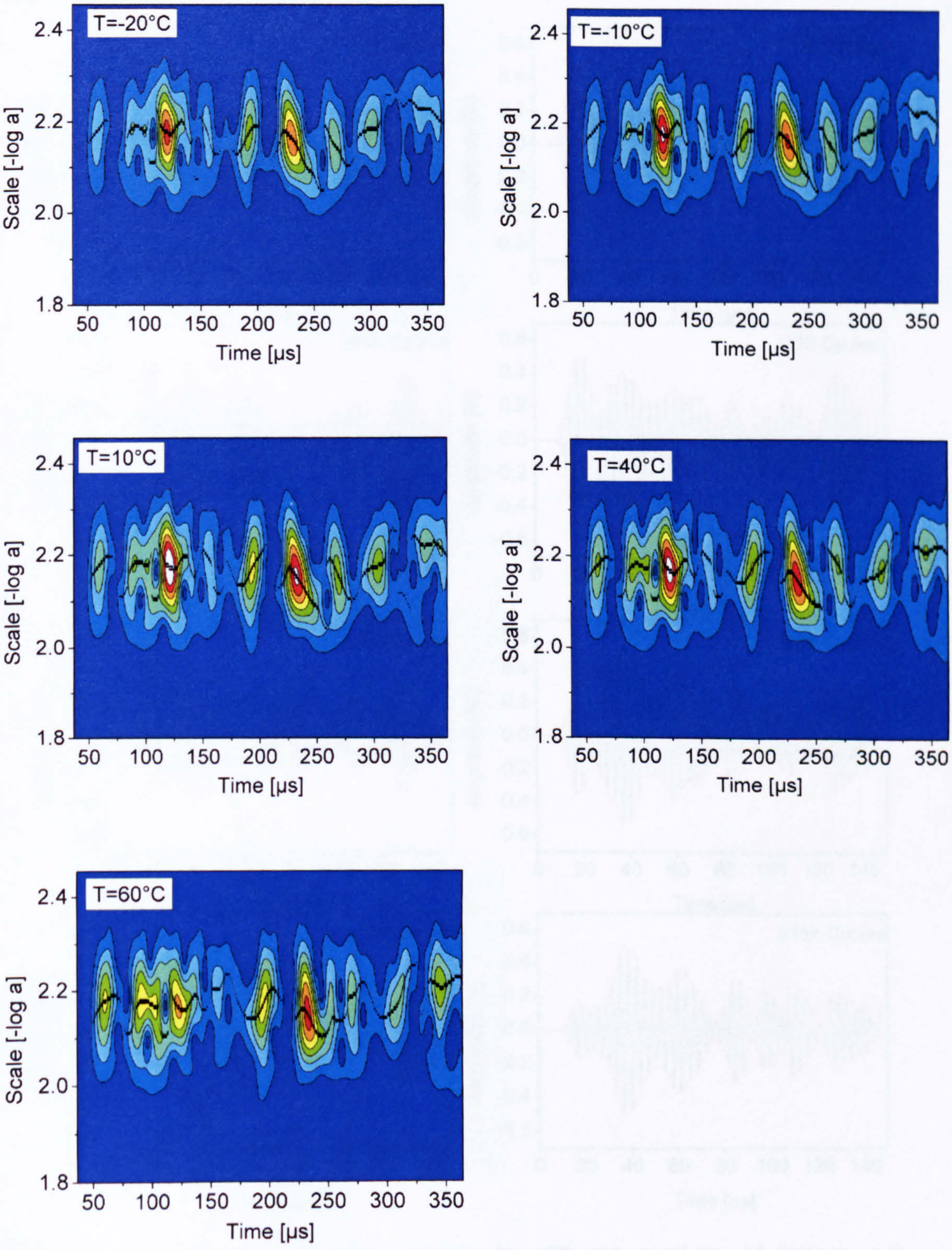

Figure I.3.: Series of CWT at different temperatures.

Appendix J: Additional Results for Fatigue Analysis Specimen 2

Original signal and envelope for FBG sensor (see Chapter 8.4)

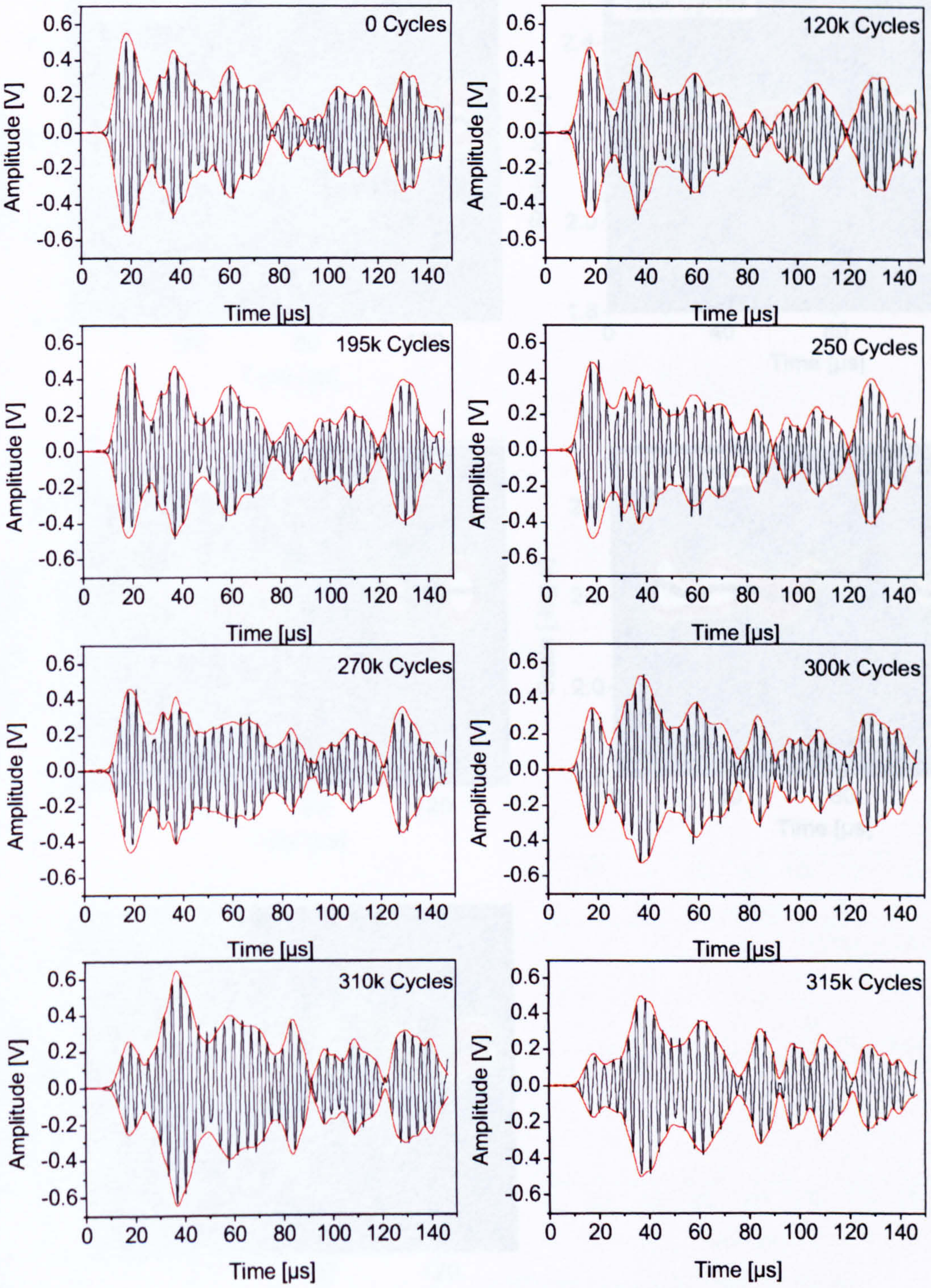

Figure J.4.: Series of Lamb wave signals for different numbers of fatigue cycles.

Continuous wavelet transform for FBG sensor

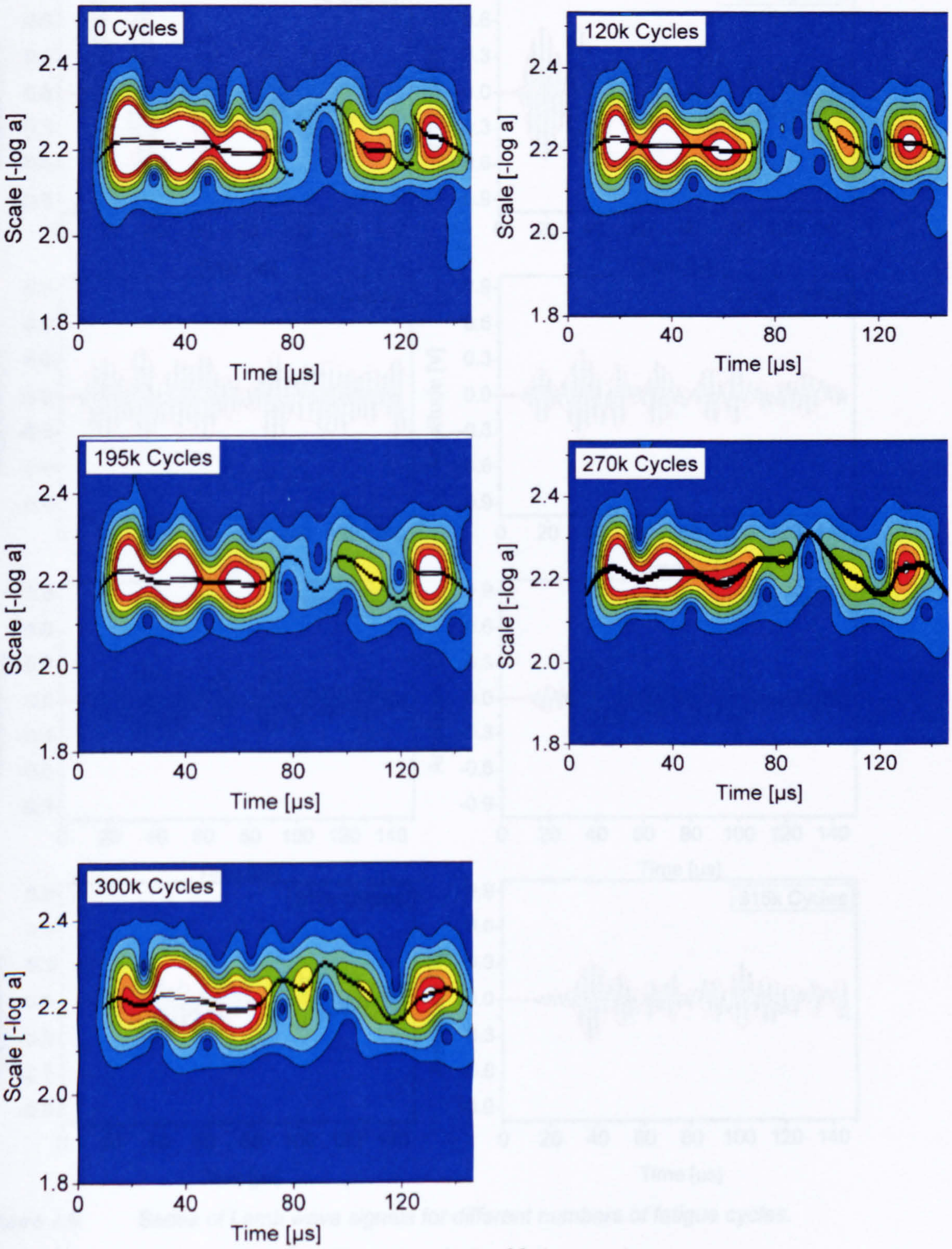

Figure J.5.: Series of CWT for different numbers of fatigue cycles.

Original signal and envelope for PZT transducer

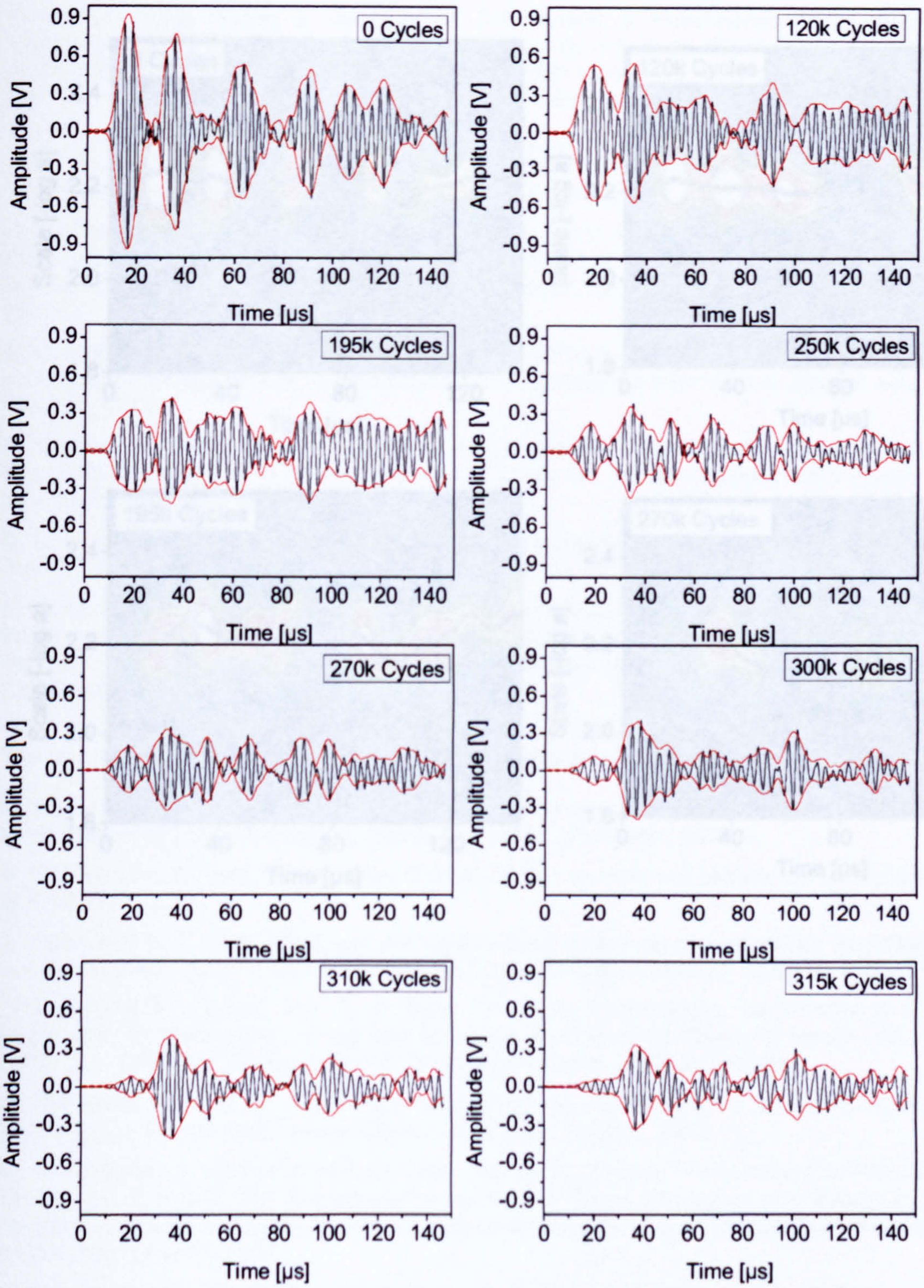

Figure J.6. Series of Lamb wave signals for different numbers of fatigue cycles.

Continuous wavelet transform for PZT transducer

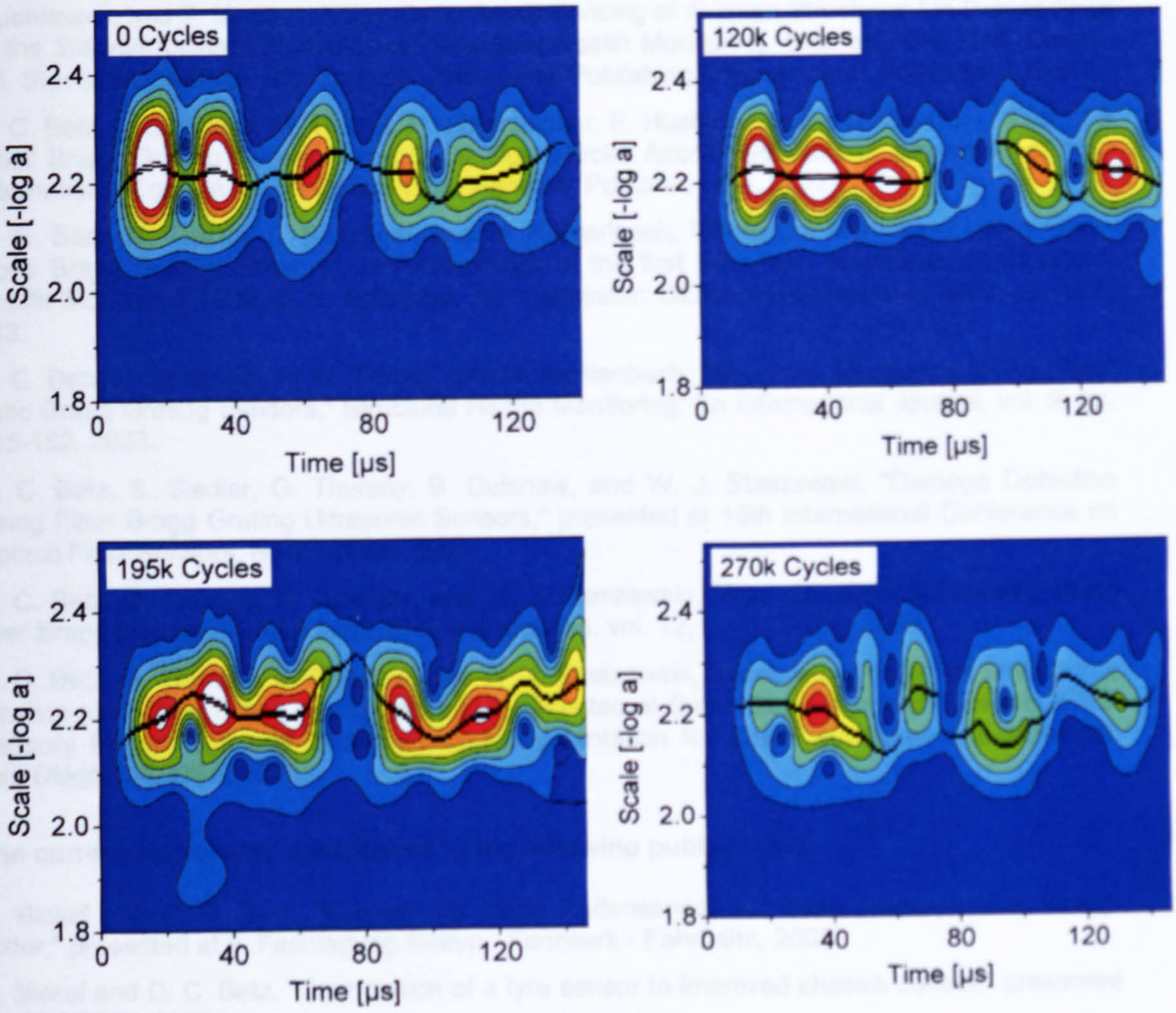

Figure J.7.: Series of CWT for different numbers of fatigue cycles.

Appendix K: Publications list

D. C. Betz, M. N. Trutzel, L. Staudigel, M. Schmuecker, E. Huelsmann, U. Czernay, H. C. Muehlmann, and T. Muellert, "Fiber-Optic Smart Sensing of Aviation Structures." in Proceedings of the 3rd International Workshop on Structural Health Monitoring, Stanford, CA, F.-K. Chang, Ed. Stanford University, Stanford, CA: Technomic Publishing Company Inc., 2001, pp. 306-315.

D. C. Betz, L. Staudigel, M. Trutzel, M. Schmuecker, E. Huelsmann, and U. Czernay, "Test of a Fiber Bragg Grating Sensor Network for Commercial Aircraft Structures," presented at 15th International Conference on Optical Fiber Sensors, Portland, USA, 2002.

D. C. Betz, M. Trutzel, L. Staudigel, and M. Kehlenbach, "Structural Monitoring Using Fiber-Optic Bragg Grating Sensors", in Proceedings of the first European Workshop on Structural Health Monitoring 2002, D. L. Balageas, Ed. Lancaster: DEStech Publications, 2002, pp. 837-843.

D. C. Betz, L. Staudigel, M. N. Trutzel, and M. Kehlenbach, "Structural Monitoring Using Fiber-optic Bragg Grating Sensors," Structural Health Monitoring: An International Journal, vol. 2, pp. 145-152, 2003.

D. C. Betz, S. Siedler, G. Thursby, B. Culshaw, and W. J. Staszewski, "Damage Detection Using Fiber Bragg Grating Ultrasonic Sensors," presented at 16th International Conference on Optical Fiber Sensors, Nara, Japan, 2003.

D. C. Betz, G. Thursby, B. Culshaw, and W. J. Staszewski, "Acousto-ultrasonic sensing using fiber Bragg gratings," Smart Material and Structures, vol. 12, pp. 122-128, 2003.

D. C. Betz, G. Thursby, B. Culshaw, and W. J. Staszewski, "Lamb wave detection and source location using fiber Bragg grating rosettes," presented at Smart Structures and Materials 2003: Sensory Phenomena and Measurement Instrumentation for Smart Structures and Materials, San Diego, CA, USA, 2003.

The current author also contributed to the following publications

B. Bickel and D. C. Betz, "Konzept für einen Reifensensor auf Basis faseroptischer Bragg-Gitter," presented at 9. Fachtagung Reifen - Fahrwerk - Fahrbahn, 2003.

B. Bickel and D. C. Betz, "Contribution of a tyre sensor to improved chassis control," presented at IFAC 2003, 2003.

C. Boller and D. C. Betz, "Beispiele der sensorischen Erfassung und adaptiven Beeinflussung von Betriebsbeanspruchungen in Fluggeräten," presented at DVM 2003, Stuttgart, 2003.

C. Boller, M. N. Trutzel, and D. C. Betz, "Emerging Technologies for Monitoring Aircraft Structures", in Proceedings of the first European Workshop on Structural Health Monitoring 2002, D. L. Balageas, Ed. Lancaster: DEStech Publications, 2002, pp. 809-816.

M. Kehlenbach and D. C. Betz, "Fiber-optic Bragg grating sensors for strain measurements inside composite materials," presented at ECCM 2002, Belgium, 2002.

M. Kehlenbach, A. Horoschenkoff, D. Betz, and M. N. Trutzel, "Performance of Fiber-Bragg Grating Sensors in CFRP Structures.," presented at Smart Structures and Materials 2001: Sensory Phenomena and Measurement Instrumentation for Smart Structures and Materials, Proceedings of SPIE, 2001.

B. Sorazu, G. Thursby, B. Culshaw, F. Dong, S. G. Pierce, Y. Yang, and D. C. Betz, "Optical Generation and Detection of Ultrasound," Strain, vol. 39, pp. 111-114, 2003.

G. Thursby, F. Dong, Y. Yong, B. Sorazu, D. C. Betz, and B. Culshaw, "Fiber Optic Polarimetric Detection of Lamb Waves," presented at OFS 2002, 15th International Conference on Optical Fiber Sensors, Portland, Oregon, USA, 2002.

G. Thursby, B. Sorazu, F. Dong, D. C. Betz, and B. Culshaw, "Damage Detection in Structural Materials using a Polarimetric Fibre Optic Sensor," presented at Smart Structures and Materials 2003: Sensory Phenomena and Measurement Instrumentation for Smart Structures and Materials, San Diego, CA, USA, 2003.